



HAL
open science

Rational functionalization of molecular magnetic materials: towards liquid crystalline phases, improved solubility and modulation of physical properties

Dmitri Mitcov

► **To cite this version:**

Dmitri Mitcov. Rational functionalization of molecular magnetic materials: towards liquid crystalline phases, improved solubility and modulation of physical properties. Other. Université de Bordeaux, 2014. English. NNT: 2014BORD0029 . tel-02126844

HAL Id: tel-02126844

<https://theses.hal.science/tel-02126844>

Submitted on 13 May 2019

HAL is a multi-disciplinary open access archive for the deposit and dissemination of scientific research documents, whether they are published or not. The documents may come from teaching and research institutions in France or abroad, or from public or private research centers.

L'archive ouverte pluridisciplinaire **HAL**, est destinée au dépôt et à la diffusion de documents scientifiques de niveau recherche, publiés ou non, émanant des établissements d'enseignement et de recherche français ou étrangers, des laboratoires publics ou privés.

THÈSE

présentée pour obtenir le grade de

DOCTEUR DE

L'UNIVERSITÉ DE BORDEAUX

École doctorale des sciences chimiques

SPÉCIALITÉ : Physico-Chimie de la Matière Condensée

par Dmitri Mitcov

**Fonctionnalisation raisonnée de matériaux moléculaires
magnétiques: vers des systèmes cristaux liquides, solubles, et
aux propriétés physiques modulables**

Sous la direction de : Rodolphe Clérac

Soutenue le 30 Avril 2014

Membres du jury :

M. Talal Mallah
M. Jaume Veciana

Professeur, Université Paris-Sud 11
Professeur, Institut de Ciència
de Materials de Barcelona

Rapporteur
Rapporteur

M. Rodolphe Clérac
M. Philippe Barois
M. Franck Camerel
M. Philippe Richetti

Directeur de recherche, CNRS
Directeur de recherche, CNRS
Chargé de Recherche, CNRS
Directeur de recherche, CNRS

Directeur de thèse
Examineur
Examineur
Examineur

There is one very important thing I learned after three and a half years of my doctoral studies – none would have been possible without the participation, support and encouragement from many people. The list of people, who assisted, supported and guided me over the past years and helped me to arrive where I am today, is very long and I wish to thank everybody who was involved in the development of this work.

*First of all, I would like to thank **Philippe Richetti** for welcoming me at the Centre of Research Paul Pascal and participating in my thesis defense jury. I thank **Prof. Talal Mallah** and **Prof. Jaume Veciana** for their time and consideration to review this thesis; **Dr. Franck Camerel** and **Dr. Philippe Barois** for their participation in the thesis defense jury. Thank you all for dedicating your time to assess my manuscript.*

*I am deeply grateful to my supervisor, **Rodolphe Clérac**, for having introduced me into an interesting research field, molecule-based magnetic materials. I thank him for the guidance, and encouragement, which he provided through this work. His constructive criticism and collaboration have been great assets throughout my PhD. I benefited from his creativity and his intuition in various situations. He has provided guidance at key moments in my work while allowing me to work independently. Thank you, **Rodolphe**, for setting up the model of a real scientist, and for your patience during the last period of my PhD.*

*I wish to dedicate special thanks to **Diana Sîrețanu Codreanu** for her help during my first year of PhD at CRPP and University of Bordeaux. She not only helped me to get acquainted with various experimental and analytical techniques at CRPP but also she was the person who guided me in the unknown world of “thousands” of documents and administrative centers that we should pass before and after becoming a PhD student.*

*I would like to thank **Corine Mathonière** who is always ready for help. Her collaboration and high pedagogical skills were very precious during all my PhD. I thank **Pierre Dechambenoit**, who arrived in the group same time with me and became fully involved in our projects. He was the person who helped to figure out the problems with single crystal diffraction experiments.*

*Most of the wonderful results obtained in this thesis were obtained as the result of collaborations with many other people. Therefore I would like to thank: (i) **Dario Bassani**, who allowed me to carry out the temperature dependent “change of colour” observations on his UV-Vis spectrometer; (ii) **Eric Collet**, **Loïc Toupet** and **Wawrzyniec Kaszub** for the photo-crystallography and ultrafast optical measurements; and (iii) **Marie-Anne Arrio**, **Philippe Saintavit**, **Edwige Otero**, **Andrei Rogalev** and **Fabrice Wilhelm** for introducing me to the synchrotron research and XMCD measurements.*

*Even if the often group and sub-group meetings are sometimes exhausting, they have their advantage in stimulating people to be hard workers and to attempt to do their best for Science. The “after” group meeting has more benefits. Therefore I would like to thank **Elizabeth Hillard** for the organization of group-*

and “after” group meetings. Thank to **Claude Coulon**, who besides Heisenberg, Ising and other Hamiltonians, taught us how a good wine should be.

Thank you to all who have passed more or less long time in the group and contributed to the development of this warm and welcoming atmosphere at work. I would like to thank **Harald Bock** and **Fabien Durola** for the fruitful discussions we had. Thanks to our postdocs **Céline Pichon**, **Daniel N. Woodruff**, **David Aguila**, **Yunnan Guo**, **Yoann Prado** and **Daniel Rosario Amorin**. I thank my dear colleagues and friends **Rodica Ababei**, **Oleg Palamarciuc**, **Ie-Rang Jeon**, **Indrani Bhowmick**, **Kasper Steen Pedersen**, **Evangelia Koumoussi**, **Vivien Pianet** and **Mihail Secu** for sharing good time in the laboratory and outside.

I express thanks to all people from CRPP. I am grateful to **Corine Amengual** who was always ready to help. I would like to thank **Nadine Laffargue** for her kindness and efficient help for my bibliographic work. I thank **Marie-France Achard**, **Ahmed Bentaleb**, **Alain Derré**, **Gilles Sigaud**, **Beatrice Agricole**, and all CRPP services: “service informatique, mission, gestion, accueil et bâtiment, cellule chimie et instrumentation, atelier mécanique”. Your help makes our ideas come true.

This work would not have been possible without the support of my friends I met here in Bordeaux. My deepest gratitude to **Rodica** and **Igor Ababei**, **Simona Ungureanu**, **Renaud Vallée**, **Oleg** and **Tatiana Palamarciuc**, **Octavian Blaj**, and **Amandine Foulet**. You were always around for my nice or bad moments in Bordeaux. I could always count on you, when I needed help in my research or simple moral support, but also for spending great time together. This, I believe, is the key to getting through a PhD program – having good friends to have fun with and complain to.

Finally, my heartiest thanks are dedicated to my family. I thank to my loving, supportive, encouraging, and patient wife, **Liuba**. We performed our PhD work in the same time; nevertheless she always found time to support me, especially during the final stages. Thank to my parents: my father **Vladimir**, my mother **Natalia**, my sister **Inga** and my grandparents **Vladimir** and **Valentina**. Without their eternal support and love from childhood until now, I would never have made it through this process or any of the hard times in my life. Thank to my parents in law (**Raisa** and **Petru**) which were always confident about my success.

Thank you all – Merci à tous – Mulțumesc tuturor

Dmitri Mitcov
Pessac, May 2014

TABLE OF CONTENTS

General Introduction	1
Chapter I – Generalities and Context	I.5
I.1. Molecule-based magnetic materials	I.7
I.1.1. Single-Molecule Magnets	I.8
I.1.1.1. Generalities	I.8
I.1.1.2. Theoretical aspects of SMMs illustrated by the Mn ₁₂ example	I.8
I.1.1.2.1. SMM properties in the absence of external field	I.9
I.1.1.2.2. SMM properties in a longitudinal magnetic field	I.11
I.1.1.2.3. Magnetization relaxation	I.11
I.1.1.2.4. Quantum tunneling of the magnetization	I.14
I.1.2. Electron transfer complexes	I.15
I.1.2.1. Generalities	I.15
I.1.2.2. Thermally and/or photo-induced ET in cyanido-bridged systems	I.16
I.1.2.3. Theoretical background	I.21
I.2. Soft hybrid molecule-based magnetic systems	I.25
I.2.1. Liquid crystalline magnetic molecular hybrids	I.25
I.2.1.1. Liquid crystalline phases – generalities	I.26
I.2.1.2. Magnetic molecule-based mesogens	I.29
I.2.2. Other soft magnetic systems	I.34
I.3. Objectives of this research work	I.36
I.4. References	I.37
Chapter II – Functionalization of Single-Molecule Magnets: Towards Liquid Crystalline Phases	II.43
II.1. Introduction	II.45
II.2. Mn ₁₂ -based SMMs: Versatile target for functionalization	II.46
II.2.1. Why Mn ₁₂ ?	II.46
II.2.2. Structure of Mn ₁₂ -based complexes	II.46
II.2.3. Chemistry of Mn ₁₂ -based complexes	II.48
II.3. Functionalization strategies towards liquid crystalline SMMs	II.50
II.4. Functionalization of Mn ₁₂ -based SMMs with strongly lipophilic groups	II.52
II.4.1. Synthetic procedures and purification	II.52
II.4.2. Analytical characterizations of substituted Mn ₁₂ complexes	II.53
II.4.2.1. Single crystal X-ray analysis of the model compound [Mn ₁₂ O ₁₂ (L ₁) ₁₆ (H ₂ O) ₃]	II.53
II.4.2.2. FT-IR spectroscopic analyses	II.55
II.4.2.3. ¹ H NMR spectroscopic analyses	II.56
II.4.2.4. Elemental and thermo-gravimetric analyses	II.56
II.4.3. Magnetic measurements	II.57
II.4.4. Thermotropic properties	II.61
II.4.4.1. [Mn ₁₂ O ₁₂ (L ²) ₁₆ (H ₂ O) ₄]	II.62
II.4.4.2. [Mn ₁₂ O ₁₂ (L ³) ₁₆ (H ₂ O) ₄]	II.63
II.4.4.3. [Mn ₁₂ O ₁₂ (L ⁴) ₁₆ (H ₂ O) ₄]	II.64
II.4.5. Description of the molecular packing inside the mesophase	II.67
II.4.6. Summary of section II.4	II.70
II.5. Functionalization of Mn ₁₂ -based SMMs by grafting a mesomorphic promoter through a flexible spacer	II.71
II.5.1. Synthetic procedures and purification	II.71
II.5.2. Analytical characterization of functionalized Mn ₁₂ complexes	II.72
II.5.2.1. FT-IR spectroscopic analyses	II.72
II.5.2.2. ¹ H NMR spectroscopic analyses	II.72

II.5.2.3. Elemental and thermo-gravimetric analyses.....	II.73
II.5.3. Magnetic measurements.....	II.74
II.5.4. Thermotropic properties.....	II.76
II.5.4.1. DSC and temperature dependent POM investigations.....	II.76
II.5.4.2. Small angle X-ray scattering (SAXS) investigations.....	II.78
II.5.5. Summary of section II.5.....	II.81
II.6. Conclusions and perspectives.....	II.81
II.7. Supporting materials.....	II.84
II.7.1. Experimental protocols.....	II.84
II.7.2. Analytical characterizations.....	II.88
II.7.2.1. Crystallographic data for $[\text{Mn}_{12}\text{O}_{12}(\text{L}^1)_{16}(\text{H}_2\text{O})_3]$	II.88
II.7.2.2. FT-IR spectroscopic analyses.....	II.90
II.7.2.3. Thermo-gravimetric analyses.....	II.94
II.7.3. Magnetic measurements.....	II.94
II.7.4. Thermotropic properties.....	II.96
II.7.4.1. DSC traces.....	II.96
II.7.4.2. Small angle X-ray scattering (SAXS) investigations.....	II.96
II.8. References.....	II.106
Chapter III – Modulating the Structural and Electron Transfer Properties of Molecular $\{\text{Fe}_2\text{Co}_2\}$ Squares in Solid State via Anion Exchange or Light Irradiation	III.109
III.1. Introduction.....	III.111
III.2. Synthesis and characterizations of molecular $\{\text{Fe}_2\text{Co}_2\}$ squares.....	III.113
III.2.1. Synthetic strategy.....	III.113
III.2.2. FT-IR spectroscopic analyses.....	III.114
III.2.3. Structural investigations of molecular $\{\text{Fe}_2\text{Co}_2\}$ squares.....	III.114
III.2.3.1. $\{[(\text{Tp}^*)\text{Fe}(\text{CN})_3]_2[\text{Co}(\text{bpy})_2]_2\}[\text{OTf}]_2 \cdot 3\text{H}_2\text{O} \cdot 3\text{DMF}$ (1).....	III.114
III.2.3.2. $\{[(\text{Tp}^*)\text{Fe}(\text{CN})_3]_2[\text{Co}(\text{diMebpy})_2]_2\}(\text{OTf})_2 \cdot \text{H}_2\text{O} \cdot 2\text{DMF}$ (2).....	III.118
III.2.3.3. $\{[(\text{Tp}^*)\text{Fe}(\text{CN})_3]_2[\text{Co}(\text{diMebpy})_2]_2\}(\text{ClO}_4)_2 \cdot 2\text{DMF}$ (3).....	III.122
III.2.3.4. $\{[(\text{Tp}^*)\text{Fe}(\text{CN})_3]_2[\text{Co}(\text{diMebpy})_2]_2\}(\text{OTs})_2 \cdot 6\text{DMF}$ (4).....	III.124
III.2.3.5. Structural comparison of compounds 2 , 3 and 4	III.125
III.2.4. Optical reflectivity studies.....	III.127
III.2.5. Magnetic measurements.....	III.128
III.3. Conclusions and perspectives.....	III.129
III.4. Supporting materials.....	III.131
III.4.1. Experimental protocols.....	III.131
III.4.2. FT-IR spectroscopic analyses.....	III.132
III.4.3. Crystallographic data for 1 , 2 , 3 and 4	III.134
III.4.4. Magnetic measurements.....	III.138
III.5. References.....	III.139
Chapter IV – Revealing and Tuning the Electron Transfer Properties by Solubilization of Functionalized Molecular Squares	IV.141
IV.1. Introduction.....	IV.143
IV.2. Synthesis and characterizations of functionalized molecular $\{\text{Fe}_2\text{Co}_2\}$ squares in solid state.....	IV.144
IV.2.1. Synthetic procedures and FT-IR characterizations.....	IV.144
IV.2.2. Structural investigations of functionalized molecular $\{\text{Fe}_2\text{Co}_2\}$ squares.....	IV.145
IV.2.2.1. $\{[(\text{Tp}^*)\text{Fe}(\text{CN})_3]_2[\text{Co}(\text{diC6bpy})_2]_2\}[\text{OTf}]_2 \cdot 2\text{DMF}$ (5).....	IV.146
IV.2.2.2. $\{[(\text{Tp}^*)\text{Fe}(\text{CN})_3]_2[\text{Co}(\text{diC13bpy})_2]_2\}[\text{OTf}]_2 \cdot \text{H}_2\text{O} \cdot 3\text{CH}_3\text{OH}$ (6).....	IV.148
IV.2.3. Reflectivity studies.....	IV.150
IV.2.4. Magnetic measurements.....	IV.151
IV.3. Analytical characterizations of functionalized molecular $\{\text{Fe}_2\text{Co}_2\}$ squares in diluted solutions.....	IV.152
IV.3.1. UV-Vis spectroscopic characterizations 5 and 6 in diluted solutions.....	IV.153

IV.3.2. Magnetic properties of 5 and 6 in solutions.....	IV.155
IV.4. Conclusions and perspectives.....	IV.158
IV.5. Supporting materials.....	IV.160
IV.5.1. Experimental protocols.....	IV.160
IV.5.2. Crystallographic data for 5 and 6	IV.161
IV.5.3. UV-Vis studies in diluted solutions of 5 and 6	IV.163
IV.5.4. Magnetic measurements in solid state.....	IV.165
IV.5.5. Magnetic measurements in solutions.....	IV.166
IV.6. References.....	IV.168
Chapter V – Functionalization of Molecular {Fe₂Co₂} Squares with Strongly Donating Methoxy Group: Electron Transfer Properties in Solid State and Solutions.....	V.169
V.1. Introduction.....	V.171
V.2. Synthesis and characterizations of functionalized molecular {Fe ₂ Co ₂ } squares in solid state.....	V.171
V.2.1. Synthetic procedures and FT-IR characterizations.....	V.171
V.2.2. Structural investigations.....	V.173
V.2.2.1. {[Tp*]Fe(CN) ₃] ₂ [Co(diMeObpy) ₂] ₂ } (OTf) ₂ ·4DMF (7).....	V.173
V.2.2.2. {[Tp*]Fe(CN) ₃] ₂ [Co(diMeObpy) ₂] ₂ } (PF ₆) ₂ ·2H ₂ O·5MeCN (8a).....	V.175
V.2.2.3. {[Tp*]Fe(CN) ₃] ₂ [Co(diMeObpy) ₂] ₂ } (PF ₆) ₂ ·6MeCN (8b).....	V.177
V.2.3. Optical reflectivity studies.....	V.179
V.2.3.1. Reflectivity measurements for compound 7	V.179
V.2.3.2. Reflectivity measurements for compound 8a	V.179
V.2.3.3. Reflectivity measurements for compound 8b	V.182
V.2.4. Photo-crystallographic investigations of compound 8a	V.185
V.2.5. Magnetic measurements.....	V.188
V.2.5.1. Magnetic properties of 7	V.188
V.2.5.2. Magnetic and photo-magnetic properties of 8a	V.189
V.2.5.3. Magnetic and photo-magnetic properties of 8b	V.190
V.3. Analytical characterizations of the methoxy functionalized molecular {Fe ₂ Co ₂ } squares in diluted solutions.....	V.192
V.3.1. UV-Vis spectroscopic characterizations of 7 and 8 in diluted solutions.....	V.193
V.3.2. Magnetic properties of 7 and 8 in solutions.....	V.195
V.4. Conclusions and perspectives.....	V.197
V.5. Preliminary XAS and XMCD investigations.....	V.200
V.6. Supporting materials.....	V.205
V.6.1. Experimental protocols.....	V.205
V.6.2. Crystallographic data for 7 , 8a and 8b	V.206
V.6.3. Optical reflectivity studies.....	V.210
V.6.4. Magnetic properties in solid state.....	V.212
V.6.5. UV-Vis spectroscopic characterizations in diluted solutions.....	V.212
V.6.6. Magnetic measurements in solutions.....	V.213
V.6.7. XAS and XMCD measurements.....	V.213
V.7. References.....	V.215
General Conclusions.....	217
Annex.....	221
Résumé.....	229

General Introduction

In the tremendously growing field of material science, molecular materials present a relatively recent and emerging interest, caused by a very rapid development of modern technology that requires better performance from existing materials. Molecule-based systems show synthetic advantages over traditional materials since they use well designed precursors with a controlled geometry and do not require energy-intensive production methods. The rational choice of the building-blocks allows an efficient control of the final structural dimensionality of the molecule-based materials and thus their related physical properties. Systems built from molecular units, that are assembled and designed to afford interesting and, sometimes, premeditated magnetic properties, give rise to the field of molecule-based magnetic materials.

Magnetic molecules are a class of fascinating materials. They contain a finite number of spin centers (e.g. paramagnetic ions) and thus provide ideal opportunities to study basic concepts of physics and magnetism. Scientists from various fields, in chemistry and physics, theoreticians and experimentalists have joined the research field on molecular magnetism in order to explore the unprecedented properties of these compounds. Molecular magnetic materials such as single-molecule magnets (SMMs), spin crossover (SC) or electron transfer (ET) complexes show tunable magnetic and/or optical properties as a function of different external stimuli (magnetic field, light, temperature or pressure). That is why these systems are promising for application in numerous areas such as information processing, high-density recording media, molecular switches, sensors and display devices.

Even though the magnetic properties are the main motivations in this field of research, building multi-functionality in a molecular magnetic material is a hot focus of research, as well. In this respect, molecular chemistry provides unique possibilities, as it allows us to design novel hybrid materials that combine in the same system several physical properties which are difficult or impossible to achieve with inorganic or solid state chemistry. In order to get hybrid magnetic materials with advanced properties, the functionalization of the organic part of interesting molecule-based magnetic materials by groups known to induce additional physical properties (liquid crystalline phases or increased solubility) is a strategy of choice as it may lead to a multifunctional behavior and/or synergetic effects.

One of the main research interests in the “Molecular Materials and Magnetism” (M^3) group at the Centre de Recherche Paul Pascal (CRPP) is the functionalization of the molecular magnetic materials towards hybrid systems possessing liquid crystalline properties and/or increased solubility. During her PhD thesis (2004-2007), Pauline Grondin developed the idea of grafting linear long alkyl chains onto triazole ligands, in order to obtain new $[\text{Fe}^{\text{II}}(\text{R-trz})_3]\text{A}_2$ compounds (where R-trz is a functionalized triazole ligand and A is a counter-anion) that showed, in addition to spin crossover, liquid crystalline properties and/or the ability to gelate various solvents. Following the same aims, the thesis work of Diana Siretanu (2008-2011) was dedicated to functionalization of Mn_{12} -based SMMs, various Fe^{II} -based SC systems and cyanido-bridged $\{\text{Fe}_2\text{Co}_2\}$ electron-transfer complexes.

To continue the foregoing works, in this thesis we are focused on further functionalization of molecule-based magnetic materials such as Mn_{12} -based SMMs and cyanido-bridged $\{\text{Fe}_2\text{Co}_2\}$ molecular squares. In the first chapter of this thesis the reader can find general information about the two classes of

magnetic complexes (single-molecule magnets and electron transfer systems) chosen for functionalization, followed by several examples of already reported hybrid magnetic materials. In the second chapter, two strategies of rational ligand functionalization of single-molecule magnets towards liquid crystalline phases are discussed. The other three chapters (Chapter III, IV and V) of this thesis are focused on cyanido-bridged $\{\text{Fe}_2\text{Co}_2\}$ molecular squares and the influence of various functionalizations, counter-anions and solvation (inside the crystal lattice) on the occurrence of the thermally and/or photo-induced electron transfer in solid state and/or in solutions. At the end of each chapter a “conclusion and perspectives” section is introduced with the aim to present a summarized overview of the obtained results and to help the reader to understand some of the problems we faced during the presented research work. Finally, a general conclusion to this work and some future perspectives to enrich the area of hybrid molecule-based materials are provided.

Chapter I

Generalities and Context

Table of Contents for Chapter I:

I.1. Molecule-based magnetic materials.....	I.7
I.1.1. Single-Molecule Magnets.....	I.8
I.1.1.1. Generalities.....	I.8
I.1.1.2. Theoretical aspects of SMMs illustrated by the Mn ₁₂ example.....	I.8
I.1.1.2.1. SMM properties in the absence of external field.....	I.9
I.1.1.2.2. SMM properties in a longitudinal magnetic field.....	I.11
I.1.1.2.3. Magnetization relaxation.....	I.11
I.1.1.2.4. Quantum tunneling of the magnetization.....	I.14
I.1.2. Electron transfer complexes.....	I.15
I.1.2.1. Generalities.....	I.15
I.1.2.2. Thermally and/or photo-induced ET in cyanido-bridged systems.....	I.16
I.1.2.3. Theoretical background.....	I.21
I.2. Soft hybrid molecule-based magnetic systems.....	I.25
I.2.1. Liquid crystalline magnetic molecular hybrids.....	I.25
I.2.1.1. Liquid crystalline phases – generalities.....	I.26
I.2.1.2. Magnetic molecule-based mesogens.....	I.29
I.2.2. Other soft magnetic systems.....	I.34
I.3. Objectives of this research work.....	I.36
I.4. References.....	I.37

I.1. Molecule-based magnetic materials

Magnetism has been known for millennia, and for millennia interpretations of the nature of this elusive force have been produced. It was in the nineteenth and twentieth centuries (AD) when the nature of magnetism was finally understood. Magnetic materials became then the origin of major technological advances indispensable in our society.^{1,2} The magnet-based materials are found everywhere in our lives: in generators, motors, loudspeakers, microphones, switches, sensors, data storage devices, medical devices and many more.

Until the 80s, magnetic materials composed of metals, metal alloys or metal oxides represented the most-studied systems.² The preparation and processing of such materials require high temperature and energy consuming metallurgical methodologies. Moreover the optimization of information storage techniques requires constant miniaturization of the size of the magnetic materials, but the traditional magnetic materials exhibit limitations towards size reduction by losing their useful magnetic properties.^{2,3} Therefore, the development of new molecule-based magnetic materials has grown considerably in recent decades. In comparison to inorganic nanoparticles that are intrinsically polydispersed in size, molecular systems exhibit perfect monodispersity in size, volume, shape and charge, since molecules are all identical to each other. They are soluble in common solvents and their modular character opens ways to fine-tune their properties. Moreover, some of these molecular materials display remarkable magnetic properties, which are rare or unknown in traditional inorganic materials. For example, molecular systems with spin crossover phenomenon (SC),⁴ photomagnetism,⁵ single-molecule magnet (SMM)⁶ or single-chain magnet (SCM)⁷ behaviors have been discovered. Furthermore, these molecule-based materials may exhibit additional features including transparency, thermo- or photochromism, solubility, conductivity/superconductivity, low density, biocompatibility and/or recyclability affording convenient solutions for new technological needs.⁸ An additional important benefit of these molecular materials is the possibility to finely tune their chemical and physical properties by the design of the molecular precursors through the modification of their ligands.

In recent years, considerable research efforts have been devoted to the fabrication of nanoscale systems, for example to reduce the size of magnetic units in information storage devices. Molecular magnetic materials could meet this expectation by giving the opportunity to store information at the nanometric or molecular scale using, for example, the promising SMMs.^{2,4-6,9} Although these physical characteristics and potential applications are often highlighted in numerous fundamental studies, to date none of these magnetic components have been exploited industrially for any commercial devices.¹⁰ Indeed, these molecule-based compounds are generally produced as powders or crystalline solids, while technological devices require that some degree of self-organization or an easy processability is imparted to the material. Therefore one of the great challenges in the field of molecular magnetism is to process these compounds into technologically sustainable materials. One of the possible solutions is the elaboration of hybrid magnetic materials via functionalization of organic ligands with various groups to improve thermal or chemical stability, to induce liquid crystalline properties or, simply, enhance the solubility.

The main objective of this thesis is to develop hybrid molecule-based materials with improved properties via rational functionalization of well-known magnetic molecular complexes. The work along this

thesis covers the following two topics: single-molecule magnets, and electron transfer systems. Therefore, the basic and essential concepts behind these two molecular systems chosen for functionalization are summarized in the first part of this chapter. The second part will provide a short bibliographical survey of the already reported functionalized magnetic molecule-based systems possessing liquid crystalline properties or improved solubility. Based on the literature review throughout the second part of this chapter and previously performed work in the “Molecular Materials and Magnetism” group from Centre de Recherche Paul Pascal (CRPP), the motivation and the objectives of this thesis work will be detailed in the end of this first chapter.

I.1.1. Single-Molecule Magnets

I.1.1.1. Generalities

It has been nearly 20 years since the discovery that single molecules of a dodecamanganese coordination complex, with formula $[\text{Mn}_{12}\text{O}_{12}(\text{O}_2\text{CCH}_3)_{16}(\text{H}_2\text{O})_4]$ ($\text{Mn}_{12}\text{-OAc}$), can act as nanomagnets at very low temperatures (i.e. $T < 10$ K).⁶ Such molecules, called Single-Molecule Magnets (SMMs), can retain their magnetization below a certain blocking temperature (the temperature at which the time, τ , taken for the magnetization to relax is 100 s),¹¹ giving rise to M vs H hysteresis loops. These molecules represent the smallest units that may potentially be used in applications such as information storage,^{6,9,10} quantum computation¹² or as low-temperature refrigerants via the magnetocaloric effect.^{12c,13}

The prerequisites for a system to act as an SMM are a high-spin ground state (S_7), a high uniaxial magnetic anisotropy (characterized by the negative zero-field splitting parameter, D , defined by the following spin Hamiltonian: $\mathcal{H} = DS^2$) with a magnetic easy axis and negligible magnetic interactions between the molecules.⁶⁻¹¹ Because of their small size, SMMs can be truly placed at the interface between the quantum and classical worlds. These objects made possible experimental observation of theoretically predicted quantum phenomena, such as quantum tunneling of the magnetization¹⁴ and quantum phase interference.¹⁵

A very fruitful research has been performed on the improvement of SMM characteristics and extraordinary advances have been made over the last two decades resulting in a huge number of new SMMs in scientific literature. Via the serendipitous self-assembly^{11,16} or rational molecular design (building block approach)^{11,17} coordination chemists were able to construct homo- or heterometallic complexes of various nuclearity (from 1 to 84 metal centers) exhibiting SMM behavior for $3d$,^{6-11,16,17} $4d$,¹⁸ $5d$,^{18a,19} $4f$,²⁰ and $5f$ ²¹ metals. Moreover, in recent years, organometallic chemistry has produced many interesting developments that account for notable “records” in terms of magnetic hysteresis and anisotropy barriers.²²

In the following paragraphs of Section I.1.1, basic theory of SMM physics is described to understand how these complexes are capable to show not only the classical magnet-like behavior but also the quantum properties.

I.1.1.2. Theoretical aspects of SMMs illustrated by the Mn_{12} example

SMM complexes are often composed of metal ions (spin carriers) bonded together by various ligands, which serve to isolate the molecular core from its neighbors and ensure their cohesion. The intramolecular

magnetic exchange between metal centers through the ligands is usually significantly larger than the intermolecular interactions. Therefore the macroscopic magnetic properties of the material basically reflect the properties of a single molecule.

The $\text{Mn}_{12}\text{-OAc}$ SMM molecule, $[\text{Mn}_{12}\text{O}_{12}(\text{O}_2\text{CCH}_3)_{16}(\text{H}_2\text{O})_4]$,^{6,23} that is used as precursor in synthesis of hybrid molecule-based materials possessing both SMM and liquid crystalline properties along this thesis work, is chosen to illustrate SMM properties in this section.

Each $\text{Mn}_{12}\text{-OAc}$ molecule contains eight Mn^{III} ($S = 2$) and four Mn^{IV} ($S = 3/2$) ions. The structure of $\text{Mn}_{12}\text{-OAc}$ can be described as a $[\text{Mn}_{12}(\mu_3\text{-O})_{12}]$ roughly planar disk containing a central $[\text{Mn}^{\text{IV}}_4\text{O}_4]^{8+}$ cube surrounded by a non-planar ring of eight Mn^{III} ions connected to the cube by eight $\mu_3\text{-O}^{2-}$ ions and four bridging carboxylates perpendicular to the plane of the disk (two on each side Figure I-1 left).

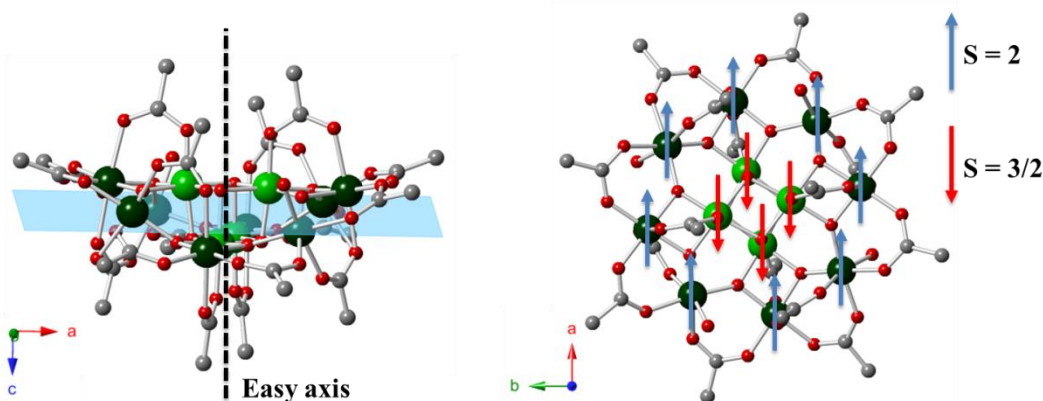


Figure I-1. Crystallographic structure of $\text{Mn}_{12}\text{-OAc}$ complex: (left) view along the crystal b -axis with illustration of the easy axis in $\text{Mn}_{12}\text{-OAc}$ complex situated along c axis of the unit cell; (right) view along the crystal c -axis with schematic representation of the spin alignments in the ground state of $\text{Mn}_{12}\text{-OAc}$ complex that gives an $S_T = 10$ ground state.^{6,23} Color scheme: Mn^{III} dark green, Mn^{IV} light green, O red, C grey. Hydrogens and lattice solvents are omitted for clarity.

SMM behavior arises from the association of a high-spin ground state with an easy-axis (i.e. Ising-type) magnetic anisotropy. The large spin ground state in $\text{Mn}_{12}\text{-OAc}$ is arising from a situation in which the spins of the four central Mn^{IV} centers are all aligned antiparallel to the spins of the eight outer Mn^{III} centers, to give $S_T = |(4 \times 3/2) + (8 \times -2)| = 10$ (see Figure I-1 right). The second ingredient required for SMM behavior is an easy-axis anisotropy, which in Mn_{12} -based complexes is brought by the nearly-parallel alignment of the eight Mn^{III} JT axes along the molecular z -axis (Figure I-1 left, see also Chapter II, Section II.2).

I.1.1.2.1. SMM properties in the absence of external field

Assuming the above mentioned SMM is a $S_T = 10$ macro-spin with the three directions of magnetization (x – hard, y – intermediate, and z – easy axis), the spin quantum number S_T possesses $2S_T + 1$ sublevels, each characterized by a projection quantum number m_S , where $-S_T \leq m_S \leq S_T$. At low temperature, when the magnetic coupling is larger than the thermal energy, SMM behavior is defined by the following Hamiltonian:

$$\mathcal{H} = DS_T^2 + E \left(S_{T_x}^2 - S_{T_y}^2 \right) \quad \text{Eq. I.1}$$

where S_T is the total spin ground state, $S_{T_x}^2$, $S_{T_y}^2$, $S_{T_z}^2$ spin operators along the three principal directions of magnetization (x – hard, y – intermediate, and z – easy axis), D and E are easy axis and transverse anisotropy parameters (that arise due to geometrical deviations from the ideal uniaxial symmetry for which $E = 0$). Hence in the absence of a magnetic field and the presence of a strong uniaxial anisotropy (D is negative and $|D| \gg E$) the Hamiltonian can be simplified to

$$\mathcal{H} = DS_{T_z}^2 \quad \text{Eq. I.2}$$

and the spin sublevels change their energy according to:

$$E_{m_s} = Dm_s^2 \quad \text{Eq. I.3.}$$

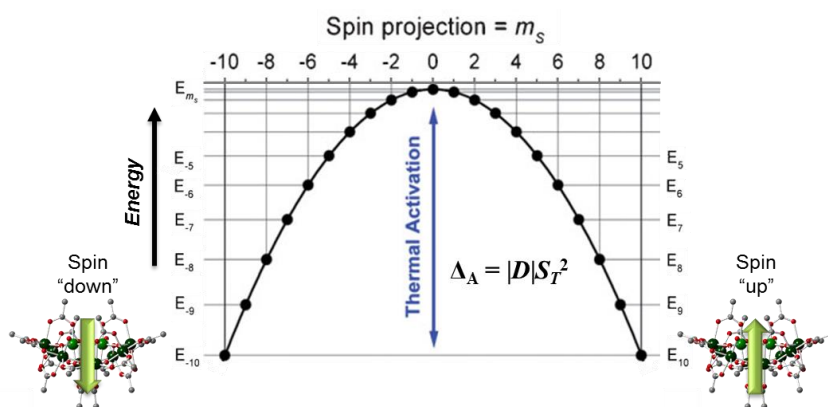


Figure I-2. Potential-energy diagram for Mn_{12} -OAc SMM with an $S_T = 10$ ground state experiencing axial zero-field splitting, $\Delta_A = |D|S_T^2$. At low temperature SMMs are blocked in the fundamental state $m_s = \pm S_T$ (± 10 in case of Mn_{12} -OAc).

As $S_T = 10$ for Mn_{12} -OAc, the spin splits in total of 21 discrete energy levels ($-S_T \leq m_s \leq S_T$) with a strong uniaxial anisotropy energy barrier (Δ_A) of about 70 K (in Mn_{12} -based complexes) and a doubly degenerated ground state $m_s = \pm 10$ in zero field. The energy barrier (Δ_A) separates two lowest energy levels of $m_s = \pm S_T$ with largest $|m_s|$ values. As illustrated in Figure I-2, the spectra of energy can be modelled as a potential energy diagram, where one side corresponds to the spin pointing up and the other to the spin pointing down. There is no energy cost to reverse the direction of the total spin in $m_s = 0$ state. The energy difference Δ_A between the states of lowest energy and those of maximum energy is defined as:

$$\Delta_A = |D|S_T^2 \quad \text{Eq. I.4}$$

where S_T is an integer total spin state and D is the zero-field splitting parameter originating from magnetic anisotropy of the system. For a half integer S_T (when an odd number of unpaired electrons is present in a molecule) the energy barrier is thus $\Delta_A = |D|(S_T^2 - 1/4)$.

In the equilibrium state at low temperature and without an applied magnetic field, half of the Mn_{12} -OAc molecules is in the $m_s = + 10$ level (“spin up”) while the other half is in $m_s = - 10$ level (“spin down”) and the total magnetization of the sample is zero. To eventually overcome the energy barrier between the positive and negative m_s states thermal population of the other m_s levels is allowed at higher temperatures.

I.1.1.2.2. SMM properties in a longitudinal magnetic field

The presence of a magnetic field changes the previously reduced Hamiltonian (Eq. I.2) to describe an SMM as followed:

$$\mathcal{H} = DS_T^2 - g\mu_B \vec{S}_T \cdot \vec{H} \quad \text{Eq. I.5}$$

where the last term is the Zeeman effect contribution which originates from the interaction of spin \vec{S}_T with external magnetic field \vec{H} . When an external longitudinal (parallel to the easy axis) magnetic field H_z is applied, the spin sublevels change their energy according to the Zeeman coupling (Figure I-3 left):

$$E_{m_S} = Dm_S^2 - g\mu_B m_S \cdot H_z \quad \text{Eq. I.6}$$

According to the Eq. I.6, the spin sublevels with $m_S > 0$ become energetically stabilized while those with $m_S < 0$ values become energetically destabilized (Zeeman effect) (Figure I-3 right). This leads to a preferred population of the $m_S = +10$ sublevel (in $\text{Mn}_{12}\text{-OAc}$). Thus a favored orientation of the microscopic magnetic moments in the direction of the external magnetic field is creating a magnetization $M \neq 0$ of the macroscopic sample.

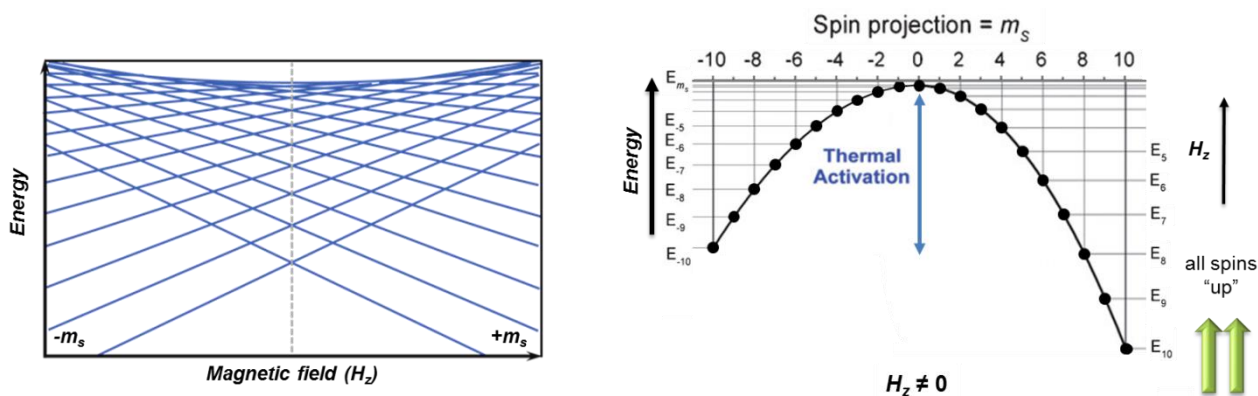


Figure I-3. (left) Zeeman diagram as a function of the external field H_z applied along the easy axis; (right) Double-well potential diagram in the presence of a longitudinal magnetic field (Zeeman effect)

I.1.1.2.3. Magnetization relaxation

On the removal of the external magnetic field, the system must go back to thermal equilibrium, the initial energy spectra are restored and spins recover their thermodynamic energy levels (Figure I-2), meaning that half of molecules return to $m_S = -10$ (in $\text{Mn}_{12}\text{-OAc}$) and magnetization relaxation is observed.

Due to the anisotropy barrier, schematized in Figure I-2, SMMs have a slow relaxation of magnetization. This relaxation process occurs through the coupling of the spin system with the environment. If there is sufficient thermal energy ($k_B T$), the molecule can absorb heat from the vibrational modes of the lattice (phonon). According to the selection rules of spin-phonon interaction, the only allowed paths are $\Delta m_S = \pm 1$ and ± 2 . Therefore, in order to relax to the equilibrium state, the system must successively absorb phonons until it reaches $m_S = 0$, then it can reach $m_S = -10$ through phonon emission. This is the origin of the thermal energy barrier to the slow relaxation of the magnetization in SMMs.

One of the ways to monitor the magnetization relaxation is by measuring the time decay of the magnetization, $M(t)$, in a zero field. First, a large *dc* field is applied to the sample at a fixed temperature to

saturate its magnetization in the easy direction. When the field is switched off, the magnetization is measured as a function of time. The experiment should be performed at different temperatures (Figure I-4). As the decay of the magnetization is usually an exponential function of time, the relaxation time τ is extracted at each temperature by taking $\tau = t$ when the magnetization reaches $1/e$. Usually, the magnetization decreases exponentially with the time at fixed temperature according to the relation:

$$M(t) = M_0 \cdot \exp(-t/\tau) \quad \text{Eq. I.7}$$

where M_0 or M_S ($t = 0$) is the saturation magnetization, $M(t)$ is the magnetization at a given time t and τ is the relaxation time. The relaxation time is temperature dependent and follows the Arrhenius law:

$$\tau = \tau_0 \cdot \exp\left(\frac{\Delta_A}{k_B T}\right) \quad \text{Eq. I.8}$$

where Δ_A is the energy barrier, k_B is the Boltzmann constant, and τ_0 is the pre-exponential factor, a constant that can be experimentally determined and depends on the nature of the SMM and its environment. In the case of Mn_{12} family, it varies in the range of $10^{-8} - 10^{-10}$ s. From the Eq. I.8, we can conclude that higher temperature means smaller relaxation time (Figure I-4).

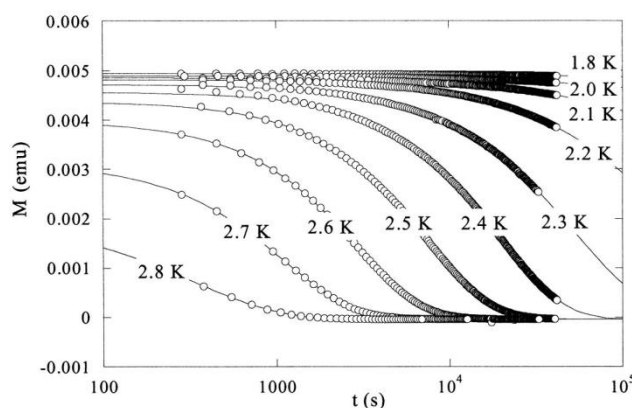


Figure I-4. Relaxation of the magnetization of Mn_{12} -OAc at different temperatures, measured at zero applied field for a single crystal after saturation at 5 T field applied along the easy axis of magnetization.²⁴

Another experimental method (and usually most commonly used) that yields information about magnetization dynamics of SMMs is the alternating current (*ac*) magnetic susceptibility measurement (with a weak field, typically 1 - 5 Oe, oscillating at a given frequency, ν_{exp}). The alternating magnetic susceptibility produces two quantities: an in-phase, or real, component χ' and an out-of-phase, or imaginary, component χ'' as:

$$\chi_{ac} = \chi' + i\chi'' \quad \text{Eq. I.9}$$

When the relaxation time τ of the compound is shorter than the characteristic experimental time τ_{exp} ($\tau_{\text{exp}} = (2\pi\nu_{\text{exp}})^{-1}$), the magnetization vector is oscillating with the *ac* field, and only a static behaviour is observed (only the real component χ'). However, when τ is longer, a dynamic behaviour is perceived and the magnetization vector is dephased (non-zero imaginary component χ''). Experimentally, we can measure the χ'' versus temperature at fixed frequency (Figure I-5 left), or/and the χ'' versus frequency at fixed temperature. The temperature or frequency where χ'' reaches its maximum value corresponds to the so-called

blocking temperature (T_B), or blocking frequency (ν_B), respectively. The relaxation time (τ) can be deduced from the maxima of the $\chi''(T)$ and/or $\chi''(\nu)$ curves at T_B (solid symbols, Figure I-5 right) and/or ν_B . For $\text{Mn}_{12}\text{-OAc}$, the experimental thermally activated energy barrier is deduced from Arrhenius law (i.e. τ vs $1/T$ plot, Eq. I.8) as $\Delta_A/k_B = 62$ K, with $\tau_0 = 2.1 \cdot 10^{-7}$ s (Figure I-5 right). To supplement these *ac* data and to ensure an accurate analysis over a wider range of temperatures, direct current (*dc*) magnetization decay data are often used.

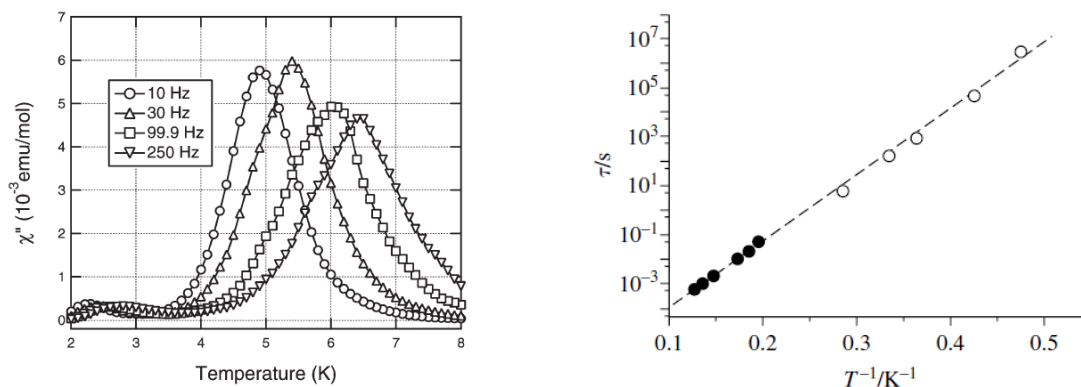


Figure I-5. (left) Imaginary component of the ac susceptibility of $\text{Mn}_{12}\text{-OAc}$ measured with frequency ranging from 10 Hz to 250 Hz.²⁵ (right) Temperature dependence of the relaxation time on a log scale of $\text{Mn}_{12}\text{-OAc}$ extracted from *ac* susceptibility data (solid symbols) in the frequency range 1-270 Hz and from time decay of the magnetization (empty symbols), the line is the fit to the Arrhenius law (Eq. I.8) with $\Delta_A/k_B = 62$ K, with $\tau_0 = 2.1 \cdot 10^{-7}$ s.¹¹

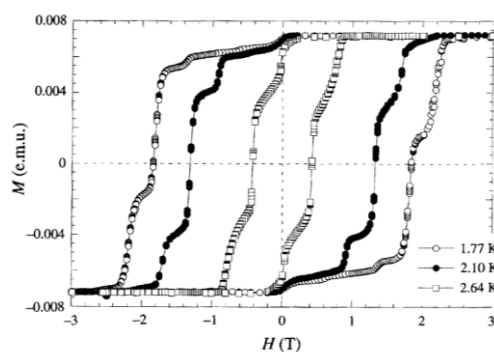


Figure I-6. Typical stepped hysteresis loops recorded on a single crystal of $\text{Mn}_{12}\text{-OAc}$ at 1.77, 2.10 and 2.64 K between 3 and -3 T with the field applied along the easy axis of magnetization with a sweep rate of 0.025 T/min.^{14b}

Like classical magnets, below the blocking temperature SMMs exhibit magnetic hysteresis loops that are temperature and magnetic field sweeping rate dependent. A series of steps were discovered in the hysteresis loops of the $\text{Mn}_{12}\text{-Ac}$ (Figure I-6). The observed steps in the hysteresis loop correspond to a faster rate of magnetization relaxation occurring when the energy levels on opposite parts of the double-well potential are at the same energy. For these particular field values where a vertical magnetization step is observed (Figure I-6), tunneling of the magnetization is enabled, and an evident increase in the relaxation rate is observed. This result can be explained by the competition between two relaxation processes (thermal and quantum) that makes short-cut of the thermal barrier (thermally assisted quantum tunneling of the magnetization). Moreover, relaxation time at very low temperatures (below 1 K) does not follow the Arrhenius law and saturates, indicating the presence of quantum tunneling of the magnetization (QTM).

I.1.1.2.4. Quantum tunneling of the magnetization

QTM occurs between energetically matched m_S levels on opposite sides of the barrier and can be observed as steps (relating to a loss or gain of magnetization) in the hysteresis loops (Figure I-6). This behavior can be described by the following spin-Hamiltonian:

$$\mathcal{H} = DS_T^2 + E \left(S_{T_x}^2 - S_{T_y}^2 \right) - g\mu_B \vec{S}_T \cdot \vec{H} \quad \text{Eq. I.10}$$

In the section I.1.1.2.1, it was assumed that due to the strong uniaxial anisotropy the SMMs behavior in an applied magnetic field can be described by the Hamiltonian from Eq I.5. As long as this Hamiltonian (Eq. I.5) is valid the two $\pm m_S$ states are orthogonal to each other, and there is no possible quantum mixing. Upon scanning the external magnetic field, they simply cross over each other and the mechanism for tunneling does not exist (Figure I-3 left). In reality, however, there is always a transverse contribution, and therefore, the contribution of the second term in Eq. I.10 cannot be neglected. The transverse term, containing $S_{T_x}^2$ or $S_{T_y}^2$ spin operators, mixes two different m_S states and creates a gap at the crossing of the m_S levels. In zero-field the $+m_S$ and $-m_S$ levels are equal in energy and this corresponds to the most favorable condition to observe tunneling. When a magnetic field is applied along the z axis (Fig. 1.3) the pairs of $\pm m_S$ levels are no longer degenerate and the tunneling is suppressed (Figure I-7 left), except for values of $H_z = nD/(g\mu_B)$ (where $n = 0, 1, 2, \dots$) when the levels are brought back into resonance again, corresponding to steps seen in hysteresis loops. When tunneling occurs between any m_S levels, this provides a faster relaxation for the magnetization resulting in the effective energy barrier (Δ_{eff}) being smaller than the theoretical upper limit (Δ_A) calculated from $S_T^2|D|$.

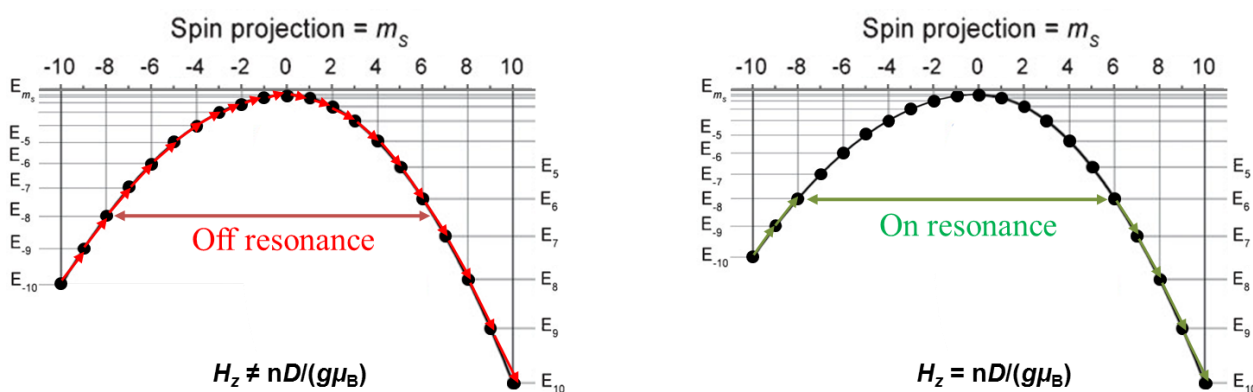


Figure I-7. Potential energy diagrams in the presence of different longitudinal fields. Resonant quantum tunneling, corresponding to vertical “steps” in hysteresis loops, occurs between m_S levels on opposite sides of the barrier at specific applied fields ($H_z = nD \cdot (g\mu_B)^{-1}$).

Basic concepts to understand SMM characteristics and associated experimental techniques were introduced based on Mn_{12} -OAc SMM in this section. In Chapter II, additional information regarding the family of Mn_{12} -based complexes may be found. Another type of interesting bistable molecules is presented in the next section of this chapter.

I.1.2. Electron transfer complexes

I.1.2.1. Generalities

Molecular materials that show a reversible change (or switching) of their physical properties as a function of external stimuli (light, temperature, pressure, magnetic or electric fields, etc.) offer appealing perspectives for the realization of energy efficient molecular-scale electronic devices.^{26,27,28} A significant extension of the application perspectives was given by the development of molecular magnetism, which led to the discovery that the switching of the magnetic properties of a molecule can be induced by temperature variation or photoexcitation. Among them, the most studied systems are those exhibiting spin crossover (SC)^{4,5a} or electron transfer (ET).^{5b,c,29} The observed phenomena in both systems are associated with the change of the electronic configuration of metal centers that results in the concomitant major changes in their structural, magnetic and optical properties.

Electron transfer (ET) systems have attracted a great interest, since this process plays a key role in most of the fundamental processes in physics, chemistry and biology.³⁰ An electron transfer (ET) represents a redox process between two units, one being the donor (reductant) while the other one – the acceptor (oxidant). Rudolph A. Marcus developed the first generally accepted theory of outer-sphere (intermolecular) ET in 1956 based on a transition state theory approach.³¹ Later, Marcus theory was extended by Hush to the problem of inner sphere (intramolecular) electron transfer reactions.³² Different other models have been developed to complete existing ones. Piepho, Krausz, and Schatz elaborated a vibronic coupling model (PKS model)³³ to calculate absorption profiles of the electron transfer systems.

A metal-to-metal electron transfer was firstly reported in the mixed valence Creutz–Taube ion, $[(H_3N)_5Ru^{II}(pyr)Ru^{III}(NH_3)_5]^{5+}$ (pyr = pyrazine).³⁴ The phenomenon of metal-to-metal electron transfer is also observed in heterometallic compounds. However, the redox sites do not necessarily have to be metallic, purely organic systems are also known.^{35,36} The discovery of ET in the 3D inorganic polymer $K_{0.2}Co_{1.4}[Fe(CN)_6] \cdot 6.9H_2O$ (Co/Fe Prussian blue analogue)^{5b} generated a great research interest due to the possibility to control magnetic properties at molecular level via temperature variation or light irradiation as the result of the metal-to-metal thermally and/or photo-induced ET occurrence. The 3D polymer contains $\{Fe(\mu-CN)Co\}$ motifs that exhibit a reversible metal-to-metal electron transfer converting diamagnetic $\{Fe^{II}_{LS}(\mu-CN)Co^{III}_{LS}\}$ ($Fe^{II}_{LS} - t^6_{2g}, S = 0$ and $Co^{III}_{LS} - t^6_{2g}, S = 0$) into paramagnetic $\{Fe^{III}_{LS}(\mu-CN)Co^{II}_{HS}\}$ ($Fe^{III}_{LS} - t^5_{2g}, S = 1/2$ and $Co^{II}_{HS} - t^5_{2g}e^2_g, S = 3/2$) units as a result of various external stimuli.

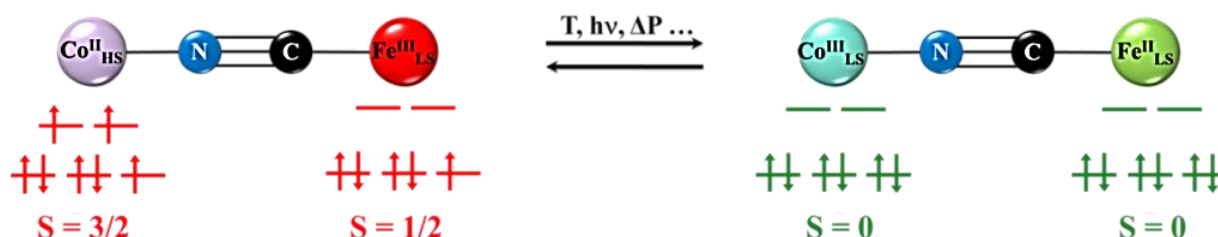


Figure I-8. Schematic representation of the metal-to-metal electron transfer induced by external stimuli in the example of $\{Fe^{II}_{LS}(\mu-CN)Co^{III}_{LS}\}$ and $\{Fe^{III}_{LS}(\mu-CN)Co^{II}_{HS}\}$ pairs.

Cyanido-bridged hetero-bimetallic molecular complexes, exhibiting switching of their magnetic and optical properties as the result of a thermally and/or photo-induced intramolecular metal-to-metal electron transfer, are another molecule-based magnetic system chosen for functionalization within this thesis work. In this regard, the following paragraphs of Section I.1.2 are dedicated to the occurrence of intramolecular metal-to-metal ET in various cyanido-bridged systems.

I.1.2.2. Thermally and/or photo-induced ET in cyanido-bridged systems

The Prussian blue analogues (PBA) of general formula, $A_jM_k[M'(CN)_6]_l \cdot nH_2O$ (A = alkali metal cation, M and M' = transition metals, Figure I-9 left), are one of the most studied bimetallic coordination compounds due to their remarkable magnetic properties. The advantages to design magnetic functionalities with these compounds can be found in their facile synthesis and the predictable magnetic couplings via CN bridge.³⁷ Moreover, certain M/M' couples of these compounds exhibit metal-to-metal electron transfer phenomenon. During the ET process, an electron is exchanged between two metal ions via a cyanide group (Figure I-8), resulting in the change of electronic, magnetic, and/or optical properties of a whole system. Electron transfer has been found to occur under the influence of temperature,³⁸ pressure,³⁹ visible light^{38,40} and X-rays⁴¹ in different PBAs.

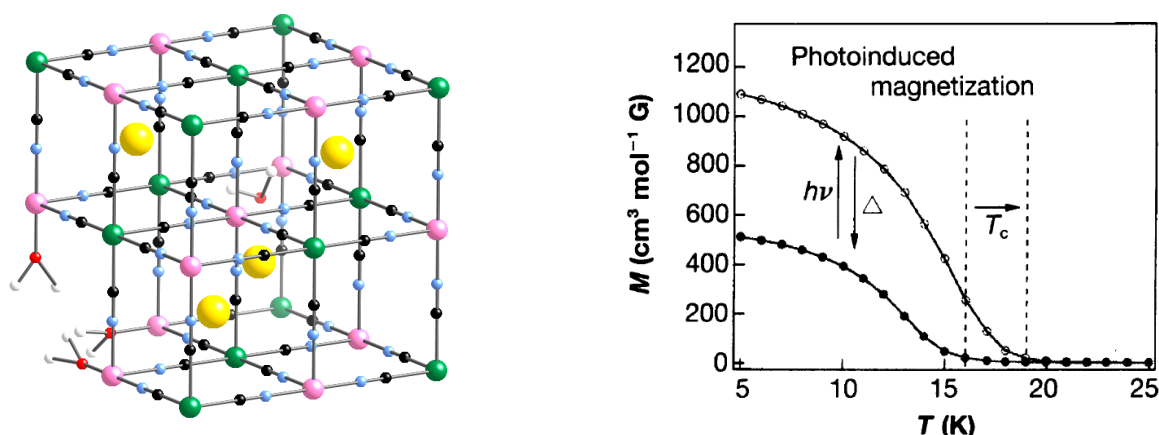


Figure I-9. (left) General structure of Prussian blue analogues, $A_jM_k[M'(CN)_6]_l \cdot nH_2O$ (A = alkali metal cation, yellow; M and M' = transition metals, pink and green; C, black; N, blue; O, red; H, white). (right) Temperature dependence of the field-cooled magnetization at $H = 5$ G, before and after red light irradiation for $K_{0.2}Co_{1.4}[Fe(CN)_6] \cdot 6.9H_2O$.^{5b}

The first example $K_{0.2}Co_{1.4}[Fe(CN)_6] \cdot 6.9H_2O$, that shows light-induced reversible magnetization changes, was briefly introduced in Section I.1.2.1. In the visible region of its electronic absorption spectra, this compound exhibits an intense metal-to-metal charge transfer absorption at 550 nm, ascribed to the conversion of $\{Fe^{II}_{LS}(\mu-CN)Co^{III}_{LS}\}$ ($Fe^{II}_{LS} - t^6_{2g}$, $S = 0$ and $Co^{III}_{LS} - t^6_{2g}$, $S = 0$) into paramagnetic $\{Fe^{III}_{LS}(\mu-CN)Co^{II}_{HS}\}$ ($Fe^{III}_{LS} - t^5_{2g}$, $S = 1/2$ and $Co^{II}_{HS} - t^5_{2g}e^2_g$, $S = 3/2$) units via the metal-to-metal ET. As shown in Figure I-9 right, the irradiation with red light (660 nm) increases the ferrimagnetic ordering temperature (Curie temperature) from 16 to 19 K and concomitantly increases the magnetization. This effect is reversed via blue light irradiation (450 nm) or heating of the sample above 150 K.

Following this seminal work, several groups reported that the photomagnetic behavior as well as thermally induced electron transfer of Fe/Co Prussian blues can be modulated by changing the Co/Fe ratio

present in the nonstoichiometric $A_jCo_k[Fe(CN)_6] \cdot nH_2O$ (A = alkali metal ion) lattices.^{5c,42} When $j < 0.5$, the Fe sites are fractionally occupied and the Co centers consequently contain one or more water molecules to satisfy their coordination spheres. The number of water molecules tunes the ligand field strength and redox potential of the Co centers. It was indeed found that an average CoN_5O coordination environment and adjacent $[Fe(CN)_6]^-$ sites are primary to result reversible thermally and photo-induced magnetization changes in the material. For example, in the case when $A = Na$, it was reported^{42e} that $Na_{0.07}Co_{1.50}[Fe(CN)_6] \cdot 6.3H_2O$ is paramagnetic and shows no thermally or photo-induced ET; $Na_{0.94}Co_{1.15}[Fe(CN)_6] \cdot 3.0H_2O$ is diamagnetic (between 2 and 350 K) and displays no photo-induced ET; while $Na_{0.60}Co_{1.37}[Fe(CN)_6] \cdot 3.9H_2O$, $Na_{0.53}Co_{1.32}[Fe(CN)_6] \cdot 4.4H_2O$ and $Na_{0.37}Co_{1.37}[Fe(CN)_6] \cdot 4.8H_2O$ besides the photo-induced electron transfer at low temperatures exhibit first-order phase transition with a thermal hysteresis between 260 – 300, 230 – 270 and 180 – 220 K, respectively, associated with an electron transfer process between diamagnetic and paramagnetic states.

Similarly to Fe/Co PBAs, Fe/Mn cyanido-bridged 3D systems exhibit a temperature-dependent ET with a large thermal hysteresis of 116 K between 147 and 263 K.^{43,44} The rubidium manganese hexacyanoferrate, $Rb_{0.88}Mn[Fe(CN)_6]_{0.96} \cdot xH_2O$, displays both thermally and photo-induced electron transfer.⁴³ This system shows a transition from the high temperature phase containing $\{Fe^{III}_{LS}(\mu-CN)Mn^{II}_{HS}\}$ pairs (Fe^{II} , $S = 1/2$; Mn^{II} , $S = 5/2$) to the low temperature phase made of $\{Fe^{II}_{LS}(\mu-CN)Mn^{III}_{HS}\}$ pairs (Fe^{II} , $S = 0$; Mn^{III} , $S = 2$). The electron transfer process is accompanied by a structural transformation from cubic to tetragonal space group due to the Jahn-Teller distortion resulting on Mn^{III} sites (some additional information about Jahn-Teller distortion in Mn^{III} ions may be found in Chapter II). The low temperature phase shows a 3D ferromagnetic order with a $T_C = 11$ K due to the interactions between Mn^{III} ions through the diamagnetic $[Fe^{II}(CN)_6]$ units. The light irradiation (532 nm) induces a ferrimagnetic phase due to a metal-to-metal charge transfer that yields reduced values of magnetization. The reverse process is also achieved via irradiation with 410 nm wavelength light source. The capability Fe/Mn PBAs to exhibit switching phenomena and their physical properties are however known to be intimately coupled to the exact system stoichiometry.⁴⁵

Besides Fe/Co or Fe/Mn PBAs, the chemistry of other 3D cyanido-bridged coordination polymers based on other d -block hexacyanidometallates was explored. Thus, bimetallic Prussian blue analogues like Fe/Cr,⁴⁶ V/Cr,⁴⁷ Mn/Cr,⁴⁸ Co/Os,⁴⁹ were reported to exhibit thermally and/or photo-induced metal-to-metal ET. Moreover, heterobimetallic networks based on octacyanidomolibdates (Cu/Mo)⁵⁰ or octacyanidotungstates (Co/W)⁵¹ were reported to display similar phenomena.

However, the high dimensionality of bimetallic assemblies of Prussian blue analogues is limiting the systematic study of structure-property relationships, and furthermore the advance towards technological application due to the processing difficulties induced by their reduced solubility. In this respect, soluble and well-defined molecular fragments of these functional networks (with preserved original properties) appear to be more promising towards future applications. Therefore an active cyanido-metallate research trend has been directed towards the synthesis and investigation of discrete PBAs that have flexible molecular and electronic structures coupled with improved solubility. In the last two decades, several groups designed, isolated and studied molecular hetero- or homobimetallic analogues (fragments of various geometry) of

Prussian blues by rational selection of capped building blocks and coordinatively unsaturated metal ions.^{52,53,54,55} This approach has been extremely successful and diverse molecular architectures have been developed to display single-molecule magnet behavior,^{17,53} spin crossover,⁵⁴ electron-transfer^{52c,54e,55} or photo-induced magnetism.⁵⁶ Thus, several heterobimetallic systems were found to exhibit thermal and/or light-induced electron transfers, such as Cu/Mo,^{56a,b} Fe/Os,^{55h} Mn/Mo,^{56c} Mn/W,^{56c} Co/W,⁵⁶ⁱ and Fe/Co^{52c,54e,55a-g,i,56d-g} that are the most studied systems due to a well established mechanism, and therefore some of these Fe/Co systems were chosen for investigations within this thesis and are discussed in following paragraphs.

Despite some earlier reports on molecular complexes containing cyanido-bridged Fe and Co ions,⁵⁷ it was only in 2004 when was reported for the first time the occurrence of an intramolecular metal-to-metal ET in a molecular $\{\text{Fe}_2\text{Co}_3\}$ complex, $\{[\text{Co}(\text{tmphen})_2]_3[\text{Fe}(\text{CN})_6]_2\}$ (tmphen = 3,4,7,8-tetramethyl-1,10-phenanthroline).^{55a} In this system of trigonal bipyramidal geometry a thermal metal-to-metal electron transfer occurs with the conversion behavior between two pairs of Fe/Co, resulting in one “extra” Co^{II} LS ion not involved in this process, in the low temperature phase. Later in 2011, the photo-sensitivity of this compound was discovered and reported.⁵⁵ⁱ

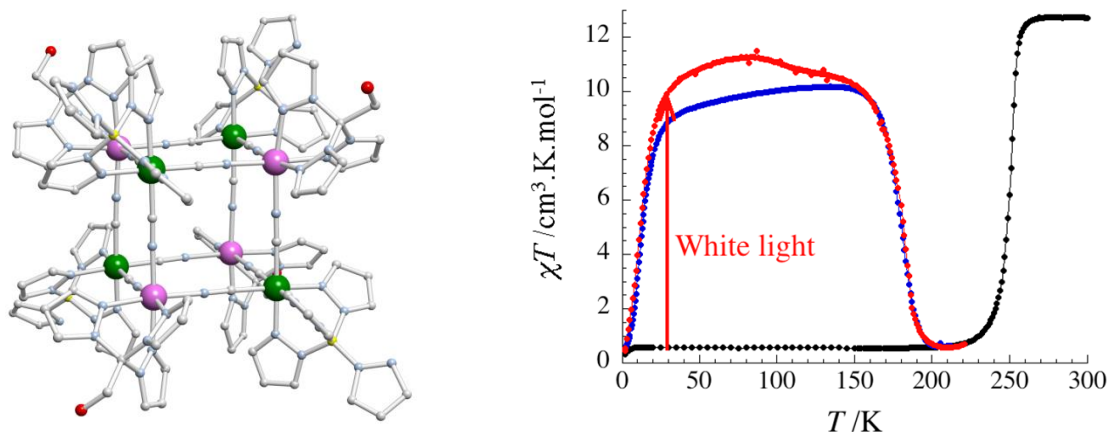


Figure I-10. (left) View of the molecular $\{\text{Fe}_4\text{Co}_4\}$ cube at 250 K. Color scheme: Fe(III) green, Co(II) pink, C grey, O red, N light blue and B yellow. Lattice solvents, anions, and hydrogen atoms are omitted for clarity. (right) Temperature dependence of the χT product (with χ defined as the molar magnetic susceptibility and equal to M/H ; M = magnetization and H = external magnetic field) for the $\{\text{Fe}_4\text{Co}_4\}$ cube before (black) and after (red) irradiation, and after thermal quenching (blue).^{55b}

The first reported example of a molecular system that mimics not only the properties (thermal and photo-induced ET) but also the structure (the cubic cell, Figure I-9 left) of Prussian blues is the $\{[(\text{pzTp})\text{Fe}^{\text{III}}(\text{CN})_3]_4[\text{Co}^{\text{II}}(\text{pz}_3\text{CCH}_2\text{OH})_4](\text{ClO}_4)_2 \cdot 4\text{H}_2\text{O} \cdot 13\text{DMF}\}$ complex (pzTp = tetrapyrazolylborate, $\text{pz}_3\text{CCH}_2\text{OH}$ = 2,2,2-tris(pyrazolyl)ethanol) (Figure I-10 left).^{55b} This compound is a stoichiometric molecular $\{\text{Fe}_4\text{Co}_4\}$ cube with alternation of Co and Fe ions at each corner with cyanide linkers on each edge. The cubes are well isolated by the presence of bulky ligands around the metallic centers: tetrapyrazolylborate (pzTp) for the Fe and 2,2,2-tris(pyrazolyl)ethanol for the Co centers (Figure I-10 left). With the use of spectroscopic, magnetic, and crystallographic methods, a fully reversible intramolecular electron transfer, interconverting diamagnetic $\{\text{Fe}^{\text{II}}_{\text{LS}}(\mu\text{-CN})\text{Co}^{\text{III}}_{\text{LS}}\}$ units into paramagnetic $\{\text{Fe}^{\text{III}}_{\text{LS}}(\mu\text{-CN})\text{Co}^{\text{II}}_{\text{HS}}\}$ ones as a function of the temperature or light, has been demonstrated. This phenomenon is also

accompanied by the change of optical properties: the red compound at room temperature turns to green at low temperature. At 30 K and under white-light irradiation, the magnetic response of the system is changing from the diamagnetic state to the paramagnetic state (Figure I-10 right, red curve). The high temperature paramagnetic state can be trapped, when the compound is rapidly cooled (30 K min⁻¹) from 300 to 5 K. Moreover, the metastable paramagnetic states obtained via light irradiation or rapid cooling, have a remarkably higher life times (~ 10 years at 120 K) compared to the 3D PBA networks (Na_{0.32}Co[Fe(CN)₆]_{0.74}·3.4H₂O, 33 hours at 120 K). This result demonstrates the interest in the development of purely molecular compounds because of their larger flexibility and comparable physical properties.

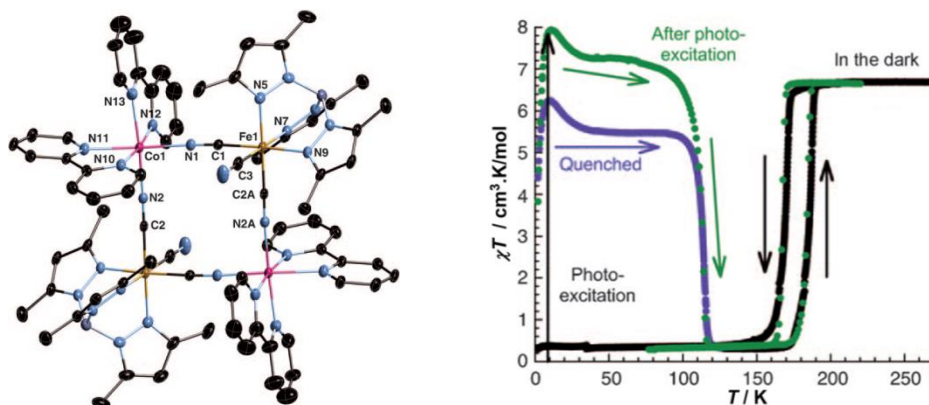


Figure I-11. (left) ORTEP-type view of the cationic portion of $\{[(\text{Tp}^*)\text{Fe}(\text{CN})_3]_2[\text{Co}(\text{bpy})_2]_2\}[\text{OTf}]_2 \cdot 2\text{H}_2\text{O} \cdot 4\text{DMF}$ at 230 K with thermal ellipsoids at 30% probability. Lattice solvent molecules, anions, and hydrogen atoms are omitted for clarity. Color scheme: C, black; Co, pink; Fe, orange; N, blue; B, gray. (right) χT vs. T data for $\{[(\text{Tp}^*)\text{Fe}(\text{CN})_3]_2[\text{Co}(\text{bpy})_2]_2\}[\text{OTf}]_2 \cdot 2\text{H}_2\text{O} \cdot 4\text{DMF}$ (at 0.4 Kmin⁻¹): in the dark (black, 0.1 T), after thermal quench (dark blue, 0.1 T), and after irradiation (green, 1 T, 3 mWcm⁻²).^{55c}

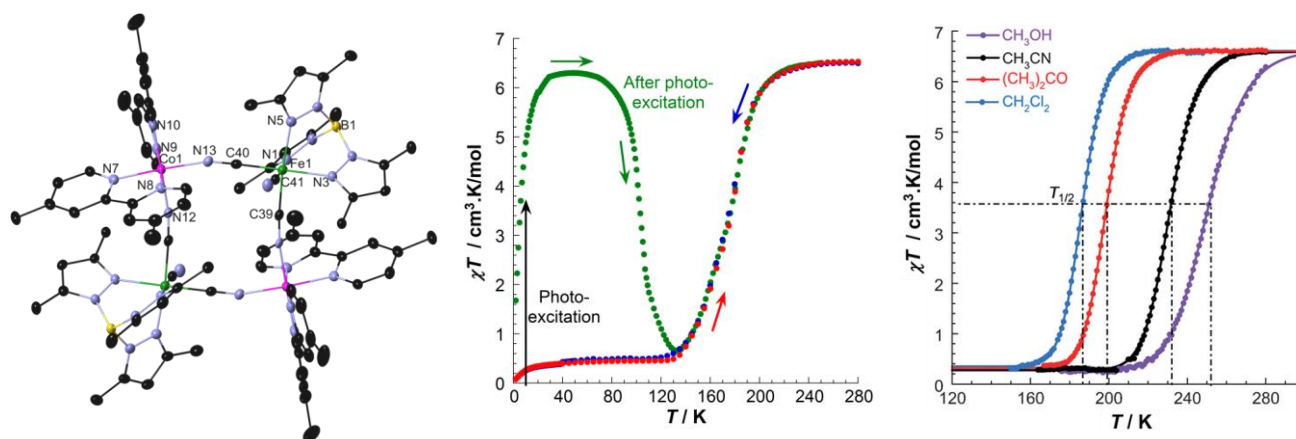


Figure I-12. (left) ORTEP-type view of the cationic part of $\{[(\text{Tp}^*)\text{Fe}(\text{CN})_3]_2[\text{Co}(\text{diMeBpy})_2]_2\}(\text{OTf})_2 \cdot \text{H}_2\text{O} \cdot 2\text{DMF}$ at 120 K with thermal ellipsoids at 30% probability level. Lattice solvents, anions, and hydrogen atoms are omitted for clarity. Colour scheme: Fe, green; Co, pink; B, yellow; N, blue; C, black. (center) χT vs. T data for $\{[(\text{Tp}^*)\text{Fe}(\text{CN})_3]_2[\text{Co}(\text{diMeBpy})_2]_2\}(\text{OTf})_2 \cdot \text{H}_2\text{O} \cdot 2\text{DMF}$: in the dark on cooling (blue, 0.5 T), and heating (red, 1 T) at 0.8 Kmin⁻¹; after irradiation (green, 1 T, 2 mWcm⁻²) at 0.4 Kmin⁻¹. (right) Temperature dependence of the χT product for $\{[(\text{Tp}^*)\text{Fe}(\text{CN})_3]_2[\text{Co}(\text{diMeBpy})_2]_2\}(\text{OTf})_2$ in methanol, acetonitrile, acetone, and dichloromethane solutions (0.4 Kmin⁻¹, 1 T; solid lines are fits to the Ideal solution model,⁵⁸ see section I.1.2.3).^{55g}

The tetranuclear $\{\text{Fe}_2\text{Co}_2\}$ squares, that also mimic structurally PBA (one face of the cubic cell) and display reversible thermally and photoinduced intramolecular electron transfer in solid state and in solution, are one of the most studied molecular systems to date.^{52c,55c-g,59} These compounds of general formula

$\{[(L^1)Fe(CN)_3]_2[Co(L^2)_2]_2\}(A)_2 \cdot S$, where L^1 is a derivative of trispyrazolylborate (Tp) and L^2 is a bidentate ligand, mostly derivatives of 2,2'-bipyridine (bpy), A is a monovalent counter-anion and S corresponds to lattice solvents. The first reported representative of this family of rationally built molecular systems, $\{[(Tp^*)Fe(CN)_3]_2[Co(bpy)_2]_2\}[OTf]_2 \cdot 2H_2O \cdot 4DMF$ (where $Tp^* = \text{tris}(3,5\text{-dimethylpyrazol-1-yl})\text{hydroborate}$, $bpy = 2,2'\text{-bipyridine}$, $OTf = \text{trifluoromethanesulfonate}$, and $DMF = N,N\text{-dimethylformamide}$, Figure I-11 left), exhibits a first-order phase transition with a thermal hysteresis of 18 K (at 0.4 Kmin^{-1}) between 186 and 168 K, associated with an electron transfer process between paramagnetic $\{Fe^{III}Co^{II}_2\}$ and diamagnetic $\{Fe^{II}Co^{III}_2\}$ states (Figure I-11 right).^{55c} It was not the case for the other square complexes that show a gradual conversion (Figure I-12 center), indicating the presence of significantly weaker elastic interactions between complexes in their crystal structures.^{55d-g,59a,b}

Solution studies of some of these tetranuclear $\{Fe_2Co_2\}$ complexes offered an opportunity to observe their unique behaviors. Thus, through the methyl functionalization of the bpy ligands on $\{[(Tp^*)Fe(CN)_3]_2[Co(bpy)_2]_2\}[OTf]_2$, a new square system was obtained, $\{[(Tp^*)Fe(CN)_3]_2[Co(\text{diMe}bpy)_2]_2\}[OTf]_2$ (Figure I-12 left) (where $\text{diMe}bpy = 4,4'\text{-methyl-2,2'-bipyridine}$), that proves the possibility to transfer the solid state properties of $\{Fe_2Co_2\}$ complexes into a wide range of solvents.^{55g} Furthermore, electron transfer and associated magnetic and optical properties could be modulated by the solvent nature (Figure I-12 right). On the other hand, another square system, $\{[(Tp^*)Fe(CN)_3]_2[Co(\text{dtbbpy})_2]_2\}(PF_6)_2 \cdot 2MeOH$ (where $\text{dtbbpy} = 4,4'\text{-di-tert-butyl-2,2'-bipyridine}$), also maintained an electron transfer process in solution, that is induced not only thermally but also by protonation.^{55e,f} The effect of the protonation was explained by the modulation of redox potential on the metal sites. All above described $\{Fe_2Co_2\}$ square complexes display a metastable $\{Fe^{III}Co^{II}_2\}$ state by light irradiation at 10 K. Whereas for the complex of formula $\{[(pzTp)Fe(CN)_3]_2[Co(\text{bik})_2]_2\}(ClO_4)_2 \cdot 2H_2O$ (where $pzTp = \text{tetrapyrazolylborate}$, $\text{bik} = \text{bis}(1\text{-methylimidazol-2-yl})\text{ketone}$), there was observed for the first time a $\{Fe^{III}Co^{II}_2\} \leftrightarrow \{Fe^{II}Co^{III}_2\}$ photo-reversibility under irradiation with light of different wavelengths at 20 K. Magnetic measurements and low-temperature single crystal X-ray diffraction experiments have shown that an intermolecular electron transfer converts the diamagnetic $\{Fe^{II}Co^{III}_2\}$ units to the paramagnetic $\{Fe^{III}Co^{II}_2\}$ metastable ones under 808 nm laser light irradiation, whereas the diamagnetic state is partially recovered under irradiation at 532 nm.^{59a} Also, in a very recent report on the $\{[(Tp)Fe(CN)_3]_2[Co(\text{diCOOEt}bpy)_2]_2\}(ClO_4)_2 \cdot 2MeOH$ complex (where $Tp = \text{tri}(\text{pyrazol-1-yl})\text{hydroborate}$ and $\text{diCOOEt}bpy = 4,4'\text{-bis}(\text{ethoxycarbonyl})\text{-2,2'-bipyridine}$) there has been shown the possibility to control the occurrence of the thermally induced ET via application of external hydrostatic pressure.^{59b}

All the mentioned above reports give a good enough motivation to work on a wise functionalization of cyanido-bridged $\{Fe_2Co_2\}$ molecular squares, since specific functional modification may open up a way for constructing novel multifunctional materials with potential practical applications. Therefore these systems were chosen as targets for rational functionalization within the frame of this thesis.

I.1.2.3. Theoretical background

As described above, ET complexes, particularly cyanido-bridged $\{\text{Fe}_2\text{Co}_2\}$ molecular squares, show experimentally interconversion between two different states (diamagnetic and paramagnetic), or eventually bistability. Therefore the following part is dedicated to the understanding the mechanism of their bistability based on a simple thermodynamic model: the binary solution model.⁵⁸

Given the fact that the ET process occurs between two different metals, we will consider an isolated pair to describe the occurrence of this process. The ET phenomena involve two states (paramagnetic and diamagnetic labeled A and B, respectively) that are energetically close and, therefore, in an equilibrium. The two different states can be easily identified by measuring the temperature dependence of the χT product (as shown in Figures I–10 - I–12), since each state is expected to be diamagnetic or paramagnetic that follows, for the latter, a Curie law. Thus, the χT product corresponds to the Curie constants (C) of each state ($C = 0$ for a diamagnetic species) and is related to their molar fraction, x , according to the following equation:

$$\chi T = x_A \cdot (\chi T)_A + x_B \cdot (\chi T)_B \quad \text{Eq. I.11}$$

where x_A and x_B represent the paramagnetic and diamagnetic fractions of a given system, respectively. Assuming that $x_A = x$, then Eq. I.11 becomes:

$$\chi T = x \cdot (\chi T)_A + (1 - x) \cdot (\chi T)_B \quad \text{Eq. I.12}$$

For the paramagnetic A and diamagnetic B states, the $(\chi T)_A$ and $(\chi T)_B$ products are usually temperature independent. Therefore the investigation of the $\chi T = f(T)$ gives a direct access to $x = f(T)$. Experimental observations have shown (Figures I–10 - I–12) that ET may occur as a conversion (Figure I–12) or a transition (Figure I–11). Therefore it was decided to describe the temperature dependence of x by both ideal and regular solution models, and finally to construct a phase diagram with the aim to understand the difference between a conversion and a transition.

Electron transfer may be described as equilibrium between two states



with a Gibbs energy change:

$$\Delta G = \Delta H - T\Delta S \quad \text{Eq. I.13}$$

This energy change ($\Delta G = G_B - G_A = \Delta H - T\Delta S = (H_B - H_A) - T(S_B - S_A)$) is positive below a temperature named T^* and negative above it. When $T = T^*$ ($\Delta G = 0$), the following relationship is verified:

$$\Delta H = T^* \Delta S \quad \text{Eq. I.14}$$

According to the ideal solution model, we assume that A and B states are mixed without any interaction. If N is the total number of molecules, then $N_A = x_A \cdot N = x \cdot N$ is the number of molecules in the A state, while $N_B = x_B \cdot N = (1-x) \cdot N$ is the number of molecules in the B state. In statistical thermodynamics, the Gibbs energy of the system can be written:

$$G = N_A G_A + N_B G_B + G_{mix} + I \quad \text{Eq. I.15}$$

where, I is the intermolecular interaction term, that is neglected in the first approximation, G_A and G_B are the molar Gibbs energy for molecules in A and B states, whereas the G_{mix} is the energy of the mixture:

$$G_{mix} = -TS_{mix} = Nk_B T [x \ln x + (1 - x) \ln(1 - x)] \quad \text{Eq. I.16}$$

hence:

$$G = xN(H_A - k_B T \ln g_A) + (1-x)N(H_B - k_B T \ln g_B) + Nk_B T [x \ln x + (1-x) \ln(1-x)] \quad \text{Eq. I.17}$$

This relationship allows describing the Gibbs energy for each molecule, g_N , as following:

$$g_N = \frac{G}{N} = x \left[\Delta H - k_B T \ln \frac{g_A}{g_B} \right] + k_B T [x \ln x + (1-x) \ln(1-x)] + G_B \quad \text{Eq. I.18}$$

Introducing the degeneracy, $a = \ln \left(\frac{g_A}{g_B} \right)$:

$$g_N = \frac{G}{N} = x [\Delta H - k_B T a] + k_B T [x \ln x + (1-x) \ln(1-x)] + G_B = g'_N(x) + G_B \quad \text{Eq. I.19}$$

The condition for equilibrium requires

$$\left(\frac{\partial g'_N}{\partial x} \right)_{T,N} = 0 \quad \text{Eq. I.20}$$

as G_B is a constant. So we get:

$$\left(\frac{\partial g'_N}{\partial x} \right)_{T,N} = \Delta H - k_B T a + k_B T \ln \frac{x_{min}}{1-x_{min}} = 0 \quad \text{Eq. I.21}$$

The equation can be rearranged in the form of

$$\frac{1-x_{min}}{x_{min}} = \exp \left(\frac{\Delta H}{k_B T} - a \right) \quad \text{Eq. I.22}$$

and:

$$x_{min} = \frac{1}{1 + \exp \left(\frac{\Delta H}{k_B T} - a \right)} \quad \text{Eq. I.23}$$

For $T = T^*$, $x_A = x_B = x^* = 0.5$ and thus $\ln \frac{x^*}{1-x^*} = 0$. Then, $\Delta H - k_B T^* \cdot a = 0$ and $a = \frac{\Delta H}{k_B T^*}$.

The expression I.23 changes in:

$$x_{min} = \frac{1}{1 + \exp \left(\frac{\Delta H_H L}{k_B} \left(\frac{1}{T} - \frac{1}{T^*} \right) \right)} = \frac{1}{1 + \exp \left(a \left(\frac{T^*}{T} - 1 \right) \right)} \quad \text{Eq. I.24}$$

or

$$\frac{T}{T^*} = \frac{a}{a + \ln \frac{1-x_{min}}{x_{min}}} \quad \text{Eq. I.25}$$

This allows plotting of the $\frac{T}{T^*} = f(x_{min})$ dependence (Figure I-13), where $T^* = \frac{\Delta H}{k_B \cdot a}$.

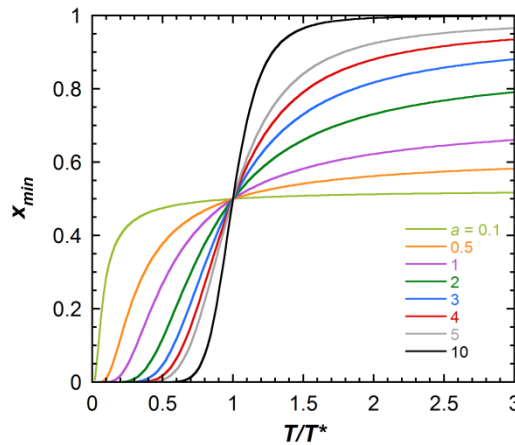


Figure I-13. Temperature dependence of the paramagnetic molar fraction x_{min} for different values of degeneracy, a , in ideal solution model.

Whatever is the value of a , the function x_{min} increases when T/T^* increases. This model predicts that at low temperature ($T/T^* \ll 1$), the system is in B state, so $x_{min} = 0$. We can observe that all curves pass through a common point, $T/T^* = 1$, and $x_{min} = 0.5$. So we can conclude that T^* is a characteristic temperature of the system. At this point, the system contains 50 % of molecules in state A and 50 % of molecules in state B. Note that in the literature, T^* is often noted $T_{1/2}$ to reflect the composition of the system.

Now let's consider a real case, for example a couple of Fe and Co ions, both in an octahedral environment. The paramagnetic state (A) consists of an Fe^{III} LS ion ($S = 1/2$, 2T_g spectroscopic term, so the spin degeneracy is 2 and the orbital degeneracy, $2L + 1$, is 3) and a Co^{II} HS ion ($S = 3/2$, 4T_g , spin degeneracy is 4, and the orbital degeneracy is 3). The diamagnetic state (B) consists of Fe^{II} LS ($S = 0$) and Co^{III} LS ($S = 0$) ions that are both corresponding to the 1A_g spectroscopic term for which the spin degeneracy is 1 and the orbital degeneracy also 1. So $g_{para} = g_A = (2 \times 3) \times (4 \times 3)$, $g_{dia} = g_B = (1 \times 1) \times (1 \times 1)$ or $g = 72$, which gives $a = \ln 72 = 4.28$. According to the simulation plot in Figure I-13 the most similar case is for $a = 4$, where x_{min} tends to 0.90 at $T/T^* > 2$. In real systems, the limit of x is, indeed, very close to 1. The entropy change in {FeCo}-based ET systems can be experimentally measured by calorimetric methods or deduced from optical and/or magnetic measurements, thus the value of a could be estimated between 6.0 and 7.1.^{55b,c,g} This shows that in real complexes not only the electronic contributions to the degeneracy are present, but also the vibrational contributions for paramagnetic and diamagnetic states that are different, because of different geometry in both states.

In a solid phase, in the crystalline lattice, the ET is directly influenced by intermolecular interactions (mostly of elastic origin). They play an important role in the macroscopic properties of the systems. The solution model called Slitcher-Drickamer,⁶⁰ assumes that the interaction energy is responsible for the cooperative effects and the interaction term, neglected in Eq. I.15, is defined as:

$$I(x) = Wx(1 - x) \quad \text{Eq. I.26}$$

where W is the intermolecular interaction parameter (in units of energy) independent of temperature. Note that $I(x)$ is a simple exchange term $Wx(1 - x) = Wx_Ax_B$ similar to a magnetic spin Hamiltonian - $H = J\vec{S}_1\vec{S}_2$. Insertion of this term in the molar Gibbs energy gives:

$$G = xN(H_A - k_B T \ln g_A) + (1 - x)N(H_B - k_B T \ln g_B) + \\ + Nk_B T [x \ln x + (1 - x) \ln(1 - x)] + Wx(1 - x) \quad \text{Eq. I.27}$$

then:

$$g'_N(x) = x[\Delta H - k_B T a] + k_B T [x \ln x + (1 - x) \ln(1 - x)] + Wx(1 - x) \quad \text{Eq. I.28}$$

and from the condition of equilibrium (Eq. I.20):

$$\Delta H - k_B T a + k_B T \ln \frac{x_{min}}{1 - x_{min}} + W(1 - 2x_{min}) = 0 \quad \text{Eq. I.29}$$

or

$$k_B T = \frac{\Delta H + W(1 - 2x_{min})}{a + \ln \frac{1 - x_{min}}{x_{min}}} \quad \text{Eq. I.30}$$

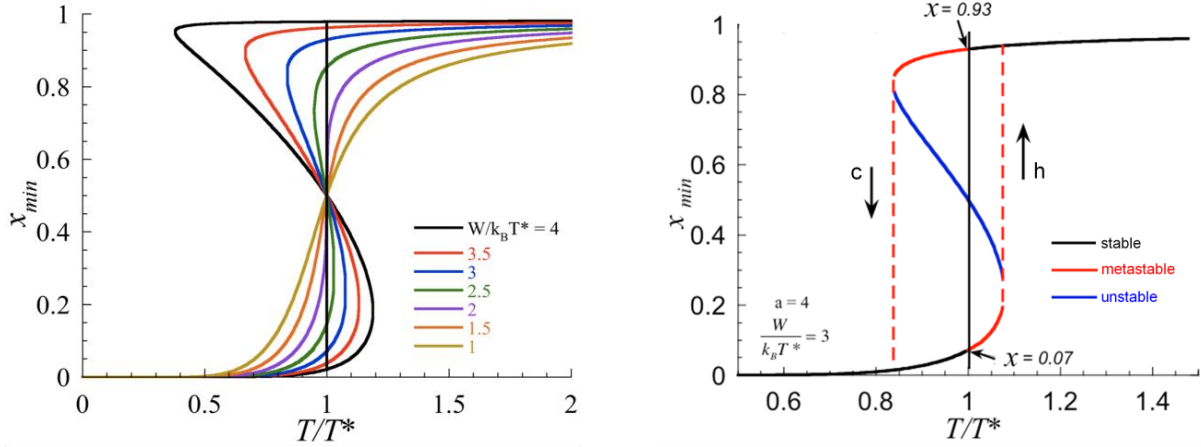


Figure I-14. (left) Temperature dependence of the paramagnetic molar fraction x for different values of $W/(k_B T^*)$ at fixed $a = 4$, in a regular solution model. (right) Thermal hysteresis when $a = 4$ and $W/(k_B T^*) = 3$, c – cooling mode, h – heating mode.

For given values of a , $\frac{T}{T^*} = f(x_{min})$ can be plotted (Figure I-14) and the function is defined by:

$$\frac{T}{T^*} = \frac{a + \frac{W}{k_B T^*} (1 - 2x_{min})}{a + \ln \frac{1 - x_{min}}{x_{min}}} \quad \text{Eq. I.31}$$

As shown in Figure I-14 (left), the inter-molecular interaction (W) plays an important role to define the stable state depending on the temperature. Therefore, three cases can be discussed:

- $W/(k_B T^*) < 2$, so x_{min} is increasing when T/T^* increases, and the corresponding curves are more and more steep for higher values of $W/(k_B T^*)$, but possess the same inflection point given by $T/T^* = 1$ and $x_{min} = 0.5$. This phenomenon is a conversion.
- $W/(k_B T^*) = 2$, there is a vertical gap of x_{min} at $T/T^* = 1$, and the corresponding curve is abrupt. This gives a first order transition at $T = T^* = T_C$ and the spin transition temperature is given by the relationship $W/(k_B T^*) = T_C$. This phenomenon is a transition at the critical point.
- $W/(k_B T^*) > 2$ the curve has an “S” shape, and for $T/T^* = 1$, not only the $x_{min} = 0.5$ solution is possible, but the Gibbs energy adopts two other local minimum values. A transition corresponding to a first order transition is observed then.

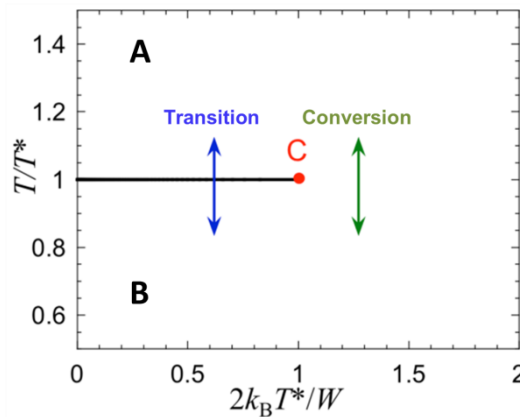


Figure I-15. Phase diagram for the regular solution model with $W > 0$ in the plane $(2k_B T^*/W, T/T^*)$.

In the last case, a first order transition is associated with a thermal hysteresis (Figure I-14 right). The blue branch of the curve corresponds to unstable points, but in fact the system describes a hysteresis, drawn in dashed lines in Figure I-14 (right). It is noteworthy to mention that, in the general case, T^* is not at the center of the thermal hysteresis. Note also that the hysteresis width does not depend on the thermodynamics but on kinetic criteria and thus on the experimental scanning rate of the temperature.

From this analysis, we can construct a phase diagram that describes the system at any temperature and any value of W . The phase diagram consists in a line of first order phase transition at $\frac{T}{T^*} = 1$ that ends with a critical point, C (red point from Figure I-15). From this phase diagram, we can predict if real system will present a conversion or a transition. If $2k_B T^*/W \leq 1$, the system crosses the transition line (blue arrow from Figure I-15) and a transition will be observed; otherwise if $2k_B T^*/W > 1$, the system is beyond the critical point (green arrow from Figure I-15) and a conversion will be observed.

In this section, the thermal ET process could be described by the binary solution model. This simple approach tells us that the interactions between the motifs responsible for the interconversion phenomena are crucial to exhibit a transition, and therefore to display bistability.

I.2. Soft hybrid molecule-based magnetic systems

Recent technological breakthroughs and the need for new functions generate an enormous demand for novel materials. Many of the well-established materials, such as metals, ceramics or plastics cannot fulfill all technological desires for the various new applications. Looking ahead, scientists must create sophisticated, miniaturized, recyclable, environmentally friendly, energy efficient, reliable, and inexpensive materials and systems. In this respect, molecular chemistry provides unique possibilities, as it allows us to design novel hybrid materials that combine in the same system several physical properties which are difficult or impossible to achieve with inorganic or solid state chemistry.

Nowadays, one of the great challenges in the molecular magnetism field is to process these compounds into technologically sustainable materials and thus to push them towards possible applications. Among interesting molecular magnetic systems, materials suitable for surface deposition,^{61,62} and nanoparticles,^{63,64} have attracted particular attention with respect to possible applications. In order to design new generation of systems, hybrid soft materials are a strategy of choice as they can be easily processed and can show multiple-properties such as improved thermal/chemical stability, self-organizational properties, enhanced the solubility, as well as possible synergetic effects. One of the possible ways towards the elaboration of such hybrid magnetic materials is the functionalization of organic ligands of known molecular magnetic materials with various groups possessing or inducing mesogenic (liquid crystalline) behavior or improve the solubility.

I.2.1. Liquid crystalline magnetic molecular hybrids

Liquid crystals (LC) are examples of soft, molecular self-assemblies that exquisitely combine order and fluidity. These systems within components self-organize into a wide diversity of mobile and long-range

ordered periodic structures.^{65,66} Moreover, LC assemblies can easily form thin films, which are intrinsically defect-tolerant because positioning errors are corrected automatically during the process of self-organization. Their dynamic nature and stimuli responsiveness abilities further render them interesting for applications in modern technologies and particularly in organic electronics.⁶⁷ The formation of ordered yet fluid LC mesophases may thus be sought as a first step in the route to controlling the organization of molecule-based magnetic materials into low-dimensional supramolecular orders for their ultimate incorporation within functional macroscopic devices.

I.2.1.1. Liquid crystalline phases - generalities

Liquid crystals have been for a long time the subject of scientific interest since the discovery of this fourth state of matter in addition to the known states of solid, liquid, and gas. In the crystalline solid state (Figure I-16 left) the arrangement of molecules is ordered, with a regularly repeating pattern in all directions of space. The molecules are held in fixed positions by intermolecular forces. In the liquid state, the motion overcomes the intermolecular forces that maintain a crystalline state, and the molecules move into random positions, without pattern in location or orientation (Figure I-16 right). The liquid crystal is an intermediate state between solid and liquid state. Molecules in a liquid-crystalline state are free to move around as in an isotropic liquid, however, they tend to orient in a preferred direction with one another, breaking the isotropy of the physical properties of the system. The arrangement of molecules in one of the liquid crystalline phases (i.e. smectic A) is represented in Figure I-16 (center). In this state, the molecules are still in layers, but within each layer they are arranged in random positions, although they remain more or less parallel to each other. Within layers, the molecules can slide around each other, and the layers can slide over one another. This molecular mobility produces the fluidity characteristic of a liquid.

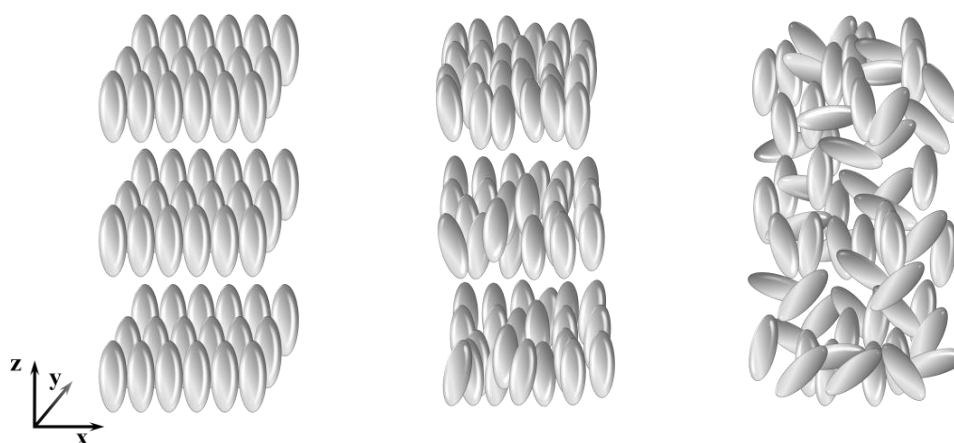


Figure I-16. (left) Schematic drawing of a crystalline, (center) liquid crystalline smectic and (right) liquid state.

In order to exhibit liquid crystallinity, the molecule must be geometrically anisotropic. Liquid crystals are anisotropic meaning that their physical properties are not identical in all directions. Therefore molecules with two antagonist parts (a rigid core and flexible ends) can form LC phases. To generate a LC a thermally induced microsegregation between the flexible chains and rigid cores is necessary.

Generally, there are three classes of LCs: lyotropic, thermotropic and amphitropic.⁶⁸ The thermotropic liquid crystals exhibit liquid-crystalline mesophases on melting from the crystal phase or cooling from the isotropic liquid, whereas the lyotropic materials exhibit liquid-crystalline mesophases when mixed with a particular solvent. The amphitropic LCs are compounds that exhibit both lyotropic and thermotropic behaviors.

The transition between a solid state and a LC state is called melting point, and it corresponds to the melting of the flexible part; the transition between the mesophase and the liquid state is called isotropic or clearing point, induced by the loss of cohesion between the molecules. When a liquid crystal melts from a solid, it exhibits one or more thermodynamically stable intermediate states called mesophases. The mesophase is called an enantiotropic when a material displays a mesophase both on cooling and heating. However, when the mesophase is solely displayed on cooling from the isotropic liquid, and below the melting point of the material, the phase is called monotropic.

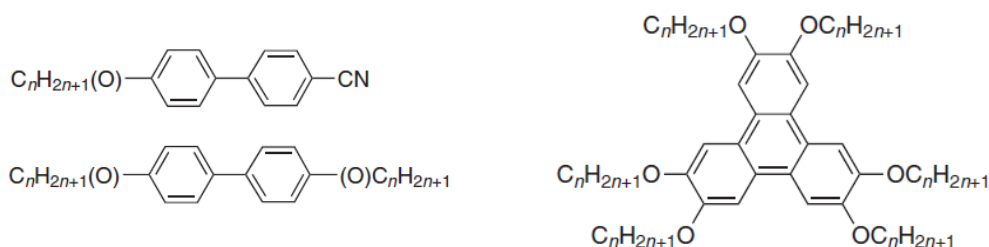


Figure I-17. Examples of calamitic (left) and discotic (right) molecules.

The organization of a mesophase is induced by the geometry of the molecules and their intermolecular interactions. The shape of the molecules can be described by two models: the disk-like molecules, called discotic and rod-like molecules, called calamitic (Figure I-17).

The nematic phase (“nêmatos” in Greek means wire, referring to its stringy texture (Schlieren) seen in microscope under polarized light) is the less ordered mesophase and is characterized by molecules that have a tendency to align parallel to each other with an organization according to a preferred direction vector \vec{n} parallel to the longitudinal axis (Figure I-18).

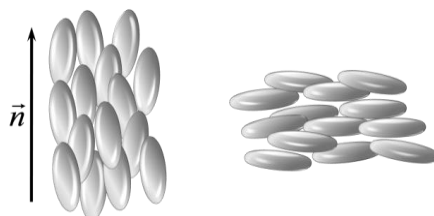


Figure I-18. Schematic representation of a nematic phase formed by calamitic or rod-like molecules (left) and discotic or disc-like molecules (right).

Smectic phases (“smectos” in Greek means soap, because the first liquid crystals of this type revealed properties similar to a soap) are formed by molecules that are arranged in layers with a positional order in addition to the orientation order found in the nematic phases. There are many smectic phases $Sm_{A,B,C,E,F,I,J,K}$, with subcategories like Sm_{A1} for monolayer and Sm_{A2} for bilayer etc.⁶⁵ Two types of smectic phases are

depicted in Figure I-19. The smectic A (Sm_A) is the least ordered smectic phase. It possesses partial translational ordering in addition to the one-dimensional orientational order of the nematic phase. The longitudinal axis of the molecules is on average perpendicular to the layer plane (Figure I-19 left). The molecules of smectic C phase (Sm_C) have an organization similar to the Sm_A , but the longitudinal axis of the molecules tilt with respect to the layer plane (Figure I-19 right). In both cases, there is no positional order within the layers.

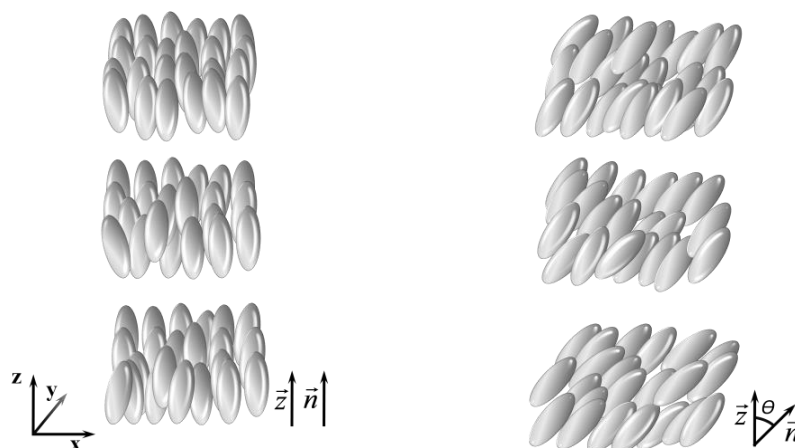


Figure I-19. Schematic representation of a smectic A phase (Sm_A) (left), and a smectic C (Sm_C) phase (right).

The columnar mesophases are formed by stacking molecules, generally disc-shaped. Structure of these mesophases is described by an arrangement of molecules in two dimensions. Flat-shaped discotic molecules are stacked one-dimensionally, forming columns. The structural order and the ways of packing of the columns define hexagonal (Col_h), rectangular (Col_r) and oblique (Col_o) columnar phases (Figure I-20).

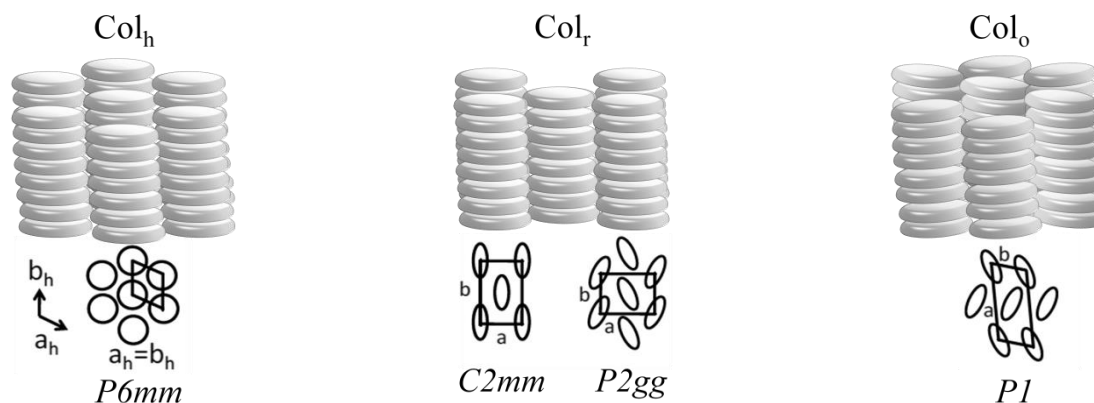


Figure I-20. Schematic representation of (left) columnar hexagonal (Col_h), (center) columnar rectangular (Col_r) and (right) columnar oblique (Col_o) phases, a side view (top) and phase cuts (bottom) are shown.

Hexagonal columnar phases are composed of disc-shaped molecules and the system has C_6 , C_3 , C_2 axes which define a hexagonal system (Figure I-20 left). The rectangular columnar phases are composed of molecules in the shape of ellipses. These molecules have lost the C_6 and/or C_3 axis of the hexagonal systems. The molecules contain only elliptical axes C_2 and symmetry planes (Figure I-20 middle).

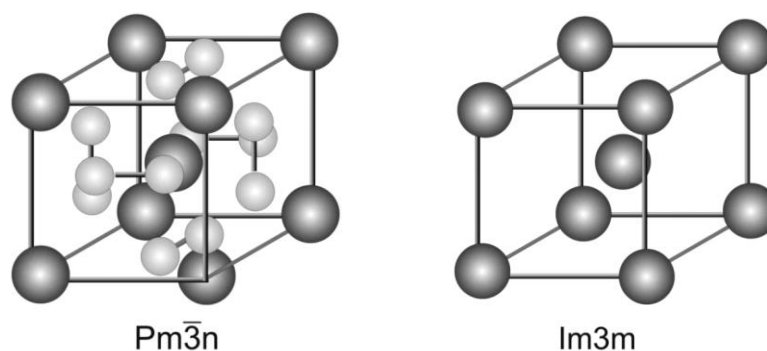


Figure I-21. Cubic lattices found for micellar cubic phases.^{70b}

Cubic mesophases (or smectic D, as they were also called^{69a}) are three dimensionally ordered supramolecular assemblies with multi-continuous⁶⁹ or a discrete micellar structures,⁷⁰ depending on the molecular self-organization within the cubic cell.⁷¹ Mesogens showing cubic phases are a special type of liquid crystals as their physical properties are not anisotropic due to the cubic symmetry. The cubic phases are very viscous, their kinetics of formation is very slow. The detection of cubic phases is complicated, in particular on cooling from the isotropic liquid phase, because of its optically isotropic (black) defect texture when viewed between crossed polarizers. The method of choice for the characterization of cubic phases is the X-ray diffraction. However, for lyotropic phases, the cubic structure is well established and two distinct molecular organizations of cubic symmetry have been described. Therefore, the lyotropic case has been used as a model for thermotropic cubic phases. In their simplest form the molecules organize into micellar assemblies, mostly, with lattice symmetries with the $Pn\bar{3}m$ and $Im\bar{3}m$ space groups (Figure I-21).^{70b} Other, less evident cubic organizations are the bicontinuous structures of $Ia\bar{3}d$, $Im\bar{3}m$ and $Pn\bar{3}m$ symmetries. The latter cubic phases can be imagined as two interwoven networks as shown in Figure I-22.^{69b} Even tricontinuous networks have been suggested for compounds containing three incompatible parts.^{69b} However, thermotropic cubic phases are not so well understood, mainly due to their rare observation.

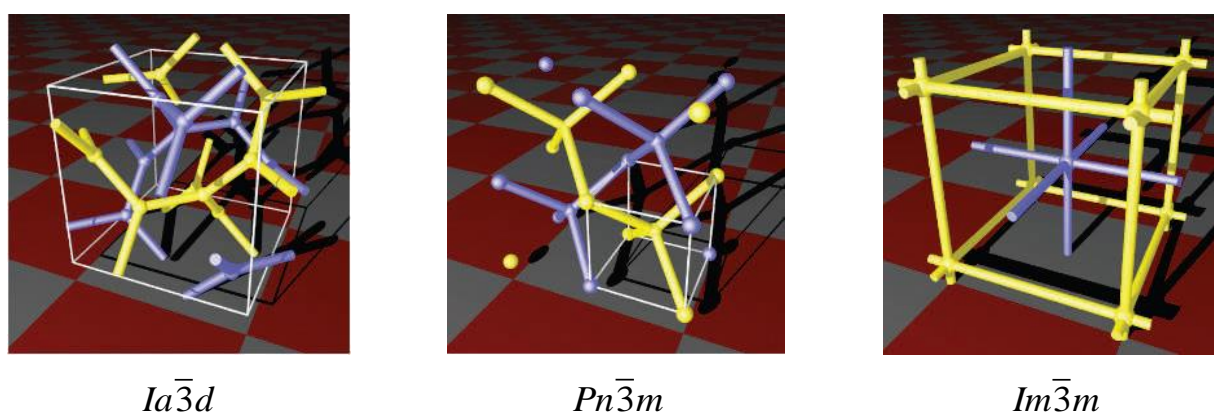


Figure I-22. Network models of the three known bicontinuous cubic phases in soft matter: $Ia\bar{3}d$ (left); $Pn\bar{3}m$ (center); $Im\bar{3}m$ (right). The two interpenetrating networks are colored blue and yellow. White lines delineate the unit cell.^{69b}

I.2.1.2. Magnetic molecule-based mesogens

The interest for novel materials with dual properties derived from metals (magnetism, optics, conductivity, color) and liquid crystals (fluidity, easy processability, order) in the late 70s was at the origin

of the metallomesogen (metal-containing liquid crystals) research.⁷² One of the objectives of this kind of combination was to obtain paramagnetic liquid crystals thanks to the presence of metal ions with unpaired electrons. It is well known that the orientation of diamagnetic, mainly organic, liquid crystalline phases can be achieved with strong magnetic or electric fields. For an eventual application in a small device, the magnetic field applied to align the mesophase should be small enough, but the threshold field for the alignment of diamagnetic liquid crystals is too high for this. Therefore, metal ions with unpaired electrons have been incorporated into liquid crystals. The design of liquid-crystalline materials containing metal ions is not a facile process. Nonetheless, over the years a wide range of mesogenic systems with improved physical properties via incorporation of different metal ions has been designed. As a result, an assortment of liquid-crystalline phases (both thermotropic and lyotropic) can be accessed with this approach.⁷²

On the other hand, the functionalization of molecule-based magnetic materials with mesogenic promoters presents a great interest in the coordination chemistry community. The self-assembling property of the LCs and the orientational behavior may affect significantly the magnetic and, generally, physical properties of molecular complexes. Particularly when the molecular materials are oriented and organized in a suitable way, their properties can be tuned or even enhanced via collective and/or synergetic effects.

In the metallomesogen design strategy described above, the main component was the mesogen while the metal ions were incorporated in it. In contrast, the development of multifunctional molecular magnetic complexes would require well-designed functionalized ligands that can coordinate without altering the magnetic core and induce mesogenic behaviors. This line of research is quite new and there are few examples of new coordination compounds exhibiting interesting magnetic phenomena combined with mesogenic properties induced by a rational ligand functionalization.

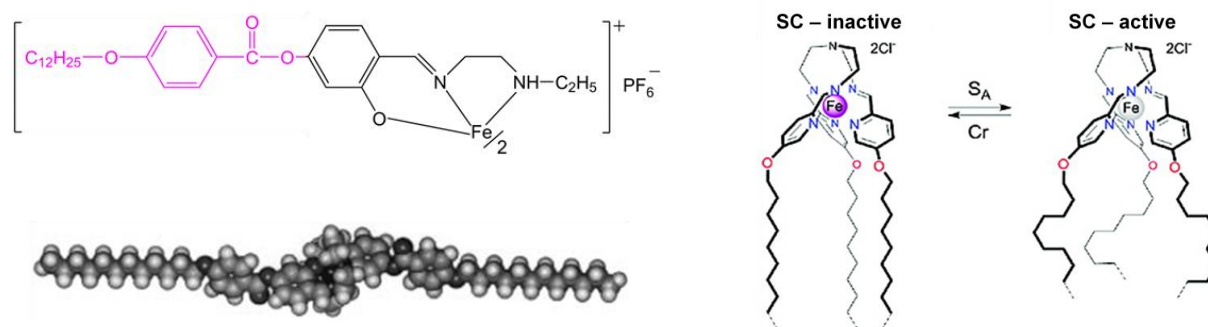


Figure I-23. (left) The chemical formula the molecular hybrid Fe(III)-based complex (top) that shows both LC and SC behaviors, the applied functionalization is shown in pink, the simulation of the molecular structure (bottom) is showed to emphasize the calamitic shape of the hybrid molecule.⁷³ (right) Schematic representation of structural changes associated with the Cr \leftrightarrow LC transition that triggers the spin state crossover in $[\text{Fe}(\text{C}_n\text{-trenR})](\text{Cl})_2$.⁷⁶

Firstly, this approach has received much attention in the case of spin crossover (SC) compounds especially because the SC phenomenon can occur around room temperature and therefore these materials are promising candidates for molecule-based optical or magnetic data storage devices. Indeed, when SC materials are modified by mesogenic ligands that show transition to a LC phase near the room temperature, there are possibilities to combine the two properties (SC and LC) and consequently to induce synergetic effects. The first example of a molecular hybrid system wherein LC and SC behaviors coexist was reported by Galyametdinov et al.⁷³ In this work, the ligand of a known Fe(III) complex⁷⁴ was modified with

dodecyloxybenzyloxy substituents (Figure I-23 left). The final complex exhibited a smectic phase above 388 K while the SC was detected below this temperature, so no synergy between these two properties of the same molecule was observed. A similar behavior was later reported for the first examples of mononuclear Fe(II) or Co(II)-based SC complex with LC phases.⁷⁵

Gaspar et al.^{76,77} developed metallomesogenic systems in which the SC and the mesophase formation occur at similar temperatures. This result suggested that the structural change associated with crystal-to-liquid crystal transition triggered the SC phenomenon (Figure I-23 right). There are also systems where both transitions coexist in the same temperature region but are not coupled, so liquid crystal phase transition is not the driving force of the spin state transition.⁷⁸ An eventual goal in the area of spin crossover metallomesogens is the switching/controlling of the spin state using the sensitivity of liquid crystalline phases to external electric and/or magnetic fields.

Several research groups have used the functionalization strategy to create hybrid systems based on the one-dimensional Fe(II)/triazole coordination polymers of general formula $[\text{Fe}(\text{R}^i\text{Trz})_3](\text{A})_2$ (R^i = 4-mesogenic substituent-1,2,4-triazole, A = anion, Figure I-24). Fujigaya et al.^{78a} and Gaspar et al.⁷⁹ modified the triazole ligand with mesogenic bis-alkyloxybenzylformylamino substituents and showed coupled LC/SC behaviors. Their studies suggested the existence of mesophases, including columnar phase, although the characteristic optical textures of these phases have not been reported. Unfortunately, the modification of ligands in these systems also induced a very gradual and incomplete SC.

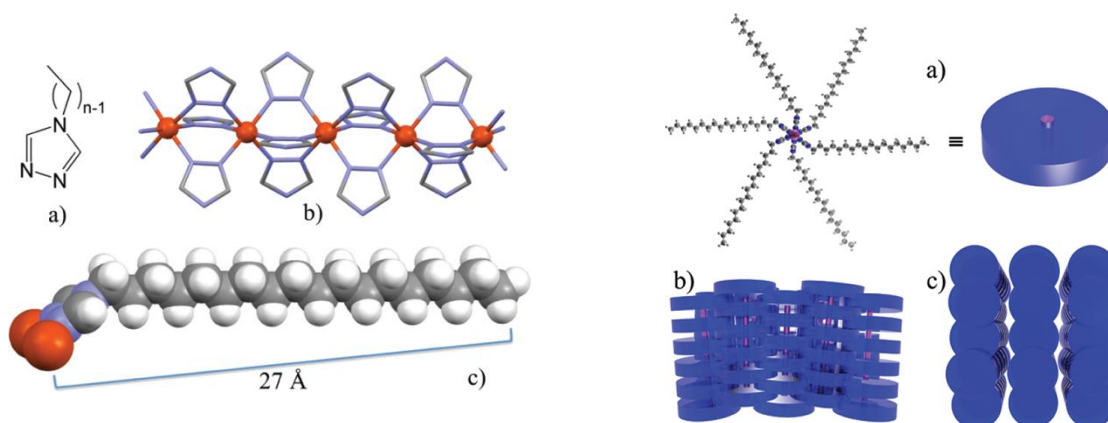


Figure I-24. (left) Representation of (a) 4-N-alkyl-1,2,4-triazole ligands, (b) the 1D chain formed through triple N1–N2 bridges upon coordination to Fe(II) or Zn(II) ions (shown as orange balls, nitrogen and carbon are, respectively, depicted as blue and gray), and (c) the space fill idealized conformation of one of these bridges with fully-stretched decyl substituent on the triazole ring. Schematic representation of (a) a hexacatenar moiety that would form repetitive triple 4-octadecyl-1,2,4-triazole bridges with fully-stretched alkyl arms in eclipsed conformation and (b and c) lamellar packing of the resulting rods with interdigitation, respectively, perpendicular and parallel to the average rod axis.⁸¹

The M^3 group at CRPP has been interested in this type of system for more than ten years. Thus, different modifications of the triazole ligand and/or the counter-anions with or without long linear alkyl chains were studied with the aim to induce gel or LC properties.^{80,81} In many cases cooperative and complete SC was observed near room temperature, while liquid-crystalline domains were unfortunately found to form at higher temperatures. Typical optical textures of lamellar phases were observed in the case of diamagnetic materials $[\text{Zn}^{\text{II}}(\text{R}^i\text{Trz})_3](\text{A})_2$, which are thermally more stable than their Fe(II) analogues. In the latter systems, mesophases were present, but the appearance of oxidation/degradation processes occurring at high

temperature, did not allow a detailed characterization of these systems. Recently, Hayami et al.^{78b} detected the presence of disordered columnar phases by functionalizing the triazole ligand with branched-alkyl chains. However, a complete investigation of thermotropic properties was not reported.

Practical applications of SMMs as molecular-scale units for high density information storage or “qubits” for quantum computation^{9,82} require the imaging, probing, and eventually manipulating of individual molecules. Regarding this aspect, it is a challenging subject for coordination chemists to obtain SMMs functionalized by mesogenic groups as liquid crystal state without changing the magnetic properties of the material. The first example was described in 2008 by Terazzi et al.^{83a} Mesomorphic dodecanuclear manganese complexes $[\text{Mn}_{12}\text{O}_{12}(\text{L}^i)_6(\text{H}_2\text{O})_4]$ were obtained by the substitution of the 16 acetate groups with functionalized gallate moieties, with methoxy (L^1), dodecyloxy (L^2), or cyanobiphenyloxyundecyloxy (L^3) groups (Figure I-25). Depending on the chosen benzoate, 1D (smectic, $\text{Mn}_{12}\text{-L}^3$, Figure I-26 left) or 3D (body centred cubic, $\text{Mn}_{12}\text{-L}^2$) organized mesophases that are stable up to 423 K were induced. The integrity of the complexes was preserved upon the exchange reaction as pointed out by the molecular structure of the model complex ($\text{Mn}_{12}\text{-L}^1$). The magnetic properties are also preserved upon functionalization (Figure I-26 right).

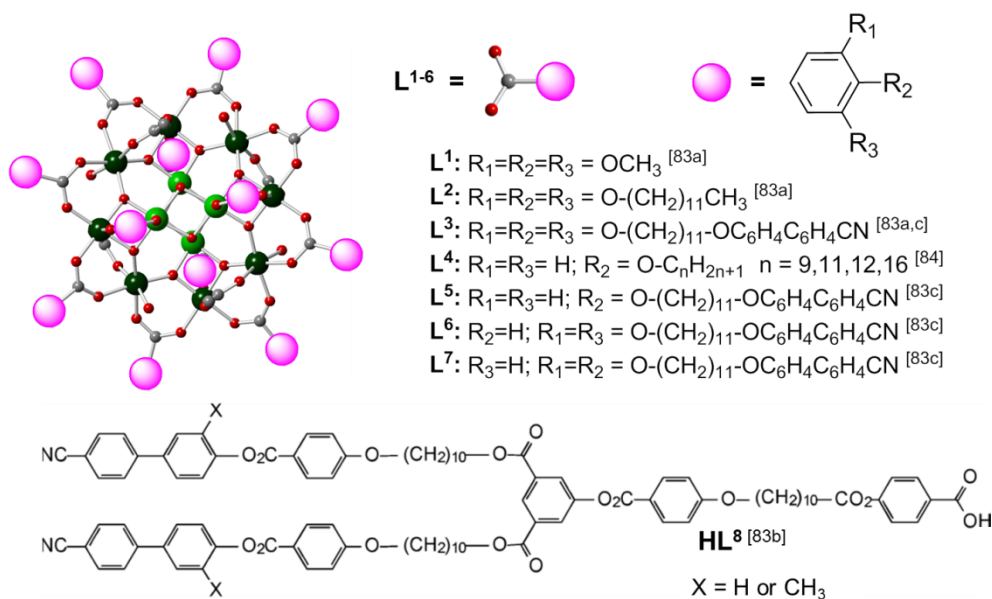


Figure I-25. Schematic representation of mesomorphic $[\text{Mn}_{12}\text{O}_{12}(\text{L}^i)(\text{H}_2\text{O})_4]$ complexes and chemical structure of mesogenic ligands used in previous reports.^{83,84} Color Scheme Mn(IV) green, Mn(III) dark green, O red, C grey, functionalized part of the ligand is shown in pink.

With the aim to design Mn_{12} -based LC systems with a reduced globular shape that preferentially leads to cubic phases, D. Siretanu, during her PhD thesis (CRPP, 2008 – 2011), employed the same strategy by using a series of *p*-*n*-alkoxybenzoic acids (i.e. nonyloxy-, decyloxy-, dodecyloxy- and hexadecyloxybenzoic acids, Figure I-25).⁸⁴ Even though all exploited functionalized *p*-*n*-alkoxybenzoic acids are well-known for their liquid crystalline properties⁸⁵ the series of prepared functionalized Mn_{12} -based complexes did not show any mesomorphic behaviour.

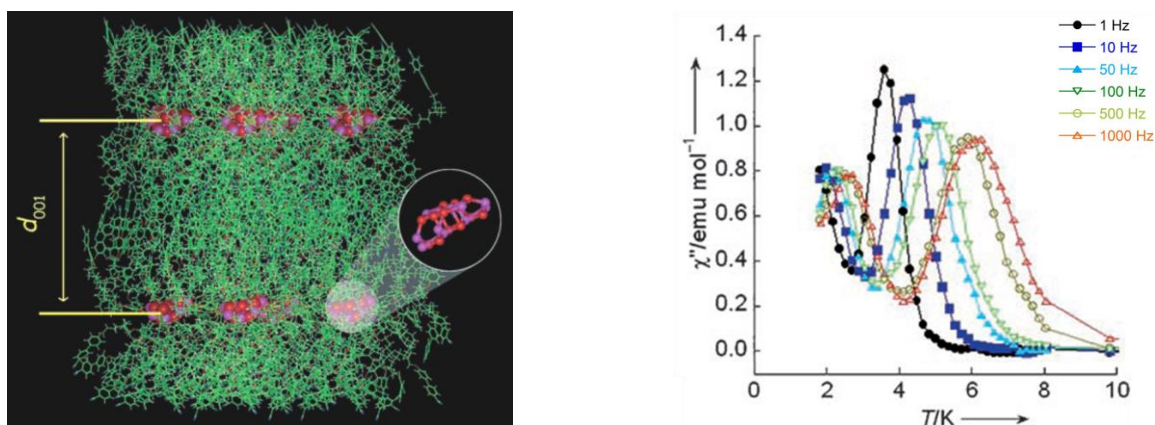


Figure I-26. (left) Side view of the lamellar packing of cyanobiphenyl groups and Mn_{12} complexes in the smectic layer. (right) Unaltered magnetic behaviour of SMM: temperature dependence of out-of-phase ac susceptibility, χ'' .^{83a}

In very recent reports, Terazzi et al.^{83b,c} have used benzoate derivatives, mono- or di-substituted with cyanobiphenyloxyundecyl chains ($L^{3,5-7}$, Figure I-25), as well as carboxylate-based ligands with two-branched dendritic structures (L^8 , Figure I-25) to prepare another series of LC Mn_{12} -based systems. In these systems, the complexes self-organize, slightly above room temperature, into smectic-like bilayers with short-ranged 2D arrangement of the magnetic units embedded in the aliphatic sublayer.

These pioneering results highlight the great potential of this hybrid approach to increase the thermal stability of Mn_{12} -based complexes without significantly affecting the magnetic properties (conservation of SMM behavior). However, tailoring precisely the mesomorphic behavior of these bulky complexes in order to control their organization is not an easy task and remains a considerable challenge.

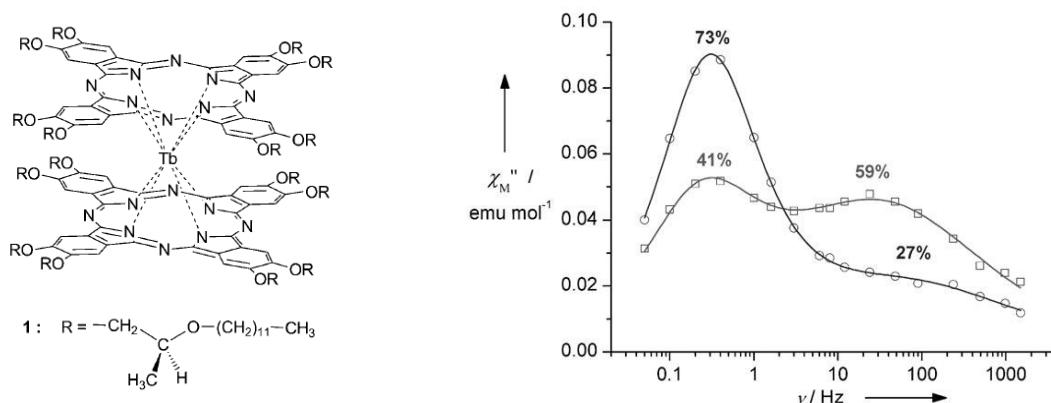


Figure I-27. (left) The structure of the functionalized Tb double-decker phthalocyanine complex. (right) The frequency dependence of the out-of-phase (χ'') susceptibility at 25 K for the quenched disordered phase (open squares) and for the crystalline phase (open circles).⁸⁶

Besides Mn_{12} -based systems the possibility to induce LC phases in a double-decker terbium phthalocyanine complex (Figure I-27 left) with chiral (*S*)-2-(dodecyloxy)propoxy groups was reported.⁸⁶ The functionalized complex exhibits hexagonal columnar mesophase at room temperature, while at low temperature it is an SMM. Moreover, this complex showed the possibility to reversibly control its magnetic properties by simple thermal treatment of the studied sample. Thus the thermally trapped disordered phase (prepared by a very rapid cooling from 333 to 150 K) and the ordered crystalline state (slowly cooled from isotropic point) show different temperature dependences of the in-phase (χ') and out-of-phase (χ'') susceptibilities measured at several frequencies (Figure I-27 left). The observed differences consisted in

different ratios between slowly and fast relaxing species in the disordered phase and in the crystalline one. This system is one of the first examples of lanthanide double-decker complex showing two different relaxation processes and it is the only system in which the ratio between these responses has been shown to be reversibly modified by simple thermal treatments.

I.2.2. Other soft magnetic systems

Gels. An alternative way towards processability of materials is their incorporation into soft-matter phases, such as gels. Hydrogels and organogels result from the self-assembly of small molecules in water or organic liquids through specific noncovalent interactions.

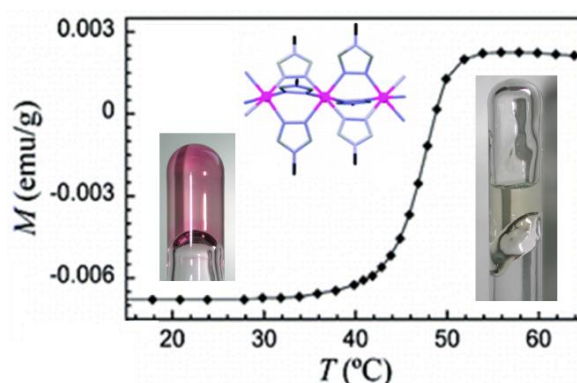


Figure I-28. Thermal dependence of the magnetization for a 3 wt% $[\text{Fe}^{\text{II}}(\text{C}_{18}\text{trz})_3](\text{ptol})_2 \cdot 2\text{H}_2\text{O}/\text{decane}$ (65%)- CHCl_3 (35%) gel. Inset: pictures corresponding to low spin gel (pink) and high spin melting gel (white), schematic representation of polymeric structure of $[\text{Fe}^{\text{II}}(\text{C}_{18}\text{trz})_3](\text{ptol})_2 \cdot 2\text{H}_2\text{O}$.^{80b}

Among the macromolecular gelators, $[\text{M}(\text{R-trz})_3]_n$ (R-trz = 4-substituted- 1,2,4-triazole) polymeric system presents a great interest. Kuroiwa et al. reported a Co^{II} /triazole system, where R is $\text{C}_{16}\text{H}_{33}$ or $\text{C}_{12}\text{H}_{25}\text{OC}_3\text{H}_6$.⁸⁷ The conversion from solution (at 273 K) to gel (at 298 K) is followed by a colour change from white to green, respectively. This property has been attributed to the conversion of the octahedral complex of cobalt in solution into a tetrahedral polymeric aggregate upon gelation. Iron(II) triazole-based coordination macromolecules are able also to gelate alkane solvents or toluene while maintaining their spin crossover related optical and magnetic switching properties.^{80,88} The spin crossover gels are potentially useful for thermoreversible magneto-optical switches.

An attempt to form SMM containing physical gel was also reported.⁸⁹ Using a universal sol-gel approach, amorphous 3D coordination polymer gels were obtained via ligand substitution technique from $\text{Mn}_{12}\text{-OAc}$ and twelve different di- or tricarboxylic acids. Mn_{12} cores were used as nodes while polycarboxylic acids as bridges in construction of the 3D coordination polymer gels. The final materials exhibited extraordinary porosity, containing ca. 95 % solvent by mass, they adopt the shape of the vessel and could be easily processed into thin-film xerogels. However, no investigations of magnetic properties were made and the goal to create processable magnetic physical gels still remains a crucial challenge.

Soluble systems. Solubility in conventional solvents should facilitate fabrication of films and coatings of magnetic materials, or even liquid phase processing.

Ligand functionalization with lipophilic chains of an Fe^{III} SC complex, [Fe^{III}(sal₂-OR₂trien)] (sal = salicylaldehyde, trien = triethylenetetramine and R = C₆H₁₃, C₈H₁₇ or C₁₈H₃₇), led to a self-assembly of the complexes in solution, preserving the spin crossover behavior.⁹⁰ When the alkyl chains are long enough (R = C₁₈H₃₇), self-assembly of the complexes in solution forms discrete (microsize and submicrosize) aggregates. Compared to the original spin crossover system, the functionalization allowed to enhance the cooperativity, in an originally poorly cooperating spin crossover Fe^{III} complex, and to increase the SC characteristic temperature.

The substitution of acetate (OAc⁻) ligands in Mn₁₂-OAc complex with various fatty acids not only improves the solubility of this magnetic system in various organic media but also leads to self-assembling into ordered vesicular aggregations.⁹¹ The dynamic light scattering (DLS) investigations showed that the assemblies with a radius about 134 nm are present in chloroform. Whereas addition of methanol improves the stability of the assemblies, and spherical morphologies are thus obtained easily from an optimized mixed solvent (3 : 1 of chloroform : methanol in volume ratio). According to the authors of this report the formation of vesicular assemblies in various solvents is the first step on the route to organizing the Mn₁₂ complexes for their eventual ordered structures.

The presence or absence of solvate molecules and packing effects often restrain the clear observation of SC⁹² or ET properties.^{55f} Investigation of these phenomena in solution (where the crystal packing effects are excluded) becomes obvious; as it highlights the molecular nature of the observed phenomena and gives information of substituent effects.^{55f,g,92} Via a subtle functionalization with methyl groups of the bpy ligands in cyanido-bridged {[Tp*]Fe(CN)₃]₂[Co(bpy)₂]₂}(OTf)₂ square complex a new system was obtained, {[Tp*]Fe(CN)₃]₂[Co(diMebpy)₂]₂}(OTf)₂·H₂O·2DMF (where diMebpy = 4,4'-dimethyl-2,2'-bipyridine), that preserved magnetic and optical switching ability driven by thermally and photo-induced intramolecular ET in solid state. The new functionalized system showed the possibility to transfer the solid state properties of {Fe₂Co₂} complexes into a wide range of solvents.^{55g} Furthermore the electron transfer and the associated changes of the magnetic and optical properties could be modulated by the solvent nature (Figure I-12 right).

The solid state properties of SMMs are relatively well understood, while it is not the case for the solution state. However, solution studies of the molecular magnetization dynamics of SMMs are crucial,⁹³ as the evolution of the magnetic properties of these systems from the solid state via solution to a surface have to be understood before being exploited. Frozen solution studies of the dynamic susceptibility allow the quantification of the contributions from solid state crystal packing effects to the molecular magnetic properties.^{93a} Nevertheless, solubility limitation of the SMM complexes and their low stability in solution hinder so far a broad exploration of this trend of research.

Therefore improving the solubilization of magnetic systems may help not only to process the material but also to study its intrinsic properties.

Throughout the sections I.1 and I.2 of this chapter, the basic concepts concerning single-molecule magnets (SMMs), electron transfer (ET) systems and soft hybrid molecule-based magnetic materials were

presented. This basic information should help the reader to follow Chapters II - V that present the main results of this thesis.

I.3. Objectives of this research work

Even though the design of novel molecular magnetic materials and the study of their physical properties represent a major research interest in the field of molecular magnetism, it is also essential to devote a part of this effort to the shaping of existing molecular materials for future applications. Hybrid materials present high versatility in physico-chemical properties, as previously mentioned. Hybrids can be applied in many branches of materials science because they are simple to process and are amenable to design on the molecular scale.

The design of hybrid molecule-based magnetic systems via rational ligand functionalization is one of the main interests of the Molecular Materials and Magnetism research group at the Centre de Recherche Paul Pascal. The employed strategy consists in selection of known complexes from different magnetic classes and modification of their organic ligands with various functional groups known to induce liquid crystalline properties or, simply, improve the solubility. Although this approach may seem obvious, it is still relatively undeveloped and only a few research groups are currently exploring this strategy to create new molecule-based hybrid magnetic materials. The functionalization of organic ligands of known systems can help: (i) to isolate and protect the magnetic core by an organic shell in order to prevent interactions between objects; (ii) to orient, align, and organize magnetic units, thanks to self-organization of the liquid crystalline phase; (iii) to have fluidity and easy processability for shaping and further applications; (iv) to improve the solubility and thermal stability; and (v) to control or optimize the chemical or physical properties of the original object.

In this work, we aim to design and study the properties of new hybrid materials by using two molecular systems known to possess remarkable magnetic properties: (a) the dodecanuclear complex $[\text{Mn}_{12}\text{O}_{12}(\text{OAc})_{16}(\text{H}_2\text{O})_4]$ that is a part of the large family of single-molecule magnets (SMMs); and (b) the tetranuclear cyanido-bridged $\{\text{Fe}_2\text{Co}_2\}$ molecular squares, $\{[(\text{Tp}^*)\text{Fe}(\text{CN})_3]_2[\text{Co}(\text{bpy})_2]_2\}[\text{OTf}]_2$, that are categorized into the class of electron transfer complexes.

Chapter II is dedicated to functionalization of Mn_{12} -based SMMs towards hybrid liquid crystalline systems via two different approaches. To help the reader, additional information regarding the family of Mn_{12} -based SMMs is also presented in the beginning of the second chapter. Chapters III – V are focused on cyanido-bridged molecular squares that exhibit thermally or photo-induced ET. Thus, in Chapter III is discussed the possibility to modulate the structural and the ET properties in $\{\text{Fe}_2\text{Co}_2\}$ molecular squares via light irradiation or counter-anion exchange. The functionalization with long aliphatic chains and its effect over the properties of $\{\text{Fe}_2\text{Co}_2\}$ molecular squares in solid state and solutions are discussed in Chapter IV. While the effect of functionalization with strongly electron density donating methoxy group over the ET properties of $\{\text{Fe}_2\text{Co}_2\}$ molecular squares is investigated in Chapter V.

I.4. References

1. Miller, J. S.; Epstein, A. J. *Molecule-based Magnets: An Introduction*, in: Turnbull, M. M.; Sugimoto, T.; Thompson, L. K. (Eds) *Molecule-Based Magnetic Materials, ACS Symposium Series*, **1996**, 644, 1-13.
2. Coey, J. M. D. *Magnetism and Magnetic Materials*, Cambridge University Press: New York, **2010**.
3. Skumryev, V.; Stoyanov, S.; Zhang, Y.; Hadjipanayis, G.; Givord, D.; Nogués, J. *Nature*, **2003**, 850-853.
4. Gütlich, P.; Goodwin, H. A. *Spin Crossover in Transition Metal Compounds I–III, Topics in Current Chemistry*; Springer-Verlag: Berlin, **2004**; Vols. 233-235.
5. (a) Decurtins, S.; Gütlich, P.; Köhler, C.P.; Spiering, H.; Hauser, A. *Chem. Phys. Lett.*, **1984**, 105, 1-4. (b) Sato, O.; Iyoda, T.; Fujishima, A.; Hashimoto, K. *Science*, **1996**, 272, 704-705; (c) Sato, O.; Einaga, Y.; A. Fujishima, A.; K. Hashimoto, K. *Inorg. Chem.*, **1999**, 38, 4405-4412.
6. (a) Caneschi, A.; Gatteschi, D.; Sessoli, R.; Barra, A. L.; Brunel, L. C.; Guillot, M. *J. Am. Chem. Soc.*, **1991**, 113, 5873-5874. (b) Sessoli, R.; Tsai, H. L.; Schake, A. R.; Wang, S. Y.; Vincent, J. B.; Folting, K.; Gatteschi, D.; Christou, G.; Hendrickson, D. N.; *J. Am. Chem. Soc.*, **1993**, 115, 1804-1816. (c) Sessoli, R.; Gatteschi, D.; Caneschi, A.; Novak, M. A. *Nature*, **1993**, 365, 141-143.
7. (a) Caneschi, A.; Gatteschi, D.; Lalioti, N.; Sangregorio, C.; Sessoli, R.; Venturi, G.; Vindigni, A.; Rettori, A.; Pini, M. G.; Novak, M. A. *Angew. Chem., Int. Ed.*, **2001**, 40, 1760-1763. (b) Clérac, R.; Miyasaka, H.; Yamashita, M.; Coulon, C. *J. Am. Chem. Soc.*, **2002**, 124, 12837-12844. (c) Coulon, C.; Miyasaka, H.; Clérac, R. *Struct. Bond.*, **2006**, 122, 163-206.
8. Linert, W.; Verdaguer, M. (Eds) *Molecular Magnets Recent Highlights*, Springer-Verlag Wien: New York, **2003**.
9. Rogez, G.; Donnio, B.; Terazzi, E.; Gallani, J.-L.; Kappler, J.-P.; Bucher, J.-P.; Drillon, M.; *Adv. Mater.*, **2009**, 21, 4323-4333.
10. Gatteschi, D.; Cornia, A.; Mannini, M.; Sessoli, R. *Inorg. Chem.*, **2009**, 48, 3408-3419 and references therein.
11. Gatteschi, D.; Sessoli, R.; Villain, J. *Molecular Nanomagnets*, Oxford University Press: Oxford, **2006**.
12. (a) Leuenberger, M. N.; Loss D. *Nature*, **2001**, 410, 789-793. (b) Tejada, J.; Chudnovsky, E. M.; del Barco, E.; Hernandez, J. M.; Spiller, T. P. *Nanotechnology*, **2001**, 12, 181-186. (c) Tejada, J. *Polyhedron*, **2001**, 20, 1751-1756.
13. Torres, F.; Hernández, J. M.; Bohigas, X.; Tejada J., *Appl. Phys. Lett.*, **2000**, 77, 3248-3250.
14. (a) Friedman, J. R.; Sarachik, M. P.; Tejada J.; Ziolo, R. *Phys. Rev. Lett.*, **1996**, 76, 3830-3833. (b) Thomas, L.; Lioni, F.; Balou, R.; Gatteschi, D.; Sessoli, R.; Barbara, B. *Nature*, **1996**, 383, 145-157.
15. Wernsdorfer W., Sessoli, R. *Science*, **1999**, 284, 133-135.
16. Winpenny, R. E. P. *J. Chem. Soc., Dalton Trans.*, **2002**, 1–10.
17. Ferko, P. J.; Holmes, S. M. *Curr. Inorg. Chem.*, **2013**, 3, 172-193.
18. (a) Wang, X.-Y.; Avendañoa, C.; Dunbar, K. R. *Chem. Soc. Rev.*, **2011**, 40, 3213-3238 and references therein. (b) Pedersen, K. S.; Dreiser, J.; Nehrkorn, J.; Gysler, M.; Schau-Magnussen, M.; Schnegg, A.; Holldack, K.; Bittl, R.; Piligkos, S.; Weihe, H.; Tregenna-Piggott, P.; Waldmann, O.; Bendix, J. *Chem. Commun.*, **2011**, 47, 6918-6920. (c) Qian, K.; Huang, X.-C.; Zhou, C.; You, X.-Z.; Wang, X.-Y.; Dunbar, K. R. *J. Am. Chem. Soc.*, **2013**, 135, 13302-13305.
19. (a) Martínez-Lillo, J.; Mastropietro, T. F.; Lhotel, E.; Paulsen, C.; Cano, J.; De Munno, G.; Faus, J.; Lloret, F.; Julve, M.; Nellutla, S.; Krzystek, J. *J. Am. Chem. Soc.*, **2013**, 135, 13737–13748. (b) Pedersen, K. S.; Sigrist, M.; Sørensen, M. A.; Barra, A.-L.; Weyhermüller, T.; Piligkos, S.; Thuesen, C. A.; Vinum, M. G.; Mutka, H.; Weihe, H.; Clérac, R.; Bendix J. *Angew. Chem., Int. Ed.*, **2014**, 53, 1351-1354.
20. Woodruff, D. N.; Winpenny, R. E. P.; Layfield, R. A. *Chem. Rev.*, **2013**, 113, 5110–5148 and references therein.
21. (a) Mougél, V.; Chatelain, L.; Pécaut, J.; Caciuffo, R.; Colineau, E.; Griveau, J. C.; Mazzanti, M. *Nat. Chem.*, **2012**, 4, 1011-1017. (b) Antunes, M. A.; Pereira, L. C. J.; Santos, I. C.; Mazzanti, M.; Marcalo, J.; Almeida, M. *Inorg. Chem.*, **2011**, 50, 9915-9917. (c) Mills, D. R.; Moro, F.; McMaster, J.; van Slageren, J.; Lewis, W.; Blake, A. J.; Liddle, S. T. *Nat. Chem.*, **2011**, 3, 454-460. (d) Rinehart, J. D.; Meihaus, K. R.; Long, J. R. *J. Am. Chem. Soc.*, **2010**, 132, 7572-7573. (e) Magnani, N.; Apostolidis, C.; Morgernstern, A.; Colineau, E.; Griveau, J. C.; Bolvin, H.; Walter, O.; Caciuffo, R. *Angew. Chem., Int. Ed.*, **2011**, 50, 1696-1698.
22. Layfield, R. A. *Organometallics*, **2014**, 33, 1084-1099.

23. Lis, T. *Acta. Cryst. B*, **1980**, *36*, 2042-2046.
24. Thomas, L.; Barbara, B. *J. Low Temp. Phys.*, **1998**, *113*, 1055-1060.
25. Awaga, K.; Suzuki, Y.; Hachisuka, H.; Takeda, K. *J. Mater. Chem.*, **2006**, *16*, 2516-2521.
26. (a) Feringa, B. L. *Molecular Switches*, Wiley-VCH: Weinheim, **2001**. (b) Balzani, V.; Credi, A.; Venturi, M. *Molecular Devices and Machines: A Journey into the Nano World*, Wiley-VCH: Weinheim, **2003**.
27. (a) Dei, A. *Angew. Chem. Int. Ed.*, **2005**, *44*, 1160-1163. (b) Sato, O.; Tao, J.; Zhang, Y.-Z. *Angew. Chem. Int. Ed.*, **2007**, *46*, 2152-2187.
28. Simão, C.; Mas-Torrent, M.; Crivillers, N.; Lloveras, V.; Artés, J. M.; Gorostiza, P.; Veciana, J.; Rovira, C. *Nat. Chem.*, **2011**, *3*, 359-364.
29. (a) Sato, O.; Tao, J.; Zhang, Y.-Z. *Angew. Chem.*, **2007**, *119*, 2200-2236. (b) Sato, O.; Tao, J.; Zhang, Y.-Z. *Angew. Chem., Int. Ed.*, **2007**, *46*, 2152-2187.
30. Prassides, K. *Mixed Valency Systems Applications in Chemistry, Physics and Biology*, Kluwer Academic Publishers: Dordrecht, **1991**.
31. Marcus, R. A. *J. Chem. Phys.*, **1956**, *24*, 966-978.
32. (a) Hush, N. S. *Prog. Inorg. Chem.*, **1967**, *8*, 391-444. (b) Hush, N. S. *Electrochim. Acta*, **1968**, *13*, 1005-1023. c) Hush, N. S. *Coord. Chem. Rev.*, **1985**, *64*, 135-157.
33. Piepho, S. B.; Krausz, E. R.; Schatz, P. N. *J. Am. Chem. Soc.*, **1978**, *100*, 2996-3005.
34. (a) Creutz, C.; Taube, H. *J. Am. Chem. Soc.*, **1969**, *91*, 3988-3989. (b) Creutz, C.; Taube, H. *J. Am. Chem. Soc.*, **1973**, *95*, 1086-1094.
35. (a) Hankache, J.; Wenger, O. S. *Chem. Rev.*, **2011**, *111*, 5138-5178. (b) Cowan, D. O.; Le Vanda, C.; Park, J.; Kaufman, F. *Acc. Chem. Res.*, **1973**, *6*, 1-7.
36. Guasch, J.; Grisanti, L.; Souto, M.; Lloveras, V.; Vidal-Gancedo, J.; Ratera, I.; Painelli, A.; Rovira, C.; Veciana, J. *J. Am. Chem. Soc.*, **2013**, *135*, 6958-6967.
37. Verdaguer, M.; Girolami, G. S. *Magnetic Prussian Blue Analogs*, in Miller, J. S.; Drillon, M. (Eds.), *Magnetism - Molecules to Materials V*, Wiley-VCH: Weinheim, **2005**, 283-346.
38. Ohkoshi, S.-i.; Tokoro, H.; Hashimoto, K. *Coord. Chem. Rev.*, **2005**, *249*, 1830-1840.
39. (a) Ksenofontov, V.; Levchenko, G.; Reiman, S.; Güttlich, P.; Bleuzen, A.; Escax, V.; Verdaguer, M. *Phys. Rev. B*, **2003**, *68*, 024415. (b) Morimoto, Y.; Hanawa, M.; Ohishi, Y.; Kato, K.; Takata, M.; Kuriki, A.; Nishibori, E.; Sakata, M.; Ohkoshi, S.-i.; Tokoro, H.; Hashimoto, K. *Phys. Rev. B*, **2003**, *68*, 144106.
40. Sato, O. *J. Photochem. Photobiol. C: Photochem. Rev.*, **2004**, *5*, 203-223 and references therein.
41. Margadonna, S.; Prassides, K.; Fitch, A. N. *Angew. Chem. Int. Ed.*, **2004**, *43*, 6316-6319.
42. (a) Bleuzen, A.; Lomenech, C.; Escax, V.; Villain, F.; Varret, F.; Cartier dit Moulin, C.; Verdaguer, M. *J. Am. Chem. Soc.*, **2000**, *122*, 6648-6652. (b) Cartier dit Moulin, C.; Villain, F.; Bleuzen, A.; Arrio, M.-A.; Sainctavit, P.; Lomenech, C.; Escax, V.; Baudalet, F.; Dartyge, E.; Gallet, J.-J.; Verdaguer, M. *J. Am. Chem. Soc.*, **2000**, *122*, 6653-6658. (c) Escax, V.; Bleuzen, A.; Cartier dit Moulin, C.; Villain, F.; Goujon, A.; Varret, F.; Verdaguer, M. *J. Am. Chem. Soc.*, **2001**, *123*, 12536-12543. (d) Campion, G.; Escax, V.; Cartier dit Moulin, C.; Bleuzen, A.; Villain, F.; Baudalet, F.; Dartyge, E.; Verdaguer, M. *J. Am. Chem. Soc.*, **2001**, *123*, 12544-12546. (e) Shimamoto, N.; Ohkoshi, S.; Sato, O.; Hashimoto, K. *Inorg. Chem.*, **2002**, *41*, 678-684.
43. (a) Tokoro, H.; Ohkoshi, S.-i. *Dalton Trans.*, **2011**, *40*, 6825-6833. (b) Tokoro, H.; Matsuda, T.; Nuida, T.; Moritomo, Y.; Ohoyama, K.; Dangui, E. D. L.; Boukheddaden, K.; Ohkoshi, S.-i. *Chem. Mater.*, **2008**, *20*, 423-428. (c) Tokoro, H.; Miyashita, S.; Hashimoto, K.; Ohkoshi S.-i. *Phys. Rev. B*, **2006**, *73*, 172415. (d) Tokoro, H.; Ohkoshi, S.-i.; Matsuda, T.; Hashimoto, K. *Inorg. Chem.*, **2004**, *43*, 5231. (e) Tokoro, H.; Ohkoshi, S.-i.; Hashimoto, K. *Appl. Phys. Lett.*, **2003**, *82*, 1245. (f) Ohkoshi, S.-i.; Tokoro, H.; Utsunomiya, M.; Mizuno, M.; Abe, M.; Hashimoto, K. *J. Phys. Chem. B*, **2002**, *106*, 2423. (g) Yokoyama, T.; Tokoro, H.; Ohkoshi, S.-i.; Hashimoto, K. *Phys. Rev. B*, **2002**, *18*, 4111.
44. (a) Lummen, T. T. A.; Gengler, R. Y. N.; Rudolf, P.; Lusitani, F.; Vertelman, E. J. M.; van Koningsbruggen, P. J.; Knupfer, M.; Molodtsova, O.; Pireaux, J.-J.; van Loosdrecht, P. H. M. *J. Phys. Chem. C*, **2008**, *112*, 14158-14167. (b) Salmon, L.; Vertelman, E. J. M.; Murgui, C. B.; Cobo, S.; Molnár, G.; van Koningsbruggen, P. J.; Bousseksou, A. *Eur. J. Inorg. Chem.*, **2009**, 760-768.

45. (a) Ohkoshi, S.-i.; Matsuda, T.; Tokoro, H.; Hashimoto, K. *Chem. Mater.*, **2005**, *17*, 81-84. (b) Vertelman, E. J. M.; Maccallini, E.; Gournis, D.; Rudolf, P.; Bakas, T.; Luzon, J.; Broer, R.; Pugzlys, A.; Lummen, T. T. A.; van Loosdrecht, P. H. M.; van Koningsbruggen, P. J. *Chem. Mater.*, **2006**, *18*, 1951-1963. (c) Cobo, S.; Fernández, R.; Salmon, L.; Molnár, G.; Bousseksou, A. *Eur. J. Inorg. Chem.*, **2007**, 1549-1555.
46. Ohkoshi, S.-i.; Einaga, Y.; Fujishima, A.; Hashimoto, K. *J. Electroanal. Chem.*, **1999**, *473*, 245-249.
47. (a) Bozdag, K. D.; Yoo, J.-W.; Raju, N. P.; McConnell, A. C.; Miller, J. S.; Epstein, A. J. *Phys. Rev. B*, **2010**, *82*, 094449. (b) Holmes, S. M.; Girolami, G. S. *J. Am. Chem. Soc.*, **1999**, *121*, 5593-5594. (c) Hatlevik, Ø.; Bushmann, W. E.; Zhang, J.; Manson, J. L.; Miller, J. S. *Adv. Mater.*, **1999**, *11*, 914-918. (d) Ferlay, S.; Mallah, T.; Ouahes, R.; Veillet, P.; Verdaguier, M. *Nature*, **1995**, *378*, 701-703.
48. Dong, W.; Zhang, W.; Ou-Yang, Y.; Zhu, L.-N.; Liao, D.-Z.; Yoshimura, K.; Jiang, Z.-H.; Yan, S.-P.; Cheng, P. J. *Magn. Magn. Mater.*, **2007**, *309*, 7-10.
49. Avendano, C.; Hilfger, M. G.; Prosvirin, A.; Sanders, C.; Stepien, D.; Dunbar, K. R. *J. Am. Chem. Soc.*, **2010**, *132*, 13123-13125.
50. (a) Ohkoshi, S.; Tokoro, H.; Hozumi, T.; Zhang, Y.; Hashimoto, K.; Mathonière, C.; Bord, I.; Rombaut, G.; Verelst, M.; Cartier dit Moulin, C.; Villain, F. *J. Am. Chem. Soc.*, **2006**, *128*, 270-277. (b) Rombaut, G.; Verelst, M.; Golhen, S.; Ouahab, L.; Mathonière, C.; Kahn, O. *Inorg. Chem.*, **2001**, *40*, 1151-1159. (c) Zhang, W.; Sun, H.-L.; Sato, O. *Dalton Trans.*, **2011**, *40*, 2735-2743. (d) Brossard, S.; Volatron, F.; Lisnard, L.; Arrio, M.-A.; Catala, L.; Mathonière, C.; Mallah, T.; Cartier dit Moulin, C.; Rogalev, A.; Wilhelm, F.; Smekhova, A.; Sainctavit, P. *J. Am. Chem. Soc.*, **2012**, *134*, 222-228.
51. (a) Ohkoshi, S.; Hamada, Y.; Matsuda, T.; Tsunobuchi, Y.; Tokoro, H. *Chem. Mater.*, **2008**, *20*, 3048-3054. (b) Ozaki, N.; Tokoro, H.; Hamada, Y.; Namai, A.; Matsuda, T.; Kaneko, S.; Ohkoshi, S. *Adv. Func. Mater.*, **2012**, *22*, 20892093.
52. (a) Beltran, L. M. C.; Long, J. R. *Acc. Chem. Res.*, **2005**, *38*, 325-334; (b) Rebilly, J.-N.; Mallah, T. *Struct. Bonding*, **2006**, *122*, 103-131; (c) Wang, S.; Ding, X.-H.; Zuo, J.-L.; You, X.-Z.; Huang, W. *Coord. Chem. Rev.*, **2011**, *255*, 1713-1732; (c) Newton, G. N.; Nihei, M.; Oshio, H. *Eur. J. Inorg. Chem.*, **2011**, 3031-3042.
53. (a) Wang, S.; Zuo, J.-L.; Zhou, H.-C.; Choi, H. J.; Ke, Y.; Long, J. R.; You, X.-Z. *Angew. Chem. Int. Ed.*, **2004**, *43*, 5940-5943; (b) Li, D.; Clérac, R.; Parkin, S.; Wang, G.; Yee, G. T.; Holmes, S. M. *Inorg. Chem.*, **2006**, *45*, 5251-5253; (c) Li, D.; Parkin, S.; Wang, G.; Yee, G. T.; Clérac, R.; Wernsdorfer, W.; Holmes, S. M. *J. Am. Chem. Soc.*, **2006**, *128*, 4214-4215; (d) Schelter, E. J.; Karadas, F.; Avendano, C.; Prosvirin, A. V.; Wernsdorfer, W.; Dunbar, K. R. *J. Am. Chem. Soc.*, **2007**, *129*, 8139-8149; (e) Freedman, D. E.; Jenkins, D. M.; Iavarone, A. T.; Long, J. R. *J. Am. Chem. Soc.*, **2008**, *130*, 2884-2885; (f) Li, D.; Parkin, S.; Wang, G.; Yee, G. T.; Prosvirin, A. V.; Holmes, S. M. *Inorg. Chem.*, **2005**, *44*, 4903-4905.
54. (a) Nihei, M.; Ui, M.; Yokota, M.; Han, L.; Maeda, A.; Kishida, H.; Okamoto, H.; Oshio, H. *Angew. Chem. Int. Ed.*, **2005**, *44*, 6484-6487; (b) Herchel, R.; Boca, R.; Gembicky, M.; Kozísek, J.; Renz, F. *Inorg. Chem.*, **2004**, *43*, 4103-4105; (c) Shatruck, M.; Dragulescu-Andrasi, A.; Chambers, K. E.; Stoian, S. A.; Bominaar, E. L.; Achim, C.; Dunbar, K. R. *J. Am. Chem. Soc.*, **2007**, *129*, 6104-6116; (d) Boldog, I.; Munoz-Lara, F. J.; Gaspar, A. B.; Munoz, M. C.; Seredyuk, M.; Real, J. A. *Inorg. Chem.*, **2009**, *48*, 3710-3719. (e) Jeon, I.-R.; Calancea, S.; Panja, A.; Piñero Cruz, D. M.; Koumoussi, E. S.; Dechambenoit, P.; Coulon, C.; Wattiaux, A.; Rosa, P.; Mathonière, C.; Clérac, R. *Chem. Sci.*, **2013**, *4*, 2463-2470.
55. (a) Berlinguette, C. P.; Dragulescu-Andrasi, A.; Sieber, A.; Galan-Mascaros, J. R.; Güdel, H.-U.; Achim, C.; Dunbar, K. R. *J. Am. Chem. Soc.*, **2004**, *126*, 6222-6223; (b) Li, D.; Clérac, R.; Roubeau, O.; Harté, E.; Mathonière, C.; Le Bris, R.; Holmes, S. M. *J. Am. Chem. Soc.*, **2008**, *130*, 252-258; (c) Zhang, Y.; Li, D.; Clérac, R.; Kalisz, M.; Mathonière, C.; Holmes, S. M. *Angew. Chem. Int. Ed.*, **2010**, *49*, 3752-3756; (d) Mercuriol, J.; Li, Y.; Pardo, E.; Risset, O.; Seuleiman, M.; Rousselière, H.; Lescouëzec, R.; Julve, M. *Chem. Commun.*, **2010**, *46*, 8995-8997; (e) Nihei, M.; Sekine, Y.; Suganami, N.; Oshio, H. *Chem. Lett.*, **2010**, *39*, 978-979; (f) Nihei, M.; Sekine, Y.; Suganami, N.; Nakazawa, K.; Nakao, H.; Murakami, Y.; Oshio, H. *J. Am. Chem. Soc.*, **2011**, *133*, 3592-3600; (g) Siretanu, D.; Li, D.; Buisson, L.; Bassani, D. M.; Holmes, S. M.; Mathonière, C.; Clérac, R. *Chem.-Eur. J.*, **2011**, *17*, 11704-11708. (h) Hilfger, M.; Chen, M.; Brinzari, T.; Nocera, T.; Shatruck, M.; Petasis, D.; Musfeldt, J.; Achim, C.; Dunbar, K. R. *Angew. Chem., Int. Ed.*, **2010**, *49*, 1410-1413; (i) Funck, K. E.; Prosvirin, A. V.; Mathonière, C.; Clérac, R.; Dunbar, K. R. *Inorg. Chem.*, **2011**, *50*, 2782-2789; (j) Bernhardt, P. V.; Martinez, M. *Inorg. Chem.*, **1999**, *38*, 424-425.
56. (a) Herrera, J. M.; Marvaud, V.; Verdaguier, M.; Marrot, J.; Kalisz, M.; Mathonière, C. *Angew. Chem. Int. Ed.*, **2004**, *43*, 5468-5471. (b) Bleuzen, A.; Marvaud, V.; Mathonière, C.; Sieklucka, B.; Verdaguier, M. *Inorg. Chem.*, **2009**, *48*, 3453-3466. (c) Mathonière, C.; Podgajny, R.; Guionneau, P.; Labrugère, C.; Sieklucka, B. *Chem. Mater.*, **2005**, *17*, 442-449. (d) Dong, D.-P.; Liu, T.; Kanegawa, S.; Kang, S.; Sato, O.; He, C.; Duan, C.-Y. *Angew. Chem. Int. Ed.*, **2012**, *51*, 5119-5123. (e) Liu, T.; Zheng, H.; Soonchul, K.; Shiota, Y.; Hayami, S.; Mito, M.; Sato, O.; Yoshizawa, K.;

- Kanegawa, S.; Duan, C. *Nat. Commun.*, **2013**, *4*, 2826. (f) Hoshino, N.; Iijima, F.; Newton, G. N.; Yoshida, N.; Shiga, T.; Nojiri, H.; Nakao, A.; Kumai, R.; Murakami, Y.; Oshio, H. *Nat. Chem.*, **2012**, *4*, 921-926. (g) Nihei, M.; Okamoto, Y.; Sekine, Y.; Hoshino, N.; Shiga, T.; Liu, I. P.-C.; Oshio, H. *Angew. Chem. Int. Ed.*, **2012**, *51*, 6361-6364. (h) Mondal, A.; Li, Y.; Herson, P.; Seuleiman, M.; Boillot, M.-A.; Rivière, E.; Julve, M.; Reichignat, L.; Bousseksou, A.; Lescouëzec, R. *Chem. Commun.*, **2012**, *48*, 5653-5655. (i) Mondal, A.; Chamoreau, L.-M.; Li, Y.; Journaux, Y.; Seuleiman, M.; Lescouëzec, R. *Chem. Eur. J.*, **2013**, *19*, 7682-7685.
57. (a) Lescouëzec, R.; Vaissermann, J.; Ruiz-Perez, C.; Lloret, F.; Carrasco, R.; Julve, M.; Verdaguer, M.; Dromzee, Y.; Gatteschi, D.; Wernsdorfer, W. *Angew. Chem. Int. Ed.*, **2003**, *42*, 1483-1486. (b) Bernhardt, P. V.; Macpherson, B. P.; Martinez, M. *J. Chem. Soc., Dalton Trans.*, **2002**, 1435-1441. (c) Bernhardt, P., V.; Macpherson, B. P.; Martinez, M. *Inorg. Chem.*, **2000**, *39*, 5203-5208. (d) Oshio, H.; Onodera, H.; Tamada, O.; Mizutani, H.; Hikichi, T.; Ito, T. *Chem.-Eur. J.*, **2000**, *6*, 2523-2530.
58. Atkins, P.; De Paula, J. *Physical Chemistry*, 8th Ed., Oxford University Press, **2006**.
59. (a) Mondal, A.; Li, Y.; Seuleiman, M.; Julve, M.; Toupet, L.; Buron-Le Cointe, M.; Lescouëzec, R. *J. Am. Chem. Soc.*, **2013**, *135*, 1653-1656. (b) Cao, L.; Tao, J.; Gao, Q.; Liu, T.; Xia, Z.; Li, D. *Chem. Commun.*, **2014**, *50*, 1665-1667. (c) Sekine, Y.; Nihei, M.; Kumai, R.; Nakao, H.; Murakami, Y.; Oshio, H. *Chem. Commun.*, **2014**, DOI: 10.1039/C3CC48820A.
60. Slichter, C. P.; Drickamer, H. G. *J. Chem. Phys.*, **1972**, *56*, 2142-2160.
61. (a) Mannini, M.; Pineider, F.; Danieli, C.; Totti, F.; Sorace, L.; Sainctavit, P.; Arrio, M.-A.; Otero, E.; Joly, L.; Cezar, J. C.; Cornia, A.; Sessoli, R. *Nature*, **2010**, *468*, 417-421. (b) Zyazin, A. S.; van den Berg, J. W. G.; Osorio, E. A.; van der Zant, H. S. J.; Konstantinidis, N. P.; Leijnse, M.; Wegewijs, M. R.; May, F.; Hofstetter, W.; Danieli, C.; Cornia, A. *Nano Lett.*, **2010**, *10*, 3307-3311. (c) Margheriti, L.; Chiappe, D.; Mannini, M.; Car, P.-E.; Sainctavit, P.; Arrio, M.-A.; Buatier de Mongeot, F.; Cezar, J. C.; Piras, F. M.; Magnani, A.; Otero, E.; Caneschi, A.; Sessoli, R. *Adv. Mater.*, **2010**, *22*, 5488-5493. (d) Mannini, M.; Pineider, F.; Sainctavit, P.; Danieli, C.; Otero, E.; Sciancalepore, C.; Talarico, A. M.; Arrio, M.-A.; Cornia, A.; Gatteschi, D.; Sessoli, R. *Nat. Mater.*, **2009**, *8*, 194-197. (e) Mannini, M.; Pineider, F.; Sainctavit, P.; Joly, L.; Fraile-Rodríguez, A.; Arrio, M.-A.; Cartier dit Moulin, C.; Wernsdorfer, W.; Cornia, A.; Gatteschi, D.; Sessoli, R. *Adv. Mater.*, **2009**, *21*, 167-171. (f) Clemente-León, M.; Soyer, H.; Coronado, E.; Mingotaud, C.; Gómez-García, C. J.; Delhaès, P. *Angew. Chem. Int. Ed.*, **1998**, *37*, 2842-2845.
62. (a) Cavallini, M.; Bergenti, I.; Milita, S.; Kengne, J. C.; Gentili, D.; Ruani, G.; Salitros, I.; Meded, V.; Ruben M. *Langmuir*, **2011**, *27*, 4076-4081. (b) Bonhommeau, S.; Molnar, G.; Galet, A.; Zwick, A.; Real, J. A.; McGarvey, J. J.; Bousseksou, A. *Angew. Chem. Int. Ed.*, **2005**, *44*, 4069-4073.
63. (a) Imaz, I.; Luis, F.; Carbonera, C.; Ruiz-Molina, D.; Maspocho, D. *Chem. Commun.*, **2008**, 1202-1204.
64. (a) Coronado, E.; Galan-Mascaros, J. R.; Monrabal-Capilla, M.; Garcia-Martinez, J.; Pardo-Ibanez, P. *Adv. Mater.*, **2007**, *19*, 1359-1361. (b) Forestier, T.; Mornet, S.; Daro, N.; Nishihara, T.; Mouri, S.; Tanaka, K.; Fouche, O.; Freysz, E.; Letard, J. F. *Chem. Commun.*, **2008**, 4327-4329. (c) Larionova, J.; Salmon, L.; Guarl, Y.; Tokarev, A.; Molvinger, K.; Molnar, G.; Bousseksou, A. *Angew. Chem. Int. Ed.*, **2008**, *47*, 8236-8240. (d) Catala, L.; Gacoin, T.; Boillot, J.-P.; Rivière, E.; Paulsen, C.; Lhotel, E.; Mallah, T. *Adv. Mater.*, **2003**, *15*, 826-829. (e) Galan-Mascaros, J. R.; Coronado, E.; Forment-Aliaga, A.; Monrabal-Capilla, M.; Pinilla-Cienfuegos, E.; Ceolin, M. *Inorg. Chem.*, **2010**, *49*, 5706-5714.
65. Demus, D.; Goodby, J. W.; Gray, G. W.; Spiess, H.-W.; Vill, V. (Eds) *Handbook of Liquid Crystals*, Wiley-VCH: Weinheim, **1998**.
66. (a) Tschierske, C. *Annu. Rep. Prog. Chem., Sect. C: Phys. Chem.*, **2001**, *97*, 191-267. (b) Binnemans, K.; Görlner-Walrand, C. *Chem. Rev.*, **2002**, *102*, 2303-2345. (c) Kato, T.; Mizoshita, N.; Kishimoto, K. *Angew. Chem. Int. Ed.*, **2006**, *45*, 38-68. (d) Donnio, B.; Buathong, S.; Bury, I.; Guillon, D. *Chem. Soc. Rev.*, **2007**, *36*, 1495-1513. (e) Tschierske, C. *Chem. Soc. Rev.*, **2007**, *36*, 1930-1970. (f) Goodby, J. W.; Saez, I. M.; Cowling, S. J.; Görtz, V.; Draper, M.; Hall, A. W.; Sia, S.; Cosquer, G.; Lee, S.-E.; Raynes, E. P. *Angew. Chem. Int. Ed.*, **2008**, *47*, 2754-2787. (g) Bruce, D. W. *Struct. Bonding*, **2008**, *126*, 161-180. (h) Bisoyi, H. K.; Kumar, S. *Chem. Soc. Rev.*, **2011**, *40*, 306-319. (i) Tschierske, C. *Top. Curr. Chem.*, **2012**, *318*, 1-108.
67. (a) Kumar, S. *Chem. Soc. Rev.*, **2006**, *35*, 83-109. (b) Laschat, S.; Baro, A.; Steinke, N.; Giesselmann, F.; Hägele, C.; Scalia, G.; Judele, R.; Kapatsina, E.; Sauer, S.; Schreivogel, A.; Tosoni, M. *Angew. Chem. Int. Ed.*, **2007**, *46*, 4832-4887. (c) Sergeev, S.; Pisula, W.; Geerts, Y. H. *Chem. Soc. Rev.*, **2007**, *36*, 1902-1929. (d) Kumar, S. *Liq. Cryst.*, **2009**, *36*, 607-638. (e) Pisula, W.; Zorn, M.; Young, J. C.; Müllen, K.; Zentel, R. *Macromol. Rapid Commun.*, **2009**, *30*, 1179-1202. (f) Kaafarani, B. R. *Chem. Mater.*, **2011**, *23*, 378-396.
68. (a) Collings, P. *Introduction to Liquid Crystals, Chemistry and Physics*, Taylor & Francis: London, **1997**. (b) Tschierske, C. *Curr. Opin. Colloid Interface Sci.*, **2002**, *7*, 355-370.

69. (a) Levelut, A. M.; Clerc, M.; *Liq. Cryst.*, **1998**, *24*, 105-115. (b) Zeng, X. B.; Ungar, G.; Impéror-Clerc, M. *Nat. Mater.*, **2005**, *4*, 562-567; (b) Impéror-Clerc, M. *Curr. Opin. Colloid Interface Sci.*, **2005**, *9*, 370-376.
70. (a) Kutsumizu, S. *Curr. Opin. Solid State Mater. Sci.*, **2002**, *6*, 537-543. (b) Diele, S. *Curr. Opin. Colloid Interface Sci.*, **2002**, *7*, 333-342.
71. (a) Percec, V.; Mitchell, C. M.; Cho, W. D.; Uchida, S.; Glodde, M.; Ungar, G.; Zeng, X.; Liu, Y.; Balagurusamy, V. S. K.; Heiney, P. A. *J. Am. Chem. Soc.*, **2004**, *126*, 6078-6094. (b) Percec, V.; Glodde, M.; Bera, T. K.; Miura, Y.; Shiyonovskaya, I.; Singer, K. D.; Balagurusamy, V. S. K.; Heiney, P. A.; Schnell, I.; Rapp, A.; Spiess, H. W.; Hudson, S. D.; Duan, H. *Nature*, **2002**, *419*, 384-387. (c) Percec, V.; Peterca, M.; Sienkowska, M. J.; Iliés, M. A.; Aqad, E.; Smidrkal, J.; Heiney, P. A. *J. Am. Chem. Soc.*, **2006**, *128*, 3324-3334.
72. (a) Giroud, A. M.; Müller-Westerhoff, U. T. *Mol. Cryst. Liq. Cryst.*, **1977**, *41*, 11-13. (b) Giroud-Godquin, A.-M.; Maitlis, P. M. *Angew. Chem. Int. Ed.*, **1991**, *30*, 375-402. (c) Serrano, J. L. *Metallomesogens*, VCH, Weinheim, **1996**. (d) Donnio, B.; Bruce, D. W. *Struct. Bond.*, **1999**, *95*, 193-247. (e) Pigué, C.; Bunzli, J. C. G.; Donnio, B.; Guillon, D. *Chem. Commun.*, **2006**, 3755-3768. (f) Date, R. W.; Iglesias, E. F.; Rowe, K. E.; Elliott, J. M.; Bruce, D. W. *Dalton Trans.*, **2003**, 1914-1931. (g) Aiello, I.; Dattilo, D.; Ghedini, M.; Golemme, A. *J. Am. Chem. Soc.*, **2001**, *123*, 5598-5599. (h) Aiello, I.; Dattilo, D.; Ghedini, M.; Bruno, A.; Termine, R.; Golemme, A. *Adv. Mater.*, **2002**, *14*, 1233-1236. (i) Ghedini, M.; Aiello, I.; Crispini, A.; Golemme, A.; La Deda, M.; Pucci, D. *Coord. Chem. Rev.*, **2006**, *250*, 1373-1390.
73. Galyametdinov, Y.; Ksenofontov, V.; Prosvirin, A.; Ovchinnikov, I.; Ivanova, G.; Guetlich, P.; Haase, W. *Angew. Chem. Int. Ed.*, **2001**, *40*, 4269-4271.
74. Haddad, M. S.; Lynch, M. W.; Federer, W. D.; Hendrickson, D. N. *Inorg. Chem.*, **1981**, *20*, 123-131.
75. (a) Hayami, S.; Danjobara, K.; Inoue, K.; Ogawa, Y.; Matsumoto, N.; Maeda, Y. *Adv. Mater.*, **2004**, *16*, 869-872. (b) Hayami, S.; Motokawa, N.; Shuto, A.; Masuhara, N.; Someya, T.; Ogawa, Y.; Inoue, K.; Maeda, Y. *Inorg. Chem.*, **2007**, *46*, 1789-1794. (c) Hayami, S.; Moriyama, R.; Shuto, A.; Maeda, Y.; Ohta, K.; Inoue, K. *Inorg. Chem.*, **2007**, *46*, 7692-7694.
76. Seredyuk, M.; Gaspar, A. B.; Ksenofontov, V.; Galyametdinov, Y.; Kusz, J.; Gütllich, P. *J. Am. Chem. Soc.*, **2008**, *130*, 1431-1439.
77. Gaspar, A. B.; Seredyuk, M.; Gütllich, R. *Coord. Chem. Rev.*, **2009**, *253*, 2399-2413.
78. (a) Fujigaya, T.; Jiang, D. L.; Aida, T. *J. Am. Chem. Soc.*, **2003**, *125*, 14690-14691. (b) Lee, Y. H.; Komatsu, Y.; Yamamoto, Y.; Kato, K.; Shimizu, T.; Ohta, A.; Matsui, T.; Hayami, S. *Inorg. Chem. Commun.*, **2011**, *14*, 1498-1500.
79. (a) Seredyuk, M.; Gaspar, A. B.; Ksenofontov, V.; Reiman, S.; Galyametdinov, Y.; Haase, W.; Rentschler, E.; Gütllich, P. *Chem. Mater.*, **2006**, *18*, 2513-2519. (b) Seredyuk, M.; Gaspar, A. B.; Ksenofontov, V.; Galyametdinov, Y.; Verdaguer, M.; Villain, F.; Gütllich, P. *Inorg. Chem.*, **2008**, *47*, 10232-10245.
80. (a) Roubeau, O.; Colin, A.; Schmitt, V.; Clérac, R. *Angew. Chem. Int. Ed.*, **2004**, *43*, 3283-3286. (b) Grondin, P.; Roubeau, O.; Castro, M.; Saadaoui, H.; Colin, A.; Clérac, R. *Langmuir*, **2010**, *26*, 5184-5195. (c) Grondin, P. *PhD thesis*, University Bordeaux 1, **2007**.
81. Grondin, P.; Siretanu, D.; Roubeau, O.; Achard, M.-F.; Clérac, R. *Inorg. Chem.*, **2012**, *51*, 5417-5426.
82. Wernsdorfer, W.; Aliaga-Alcade, N.; Hendrickson, D. N.; Christou, G. *Nature*, **2002**, *416*, 406-409.
83. (a) Terazzi, E.; Bourgogne, C.; Welter, R.; Gallani, J.-L.; Guillon, D.; Rogez, G.; Donnio, B. *Angew. Chem., Int. Ed.* **2008**, *47*, 490-495. (b) Terazzi, E.; Jensen, T. B.; Donnio, B.; Buchwalder, K.; Bourgogne, C.; Rogez, G.; Heinrich, B.; Gallani, J.-L.; Pigué, C. *Dalton Trans.*, **2011**, *40*, 12028-12032. (c) Terazzi, E.; Rogez, G.; Gallani, J.-L.; Donnio, B. *J. Am. Chem. Soc.*, **2013**, *135*, 2708-2722.
84. Siretanu, D. *PhD thesis*, University Bordeaux 1, **2011**.
85. (a) Herbert, A. J. *Trans. Faraday Soc.* **1967**, *63*, 555-560. (b) Blumstein, A.; Platel, L. *Mol. Cryst. Liq. Cryst.* **1978**, *48*, 151-164. (c) Gray, G. W.; Jones, B. *J. Chem. Soc.* **1953**, 4179-4180. (d) Bryan, R. F.; Hartley, P.; Miller, R. W.; Shen, M. S. *Mol. Cryst. Liq. Cryst.* **1980**, *62*, 281-309. (e) Bryan, R. F.; Hartley, P. *Mol. Cryst. Liq. Cryst.* **1980**, *62*, 259-279. (f) Babkov, L. M.; Gorshkov, O. V.; Golovina, N. A.; Puchkovskaya, G. A.; Khakimov, I. N. *J. Struct. Chem.* **1995**, *36*, 302-308. (g) Kato, T.; Kubota, Y.; Nakano, M.; Uryu, T. *Chem. Lett.* **1995**, 1127-1128. (h) Plass, M. Z. *Phys. Chem. Int. Ed.* **1996**, *194*, 223-230. (i) Painter, P.; Cleveland, C.; Coleman, M. *Mol. Cryst. Liq. Cryst.* **2000**, *348*, 269-293. (j) Paleos, C. M.; Tsiourvas, D. *Liquid Crystals* **2001**, *28*, 1127-1161.
86. Gonidec, M.; Luis, F.; Vilchez, Á.; Esquena, J.; David B. Amabilino, D. B.; Veciana, J. *Angew. Chem. Int. Ed.*, **2010**, *49*, 1623-1626.

87. Kuroiwa, K.; Shibata, T.; Takada, A.; Nemoto, N.; Kimizuka, N. *J. Am. Chem. Soc.*, **2004**, *126*, 2016-2021.
88. Fujigaya, T., Jiang, D.-L.; Aida, T. *Chem. Asian J.*, **2007**, *2*, 106-113.
89. Luisi, B. S.; Rowland, K. D.; Moulton, B. *Chem. Commun.*, **2007**, 2802-2804.
90. Gandolfi, C.; Moitzi, C.; Schurtenberger, P.; G. Morgan, G. G.; Albrecht, M. *J. Am. Chem. Soc.*, **2008**, *130*, 14434-14435.
91. Li, W.; Li, B.; Wang, Y.; Zhang, J.; Wang S.; Wu, L. *Chem. Commun.*, **2010**, *46*, 6548-6550.
92. (a) Ni, Z.; Fiedler, S. R.; Shores, M. P. *Dalton Trans.*, **2011**, *40*, 944-950. (b) Ni, Z.; McDaniel, A. M.; Shores, M. P.; *Chem. Sci.*, **2010**, *1*, 615-621. (c) Ni, Z.; Shores, M. P. *J. Am. Chem. Soc.*, **2009**, *131*, 32-33.
93. (a) Inglis, R.; Bendix, J.; Brock-Nannestad, T.; Weihe, H.; Brechin, E. K.; Piligkos, S. *Chem. Sci.*, **2010**, *1*, 631636. (b) Schlegel, C.; Burzuri, E.; Luis, F.; Moro, F.; Manoli, M.; Brechin, E. K.; Murrie, M.; van Slageren, J. *Chem. Eur. J.*, **2010**, *16*, 10178-10185. (c) Schlegel, C.; van Slageren, J.; Manoli, M.; Brechin, E. K.; Dressel, M. *Polyhedron*, **2009**, *28*, 1834-1837. (d) El Hallak, F., van Slageren, J., Gómez-Segura, J., Ruiz-Molina, D., Dressel, M. *Phys. Rev. B*, **2007**, *75*, 104403. (e) Caneschi, A.; Ohm, T.; Paulsen, C.; Rovai, D.; Sangregorio, C.; Sessoli, R. *J. Magn. Magn. Mater.*, **1998**, *177-181*, 1330-1336. (f) Sessoli, R. *Mol. Cryst. Liq. Cryst. Sci. Technol. A* **1995**, *274*, 145-157.

Chapter II

**Functionalization of Single-Molecule Magnets:
Towards Liquid Crystalline Phases**

Table of Contents for Chapter II:

II.1. Introduction.....	II.45
II.2. Mn ₁₂ -based SMMs: Versatile target for functionalization.....	II.46
II.2.1. Why Mn ₁₂ ?.....	II.46
II.2.2. Structure of Mn ₁₂ -based complexes	II.46
II.2.3. Chemistry of Mn ₁₂ -based complexes	II.48
II.3. Functionalization strategies towards liquid crystalline SMMs	II.50
II.4. Functionalization of Mn ₁₂ -based SMMs with strongly lipophilic groups	II.52
II.4.1. Synthetic procedures and purification	II.52
II.4.2. Analytical characterizations of substituted Mn ₁₂ complexes	II.53
II.4.2.1. Single crystal X-ray analysis of the model compound [Mn ₁₂ O ₁₂ (L ¹) ₁₆ (H ₂ O) ₃].....	II.53
II.4.2.2. FT-IR spectroscopic analyses	II.55
II.4.2.3. ¹ H NMR spectroscopic analyses	II.56
II.4.2.4. Elemental and thermo-gravimetric analyses	II.56
II.4.3. Magnetic measurements	II.57
II.4.4. Thermotropic properties	II.61
II.4.4.1. [Mn ₁₂ O ₁₂ (L ²) ₁₆ (H ₂ O) ₄]	II.62
II.4.4.2. [Mn ₁₂ O ₁₂ (L ³) ₁₆ (H ₂ O) ₄]	II.63
II.4.4.3. [Mn ₁₂ O ₁₂ (L ⁴) ₁₆ (H ₂ O) ₄]	II.64
II.4.5. Description of the molecular packing inside the mesophase	II.67
II.4.6. Summary of section II.4	II.70
II.5. Functionalization of Mn ₁₂ -based SMMs by grafting a mesomorphic promoter through a flexible spacer.....	II.71
II.5.1. Synthetic procedures and purification	II.71
II.5.2. Analytical characterization of functionalized Mn ₁₂ complexes	II.72
II.5.2.1. FT-IR spectroscopic analyses	II.72
II.5.2.2. ¹ H NMR spectroscopic analyses	II.72
II.5.2.3. Elemental and thermo-gravimetric analyses	II.73
II.5.3. Magnetic measurements	II.74
II.5.4. Thermotropic properties	II.76
II.5.4.1. DSC and temperature dependent POM investigations.....	II.76
II.5.4.2. Small angle X-ray scattering (SAXS) investigations	II.78
II.5.5. Summary of section II.5	II.81
II.6. Conclusions and perspectives	II.81
II.7. Supporting materials.....	II.84
II.7.1. Experimental protocols.....	II.84
II.7.2. Analytical characterizations.....	II.88
II.7.2.1. Crystallographic data for [Mn ₁₂ O ₁₂ (L ¹) ₁₆ (H ₂ O) ₃]	II.88
II.7.2.2. FT-IR spectroscopic analyses	II.90
II.7.2.3. Thermo-gravimetric analyses	II.94
II.7.3. Magnetic measurements	II.94
II.7.4. Thermotropic properties	II.96
II.7.4.1. DSC traces	II.96
II.7.4.2. Small angle X-ray scattering (SAXS) investigations	II.96
II.8. References	II.106

II.1. Introduction

An important research field at the interface of classical and quantum worlds was opened after the discovery that certain molecules can retain magnetization at molecular level. Thanks to the fact that they represent the most significant level of miniaturization for a magnet, they were later called single molecule magnets (SMM).¹ These molecular objects appear to be promising units for the development of future integrated nanodevices, such as molecular transistors, single-molecule spin-valves, quantum computers, “nanosquid” junctions, or magnetic random access memories.^{2,3} The potential use of these molecular materials in a device, *i.e.* for high density information storage, would require a close control of their self-organization. The organization of SMMs has been reported on surfaces, in mesoporous materials or by coordination chemistry,⁴ but another promising strategy towards their controlled organization and eventual use is the development of new functional hybrid molecular materials with self-organization abilities. Metallomesogens (liquid crystalline materials incorporating metal ions) are very good candidates for such multifunctional materials, because they combine anisotropy related properties of liquid crystals with the original properties of metallic complexes.⁵ Thus, the functionalization of organic ligands of known SMMs can help: (i) to isolate and protect the magnetic core by an organic shell in order to prevent interactions between objects; (ii) to orient, align, and organize magnetic units to keep easy axes in a quasi-same direction (see Chapter I), thanks to self-organization of the liquid crystalline phase; and (iii) to have fluidity and easy processability for shaping and further applications.

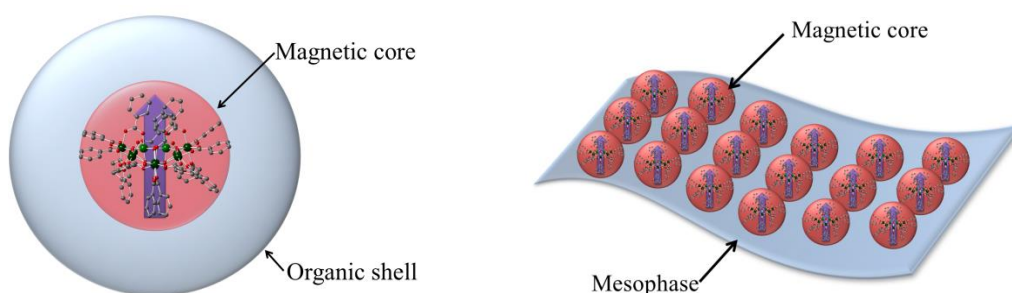


Figure II-1. Schematic representation emphasizing the benefits of ligand functionalization in SMMs: (left) functionalization with ligands possessing strongly lipophilic groups (long alkyl chains) can protect and isolate magnetic cores from contacts between them; (right) the self-organization of liquid crystalline phase can help to orient, align, and organize SMMs.

Thus the formation of liquid crystalline mesophases may be considered as a first step towards the control of SMM self-organization into low-dimensional orders for their future incorporation into a functional device.

In this chapter our discussions are focused on functionalization of SMMs. The chapter starts with a short description of the Mn_{12} -based SMM family chosen for our investigations, followed by previously reported attempts and the selected functionalization strategies to induce liquid crystalline organization. For a better understanding of functionalization effect over thermotropic and magnetic properties, the series of prepared Mn_{12} -based complexes is divided into two groups according to the applied functionalization. The analytical characterizations as well as magnetic and thermotropic properties are then described and discussed for each group separately.

II.2. Mn₁₂-based SMMs: Versatile target for functionalization

II.2.1. Why Mn₁₂?

One of the most famous and, respectively, widely studied families of SMMs is the one derived from dodecanuclear manganese complex with a general formula [Mn^{III}₈Mn^{IV}₄O₁₂(CH₃COO)₁₆(H₂O)₄] (Mn₁₂-OAc or Mn₁₂-acetate for short, Figure II-2). In 1980, it was serendipitously synthesized by Lis, while in 1993 for the first time it was discovered that Mn₁₂-OAc shows slow relaxation of the magnetization at low temperature.¹ Under these conditions, if magnetized by an applied field it retains the magnetization for months and one single molecule functions as a nanoscale magnet. A deep and broad understanding of molecular magnetism became possible thanks to a systematic study of the family of Mn₁₂ SMMs. Besides its prominent magnetic properties, characterized by a high-spin ground state $S_T = 10$, the presence of strong uniaxial magnetic anisotropy and a relatively high energy barrier (~ 74 K)⁶ (beaten only by hexanuclear manganese complexes⁷ and lanthanide-based SMMs⁸), Mn₁₂-OAc and its derivatives are versatile from the chemical point of view. Its synthesis is cheap, easy and, in addition, it is possible to modify easily the organic moiety that surrounds the inorganic core without significant modification of the magnetic properties. Moreover, it is well known that chemical modification of Mn₁₂-OAc allows a relative control of its solubility and redox potentials.⁹ All these give a good enough motivation to work on a wise functionalization of ligands surrounding the Mn₁₂ core to get hybrid molecular materials, eventually with liquid crystalline phases.

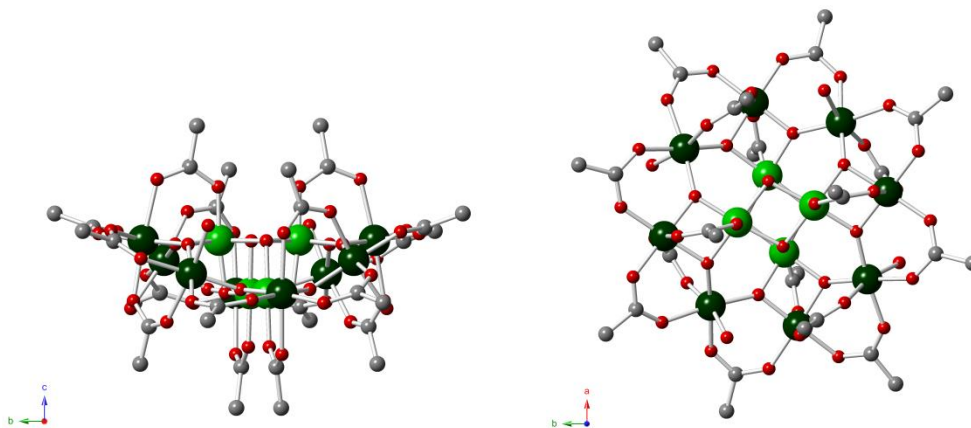


Figure II-2. Crystallographic structure of Mn₁₂-OAc complex (left) along the crystal a-axis, and (right) along the crystal c-axis. Color scheme: Mn^{III} dark green, Mn^{IV} light green, O red, C grey. Hydrogens are omitted for clarity.

II.2.2. Structure of Mn₁₂-based complexes

The structure of Mn₁₂-OAc (Figure II-2) and its derivatives can be described as a [Mn₁₂(μ_3 -O)₁₂] roughly planar disk containing a central [Mn^{IV}₄O₄]⁸⁺ cubane unit held within a non-planar ring of eight Mn^{III} ions connected to the cube by eight μ_3 -O²⁻ ions and four bridging carboxylates perpendicular to the plane of the disk (two on each side). The peripheral eight Mn^{III} ions are connected to each other by eight equatorial and four axial (two on each side of the disk) bridging carboxylate-based ligands. The Mn^{III} ions of the outer ring are alternatively doubly bridged to one and singly bridged to two Mn^{IV} ions (also called Mn^{III} of type I

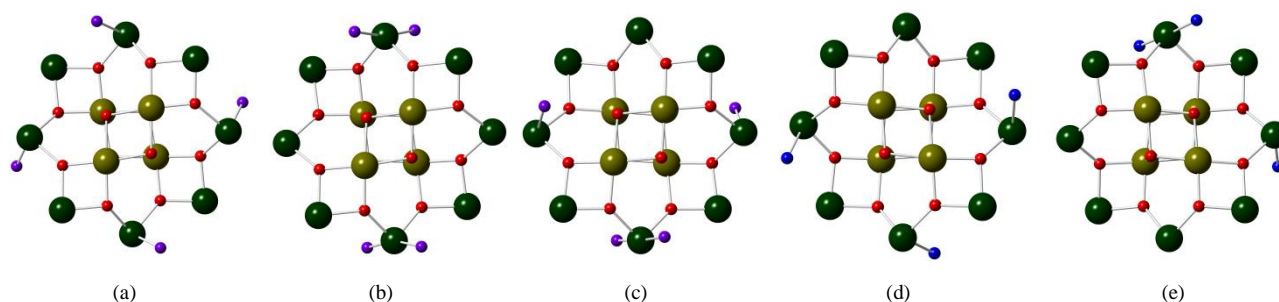


Figure II-3. Schematic representation of several Mn_{12} cores with different number and coordination positions of axially coordinated H_2O molecules: (a) $[\text{Mn}_{12}\text{O}_{12}(\text{CH}_3\text{COO})_{16}(\text{H}_2\text{O})_4]$, 1:1:1:1 isomer; (b) $[\text{Mn}_{12}\text{O}_{12}(\text{CF}_3\text{COO})_{16}(\text{H}_2\text{O})_4]$, 2:0:2 isomer; (c) $[\text{Mn}_{12}\text{O}_{12}(p\text{-Me-PhCOO})_{16}(\text{H}_2\text{O})_4]$, 1:2:1 isomer; (d) $[\text{Mn}_{12}\text{O}_{12}(\text{C}_2\text{H}_5\text{COO})_{16}(\text{H}_2\text{O})_3]$, 1:1:1 isomer; (e) $[\text{Mn}_{12}\text{O}_{12}(\text{CHCl}_2\text{COO})_8(\text{Bu}'\text{CH}_2\text{COO})_8(\text{H}_2\text{O})_3]$, 2:0:1. Color scheme: Mn(III) dark green, Mn(IV) green, O red, O_{water} blue.

or II, respectively). Three or four H_2O molecules are bound only to Mn^{III} ions of type II. The original $\text{Mn}_{12}\text{-OAc}$ has a 1:1:1:1 arrangement of coordinated H_2O molecules (Figure II-3a, one H_2O ligand on each Mn^{III} ion in the set of four type II Mn^{III}). The four water molecules in $[\text{Mn}_{12}\text{O}_{12}(\text{PhCOO})_{16}(\text{H}_2\text{O})_4]$ and in $[\text{Mn}_{12}\text{O}_{12}(\text{CF}_3\text{COO})_{16}(\text{H}_2\text{O})_4]$ are arranged in a 2:0:2 fashion (Figure II-3b, two H_2O ligands on two Mn^{III} type II ions).^{9,10} Also, 1:2:1 and 1:1:2 isomers (Figure II-3c) have been found in different Mn_{12} -based molecules.^{1d,11} The exact number and the coordination position of the water molecules can vary from one Mn_{12} complex to another. Thus, $[\text{Mn}_{12}\text{O}_{12}(\text{C}_2\text{H}_5\text{COO})_{16}(\text{H}_2\text{O})_3]$ has only three coordinated water molecules in a 1:1:1 fashion (Figure II-3d), with one type II Mn^{III} ion that is five-coordinated. While for $[\text{Mn}_{12}\text{O}_{12}(\text{CHCl}_2\text{COO})_8(\text{Bu}'\text{-CH}_2\text{COO})_8(\text{H}_2\text{O})_3]$, the 2:0:1 isomer was reported (Figure II-3e).¹² Moreover there were isolated complexes with methanol molecules in axial positions instead of water.¹³ Nevertheless, all these Mn_{12} isomers preserved their SMM property.

As a consequence of the arrangement of Mn^{IV} and Mn^{III} ions in the oxo-metallic core, Mn_{12} complexes have a high spin ground state $S_T = 10$, which can be understood after the analysis of the magnetic core's structure. Assuming that the Mn^{IV} ($S = 3/2$) of the central $[\text{Mn}^{\text{IV}}_4\text{O}_4]^{8+}$ cubane are coupled ferromagnetically and so are all of the Mn^{III} ($S = 2$) from the external ring, the antiferromagnetic coupling between two subsets of Mn ions yields an $S_T = 10$ value of spin ground state.

Most of the magnetic anisotropy of the ground state in $\text{Mn}_{12}\text{-OAc}$ comes from the magnetic anisotropy of outer eight Mn^{III} ions. The coordination around each Mn^{III} ion is actually not a regular octahedron, but is axially distorted, as two bonds are longer than the other four. In the case of high spin d^4 ion like Mn^{III} ($S = 2$), the fourth electron can go into either one of the e_g orbitals and a Jahn-Teller (JT) distortion arises, causing a tetragonal elongation of axial $\text{Mn}^{\text{III}}\text{-O}$ bonds (Figure II-4).¹⁴ In Mn_{12} complexes, the axial elongation of two *trans* bonds increases typically by 0.1–0.2 Å.⁹ These JT elongation axes do not involve the $\text{Mn}^{\text{III}}\text{-}\mu_3\text{-O}^{2-}$ bonds, as they are the strongest bonds in the molecule. JT axes are all axially disposed, nearly perpendicularly to the plane of the $[\text{Mn}_{12}\text{O}_{12}]$ disk-like core (Figure II-5 left). The nearly-parallel alignment of the eight Mn^{III} JT axes along the molecular z -axis is the origin of the significant uniaxial magnetic anisotropy that greatly influences the magnetic properties of Mn_{12} -based systems.

In the structures of some Mn_{12} complexes, it was observed that one Mn^{III} JT elongation axis can be oriented equatorially rather than axially in regard to the Mn_{12} planar core (Figure II-5 right).¹⁵ This abnormal

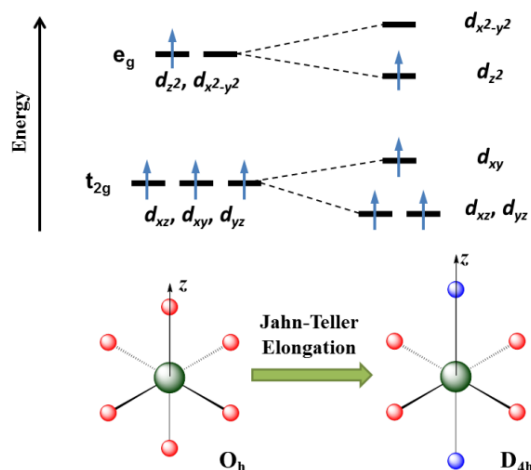


Figure II-4. (top) d Orbital electronic configurations of distorted d^4 high spin octahedral complexes, emphasizing the effect of tetragonal elongation on the energies of d orbitals; (bottom) Schematic representation of regular octahedral complex (O_h), where all six ligands are identical and equidistant from the metal center, and the Jahn-Teller distortion with axial elongation, where two ligands in *trans* positions to each other are further than the other planar four ligands.

orientation is a local higher-energy situation stabilized by crystal packing effects and can be reoriented if the latter are relaxed. For example, the loss of co-crystallized solvent upon drying or the recrystallization from different solvents can convert to the isomer with normal orientation.¹⁶ The ability of a molecule to exist in two distinct forms differing only in the relative orientation of one or more JT axes has been named Jahn-Teller isomerism. Thus, not only coordinated water molecules are responsible for the existence of different structural isomers of Mn_{12} core, but also Mn^{III} ions are. This structural distortion involving JT axes is at the origin of the low temperature (or fast relaxing) ac susceptibility signal, since the abnormal orientation of one JT axis alters the nearly-parallel alignment and, thus, influences the uniaxial magnetic anisotropy.

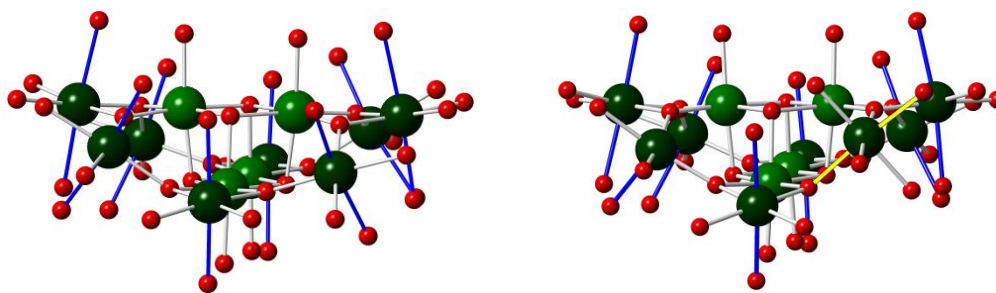
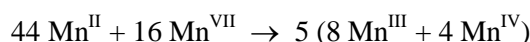


Figure II-5. Structural view parallel to the molecular plane of different Mn_{12} -based cores, emphasizing the orientation of the JT axes: (left) Mn_{12} -OAc with JT axes axially disposed, and (right) $[Mn_{12}O_{12}(CHCl_2COO)_8(Bu^t-CH_2COO)_8(H_2O)_3]$ with one abnormally oriented JT axis. Color scheme: normally oriented JT axes are shown in blue and the abnormally oriented JT axis is shown in yellow, Mn^{III} dark green, Mn^{IV} green, O red. Hydrogen and carbon atoms are omitted for clarity.

II.2.3. Chemistry of Mn_{12} -based complexes

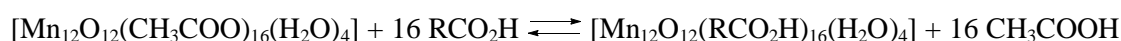
There are basically two synthetic procedures available for making new $[Mn_{12}O_{12}(O_2CR)_{16}(H_2O)_4]$ complexes. The first involves the comproportionation between a Mn^{II} source and Mn^{VII} from MnO_4^- in the presence of the desired carboxylic acid ($RCOOH$). This was the original method used by Lis^{1a} to synthesize $[Mn_{12}O_{12}(CH_3COO)_{16}(H_2O)_4]$ complex with a high yield of crystalline material. The method includes the

reaction between $\text{Mn}(\text{CH}_3\text{COO})_2$ and KMnO_4 in 60% aq. acetic acid in an appropriate ratio, according to the following simplified equation:



Similarly, $[\text{Mn}_{12}\text{O}_{12}(\text{PhCOO})_{16}(\text{H}_2\text{O})_4]$ can be obtained by comproportionation of $n\text{Bu}_4\text{NMnO}_4$ with $\text{Mn}(\text{CH}_3\text{COO})_2$ in the presence of benzoic acid,^{1c} and $[\text{Mn}_{12}\text{O}_{12}(p\text{-R-PhCOO})_{16}(\text{H}_2\text{O})_4]$ ($\text{R} = \text{Cl}, \text{CH}_3, t\text{Bu}$) by the analogous reaction of $\text{Mn}(\text{ClO}_4)_2$ and $n\text{Bu}_4\text{NMnO}_4$ in ethanol in the presence of $p\text{-R-C}_6\text{H}_4\text{COOH}$;¹⁷ the yields are generally less than those obtained by carboxylate substitution method (see below).

The second method of Mn_{12} derivatives synthesis is based on ligand substitution reactions,¹⁸ which are driven by the greater acidity of the added carboxylic acids RCO_2H and/or the removal by distillation of an azeotrope of acetic acid and toluene:



It has to be emphasized that ligand substitution is a reversible process. In order to shift the reaction equilibrium towards the formation of desired products, several treatments with the new carboxylic acid are sometimes needed (to replace all acetate groups) or the reactions are carried out in the presence of an excess of the substituting ligands. The main advantage of this technique is that reaction yields are generally larger than those obtained in the previous approach. Many carboxylate substitutions have been successful in the Mn_{12} chemistry using this approach.¹⁸

Derivatives of Mn_{12} -based SMMs with ligands other than carboxylates or with site-specific modifications yielding mixed-carboxylate $[\text{Mn}_{12}\text{O}_{12}(\text{RCOO})_8(\text{R}'\text{COO})_8(\text{H}_2\text{O})_4]$ type complexes, have been achieved.¹² The structural JT distortion (discussed above) has also important consequences on the relative reactivity of the carboxylate groups. The JT elongation of a metal-ligand bond weakens that bond. For a donor ligand such as carboxylate, JT elongation will serve to maintain a greater electron density on their O atoms compared with the O atoms of Mn-O bonds which are not elongated by JT effect. This will make RCOO^- groups possessing an O atom lying on a JT axis more sensitive to electrophilic attack at the O atom. This remark could form the basis for selective subtraction of these RCOO^- groups. Thus, addition of 8 equivalents of $\text{R}'\text{COOH}$ to a pre-formed $[\text{Mn}_{12}\text{O}_{12}(\text{RCOO})_{16}(\text{H}_2\text{O})_4]$ (where $\text{R}'\text{COOH}$ is a stronger acid than RCOOH) allows direct access to the mixed-carboxylate product $[\text{Mn}_{12}\text{O}_{12}(\text{RCOO})_8(\text{R}'\text{COO})_8(\text{H}_2\text{O})_4]$:



This is, indeed, not generally a useful method to obtain mixed-carboxylates, because a smaller pK_a difference between the incoming and leaving acids yields a mixture containing species with different carboxylate compositions. A better approach used to prepare mixed-carboxylate complexes is to use an equimolar reaction of Mn_{12} homo-carboxylate species containing 16 RCOO^- ligands, and 16 $\text{R}'\text{COO}^-$ ligands, respectively. The resulting 8:8 product has ligands originating from a stronger acid (small pK_a , ex. $\text{R}' = \text{Cl}_2\text{CH}$) in the axial positions and ligands originating from a weaker acid (higher pK_a , ex. $\text{R} = t\text{BuCH}_2$) in the equatorial positions. Two examples of such mixed carboxylate complexes are $[\text{Mn}_{12}\text{O}_{12}(\text{Cl}_2\text{CHCOO})_8(t\text{BuCH}_2\text{COO})_8(\text{H}_2\text{O})_4]$ and $[\text{Mn}_{12}\text{O}_{12}(\text{Cl}_2\text{CHCOO})_8(\text{C}_2\text{H}_5\text{COO})_8(\text{H}_2\text{O})_4]$.¹²

In a site-specific way, Mn_{12} ligands can be replaced with non-carboxylate ligands. The treatment of Mn_{12} -OAc with 8 eq. of benzenesulfonic acid yields $[Mn_{12}O_{12}(CH_3COO)_8(PhSO_3)_8(H_2O)_4]$ complex with the $PhSO_3^-$ ligands on the eight axial sites above and below the disk-like magnetic core, as expected for ligands originating from a stronger acid.¹⁹ The non-carboxylate substituents have no significant effect on the electronic properties of the core as magnetic properties of the resulting compounds preserve the S_7 , D , and Δ_{eff} values within the normal range for Mn_{12} carboxylate complexes.

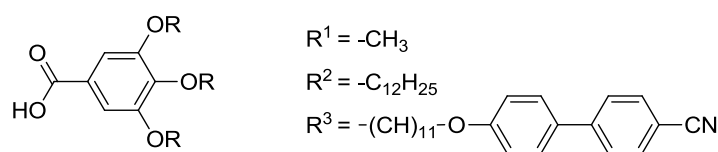
All of the above reported methodologies could be useful for introduction of different groups in order to design hybrid molecular materials, eventually with functional groups able to induce liquid crystalline properties.

II.3. Functionalization strategies towards liquid crystalline SMMs

Two different strategies can be applied on the Mn_{12} -OAc complex in order to induce mesomorphic properties. These procedures consist in: (a) the functionalization of peripheral ligands with strongly lipophilic groups (long alkyl chains), or (b) the grafting of a mesomorphic promoter through a flexible aliphatic spacer. Both strategies allow improving interfaces and area compatibilities between moieties (rigid and soft) and were successfully used to obtain thermotropic mesophases with fullerenes,²⁰ octahedral coordination complexes,²¹ polyoxometalates²² or metallic clusters.²³

There are only a few examples of coordination compounds combining SMM behavior and mesomorphic properties induced by functionalization of peripheral ligands.^{24,25} The first attempt to introduce liquid crystalline properties to a Mn_{12} -based SMM was reported in 2008 by Terazzi et al.^{24a} Thus, by applying strategies mentioned above it was possible to modify original Mn_{12} -OAc complex by the replacement of 16 acetate groups with gallic acid derivatives, which had three dodecyl or (cyanobiphenyloxy)undecyl chains (Scheme II-1). The magnetic properties were preserved, thermal stability (up to 425 K) was improved (if compared with the original Mn_{12} -OAc starting material; < 330 K), and it was possible to induce smectic or cubic mesophases in the final compounds.

Scheme II-1. Chemical structures of gallic acid derivatives used by Terazzi et al.^{24a}



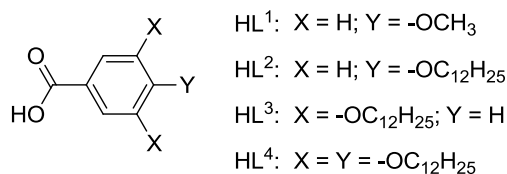
The complex containing strongly lipophilic ligand (R^2 on Scheme II-1) such as tris(dodecyloxy)benzoic acid shows a 3D body-centered cubic mesophase^{24a}, that could be induced by the large number (48) of long alkyl chains. The large lipophilic density around the rigid magnetic core, formed functionalized molecules of almost spherical (spherulitic) shape that caused a cubic organization, since the systems of spherulitic shape tend to form cubic phases.²⁶

Besides the report of Terazzi et al.,^{24a} the work on functionalization of Mn_{12} -based SMMs was started almost at the same time in our team by Diana Siretanu during her PhD thesis (CRPP, 2008 – 2011).²⁷ During this work a series of *p*-*n*-alkoxybenzoic acids (i.e. nonyloxy-, decyloxy-, dodecyloxy- and

hexadecyloxybenzoic acids) was chosen for functionalization of Mn_{12} -based SMMs. Even though all exploited functionalized *p*-*n*-alkoxybenzoic acids are well-known for their liquid crystalline properties²⁸ the series of prepared functionalized Mn_{12} -based complexes did not show any mesomorphic behaviour.

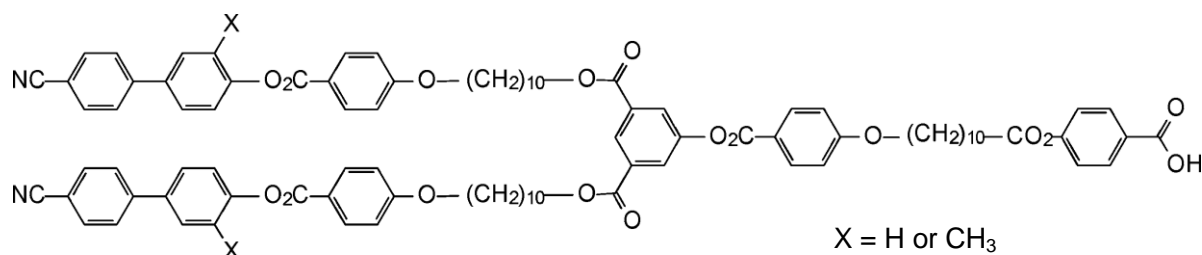
In the first part of our work focused on SMM functionalization with lipophilic groups (section II.4) we have chosen ligands HL^i (Scheme II-2) containing one, two or three long dodecyl chains attached to benzoate moiety. Our goal was to test if the variation of lipophilic chains density would offer reduced globular bulkiness of the final products, and ultimately less oriented and symmetric phases than the cubic one observed by Terazzi et al.^{24a} For a better understanding and confirmation of complete acetate substitution, long chain substituted compounds were compared with a model compound $[Mn_{12}O_{12}(L^1)_{16}(H_2O)_3]$ with a very short terminal methoxy group. The complex containing tris(dodecyloxy)benzoic acid as peripheral ligand $[Mn_{12}O_{12}(L^4)_{16}(H_2O)_4]$ reported by Terazzi et al.^{24a} was resynthesized and characterized, as well, in order to have a full series of compounds for comparison, this should allow a better understanding and rationalization of the influence of specific structural variations on the magnetic and self-organizational properties of the Mn_{12} complexes containing a varying density of lipophilic groups.

Scheme II-2. Chemical structure of HL^i ($i=1-4$) ligands, based on modified benzoic acid scaffold, for Mn_{12} functionalization.



Grafting a mesogenic promoter through a flexible aliphatic spacer to Mn_{12} -based core is another strategy that was applied by Terazzi et al.^{24a} in functionalization of Mn_{12} -based SMMs. The compound, in which all of the sixteen axial and equatorial acetates were replaced by the ligand with R^3 (Scheme II-1), displayed a supramolecular lamellar-like organization, with a short-ranged 2D intralayer hexagonal or square-like ordering of rigid magnetic cores above 313 K.^{24a} The main disadvantage of this system is the impossibility of reaching the clearing point without decomposing the compound, fact that may limit the further processing, like transposing the bulk ordering on surfaces. Later in 2011, the same team reported^{24b} an attempt to decrease the clearing temperature by functionalization of benzoate-based ligands with two-branched dendritic structures (Scheme II-3) containing as terminal groups original and methylated

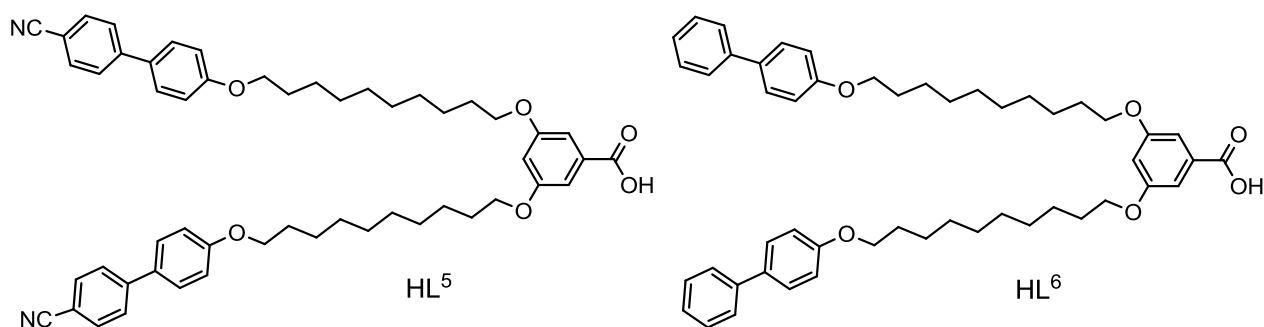
Scheme II-3. Structure of dendritic ligands reported to obtain Mn_{12} -based complexes showing cyanobiphenyl induced lamellar phases.^{24b}



cyanobiphenyl groups. Even though the methylation of cyanobiphenyl group helped decreasing the clearing point by 60 degrees, it still remained quite high; i.e. 411 K.

Later in 2013, a series of Mn_{12} -based complexes with benzoic acid derivatives containing a varying number of (cyanobiphenyloxy)undecyl chains was reported.^{24c} The clearing point was above decomposition temperature and the self-organization of the reported complexes inside the liquid crystalline phase was influenced by the presence of strong intermolecular interactions driven by cyanobiphenyl mesogenic group, and not by the number of attached mesogenic groups or ligand symmetry similarly to the compounds reported in 2011.^{24b,c}

Scheme II-4. Chemical structure of HL^i ($i = 5-6$) ligands, based on modified 3,5-dihydroxybenzoic acid, for Mn_{12} functionalization.



In the second part of our work focused on SMM functionalization (section II.5), we have chosen to functionalize 3,5-dihydroxybenzoic acid with (cyanobiphenyloxy)decyl and (biphenyloxy)decyl chains (Scheme II-4) and to study the corresponding Mn_{12} complexes. With the aim to weaken the intermolecular interactions and, thus, to decrease the clearing point temperature the biphenyl moiety is used as the mesogenic terminal group (in the case of HL^6 ligand) and compared with cyanobiphenyl analogue (ligand HL^5).

II.4. Functionalization of Mn_{12} -based SMMs with strongly lipophilic groups

II.4.1. Synthetic procedures and purification

The Mn_{12} -based hybrids were obtained from $[Mn_{12}O_{12}(OAc)_{16}(H_2O)_4]$ by ligand exchange technique, taking the advantage of the ability of Mn_{12} molecules to undergo carboxylate substitution (via ligand exchange on the pre-formed Mn_{12} complex). This feature provides an extremely useful and convenient approach to get other carboxylate derivatives of Mn_{12} . The acetate groups were substituted by corresponding carboxylic derivatives (HL^i):



The ligand substitution is a reversible process. In order to shift the reaction equilibrium towards the formation of desired products, the reactions were carried out in the presence of an excess of the substituting ligands (HL^i), followed by the removal of AcOH as azeotrope mixture with toluene. In order to obtain the Mn_{12} -OAc precursor, the procedure reported by Lis in 1980 was slightly modified (See Supporting information). Some of the benzoic acid derivatives (HL^{1-2}), used to replace the 16 acetate groups, were

commercially available while others HL³ and HL⁴ were prepared by slightly modified published methods (see Supporting materials, Section II.7.1).

Several purification techniques were used to separate the substituted complexes from the reaction mixture and ligand excess. The compound with 4-methoxybenzoic (HL¹) acid was crystallized and purified by recrystallization. In our investigations, this compound served as a model system for this type of substitution. Since its structure was determined by single crystal X-ray diffraction, other analytical characterizations (including FT-IR and ¹H NMR spectroscopies) of this compound were very helpful in proving the ligand substitution and the purity of the synthesized hybrid compounds. Complexes substituted by long alkoxy chains were purified by size exclusion column chromatography, in order to separate the unreacted ligand or the partially substituted complex from the fully substituted Mn₁₂-complexes. Bio-Beads S-X3 beads (neutral, porous styrene divinylbenzene copolymer beads) swelled with CH₂Cl₂ were used as stationary phase. The ligand is more retained inside the column compared to the final product, but the separation was not easy to control. Thus, each small volume (~ 1-2 mL) of eluents was collected one by one, and then each of them was characterized by FT-IR to check the eventual presence of free ligand, acetic acid or unsubstituted acetate. This procedure was repeated twice. Three new compounds, with the general formula [Mn₁₂O₁₂(Lⁱ)₁₆(H₂O)_x] (*i* = 1-3, *x* = 3 or 4), and the previously reported [Mn₁₂O₁₂(L⁴)₁₆(H₂O)₄] complex, were synthesized and purified by the methods presented above. The structural and physical properties of synthesized complexes were characterized by different techniques.

II.4.2. Analytical characterizations of substituted Mn₁₂ complexes

II.4.2.1. Single crystal X-ray analysis of the model compound [Mn₁₂O₁₂(L¹)₁₆(H₂O)₃]

The crystal structure of the 4-methoxybenzoate-substituted compound, [Mn₁₂O₁₂(L¹)₁₆(H₂O)₃], validated the chosen synthetic method for substitution of acetate groups of the original Mn₁₂-OAc complex and allowed to check the bonding mode of the benzoate groups on the Mn₁₂ core. Crystals, suitable for X-ray diffraction experiment, were prepared by slow diethyl ether diffusion into dichloromethane solution of [Mn₁₂O₁₂(L¹)₁₆(H₂O)₃] in refrigerator at 277 K (4°C), and then re-crystallized by the same method. The compound crystallized in the triclinic *P*-1 space group with two Mn₁₂ molecules in the unit cell related by crystallographic center of inversion. Two water molecules and one disordered diethyl ether molecule are present in the unit cell. Structural parameters can be found in Table S.II-1.

The structure of [Mn₁₂O₁₂(L¹)₁₆(H₂O)₃] (Figure II-6) is quite similar in many aspects to the previously reported Mn₁₂-family complexes.^{1,6,9,11a,18,24a} There is a central [Mn^{IV}₄O₄] cube-like core surrounded by a non-planar ring of eight outer Mn^{III} ions, which are bridged and connected to the central cube via μ₃-O²⁻ ions. The peripheral ligation is achieved by sixteen bridging 4-methoxybenzoate ligands (eight in equatorial, in-plane, and eight in axial, out-of-plane, positions) and only three terminal H₂O molecules (rather than four usually found in Mn₁₂ complexes), two on Mn10 and one on Mn12, as it was previously observed in several other cases.^{11,12} There are two types of Mn^{III} ions inside the magnetic core. Those doubly bridged to one Mn^{IV} are type I, and those singly bridged to two Mn^{IV} are type II. The water molecules are bound to type II ions. As was mentioned in the paragraph II.2.2, the isomers of Mn₁₂ molecules can be differentiated depending on the

way of water molecules coordination on type II Mn^{III} ions. The present compound corresponds to the 2:0:1 form (see Figure II-3) as two of three water molecules are on the same Mn^{III} ion and the third is on another Mn^{III} ion, whereas the predominant isomer in precursor is the 1:1:1:1 form where one water molecule per type II ion is present.^{1b,29} One of Mn^{III} ions (Mn6) in [Mn₁₂O₁₂(L¹)₁₆(H₂O)₃] is consequently five-coordinated with square-pyramidal geometry (Figure II-7). This is certainly induced by a solid-state effect, and in solution, it is anticipated that all Mn^{III} ions are six-coordinate as described previously.¹²

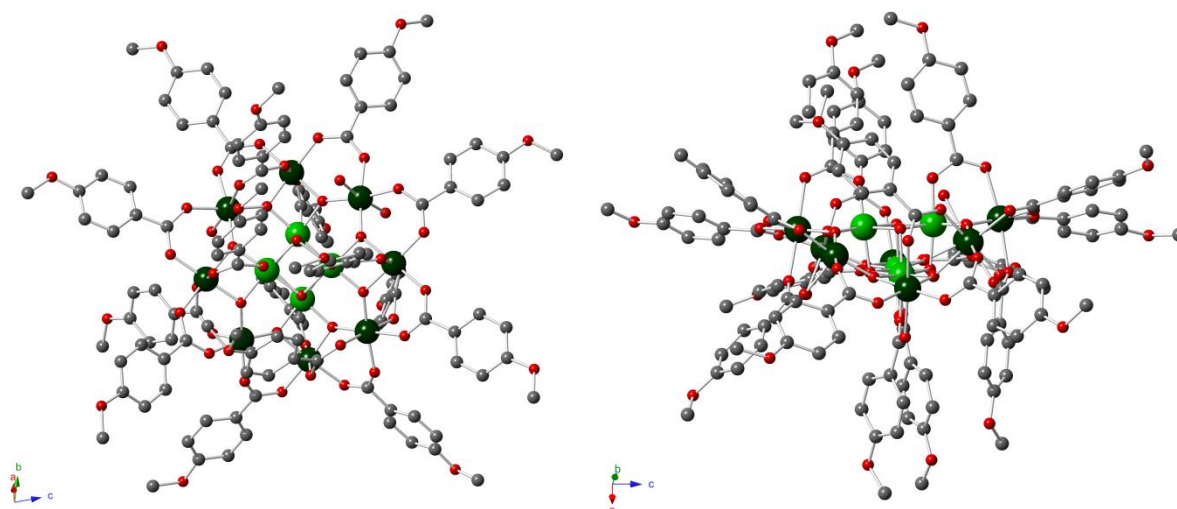


Figure II-6. Crystal structure at 100 K of [Mn₁₂O₁₂(L¹)₁₆(H₂O)₃] viewed in the *bc* plane (left) and in the *ac* plane (right). Lattice solvent molecules and hydrogen atoms are omitted for clarity. Color scheme: Mn^{IV} green, Mn^{III} dark green, O red, C grey.

The Mn-O bond distances (Table S.II-2) indicate without ambiguity that the four metal ions in the cube-like core are Mn^{IV}, while the surrounding manganese ring consists of eight Mn^{III} ions. Indeed a comparison between Mn^{IV}-O_b (where O_b is 4-methoxybenzoate oxygen; av. = 1.906 Å) and Mn^{III}-O_b (av. = 1.963 Å; oxygen from in-plane 4-methoxybenzoate) indicates that the cubane manganese ions are in a higher oxidation state. These assignments are supported by the Jahn-Teller elongation of the axial Mn-O bonds (2.075 – 2.261 Å), which are on average longer than the equatorial Mn-O bonds (1.908 – 1.972 Å). In contrast, the six Mn^{IV}-O distances around each of the central cubane Mn^{IV} ions are on average shorter and in a comparatively narrower range (1.836 – 1.939 Å), due to the different O atoms involved, 4-methoxybenzoate vs. bridging μ₃-O²⁻. A closer examination of the crystal structure showed that one JT axis is abnormally oriented as shown in Figure II-7 in yellow. The bond distances support this distortion. The two bonds on Mn8 connected to the out-of-plane 4-methoxybenzoate ligand (Mn8-O_b) are 1.933 and 1.950 Å, instead of usual elongated values. Similarly, the Mn8-μ₃-O²⁻ (2.106 Å) and Mn8-O_b (2.131 Å; oxygen from in-plane 4-methoxybenzoate) bonds are noticeably longer than those on other Mn^{III} ions. This abnormal orientation is a local lower-energy situation stabilized by complicated crystal packing effects and can be reoriented if the latter are relaxed.^{16a} This structural distortion, involving JT axes, is at the origin of the low temperature (or fast relaxing) χ'' ac susceptibility signal, since the abnormal orientation of one JT axis alters the nearly-parallel alignment and, thus, decreases the uniaxial magnetic anisotropy.³⁰

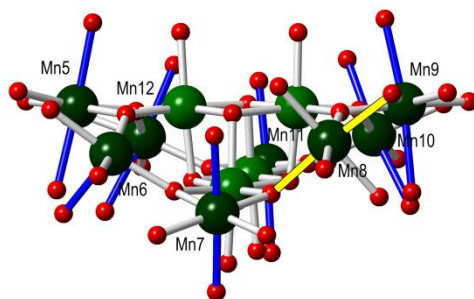


Figure II-7. Structural view of $[\text{Mn}_{12}\text{O}_{12}(\text{L}^1)_{16}(\text{H}_2\text{O})_3]$ parallel to the molecular plane. JT axes are shown in blue and the abnormally oriented JT axis is shown in yellow. Colour scheme: Mn^{IV} green, Mn^{III} dark green, O red.

Several intermolecular interactions are present in the crystal packing. In one Mn_{12} -molecule, two of the three water molecules coordinated to Mn^{III} ions form $\text{O}\cdots\text{O}$ hydrogen bonds ($\text{O}\cdots\text{O}$, $\sim 2.71\text{--}2.75$ Å) with methoxy oxygen atoms from the ligands of other two Mn_{12} -molecules. The third water molecule coordinated to Mn_{12} core is directly H-bonded with the lattice water molecule ($\text{O}\cdots\text{O}$, ~ 2.69 Å). Moreover, close π - π contacts (ca. 3.69 Å, Figure S.II-1) are formed between 4-methoxybenzoate ligands of two adjacent complexes. Thus, inside the packing, one molecule is hydrogen-bonded with two others and with a third one via π -stacking. Such structural interactions have significant influence on magnetic properties and can lead to intermolecular antiferromagnetic interactions, especially when molecules have one or several reversed neighboring molecules.³¹

As it was mentioned previously, the single crystal structure of the 4-methoxybenzoate substituted complex $[\text{Mn}_{12}\text{O}_{12}(\text{L}^1)_{16}(\text{H}_2\text{O})_3]$ confirmed our synthetic method to replace acetate ligands from the original $\text{Mn}_{12}\text{-OAc}$ complex. Other analytical characterizations of $[\text{Mn}_{12}\text{O}_{12}(\text{L}^1)_{16}(\text{H}_2\text{O})_3]$ such as FT-IR, $^1\text{H-NMR}$, TGA and elemental analysis helped us to confirm the structure of the $[\text{Mn}_{12}\text{O}_{12}(\text{L}^{2-4})_{16}(\text{H}_2\text{O})_4]$ analogues.

II.4.2.2. FT-IR spectroscopic analyses

FT-IR spectroscopy is a helpful tool to study the ligand exchange in Mn_{12} -based complexes. It allows not only to confirm that the acetate ligand was replaced by another carboxylate-based ligand, but also to observe in the obtained compound if the substitution was complete or if it contains impurities such as free acetic acid or other carboxylate based ligand. Each of the benzoic acid based ligands shows very strong bands for $\text{C}=\text{O}$ and $\text{C}-\text{O}$ stretches that appear around $1670\text{--}1687\text{ cm}^{-1}$ and $1254\text{--}1276\text{ cm}^{-1}$, respectively. In the FT-IR spectra of the final compounds, the strong $\text{C}=\text{O}$ band ($1670\text{--}1687\text{ cm}^{-1}$) from acidic ligand disappears, while two other bands around $1577\text{--}1587\text{ cm}^{-1}$ and $1406\text{--}1412\text{ cm}^{-1}$ appear (red curves in Figure S.II-2 - Figure S.II-5). These vibrations correspond to antisymmetrical and symmetrical OCO stretches of carboxylate ligands in their bidentate bridging mode.³² This result suggests that the deprotonated ligand was covalently grafted onto the manganese core and no free ligand or acetic acid were present in the sample. It is worth noting that the precursor complex, $[\text{Mn}_{12}\text{O}_{12}(\text{CH}_3\text{COO})_{16}(\text{H}_2\text{O})_4]$, (Figure S.II-6) shows $\text{C}=\text{O}$ stretching band ($\sim 1700\text{ cm}^{-1}$) arising from free acetic acids existing in the channels formed by the packing of the complex. In the case of our compounds, the ligand itself is probably too bulky to stay in the inter-molecular void space. Also, the FT-IR spectra indicate that the removal of acetic acid as its toluene azeotrope was complete. Furthermore, no significant changes for $\text{C}-\text{O}$ ($\approx 1260\text{ cm}^{-1}$) and $\text{C}-\text{H}$ ($\approx 2900\text{ cm}^{-1}$)

stretching bands indicate that the reacted ligand was well preserved without any major structural deformation after the reaction, except for the deprotonation.

II.4.2.3. ^1H NMR spectroscopic analyses

Due to the presence of paramagnetic centers, ^1H NMR spectroscopy may appear to be an inappropriate analysis technique because serious signal broadening and shifts may not allow proper peak attribution. However, it is known that nonequivalency of the binding sites on original $\text{Mn}_{12}\text{-OAc}$ core causes apparition of three peaks at $\delta = 13.7$, 40.9 and 47.8 ppm corresponding to methyl groups from coordinated acetic acid.^{11a} Thus, the absence of these peaks in the ^1H NMR spectra of prepared complexes indicates complete substitution of acetate by functionalized benzoate-based ligands (Figure II-8).

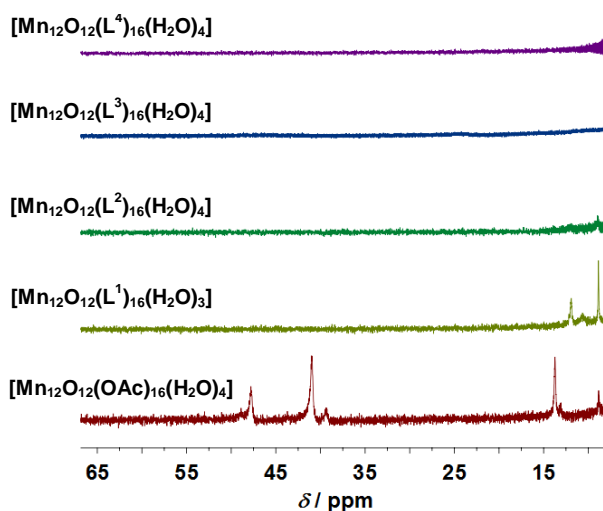


Figure II-8. ^1H NMR spectra of $[\text{Mn}_{12}\text{O}_{12}(\text{OAc})_{16}(\text{H}_2\text{O})_4]$ in CD_3CN and $[\text{Mn}_{12}\text{O}_{12}(\text{L}^{i=1-4})_{16}(\text{H}_2\text{O})_{x=3 \text{ or } 4}]$ in CDCl_3 at 298 K.

II.4.2.4. Elemental and thermo-gravimetric analyses

The complete substitution in 16 positions by benzoate-based ligands was also demonstrated by elemental analysis which is in good agreement with the proposed formulas. The results from elemental analysis (Table II-1) were completed with the help of thermo-gravimetric analysis (TGA).

Table II-1. Elemental analyses of $[\text{Mn}_{12}\text{O}_{12}(\text{L}^{1-4})_{16}(\text{H}_2\text{O})_x]$ ($x = 3$ or 4) complexes

Compound	%C (found)	%H (found)	%C (calc.)	%H (calc.)
$[\text{Mn}_{12}\text{O}_{12}(\text{L}^1)_{16}(\text{H}_2\text{O})_3] \cdot \text{H}_2\text{O}$ $\text{C}_{128}\text{H}_{120}\text{Mn}_{12}\text{O}_{64}$	46.05	3.73	46.01	3.62
$[\text{Mn}_{12}\text{O}_{12}(\text{L}^2)_{16}(\text{H}_2\text{O})_4] \cdot 2\text{H}_2\text{O}$ $\text{C}_{304}\text{H}_{476}\text{Mn}_{12}\text{O}_{66}$	62.30	8.19	62.28	8.21
$[\text{Mn}_{12}\text{O}_{12}(\text{L}^3)_{16}(\text{H}_2\text{O})_4] \cdot 6\text{H}_2\text{O}$ $\text{C}_{496}\text{H}_{868}\text{Mn}_{12}\text{O}_{86}$	67.58	10.01	67.18	9.87
$[\text{Mn}_{12}\text{O}_{12}(\text{L}^4)_{16}(\text{H}_2\text{O})_4] \cdot \text{H}_2\text{O}$ $\text{C}_{688}\text{H}_{1246}\text{Mn}_{12}\text{O}_{99}$	69.89	10.73	70.25	10.68

From the thermo-gravimetric analyses (Figure S.II-9), it was determined that there were present co-crystallized water molecules in the inter-complex void space because of the first weight loss around 370 K. The amount of absorbed water molecules in each complex was determined using both TG and elemental

analysis. In the case of $[\text{Mn}_{12}\text{O}_{12}(\text{L}^1)_{16}(\text{H}_2\text{O})_3]$, it was possible to detect the co-crystallized water molecules and not the lattice diethyl ether molecule. Thus, it is likely that the lattice diethyl ether molecule was lost easily as a function of exposure time in the air, because the crystals for TGA were kept in air outside mother liquor more time (about an hour) than the one chosen for X-ray analysis. Upon further heating above 420 K, all samples begin to decompose due to elimination of coordinated water, observed as a second weight lost. Complex $[\text{Mn}_{12}\text{O}_{12}(\text{L}^1)_{16}(\text{H}_2\text{O})_3]$, with the shortest alkoxy group on its ligand, shows good thermal stability up to 500 K compared to those with long alkoxy chains that begin to decompose above 420 K (Figure S.II-9). Above 550 K the decomposition leads ultimately to Mn_3O_4 phase according to previous studies.³³

II.4.3. Magnetic measurements

Direct evidence that the Mn_{12} core preserved its structural integrity and physical properties is given by magnetic measurements. Complexes were checked for SMM behavior by investigation of their magnetic properties using *ac* and *dc* modes.

The presence of frequency dependent out-of-phase *ac* signal (χ'') is considered to be the characteristic feature of superparamagnetic-like or SMM behaviour.¹ An out-of-phase *ac* magnetic susceptibility signal is observed when the rate at which the magnetic moment of a molecule flips is close to the operating frequency of the *ac* magnetic field. The system is able to follow the *ac* field only when the magnetization relaxation is fast. Thus a non-zero frequency dependent χ'' signal suggests the presence of slow relaxation of magnetization. From the *ac* susceptibility study, the effective energy barrier (Δ_A) for the relaxation of magnetization can be estimated. Moreover, this study can also give the information about the nature of the magnetization relaxation process.

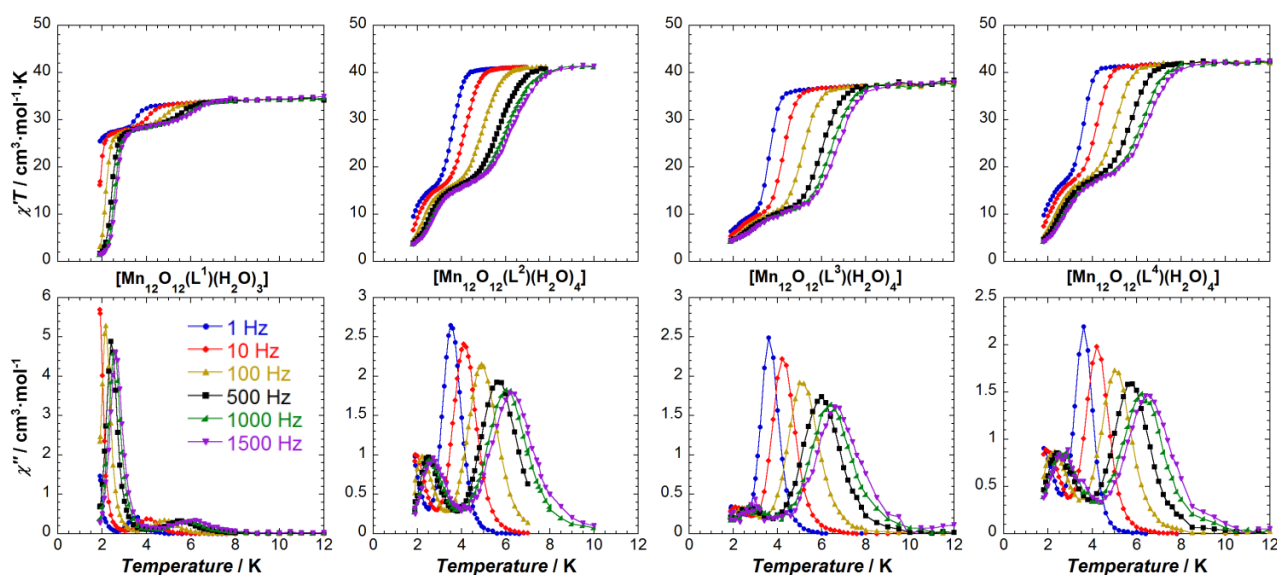


Figure II-9. Temperature dependence of $\chi'T$ and χ'' for $[\text{Mn}_{12}\text{O}_{12}(\text{L}^i)_{16}(\text{H}_2\text{O})_x]$ ($i = 1 - 4$, $x = 3 - 4$) measured under various oscillating frequencies (1-1500 Hz) in zero dc field. The solid lines are guides for the eyes.

The temperature dependence of the in-phase (χ') and out-of-phase (χ'') components of the *ac* susceptibility were measured in a zero static external field with different frequencies ranging from 1 to 1500 Hz (Figure II-9). The frequency-dependent decrease in $\chi'T$ at low temperature is attributed to a blocking process of the magnetization and was observed in all complexes. The values of $\chi'T$ at the plateau (8 - 10 K)

are $34.5 - 42 \text{ cm}^3 \cdot \text{K/mol}$ and correspond to a ground state of $S_T = 9$ (while for the original $\text{Mn}_{12}\text{-OAc}$ $S_T = 10$) with $g = 1.75 - 1.93$. This behavior is not surprising, since the substitution of the acetate from $\text{Mn}_{12}\text{-OAc}$ with benzoate,^{1c} propionate,^{11a} 3-chlorobenzoate³⁴ ligands or with some of functionalized benzoic acids,^{24,27} leads to Mn_{12} complexes with the ground state $S_T = 9$, while low values of g factor were reported for Mn_{12} complex with *p*-phenylbenzoic acid ($g = 1.73$) and for a mixed carboxylate complex with four acetates and twelve *o*-cyanobenzoates ($g = 1.70$).^{35,36} The substitution of the ligand influences the intra- and inter-molecular organizations, and thus the couplings, that lead to ground states different from parent compound. A second plateau can be observed at lower temperatures, suggesting that there are two different relaxation processes. The origin of these two relaxations is attributed to Jahn-Teller (JT) isomerism.^{16a,33} The ratio of each isomer present in the measured sample can be quantified by the difference of the two plateaus present in $\chi'T$ vs T plots. In the $[\text{Mn}_{12}\text{O}_{12}(\text{L}^1)_{16}(\text{H}_2\text{O})_3]$ sample, a ratio of 85% to 15 % of low temperature (LT) to high temperature (HT) JT isomers is present, while in other Mn_{12} -functionalized samples reported herein the amount of HT species is predominant and varies between 60% and 80% (Table II-2).

Table II-2. Magnetic Properties for $[\text{Mn}_{12}\text{O}_{12}(\text{L}^i)_{16}(\text{H}_2\text{O})_x]$ ($i = 1 - 4$, $x = 3$ or 4)

Compound	S	g	JT isomers ratios LT (%) / HT (%)	Low temperature (LT) or fast relaxing (FR) JT isomer		High temperature (HT) or slow relaxing (SR) JT isomer		$\mu_0 H_C$ (T)
				Δ_{eff}/k_B (K)	τ_0 (s)	Δ_{eff}/k_B (K)	τ_0 (s)	
				$[\text{Mn}_{12}\text{O}_{12}(\text{L}^1)_{16}(\text{H}_2\text{O})_3]$	9	1.75	85 / 15	
$[\text{Mn}_{12}\text{O}_{12}(\text{L}^2)_{16}(\text{H}_2\text{O})_4]$	9	1.91	30 / 70	34.7	2.7×10^{-10}	59.1	9.7×10^{-9}	0.55
$[\text{Mn}_{12}\text{O}_{12}(\text{L}^3)_{16}(\text{H}_2\text{O})_4]$	9	1.82	20 / 80	33.2	2.7×10^{-9}	58.2	1.9×10^{-8}	0.83
$[\text{Mn}_{12}\text{O}_{12}(\text{L}^4)_{16}(\text{H}_2\text{O})_4]$	9	1.93	40 / 60	37.6	4.1×10^{-10}	58.0	2.0×10^{-8}	0.53

S : spin ground state; g : Lande factor of ground state; Δ_{eff} : potential energy barrier; τ_0 : pre-exponential factor; $\mu_0 H_C$: coercive field measured at $T = 1.9 \text{ K}$ and at $0.035 \text{ T} \cdot \text{min}^{-1}$ sweep rate.

As the temperature decreases, there is a temperature ($\sim 8 \text{ K}$) below which the magnetic moment of the complex cannot stay in phase with the oscillating field for ac frequencies between 1 and 1500 Hz. In accordance, χ'' signals appeared at the corresponding temperatures, indicating that the SMM behaviour of the samples was preserved. The maxima of the peaks in χ'' signal shift to higher temperature as the operating frequency increases. In all of the four complexes, two peaks in out-of-phase susceptibility were observed in the temperature regions of 2-3 K and 4-7 K, confirming two different relaxation processes. Complex $[\text{Mn}_{12}\text{O}_{12}(\text{L}^1)_{16}(\text{H}_2\text{O})_3]$ has a predominant peak in the 2-3 K region (85% of the sample, Figure II-9), whereas the other $[\text{Mn}_{12}\text{O}_{12}(\text{L}^{i=2-4})_{16}(\text{H}_2\text{O})_4]$ complexes show higher intensity peaks in 4-7 K region (60-80% of the sample). The lower-temperature (LT) signal indicates the presence of fast-relaxing (FR) Mn_{12} species involving abnormally oriented Mn^{III} JT axis that is almost perpendicular to the elongation axis of the other Mn^{III} centres. This unusual JT orientation makes the molecule to have lower symmetry and magnetic anisotropy that is important for slow relaxation, and induces a significant rhombic (transverse) anisotropic term within the molecules. In Figure II-7, it is showed that one of the Mn^{III} ions in $[\text{Mn}_{12}\text{O}_{12}(\text{L}^1)_{16}(\text{H}_2\text{O})_3]$ has a Jahn–Teller elongation axis almost perpendicular to the other. According to the crystal structure of $[\text{Mn}_{12}\text{O}_{12}(\text{L}^1)_{16}(\text{H}_2\text{O})_3]$ the JT distorted isomer is predominantly present in this complex, that explains the

occurrence of a significant out-of-phase signal at a lower temperature than for the parent $[\text{Mn}_{12}\text{O}_{12}(\text{CH}_3\text{COO})_{16}(\text{H}_2\text{O})_4]$ compound.⁹ There are several examples reported previously which showed the same behaviour (predominant LT isomer), and this can be affected by either the change of ligand or of co-crystallized solvent.^{16a,33} For the other complexes, for which no structure of the core is available, the presence of two strong peaks suggests the coexistence of different JT isomers within the sample, as already observed for many Mn_{12} derivatives.^{18,24,36}

From the position of the peak maximum in the χ'' versus T plot (Figure II-9), values of magnetization relaxation time (τ) could be determined as $\tau = (2\pi\nu_{\text{max}})^{-1}$ (where ν_{max} is the frequency of the oscillating magnetic field) at various temperatures (Figure II-10). The fitting to the Arrhenius law ($\tau = \tau_0 \cdot \exp(\Delta_{\text{eff}}/k_{\text{B}}T)$, where τ is the relaxation time, k_{B} is the Boltzmann constant, $\Delta_{\text{eff}}/k_{\text{B}}$ is the energy barrier of the thermally activated regime and τ_0 a pre-exponential factor), allowed us to determine $\Delta_{\text{eff}}/k_{\text{B}}$ with values for LT species between 32.5 – 37.6 K and between 58 – 62.5 K for HT species (Table II-2). Obtained $\Delta_{\text{eff}}/k_{\text{B}}$ values for the high temperature relaxation are in the range of 55 – 72 K reported for other Mn_{12} derivatives. The $\Delta_{\text{eff}}/k_{\text{B}}$ for the LT species is consistent with molecules possessing abnormally oriented JT axes, generating fast relaxing species.^{16a}

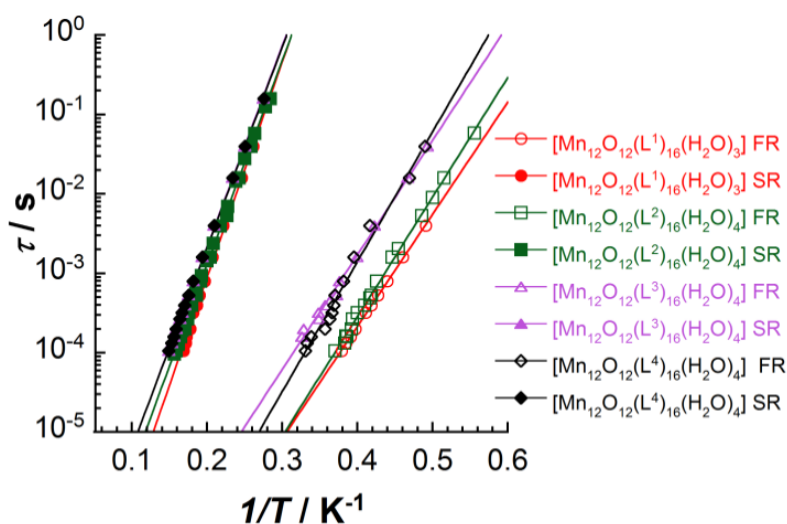


Figure II-10. Inverse temperature dependence of the relaxation time in semi-logarithmic scale for synthesized $[\text{Mn}_{12}\text{O}_{12}(\text{L}^{1-4})_{16}(\text{H}_2\text{O})_{3-4}]$ complexes using χ'' vs T data for the FR and SR species from Figure II-9. Full lines are the best fits to an Arrhenius law.

Direct-current (dc) magnetic susceptibility studies of functionalized Mn_{12} complexes have been carried out in an applied magnetic field of 1 kOe in the 300 – 1.8 K temperature range. The χT versus T data, where χ is the molar magnetic susceptibility, are shown in Figure S.II-10 left. The observed χT values at 280 K are in the range 17 – 20 $\text{cm}^3 \cdot \text{K} \cdot \text{mol}^{-1}$ that is in a good agreement with previously reported Mn_{12} complexes.^{1,2,11} The values of χT product slightly decrease between 280 and 120 K, suggesting a ferrimagnetic arrangement. As expected, the χT products increase significantly below 50 K, to reach maximum values of 35 – 42 $\text{cm}^3 \cdot \text{K} / \text{mol}$ at 12 – 13 K. At lower temperatures, the χT products decrease rapidly due to Zeeman and zero-field splitting (zfs) effects. Low temperature χT values for $[\text{Mn}_{12}\text{O}_{12}(\text{L}^i)_{16}(\text{H}_2\text{O})_x]$ compounds are lower than in the original $\text{Mn}_{12}\text{-OAc}$ complex confirming an $S_T = 9$ spin ground state as measured with ac susceptibility measurements.

Magnetization hysteresis loops at low temperatures are also an experimental manifestation of the SMM behavior. In all of the four samples, the field dependence of magnetization presents hysteresis loops with coercive fields varying from 0.03 to 0.83 T at 1.9 K with a field sweep rate of about $0.035 \text{ T} \cdot \text{min}^{-1}$ (Figure II-11). An interesting feature is the dramatic increase of the coercivity after functionalization with long alkyl chains (from 0.03 T for complex with HL^1 ligand to 0.53–0.83 T for complexes with functionalized HL^2 - HL^4 ligands), as a consequence of larger SR/FR species ratios (vide supra). The shape of magnetization vs. field curves and magnetization values at high fields ($\approx 16 \mu_B$) show an absence of magnetization saturation (Figure S.II-11) which is consistent with magnetic anisotropy and high spin ground state ($S > 8$) in a randomly oriented polycrystalline samples. This is also confirmed by the M vs. H/T plots (Figure S.II-12) at different temperatures (from 1.9 to 10 K).

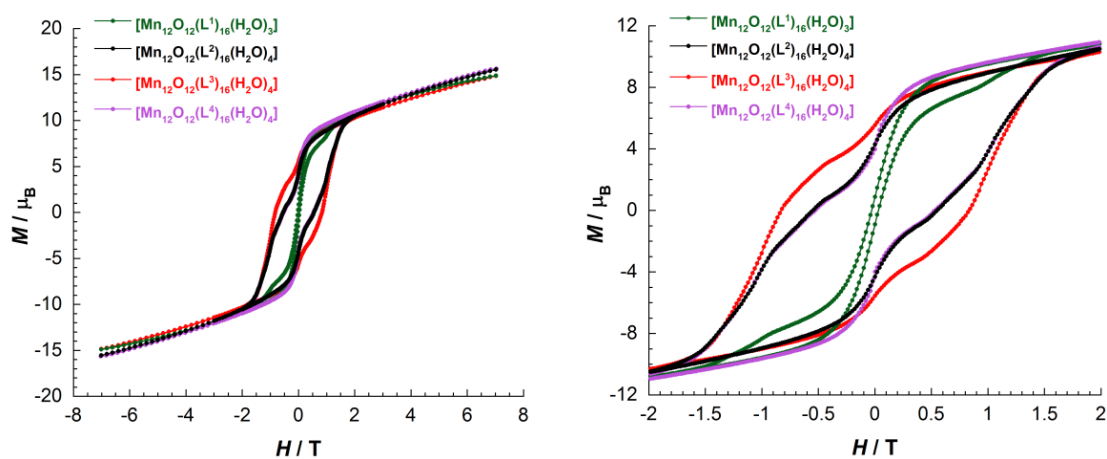


Figure II-11. Magnetization vs. applied field at 1.9 K and at $0.035 \text{ T} \cdot \text{min}^{-1}$ sweep rate for all $[\text{Mn}_{12}\text{O}_{12}(\text{L}^{1-4})_{16}(\text{H}_2\text{O})_{3-4}]$ complexes, the right figure is a zoom of the figure on the left side.

The magnetic properties of the synthesized complexes are influenced by their molecular structure that is strongly dependent of the peripheral ligand substitution patterns. The relative proportion between SR and FR species seems to be dependent on the structure of functionalized benzoate ligand. For the series of Mn_{12} -based SMMs substituted with (cyanobiphenyloxyundecyloxy)benzoates, it was reported that the position and the number of electron-donor alkoxy groups alter the electronic density of the ligand's aromatic ring, and consequently the Mn^{III} ligand field, that plays a crucial role in stabilization of the JT elongation along the main symmetry axis of the Mn_{12} -core.^{24c} Apparently, when the functionalization with electron-donor groups is done in 3-, 4-, and 5- positions the SR (HT) phase is found to be more stable, whereas the presence of cyanobiphenyloxyundecyloxy groups in 3- and 5- (*meta*-) positions or in 4- (*para*) contributes to an increase of the FR (LT) species fraction. Therefore the dependence of SR/FR ratio was reported as: (3-, 4- and 5-substituted) > (3- and 5- substituted) > (4- substituted).^{24c} In the family of functionalized complexes, reported in this work, the SR/FR ratio follows the trend HL^3 (3- and 5- substituted) > HL^4 (3-, 4- and 5- substituted) > HL^2 (4- substituted). This dependence slightly differs from the one reported for the series of compounds with different (cyanobiphenyloxyundecyloxy)benzoates.^{24c} It appears that the difference between the trends in SR/FR ratios may come from the pulling and pressure effects of peripheral mesogens (in other words the packing) that distort the magnetic core and affect its properties. In order to identify which of the factors (donor-acceptor nature or the packing effect of the functional groups) has a greater influence on the SR/FR

species ratio, the data obtained in this work was compared with previous reports concerning Mn_{12} complexes with various benzoate based ligands. The model $[Mn_{12}O_{12}(L^1)_{16}(H_2O)_3]$ compound with 4-methoxybenzoic acid, reported in this work, shows a high fraction of FR (LT) species ~ 85% that is in agreement with both trends reported above. Whereas the Mn_{12} complex with 3,4,5-trimethoxybenzoic acid^{24a} shows almost 100 % of FR (LT) species, that is not at all in agreement with trends established above. Moreover, the complex of 4-methylbenzoic acid, with a weaker donor group, shows a 15/85 (SR/FR) ratio when it is co-crystallized with one molecule of 4-methylbenzoic acid and a 95/5 (SR/FR) ratio when it is crystallized without the ligand molecule.^{17,37} Other Mn_{12} complexes do not show any influence of the functional group's donor nature as well. Thus, the complex with 4-*t*-butylbenzoic acid shows 100 % of FR (LT) species,³⁷ the ones with 4-nonyloxy- and 4-hexadecyloxybenzoic acids show SR/FR ratios of 70/30 and 50/50, respectively, while the complex with 4-decyloxybenzoic acid shows 100 % of SR (HT) species.²⁷ The analysis of this data, indeed, shows that the bulkiness of the functional groups influences the geometry of the core through the packing effects and intermolecular interactions inside the crystal or the mesophase. Therefore, we can state that the variation of the density of strongly lipophilic groups allows a better isolation of the magnetic cores and a certain control of magnetic properties through variation of the SR/FR ratio.

II.4.4. Thermotropic properties

The thermal and mesomorphic properties of synthesized complexes were first investigated by TGA, temperature dependent polarized optical microscopy (POM), and differential scanning calorimetry (DSC). The nature of observed phase transitions was thereafter determined with small angle X-ray scattering (SAXS) investigations. Thermal data of phase transitions and thermodynamic parameters for functionalized $[Mn_{12}O_{12}(L^{2-4})_{16}(H_2O)_4]$ complexes are summarized in Table II-3.

Table II-3. Thermal data for functionalized $[Mn_{12}O_{12}(L^{2-4})_{16}(H_2O)_4]$ complexes obtained by DSC at 5 Kmin⁻¹.

Compound	Transition ^a	T / K	ΔH / kJ·mol ⁻¹
$[Mn_{12}O_{12}(L^2)_{16}(H_2O)_4]$	Cr – I ^b	380*	25.5*
$[Mn_{12}O_{12}(L^3)_{16}(H_2O)_4]$	Cr – Cub	242	94.6
	Cub – I	295	23.9
$[Mn_{12}O_{12}(L^4)_{16}(H_2O)_4]$	Cr – Cub	276	205.9
	Cub – dec	423 ^c	-

^a onset point on second heating, Cr = crystal, I = isotropic liquid, Cub = cubic phase, dec = decomposition; ^b this transition was observed only on first heating in DSC; ^c determined according to TGA; * data obtained on first heating.

As expected, our model compound $[Mn_{12}O_{12}(L^1)_{16}(H_2O)_3]$ did not show any mesomorphic properties and remains crystalline until its decomposition around 500 K, whereas other three compounds exhibit thermotropic properties strongly dependent on the density of lipophilic chains attached to the rigid oxo-metallic core.

At room temperature, $[Mn_{12}O_{12}(L^2)_{16}(H_2O)_4]$ looks like a brown glassy solid, $[Mn_{12}O_{12}(L^3)_{16}(H_2O)_4]$ is a dark-brown viscous liquid, and $[Mn_{12}O_{12}(L^4)_{16}(H_2O)_4]$ is a very sticky dark-brown solid. No birefringent texture could be observed using polarized optical microscopy for these Mn_{12} compounds in the explored

temperature ranges (293 – 400 K). On increasing the temperature in the case of the complex functionalized with a ligand containing only one dodecyl chain, $[\text{Mn}_{12}\text{O}_{12}(\text{L}^2)_{16}(\text{H}_2\text{O})_4]$, melting of the glassy solid around 383 K and the formation of large brown (optically isotropic) viscous areas are observed. Upon cooling, the compound becomes a solid glass again, showing no anisotropic region under crossed polarizers. The $[\text{Mn}_{12}\text{O}_{12}(\text{L}^3)_{16}(\text{H}_2\text{O})_4]$ complex, which has two dodecyl chains attached to its ligand, is an isotropic liquid on both heating or cooling from room temperature to 373 K. Upon heating, the $[\text{Mn}_{12}\text{O}_{12}(\text{L}^4)_{16}(\text{H}_2\text{O})_4]$ complex shows an increase in viscosity at higher temperatures, and no birefringence was observed even after applying a shear distortion. These observations were not enough to determine the presence or formation of any mesophase in the investigated samples. The identification and clear assignment of mesophases and phase transitions was achieved by the combination of the results obtained using DSC and SAXS.

II.4.4.1. $[\text{Mn}_{12}\text{O}_{12}(\text{L}^2)_{16}(\text{H}_2\text{O})_4]$

Neither in DSC nor in SAXS $[\text{Mn}_{12}\text{O}_{12}(\text{L}^2)_{16}(\text{H}_2\text{O})_4]$ complex showed a thermally reversible behavior. Even though in microscopy we observe a kind of melting for this sample, DSC traces on first heating contain a very broad peak around 340 K, which is not present anymore on cooling and second heating (Figure S.II-13), probably due to the very slow dynamics of the existing transition. SAXS measurements for $[\text{Mn}_{12}\text{O}_{12}(\text{L}^2)_{16}(\text{H}_2\text{O})_4]$ were carried out at different temperatures. At 303 K, up to 13 sharp reflections (Figure S.II-15 left) were detected in the low and high angle range for which the reciprocal q spacings were in the ratios $\sqrt{2}:\sqrt{3}:\sqrt{6}:\sqrt{9}:\sqrt{12}:\sqrt{14}:\sqrt{20}:\sqrt{29}:\sqrt{33}:\sqrt{38}:\sqrt{49}:\sqrt{76}:\sqrt{83}$ suggesting a cubic lattice. All summarized indexation parameters at 303 K are shown in Table S.II-3. The reflections were indexed as (110), (111), (211), (221/300), (222), (321), (420), (432/520), (441/522), (532/611), (632/700), (662), and (753). Examination of the general and systematic absences and the fail to meet the reflection conditions allowed to eliminate the face-centered (F) cubic (reflection conditions $hkl: h + k = 2n, h + l = 2n, k + l = 2n$), body-centered (I) cubic (reflection conditions $hkl: h + k + l = 2n$), and some of the primitive (P) cubic (reflection conditions $0kl: k + l = 2n, hhl: l = 2n, 00l: l = 2n \text{ or } 4n$) space groups.³⁸ The presence or absence of a center of symmetry cannot be detected on the basis of these experiments (Friedel's law),³⁹ therefore all non-centrosymmetric groups (with Laue classes 23, 432 and $\bar{4}3m$) are unlikely. This leaves only $Pm\bar{3}$ and $Pm\bar{3}m$ space groups. The exact nature of the space group is still undetermined, thus both of them are theoretically possible. Finally the latter $Pm\bar{3}m$ space group was retained due to its higher symmetry. The reciprocal spacing (q) of cubic phases is related to the lattice parameter (a) by: $q_{hkl} = 2\pi\sqrt{h^2 + k^2 + l^2} / a$, where h, k, l are Miller indices. Therefore, the lattice parameter can be calculated from the slope of the $2\pi/q$ vs $1/\sqrt{h^2 + k^2 + l^2}$ plot (Figure S.II-16). From this plot, we can observe that the experimental data fit well with a straight line and the cubic lattice parameter $a = 37.8 \text{ \AA}$ was deduced. The absence of liquid-crystalline phase in the material is confirmed by the absence of a broad scattering halo located around $q = 13 \text{ nm}^{-1}$ characteristic of the liquid like order of the molten aliphatic chains. Sharp peaks in wide angle region were present up to 380 K (Figure S.II-15 left). Thus, this information suggests a crystalline phase with a cubic symmetry in the thermally untreated complex below 380 K. At highest temperature, 393 K (below

decomposition temperature of ca 420 K), in small angle region, two broad reflections at 1.8 and 2.2 nm⁻¹ are still present in the X-ray diffraction profile, suggesting a remnant order or a short range ordering of the objects (Figure S.II-15 left). At wide angles a broad halo appears around 13 nm⁻¹, suggesting the presence of molten alkyl chains. However, as previously mentioned, no birefringent texture could be observed in POM, even if a large brown viscous area is forming on increasing temperature. As observed from DSC analyses, this thermal behavior is irreversible and is consistent with the fact that the SAXS profile remains unchanged as the temperature decreases after the first thermal cycle (Figure S.II-15 right). This irreversibility is likely caused by a very slow dynamics of the phase transition process.

II.4.4.2. [Mn₁₂O₁₂(L³)₁₆(H₂O)₄]

The DSC thermogram of [Mn₁₂O₁₂(L³)₁₆(H₂O)₄] between 160 and 340 K shows two endothermic transitions which are thermally reversible (Figure II-12 left). The broad peak with a maximum at 242 K corresponds to a transition involving melting of alkyl chains and to the formation of a mesophase that was identified as cubic with the help of X-ray diffraction investigations (vide infra). The second peak observed in the DSC traces at 301 K is corresponding to the clearing point. On cooling the reverse sequence of transitions occurs, with a 20 K thermal hysteresis (at 5 K/min) for clearing point (280 K), while the maximum of the broad transition at lower temperature remained unchanged. The enthalpy change (ΔH) during the broad phase transition is about 94.6 kJ/mol (or 3 kJ/mol per dodecyl chain, if divided by the number of attached alkyl chains) and corresponds to a typical transition enthalpy of melting for dodecyl chains.⁴⁰

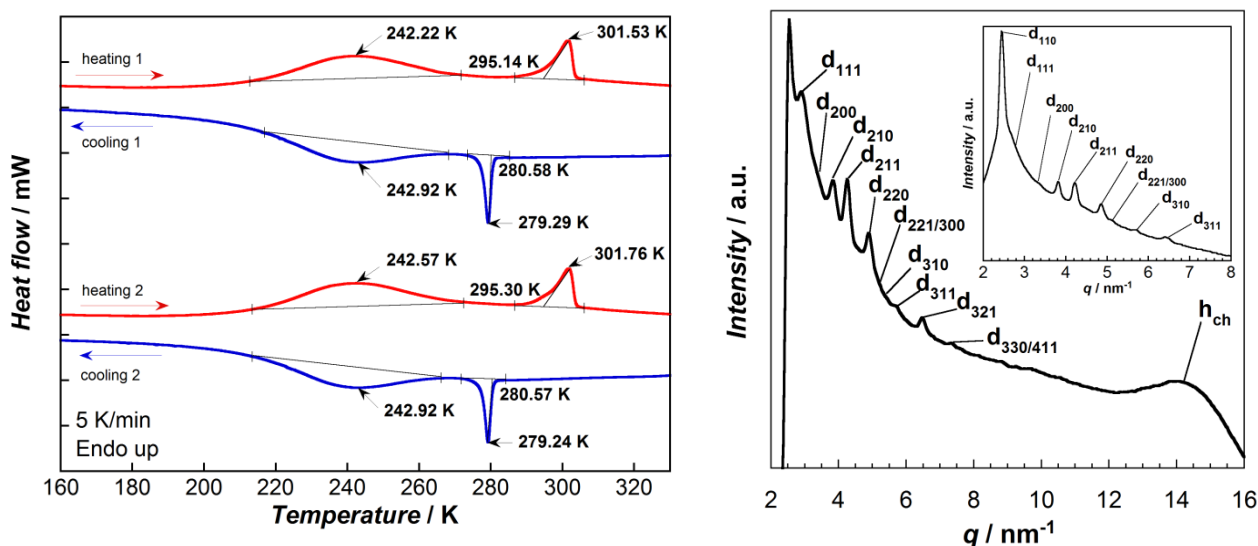


Figure II-12. (left) DSC traces of [Mn₁₂O₁₂(L³)₁₆(H₂O)₄] complex between 160 and 330 (5 K/min). (right) Indexed SAXS diffraction profile of [Mn₁₂O₁₂(L³)₁₆(H₂O)₄] at 283 K, in the inset diffraction profile at small angle range, intensity axis is in logarithmic scale.

To gain more insights regarding the arrangement of the molecules in the mesophase, temperature-dependent SAXS measurements were performed on heating the sample from 283 K (the sample was preliminary heated to 320 K to bypass the clearing point, then cooled down to 255 K in freezer, and, finally, quickly transferred to sample chamber cooled to 283 K). The pattern collected at 283 K contained 10

reflections in the low angle region, and a diffuse scattering halo in the wide angle region centered around 14 nm^{-1} (h_{ch} in Figure II-12 right), which corresponds to the lateral short range order of the molten chains, confirming the liquid crystalline nature of the mesophase. Reflections observed in the low-angle region (Figure II-12 right) are in the ratio of $\sqrt{2}:\sqrt{3}:\sqrt{4}:\sqrt{5}:\sqrt{6}:\sqrt{8}:\sqrt{9}:\sqrt{10}:\sqrt{11}:\sqrt{14}$ and were indexed as (110), (111), (200), (210), (211), (220), (300/221), (310), (311), and (321), which are consistent with a cubic lattice (see also Table S II-4) with a primitive network (*P*). The average unit cell parameter was calculated as $a = 36.5 \text{ \AA}$, from the slope of the $2\pi/q$ vs $1/\sqrt{h^2+k^2+l^2}$ plot (Figure S.II-17 right). The analysis of the general and systematic absences and the fail to meet the reflection conditions corresponding to the face-centered (*F*), body-centered (*I*) and some of the primitive (*P*) cubic space groups suggested that the space group is theoretically compatible with $Pm\bar{3}m$ like for $[\text{Mn}_{12}\text{O}_{12}(\text{L}^4)_{16}(\text{H}_2\text{O})_4]$. Diffraction patterns collected above 300 K on further heating (Figure S.II-17 left) showed no reflections in small angle range, confirming the presence of a transition into the isotropic liquid assigned to the second endothermic peak observed in DSC traces around 301 K on heating (Figure II-12 left).

II.4.4.3. $[\text{Mn}_{12}\text{O}_{12}(\text{L}^4)_{16}(\text{H}_2\text{O})_4]$

A mesophase with a supramolecular cubic organization and $Im\bar{3}m$ symmetry was previously reported for $[\text{Mn}_{12}\text{O}_{12}(\text{L}^4)_{16}(\text{H}_2\text{O})_4]$.^{24a} Similarly to previous report, we could observe only one intense endothermic peak in DSC thermograms at low temperatures and no birefringent texture in POM in a wide temperature range. But, from the first SAXS measurements we could not deduce a cubic arrangement even though we obtained a diffraction pattern quite similar to the one reported earlier.^{24a} Thus the thermal behavior of $[\text{Mn}_{12}\text{O}_{12}(\text{L}^4)_{16}(\text{H}_2\text{O})_4]$ was studied in more details using SAXS technique performing several heating-cooling cycles. Thermogravimetric measurements combined with POM observations showed that $[\text{Mn}_{12}\text{O}_{12}(\text{L}^4)_{16}(\text{H}_2\text{O})_4]$ is stable in the 298 – 423 K temperature range. The DSC traces reproducibly showed

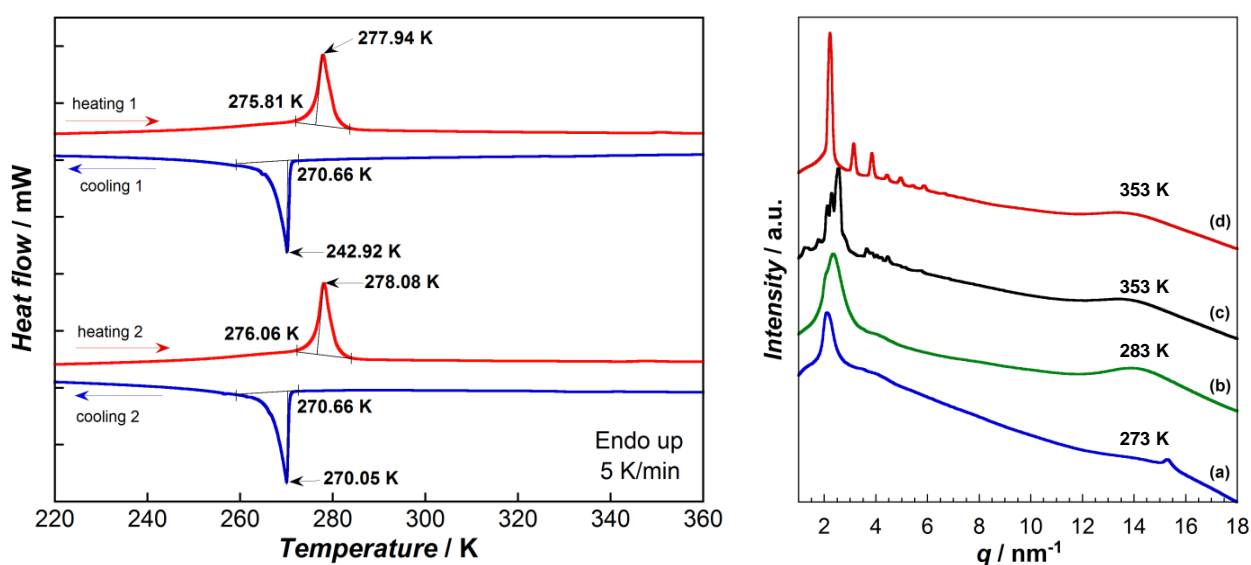


Figure II-13. (left) DSC traces of $[\text{Mn}_{12}\text{O}_{12}(\text{L}^4)_{16}(\text{H}_2\text{O})_4]$ complex between 220 and 360 (5 K/min). (right) SAXS diffraction profiles of $[\text{Mn}_{12}\text{O}_{12}(\text{L}^4)_{16}(\text{H}_2\text{O})_4]$ (intensities are in logarithmic scale): (a) at 273 K before first heating; (b) at 283 K on first heating; (c) at 353 K on first heating; (d) at 353 K on fourth heating.

a single endothermic first order transition centered at 278 K on heating and 270 K on cooling (Figure II-13 left), which we were able to assign to the melting of $[\text{Mn}_{12}\text{O}_{12}(\text{L}^4)_{16}(\text{H}_2\text{O})_4]$ with the help of SAXS measurements after comparison of diffraction patterns collected at 273 K and after heating to 283 K (see Figure II-13 right). At 273 K, the diffraction pattern showed a sharp reflection (centered around 15.3 nm^{-1}) and a very weak scattering halo in the wide angle region, suggesting that the sample is close to the melting point. Also, if the enthalpy change of 205.9 kJ/mol is divided by 48 (the number of dodecyl chains) a value of 4 kJ/mol is obtained, that is in the range specific to the melting of dodecyl chains.⁴⁰ It is noticeable that the melting enthalpy of $[\text{Mn}_{12}\text{O}_{12}(\text{L}^4)_{16}(\text{H}_2\text{O})_4]$ is larger than that of $[\text{Mn}_{12}\text{O}_{12}(\text{L}^3)_{16}(\text{H}_2\text{O})_4]$, this could be due to differences in the starting crystalline phase.

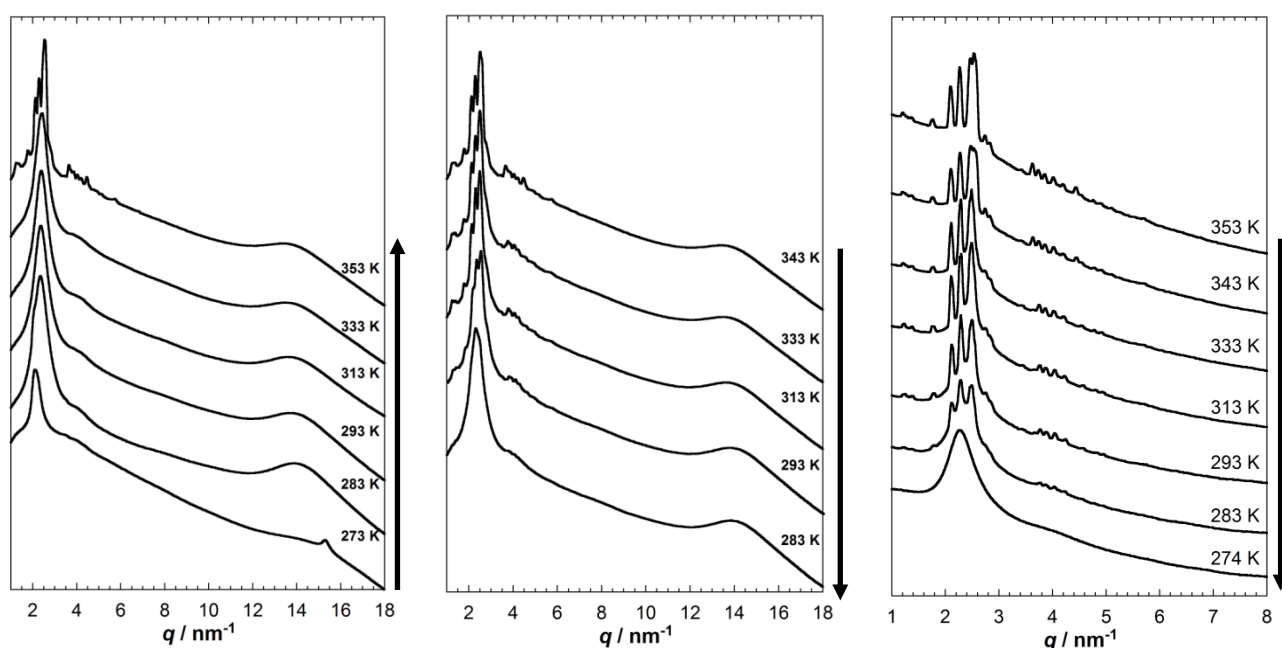


Figure II-14. Small angle X-ray diffraction profiles of $[\text{Mn}_{12}\text{O}_{12}(\text{L}^4)_{16}(\text{H}_2\text{O})_4]$: (left) on 1st heating from 273 K to 353 K; (center) on 1st cooling from 353 K to 283 K; and (right) on 2nd cooling from 353 K to 274 K and at a bigger detector distance than in the profiles showed on left and in the center.

At temperatures between 283 and 333 K, $[\text{Mn}_{12}\text{O}_{12}(\text{L}^4)_{16}(\text{H}_2\text{O})_4]$ complex showed liquid-like weakly ordered phase, as SAXS experiments only showed a broad intense peak at 2.3 nm^{-1} corresponding to some short range organization of Mn_{12} -cores with an average distance of about 26.4 \AA (Figure II-14 left) and a diffuse scattering halo in wide angle region at 14 nm^{-1} , which corresponds to the lateral short range order of the molten alkyl chains. Further heating induces the organization of functionalized molecules such that 18 reflections were detected in the low angle range at 353 K (Figures II-13 right and II-14 left). Even though the diffraction pattern was very similar to the one obtained previously,^{24a} the reciprocal spacings for the observed reflections were not in the reported ratios and we were not able to confirm the reported cubic lattice. On cooling from 353 K to 313 K the diffraction pattern remained unchanged, at 293 K weak diffraction peaks disappeared while the intense ones broadened and at 283 K the system recovered its liquid-like weakly ordered phase (Figure II-14 center). Taking into the account that this surprising thermal behavior (the evolution of an apparent isotropic liquid into an organized phase between 333 and 353 K) was observed after first heating-cooling cycle, it was decided to check the reversibility by performing additional thermal

cycles at longer detector distance, in order to better separate the reflections in the organized mesophase present at higher temperatures in low angle region. Indeed, upon second cooling from 353 K (Figure II-14 right) the analyzed sample of $[\text{Mn}_{12}\text{O}_{12}(\text{L}^4)_{16}(\text{H}_2\text{O})_4]$ complex showed similar thermal behavior, but with a shift of the liquid-like weakly ordered phase appearance to lower temperatures (between 283 and 274 K). This type of behavior termed “inverse melting” or “inverse freezing” has been observed in polymers, colloidal compounds, high-temperature superconductors, proteins, ultra-thin films, liquid crystals, and metallic alloys.⁴¹ Different kinds of phase transitions are related to this phenomenon, in particular the solidification or appearance of an ordered phase from an isotropic liquid upon heating. In the field of liquid crystals, it is more precisely called the “re-entrance of the isotropic phase” and has been experimentally observed and theoretically explained.^{41a} Also, it is important to mention that no peaks were observed in DSC traces (Figure II-13 left) corresponding to this transition. This could simply mean that the transition is strongly second order. Therefore, it is difficult to give precisely the transition temperature because we detected it through the appearance of reflections in the X-ray diffraction profile, and this can only be done when a certain amount of material has already transited. Up to 20 reflections were identified after the detailed investigation of the low angle region in the temperature range between 303 and 393 K (Figure S.II-18). The diffuse halo in the wide angle region with a maximum at 14 nm^{-1} , corresponding to the molten alkyl chains, was present as well. But again it was impossible to index them with the reported cubic lattice.^{24a}

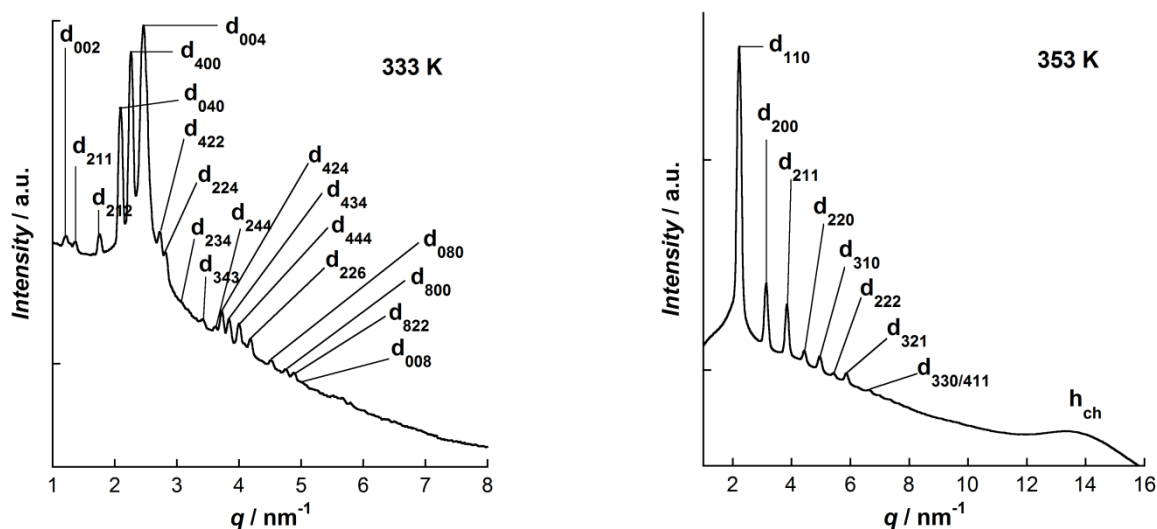


Figure II-15. Indexed SAXS profiles for $[\text{Mn}_{12}\text{O}_{12}(\text{L}^4)_{16}(\text{H}_2\text{O})_4]$: (left) at 333 K on 3rd heating, corresponding to an intermediate mesophase with orthorhombic symmetry, only the small angle region is shown; and (right) at 353 K on 4th cooling corresponding to a cubic mesophase with $Im\bar{3}m$ symmetry.

The analysis of reciprocal spacings allowed sorting of observed reflections into three groups according to ratios between their positions. The presence of three sets of reflections suggested the existence of three distances characteristic to the organization of functionalized complexes inside the mesophase. As the result we were able to index all of the observed reflections (Figure II-15 left) on an orthorhombic lattice $a = 110.8 \text{ \AA}$, $b = 119.7 \text{ \AA}$, $c = 101.9 \text{ \AA}$ at 303 and $a = 116.5 \text{ \AA}$, $b = 123.0 \text{ \AA}$, $c = 104.5 \text{ \AA}$ at 393 K (Tables S.II-5 and S.II-6). The large values of unit cell parameters are of the same order as the lattice parameter ($a = 106.1 - 108.1 \text{ \AA}$) of the previously reported supramolecular cubic organization with $Im\bar{3}m$ symmetry.^{24a} The

indexation of X-ray diffraction data obtained at this point, indeed, may correspond to a supramolecular organization (the number of $[\text{Mn}_{12}\text{O}_{12}(\text{L}^4)_{16}(\text{H}_2\text{O})_4]$ complexes per unit cell Z is varying between 70 to 77, if density is considered 1 g/cm^3), but with an imperfect 3D arrangement of Mn_{12} -based cores inside the mesophase. Similar imperfect 3D organization was reported, as well, in the case of some cone-shaped molecules and is caused by not uniformly spread aliphatic chains around the rigid core.⁴² On third cooling from 393 K, the shape of the diffraction profiles started to change (Figure S.II-18 right). The re-entrance of the isotropic phase was observed again since the number of reflections decreased from 20 at 393 K to 9 at 303 K (indexation of observed reflections with an orthorhombic lattice was still possible and is summarized in Table S.II-7). A fourth heating-cooling cycle was performed to probe the evolution of observed thermal behavior in $[\text{Mn}_{12}\text{O}_{12}(\text{L}^4)_{16}(\text{H}_2\text{O})_4]$ complex. Surprisingly, on heating a new diffraction pattern started to form between 353 and 373 K. Thus, 10 sharp reflections were well formed at 413 K (Figure S.II-19 left). The diffuse signal centered at 14 nm^{-1} of the molten alkyl chains was present in the wide-angle as well (Figures II-13 and II-15 both right). On cooling the system maintained the diffraction pattern until 274 K, showing no re-entrance of the isotropic phase. The reciprocal spacings were in the ratios $\sqrt{1}:\sqrt{2}:\sqrt{3}:\sqrt{4}:\sqrt{5}:\sqrt{6}:\sqrt{7}:\sqrt{8}:\sqrt{9}:\sqrt{11}$ for the set of the observed 10 small angle reflections. The presence of reflection corresponding to $\sqrt{7}$ might be consistent with a 2D hexagonal arrangement, but no birefringence in POM and the presence of several other reflections as $\sqrt{2}, \sqrt{5}, \sqrt{6}, \sqrt{8}, \sqrt{11}$ allowed immediate elimination of such an organization. Thus, the considered ratio sequence must be $\sqrt{2}:\sqrt{4}:\sqrt{6}:\sqrt{8}:\sqrt{10}:\sqrt{12}:\sqrt{14}:\sqrt{16}:\sqrt{18}:\sqrt{22}$ with reflections indexed as (110), (200), (211), (220), (310), (222), (321), (400), (330/411) and (332) (Figure II-15 left, Tables S.II-8 and S.II-9). All reflections satisfied $hkl: k + l = 2n$, $hhl: l = 2n$, $h00: h = 2n$ conditions compatible with a body-centered cubic lattice. The presence of forbidden reflections and the exclusion of all non-centrosymmetric space groups allowed reducing the number of compatible body-centered cubic space groups to $Im\bar{3}$ and $Im\bar{3}m$ (which are with the same general conditions of extinction). Due to its higher symmetry the $Im\bar{3}m$ group was retained. The cubic lattice parameter is almost temperature-independent ($a = 39.6 \text{ \AA}$ at 274 K and $a = 40.3 \text{ \AA}$ at 393 K), slightly bigger in value than those obtained for $[\text{Mn}_{12}\text{O}_{12}(\text{L}^2)_{16}(\text{H}_2\text{O})_4]$ ($a = 37.8 \text{ \AA}$, crystalline primitive cubic) and $[\text{Mn}_{12}\text{O}_{12}(\text{L}^3)_{16}(\text{H}_2\text{O})_4]$ ($a = 36.5 \text{ \AA}$, cubic mesophase with primitive lattice), and about 2.5 times smaller than the one reported ($a = 106.1 - 108.1 \text{ \AA}$).^{24a}

This complex thermal behavior exhibited by $[\text{Mn}_{12}\text{O}_{12}(\text{L}^4)_{16}(\text{H}_2\text{O})_4]$ is not surprising since it is known that the presence of intermediate metastable mesophases (with large lattice parameters) and strong influence of thermal cycles are characteristic to thermotropic cubic phases.⁴³

II.4.5. Description of the molecular packing inside the mesophase

The determination of the exact space group is very important for the possible description of molecules packing inside the mesophase. In the literature, thermotropic cubic phases are relatively rare and most of them possess $Pn\bar{3}m$ (bicontinuous), $Im\bar{3}m$ or $Ia\bar{3}d$ (that may be bicontinuous or tricontinuous) symmetries.^{43,44} Due to the supramolecular nature of the reported cubic phases (including both lyotropic and

thermotropic) the elementary cell of a cubic phase may contain up to several hundreds of molecules. The discontinuous (micellar) and multicontinuous models are generally used to describe the 3D organization inside the cubic phases with $Im\bar{3}m$ symmetry. The multicontinuous model's structure consists of multiple interwoven, infinite 3D networks (formed by the rigid parts of mesogenic molecules) separated from each other by lipophilic regions, formed by the molten aliphatic chains.⁴⁵ The discontinuous micellar model can be easily exemplified by dendrimers with strongly amphiphilic characters.^{44h,i} Such dendrimers are known to adopt conical shapes that can self-assemble into pseudospherical (spherulitic) supramolecular micelles. The structure of such self-assembled supramolecular micelles is composed of a polar (rigid) nucleus embedded in a non-polar soft aliphatic shell. Then, the resulting supramolecular micelles subsequently pack into three dimensional lattices (Figure II-16a).^{44h,i}

For the cubic phases with $Pm\bar{3}m$ symmetry there is no certain description of molecular arrangement inside the lattice, since there are only a few reported examples.⁴⁶ In the case of some imidazolium based T-shaped ionic liquid crystals, a supramolecular multicontinuous structure was proposed consisting of multiple interwoven, infinite three dimensional (column-like) networks (formed by the cationic rigid cores) separated from each other by lipophilic regions (formed by the molten aliphatic chains).^{46b} While in the case of some tetra-N-alkylammonium polyoxometalate ionic complexes an arrangement similar to discontinuous (micellar) model for $Im\bar{3}m$ is considered with core-shell spheroidal aggregates located only in the corner of the cubic cell (Figure II-16 b).^{46c}

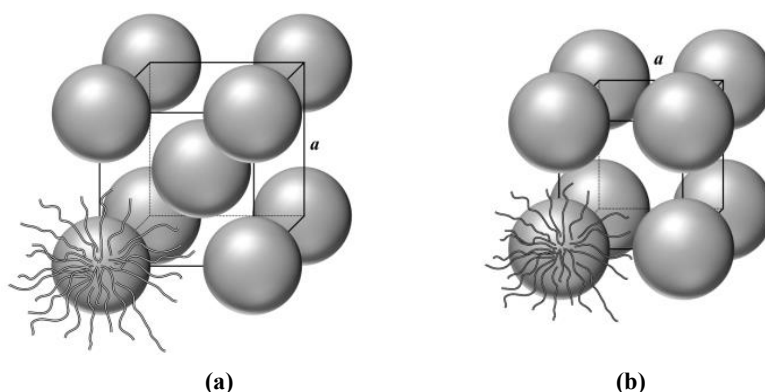


Figure II-16. (a) Schematic representation of the “inverse micellar” type body-centered cubic liquid crystalline lattice with $Im\bar{3}m$ symmetry, the spheres represent the preferred locations of rigid cores, the interstitial space is filled with aliphatic chains, a is the lattice parameter of the cubic cell. (b) Schematic representation of the “inverse micellar” type primitive cubic liquid crystalline lattice with $Pm\bar{3}m$ symmetry.

Single crystal structure of the $[Mn_{12}O_{12}(L^1)_{16}(H_2O)_3]$ compound allowed to model the structure of the functionalized molecules using Chem3D software. The idealized structure of $[Mn_{12}O_{12}(L^3)_{16}(H_2O)_4]$ complex molecule (Figure II-17) has a micelle-like spherulitic shape, where the rigid nucleus (of ~ 20 Å diameter, Figure II-17) is composed of the oxo-metallic core surrounded by 16 benzoate units, while the shell is formed from the dodecyl chains anchored to aromatic rings and is ~ 15 Å thick. Thus, the micellar (discontinuous) model appears to be more probable to describe the organization of functionalized Mn_{12} -based molecules inside the cubic phases with both P and I symmetries (Figure II-16). Also, the theoretical size of the functionalized molecules and the determined values of lattice parameters show that the cubic lattice inside the mesophase is formed by self-organized molecules and not by supramolecular aggregates as it

was reported in 2008 for $[\text{Mn}_{12}\text{O}_{12}(\text{L}^4)_{16}(\text{H}_2\text{O})_4]$ complex^{24a} and for other compounds exhibiting cubic phases.⁴⁴

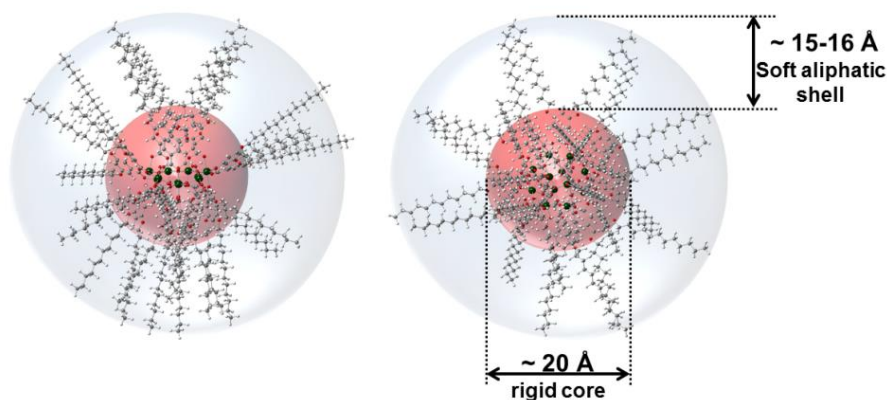


Figure II-17. Structural model (calculated) of the $[\text{Mn}_{12}\text{O}_{12}(\text{L}^3)_{16}(\text{H}_2\text{O})_4]$ molecule viewed from equatorial (left) and axial (right) sides. The inner red sphere indicates the imaginary edge of the rigid core, the outer grey sphere is corresponding to soft aliphatic shell. Color scheme: Mn dark green, O red, C grey, H white.

The calculated cubic lattice parameters, 37.8 Å for $[\text{Mn}_{12}\text{O}_{12}(\text{L}^2)_{16}(\text{H}_2\text{O})_4]$, 36.5 Å for $[\text{Mn}_{12}\text{O}_{12}(\text{L}^3)_{16}(\text{H}_2\text{O})_4]$ and 40 Å for $[\text{Mn}_{12}\text{O}_{12}(\text{L}^4)_{16}(\text{H}_2\text{O})_4]$ are smaller than the theoretical diameter ~ 50 Å of idealized molecules with alkyl chains in their most extended conformation (Figure II-17). The maximal thickness of the soft organic shell around the magnetic core is about 15 Å while the radius of the rigid core is close 10 Å. The cubic lattice parameter a represents the distance between the centers of two neighboring molecules located in the corners of the cubic cell. Thus, after taking into account a complete interdigitation of the aliphatic chains, and/or some elastic deformations favoring different conformations of alkyl chains and contact area minimization, it is possible to get a minimal theoretical distance of 35 Å between centers of two molecules ($a_{\text{theor}} = 2r_{\text{core}} + l_{\text{shell}}$, where a_{theor} is the minimal theoretical distance between two Mn_{12} molecules situated in the corners of a cubic cell, r_{core} is the radius of the rigid oxo-metallic core, and l_{shell} is the maximal thickness of the soft aliphatic shell, Figure II-18). This calculated value is in agreement with measured lattice parameters.

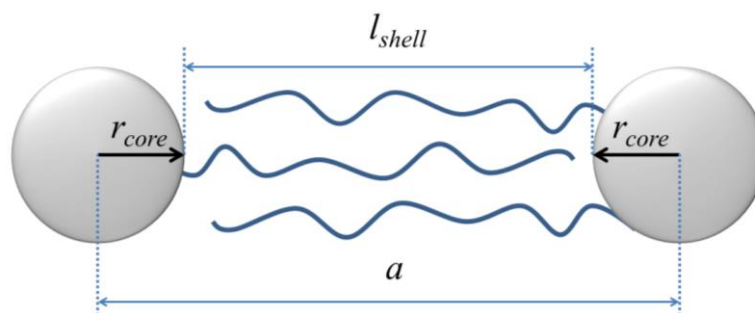


Figure II-18. Schematic representation of complete interdigitation of aliphatic chains.

Similarly to the magnetic properties, the thermotropic properties and the self-organization inside the mesophase are dependent on the density of lipophilic chains and their positions inside benzoate ligands. The $[\text{Mn}_{12}\text{O}_{12}(\text{L}^2)_{16}(\text{H}_2\text{O})_4]$ complex, which has the lowest density of dodecyl chains, has a thermally irreversible behavior and exhibits a crystalline cubic phase with, likely, the same $Pm\bar{3}m$ symmetry as the cubic

mesophase of $[\text{Mn}_{12}\text{O}_{12}(\text{L}^3)_{16}(\text{H}_2\text{O})_4]$ (vide supra). The lattice parameter of the crystalline phase in $[\text{Mn}_{12}\text{O}_{12}(\text{L}^2)_{16}(\text{H}_2\text{O})_4]$ complex (37.8 Å) is 1.3 Å greater than the lattice parameter of the cubic mesophase of $[\text{Mn}_{12}\text{O}_{12}(\text{L}^3)_{16}(\text{H}_2\text{O})_4]$ complex (36.5 Å), which has a twice bigger number of attached dodecyl chains. This surprising difference may be explained by different functionalization positions inside the ligands used in the preparation of these two complexes. Thus, the benzoic ligand with a single chain in 4- (*para*-) position on the aromatic ring has a bigger average length and contributes to a little bit bigger lattice parameter than in the case with benzoic ligand with two dodecyl chains in 3- and 5- (*meta*-) positions. Further increase of the aliphatic density around the magnetic core, as in $[\text{Mn}_{12}\text{O}_{12}(\text{L}^4)_{16}(\text{H}_2\text{O})_4]$ complex, causes a very complex thermal history behavior that can be stabilized as a cubic phase with $Im\bar{3}m$ symmetry.

II.4.6. Summary of section II.4

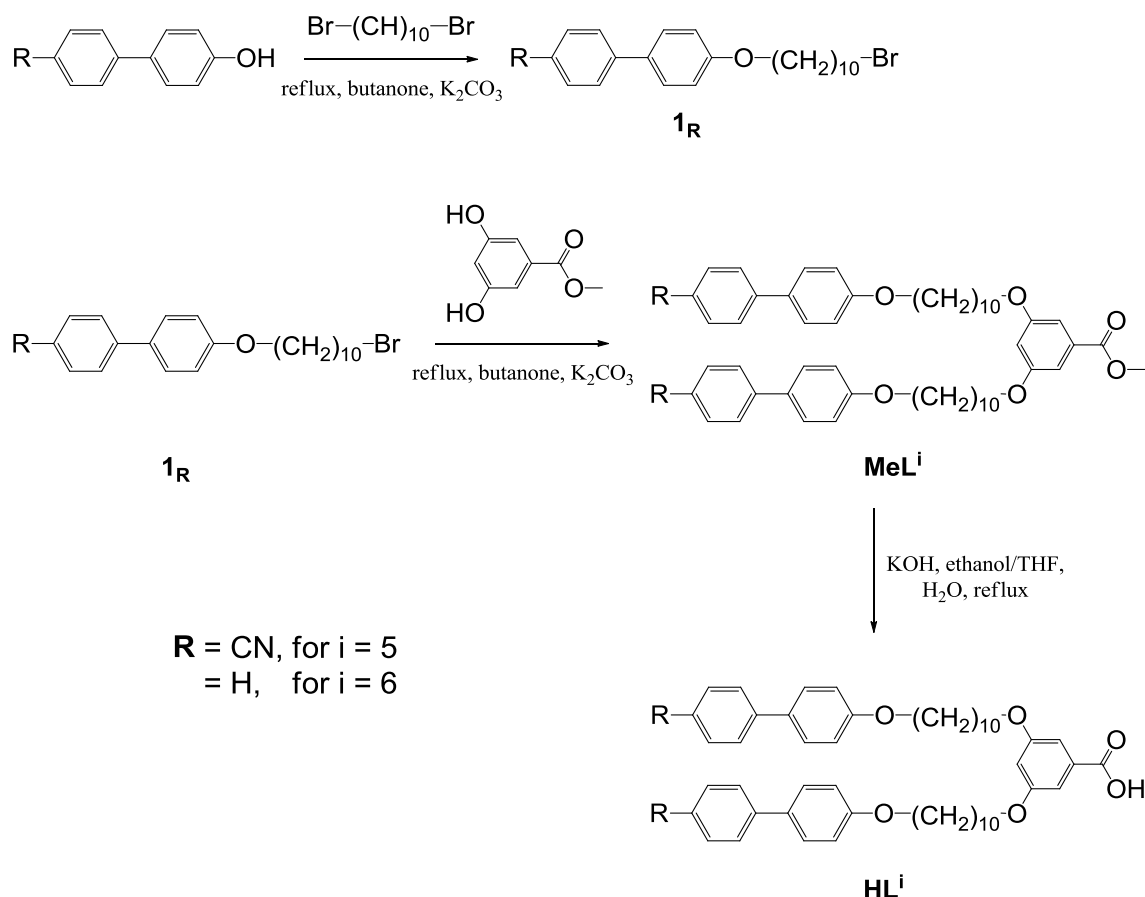
A series of four functionalized Mn_{12} -based complexes was synthesized and characterized. Various alkoxybenzoic acids have replaced acetate ligands in $[\text{Mn}_{12}\text{O}_{12}(\text{CH}_3\text{COO})_{16}(\text{H}_2\text{O})_4]$ by ligand substitution reaction, in order to organize single molecule magnets into a fluid liquid crystalline phase. In marked contrast with the original Mn_{12} -Ac, which is unstable above 320 K, obtained compounds are thermally stable up to 420 K with the ligands bearing long chains and up to 470 K with *p*-methoxybenzoate ligand. From the *ac* magnetic measurements, the conservation of Mn_{12} SMM property was confirmed. Our complexes exhibit JT isomerism as shown in *ac* out-of-phase susceptibility and X-ray crystal structure of the model compound. Significant differences in magnetic relaxation were observed, resulting from the different ratio of JT isomers, which is itself dependent on the density of lipophilic chains, their positions inside ligand's aromatic ring and the electronic density donating-accepting nature of grafted groups of benzoate-based ligand. Our applied design strategy, consisting in grafting a various number of lipophilic chains around the rigid Mn_{12} core, failed in obtaining products with less oriented and symmetric phases, but still resulted to be successful in the control of thermally induced 3D self-organization of hybrid molecules. Thus, by varying chain density around the rigid core, it is possible to stabilize crystalline cubic organization for $[\text{Mn}_{12}\text{O}_{12}(\text{L}^2)_{16}(\text{H}_2\text{O})_4]$ or thermotropic cubic mesophases of different symmetry for $[\text{Mn}_{12}\text{O}_{12}(\text{L}^3)_{16}(\text{H}_2\text{O})_4]$ and $[\text{Mn}_{12}\text{O}_{12}(\text{L}^4)_{16}(\text{H}_2\text{O})_4]$. The organization inside the cubic mesophases has a molecular nature and is governed by the overall shape of rigid aromatic core, while aliphatic chains offer necessary fluid environment for self-organization. Similarly to magnetic properties, the organization and symmetry inside the observed cubic mesophases is dependent not only on the number of functional groups but on the substitution pattern inside benzoate ligands as well. The specific molecular design in this case contributed to formation of hybrid molecular materials possessing several properties and allowed the tuning of parameters characteristic to the original Mn_{12} -based core. Obviously multiple possibilities exist for further development and optimization of magnetic and mesomorphic properties to design novel SMM complexes with liquid crystalline properties. The strategy based on the grafting of mesomorphic units through a flexible aliphatic spacer can be used (and is applied in the next section of this chapter), as it has been already successfully applied to obtain thermotropic mesophases in many cases including Mn_{12} -based SMMs.^{23,24}

II.5. Functionalization of Mn₁₂-based SMMs by grafting a mesomorphic promoter through a flexible spacer

II.5.1. Synthetic procedures and purification

In order to apply the functionalization strategy of grafting a mesogenic moiety through a flexible aliphatic chain to produce Mn₁₂-based complexes with fluid mesophases at lower temperature, structurally related ligands HL⁵ and HL⁶ (Scheme II-4) were synthesized. The ligands were obtained in three steps (see Scheme II-5 and Supporting Materials for detailed protocols) following procedures reported for similar compounds.²³ Firstly, the precursors (**1_{CN}** and **1_H**) containing the mesogenic unit and the aliphatic spacer were prepared. Methyl esters MeL⁵ and MeL⁶ were obtained by Williamson etherification of precursor (**1_{CN}** or **1_H**) with methyl 3,5-dihydroxybenzoate in butanone. Finally, the methyl esters were hydrolysed into the corresponding carboxylic acids HL⁵ and HL⁶.

Scheme II-5. Synthetic scheme for HL⁵ and HL⁶ ligands preparation.



The functionalization of the outer shell of the Mn₁₂-based magnetic cores with (L⁵)⁻ or (L⁶)⁻ ligands was achieved by ligand-exchange reaction between the original Mn₁₂-OAc with a large excess (28 eq.) of functionalized acid (HL⁵ or HL⁶) in CH₂Cl₂/toluene 1:1 mixture, similarly to the complexes modified with aliphatic chains (see sections II.2.3 and II.4.1 for details). The [Mn₁₂O₁₂(L⁵)₁₆(H₂O)₄] complex is poorly soluble in toluene, thus in order to efficiently remove the resulting acetic acid by successive azeotropic distillations with toluene it is necessary, firstly, to dissolve the residue in CH₂Cl₂, then add toluene, stir for

additional 3 hours, and finally evaporate to dryness. To displace favourably the equilibrium, the distillations must be repeated at least four times.

The crude functionalized molecules were purified by size exclusion column chromatography, using Bio-Beads S-X3 beads swelled with CH_2Cl_2 (see section II.4.1) as stationary phase. The final products after drying in vacuum are vitreous dark brown solids at room temperature. The structural and physical properties of synthesized complexes were characterized by various techniques (vide infra).

II.5.2. Analytical characterization of the functionalized Mn_{12} complexes

Similarly to the previously functionalized complexes (section II.4), the demonstration of complete substitution on the 16 coordination sites, as well as complete removal of the ligands taken in excess, relayed on the combination of several analytical techniques. Thus, the structural characterizations of functionalized complexes were performed in both solid state (FT-IR spectroscopy, elemental and thermo-gravimetric analyses) and in solution (^1H NMR spectroscopy).

II.5.2.1. FT-IR spectroscopic analyses

Once the substitution reaction was completed and the benzoic acid derived ligands were covalently grafted onto the Mn_{12} core, the characteristic stretching vibration band of the carbonyl groups ($\sim 1676\text{ cm}^{-1}$) of the free benzoates disappeared (Figure S.II-7). The absence of this band and of another one around 1700 cm^{-1} indicates that no free ligand or acetate is present in the sample. Furthermore, no significant change of the C-O ($\approx 1260\text{ cm}^{-1}$) and C-H ($\approx 2900\text{ cm}^{-1}$) stretching bands indicate that the reacted ligand was preserved after the reaction, except for the deprotonation. In the case of $[\text{Mn}_{12}\text{O}_{12}(\text{L}^5)_{16}(\text{H}_2\text{O})_4]$ complex, the stretching vibration at 2224 cm^{-1} corresponding to CN group confirms the grafting of mesogenic cyanobiphenyl moiety (Figure S.II-7).

II.5.2.2. ^1H NMR spectroscopic analyses

The absence of the three peaks at $\delta = 13.7$, 40.9 and 47.8 ppm (corresponding to methyl groups from coordinated acetic acid) in the ^1H NMR spectra of prepared complexes confirms complete substitution of acetate by functionalized benzoate-based ligands (Figure II-19).

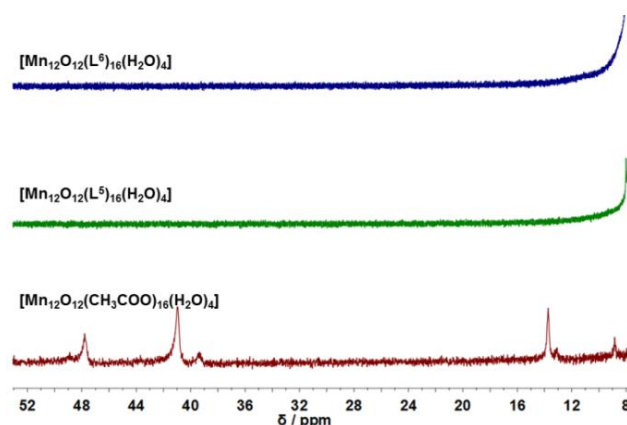


Figure II-19. ^1H NMR spectra of $[\text{Mn}_{12}\text{O}_{12}(\text{OAc})_{16}(\text{H}_2\text{O})_4]$ in CD_3CN and $[\text{Mn}_{12}\text{O}_{12}(\text{L}^{5-6})_{16}(\text{H}_2\text{O})_4]$ in CDCl_3 at 298 K.

The signals of the protons located close to the paramagnetic core are very broad to be observed, but the peripheral protons of the terminal mesogenic biphenyl and cyanobiphenyl groups are less affected (the signals are weakly broadened and their positions are slightly shifted). Thus, ^1H NMR spectroscopy can be used as a useful probe to determine whether the functionalized ligand is grafted or not (Figure II-20).

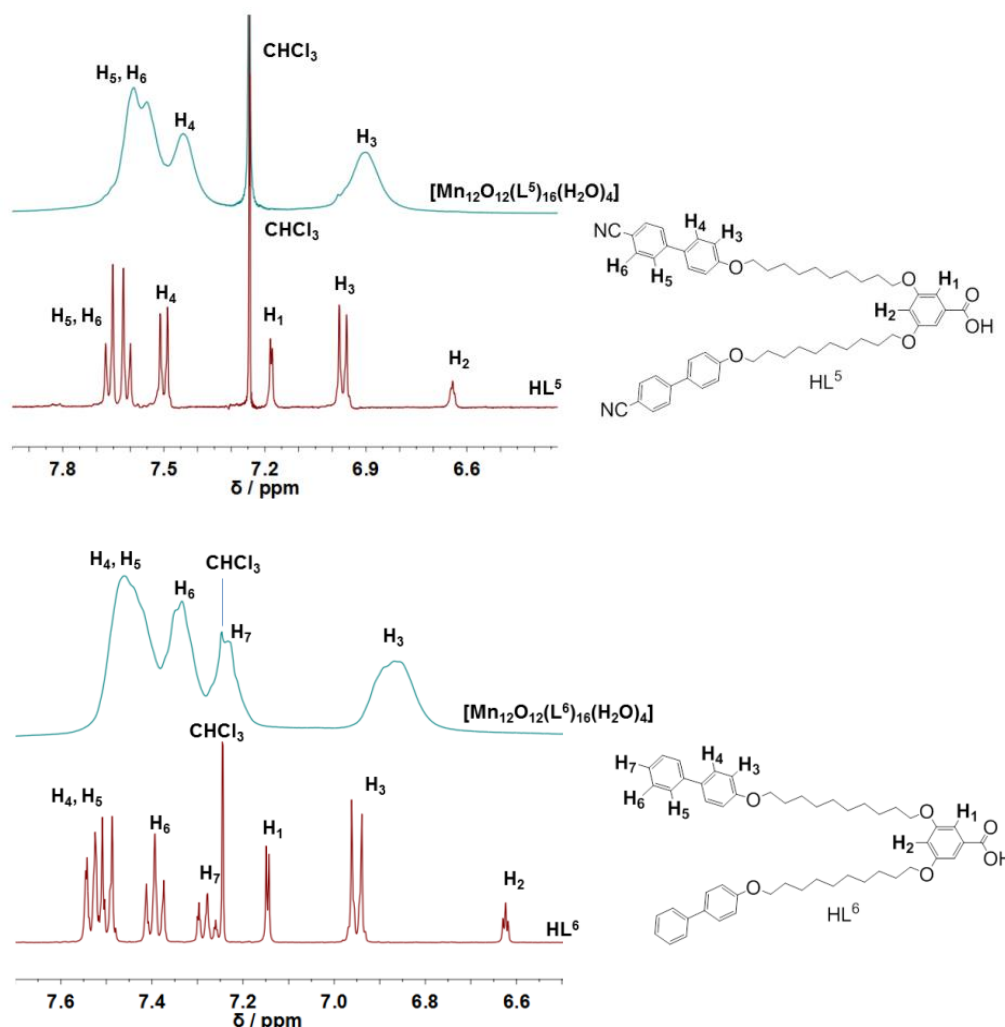


Figure II-20. Aromatic region of ^1H NMR spectra in CDCl_3 at 298 K: (top) HL^5 and $[\text{Mn}_{12}\text{O}_{12}(\text{L}^5)_{16}(\text{H}_2\text{O})_4]$; (bottom) HL^6 and $[\text{Mn}_{12}\text{O}_{12}(\text{L}^6)_{16}(\text{H}_2\text{O})_4]$.

As the result of the ligands grafting and the proximity to paramagnetic core, the signals corresponding to protons H_1 and H_2 have totally disappeared. Also, the absence of signals corresponding to these protons corresponds to complete removal of unreacted ligand (used in a large excess in preparation) and validates the purification technique. The presence of sets of protons $\text{H}_3\text{-H}_6$ for $[\text{Mn}_{12}\text{O}_{12}(\text{L}^5)_{16}(\text{H}_2\text{O})_4]$ and $\text{H}_3\text{-H}_7$ for $[\text{Mn}_{12}\text{O}_{12}(\text{L}^6)_{16}(\text{H}_2\text{O})_4]$, although broadened, confirmed the grafting of the functionalized ligands (Figure II-20).

II.5.2.3. Elemental and thermo-gravimetric analyses

The complete substitution of 16 acetates from the parent $\text{Mn}_{12}\text{-OAc}$ complex by functionalized ligands was also demonstrated with the help of elemental and thermo-gravimetric (TG) analyses which were found to be in good agreement with proposed stoichiometries (Table II-4).

The presence of co-crystallized water molecules in the inter-complex void space was determined from the first mass loss between 360 and 400 K in TG analysis. Upon further heating above 420 K, the weight loss higher than 2 % suggests that both samples begin to decompose due to elimination of coordinated water and carboxylate-based organic ligands (Figure S.II-9).

Table II-4. Elemental analyses of $[\text{Mn}_{12}\text{O}_{12}(\text{L}^{5-6})_{16}(\text{H}_2\text{O})_4]$ complexes

Compound	%C (found)	%H (found)	%N (found)	%C (calc.)	%H (calc.)	%N (calc.)
$[\text{Mn}_{12}\text{O}_{12}(\text{L}^5)_{16}(\text{H}_2\text{O})_4] \cdot 12\text{H}_2\text{O}$ $\text{C}_{848}\text{H}_{976}\text{Mn}_{12}\text{N}_{32}\text{O}_{124}$	71.39	6.93	3.32	71.42	6.90	3.14
$[\text{Mn}_{12}\text{O}_{12}(\text{L}^6)_{16}(\text{H}_2\text{O})_4] \cdot 9\text{H}_2\text{O}$ $\text{C}_{816}\text{H}_{1002}\text{Mn}_{12}\text{O}_{121}$	73.08	7.61	-	73.11	7.53	-

II.5.3. Magnetic measurements

Functionalized $[\text{Mn}_{12}\text{O}_{12}(\text{L}^5)_{16}(\text{H}_2\text{O})_4]$ and $[\text{Mn}_{12}\text{O}_{12}(\text{L}^6)_{16}(\text{H}_2\text{O})_4]$ complexes were checked for SMM behavior by investigation of their magnetic properties that give direct evidence, that the dodecanuclear oxo-metallic core preserved its structural integrity.

To detect the slow relaxation of the magnetization, the temperature dependence of the in-phase (χ') and out-of-phase (χ'') ac magnetic measurements were carried out in the 1.9-15 K range at several oscillation frequencies from 1 to 1500 Hz (Figure II-21).

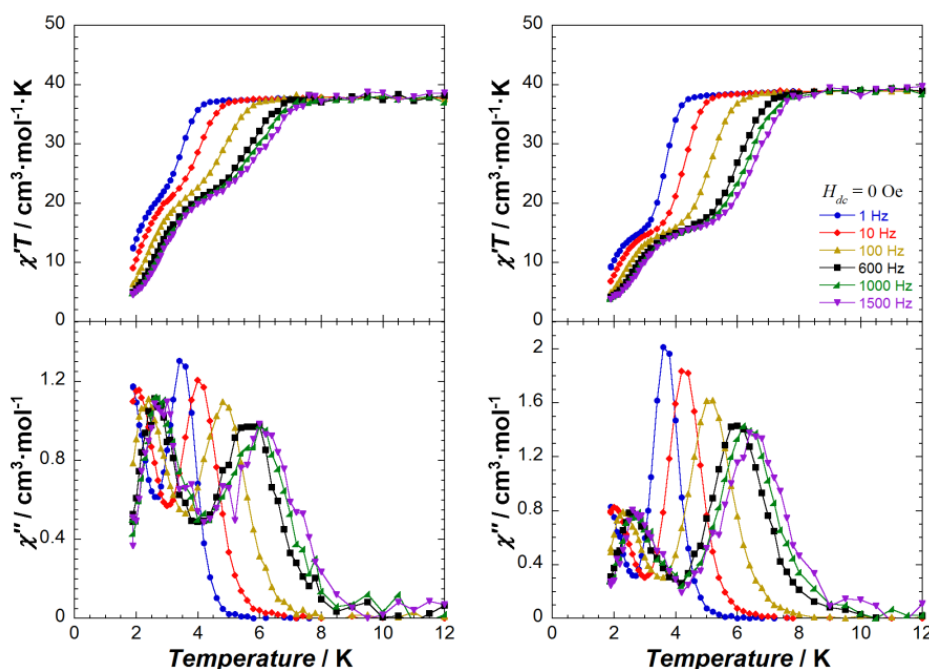


Figure II-21. Temperature dependence of $\chi'T$ (top) and χ'' (bottom) for $[\text{Mn}_{12}\text{O}_{12}(\text{L}^5)_{16}(\text{H}_2\text{O})_4]$ (left) and $[\text{Mn}_{12}\text{O}_{12}(\text{L}^6)_{16}(\text{H}_2\text{O})_4]$ (right) measured under various oscillating frequencies (1-1500 Hz) in zero dc field. The solid lines are guides for the eyes.

Constant values of $\chi'T = 37.7 \text{ cm}^3 \cdot \text{K} \cdot \text{mol}^{-1}$ for $[\text{Mn}_{12}\text{O}_{12}(\text{L}^5)_{16}(\text{H}_2\text{O})_4]$ and $39.1 \text{ cm}^3 \cdot \text{K} \cdot \text{mol}^{-1}$ for $[\text{Mn}_{12}\text{O}_{12}(\text{L}^6)_{16}(\text{H}_2\text{O})_4]$ are observed in the 8–12 K range, which correspond to $\chi'T$ values expected for complexes with $S_T = 9$ ($g = 1.83$ for $[\text{Mn}_{12}\text{O}_{12}(\text{L}^5)_{16}(\text{H}_2\text{O})_4]$ and 1.86 for $[\text{Mn}_{12}\text{O}_{12}(\text{L}^6)_{16}(\text{H}_2\text{O})_4]$) in the ground state. The decrease of $\chi'T$ product below 8 K is accompanied by the appearance of the systematic frequency dependent out-of-phase χ'' ac susceptibility. The presence of two peaks in the χ'' vs T plots, as well

as, the second plateau in $\chi'T$ vs T plots is suggesting that there are two different relaxation processes. These two magnetization relaxation processes in Mn_{12} complexes have been elucidated by the Jahn-Teller isomerism, characteristic to Mn_{12} family (see sections II.2.2 and II.4.3). The HT (high temperature or slowly relaxing) species contain Jahn–Teller (JT) isomers with a near parallel alignment of the eight Mn^{III} JT axes along the molecular z -axis (normal orientation), whereas in the LT (low temperature or fast relaxing) species, one or more Mn^{III} JT elongation axes are abnormally oriented (equatorially rather than axially). The ratio of each isomer present in the measured sample can be quantified by the difference of the two plateaus present in $\chi'T$ vs T plots, thus for $[Mn_{12}O_{12}(L^5)_{16}(H_2O)_4]$ the LT(%) / HT(%) ratio is 55/45 and for $[Mn_{12}O_{12}(L^6)_{16}(H_2O)_4]$ it is 35/65.

Table II-5. Magnetic Properties for $[Mn_{12}O_{12}(L^{5-6})_{16}(H_2O)_4]$ complexes

Compound	S	g	JT isomers ratios LT (%) / HT (%)	Low temperature (LT) or fast relaxing (FR) JT isomer		High temperature (HT) or slow relaxing (SR) JT isomer		$\mu_0 H_C$ (T)
				Δ_{eff}/k_B (K)	τ_0 (s)	Δ_{eff}/k_B (K)	τ_0 (s)	
$[Mn_{12}O_{12}(L^5)_{16}(H_2O)_4]$	9	1.83	55 / 45	32.5	1.6×10^{-9}	60.4	6.2×10^{-9}	0.22
$[Mn_{12}O_{12}(L^6)_{16}(H_2O)_4]$	9	1.86	35 / 65	31.7	1.9×10^{-9}	60.8	1.1×10^{-8}	0.72

S: spin ground state; *g*: Lande factor of ground state; Δ_A : potential energy barrier; τ_0 : pre-exponential factor; $\mu_0 H_C$: coercive field measured at $T = 1.9$ K and at 0.035 T·min⁻¹ sweep rate.

Both peaks from χ'' vs T plots shift towards higher temperatures when the frequency increases. The deduced relaxation time follows an Arrhenius law as shown in Figure II-22. The activation energy barriers Δ_{eff}/k_B and the pre-exponential factors τ_0 were estimated for both HT and LT relaxing species (Table II-5). Obtained values are almost the same for both $[Mn_{12}O_{12}(L^5)_{16}(H_2O)_4]$ and $[Mn_{12}O_{12}(L^6)_{16}(H_2O)_4]$ and are close to those observed for other Mn_{12} complexes (see Table II-5).

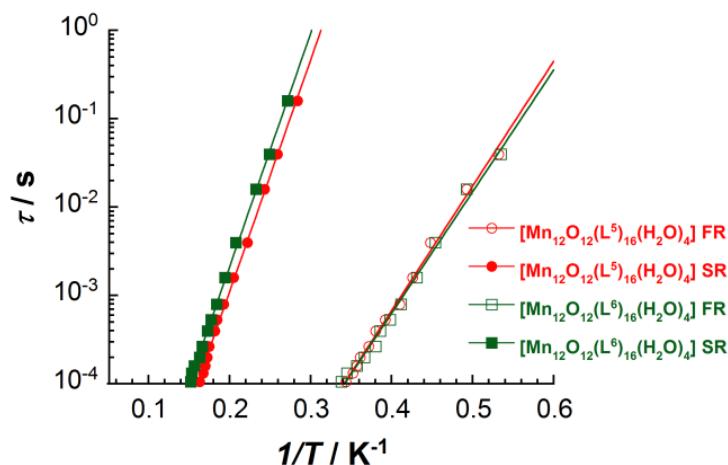


Figure II-22. Inverse temperature dependence of the relaxation time in semi-logarithmic scale for $[Mn_{12}O_{12}(L^{5-6})_{16}(H_2O)_4]$ complexes using χ'' vs T data for the FR (LT) and SR (HT) species from Figure II-21. Full lines are the best fits to an Arrhenius law.

Variable-temperature dc magnetic susceptibility (χ) data were collected on complexes $[Mn_{12}O_{12}(L^5)_{16}(H_2O)_4]$ and $[Mn_{12}O_{12}(L^6)_{16}(H_2O)_4]$ in the 1.8 - 280 K range in a 0.1 T magnetic field (Figure S.II-10 right). The χT versus T dependences are similar to those of previously studied $[Mn_{12}O_2(L^{1-4})_{16}(H_2O)_4]$ complexes, exhibiting a nearly temperature-independent value of 18 cm³·K·mol⁻¹ in the 150-280 K range

which then increases rapidly to a maximum of $39 - 40 \text{ cm}^3 \cdot \text{K} \cdot \text{mol}^{-1}$ at 12 K before decreasing rapidly to $27 - 29 \text{ cm}^3 \cdot \text{K} \cdot \text{mol}^{-1}$ at 1.8 K. The maximum indicates a large ground-state spin (S_T) value, and the low temperature decrease is primarily due to zero-field splitting effects.

The opening of a hysteresis loop in the field dependence of magnetization, observed for both $[\text{Mn}_{12}\text{O}_{12}(\text{L}^{5-6})_{16}(\text{H}_2\text{O})_4]$ complexes, is another feature specific to SMMs and bulk magnets. Thus, the M vs H plots (Figure II-23) measured for both samples at 1.9 K with a sweep rate of about $0.035 \text{ T} \cdot \text{min}^{-1}$ revealed coercive fields of 0.22 T for $[\text{Mn}_{12}\text{O}_{12}(\text{L}^5)_{16}(\text{H}_2\text{O})_4]$ and 0.72 T for $[\text{Mn}_{12}\text{O}_{12}(\text{L}^6)_{16}(\text{H}_2\text{O})_4]$.

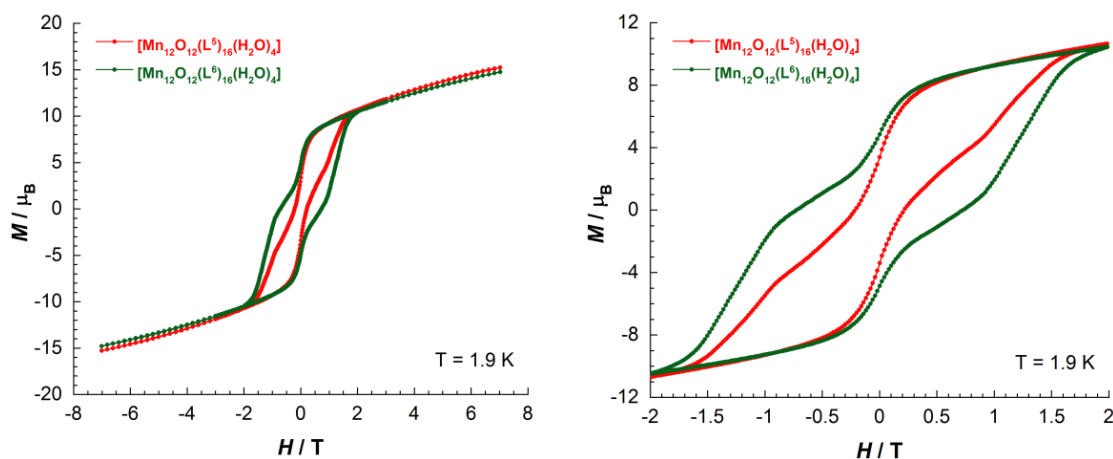


Figure II-23. Magnetization vs. applied field at 1.9 K and at $0.035 \text{ T} \cdot \text{min}^{-1}$ sweep rate for $[\text{Mn}_{12}\text{O}_{12}(\text{L}^{5-6})_{16}(\text{H}_2\text{O})_4]$ complexes, the right figure is a zoom of the figure on the left side.

Despite the facts that HL^5 and HL^6 ligands have almost similar structures and final complexes are characterized by magnetic parameters (S , g , Δ_{eff}/k_B) of almost similar values, the ratios of JT isomers is considerably different. This may confirm the hypothesis that peripheral cyanobiphenyl moieties form stronger intermolecular interactions that distort the magnetic core by pulling and pressure effects and, as result, affect its properties.

II.5.4. Thermotropic properties

II.5.4.1. DSC and temperature dependent POM investigations

The thermal properties of both compounds were firstly investigated by differential scanning calorimetry (DSC) and temperature dependent polarized optical microscopy (POM). Thermal data are summarized in Table II-6.

Table II-6. Thermal data for $[\text{Mn}_{12}\text{O}_{12}(\text{L}^{5-6})_{16}(\text{H}_2\text{O})_4]$ complexes obtained by DSC at 5 Kmin^{-1} .

Compound	Transition ^a	T / K	$\Delta C_p / \text{kJ} \cdot \text{mol}^{-1} \cdot \text{K}^{-1}$	$\Delta H / \text{kJ} \cdot \text{mol}^{-1}$
$[\text{Mn}_{12}\text{O}_{12}(\text{L}^5)_{16}(\text{H}_2\text{O})_4]$	g – Sm ^b	301	7.6	-
	Sm – I ^c	442.5	-	50.1
$[\text{Mn}_{12}\text{O}_{12}(\text{L}^6)_{16}(\text{H}_2\text{O})_4]$	g – Sm	295.6	8.3	-
	Sm – I	347.5	-	73.3

^a data obtained on second heating, g = glass, Sm = smectic phase, I = isotropic liquid; ^b the smectic nature of the observed mesophase was determined using SAXS technique; ^c this transition temperature was taken at first heating due to the decomposition on further heating cycles.

POM investigations of the functionalized $[\text{Mn}_{12}\text{O}_{12}(\text{L}^{5-6})_{16}(\text{H}_2\text{O})_4]$ complexes revealed presence of birefringent optical textures (Figure II-24). Above room temperature the fluidity of the observed birefringent

mesophases was increasing as the temperature was raised. The assignment of a certain mesophase to the textures observed on heating or on cooling from isotropic melt was not possible since no specific natural texture (schlieren, fingerprint, focal-conic fan or others) could be obtained. However, it was possible to assign the transition to isotropic liquid due to the formation of fluid optically isotropic (black) areas. In the case of $[\text{Mn}_{12}\text{O}_{12}(\text{L}^5)_{16}(\text{H}_2\text{O})_4]$ the clearing point was observed around 445 K, that is the same as the Mn_{12} -based core decomposition temperature observed in TGA, while the $[\text{Mn}_{12}\text{O}_{12}(\text{L}^6)_{16}(\text{H}_2\text{O})_4]$ compound showed the formation of the isotropic liquid around 348 K.

DSC thermograms were in agreement with POM observations. Both compounds showed a glass transition, corresponding to the melting/freezing of the mesophase, around 295-305 K. Only the glass transition was observed for $[\text{Mn}_{12}\text{O}_{12}(\text{L}^5)_{16}(\text{H}_2\text{O})_4]$ complex (Figure II-25 left) in 280-410 K temperature range (in order to avoid decomposition) on several subsequent heating-cooling cycles. Thus, in order to determine the clearing point temperature fast (10 K/min) subsequent heating-cooling cycles in 300-450 K range were afterwards performed. Large and asymmetric peak assigned to the clearing point with POM was observed at 442 K on both heating and cooling. Further thermal cycles showed peak broadening and a significant decrease of enthalpy value, which may be explained by the decomposition of functionalized compound, confirmed by TG analysis.

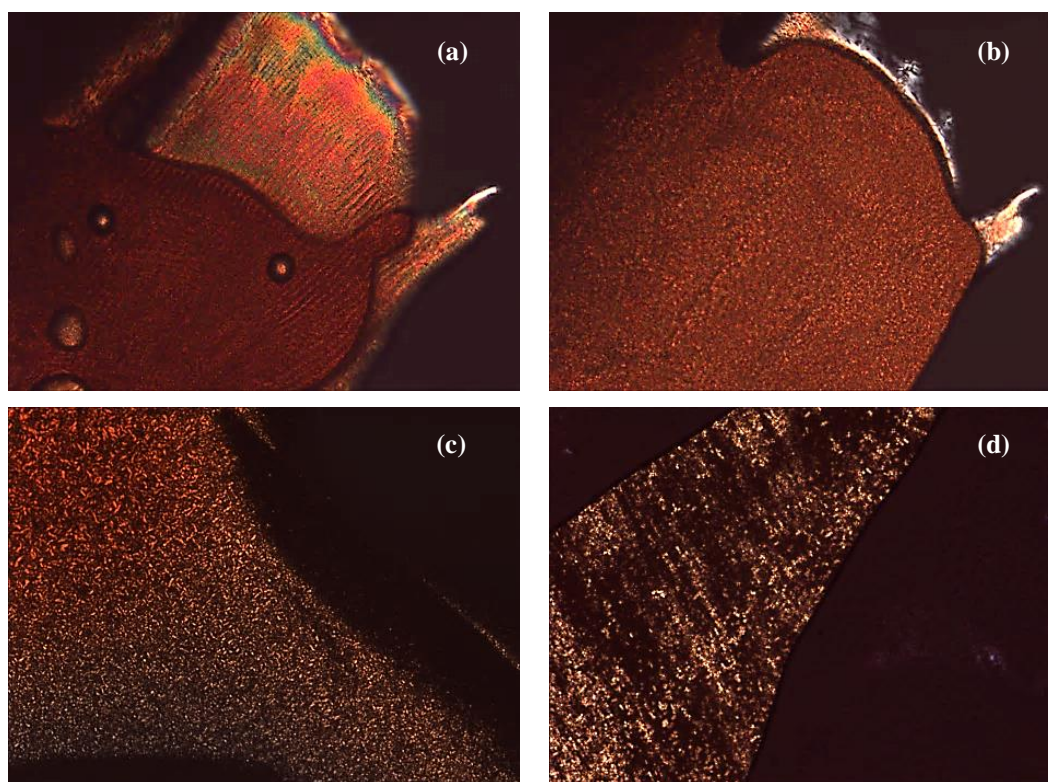


Figure II-24. Birefringent textures observed with POM: (a) for $[\text{Mn}_{12}\text{O}_{12}(\text{L}^5)_{16}(\text{H}_2\text{O})_4]$ at 393 K on heating from room temperature; (b) for $[\text{Mn}_{12}\text{O}_{12}(\text{L}^5)_{16}(\text{H}_2\text{O})_4]$ at 423 K on heating from room temperature; (c) for $[\text{Mn}_{12}\text{O}_{12}(\text{L}^6)_{16}(\text{H}_2\text{O})_4]$ at 343 K on heating from room temperature; (d) for $[\text{Mn}_{12}\text{O}_{12}(\text{L}^6)_{16}(\text{H}_2\text{O})_4]$ at 323 K on cooling from isotropic liquid.

The $[\text{Mn}_{12}\text{O}_{12}(\text{L}^6)_{16}(\text{H}_2\text{O})_4]$ complex showed a reversible sharp peak at 347.5 K, corresponding to the transition from liquid crystal phase to isotropic liquid (Figure II-25). The enthalpy change of both transitions (50.1 kJ/mol for $[\text{Mn}_{12}\text{O}_{12}(\text{L}^5)_{16}(\text{H}_2\text{O})_4]$ and 73.3 kJ/mol for $[\text{Mn}_{12}\text{O}_{12}(\text{L}^6)_{16}(\text{H}_2\text{O})_4]$) have very high values when compared to the normal range specific to clearing point of a mesophase.⁴⁷ However, it is possible to

explain these high values by considering a large amount of attached mesogenic promoters. Therefore, if the enthalpy changes are divided by the number of attached mesogenic groups (32), values of 1.6 and 2.3 kJ/mol per mesogenic unit are then obtained. The values of enthalpy changes occurring at the clearing temperature are comparable with those observed for other biphenyl or cyanobiphenyl functionalized compounds.^{23,24b,26,48} Indeed this result shows that the oxo-metallic core play a minor role in the clearing processes, which are governed by the organic moieties. Also, it is important to mention that functionalization with biphenyl moieties allowed to decrease the clearing temperature almost by 100 K in comparison with cyanobiphenyl analogue.

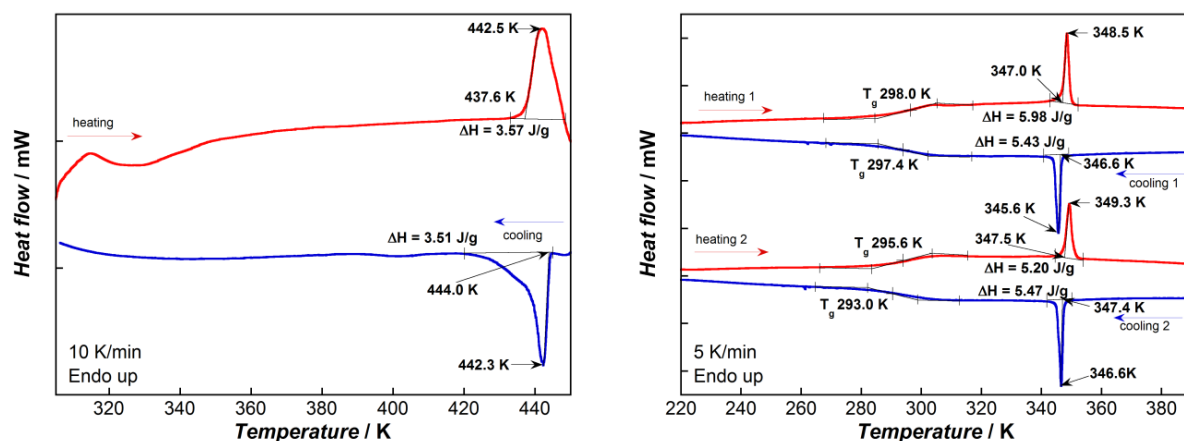


Figure II-25. DSC traces of $[\text{Mn}_{12}\text{O}_{12}(\text{L}^5)_{16}(\text{H}_2\text{O})_4]$ on third heating-cooling cycle between 300 and 450 K at 10 K/min (left) and DSC traces of $[\text{Mn}_{12}\text{O}_{12}(\text{L}^6)_{16}(\text{H}_2\text{O})_4]$ recorded on first two heating-cooling cycles between 220 and 390 K at 5 K/min (right).

II.5.4.2. Small angle X-ray scattering (SAXS) investigations

More insights regarding the mesophase in both $[\text{Mn}_{12}\text{O}_{12}(\text{L}^{5-6})_{16}(\text{H}_2\text{O})_4]$ systems were revealed with the help of temperature-dependent small and wide angle X-ray scattering investigations. The experiments were carried out on several heating-cooling cycles to allow thermal annealing of the mesophase in the studied samples. Thus, $[\text{Mn}_{12}\text{O}_{12}(\text{L}^5)_{16}(\text{H}_2\text{O})_4]$ with high clearing point temperature, was firstly heated from room temperature to 373 K and kept for several hours (with acquisition of several diffraction patterns in order to verify if the sample is stable at this temperature), then the sample was slowly cooled to 303 K and diffractograms were obtained on subsequent heating-cooling cycles in the 303-413 K temperature range (in order to avoid decomposition of the sample). Finally a set of diffraction images was acquired on heating the sample above the observed clearing point (445 K). Due to the stability of the $[\text{Mn}_{12}\text{O}_{12}(\text{L}^6)_{16}(\text{H}_2\text{O})_4]$ complex above clearing temperature, SAXS investigations were performed between 298 and 353 K on cooling and heating.

Diffraction patterns recorded for both $[\text{Mn}_{12}\text{O}_{12}(\text{L}^{5-6})_{16}(\text{H}_2\text{O})_4]$ were quite similar. Each contained two sets of reflections in small angle region and a diffuse scattering halo in the wide angle region centered around 4.4 Å (or at 14.2-14.3 nm⁻¹ showed as h_{ch} in Figure II-26). The presence of diffuse halo corresponds to the lateral short range order of the molten chains and mesogenic (biphenyl or cyanobiphenyl) moieties, confirming the liquid crystalline nature of the mesophase.

The SAXS profiles recorded at different temperatures are all qualitatively equivalent and contain two sharp small angle reflections (and a third, very weak one, in the case of $[\text{Mn}_{12}\text{O}_{12}(\text{L}^6)_{16}(\text{H}_2\text{O})_4]$) characteristic to a layered arrangement with reciprocal spacing in the 1:2 ($1:\sqrt{4}$) ratio for $[\text{Mn}_{12}\text{O}_{12}(\text{L}^5)_{16}(\text{H}_2\text{O})_4]$ and 1:2:3 ($1:\sqrt{4}:\sqrt{9}$) ratios for $[\text{Mn}_{12}\text{O}_{12}(\text{L}^6)_{16}(\text{H}_2\text{O})_4]$. Observed reflections were indexed with 001, 002 and 003 Miller indices ($00l$) and, by applying the Bragg's law, interlayer distances of 38.8 Å for $[\text{Mn}_{12}\text{O}_{12}(\text{L}^5)_{16}(\text{H}_2\text{O})_4]$ and 32.8 Å for $[\text{Mn}_{12}\text{O}_{12}(\text{L}^6)_{16}(\text{H}_2\text{O})_4]$ were calculated.

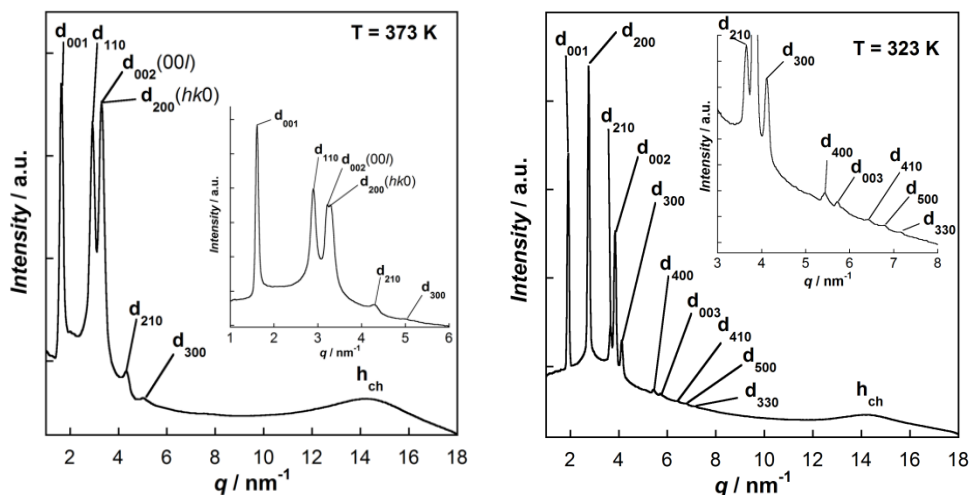


Figure II-26. Indexed SAXS profiles for: (left) $[\text{Mn}_{12}\text{O}_{12}(\text{L}^5)_{16}(\text{H}_2\text{O})_4]$ at 373 K on second heating from room temperature, in the inset is showed the small angle region emphasizing very close proximity of 002 and 200 reflections originating, respectively, from the lamellar ordering ($00l$) and from hexagonal ($hk0$) interlayer arrangement of electron-rich Mn_{12} cores; and (right) for $[\text{Mn}_{12}\text{O}_{12}(\text{L}^6)_{16}(\text{H}_2\text{O})_4]$ at 323 K on cooling from isotropic liquid, in the inset weak reflections between 5 and 8 nm^{-1} are emphasized.

Besides the reflections corresponding to the lamellar arrangement, several additional reflections of variable intensity were observed. These reflections were indexed in a hexagonal network as $(hk0) = (110)$, (200) , (210) , (300) corresponding to the reciprocal spacings ratios $\sqrt{3}:\sqrt{4}:\sqrt{7}:\sqrt{9}$ for $[\text{Mn}_{12}\text{O}_{12}(\text{L}^5)_{16}(\text{H}_2\text{O})_4]$ and as $(hk0) = (200)$, (210) , (300) , (400) , (410) , (500) , (330) with reciprocal spacings ratios $\sqrt{4}:\sqrt{7}:\sqrt{9}:\sqrt{16}:\sqrt{21}:\sqrt{25}:\sqrt{27}$ for $[\text{Mn}_{12}\text{O}_{12}(\text{L}^6)_{16}(\text{H}_2\text{O})_4]$ (see also tables S.II–10 and S.II–11). The sharp shape and the strong intensity of some of these reflections indicate a long range hexagonal ordering of the electron-rich cores within the layer for both functionalized complexes. The average in-plane inter-core (or intra-layer) distances (a) of 43.5 Å for $[\text{Mn}_{12}\text{O}_{12}(\text{L}^5)_{16}(\text{H}_2\text{O})_4]$ and 52.7 Å for $[\text{Mn}_{12}\text{O}_{12}(\text{L}^6)_{16}(\text{H}_2\text{O})_4]$ at 323 K were calculated. The interlayer distances (corresponding to d_{001} reflections) are weakly temperature dependent and usually slightly increase with temperature decrease, while the inter-core distances decreases by 1-2 Å (see also tables S.II–10 and S.II–11). The shortening of the lamellar interlayer distance when cyanobiphenyl unit is exchanged by biphenyl moiety may correspond to a higher interdigitation of the biphenyl moieties, as confirmed by an increase of in-plane inter-core distances and, thus, of molecular area (1617 Å² for $[\text{Mn}_{12}\text{O}_{12}(\text{L}^5)_{16}(\text{H}_2\text{O})_4]$ and 2405 Å² for $[\text{Mn}_{12}\text{O}_{12}(\text{L}^6)_{16}(\text{H}_2\text{O})_4]$ at 323 K). Apparently shorter inter-planar distances are specific to biphenyl moieties, since similar result was observed and reported for a series of $(\text{nBu}_4\text{N})_2[\text{Mo}_6\text{Br}_8(\text{L}^i)_6]$ functionalized clusters,²³ where L^i are gallic acid based ligands modified with $[\text{((biphenyl)yl)oxy}]$ - or $[\text{((4-cyanobiphenyl)yl)oxydecyl}]$ groups (exactly the

same as those used in our work). Due to the absence of a strongly electron density withdrawing cyano (-CN) group (as it is schematically represented in Figure II-27 top right), the biphenyl moieties are much less polar than cyanobiphenyl ones (as it is schematically represented in Figure II-27 top right). Therefore electrostatic interactions between biphenyl groups are much weaker than those observed between cyanobiphenyl groups. This explains quite well the decrease of the isotropic transition temperature, a higher interdigitation between the [(biphenyl)yl]oxydecyl chains and, thus, a shorter interplanar distance (Figure II-27 left and center).

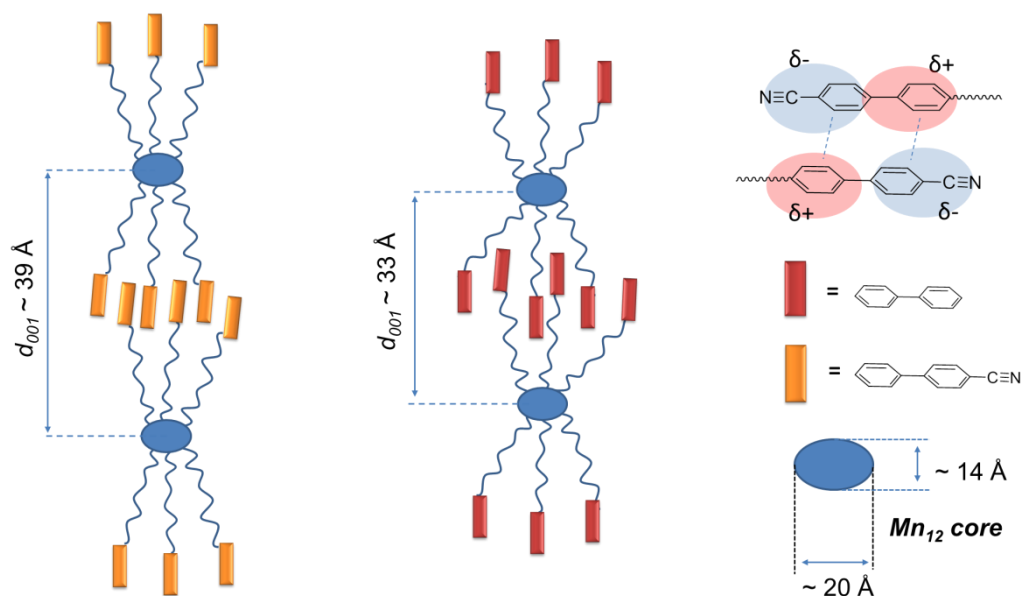


Figure II-27. Schematic representation of the idealized intermolecular interactions leading to different inter-planar distances in the mesophases observed for $[\text{Mn}_{12}\text{O}_{12}(\text{L}^{5-6})_{16}(\text{H}_2\text{O})_4]$ complexes, only the ligands in axial positions are shown.

Theoretical distances calculated for the both biphenyl-based mesogens (9 – 10 Å), the aliphatic spacer (~ 13 Å, idealized conformation), and the rigid Mn_{12} core, including benzoate moieties from the ligands (height ~ 14 Å and diameter ~ 20 Å) allow existence of the calculated interlamellar distances, moreover these data suggests that mainly the ligands in axial positions are contributing to the formation of the lamellar structure. Whereas the in plane distance (a) corresponding to a 2D hexagonal arrangement of the magnetic cores inside the plane is influenced by the interdigitation of the mesogenic promoters (the higher is the interdigitation of the axially situated promoters the bigger is the molecular area, as can be observed from the schemes in Figure II-27) and the functional groups present in equatorial positions, that, apparently form only short contacts with other neighbors.

The analysis of SAXS profiles at temperatures close to clearing points (Figures S.II-22 and S.II-23) confirms the presence of a lamellar structure and weaker in plane intermolecular interactions. Only the reflections corresponding to the layered morphology are present close to clearing temperatures, while those assigned to intra-layer ordering shift and broaden, forming in small-angle region a broad diffusion d' that corresponds to an average short-range correlation distance between oxo-metallic cores within the layer. Thus, the mesophase observed for $[\text{Mn}_{12}\text{O}_{12}(\text{L}^5)_{16}(\text{H}_2\text{O})_4]$ and $[\text{Mn}_{12}\text{O}_{12}(\text{L}^6)_{16}(\text{H}_2\text{O})_4]$ complexes can be surely described by a smectic phase, consisting of alternating layers of interdigitated mesogens and Mn_{12} cores arranged into a hexagonal array and separated by aliphatic sub-layers (Figure II-28).

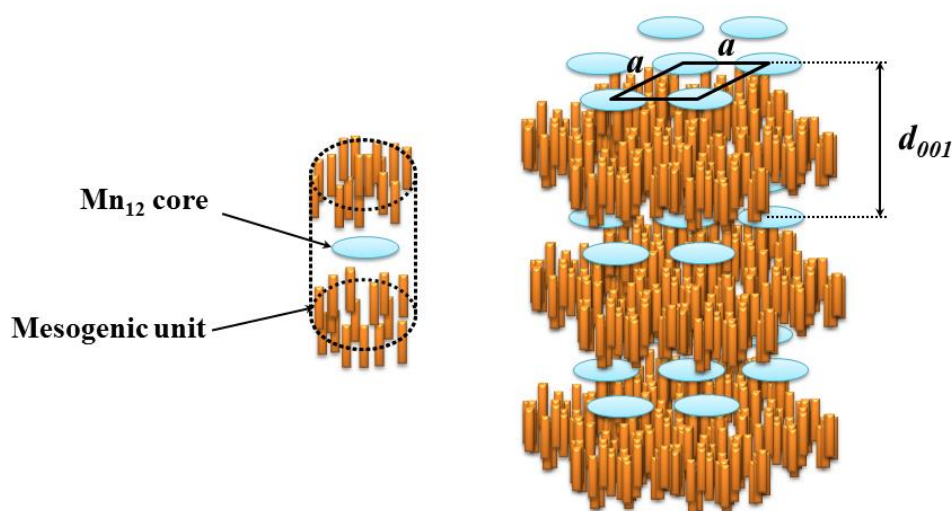


Figure II-28. Schematic representation of the lamellar packing of $[\text{Mn}_{12}\text{O}_{12}(\text{L}^{5-6})_{16}(\text{H}_2\text{O})_4]$ complexes inside the smectic mesophase, the equatorial groups are omitted for clarity.

Even though, a few Mn_{12} -based complexes bearing mesogenic promoters (cyanobiphenyl group) were also reported with smectic mesophases, the arrangement of magnetic cores was difficult to deduce from previous SAXS investigations.²⁴ Only the presence of broad diffusion along with two sharp interlayer reflections was reported in small angle region between 313 and 413 K. Thus, the square-like short-ranged 2D order of Mn_{12} cores within the layer was deduced from molecular dynamic calculations.^{24c} In the case of the functionalized compounds reported in this work, it was possible to observe experimentally the short range hexagonal order of the magnetic units within the layers from SAXS profiles. Probably, the shortening of the length of the aliphatic spacer by one carbon allowed a certain stabilization of Mn_{12} -cores arrangement within the lamellar structure induced by organic mesogens.

II.5.5. Summary of section II.5

By applying the functionalization strategy of grafting a mesogenic promoter via a flexible spacer, it was possible to obtain two new hybrid complexes possessing SMM and liquid crystalline properties. Two different mesogenic promoters were used in this work. Despite the bulkiness of the Mn_{12} core, it was possible in both cases to induce thermotropic smectic phases. Moreover, grafting of biphenyl groups allowed decreasing the clearing point and, to the best of our knowledge, the reported $[\text{Mn}_{12}\text{O}_{12}(\text{L}^6)_{16}(\text{H}_2\text{O})_4]$ complex has the lowest clearing temperature among Mn_{12} complexes functionalized with mesogenic promoters. Even though that both systems have similar structures and have the same packing inside the mesophase, the ratio of magnetic JT isomers is considerably different. This may be related to the presence of peripheral biphenyl moieties that induce a higher interdigitation comparing to cyanobiphenyl units. Thus, intermolecular interactions induced by cyanobiphenyl or biphenyl groups differently distort the magnetic core and, as result, affect differently their magnetic properties.

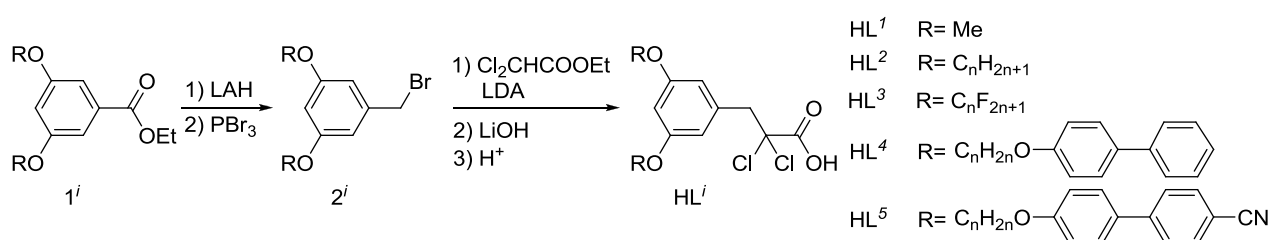
II.6. Conclusions and perspectives

Two different functionalization strategies were applied to obtain hybrid molecular materials. The functionalization with strongly lipophilic groups failed in obtaining products with less oriented and

symmetric phases, but still resulted to be successful in the control of thermally induced 3D self-organization of the Mn_{12} SMMs. Thus, by varying chain density around the rigid core, it was possible to stabilize crystalline cubic organization or thermotropic cubic mesophases of different symmetries. The organization inside the cubic mesophases has a molecular origin and is governed by the overall shape of rigid magnetic core, while aliphatic chains offer necessary fluid environment for self-organization. The second chosen strategy, functionalization by grafting a mesogenic promoter via a flexible spacer, showed that functionalized complexes form a hexagonal self-organization in layered smectic phase over a wide range of temperatures. The rational choice of the mesogenic promoter allowed controlling the thermal properties of hybrid molecular materials. The specific molecular design in this case contributed to formation of hybrid molecular materials possessing several properties and allowed tuning of parameter characteristics to the original Mn_{12} -based core. All synthesized complexes preserved their magnetic properties after the functionalization process. Significant difference in magnetic relaxation was observed, resulting from the different ratio of JT isomers, which appears to be influenced by the structure of the ligand and the intermolecular interactions it may induce.

To further develop these fundamental aspects and to optimize the magnetic and mesomorphic properties, it is necessary to design new liquid crystalline Mn_{12} complexes or to adapt and extend functionalization strategies to other types of SMMs. In order to tailor more precisely the mesomorphic features functionalized Mn_{12} complex should have a more anisotropic structure than a globular geometrical shape. For achieving this, it is necessary to introduce mesogenic ligands only in specific positions of the complex. Indeed, the 16 acetates of the Mn_{12} complex are equitably distributed on equatorial and axial positions and several studies have shown that the acetates can be exchanged selectively depending on their position occupancies. Thus, numerous heterogeneous Mn_{12} analogues, of formula $[Mn_{12}O_{12}(L)_8^{ax}(L')_8^{eq}(H_2O)_x]$ (where L and L' are two different ligands occupying the positions axial and equatorial respectively), have been reported (see section II.2.3).¹² Based upon these studies, it is possible to functionalize the Mn_{12} core regio-selectively with mesogenic ligands. The two functionalization modes (axial and equatorial) can be explored. By functionalizing the axial positions with mesogenic ligands, the complex can adopt a rod-like shape (calamitic) favoring the formation of smectic phases. In the second case (equatorial-mode functionalization), the molecular structure may adopt a disk-like form and lead, depending on intermolecular cohesion, to nematic or columnar mesophases. The regioselective substitution in Mn_{12} derivatives is dependent on the acidity of carboxylic acids. Thus, in order to selectively modify original Mn_{12} -OAc complex in its axial positions it will be necessary to obtain functionalized ligands with pK_a lower than that of acetic acid as it is proposed in the scheme below:

Scheme II-6. Synthetic pathway for the preparation of mesogenic ligands with a low pK_a .



To prepare the final complexes, a methodology described previously for the synthesis of heterogeneous Mn_{12} must be employed.¹² The general procedure involves synthesis of homogeneous complexes $[Mn_{12}O_{12}(L^i)_{16}(H_2O)_4]$ and $[Mn_{12}O_{12}(AcO)_{16}(H_2O)_4]$. A ligand exchange reaction between the two compounds will generate heterogeneous $[Mn_{12}O_{12}(L^i)_8^{ax}(AcO)_8^{eq}(H_2O)_x]$.

On the other hand the functionalized complexes presented in this work, $[Mn_{12}O_{12}(L^{3-6})_{16}(H_2O)_4]$, can be used as precursors for systems of discotic geometry. The HL^{3-6} ligands are weak acids, therefore the treatment of one of the $[Mn_{12}O_{12}(L^{3-6})_{16}(H_2O)_4]$ complexes with a complex containing a stronger carboxylic acid, i.e. $[Mn_{12}O_{12}(Cl_2CHCOO)_{16}(H_2O)_4]$, may lead to heterogeneous $[Mn_{12}O_{12}(L^i)_8^{eq}(Cl_2CHCOO)_8^{ax}(H_2O)_x]$. Since the acid with a lower pKa will go preferentially to axial positions whereas the functionalized ligands will remain in (or occupy) the equatorial positions, thus, forming a hybrid discotic molecule.

The proposed strategies will be developed during the PhD thesis of Elena Darbinean (2013-2016), who will carry on the regioselective functionalization of SMMs in order to get liquid crystalline phases with columnar or nematic orders.

II.7. Supporting materials

II.7.1. Experimental protocols

Solvents, starting materials, 4-methoxybenzoic acid (HL^1) and 4-dodecyloxybenzoic acid (HL^2) were purchased from Acros, Alfa Aesar or Aldrich, and used without further purification unless otherwise stated.

Preparation of 3,5-bis(dodecyloxy)benzoic acid (HL^3). To a solution of methyl 3,5-dihydroxybenzoate (3.65 g, 21.7 mmol) in 150 mL of acetone, anhydrous potassium carbonate (26.95 g, 195.1 mmol) was added. The mixture was heated to reflux and 1-bromododecane (13.00 g, 52.20 mmol) and a catalytic amount of potassium iodide were added. The reaction mixture was then refluxed for 4 days. The solvent was removed and CH_2Cl_2 (200 mL) was added. The suspension was washed with water (3x100 mL). The organic layer was dried over anhydrous sodium sulfate, filtrated and concentrated. The obtained white vitreous solid (MeL^3) was recrystallized from ethanol (500 mL), filtrated, washed with cold ethanol and dried under vacuum. Ethanol (150 mL) and potassium hydroxide (5.00 g, 89.10 mmol), dissolved previously in 20 mL of water, were added to MeL^3 . The solution was refluxed for 12 h, H_2O (100 mL) was added and then acidified to pH = 1 with a 37 % HCl aqueous solution. Ethanol was removed and the resulting mixture was washed with CH_2Cl_2 (3x100 mL). The organic layers were combined and dried over anhydrous sodium sulfate and concentrated. The product was dried for 24 h under vacuum and 8.19 g (16.22 mmol, 74%) of HL^3 were obtained, as a white vitreous solid. 1H NMR (400 MHz) in $CDCl_3$ (δ , ppm): 7.22 (d, $J = 2.3$ Hz, 2H), 6.69 (t, $J = 2.3$ Hz, 1H), 3.98 (t, $J = 6.5$ Hz, 4H), 1.83 – 1.73 (m, 4H), 1.50 – 1.40 (m, 4H), 1.38 – 1.23 (m, 32H), 0.88 (t, $J = 6.8$ Hz, 6H). Elemental analysis – Calc. (Found) for $C_{31}H_{54}O_4$: C, 75.87 (75.90); H, 11.09 (11.15). Selected FT-IR data (ATR, cm^{-1}): 2916 (vs), 2847 (s), 1687 (vs), 1594 (s), 1420 (vs), 1301 (s), 1170 (s).

Preparation of 3,4,5-tris(dodecyloxy)benzoic acid (HL^4). To a solution of methyl 3,4,5-trihydroxybenzoate (4.00 g, 21.7 mmol) in 150 mL of acetone, anhydrous potassium carbonate (26.95 g, 195.1 mmol) was added. The mixture was heated to reflux and 1-bromododecane (19.20 g, 77.0 mmol) and a catalytic amount of potassium iodide were added. The reaction mixture was then refluxed for 4 days. The solvent was removed and CH_2Cl_2 (200 mL) was added. The suspension was washed with water (3x100 mL). The organic layer was dried over anhydrous sodium sulfate, filtrated and concentrated. The obtained white vitreous solid (MeL^4) was recrystallized from ethanol (500 mL), filtrated, washed with cold ethanol and dried under vacuum. Ethanol (150 mL) and potassium hydroxide (5.00 g, 89.1 mmol), dissolved previously in 20 mL of water, were added to MeL^4 . The solution was refluxed for 12 h, H_2O (100 mL) was added and then acidified to pH = 1 with a 37 % HCl aqueous solution. Ethanol was removed and the resulting mixture was washed with CH_2Cl_2 (3x100 mL). The organic layers were combined and dried over anhydrous sodium sulfate and concentrated. The product was dried for 24 h under vacuum and 10.45 g (15.48 mmol, 71%) of HL^4 were obtained, as a white vitreous solid. 1H NMR (400 MHz) in $CDCl_3$ (δ , ppm): 7.29 (s, 2H), 4.06 – 3.98 (m, 6H), 1.85 – 1.69 (m, 6H), 1.51 – 1.42 (m, 6H), 1.36 – 1.21 (m, 48H), 0.86 (t, $J = 6.8$ Hz, 9H). Elemental analysis – Calc. (Found) for $C_{43}H_{78}O_5$: C, 76.50 (75.53); H, 11.65 (11.72). Selected FT-IR data (ATR, cm^{-1}): 2954 (m), 2917 (vs), 2848 (s), 1679 (vs), 1585 (s), 1429 (s), 1225 (s), 1119 (vs).

Preparation of $[\text{Mn}_{12}\text{O}_{12}(\text{CH}_3\text{COO})_{16}(\text{H}_2\text{O})_4]$. $\text{Mn}(\text{CH}_3\text{COO})_2 \cdot 4\text{H}_2\text{O}$ (4.00 g, 16.32 mmol) was dissolved in 40 mL of 60 % CH_3COOH at room temperature. After cooling down the solution to 0°C , KMnO_4 (1.00 g, 6.33 mmol) was slowly added. The mixture was then warmed up to room temperature while stirring during 30 minutes (until the KMnO_4 was totally dissolved). The solution was filtered and the filtrate was allowed to stand at room temperature for 1 day. The resulting black crystals were filtrated and washed with acetone (100 mL) and tetrahydrofuran (THF, 100 mL). The yield was 57.8 % (2.20 g). Selected FT-IR data (ATR, cm^{-1}): 3400 (br), 2986 (w), 2934 (w), 1754 (w) 1709 (m), 1560 (s), 1413 (s), 1381 (s), 1017 (m), 709 (m), 666 (s).

Preparation of $[\text{Mn}_{12}\text{O}_{12}(\text{L}^1)_{16}(\text{H}_2\text{O})_3]$. To a suspension of $[\text{Mn}_{12}\text{O}_{12}(\text{CH}_3\text{COO})_{16}(\text{H}_2\text{O})_4]$ (0.10 g, $5.25 \cdot 10^{-2}$ mmol) in 20 mL of CH_2Cl_2 /toluene 1:1, 4-methoxybenzoic acid (HL^1) (0.22 g, 1.46 mmol, 28 eq.) was added. The mixture was stirred at 45°C during 24 h. The color of solution changed from brown to brownish black. The solution was filtrated and the solvent was evaporated. Toluene (20 mL) was added to the residue, stirred for 3 hours, and then evaporated to dryness. This procedure was repeated three more times. The residue was re-dissolved in CH_2Cl_2 (5 mL) and crystallized by slow diffusion of Et_2O after 3 days at 4°C . The resulting crystals were collected by filtration, washed with Et_2O . The yield was 0.13 g (72.6 %). The crystals for X-ray diffraction study were re-crystallized with the same method. Elemental analysis – Calc. (Found) for $\text{C}_{128}\text{H}_{120}\text{Mn}_{12}\text{O}_{64}$ ($[\text{Mn}_{12}\text{O}_{12}(\text{L}^1)_{16}(\text{H}_2\text{O})_3] \cdot \text{H}_2\text{O}$): C, 46.01 (46.05); H, 3.62 (3.73). Selected FT-IR data (ATR, cm^{-1}): 2905 (w), 2836 (w), 1602 (s), 1412 (vs), 1250 (s), 1170 (s), 1026 (m), 847 (w), 776 (m).

Preparation of $[\text{Mn}_{12}\text{O}_{12}(\text{L}^i)_{16}(\text{H}_2\text{O})_4]$ ($i = 2-4$). To a suspension of $[\text{Mn}_{12}\text{O}_{12}(\text{CH}_3\text{COO})_{16}(\text{H}_2\text{O})_4]$ (0.10 g, $5.25 \cdot 10^{-2}$ mmol) in 20 mL of CH_2Cl_2 /toluene 1:1, HL^i (0.45 g (HL^2), 0.72 g (HL^3), or 0.98 g (HL^4); 1.46 mmol, 28 eq.) was added. The mixture was stirred at 45°C during 24 h. The color of solution changed from brown to brownish black. The solution was filtrated and the solvent was then evaporated. Toluene (20 mL) was added to the residue, stirred for 3 hours, and then evaporated to dryness. This procedure was repeated three times more. The resulting residue was re-dissolved in CH_2Cl_2 (1-2 mL) affording a viscous mixture, which was purified by two successive gel permeation chromatography with Biorad S-X3 beads swelled with CH_2Cl_2 . The product was dried in vacuum at 40°C overnight. The yields were 66 % for $[\text{Mn}_{12}\text{O}_{12}(\text{L}^2)_{16}(\text{H}_2\text{O})_4]$, 57 % for $[\text{Mn}_{12}\text{O}_{12}(\text{L}^3)_{16}(\text{H}_2\text{O})_4]$ and 62 % for $[\text{Mn}_{12}\text{O}_{12}(\text{L}^4)_{16}(\text{H}_2\text{O})_4]$, based on $[\text{Mn}_{12}\text{O}_{12}(\text{CH}_3\text{COO})_{16}(\text{H}_2\text{O})_4]$. Elemental analysis – Calc. (Found) for $\text{C}_{304}\text{H}_{476}\text{Mn}_{12}\text{O}_{66}$ ($[\text{Mn}_{12}\text{O}_{12}(\text{L}^2)_{16}(\text{H}_2\text{O})_4] \cdot 2\text{H}_2\text{O}$): C, 62.28 (62.30); H, 8.21 (8.19). Selected FT-IR data (ATR, cm^{-1}): 2925 (m), 2853 (m), 1607 (s), 1410 (vs), 1257 (s), 1173 (m), 849 (w), 780 (w). Elemental analysis – Calc. (Found) for $\text{C}_{496}\text{H}_{868}\text{Mn}_{12}\text{O}_{86}$ ($[\text{Mn}_{12}\text{O}_{12}(\text{L}^3)_{16}(\text{H}_2\text{O})_4] \cdot 6\text{H}_2\text{O}$): C, 67.18 (67.58); H, 9.87 (10.01). Selected FT-IR data (ATR, cm^{-1}): 2920 (s), 2852 (s), 1595 (s), 1412 (vs), 1164 (m), 840 (w), 779 (w). Elemental analysis – Calc. (Found) for $\text{C}_{688}\text{H}_{1246}\text{Mn}_{12}\text{O}_{99}$ ($[\text{Mn}_{12}\text{O}_{12}(\text{L}^4)_{16}(\text{H}_2\text{O})_4] \cdot \text{H}_2\text{O}$): C, 70.25 (69.89); H, 10.68 (10.73). Selected FT-IR data (ATR, cm^{-1}): 2920 (s), 2852 (s), 1567 (s), 1409 (vs), 1227 (s), 1112 (m), 868 (w), 777 (w).

Preparation of 4'-((10-bromodecyl)oxy)biphenyl-4-carbonitrile (I_{CN}). To a solution of 4'-hydroxybiphenyl-4-carbonitrile (2.5 g, 12.81 mmol) with anhydrous potassium carbonate (3.54 g, 25.62 mmol) in butanone (125 mL) was added 1,10-dibromodecane (14.34 mL, 64.03 mmol). The mixture was

stirred under reflux overnight. After filtration, washing with CH_2Cl_2 and evaporation of the solvent, the crude product was purified by silica gel column chromatography (CH_2Cl_2 /pentane 1:9). The pale yellow solid was collected after solvent evaporation, then, filtrated and washed with pentane. The product was dried at 60°C overnight under vacuum to obtain compound 1_{CN} as white crystalline solid (3.87 g, 73%). ^1H NMR (400 MHz) in CDCl_3 (δ , ppm): 7.66 (dd, $J = 20.5, 8.1$ Hz, 4H), 7.52 (d, $J = 8.9$ Hz, 2H), 6.99 (d, $J = 8.3$ Hz, 2H), 4.00 (t, $J = 6.5$ Hz, 2H), 3.41 (t, $J = 6.6$ Hz, 2H), 1.89 – 1.77 (m, 4H), 1.52 – 1.40 (m, 4H), 1.30 (m, 8H). Elemental analysis – Calc. (Found) for $\text{C}_{23}\text{H}_{28}\text{BrNO}$: C, 66.67 (66.59); H, 6.81 (6.89); N, 3.38 (3.45).

Preparation of methyl 3,5-bis[(10-(4'-cyanobiphenyl-4-yloxy)decyl)oxy]benzoate (MeL^5). To a solution of methyl 3,5-dihydroxybenzoate (452 mg, 2.69 mmol) with anhydrous potassium carbonate (1.9 g, 13.45 mmol) in butanone (100 mL) was added 1_{CN} (2.45 g, 5.92 mmol) and KI in catalytic amounts. The mixture was stirred at reflux under argon atmosphere for 2 days. After addition of H_2O (150 mL), the product was extracted with CH_2Cl_2 (4x50 mL). The organic layer was washed with H_2O (3x50 mL), dried over anhydrous Na_2SO_4 , filtrated and evaporated. The crude product was purified by silica gel column chromatography (CH_2Cl_2 /pentane 2:8). The final product was dried at 60°C under vacuum over night to obtain compound MeL^5 as white solid (1.52 g, 66%). ^1H NMR (400 MHz) in CDCl_3 (δ , ppm): 7.64 (dd, $J = 20.9, 8.6$ Hz, 8H), 7.51 (d, $J = 8.8$ Hz, 4H), 7.15 (d, $J = 2.3$ Hz, 2H), 6.97 (d, $J = 8.8$ Hz, 4H), 6.62 (t, $J = 2.3$ Hz, 1H), 3.97 (dt, $J = 15.7, 6.5$ Hz, 8H), 3.88 (s, 3H), 1.84 – 1.71 (m, 8H), 1.51 – 1.28 (m, 24H). Elemental analysis – Calc. (Found) for $\text{C}_{54}\text{H}_{62}\text{N}_2\text{O}_6$: C, 77.67 (77.61); H, 7.48 (7.53); N, 3.35 (3.49).

Preparation of 3,5-bis[(10-(4'-cyanobiphenyl-4-yloxy)decyl)oxy]benzoic acid (HL^5). To a solution of MeL^5 (1.48 g, 1.77 mmol) in 100 mL of THF/EtOH 1:1 was added a solution of KOH (250 mg, 4.43 mmol) in water (5 mL). The mixture was stirred under reflux for 4 h, then H_2O (250 mL) was added and acidified to pH = 1 with a 37 % HCl aqueous solution and stirred for 1 h. Ethanol and THF were removed and the resulting mixture was washed with CH_2Cl_2 (3x100 mL). The organic layers were combined and dried over anhydrous sodium sulfate and concentrated. The crude product was purified by silica gel column chromatography (CH_2Cl_2 /MeOH 100:0 and 98.5:2.5 at the end of the column). The final product was dried under vacuum over night to afford compound HL^5 as white solid in (0.99 g, 68%). ^1H NMR (400 MHz) in CDCl_3 (δ , ppm): 7.64 (dd, $J = 20.9, 8.3$ Hz, 8H), 7.50 (d, $J = 8.7$ Hz, 4H), 7.18 (d, $J = 2.2$ Hz, 2H), 6.97 (d, $J = 8.7$ Hz, 4H), 6.64 (t, $J = 2.1$ Hz, 1H), 3.98 (t, $J = 6.6$ Hz, 4H), 3.95 (t, $J = 6.6$ Hz, 4H), 1.84 – 1.70 (m, 8H), 1.51 – 1.39 (m, 8H), 1.39 – 1.27 (m, 16H). Elemental analysis – Calc. (Found) for $\text{C}_{53}\text{H}_{60}\text{N}_2\text{O}_6$: C, 77.53 (77.49); H, 7.37 (7.42); N, 3.41 (3.51). Selected FT-IR data (ATR, cm^{-1}): 2922 (vs), 2852 (s), 2224 (s), 1687 (vs), 1601 (s), 1484 (s), 1301 (s), 1155 (s).

Preparation of 4-((10-bromodecyl)oxy)biphenyl (1_{H}). A mixture of 4-hydroxybiphenyl (2 g, 11.8 mmol), 1,10-dibromodecane (17.62 g, 58.7 mmol), and anhydrous potassium carbonate (3.24 g, 23.5 mmol) in 50 mL butanone was heated under reflux for 24 h. The mixture was filtered hot and washed with CH_2Cl_2 . After removal of the solvent, the mixture was purified by flash column chromatography on silica gel using pentane/dichloromethane (9:1) as eluent to yield 2.6 g (56%) of white crystals. ^1H NMR (400 MHz) in CDCl_3 (δ , ppm): 7.52 (dd, $J = 13.8, 8.0$ Hz, 4H), 7.40 (t, $J = 7.6$ Hz, 2H), 7.29 (t, $J = 7.3$ Hz, 1H), 6.96 (d, J

= 8.6 Hz, 2H), 3.98 (t, $J = 6.6$ Hz, 2H), 3.40 (t, $J = 6.9$ Hz, 2H), 1.90 – 1.75 (m, 4H), 1.51 – 1.38 (m, 4H), 1.39 – 1.24 (m, 8H). Elemental analysis – Calc. (Found) for $C_{22}H_{29}BrO$: C, 66.86 (66.79); H, 7.51 (7.58).

Preparation of methyl 3,5-bis((10-(biphenyl-4-yloxy)decyl)oxy)benzoate (MeL⁶). A mixture of methyl 3,5-dihydroxybenzoate (0.33 g, 1.96 mmol), 1_H (1.57 g, 4.03 mmol) and anhydrous potassium carbonate (1.42g, 10.3 mmol) in 50 mL butanone was heated under reflux for 4 days. After cooling the mixture to room temperature, 100 mL of water was added. The resulting mixture was extracted several times with CH_2Cl_2 . Combined organic fractions were dried over anhydrous Na_2SO_4 . The solvent was removed under reduced pressure. The obtained solid was purified by flash column chromatography on silica gel using pentane/dichloromethane (7:3) as eluent to yield 1.47 g (62%) of white crystals. 1H NMR (400 MHz) in $CDCl_3$ (δ , ppm): 7.57 – 7.47 (m, 8H), 7.39 (t, $J = 7.7$ Hz, 4H), 7.31 – 7.25 (m, 2H), 7.15 (d, $J = 2.3$ Hz, 2H), 6.95 (d, $J = 8.6$ Hz, 4H), 6.62 (t, $J = 2.3$ Hz, 1H), 4.02 – 3.93 (m, 8H), 3.88 (s, 3H), 1.87 – 1.72 (m, 8H), 1.51 – 1.39 (m, 8H), 1.33 (s, 16H). Elemental analysis – Calc. (Found) for $C_{52}H_{64}O_6$: C, 79.56 (79.49); H, 8.22 (8.31).

Preparation of 3,5-bis((10-(biphenyl-4-yloxy)decyl)oxy)benzoic acid (HL⁶). To a solution of MeL⁶ (1.43g, 1.82 mmol) in ethanol/THF (1:1) was added KOH (0.36 g, 6.1 mmoles) dissolved in a minimum amount of water. The mixture was stirred under reflux overnight. Then H_2O (250 mL) was added and acidified to pH = 1 with a 37 % HCl aqueous solution and stirred for 1 h. Ethanol and THF were removed and the resulting mixture was washed with CH_2Cl_2 (3x100 mL). The organic layers were combined and dried over anhydrous sodium sulfate and concentrated. The final product was dried under vacuum overnight to afford compound HL⁶ as white solid. The yield was 1 g (71%). 1H NMR (400 MHz) in $CDCl_3$ (δ , ppm): 1H NMR (400 MHz,) δ 7.59 – 7.46 (m, 8H), 7.40 (t, $J = 6.7$ Hz, 4H), 7.28 (t, $J = 6.4$ Hz, 2H), 6.96 (dd, $J = 8.7$, 2.1 Hz, 4H), 6.68 (d, $J = 2.1$ Hz, 1H), 4.03 – 3.93 (m, 8H), 1.86 – 1.71 (m, 8H), 1.46 (d, $J = 6.1$ Hz, 8H), 1.34 (s, 16H). Elemental analysis – Calc. (Found) for $C_{51}H_{62}O_6$: C, 79.44 (79.51); H, 8.10 (8.20). Selected FT-IR data (ATR, cm^{-1}): 2918 (vs), 2849 (s), 2224 (s), 1676 (vs), 1602 (vs), 1488 (s), 1271 (s), 1171 (s).

Preparation of $[Mn_{12}O_{12}(L^5)_{16}(H_2O)_4]$. To a suspension of $[Mn_{12}O_{12}(CH_3COO)_{16}(H_2O)_4]$ (55 mg, $2.67 \cdot 10^{-2}$ mmol) in 50 mL of CH_2Cl_2 /toluene 1:1, 0.615g of HL⁵ (0.75 mmol, 28 eq.) was added. The mixture was stirred at 55°C during 24 h. The color of solution changed from brown to brownish black. The solution was filtrated and the solvent was then evaporated. The final compound is poorly soluble in toluene, thus the dried reaction mixture was firstly dissolved in 20 mL of CH_2Cl_2 and then toluene (20 mL) was added, stirred for 3 hours, and then evaporated to dryness. This procedure was repeated at least three more times to remove acetic acid. The resulting residue was purified by two successive gel permeation chromatographic columns with Biorad S-X3 beads swelled with CH_2Cl_2 . The final product was dried in vacuum at 40°C overnight. The yield was 42% based on $[Mn_{12}O_{12}(CH_3COO)_{16}(H_2O)_4]$. Elemental analysis – Calc. (Found) for $C_{848}H_{976}Mn_{12}N_{32}O_{124}$ ($[Mn_{12}O_{12}(L^5)_{16}(H_2O)_4] \cdot 12H_2O$): C, 71.42 (71.39); H, 6.90 (6.93); N 3.14 (3.32). Selected FT-IR data (ATR, cm^{-1}): 2922 (m), 2852 (m), 2224 (m) 1601 (s), 1577 (s), 1410 (s), 1249 (vs), 1159 (vs), 820 (vs), 780 (m), 730 (s).

Preparation of $[Mn_{12}O_{12}(L^6)_{16}(H_2O)_4]$. To a suspension of $[Mn_{12}O_{12}(CH_3COO)_{16}(H_2O)_4]$ (55 mg, $2.67 \cdot 10^{-2}$ mmol) in 50 mL of CH_2Cl_2 /toluene 1:1, 0.619 g of HL⁶ (0.75 mmol, 28 eq.) was added. The

mixture was stirred at 55°C during 24 h. The color of solution changed from brown to brownish black. The solution was filtrated and the solvent was then evaporated. Toluene (20 mL) was then added, stirred for 3 hours, and then evaporated to dryness. This procedure was repeated at least three more times to remove acetic acid. The resulting residue was purified by two successive gel permeation chromatographic columns with Biorad S-X3 beads swelled with CH₂Cl₂. The final product was dried in vacuum at 40°C overnight. The yield was 45 % based on [Mn₁₂O₁₂(CH₃COO)₁₆(H₂O)₄]. Elemental analysis – Calc. (Found) for C₈₁₆H₁₀₀₂Mn₁₂O₁₂₁ ([Mn₁₂O₁₂(L⁶)₁₆(H₂O)₄]₉·9H₂O): C, 73.11 (73.08); H, 7.53 (7.61). Selected FT-IR data (ATR, cm⁻¹): 2924 (m), 2852 (m), 1607 (s), 1577 (s), 1412 (vs), 1248 (s), 1165 (m), 832 (m), 762 (vs).

II.7.2. Analytical characterizations

II.7.2.1. Crystallographic data for [Mn₁₂O₁₂(L¹)₁₆(H₂O)₃]

Table S.II-1. Crystal data and structure refinement for [Mn₁₂O₁₂(L¹)₁₆(H₂O)₃] at 100K.

Moiety formula	2(C ₁₂₈ H ₁₁₈ Mn ₁₂ O ₆₃), C ₄ H ₁₀ O, 2(H ₂ O)
Empirical formula	C ₂₆₀ H ₂₅₀ Mn ₂₄ O ₁₂₉
Formula weight	6757.16
Crystal system	Triclinic
Space group	P $\bar{1}$
Wavelength, Å	0.71073
a, Å	15.5955(14)
b, Å	17.3439(15)
c, Å	29.249(3)
α , °	74.666(4)
β , °	83.808(5)
γ , °	64.860(4)
V, Å ³	6907.0(10)
Z	1
ρ_{calcd} , g/cm ³	1.625
μ , 1/mm	1.156
Reflections collected	208696
Independent reflections	25469
R_1^a	0.0785
wR_2^a	0.2348
GoF ^a	1.006

$$^a I > 2\sigma(I), R_1 = \Sigma(|F_o| - |F_c|) / \Sigma|F_o|.$$

$$wR_2 = \{\Sigma[w(F_o^2 - F_c^2)^2] / \Sigma[w(F_o^2)^2]\}^{1/2}.$$

$$\text{GoF (goodness of fit on } F^2) = \{\Sigma[w(F_o^2 - F_c^2)^2] / (n-p)\}^{1/2},$$

where n is the number of reflections and p is the total number of refined parameters.

Table S.II-2. Selected distances in Å for $[\text{Mn}_{12}\text{O}_{12}(\text{L}^1)_{16}(\text{H}_2\text{O})_3] \cdot 1/2\text{C}_4\text{H}_{10}\text{O} \cdot \text{H}_2\text{O}$

Atom1	Atom2	Length / Å	Atom1	Atom2	Length / Å
Mn1	Mn2	2.834(2)	Mn6	O7	1.860(6)
Mn1	Mn3	2.917(3)	Mn6	O34	1.927(8)
Mn1	Mn4	2.818(2)	Mn6	O6	1.872(7)
Mn1	Mn11	2.784(3)	Mn6	O32	1.945(7)
Mn1	O43	1.898(5)	Mn6	O50	2.075(6)
Mn1	O1	1.937(8)	Mn7	O7	1.943(6)
Mn1	O2	1.927(6)	Mn7	O46	2.182(7)
Mn1	O11	1.879(8)	Mn7	O37	2.001(6)
Mn1	O4	1.891(5)	Mn7	O61	2.142(7)
Mn1	O12	1.867(6)	Mn7	O8	1.846(8)
Mn2	Mn9	2.795(2)	Mn7	O35	1.952(8)
Mn2	Mn3	2.852(2)	Mn8	O16	2.131(6)
Mn2	Mn4	2.906(2)	Mn8	O9	1.882(7)
Mn2	O3	1.908(7)	Mn8	O41	1.933(6)
Mn2	O9	1.848(6)	Mn8	O62	1.950(6)
Mn2	O52	1.908(5)	Mn8	O8	2.106(6)
Mn2	O2	1.894(5)	Mn8	O38	1.943(8)
Mn2	O4	1.939(5)	Mn9	O9	1.876(8)
Mn2	O10	1.854(8)	Mn9	O40	2.261(5)
Mn3	Mn4	2.830(2)	Mn9	O53	2.232(5)
Mn3	Mn7	2.757(3)	Mn9	O10	1.909(6)
Mn3	O7	1.875(8)	Mn9	O19	1.948(8)
Mn3	O47	1.902(6)	Mn9	O17	1.934(6)
Mn3	O1	1.929(6)	Mn10	O22	1.953(9)
Mn3	O3	1.933(5)	Mn10	O14W	2.175(5)
Mn3	O2	1.924(8)	Mn10	O13W	2.197(5)
Mn3	O8	1.836(6)	Mn10	O20	1.932(6)
Mn4	O1	1.889(5)	Mn10	O11	1.877(6)
Mn4	O6	1.873(8)	Mn10	O10	1.889(8)
Mn4	O5	1.878(6)	Mn11	O44	2.237(5)
Mn4	O3	1.910(5)	Mn11	O56	2.165(5)
Mn4	O4	1.895(7)	Mn11	O25	1.950(7)
Mn4	O59	1.917(5)	Mn11	O11	1.904(6)
Mn5	Mn4	2.772(2)	Mn11	O12	1.884(8)
Mn5	O58	2.171(6)	Mn11	O23	1.960(8)
Mn5	O6	1.893(6)	Mn12	O28	1.959(6)
Mn5	O5	1.898(8)	Mn12	O15W	2.228(8)
Mn5	O29	1.941(6)	Mn12	O55	2.141(6)
Mn5	O31	1.957(9)	Mn12	O5	1.884(8)
Mn5	O49	2.190(5)	Mn12	O26	1.972(9)
			Mn12	O12	1.888(6)

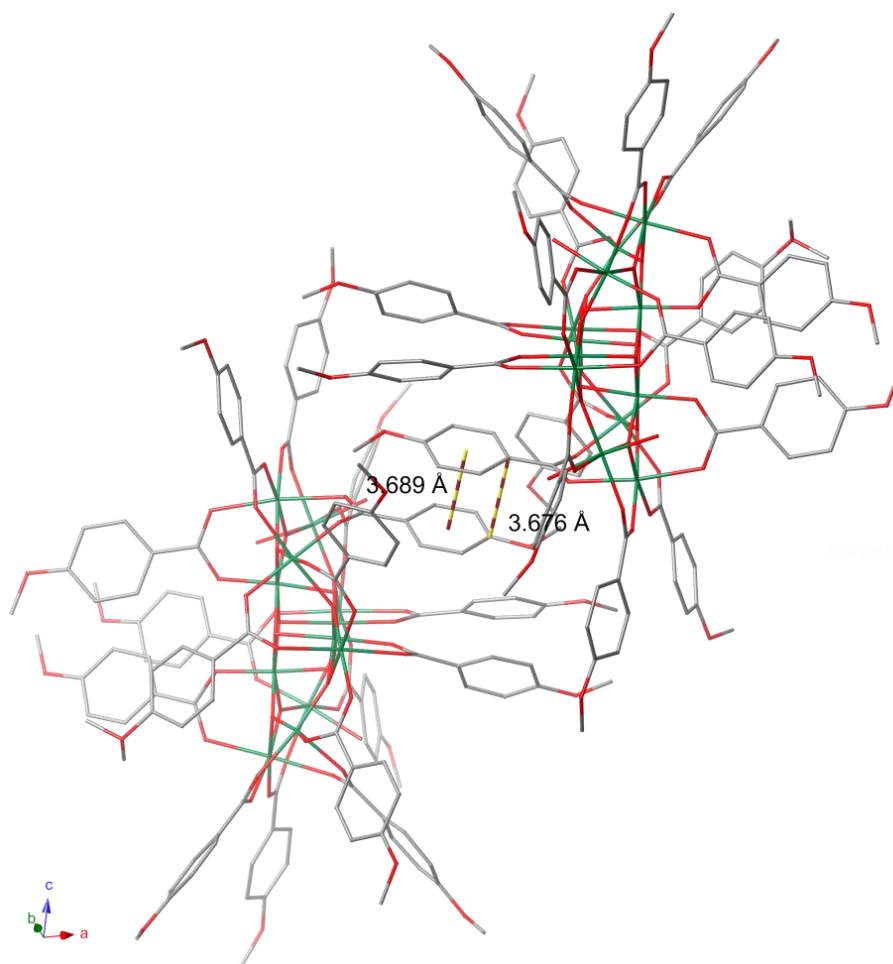


Figure S.II-1. Packing arrangement illustrating π - π interactions present between adjacent $[\text{Mn}_{12}\text{O}_{12}(\text{L}^1)_{16}(\text{H}_2\text{O})_3]$ complexes

II.7.2.2. FT-IR spectroscopic analyses

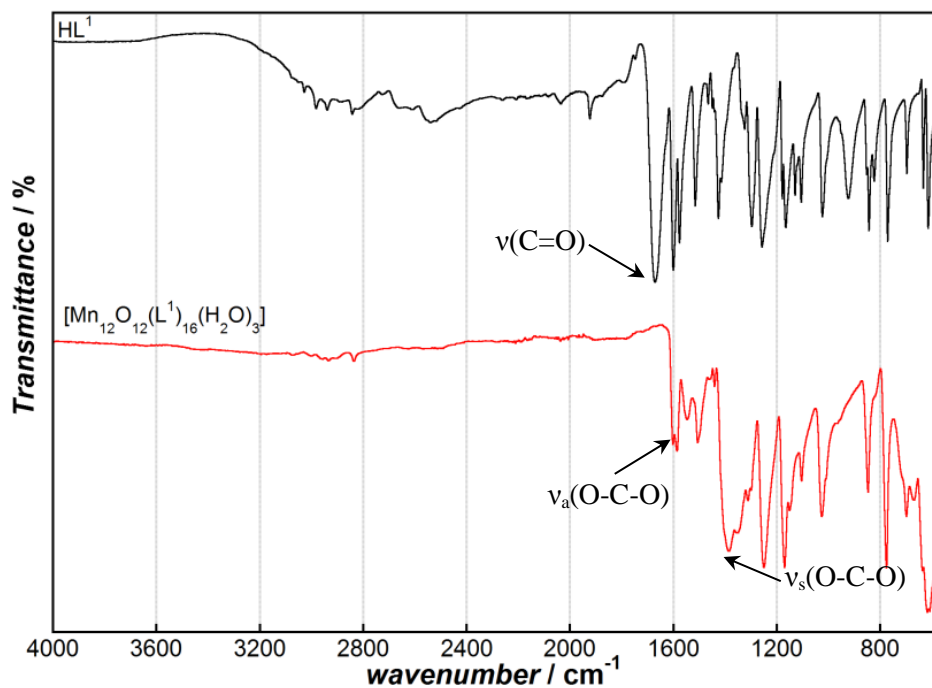


Figure S.II-2. FT-IR spectra of HL^1 (black) and $[\text{Mn}_{12}\text{O}_{12}(\text{L}^1)_{16}(\text{H}_2\text{O})_3]$ (red).

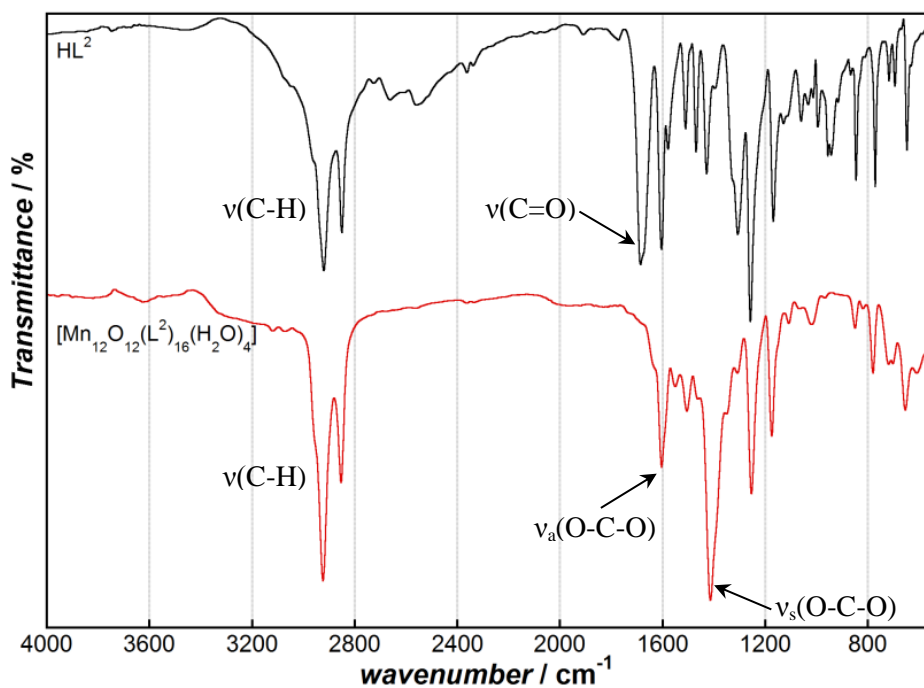


Figure S.II-3. FT-IR spectra of HL^2 (black) and $[Mn_{12}O_{12}(L^2)_{16}(H_2O)_3]$ (red).

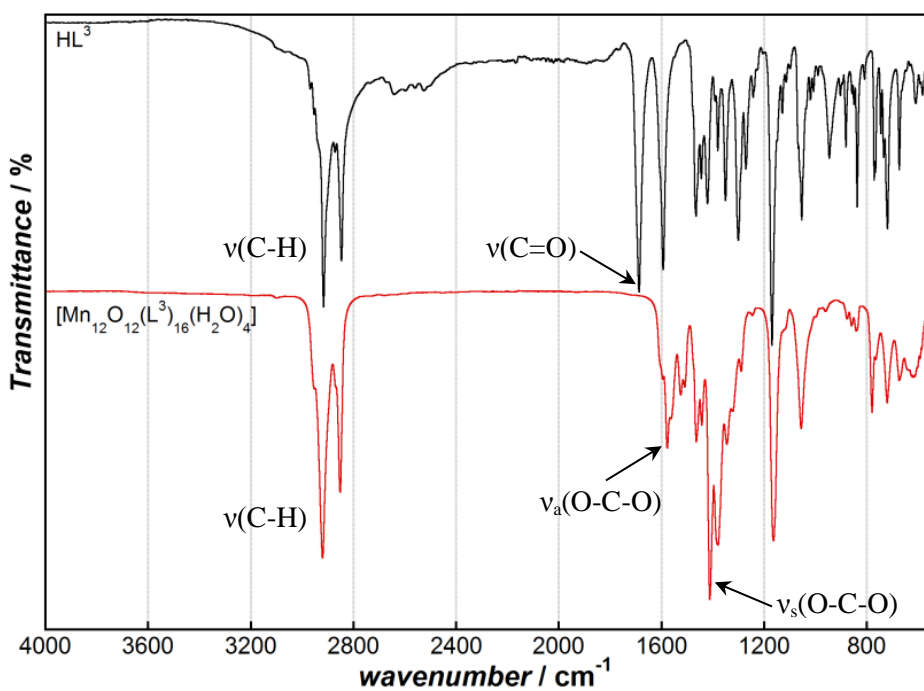


Figure S.II-4. FT-IR spectra of HL^3 (black) and $[Mn_{12}O_{12}(L^3)_{16}(H_2O)_3]$ (red).

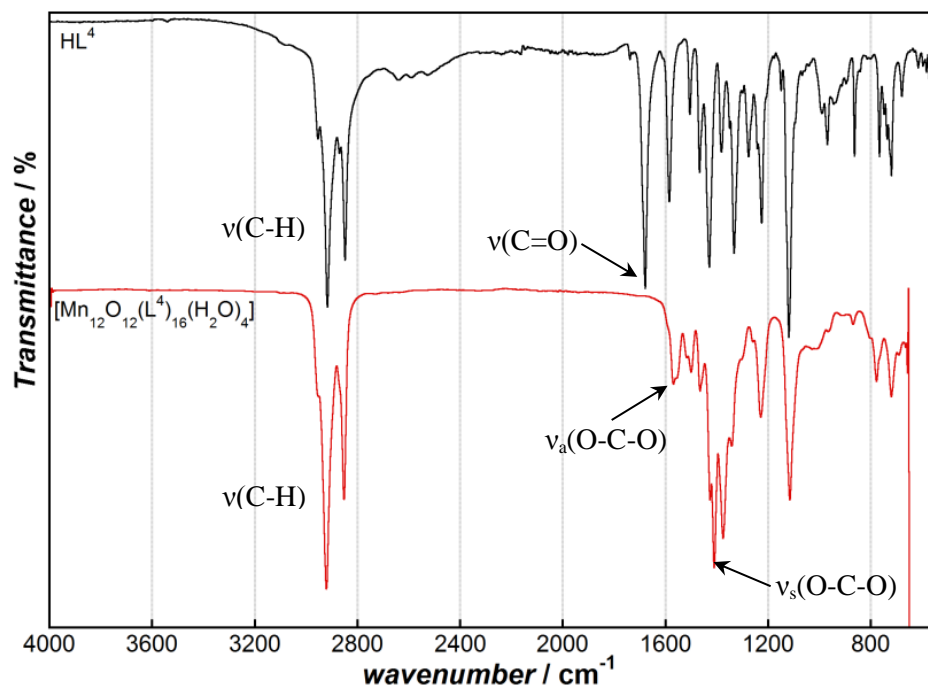


Figure S.II-5. FT-IR spectra of HL^4 (black) and $[Mn_{12}O_{12}(L^4)_{16}(H_2O)_3]$ (red).

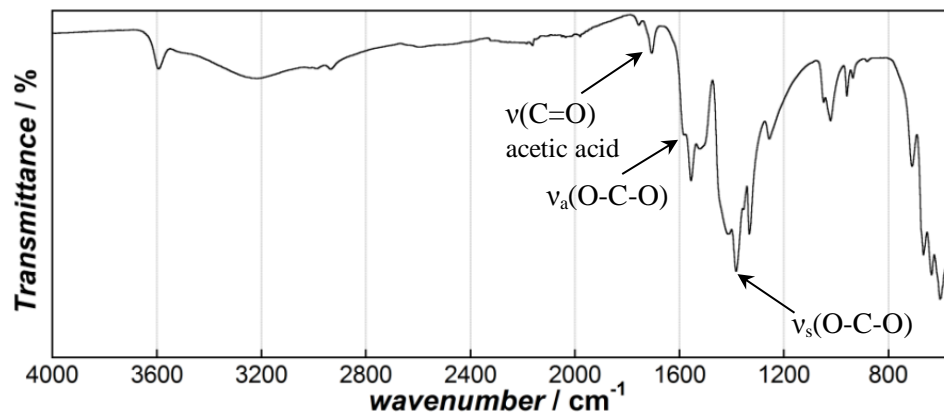


Figure S.II-6. FT-IR spectrum of $[Mn_{12}O_{12}(CH_3COO)_{16}(H_2O)_4]$.

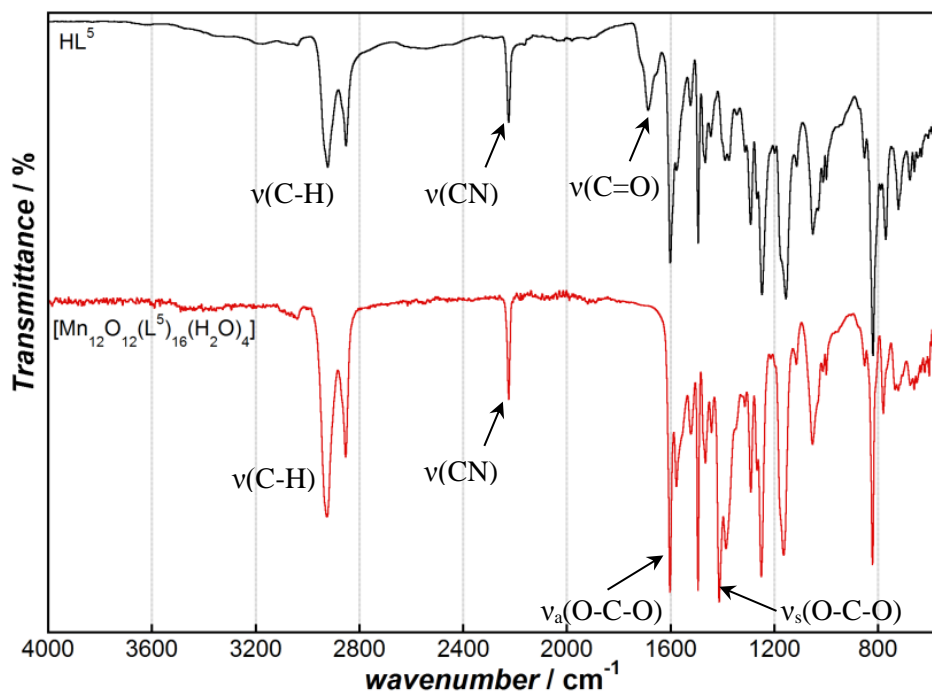


Figure S.II-7. FT-IR spectra of HL^5 (black) and $[Mn_{12}O_{12}(L^5)_{16}(H_2O)_3]$ (red).

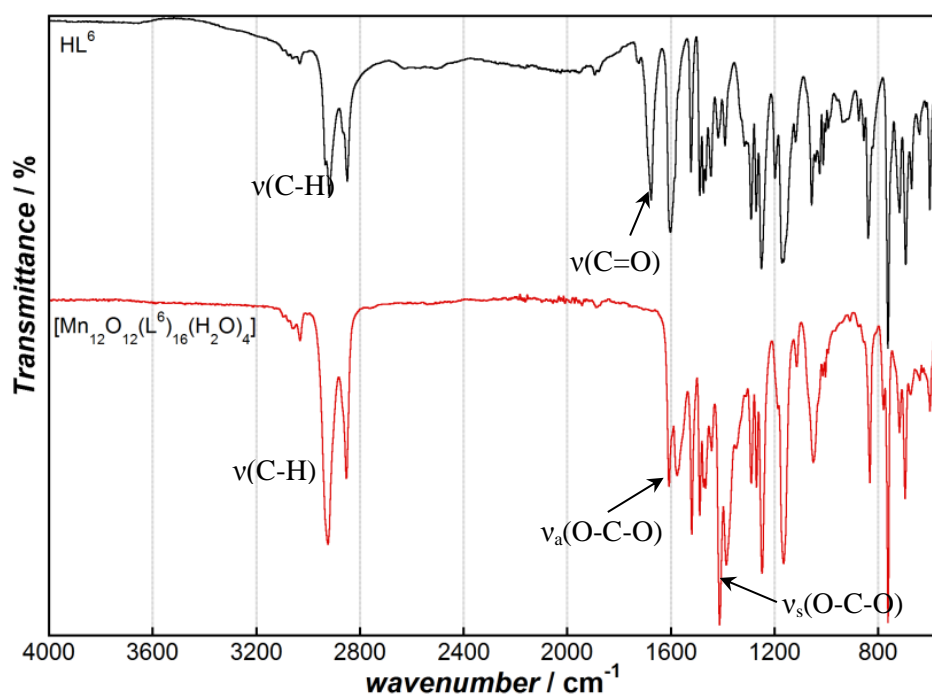


Figure S.II-8. FT-IR spectra of HL^6 (black) and $[Mn_{12}O_{12}(L^6)_{16}(H_2O)_3]$ (red).

II.7.2.3. Thermo-gravimetric analyses

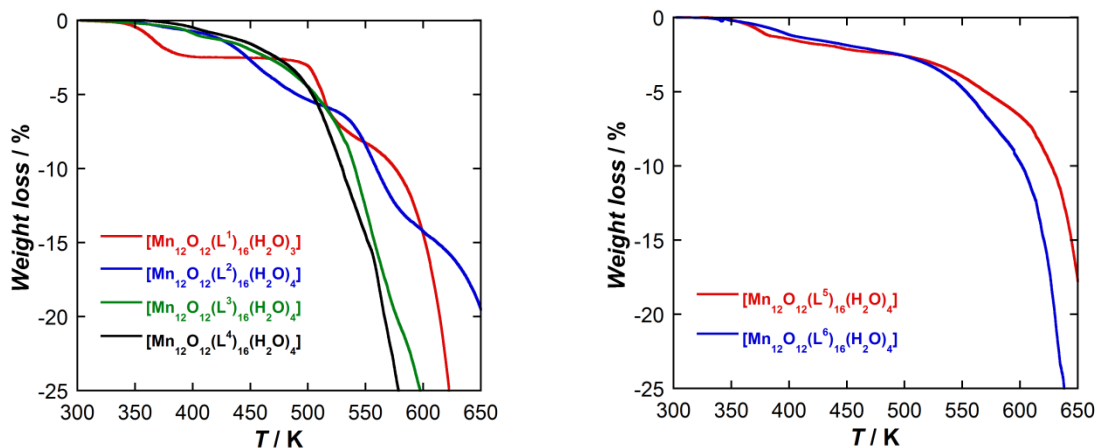


Figure S.II-9. TGA curves obtained for $[\text{Mn}_{12}\text{O}_{12}(\text{L}^{1-4})_{16}(\text{H}_2\text{O})_{3-4}]$ complexes (left) and for $[\text{Mn}_{12}\text{O}_{12}(\text{L}^{5-6})_{16}(\text{H}_2\text{O})_4]$ complexes (right).

II.7.3. Magnetic measurements

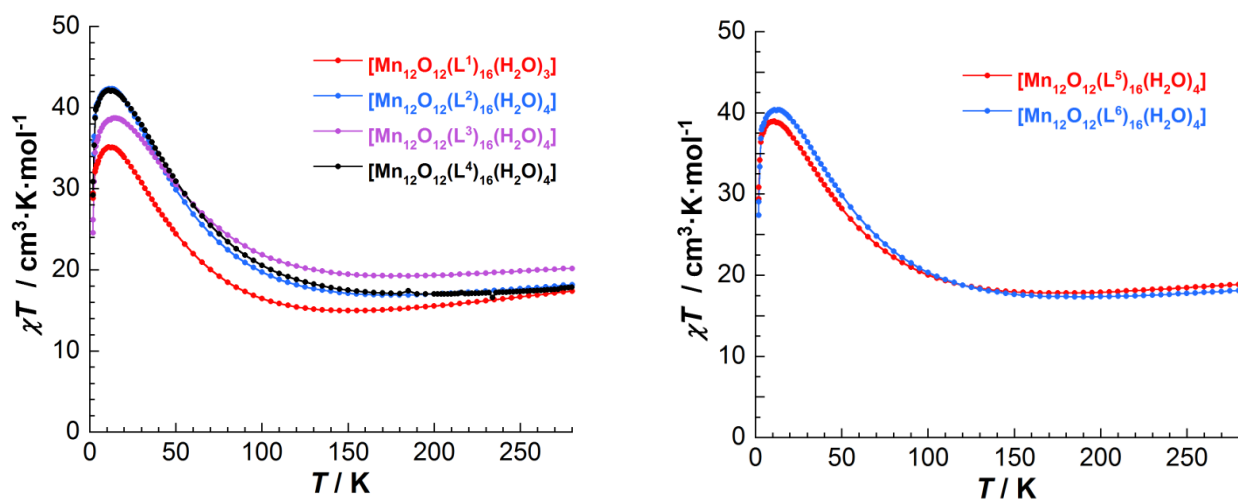


Figure S.II-10. χT versus T plots at 0.1 T (with χ being the molar magnetic susceptibility defined as M/H per complex) for $[\text{Mn}_{12}\text{O}_{12}(\text{L}^{1-4})_{16}(\text{H}_2\text{O})_{3-4}]$ complexes (left) and for $[\text{Mn}_{12}\text{O}_{12}(\text{L}^{5-6})_{16}(\text{H}_2\text{O})_4]$ (right). The solid lines are guides for the eyes.

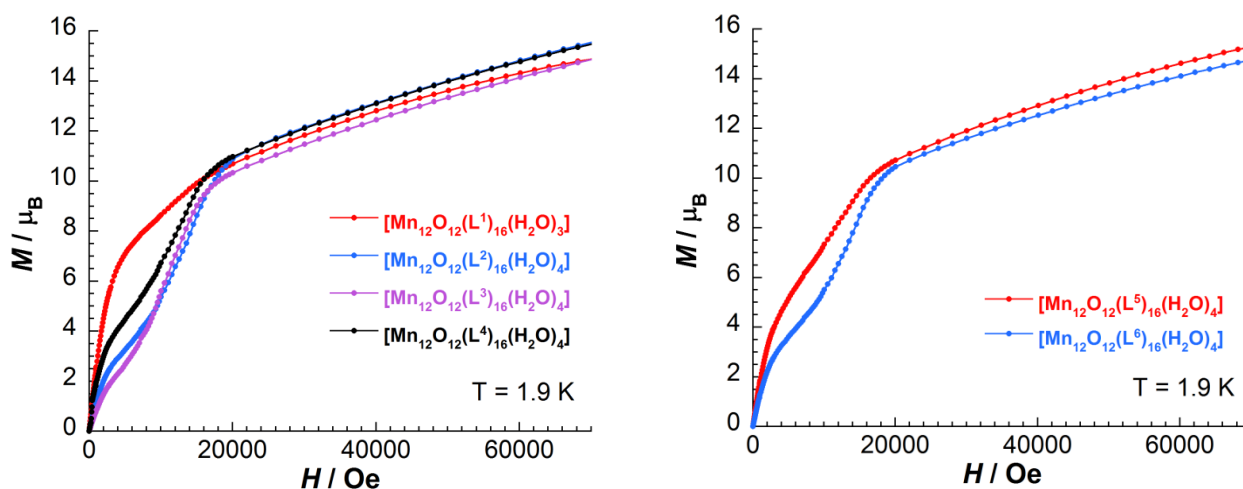


Figure S.II-11. M vs. H plot at 1.9 K for $[\text{Mn}_{12}\text{O}_{12}(\text{L}^{1-4})_{16}(\text{H}_2\text{O})_{3-4}]$ complexes (left) and for $[\text{Mn}_{12}\text{O}_{12}(\text{L}^{5-6})_{16}(\text{H}_2\text{O})_4]$ (right). The solid lines are guides for the eyes.

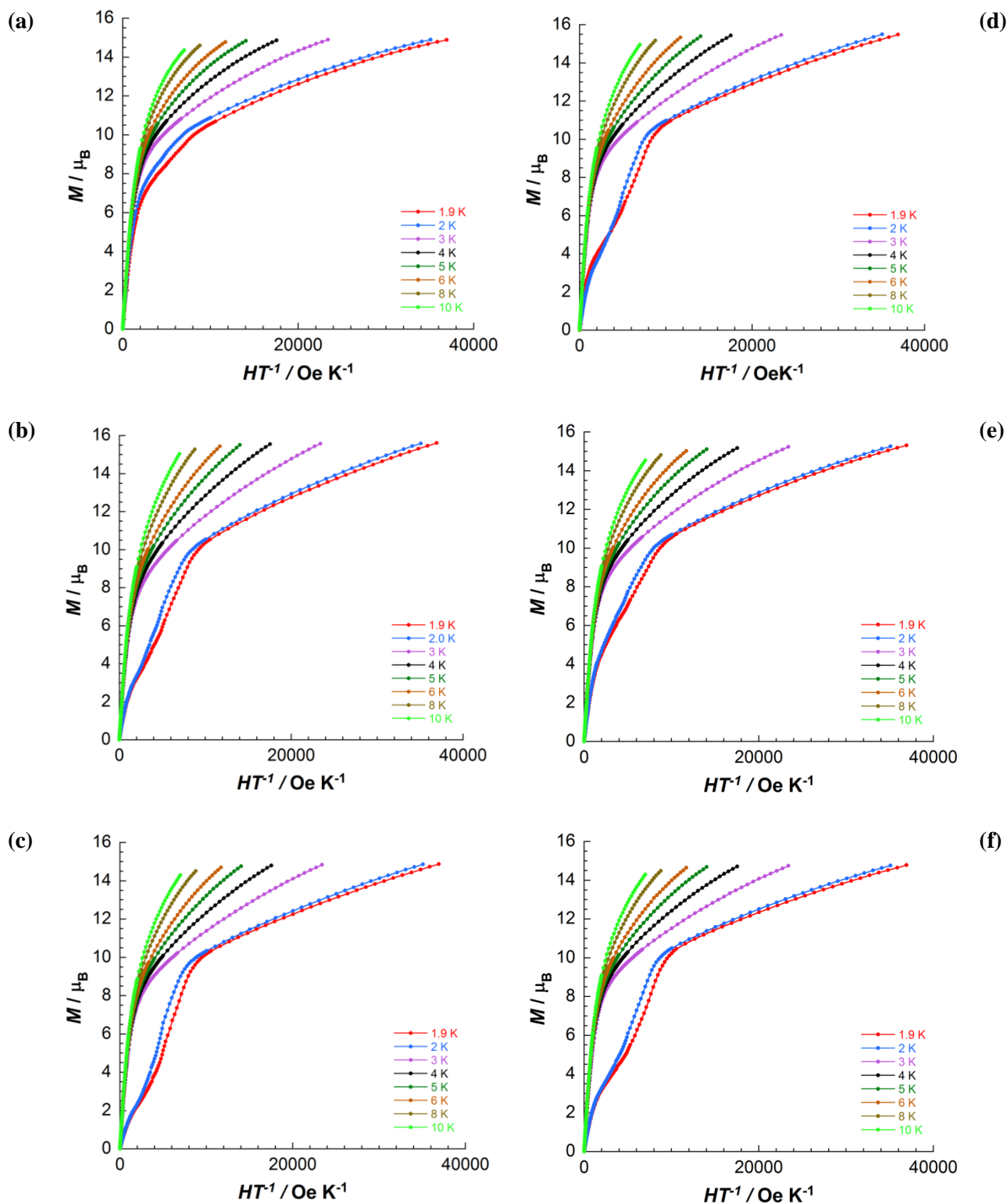


Figure S.II-12. M vs. H/T plots at different temperatures: (a) $[\text{Mn}_{12}\text{O}_{12}(\text{L}^1)_{16}(\text{H}_2\text{O})_3]$; (b) $[\text{Mn}_{12}\text{O}_{12}(\text{L}^2)_{16}(\text{H}_2\text{O})_4]$; (c) $[\text{Mn}_{12}\text{O}_{12}(\text{L}^3)_{16}(\text{H}_2\text{O})_4]$; (d) $[\text{Mn}_{12}\text{O}_{12}(\text{L}^4)_{16}(\text{H}_2\text{O})_4]$; (e) $[\text{Mn}_{12}\text{O}_{12}(\text{L}^5)_{16}(\text{H}_2\text{O})_4]$; (f) $[\text{Mn}_{12}\text{O}_{12}(\text{L}^6)_{16}(\text{H}_2\text{O})_4]$.

II.7.4. Thermotropic properties

II.7.4.1. DSC traces

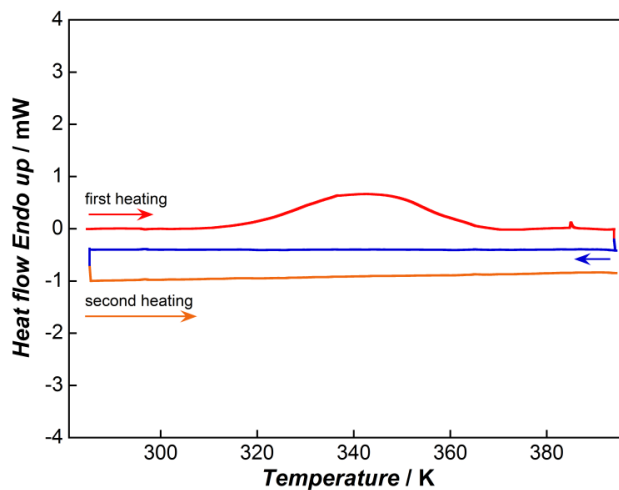


Figure S.II-13. DSC traces of $[\text{Mn}_{12}\text{O}_{12}(\text{L}^2)_{16}(\text{H}_2\text{O})_4]$ complex between 280 and 400 (5 K/min).

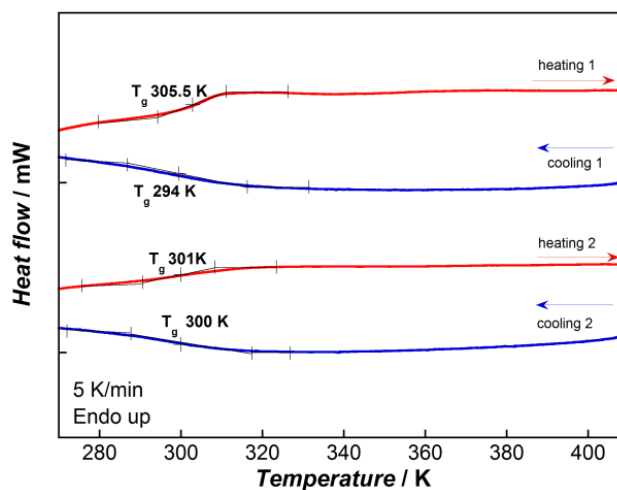


Figure S.II-14. DSC traces of $[\text{Mn}_{12}\text{O}_{12}(\text{L}^5)_{16}(\text{H}_2\text{O})_4]$ on first two heating-cooling cycles between 270 and 410 K at 5 K/min.

II.7.4.2. Small angle X-ray scattering (SAXS) investigations

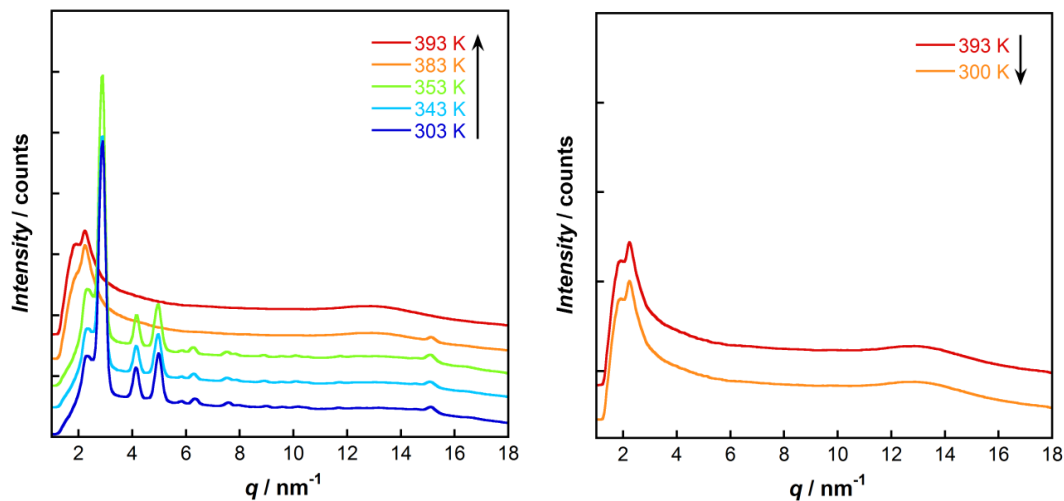


Figure S.II-15. Small and wide angle X-ray diffraction profile of the $[\text{Mn}_{12}\text{O}_{12}(\text{L}^2)_{16}(\text{H}_2\text{O})_4]$ at different temperatures: (left) on heating from 303 K to 393 K; (right) on cooling from 393 K to 300 K.

Table S.II-3. Indexation of observed reflections at 303 K for $[\text{Mn}_{12}\text{O}_{12}(\text{L}^2)_{16}(\text{H}_2\text{O})_4]$.

T / K	Peak number	$q_{(\text{obs})} / \text{nm}^{-1}$	$d_{(\text{obs})} / \text{Å}$	hkl	$h^2+k^2+l^2$	$d_{(\text{calc})} / \text{Å}$	Calculated cell parameters
303 heating	1	2.34	26.84	110	2	26.72	a = 37.79 Å V = 53967.30 Å ³ Z ≈ 6
	2	2.89	21.73	111	3	21.82	
	3	4.10	15.32	211	6	15.43	
	4	4.97	12.64	221/300	9	12.60	
	5	5.75	10.92	222	12	10.91	
	6	6.21	10.11	321	14	10.10	
	7	7.41	8.48	420	20	8.45	
	8	8.91	7.05	432/520	29	7.02	
	9	9.50	6.61	441/522	33	6.58	
	10	10.19	6.16	532/611	38	6.13	
	11	11.60	5.41	632/700	49	5.40	
	12	14.43	4.35	662	76	4.33	
	13	15.08	4.16	753	83	4.15	

$q_{(\text{obs})}$ is the observed/measured reciprocal spacing, $q = 4\pi \sin\theta/\lambda$, where λ is the wavelength, 2θ is the diffraction angle, $d_{(\text{obs})}$ and $d_{(\text{calc})}$ are observed and calculated diffraction spacings: $d_{(\text{obs})} = 2\pi/q_{(\text{obs})}$, $d_{(\text{calc})} = a/\sqrt{h^2 + k^2 + l^2}$, a is the lattice parameter of the cubic phase, V is the volume of the cubic cell unit ($V = a^3$), Z is the number of complexes per cubic cell, $Z = (\rho \cdot V \cdot N_A)/Mw$, where ρ is the density $\approx 1 \text{ g/cm}^3$, N_A is the Avogadro constant $6.0225 \cdot 10^{23}$ (note: $1 \text{ Å}^3 = 1.0 \cdot 10^{-24} \text{ cm}^3$).

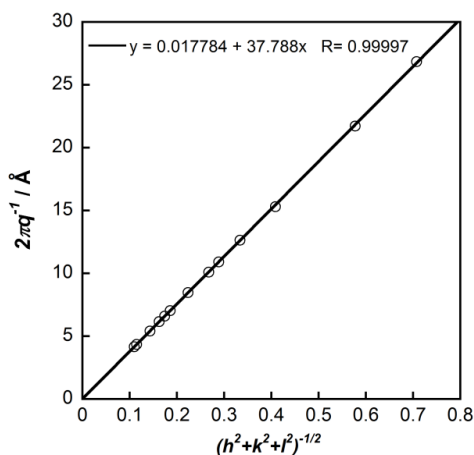


Figure S.II-16. The lattice spacing of the cubic phase, $a = d_{100}$, of the $[\text{Mn}_{12}\text{O}_{12}(\text{L}^2)_{16}(\text{H}_2\text{O})_4]$ complex can be calculated from the reciprocal gradient of the plot $2\pi/q$ vs $1/\sqrt{h^2 + k^2 + l^2}$. Solid black line is the linear fit. The lattice parameter $a = 37.8 \text{ Å}$ corresponds to the slope of the linear fit.

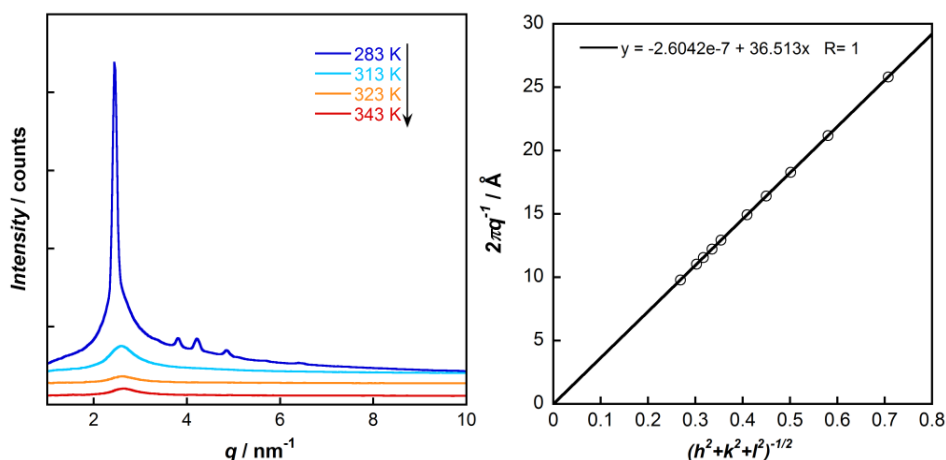


Figure S.II-17. (left) Small angle X-ray diffraction profile of $[\text{Mn}_{12}\text{O}_{12}(\text{L}^2)_{16}(\text{H}_2\text{O})_4]$ on heating from 283 K to 343 K, emphasizing the transition to the isotropic phase; (right) $2\pi/q$ vs $1/\sqrt{h^2 + k^2 + l^2}$ plot. Solid black line is the linear fit. The lattice parameter $a = 36.5 \text{ Å}$ corresponds to the slope of the linear fit.

Table S II-4. Indexation of the reflections at 283 K for $[\text{Mn}_{12}\text{O}_{12}(\text{L}^3)_{16}(\text{H}_2\text{O})_4]$.

T / K	Peak number	$q_{(\text{obs})} / \text{nm}^{-1}$	$d_{(\text{obs})} / \text{Å}$	hkl	$h^2+k^2+l^2$	$d_{(\text{calc})} / \text{Å}$	Calculated cell parameters
283 heating	1	2.43	25.82	110	2	25.85	a = 36.51 Å V = 49000.64 Å ³ Z ≈ 3 - 4
	2	2.97	21.19	111	3	21.11	
	3	3.43	18.30	200	4	18.28	
	4	3.83	16.42	210	5	16.35	
	5	4.21	14.94	211	6	14.93	
	6	4.86	12.94	220	8	12.93	
	7	5.14	12.23	221/300	9	12.19	
	8	5.43	11.56	310	10	11.56	
	9	5.69	11.05	311	11	11.02	
	10	6.42	9.79	321	14	9.77	

$q_{(\text{obs})}$ is the observed/measured reciprocal spacing, $q = 4\pi \sin\theta/\lambda$, where λ is the wavelength, 2θ is the diffraction angle, $d_{(\text{obs})}$ and $d_{(\text{calc})}$ are observed and calculated diffraction spacings: $d_{(\text{obs})} = 2\pi/q_{(\text{obs})}$, $d_{(\text{calc})} = a/\sqrt{h^2 + k^2 + l^2}$, a is the lattice parameter of the cubic phase, V is the volume of the cubic cell unit ($V = a^3$), Z is the number of complexes per cubic cell, $Z = (\rho \cdot V \cdot N_A)/Mw$, where ρ is the density $\approx 1 \text{ g/cm}^3$, N_A is the Avogadro constant $6.0225 \cdot 10^{23}$ (note: $1 \text{ Å}^3 = 1.0 \cdot 10^{-24} \text{ cm}^3$).

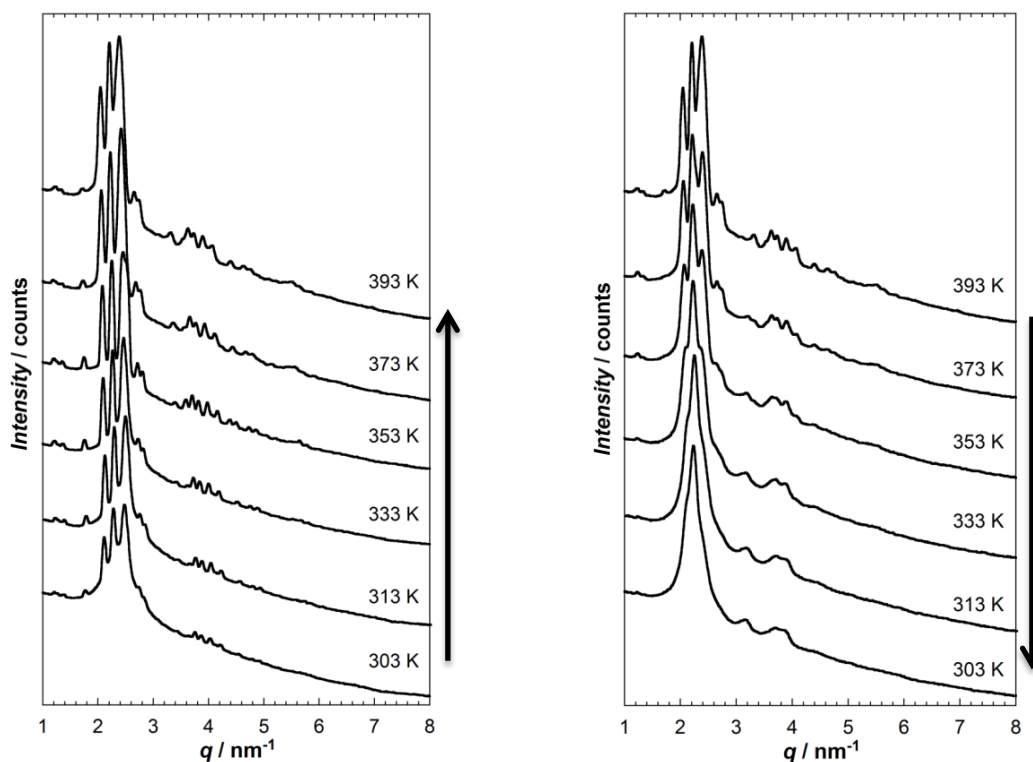


Figure S.II-18. Small angle X-ray diffraction profiles of $[\text{Mn}_{12}\text{O}_{12}(\text{L}^4)_{16}(\text{H}_2\text{O})_4]$ (left) on 3rd heating from 303 K to 393 K and (right) on 3rd cooling from 393 K to 303 K.

Table S.II-5. Indexation of the reflections on 3rd heating for [Mn₁₂O₁₂(L⁴)₁₆(H₂O)₄], part 1.

T / K	Peak number	$q_{(obs)} / \text{nm}^{-1}$	$d_{(obs)} / \text{Å}$	hkl	$d_{(calc)} / \text{Å}$	Calculated cell parameters
303 K heating	1	1.23	51.01	002	50.94	a = 110.80 Å b = 119.74 Å c = 101.87 Å V = 1.3515 · 10 ⁶ Å ³ Z ≈ 69
	2	1.38	45.39	211	45.09	
	3	1.77	35.50	212	35.78	
	4	2.11	29.76	040	29.94	
	5	2.28	27.53	400	27.70	
	6	2.49	25.27	004	25.47	
	7	2.75	22.85	422	22.54	
	8	2.86	21.99	224	21.58	
	9	3.09	20.31	234	20.02	
	10	3.42	18.36	244	18.31	
	11	3.64	17.25	424	17.89	
	12	3.76	16.72	434	16.97	
	13	3.88	16.21	444	15.89	
	14	4.03	15.58	226	15.67	
	15	4.22	14.90	080	14.97	
	16	4.54	13.83	800	13.85	
	17	4.80	13.10	822	13.04	
	18	4.93	12.76	008	12.73	
333 K heating	1	1.21	51.78	002	51.56	a = 111.54 Å b = 120.70 Å c = 103.11 Å V = 1.388 · 10 ⁶ Å ³ Z ≈ 71
	2	1.37	45.77	211	45.44	
	3	1.76	35.64	212	36.12	
	4	2.09	30.06	040	30.18	
	5	2.27	27.72	400	27.89	
	6	2.46	25.50	004	25.78	
	7	2.73	22.98	422	22.72	
	8	2.83	22.16	224	21.82	
	9	3.07	20.48	234	20.23	
	10	3.20	19.64	343	19.36	
	11	3.42	18.35	244	18.49	
	12	3.59	17.51	424	18.06	
	13	3.72	16.89	434	17.13	
	14	3.85	16.32	444	16.03	
	15	4.01	15.68	226	15.85	
	16	4.19	15.00	080	15.09	
	17	4.53	13.87	800	13.94	
	18	4.75	13.22	822	13.14	
	19	4.90	12.83	008	12.89	
	20	5.06	12.43	448	12.29	

$q_{(obs)}$ is the observed/measured reciprocal spacing, $q = 4\pi \cdot \sin \theta / \lambda$, where λ is the wavelength, 2θ is the diffraction angle, $d_{(obs)}$ and $d_{(calc)}$ are observed and calculated diffraction spacings: $d_{(obs)} = 2\pi/q_{(obs)}$, $d_{(calc)} = 1/\sqrt{h^2/a^2 + k^2/b^2 + l^2/c^2}$, a , b and c are the lattice parameters of an orthorhombic cell, V is the volume of the orthorhombic cell unit ($V = a \cdot b \cdot c$), Z is the number of complexes per orthorhombic cell, $Z = (\rho \cdot V \cdot N_A) / Mw$, where ρ is the density $\approx 1 \text{ g/cm}^3$, N_A is the Avogadro constant $6.0225 \cdot 10^{23}$ (note: $1 \text{ Å}^3 = 1.0 \cdot 10^{-24} \text{ cm}^3$).

Table S.II-6. Indexation of the reflections on 3rd heating for $[\text{Mn}_{12}\text{O}_{12}(\text{L}^4)_{16}(\text{H}_2\text{O})_4]$, part 2.

T / K	Peak number	$q_{(\text{obs})} / \text{nm}^{-1}$	$d_{(\text{obs})} / \text{Å}$	hkl	$d_{(\text{calc})} / \text{Å}$	Calculated cell parameters
363 K heating	1	1.22	51.45	002	51.48	$a = 113.12 \text{ Å}$ $b = 121.65 \text{ Å}$ $c = 102.95 \text{ Å}$ $V = 1.417 \cdot 10^6 \text{ Å}^3$ $Z \approx 72$
	2	1.37	45.86	211	45.91	
	3	1.73	36.33	212	36.33	
	4	2.07	30.35	040	30.41	
	5	2.24	28.03	400	28.28	
	6	2.44	25.76	004	25.74	
	7	2.70	23.23	422	22.95	
	8	2.80	22.46	224	21.86	
	9	3.03	20.73	234	20.28	
	10	3.39	18.55	244	18.56	
	11	3.54	17.76	424	18.17	
	12	3.69	17.02	434	17.23	
	13	3.81	16.51	444	16.13	
	14	3.96	15.86	226	15.85	
	15	4.14	15.16	080	15.21	
	16	4.30	14.62	426	14.26	
	17	4.48	14.03	800	14.14	
	18	4.70	13.36	822	13.30	
	19	4.84	12.97	008	12.87	
	20	5.60	11.21	428	11.50	
393 K heating	1	1.20	52.21	002	52.25	$a = 116.46 \text{ Å}$ $b = 123.01 \text{ Å}$ $c = 104.51 \text{ Å}$ $V = 1.497 \cdot 10^6 \text{ Å}^3$ $Z \approx 76 - 77$
	2	1.34	46.94	211	47.01	
	3	1.70	36.97	212	37.08	
	4	2.03	30.95	040	30.75	
	5	2.20	28.50	400	29.11	
	6	2.40	26.16	004	26.13	
	7	2.68	23.48	422	23.50	
	8	2.76	22.80	224	22.23	
	9	3.10	20.26	234	20.60	
	10	3.31	18.98	244	18.84	
	11	3.50	17.95	424	18.54	
	12	3.63	17.32	434	17.56	
	13	3.77	16.66	444	16.44	
	14	3.89	16.15	425	16.36	
	15	4.07	15.44	080	15.38	
	16	4.25	14.79	800	14.56	
	17	4.40	14.28	426	14.52	
	18	4.61	13.62	822	13.67	
	19	4.76	13.19	008	13.06	
	20	5.06	12.43	228	12.48	

$q_{(\text{obs})}$ is the observed/measured reciprocal spacing, $q = 4\pi \sin\theta/\lambda$, where λ is the wavelength, 2θ is the diffraction angle, $d_{(\text{obs})}$ and $d_{(\text{calc})}$ are observed and calculated diffraction spacings: $d_{(\text{obs})} = 2\pi/q_{(\text{obs})}$, $d_{(\text{calc})} = 1/\sqrt{h^2/a^2 + k^2/b^2 + l^2/c^2}$, a , b and c are the lattice parameters of an orthorhombic cell, V is the volume of the orthorhombic cell unit ($V = a \cdot b \cdot c$), Z is the number of complexes per orthorhombic cell, $Z = (\rho \cdot V \cdot N_A)/Mw$, where ρ is the density $\approx 1 \text{ g/cm}^3$, N_A is the Avogadro constant $6.0225 \cdot 10^{23}$ (note: $1 \text{ Å}^3 = 1.0 \cdot 10^{-24} \text{ cm}^3$).

Table S.II-7. Indexation of the reflections on 3rd cooling for [Mn₁₂O₁₂(L⁴)₁₆(H₂O)₄].

T / K	Peak number	$q_{(obs)}/\text{nm}^{-1}$	$d_{(obs)}/\text{Å}$	hkl	$d_{(calc)}/\text{Å}$	Calculated cell parameters
373 K cooling	1	1.21	51.78	002	51.99	a = 115.57 Å b = 121.98 Å c = 103.97 Å V = 1.466 · 10 ⁶ Å ³ Z ≈ 75
	2	1.35	46.64	211	46.67	
	3	1.72	36.48	212	36.84	
	4	2.05	30.64	040	30.50	
	5	2.21	28.41	400	28.89	
	6	2.41	26.09	004	25.99	
	7	2.66	23.65	422	23.33	
	8	2.78	22.60	224	22.09	
	9	3.14	20.03	234	20.48	
	10	3.34	18.84	244	18.72	
	11	3.62	17.37	434	17.45	
	12	3.78	16.62	444	16.32	
	13	3.91	16.09	425	16.27	
	14	4.09	15.36	080	15.25	
	15	4.40	14.27	426	14.45	
	16	4.62	13.59	822	13.57	
	17	4.77	13.18	008	13.00	
353 K cooling	1	1.20	52.24	002	52.67	a = 115.14 Å b = 123.8 Å c = 105.34 Å V = 1.502 · 10 ⁶ Å ³ Z ≈ 77
	2	1.34	46.89	211	46.77	
	3	2.04	30.75	040	30.95	
	4	2.22	28.27	400	28.79	
	5	2.40	26.19	004	26.34	
	6	2.65	23.69	422	23.39	
	7	2.78	22.57	224	22.33	
	8	3.20	19.66	334	19.22	
	9	3.61	17.39	434	17.58	
	10	3.74	16.80	444	16.46	
	11	3.90	16.13	425	16.39	
	12	4.10	15.33	080	15.48	
	13	4.40	14.27	426	14.39	
	14	4.61	13.63	822	13.55	
	15	4.77	13.18	008	13.17	
333 K cooling	1	1.20	52.24	002	52.79	a = 114.28 Å b = 123.08 Å c = 105.57 Å V = 1.485 · 10 ⁶ Å ³ Z ≈ 76
	2	2.04	30.75	040	30.77	
	3	2.22	28.27	400	28.57	
	4	2.40	26.19	004	26.39	
	5	2.65	23.69	422	23.26	
	6	2.78	22.57	224	22.33	
	7	3.20	19.66	334	19.18	
	8	3.61	17.39	434	17.53	
	9	3.90	16.13	425	16.37	
	10	4.10	15.33	080	15.39	
	11	4.40	14.27	426	14.29	
303 K cooling	1	1.20	52.21	002	52.37	a = 113.48 Å b = 123.12 Å c = 104.73 Å V = 1.463 · 10 ⁶ Å ³ Z ≈ 75
	2	2.07	30.29	040	30.78	
	3	2.23	28.13	400	28.37	
	4	2.42	25.93	004	26.18	
	5	2.65	23.69	422	23.12	
	6	3.16	19.88	334	19.06	
	7	3.68	17.07	434	17.42	
	8	3.89	16.16	425	16.25	
	9	4.44	14.14	426	14.19	

$q_{(obs)}$ is the observed/measured reciprocal spacing, $q = 4\pi \cdot \sin\theta/\lambda$, where λ is the wavelength, 2θ is the diffraction angle, $d_{(obs)}$ and $d_{(calc)}$ are observed and calculated diffraction spacings: $d_{(obs)} = 2\pi/q_{(obs)}$, $d_{(calc)} = 1/\sqrt{h^2/a^2 + k^2/b^2 + l^2/c^2}$, a , b and c are the lattice parameters of an orthorhombic cell, V is the volume of the orthorhombic cell unit ($V = a \cdot b \cdot c$), Z is the number of complexes per orthorhombic cell, $Z = (\rho \cdot V \cdot N_A)/Mw$, where ρ is the density $\approx 1 \text{ g/cm}^3$, N_A is the Avogadro constant $6.0225 \cdot 10^{23}$ (note: $1 \text{ Å}^3 = 1.0 \cdot 10^{-24} \text{ cm}^3$).

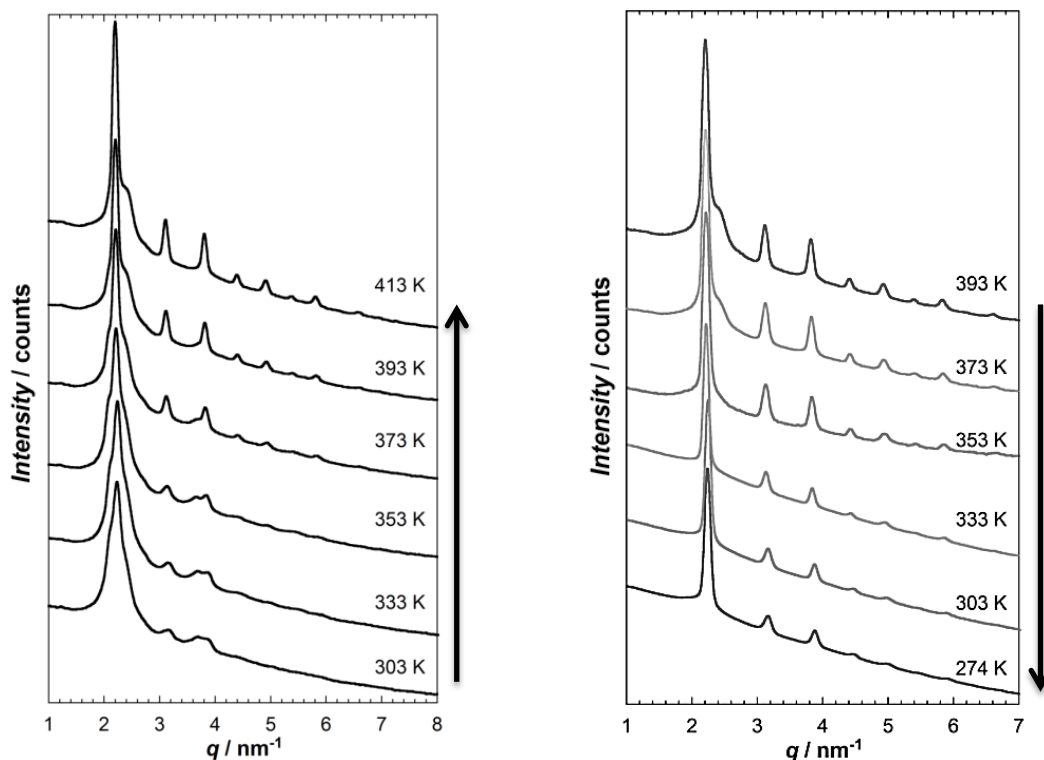


Figure S.II-19. Small angle X-ray diffraction profiles of $[\text{Mn}_{12}\text{O}_{12}(\text{L}^4)_{16}(\text{H}_2\text{O})_4]$ (left) on 4th heating from 303 K to 413 K and (right) on 4th cooling from 413 K to 274 K.

Table S.II-8. Indexation of the reflections on 4th cooling for $[\text{Mn}_{12}\text{O}_{12}(\text{L}^4)_{16}(\text{H}_2\text{O})_4]$, part 1.

T / K	Peak number	$q_{(\text{obs})} / \text{nm}^{-1}$	$d_{(\text{obs})} / \text{Å}$	hkl	$h^2+k^2+l^2$	$d_{(\text{calc})} / \text{Å}$	Calculated cell parameters
393 cooling	1	2.21	28.46	110	2	28.53	a = 40.35 Å V = 65701 Å ³ Z ≈ 3 - 4
	2	3.11	20.23	200	4	20.18	
	3	3.81	16.48	211	6	16.47	
	4	4.40	14.27	220	8	14.27	
	5	4.92	12.77	310	10	12.76	
	6	5.40	11.63	222	12	11.65	
	7	5.84	10.77	321	14	10.78	
	8	6.22	10.11	400	16	10.09	
	9	6.60	9.52	330	18	9.51	
	10	7.32	8.59	332	22	8.60	
373 cooling	1	2.20	28.50	110	2	28.44	a = 40.22 Å V = 65094 Å ³ Z ≈ 3 - 4
	2	3.12	20.16	200	4	20.11	
	3	3.83	16.39	211	6	16.42	
	4	4.42	14.21	220	8	14.22	
	5	4.94	12.73	310	10	12.72	
	6	5.42	11.60	222	12	11.61	
	7	5.85	10.74	321	14	10.75	
	8	6.64	9.46	330	18	9.48	
353 cooling	1	2.21	28.41	110	2	28.37	a = 40.12 Å V = 64602 Å ³ Z ≈ 3 - 4
	2	3.13	20.06	200	4	20.06	
	3	3.84	16.38	211	6	16.38	
	4	4.43	14.19	220	8	14.19	
	5	4.96	12.68	310	10	12.69	
	6	5.43	11.57	222	12	11.58	
	7	5.86	10.73	321	14	10.72	
	8	6.66	9.44	330	18	9.46	

$q_{(\text{obs})}$ is the observed/measured reciprocal spacing, $q = 4\pi \sin\theta/\lambda$, where λ is the wavelength, 2θ is the diffraction angle, $d_{(\text{obs})}$ and $d_{(\text{calc})}$ are observed and calculated diffraction spacings: $d_{(\text{obs})} = 2\pi/q_{(\text{obs})}$, $d_{(\text{calc})} = a/\sqrt{h^2+k^2+l^2}$, a is the lattice parameter of the cubic phase, V is the volume of the cubic cell unit ($V = a^3$), Z is the number of complexes per cubic cell, $Z = (\rho \cdot V \cdot N_A)/Mw$, where ρ is the density $\approx 1 \text{ g/cm}^3$, N_A is the Avogadro constant $6.0225 \cdot 10^{23}$ (note: $1 \text{ Å}^3 = 1.0 \cdot 10^{-24} \text{ cm}^3$).

Table S.II-9. Indexation of the reflections on 4th cooling for $[\text{Mn}_{12}\text{O}_{12}(\text{L}^4)_{16}(\text{H}_2\text{O})_4]$, part 2.

T / K	Peak number	$q_{(\text{obs})} / \text{nm}^{-1}$	$d_{(\text{obs})} / \text{Å}$	hkl	$h^2+k^2+l^2$	$d_{(\text{calc})} / \text{Å}$	Calculated cell parameters
333 cooling	1	2.22	28.34	110	2	28.35	a = 40.09 Å V = 64452 Å ³ Z ≈ 3 - 4
	2	3.13	20.10	200	4	20.05	
	3	3.84	16.37	211	6	16.37	
	4	4.44	14.17	220	8	14.18	
	5	4.96	12.68	310	10	12.68	
	6	5.43	11.57	222	12	11.57	
	7	5.87	10.70	321	14	10.72	
	8	6.64	9.46	330	18	9.45	
303 cooling	1	2.23	28.18	110	2	28.21	a = 39.90 Å V = 63507 Å ³ Z ≈ 3 - 4
	2	3.15	19.93	200	4	19.95	
	3	3.86	16.27	211	6	16.29	
	4	4.46	14.09	220	8	14.11	
	5	4.98	12.61	310	10	12.62	
	6	5.45	11.52	222	12	11.52	
	7	5.89	10.66	321	14	10.66	
274 cooling	1	2.24	28.01	110	2	28.04	a = 39.65 Å V = 62355 Å ³ Z ≈ 3 - 4
	2	3.17	19.83	200	4	19.83	
	3	3.88	16.21	211	6	16.19	
	4	4.49	14.01	220	8	14.02	
	5	5.01	12.55	310	10	12.54	
	6	5.51	11.40	222	12	11.45	
	7	5.92	10.61	321	14	10.60	

$q_{(\text{obs})}$ is the observed/measured reciprocal spacing, $q = 4\pi \sin\theta/\lambda$, where λ is the wavelength, 2θ is the diffraction angle, $d_{(\text{obs})}$ and $d_{(\text{calc})}$ are observed and calculated diffraction spacings: $d_{(\text{obs})} = 2\pi/q_{(\text{obs})}$, $d_{(\text{calc})} = a/\sqrt{h^2 + k^2 + l^2}$, a is the lattice parameter of the cubic phase, V is the volume of the cubic cell unit ($V = a^3$), Z is the number of complexes per cubic cell, $Z = (\rho \cdot V \cdot N_A)/Mw$, where ρ is the density $\approx 1 \text{ g/cm}^3$, N_A is the Avogadro constant $6.0225 \cdot 10^{23}$ (note: $1 \text{ Å}^3 = 1.0 \cdot 10^{-24} \text{ cm}^3$).

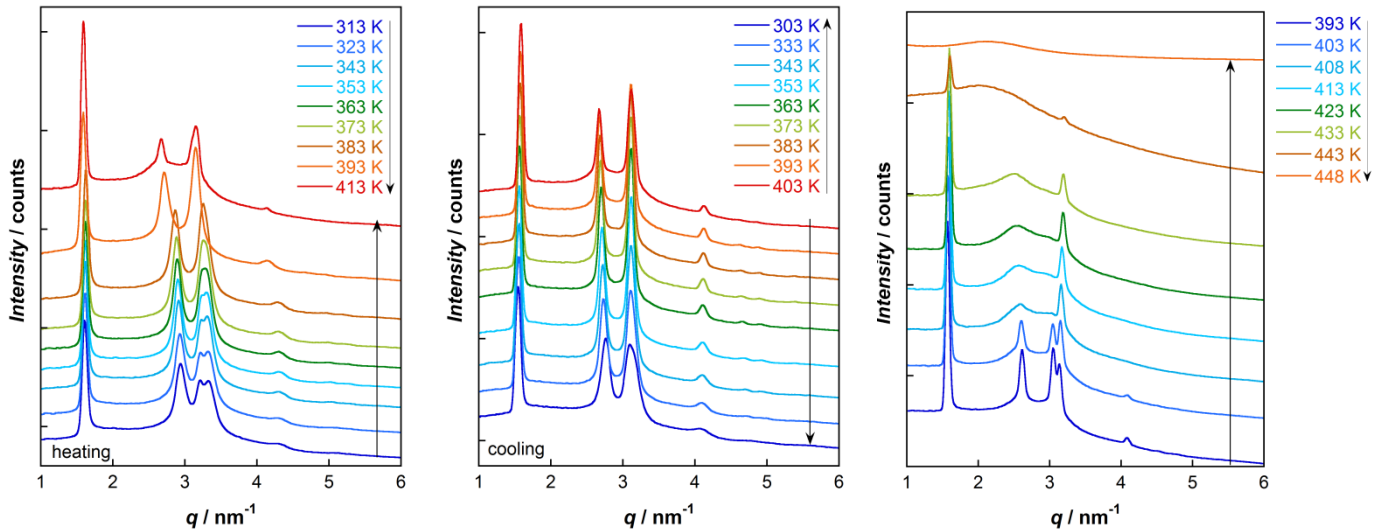

Figure S.II-20. Small angle X-ray diffraction profiles of $[\text{Mn}_{12}\text{O}_{12}(\text{L}^5)_{16}(\text{H}_2\text{O})_4]$: (left) on 2nd heating from 313 K to 413 K; (center) on 2nd cooling from 413 K to 303 K; (right) on 3rd heating from 393 K to 448 K.

Table S.II-10. Indexation of the reflections on 3rd heating for [Mn₁₂O₁₂(L⁵)₁₆(H₂O)₄].

T / K	Peak number	$q_{(obs)} / \text{nm}^{-1}$	$d_{(obs)} / \text{Å}$	hkl	h^2+k^2+hk	$d_{(calc)} / \text{Å}$	Calculated cell parameters
423 K heating	1	1.60	39.34	001	-	39.42	periodicity $d = 39.42 \text{ Å}$
	2	2.54	24.72	d'	-		
	3	3.18	19.75	002	-	19.71	
403 K heating	1	1.58	39.89	001	-	39.88	$a = 47.71 \text{ Å}$ $c = 39.88 \text{ Å}$ $V = 78592 \text{ Å}^3$ $S = 1971 \text{ Å}^2$
	2	2.67	23.57	110	3	23.51	
	3	3.15	19.93	002	-	19.94	
	4	4.07	15.45	200	4	20.36	
	5	5.40	11.63	210	7	15.39	
393 K heating	1	1.57	40.10	001	-	40.10	$a = 47.75 \text{ Å}$ $c = 40.10 \text{ Å}$ $V = 79164 \text{ Å}^3$ $S = 1974 \text{ Å}^2$
	2	2.67	23.57	110	3	23.51	
	3	3.13	20.05	002	-	20.05	
	4	4.07	15.45	200	4	20.36	
	5	5.40	11.63	210	7	15.39	
	6	5.74	10.95	300	9	13.57	
343 K heating	1	1.62	38.83	001	-	38.78	$a = 43.50 \text{ Å}$ $c = 38.78 \text{ Å}$ $V = 63556 \text{ Å}^3$ $S = 1639 \text{ Å}^2$
	2	2.92	21.49	110	3	21.75	
	3	3.24	19.37	002	-	19.39	
	4	3.31	18.97	200	4	18.84	
	5	4.37	14.39	210	7	14.24	
	6	5.03	12.49	300	9	12.56	
323 K heating	1	1.62	38.83	001	-	38.78	$a = 43.21 \text{ Å}$ $c = 38.78 \text{ Å}$ $V = 62699 \text{ Å}^3$ $S = 1617 \text{ Å}^2$
	2	2.91	21.59	110	3	21.60	
	3	3.24	19.37	002	-	19.39	
	4	3.35	18.76	200	4	18.71	
	5	4.44	14.15	210	7	14.14	
	6	5.05	12.44	300	9	12.47	
313 K heating	1	1.61	39.03	001	-	39.18	$a = 43.05 \text{ Å}$ $c = 39.18 \text{ Å}$ $V = 62861 \text{ Å}^3$ $S = 1604 \text{ Å}^2$
	2	2.92	21.52	110	3	21.53	
	3	3.21	19.57	002	-	19.59	
	4	3.37	18.65	200	4	18.64	
	5	4.45	14.12	210	7	14.09	
	6	5.07	12.39	300	9	12.43	

$q_{(obs)}$ is the observed/measured reciprocal spacing, $q = 4\pi \cdot \sin\theta/\lambda$, where λ is the wavelength, 2θ is the diffraction angle, $d_{(obs)}$ and $d_{(calc)}$ are observed and calculated diffraction spacings: $d_{(obs)} = 2\pi/q_{(obs)}$, $d_{(calc)} = \frac{a\sqrt{3}}{2\sqrt{h^2+hk+k^2}}$, a and c are lattice parameters of the average hexagonal organization in layers, also c corresponds to average lamellar periodicity between the layers formed by magnetic cores: $c = \frac{1}{n} \sum_{i=1}^n i \cdot d_{00i}$. V is the volume of the average hexagonal unit cell $V = a^2 \cdot c \cdot \cos(\pi/6)$. S corresponds to the hexagonal basal (ab) plane area. d' is average short-range correlation distance between oxo-metallic cores within the layer

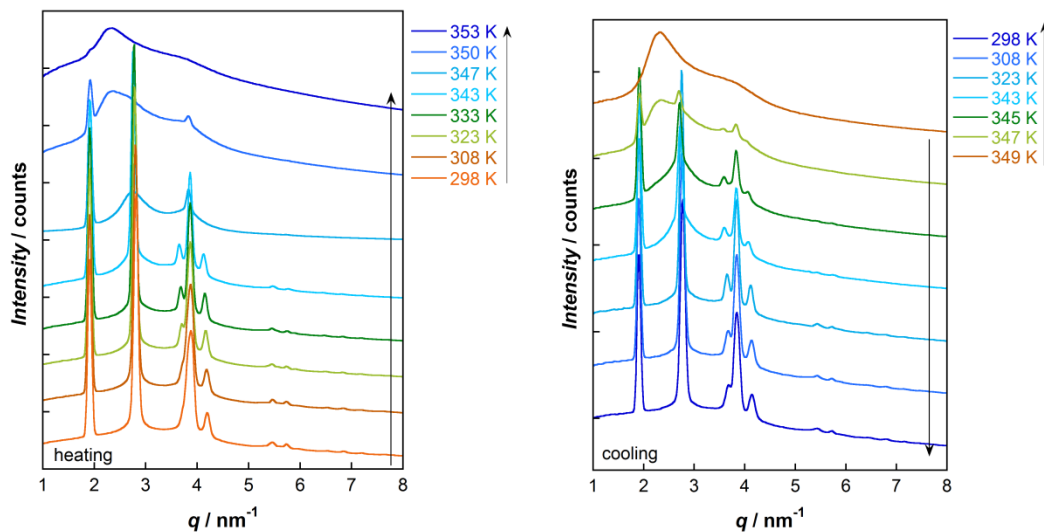

Figure S II-21. Small angle X-ray diffraction profiles of [Mn₁₂O₁₂(L⁶)₁₆(H₂O)₄]: (left) on 2nd heating from 298 K to 353 K; (right) on 2nd cooling from 349 K to 298 K.

Table S.II-11. Indexation of reflections on cooling for $[\text{Mn}_{12}\text{O}_{12}(\text{L}^6)_{16}(\text{H}_2\text{O})_4]$

T / K	Peak number	$q_{(\text{obs})} / \text{nm}^{-1}$	$d_{(\text{obs})} / \text{Å}$	hkl	h^2+k^2+hk	$d_{(\text{calc})} / \text{Å}$	Calculated cell parameters
347 K cooling	1	1.92	32.78	001	-	32.80	$a = 53.80 \text{ Å}$
	2	2.35	26.77	110	3	26.90	$c = 32.80 \text{ Å}$
	3	2.69	23.32	200	4	23.30	$V = 82213 \text{ Å}^3$
	4	3.57	17.60	210	7	17.61	$S = 2507 \text{ Å}^2$
	5	3.83	16.41	002	-	16.40	
	6	4.03	15.60	300	9	15.53	
345 K cooling	1	1.92	32.78	001	-	32.80	$a = 53.55 \text{ Å}$
	2	2.72	23.13	200	4	23.24	$c = 32.80 \text{ Å}$
	3	3.58	17.53	210	7	17.57	$V = 81470 \text{ Å}^3$
	4	3.83	16.39	002	-	16.40	$S = 2483 \text{ Å}^2$
	5	4.07	15.45	300	9	15.50	
	6	5.40	11.63	400	16	11.62	
	7	5.74	10.95	003	-	10.93	
323 K cooling	1	1.92	32.78	001	-	32.78	$a = 52.70 \text{ Å}$
	2	2.75	22.85	200	4	22.82	$c = 32.78 \text{ Å}$
	3	3.64	17.27	210	7	17.25	$V = 78850 \text{ Å}^3$
	4	3.83	16.39	002	-	16.39	$S = 2405 \text{ Å}^2$
	5	4.13	15.23	300	9	15.21	
	6	5.50	11.43	400	16	11.41	
	7	5.75	10.93	003	-	10.93	
	8	6.35	9.89	410	21	9.96	
	9	6.87	9.15	500	25	9.13	
	10	7.16	8.78	330	27	8.78	
308 K cooling	1	1.91	32.90	001	-	32.86	$a = 52.40 \text{ Å}$
	2	2.78	22.64	200	4	22.69	$c = 32.86 \text{ Å}$
	3	3.68	17.10	210	7	17.15	$V = 78157 \text{ Å}^3$
	4	3.85	16.32	002	-	16.43	$S = 2379 \text{ Å}^2$
	5	4.16	15.10	300	9	15.13	
	6	5.51	11.40	400	16	11.34	
	7	5.73	10.97	003	-	10.95	
	8	6.35	9.89	41	21	9.90	
	9	6.91	9.09	50	25	9.08	
	10	7.18	8.75	33	27	8.73	
298 K cooling	1	1.90	33.07	001	-	33.04	$a = 52.35 \text{ Å}$
	2	2.77	22.69	200	4	22.69	$c = 33.04 \text{ Å}$
	3	3.67	17.13	210	7	17.15	$V = 78429 \text{ Å}^3$
	4	3.83	16.41	002	-	16.52	$S = 2373 \text{ Å}^2$
	5	4.15	15.13	300	9	15.13	
	6	5.55	11.32	400	16	11.34	
	7	5.67	11.08	003	-	11.01	
	8	6.39	9.83	410	21	9.90	
	9	6.91	9.09	500	25	9.08	
	10	7.18	8.75	330	27	8.73	

$q_{(\text{obs})}$ is the observed/measured reciprocal spacing, $q = 4\pi \cdot \sin\theta / \lambda$, where λ is the wavelength, 2θ is the diffraction angle, $d_{(\text{obs})}$ and $d_{(\text{calc})}$ are observed and calculated diffraction spacings: $d_{(\text{obs})} = 2\pi/q_{(\text{obs})}$, $d_{(\text{calc})} = \frac{\sqrt{3}}{2} \cdot \frac{a}{\sqrt{h^2+hk+k^2}}$, a and c are lattice parameters of the average hexagonal organization in layers, also c corresponds to average lamellar periodicity between the layers formed by magnetic cores: $c = \frac{1}{n} \sum_{i=1}^n i \cdot d_{00i}$. V is the volume of the average hexagonal unit cell $V = a^2 \cdot c \cdot \cos(\pi/6)$. S corresponds to the hexagonal basal (ab) plane area.

II.8. References

- (a) Lis, T. *Acta. Cryst. B* **1980**, *36*, 2042-2046. (b) Caneschi, A.; Gatteschi, D.; Sessoli, R.; Barra, A. L.; Brunel, L. C.; Guillot, M. *J. Am. Chem. Soc.* **1991**, *113*, 5873-5874. (c) Sessoli, R.; Tsai, H. L.; Schake, A. R.; Wang, S. Y.; Vincent, J. B.; Folting, K.; Gatteschi, D.; Christou, G.; Hendrickson, D. N.; *J. Am. Chem. Soc.* **1993**, *115*, 1804-1816. (d) Sessoli, R.; Gatteschi, D.; Caneschi, A.; Novak, M. A. *Nature* **1993**, *365*, 141-143. (e) Thomas, L.; Lioni, F.; Balou, R.; Gatteschi, D.; Sessoli, R.; Barbara, B. *Nature* **1996**, *383*, 145-157.
- Rogez, G.; Donnio, B.; Terazzi, E.; Gallani, J.-L.; Kappler, J.-P.; Bucher, J.-P.; Drillon, M.; *Adv. Mater.* **2009**, *21*, 4323-4333.
- Bogani, L.; Wernsdorfer W. *Nature Materials* **2008**, *7*, 179-186
- (a) Cornia, A.; Fabretti, A. C.; Pacchioni, M.; Bonacchi, D.; Caneschi, A.; Gatteschi, D.; Biagi, R.; Del Penino, U.; De Renzi, V.; Gurevich, L.; Van der Zant, H. S. J. *Angew. Chem. Int. Ed.* **2003**, *42*, 1645-1648. (b) Condorelli, G. G.; Motta A.; Fragala, I. L.; Giannazzo, F.; Raineri, V.; Caneschi A.; Gatteschi, D. *Angew. Chem. Int. Ed.* **2004**, *43*, 4081-4084. (c) Naitabdi, A.; Bucher, J.-P.; Gerbier, P.; Rabu, P.; Drillon, M. *Adv. Mater.* **2005**, *17*, 1612-1616. (d) Mannini, M.; Pineider F.; Sainctavit, P.; Danieli, C.; Otero, E.; Sciancalepore, C.; Talarico, A. M.; Arrio, M.-A.; Cornia, A.; Gatteschi, D.; Sessoli, R. *Nature Materials* **2009**, *8*, 194-197. (e) Ababei, R.; Li, Y.-G.; Roubeau, O.; Kalisz, M.; Bréfuel, N.; Coulon, C.; Harté, E.; Liu, X.; Mathonière, C.; Clérac, R. *New J. Chem.* **2009**, *33*, 1237-1248. (f) Jeon, I.-R.; Ababei, R.; Lecren, L.; Li, Y.-G.; Wernsdorfer, W.; Roubeau, O.; Mathonière, C.; Clérac, R. *Dalton Trans.*, **2010**, *39*, 4744-4746.
- Binnemans, K. *Physical Properties of Metallomesogens*, in: Bruce, D.W.; O'Hare, D.; Walton, R.I. (Eds) *Inorganic Materials Series: Molecular Materials*, John Wiley & Sons, Ltd.: Chichester, **2010**, 61-141.
- Chakov, N. E.; Lee, S.-C.; Harter, A. G.; Kuhns, P. L.; Reyes, A. P.; Hill, S. O.; Dalal, N. S.; Wernsdorfer, W.; Abboud, K.; Christou, G. *J. Am. Chem. Soc.* **2006**, *128*, 6975-6989.
- Milios, C. J.; Vinslava, A.; Wernsdorfer, W.; Moggach, S.; Parsons, S.; Perlepes, S. P.; Christou, G.; Brechin, E. K. *J. Am. Chem. Soc.* **2007**, *129*, 2754-2755.
- (a) Blagg, R.; Muryn, C. A.; McInnes, E. J. L.; Tuna, F.; Winpenny, R. E. P. *Angew. Chem., Int. Ed.* **2011**, *50*, 6530-6533. (b) Hewitt, I. J.; Tang, J.; Madhu, N. T.; Anson, C. E.; Lan, Y.; Luzon, J.; Etienne, M.; Sessoli, R.; Powell, A. K. *Angew. Chem., Int. Ed.* **2010**, *49*, 6352-6355. (c) Guo, Y.-N.; Xu, G.-F.; Gamez, P.; Zhao, L.; Lin, S.-Y.; Deng, R.; Tang, J.; Zhang, H.-J. *J. Am. Chem. Soc.* **2010**, *132*, 8538-8539. (d) Lin, P.-H.; Burchell, T. J.; Ungur, L.; Chibotaru, L. F.; Wernsdorfer, W.; Murugesu, M. *Angew. Chem., Int. Ed.* **2009**, *48*, 9489-9492. (e) Carolina R. Ganiwet, C. R.; Ballesteros, B.; de la Torre, G.; Clemente-Juan, J. M.; Coronado, E.; Torres, T. *Chem. Eur. J.* **2013**, *19*, 1457-1465.
- Bagai, R.; Christou, G. *Chem. Soc. Rev.* **2009**, *38*, 1011-1026.
- Zhao, H. H.; Berlinguette, C. P.; Bacsá, J.; Prosvirin, A. V.; Bera, J. K.; Tichy, S. E.; Schelter, E. J.; Dunbar, K. R. *Inorg. Chem.* **2004**, *43*, 1359-1369.
- (a) Eppley, H. J.; Tsai, H.; Vries, N.; Folting, K.; Christou, G.; Hendrickson, D. N. *J. Am. Chem. Soc.* **1995**, *117*, 301-317. (b) Coronado, E.; Forment-Aliaga, A.; Gaita-Ariño, A.; Giminéz-Saiz, C.; Romero, F. M.; Wernsdorfer, W. *Angew. Chem., Int. Ed.* **2004**, *43*, 6152-6156. (c) Ruiz-Molina, D.; Mas-Torrent, M.; Gomez, J.; Balana, A. I.; Domingo, N.; Tejada, J.; Martinez, M. T.; Rovira, C.; Veciana, J. *Adv. Mater.* **2003**, *15*, 42-45.
- Soler, M.; Artus, P.; Folting, K.; Huffman, J. C.; Hendrickson, D. N.; Christou, G. *Inorg. Chem.* **2001**, *40*, 4902-4912.
- (a) Hill, S.; Anderson, N.; Wilson, A.; Takahashi, S.; Petukhov, K.; Chakov, N. E.; Murugesu, M.; North, J. M.; del Barco, E.; Kent, A. D.; Dalal, N. S.; Christou, G. *Polyhedron* **2005**, *24*, 2284-2292; (b) Bian, G. Q.; Kuroda-Sowa, T.; Gunjima, N.; Maekawa M.; Munakata, M. *Inorg. Chem. Commun.*, **2005**, *8*, 208-211.
- (a) Halcrow, M. A. *Chem. Soc. Rev.* **2013**, *42*, 1784-1795. (b) Winter, M. J. *d-Block Chemistry*, Oxford University Press: Oxford, **1994**, 83-86.
- Ruiz, D.; Sun, Z. M.; Albela, B.; Folting, K.; Ribas, J.; Christou, G.; Hendrickson, D. N. *Angew. Chem., Int. Ed.* **1998**, *37*, 300-302.
- (a) Soler, M.; Wernsdorfer, W.; Sun, Z. M.; Huffman, J. C.; Hendrickson, D. N.; Christou, G. *Chem. Commun.* **2003**, 2672-2673. (b) Cornia, A.; Sessoli, R.; Sorace, L.; Gatteschi, D.; Barra, A. L.; Daguebonne, C. *Phys. Rev. Lett.* **2002**, *89*, 257201.
- Aubin, M. J. S.; Sun, Z.; Guzei, I. A.; Rheingold, A. L.; Christou, G.; Hendrickson, D. N. *Chem. Commun.*, **1997**, 2239-2240.

18. (a) Gerbier, P.; Ruiz-Molina, D.; Domingo, N.; Amabilino, D. B.; Vidal-Gancedo, J.; Tejada, J.; Hendrickson, D. N.; Veciana, J. *Monatsh. Chem.* **2003**, *134*, 265-276. (b) Coronado, E.; Forment-Aliaga, A.; Gaita-Ariño, A.; Giminéz-Saiz, C.; Romero, F. M.; Wernsdorfer, W. *Angew. Chem., Int. Ed.* **2004**, *43*, 6152-6156. (c) Park, C.-D.; Jung, D.-Y. *Bull. Korean Chem. Soc.* **2001**, *22*, 611-615. (d) Sun, H.; Li, W.; Wollenberg, L.; Li, B.; Wu, L.; Li, F.; Xu, L. *J. Phys. Chem. B* **2009**, *113*, 14674-14680. (e) Li, W.; Li, B.; Wang, Y.; Zhang, J.; Wang, S.; Wu, L. *Chem. Commun.* **2010**, *46*, 6548-6550. (f) Wang, Y.; Li, W.; Zhou, S.; Kong, D.; Yang, H.; Wu, L. *Chem. Commun.* **2011**, *47*, 3541-3543. (g) Heersche, H. B.; De Groot, Z.; Folk, J. A.; van der Zant, H. S. J.; Romeike, C.; Wegewijs, M. R.; Zobbi, L.; Barreca, D.; Tondello, E.; Cornia, A. *Phys. Rev. Lett.* **2006**, *96*, 206801. (h) Bian, G. Q.; Kuroda-Sowa, T.; Nogami, T.; Sugimoto, K.; Maekawa, M.; Munakata, M.; Miyasaka, H.; Yamashita, M. *Bull. Chem. Soc. Jpn.* **2005**, *78*, 103210-39. (i) Willemin, S.; Donnadiou, B.; Lecren, L.; Henner, B.; Clérac, R.; Guérin, C.; Meyer, A.; Pokrovskii A. V.; Larionova, J. *New J. Chem.* **2004**, *28*, 919-928. (j) Burgert, M.; Voss, S.; Herr, S.; Fonin, M.; Groth, U.; Ruediger, U. *J. Am. Chem. Soc.* **2007**, *129*, 14362-14366. (k) Cornia, A.; Fabretti, A. C.; Pacchioni, M.; Zobbi, L.; Bonacchi, D.; Caneschi, A.; Gatteschi, D.; Biagi, R.; Del Pennino, U.; De Renzi, V.; Gurevich, L.; Van der Zant, H. S. J. *Angew. Chem., Int. Ed.* **2003**, *42*, 1645-1648. (l) Pacchioni, M.; Cornia, A.; Fabretti, A. C.; Zobbi, L.; Bonacchi, D.; Caneschi, A.; Chastanet, G.; Gatteschi, D.; Sessoli, R. *Chem. Commun.* **2004**, 2604-2605.
19. (a) Chakov, N. E.; Wernsdorfer, W.; Abboud, K. A.; Hendrickson, D. N.; Christou, G. *Dalton Trans.* **2003**, 2243-2248. (b) Chakov, N. E.; Abboud, K. A.; Zakharov, L. N.; Rheingold, A. L.; Hendrickson, D. N.; Christou, G. *Polyhedron* **2003**, *22*, 1759-1763.
20. (a) Tirelli, N.; Cardullo, F.; Habicher, T.; Suter, U.W.; Diederich, F. *J. Chem. Soc. Perkin Trans. 2* **2000**, 193-198. (b) Deschenaux, R.; Donnio, B.; Guillon, D. *New J. Chem.* **2007**, *31*, 1064-1073.
21. (a) Date, R.W.; Fernandez Iglesias, E.; Rowe, K. E.; Elliott, J. M.; Bruce, D.W. *Dalton Trans.* **2003**, 1914-1931. (b) Camerel, F.; Ziessel, R.; Donnio, B.; Guillon, D. *New J. Chem.* **2006**, *30*, 135-139.
22. Zhang, T.; Liu, S.; Kurth, D. G.; Faul, C. F. J. *Adv. Funct. Mater.* **2009**, *19*, 642-652.
23. (a) Molard, Y.; Dorson, F.; Cîrcu, V.; Roisnel, T.; Artzner, F.; Cordier, S. *Angew. Chem. Int. Ed.* **2010**, *49*, 3351-3355. (b) Mocanu, A. S.; Amela-Cortes, M.; Molard, Y.; Cîrcu, V.; Cordier, S. *Chem. Commun.* **2011**, *47*, 2056-2058
24. (a) Terazzi, E.; Bourgogne, C.; Welter, R.; Gallani, J.-L.; Guillon, D.; Rogez, G.; Donnio, B. *Angew. Chem., Int. Ed.* **2008**, *47*, 490-495. (b) Terazzi, E.; Jensen, T. B.; Donnio, B.; Buchwalder, K.; Bourgogne, C.; Rogez, G.; Heinrich, B.; Gallani, J.-L.; Piguët, C. *Dalton Trans.*, **2011**, *40*, 12028-12032. (c) Terazzi, E.; Rogez, G.; Gallani, J.-L.; Donnio, B. *J. Am. Chem. Soc.*, **2013**, *135*, 2708-2722.
25. Gonidec, M.; Luis, F.; Vilchez, Á.; Esquena, J.; Amabilino, D. B.; Veciana, J. *Angew. Chem., Int. Ed.* **2010**, *49*, 1-5.
26. Saez, I. M.; Goodby J. W. *Struct. Bond.* **2008**, *128*, 1-62.
27. Siretanu, D. *PhD Thesis*, Univ. of Bordeaux I, **2011**.
28. (a) Herbert, A. J. *Trans. Faraday Soc.* **1967**, *63*, 555-560. (b) Blumstein, A.; Platel, L. *Mol. Cryst. Liq. Cryst.* **1978**, *48*, 151-164. (c) Gray, G. W.; Jones, B. *J. Chem. Soc.* **1953**, 4179-4180. (d) Bryan, R. F.; Hartley, P.; Miller, R. W.; Shen, M. S. *Mol. Cryst. Liq. Cryst.* **1980**, *62*, 281-309. (e) Bryan, R. F.; Hartley, P. *Mol. Cryst. Liq. Cryst.* **1980**, *62*, 259-279. (f) Babkov, L. M.; Gorshkov, O. V.; Golovina, N. A.; Puchkovskay, G. A.; Khakimov, I. N. *J. Struct. Chem.* **1995**, *36*, 302-308. (g) Kato, T.; Kubota, Y.; Nakano, M.; Uryu, T. *Chem. Lett.* **1995**, 1127-1128. (h) Plass, M. Z. *Phys. Chem. Int. Ed.* **1996**, *194*, 223-230. (i) Painter, P.; Cleveland, C.; Coleman, M. *Mol. Cryst. Liq. Cryst.* **2000**, *348*, 269-293. (j) Paleos, C. M.; Tsiourvas, D. *Liquid Crystals* **2001**, *28*, 1127-1161.
29. (a) Sessoli, R. *Mol. Cryst. Liq. Cryst.* **1995**, *274*, 145-157. (b) Gatteschi, D.; Sessoli, R. *Angew. Chem., Int. Ed.* **2003**, *42*, 268-297.
30. Sun, Z.; Ruiz, D.; Dilley, N. R.; Soler, M.; Ribas, J.; Folting, K.; Maple, M. B.; Christou, G.; Hendrickson, D. N. *Chem. Commun.* **1999**, 1973-1974.
31. Wernsdorfer, W.; Aliaga-Alcalde, N.; Hendrickson, D. N.; Christou, G. *Nature* **2002**, *416*, 406-409; Tiron, R.; Wernsdorfer, W.; Foguet-Albiol, D.; Aliaga-Alcalde, N.; Christou, G. *Phys. Rev. Lett.* **2003**, *91*, 227203.
32. Nakamoto, K. *Infrared and Raman Spectra of Inorganic and Coordination Compounds*, 2nd edition, Wiley Interscience: New York, **1970**.
33. Larionova, J.; Clérac, R.; Boury, B.; Bideau, J. L.; Lecren, L.; Willemin, S. *J. Mater. Chem.* **2003**, *13*, 795-799.
34. An, J.; Chen, Z.-D.; Bian, J.; Chen, J.-T.; Wang, S.-X.; Gao, S.; Xu, G.-X. *Inorg. Chim. Acta* **2000**, *299*, 28-34.
35. Ruiz-Molina, D.; Gerbier, P.; Rumberger, E.; Amabilino, D. B.; Guzei, I. A.; Folting, K.; Huffman, J. C.; Rheingold, A.; Christou, G.; Veciana J.; Hendrickson D. N. *J. Mater. Chem.*, **2002**, *12*, 1152-1161.

36. Kushch, L. A.; Sasnovskayaa, V. D.; Dmitriev, A. I.; Yagubskii, E. B.; Koplak, O. V.; Zorina, L. V.; Boukhvalov D. W. *Dalton Trans.* **2012**, 41, 13747-13754.
37. (a) Sun, Z.; Ruiz, D.; Rumberger, E.; Incarvito, C. D.; Folting, K.; Rheingold, A. L.; Christou, G.; Hendrickson, D. N. *Inorg. Chem.* **1998**, 37, 4758-4759. (b) Aubin, S. M. J.; Sun, Z.; Eppley, H. J.; Rumberger, E. M.; Guzei, I. A.; Folting, K.; Gantzel, P. K.; Rheingold, A. L.; Christou, G.; Hendrickson, D. N. *Inorg. Chem.* **2001**, 40, 2127-2146.
38. (a) Kasper, J. S.; Lonsdale, K. (Eds.) *International Tables for X-Ray Crystallography, Vol. II, 3rd ed.*, Kynoch Press: Birmingham, **1972**, 147-149. (b) Hahn, Th. (Ed.) *International Tables for Crystallography, Vol. A, 5th ed.*, Springer: Dordrecht, **2005**, 47-53.
39. Hammond, C. *The Basics of Crystallography and Diffraction*, 2nd ed., Oxford University Press: New York, **2001**.
40. (a) Nakanishi, T.; Morita, M.; Murakami, H.; Sagara, T.; Nakashima, N. *Chem. Eur. J.* **2002**, 8, 1641-1648. (b) Zhang, T.; Liu, S.; Kurth, D. G.; Faul, C. F. J. *Adv. Funct. Mater.* **2009**, 19, 642-652.
41. (a) Terzis, A. F.; Vanakaras, A. G.; Photinos, D. J. *Mol. Cryst. Liq. Cryst.* **2000**, 352, 265-274; (b) Crisanti, A.; Leuzzi, L. *Phys. Rev. Lett.* **2005**, 95, 087201 and references therein.
42. Levelut, A.M.; Malthête, J.; Collet, A. *J. Physique*, **1986**, 47, 351-357
43. (a) Kutsumizu, S. *Curr. Opin. Solid State Mater. Sci.* **2002**, 6, 537-543. (b) Diele, S. *Curr. Opin. Colloid Interface Sci.* **2002**, 7, 333-342. (c) Impéror-Clerc, M. *Curr. Opin. Colloid Interface Sci.* **2005**, 9, 370-376.
44. (a) Alam, M. A.; Motoyanagi, J.; Yamamoto, Y.; Fukushima, T.; Kim, J., Kato, K.; Takata, M.; Saeki, A.; Seki, S.; Tagawa, S.; Aida, T. *J. Am. Chem. Soc.* **2009**, 131, 17722 –17723. (b) Ichihara, M.; Suzuki, A.; Hatsusaka, K.; Ohta, K. *Liq. Cryst.* **2007**, 34, 555 – 567. (c) Zeng, X. B.; Ungar, G.; Impéror-Clerc, M. *Nat. Mater.* **2005**, 4, 562 –567; (d) Levelut, A. M.; Clerc, M.; *Liq. Cryst.* **1998**, 24, 105 – 115. (e) Bury, I.; Heinrich, B.; Bourgogne, C.; Guillon, D.; Donnio, B. *Chem. Eur. J.* **2006**, 12, 8396-8413. (f) Donnio, B.; García-Vásquez, P.; Gallani, J.-L.; Guillon, D.; Terazzi, E. *Adv. Mater.* **2007**, 19, 3534-3539. (g) Ichikawa, T.; Yoshio, M.; Hamasaki, A.; Taguchi, S.; Liu, F.; Zeng, X.-B.; Ungar, G.; Ohno, H.; Kato, T. *J. Am. Chem. Soc.* **2012**, 134, 2634–2643. (h) Yeardley, D. J. P.; Ungar, G.; Percec, V.; Holerca, M. N.; Johansson, G. *J. Am. Chem. Soc.* **2000**, 122, 1684-1689. (i) Duan, H.; Hudson, S. D.; Ungar, G.; Holerca, M. N.; Percec, V. *Chem. Eur. J.* **2001**, 7, 4134-4141. (j) Ungar, G.; Zeng, X. *Soft Matter*, **2005**, 95-106, (k) Kim, J.-K.; Hong, M.-K.; Ahn, J.-H.; Lee, M. *Angew. Chem., Int. Ed.* **2005**, 44, 328-332. (l) Sun, R. G.; Zhang, J. *J. Phys. D: Appl. Phys.* **2004**, 37, 463-467.
45. Tschierske, C. *Chem. Soc. Rev.* **2007**, 36, 1930 –1970.
46. (a) Hatano, T.; Kato, T. *Chem. Commun.* **2006**, 1277-1279. (b) Goossens, K.; Wellens, S.; Van Hecke, K.; Van Meervelt, L.; Cardinaels, T.; Binnemans, K. *Chem. Eur. J.* **2011**, 17, 4291-4306. (c) Jiang, Y.; Liu, S.; Wu, L. *Dalton Trans.*, **2013**, 42, 7643-7650.
47. Singh, S. *Phys. Rep.*, **2000**, 324, 107-269.
48. (a) Dardel, B.; Guillon, D.; Heinrich B.; Deschenaux R. *J. Mater. Chem.* **2001**, 11, 2814–2831. (b) Chuard, T.; Deschenaux, R.; Hirsch, A.; Schonberger, H. *Chem. Commun.* **1999**, 2103-2104. (c) Deschenaux, R.; Donnio B.; Guillon, D. *New J. Chem.* **2007**, 31, 1064-1073. (d) Mehl, G. H.; Saez, I. M. *Appl. Organomet. Chem.* **1999**, 13, 261-272. (e) Donnio B.; Guillon, D. *Adv. Polym. Sci.* **2006**, 201, 45-155.

Chapter III
Modulating the Structural and Electron
Transfer Properties of Molecular {Fe₂Co₂}
Squares in Solid State via Anion Exchange or
Light Irradiation

Table of Contents for Chapter III:

III.1. Introduction	III.111
III.2. Synthesis and characterizations of molecular $\{\text{Fe}_2\text{Co}_2\}$ squares	III.113
III.2.1. Synthetic strategy	III.113
III.2.2. FT-IR spectroscopic analyses	III.114
III.2.3. Structural investigations of molecular $\{\text{Fe}_2\text{Co}_2\}$ squares	III.114
III.2.3.1. $\{[(\text{Tp}^*)\text{Fe}(\text{CN})_3]_2[\text{Co}(\text{bpy})_2]_2\}[\text{OTf}]_2 \cdot 3\text{H}_2\text{O} \cdot 3\text{DMF}$ (1)	III.114
III.2.3.2. $\{[(\text{Tp}^*)\text{Fe}(\text{CN})_3]_2[\text{Co}(\text{diMebpy})_2]_2\}(\text{OTf})_2 \cdot \text{H}_2\text{O} \cdot 2\text{DMF}$ (2)	III.118
III.2.3.3. $\{[(\text{Tp}^*)\text{Fe}(\text{CN})_3]_2[\text{Co}(\text{diMebpy})_2]_2\}(\text{ClO}_4)_2 \cdot 2\text{DMF}$ (3)	III.122
III.2.3.4. $\{[(\text{Tp}^*)\text{Fe}(\text{CN})_3]_2[\text{Co}(\text{diMebpy})_2]_2\}(\text{OTs})_2 \cdot 6\text{DMF}$ (4)	III.124
III.2.3.5. Structural comparison of compounds 2 , 3 and 4	III.125
III.2.4. Optical reflectivity studies	III.127
III.2.5. Magnetic measurements	III.128
III.3. Conclusions and perspectives	III.129
III.4. Supporting materials	III.131
III.4.1. Experimental protocols	III.131
III.4.2. FT-IR spectroscopic analyses	III.132
III.4.3. Crystallographic data for 1 , 2 , 3 and 4	III.134
III.4.4. Magnetic measurements	III.138
III.5. References	III.139

III.1. Introduction

The chemistry of cyanido-bridged heterometallic materials with tunable optical and magnetic properties became a forefront topic after the report on the first photo-magnetic Co/Fe Prussian blue (PB) analogue by Hashimoto.¹ However, the high dimensionality of bimetallic assemblies of Prussian blue analogues and their non-stoichiometric lattice defects make difficult the systematic structure-property correlation investigations. Moreover, the reduced solubility of these inorganic 3D polymers limits their potential applications and requires elaboration of strategies for nanoparticles design, to increase their solubility and to create multi-functionalities at nano-scale.² Therefore an active cyanido-metallate research trend has been directed towards the synthesis and investigation of discrete PB analogues that have flexible molecular and electronic structures coupled with improved solubility. In the last two decades, several groups designed, isolated and studied molecular analogues (fragments of various geometry) of Prussian blue by rational selection of various capping ligands.^{3,4,5,6} This approach has been extremely successful and diverse molecular architectures have been obtained with interesting magnetic properties such as single-molecule magnets,⁴ spin crossover,⁵ electron-transfer⁶ and photo-induced magnetism.⁷ Amongst these fragments, the most important complexes may be considered octanuclear cube^{4b-d,6b,8} and tetranuclear square^{3c,4f,5a,d,6c-g} complexes, which mimic the properties and the structural units of the infinite Prussian blue network (their unit cell and a face of their cubic unit cell).

Tetranuclear cyanido-bridged $\{Fe_2Co_2\}$ squares,^{6c-g} that display an electron transfer associated with a reversible switching of the magnetic and optical properties, are promising units for the development and investigation of switchable molecular materials. The first reported tetranuclear cyanido-bridged molecular square complex (by our group in 2010)^{6c}, $\{[(Tp^*)Fe(CN)_3]_2[Co(bpy)_2]_2\}(OTf)_2 \cdot 2H_2O \cdot 4DMF$ (where Tp^* = tris(3,5-dimethylpyrazol-1-yl)hydroborate, OTf = trifluoromethanesulfonate, bpy = 2,2'-bipyridine and DMF = N,N-dimethylformamide), exhibits both thermally and photoinduced intramolecular electron transfer process between paramagnetic $\{Fe^{III}_2Co^{II}_2\}$ and diamagnetic $\{Fe^{II}_2Co^{III}_2\}$ states.^{6c} Moreover, an electron transfer associated with first-order phase transition was observed for this system with a thermal hysteresis of 18 K (at a temperature sweep rate of 0.4 Kmin⁻¹) between 186 and 168 K (see Figure III-1 left). The other two $\{Fe_2Co_2\}$ molecular squares, reported later the same year,^{6d,e} had different capping ligands on Co or Fe sites and as a result showed different ET related behaviors. The complex of formula $\{[(pzTp)Fe(CN)_3]_2[Co(bik)_2]_2\}(ClO_4)_2 \cdot 2H_2O$ (where $pzTp$ = tetrapyrazolylborate, bik = bis(1-methylimidazol-2-yl)ketone) is a diamagnetic cyanido-bridged $\{Fe^{II}_2Co^{III}_2\}$ square over the 2 – 300 K temperature range and can be converted into the corresponding paramagnetic $\{Fe^{III}_2Co^{II}_2\}$ species under light irradiation below 100 K.^{6d} On the other hand, the $\{[(Tp^*)Fe(CN)_3]_2[Co(dtbbpy)_2]_2\}(PF_6)_2 \cdot 2MeOH$ (where $dtbbpy$ = 4,4'-di-*tert*-butyl-2,2'-bipyridine) complex exhibits a two-step thermally induced electron transfer process between paramagnetic $\{Fe^{III}_2Co^{II}_2\}$, intermediate $\{Fe^{III}_2Co^{II}_2\} + \{Fe^{II}_2Co^{III}_2\}$ (1:1) and diamagnetic $\{Fe^{II}_2Co^{III}_2\}$ states.^{6e} Later in 2011 the same authors^{6f} observed a photoinduced electron transfer below 80 K for this molecular system as well. Thus, for these cyanido-bridged $\{Fe_2Co_2\}$ squares, the nature of the capping ligands can tune magneto-optical bistability or stabilize paramagnetic or diamagnetic units that show no thermally and/or photoinduced intramolecular electron transfer process.^{6c-g}

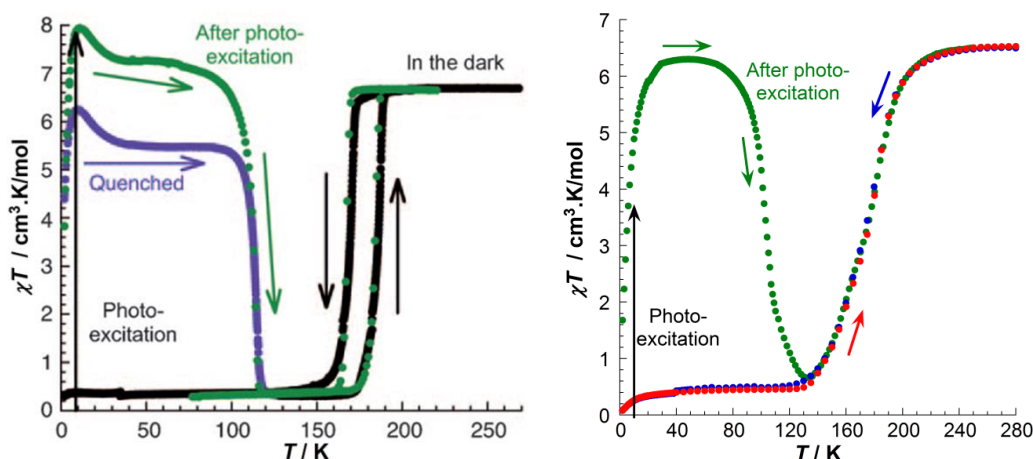


Figure III-1. (left) χT vs. T data for $\{[(\text{Tp}^*)\text{Fe}(\text{CN})_3]_2[\text{Co}(\text{bpy})_2]_2\}(\text{OTf})_2 \cdot 2\text{H}_2\text{O} \cdot 4\text{DMF}$ (**1**) (at 0.4 Kmin^{-1} , with χ defined as the molar magnetic susceptibility and equal to M/H ; M = magnetization and H = external magnetic field): in the dark (black, 0.1 T), after thermal quench (purple, 0.1 T), and after irradiation (green, 1 T, 3 mWcm^{-2});^{6c} (right) χT vs. T data for $\{[(\text{Tp}^*)\text{Fe}(\text{CN})_3]_2[\text{Co}(\text{diMe bpy})_2]_2\}(\text{OTf})_2 \cdot \text{H}_2\text{O} \cdot 2\text{DMF}$ (**2**) in the dark on cooling (blue, 0.5 T), and heating (red, 1 T) at 0.8 Kmin^{-1} , and after irradiation (green, 1 T, 2 mWcm^{-2}) at 0.4 Kmin^{-1} .^{6g}

Due to their ET associated magnetic and optical bistabilities, cyanido-bridged molecular $\{\text{Fe}_2\text{Co}_2\}$ squares became interesting molecular objects for functionalization and design of hybrid systems. Successful attempts of rational functionalization of molecular $\{\text{Fe}_2\text{Co}_2\}$ squares were performed by Diana Siretanu during her PhD thesis (CRPP, 2008 – 2011).⁹ Through the methyl functionalization of the bpy ligands of the $\{[(\text{Tp}^*)\text{Fe}(\text{CN})_3]_2[\text{Co}(\text{bpy})_2]_2\}^{2+}$, a new system was obtained, $\{[(\text{Tp}^*)\text{Fe}(\text{CN})_3]_2[\text{Co}(\text{diMe bpy})_2]_2\}(\text{OTf})_2 \cdot \text{H}_2\text{O} \cdot 2\text{DMF}$ (where diMe bpy = 4,4'-dimethyl-2,2'-bipyridine), that preserved magnetic and optical switching ability driven by thermally and photo-induced intramolecular electron transfer process. This result proved the possibility to transfer and tune the solid state properties of $\{\text{Fe}_2\text{Co}_2\}$ complexes into a wide range of solvents.^{6g,9} In the case of the methyl functionalized square, the electron transfer was not associated with a first-order phase transition with a thermal hysteresis. The square complex shows a gradual conversion between paramagnetic $\{\text{Fe}^{\text{III}}_2\text{Co}^{\text{II}}_2\}$ state and diamagnetic $\{\text{Fe}^{\text{II}}_2\text{Co}^{\text{III}}_2\}$ state (Figure III-1 right), indicating the presence of significantly weaker elastic interactions between complexes in the crystal structure.^{6g,9}

The study presented in this chapter focuses on the structural investigations of tetranuclear $\{\text{Fe}_2\text{Co}_2\}$ square complexes (recently reported by our team)^{6c,g,9} and on the perturbation of ET process in functionalized $\{[(\text{Tp}^*)\text{Fe}(\text{CN})_3]_2[\text{Co}(\text{diMe bpy})_2]_2\}^{2+}$ system in solid state through changing the counter-anion X. While this kind of modification has been extensively studied for spin crossover complexes,¹⁰ the effect of counter-anion exchange has not been investigated so far for $\{\text{Fe}_2\text{Co}_2\}$ -based ET systems.

Herein, we present the synthesis and characterizations of four $\{\text{Fe}_2\text{Co}_2\}$ square complexes:

- (1) – $\{[(\text{Tp}^*)\text{Fe}(\text{CN})_3]_2[\text{Co}(\text{bpy})_2]_2\}(\text{OTf})_2 \cdot 3\text{H}_2\text{O} \cdot 3\text{DMF}$;^{6c}
- (2) – $\{[(\text{Tp}^*)\text{Fe}(\text{CN})_3]_2[\text{Co}(\text{diMe bpy})_2]_2\}(\text{OTf})_2 \cdot \text{H}_2\text{O} \cdot 2\text{DMF}$;^{6g,9}
- (3) – $\{[(\text{Tp}^*)\text{Fe}(\text{CN})_3]_2[\text{Co}(\text{diMe bpy})_2]_2\}(\text{ClO}_4)_2 \cdot 2\text{DMF}$;
- (4) – $\{[(\text{Tp}^*)\text{Fe}(\text{CN})_3]_2[\text{Co}(\text{diMe bpy})_2]_2\}(\text{OTs})_2 \cdot 6\text{DMF}$,

where bpy = 2,2'-bipyridine, diMe bpy = 4,4'-dimethyl-2,2'-bipyridine, Tp* = tris(3,5-dimethylpyrazol-1-yl)hydroborate, OTf = trifluoromethanesulfonate, OTs = *para*-toluenesulfonate, and DMF = N,N-

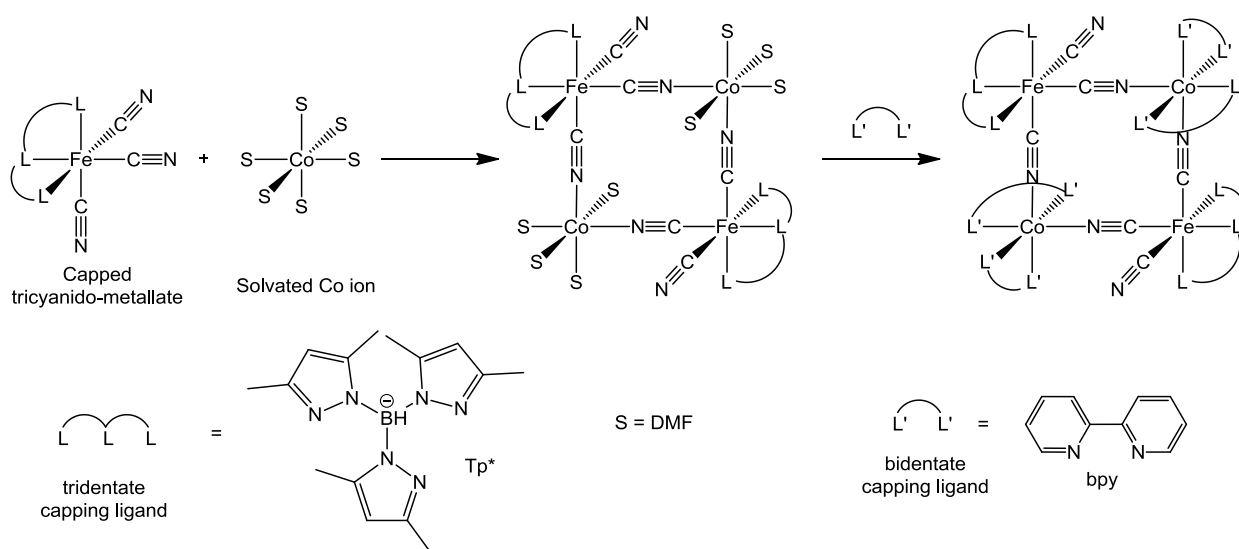
dimethylformamide. For compounds **1** and its functionalized analogue **2**, chosen as model systems displaying thermally and photoinduced ET, additional single-crystal X-ray diffraction experiments under continuous white light irradiation were performed. While for complexes **2**, **3** and **4**, the counter-anion effect on the ET behavior is discussed on the basis of structural, optical and magnetic characterizations.

III.2. Synthesis and characterizations of molecular $\{Fe_2Co_2\}$ squares

III.2.1. Synthetic strategy

The general synthetic approach adopted in the preparation of molecular Prussian blue analogues is to combine solvated metal cations with cyanido-metallate ions. In order to prevent polymerization, it is necessary to employ capping ligands, which will dictate the number and relative position of the available binding sites on the metal ions. A capped cyanido-metallate mononuclear building block may be added to a solution of solvated metal ions (or of a second capped metal ion precursor) resulting in the crystallization of cyanido-bridged molecular species whose topology is dependent upon the angle between the available binding sites of the cyanido-metallate ion. Considering cyanido-bridged square molecules, the capped metal ions should have at least two available *cis* binding sites to allow coordination with an angle of approximately 90° between the coordination vectors.

Scheme III-1. Schematic representation of the approach used to synthesize cyanido-bridged molecular $\{Fe_2Co_2\}$ squares, charges on metal ions and counter-ions are omitted.



To generate a family of closely related complexes, a common solvent and synthetic strategy were used systematically, since it is known that synthetic variations can affect the crystal structure and the properties of the final compounds. In this work, similarly to previous reports,^{6c,g} the synthetic procedure consisted (Scheme III-1) in reaction of the tricyanido-metallate precursor $(NEt_4)[(Tp^*)Fe(CN)_3]$ with DMF solution of corresponding Co^{2+} salt ($Co(OTf)_2$ for **1** and **2**, $Co(ClO_4)_2 \cdot 6H_2O$ for **3**, and $Co(OTs)_2 \cdot 6H_2O$ for **4**), followed by subsequent addition of bidentate bpy-based ligand (2,2'-bipyridine for **1** and 4,4'-dimethyl-2,2'-bipyridine for **2-4**). The crystallizations were carried out by subjecting the filtered reaction mixtures to vapor diffusion of diethyl ether.

Both bpy-based ligands and $\text{Co}(\text{ClO}_4)_2 \cdot 6\text{H}_2\text{O}$ are commercially available. The Co^{2+} salts such as $\text{Co}(\text{OTf})_2$ and $\text{Co}(\text{OTs})_2 \cdot 6\text{H}_2\text{O}$ were prepared by treatment of CoCO_3 with corresponding acid (see Section III.4 for detailed protocols). The cyanido-metallate $(\text{Et}_4\text{N})[(\text{Tp}^*)\text{Fe}(\text{CN})_3]$ complex has been prepared via ligand metathesis reactions. The literature reported method¹¹ was modified using iron(III) acetylacetonate ($\text{Fe}^{\text{III}}(\text{acac})_3$) precursor salt instead of iron(II) acetate ($\text{Fe}^{\text{II}}(\text{CH}_3\text{COO})_2$). Treatment of $\text{Fe}^{\text{III}}(\text{acac})_3$ with potassium tris(3,5-dimethylpyrazol-1-yl)-hydroborate (KTp^*) in methanol rapidly affords a red precipitate. Subsequent treatment of the obtained precipitate with an excess of tetraethylammonium cyanide in acetonitrile affords a red hydrated iron(III) cyanido-metallate complex of formula $(\text{Et}_4\text{N})[(\text{Tp}^*)\text{Fe}(\text{CN})_3] \cdot 2\text{H}_2\text{O}$. This compound was purified by flash silica gel column chromatography, to eliminate the large excess of uncoordinated cyanide.

III.2.2. FT-IR spectroscopic analyses

The stretching bands specific to cyanide groups ($\bar{\nu}_{\text{CN}}$) are sensitive to their coordination mode (bridging or terminal) and the oxidation states of the coordinated metal ions.¹² Therefore FT-IR spectroscopy is an efficient technique to study the self-assembly of Fe^{III} -based cyanide-containing building block with Co^{II} ions during the formation of molecular cyanide-bridged $\{\text{Fe}_2\text{Co}_2\}$ molecular squares. The FT-IR spectrum of the tricyanido-metallate precursor, $(\text{NEt}_4)[(\text{Tp}^*)\text{Fe}(\text{CN})_3]$, exhibits one strong $\bar{\nu}_{\text{CN}}$ stretching at 2115 cm^{-1} and another one of medium intensity corresponding to $\bar{\nu}_{\text{BH}}$ at 2549 cm^{-1} (Figure S.III-1).^{6c,g,9} The stretching band of the cyanide groups in cyanido-bridged $\{\text{Fe}_2\text{Co}_2\}$ molecular squares **1** - **4** (Figure S.III-2) at room temperature is shifted to higher energies and splitted into two bands: one at $2146 - 2151 \text{ cm}^{-1}$ characteristic of bridging cyanides within $\{\text{Fe}^{\text{III}}_{\text{LS}}(\mu\text{-CN})\text{Co}^{\text{II}}_{\text{HS}}\}$ units and a second one at $2116 - 2128 \text{ cm}^{-1}$ assigned to terminal cyanide.^{6c,g,9} The energy of $\bar{\nu}_{\text{BH}}$ stretching band remained almost unchanged ($2542 - 2546 \text{ cm}^{-1}$) suggesting that the electronic state of the Fe^{III} ion remained the same as the tricyanido-metallate precursor. In the FT-IR spectra of the final compounds contain a strong C=O band ($1663 - 1672 \text{ cm}^{-1}$) suggesting the presence of co-crystallized DMF molecules.

III.2.3. Structural investigations of molecular $\{\text{Fe}_2\text{Co}_2\}$ squares

In order to study the photo-induced ET on single crystals and to describe the structure of photo-induced state, a set of single crystal X-ray diffraction (XRD) studies was carried out under light irradiation at low temperatures for complexes **1** and **2**. Detailed studies of structural changes associated with thermally induced ET in complexes **1** and **2** were reported previously,^{6c,g,9} but were repeated with the aim to compare them with the photo-induced state.

Single crystals of compounds **1** - **4** were obtained using the same solvents and crystallization method. This technical aspect is important in establishing trends such as the counter-anion effect on the properties of cyanido-bridged $\{\text{Fe}_2\text{Co}_2\}$ molecular squares **2** - **4**.

III.2.3.1. $\{[(\text{Tp}^*)\text{Fe}(\text{CN})_3]_2[\text{Co}(\text{bpy})_2]_2\}[\text{OTf}]_2 \cdot 3\text{H}_2\text{O} \cdot 3\text{DMF}$ (**1**)

Complex **1** is the first reported example of cyanide-bridged $\{\text{Fe}_2\text{Co}_2\}$ molecular square that displays thermally and photo-induced ET associated reversible switching of magnetic and optical properties.^{6c} As the

result of the intramolecular electron transfer and intercomplex elastic interactions, it exhibits a first-order phase transition with an 18 K thermal hysteresis loop (between 186 and 168 K, at a temperature sweep rate of 0.4 Kmin⁻¹) between paramagnetic $\{Fe^{III}_2Co^{II}_2\}$ and diamagnetic $\{Fe^{II}_2Co^{III}_2\}$ states (Figure III-1 left).^{6c} Under white-light irradiation at 10 K, it is possible to convert the diamagnetic $\{Fe^{II}_2Co^{III}_2\}$ phase into a paramagnetic $\{Fe^{III}_2Co^{II}_2\}$ one. Also, it is important to mention that a metastable $\{Fe^{III}_2Co^{II}_2\}$ paramagnetic phase can be also trapped by fast cooling from 298 K to 10 K (at a temperature sweep rate > 50 Kmin⁻¹). The thermally quenched and photo-induced paramagnetic phases possess similar crystal structures and exhibit nearly identical magnetic data (Figure III-1 left).^{6c} However, the χT values are consistently lower in quenched phase (Figure III-1 left).^{6c} The crystal structures have previously been reported for the high temperature phase at 230 K, for the low temperature phase at 120 K and for the quenched phase at 90 K (after flash cooling to 90 K from 300 K).^{6c}

Table III-1. Unit-cell parameters, average metal-to-ligand bond lengths, and deformation of the Co coordination sphere for **1** under different experimental conditions.

	[[(Tp*) Fe(CN) ₃] ₂ [Co(bpy) ₂] ₂][OTf] ₂ ·3H ₂ O·3DMF (1)			
	230 K {Fe ^{III} ₂ Co ^{II} ₂ }	90 K quenched {Fe ^{III} ₂ Co ^{II} ₂ }	83 K light on {Fe ^{III} ₂ Co ^{II} ₂ }	84 K light off {Fe ^{II} ₂ Co ^{III} ₂ }
Crystal color	dark red	dark red	dark red	dark green
Crystal system	Triclinic	Triclinic	Triclinic	Triclinic
Space group	P $\bar{1}$	P $\bar{1}$	P $\bar{1}$	P $\bar{1}$
a, Å	13.6685(11)	13.560(2)	13.5151(7)	13.3171(9)
b, Å	13.8537(9)	13.7708(19)	13.7665(5)	13.4405(8)
c, Å	14.8485(12)	14.805(2)	14.7657(7)	14.7961(10)
α , °	99.514(3)	99.932(6)	99.894(2)	100.494(3)
β , °	93.620(3)	94.494(7)	94.611(2)	94.330(3)
γ , °	107.868(3)	107.213(6)	107.283(2)	106.519(3)
V, Å ³	2619.8(3)	2576.4(7)	2558.8(2)	2473.7(3)
<Fe-C>, Å	1.919	1.925	1.920	1.894
<Fe-N>, Å	2.002	2.019	1.997	2.041
<Co-N>, Å	2.122	2.083	2.111	1.935
Fe(1)···Co(1), Å	5.134	5.102	5.131	4.940
Fe(1)···Co(1)', Å	5.165	5.144	5.162	4.948
Fe···Fe, Å	7.652	7.584	7.642	7.201
Co···Co, Å	6.894	6.890	6.895	6.776
$\Sigma(N-Co-N)^a$, °	65.87	58.02	62.70	43.21

$$^a \Sigma = \sum_{i=1}^{12} |90 - \varphi_i|, \text{ where } \varphi_i \text{ are N-Co-N bond angles}$$

In order to describe the effects of the photo- and thermally induced ET transitions on the structure, in particular to compare photo-excited, thermally trapped and high temperature $\{Fe^{III}_2Co^{II}_2\}$ structures, the structure of **1** was refined in four different states at five different temperatures (Figure III-2, Tables III-1 and S.III-1). To avoid crystal fracture that often arises from a first-order phase transition, the following thermal treatment protocol was employed: the crystal was quenched from 300 to 90 K (1st crystal structure collected); warmed from 90 to 120 K (at 0.4 Kmin⁻¹), and kept at 120 K for 24 h to allow complete and slow conversion to the thermodynamic diamagnetic phase (2nd crystal structure collected); cooled to 84 K in the dark (3rd crystal structure collected); irradiated with white light ($P = 3 \text{ mW/cm}^2$) for 24 h at 83 K (4th crystal structure collected); and, finally, the crystal was rapidly removed from the cryostream, kept for 1 h at room temperature and placed back under cryostream, preliminary warmed to 230 K (5th crystal structure collected). First experimental trials showed that the crystals of **1** loose crystallinity over time even if they are kept in oil at 90 K. Therefore a red prismatic crystal of **1** was placed into a sealed glass capillary with a small amount of

mother liquor allowing to preserve the crystallinity and to perform the entire set of structural investigations on the same crystal.

Complex **1** crystallizes in the triclinic *P-1* space group without any symmetry change after thermally and photo-induced ET associated transitions (Tables III-1 and S.III-1). Adjacent Fe and Co ions reside in alternate corners and are linked by cyanide ligands to form $\{\text{Fe}(\mu\text{-CN})\text{Co}\}$ pairs; each Fe center bears one terminal cyanide ligand that adopts an *anti* orientation relative to the $\{\text{Fe}_2(\mu\text{-CN})_4\text{Co}_2\}$ plane. The Fe ions are coordinated by tridentate Tp* with facial configuration and two bidentate bpy ligands coordinate each Co ion (Figure III-2). The asymmetric unit is composed of a half of the complex cation, $[(\text{Tp}^*)\text{Fe}(\text{CN})_3\text{Co}(\text{bpy})_2]$, a free trifluoromethanesulfonate ion and co-crystallized solvent molecules (water and DMF). It is important to note that the solvation observed in the analyzed single crystal of **1**, $\{[(\text{Tp}^*)\text{Fe}(\text{CN})_3]_2[\text{Co}(\text{bpy})_2]_2\}[\text{OTf}]_2 \cdot 3\text{H}_2\text{O} \cdot 3\text{DMF}$, does not exactly match that of the bulk sample used for elemental analysis, which corresponded better to $\{[(\text{Tp}^*)\text{Fe}(\text{CN})_3]_2[\text{Co}(\text{bpy})_2]_2\}[\text{OTf}]_2 \cdot 2\text{H}_2\text{O} \cdot 4\text{DMF}$ and was in agreement with previous reports.^{6c,9}

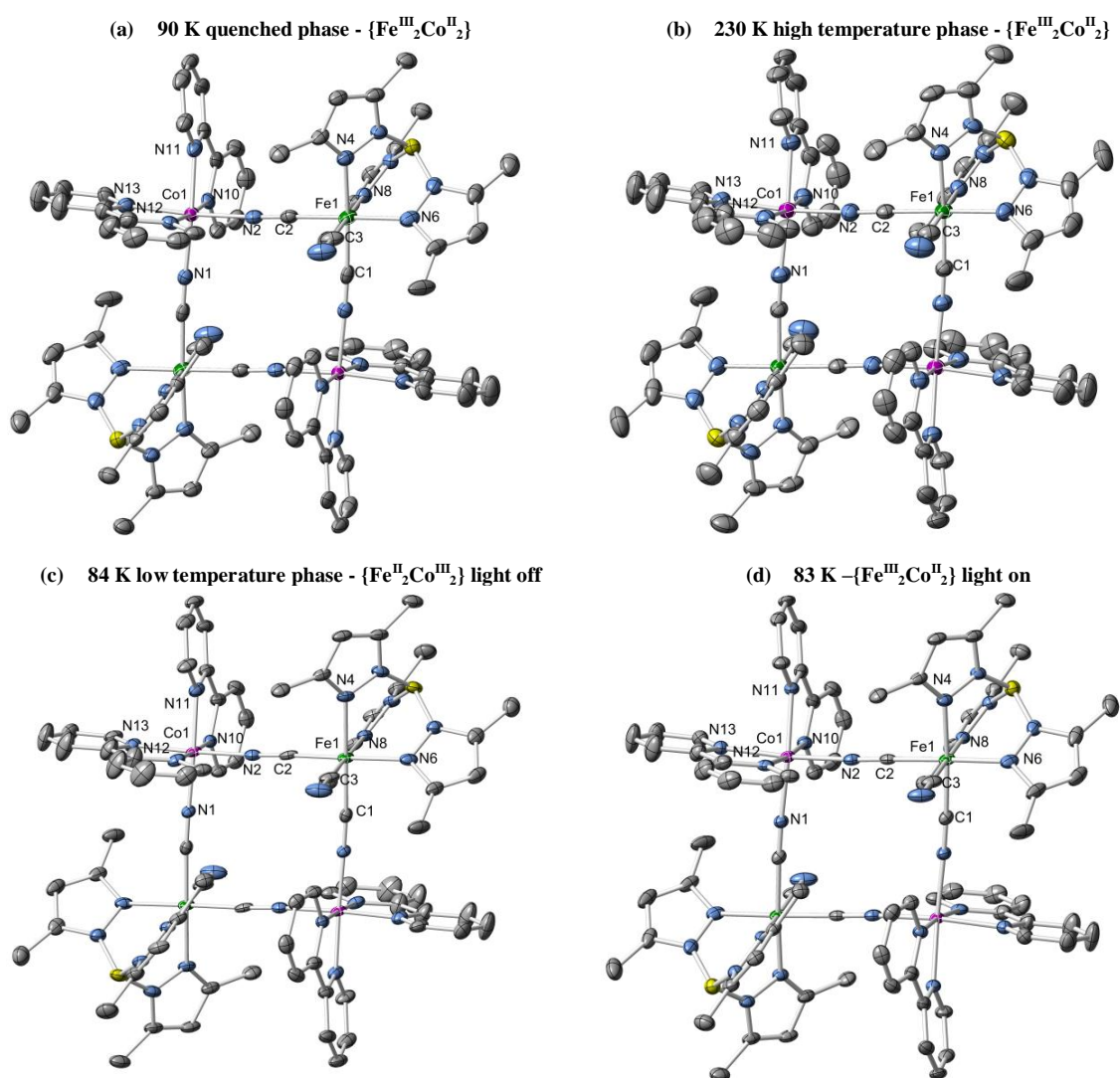


Figure III-2. Cationic portion of **1** in its: (a) quenched phase at 90K (quickly cooled from 300 to 90 K); (b) high temperature phase at 230 K; (c) low temperature phase collected at 84 K; and (d) photo-induced metastable paramagnetic phase at 83 K. Thermal ellipsoids are at 50% probability. All anions, lattice solvent molecules, and hydrogen atoms are omitted for clarity. Color scheme: C grey, Co pink, Fe green, N blue, B yellow.

As the result of the thermally and photo-induced ET transitions, differences were observed in unit cell parameters, in metal-to-ligand bond lengths and in coordination sphere deformation (especially around Co ions) (Tables III–1 and S.III–1).

At 230 K, single-crystal XRD studies showed that $\{Fe_2(\mu-CN)_4Co_2\}$ core is in paramagnetic state since it contains divalent Co ions in high spin (HS) configuration (confirmed by average Co-N bond distance of approximately 2.12 Å, Table III-1) and Fe^{III} ions, as results of the charge balance. The $\{Fe_2(\mu-CN)_4Co_2\}$ core is nearly planar since the Fe-C-N angles range between 175.5(4) and 178.8(5)° while Co-N-C angles range between 173.8(4) and 176.6(4)° (Table S.III-1). The separations between adjacent metal ions within the tetranuclear core through the cyanide bridges (Fe(1)···Co(1) and Fe(1)···Co(2)) are 5.13 and 5.16 Å, respectively. Nevertheless, the C(1)-Fe(1)-C(2) angle (85.52°), Fe···Fe (7.65 Å) and Co···Co (6.89 Å) distances indicate that **1** adopts a distorted square structure (Figure III-2b). The two Fe^{III} ions show a slightly distorted six-coordinated octahedral environment, FeC_3N_3 , formed by three pyrazol nitrogen atoms from the capping Tp^* ligand and three carbon atoms from bridging and terminal cyanide groups. The average Fe-C and Fe-N bond lengths are of 1.92 and 2.00 Å (Table S.III-1), respectively. The two Co^{II} ions exhibit a distorted octahedral environment, CoN_6 , which is formed by four bipyridine nitrogen atoms and two nitrogen atoms from bridging cyanide groups. The values of N-Co-N angles (Table S.III-1) in the coordination sphere of the HS Co^{II} ion depart significantly from orthogonality, as can be observed from the $\Sigma_{(N-Co-N)}$ parameter of 65.87° (Table III-1), that is the sum of the deviations from 90° of the 12 *cis* Φ angles in the coordination sphere of a metal ion (Co^{II} in our case) to estimate the distortion.¹³ The Co- N_{CN} bonds are slightly shorter (~2.09 Å) than Co- N_{bpy} bonds (2.13 – 2.15 Å). Hydrogen-bonding interactions along the *c* axis are present between the N(3) atom from terminal cyanide ligand, lattice water and one DMF molecule (N(3)···O(1)_w, 2.835 Å and O(1)_w···O(5)_{DMF}, 3.009 Å, Figure S.III-4b). Also, weak intermolecular π - π type interactions between several adjacent bpy ligands coordinated to Co^{II} ions occur along *b*-axis, with centroid-centroid distance between bpy planes of 3.879 Å (Figure S.III-3b).

Single-crystal X-ray studies of **1** obtained after rapid cooling (quenching) to 90 K (Figure III-2a, Tables III–1 and S.III–1) are in agreement with magnetic measurements (Figure III-1 left), suggesting that thermal quenching is not a very efficient way to obtain the metastable paramagnetic $\{Fe^{III}_{LS}(\mu-CN)Co^{II}_{HS}\}$ phase. The observed decrease of 0.04 Å in average Co–N distances (2.08 Å) and the decrease of the $\Sigma_{(N-Co-N)}$ parameter to 58°, originating from the change in N-Co-N angles, are consistent with the presence of a certain small amount of diamagnetic $\{Fe^{II}_{LS}(\mu-CN)Co^{III}_{LS}\}$ species. That may be indirectly confirmed by higher refinement factors of the crystal structure ($R_1 = 7.17\%$, $wR_2 = 20.67\%$) if compared to the structures of other phases observed on the same crystal of **1** (Table S.III-1).

The data collected at 120 K (after relaxation from quenched phase at 90 K) and at 84 K (after cooling from 120 K in the dark) (Figure III-2c, Tables III–1 and S.III–1) show a marked decrease in unit cell volume and in the average Co–N distance (ca. 0.18 Å), which is consistent with the conversion of paramagnetic $\{Fe^{III}_{LS}(\mu-CN)Co^{II}_{HS}\}$ into diamagnetic $\{Fe^{II}_{LS}(\mu-CN)Co^{III}_{LS}\}$. The values of N-Co-N angles in the coordination sphere of Co^{III} LS ion depart less from orthogonality ($\Sigma_{(N-Co-N)} = 43.2^\circ$) than those measured for Co^{II} HS. Although, the Fe coordination sphere showed much smaller differences comparing to Co site, the

change in the Fe charge is visible in the values of Fe-C bond lengths (ca. 1.92 Å at 230 K and ca. 1.89 Å at 84 K, Tables III–1 and S.III–1). Moreover, weaker intermolecular π - π type interactions are found between adjacent $\{\text{Fe}_2\text{Co}_2\}$ complexes (centroid-centroid distance between bpy planes increased to 4.142 Å, Figure S.III-3c), while the H-bonds decreased between the N(3) atom from terminal cyanide ligand, lattice water and one DMF molecule ($\text{N}(3)\cdots\text{O}(1)_w$, 2.681 Å and $\text{O}(1)_w\cdots\text{O}(5)_{\text{DMF}}$, 2.809 Å, Figure S.III-4c).

After the irradiation with the white light ($P = 3 \text{ mW/cm}^2$) at 83 K, it was possible to determine the structure of the photo-induced paramagnetic $\{\text{Fe}^{\text{III}}_{\text{LS}}(\mu\text{-CN})\text{Co}^{\text{II}}_{\text{HS}}\}$ phase (Figure III-2d). The conversion was achieved in less than an hour (the unit cell parameters after 1 h of irradiation were the same as those corresponding to 24 h of irradiation), but the crystal was kept under white light at 83 K for 24 h to allow full conversion to the paramagnetic state and to check the stability of the crystal under these experimental conditions. Similarly to previous structures, significant changes in Co coordination sphere occurred as the result of photo-induced ET associated with the conversion from the thermodynamic diamagnetic $\{\text{Fe}^{\text{II}}_{\text{LS}}(\mu\text{-CN})\text{Co}^{\text{III}}_{\text{LS}}\}$ phase to the metastable paramagnetic $\{\text{Fe}^{\text{III}}_{\text{LS}}(\mu\text{-CN})\text{Co}^{\text{II}}_{\text{HS}}\}$ phase. Thus, the average Co-N distance increased to 2.11 Å and the values of the N-Co-N angles show a more distorted coordination sphere around $\text{Co}^{\text{II}}_{\text{HS}}$ ion ($\Sigma_{(\text{N-Co-N})} = 62.7^\circ$) than the one observed in diamagnetic phase around the $\text{Co}^{\text{III}}_{\text{LS}}$ ion at 84 or 120 K (Tables III–1 and S.III–1). The average Fe-C and Fe-N bond lengths are of 1.92 and 2.00 Å (Table S.III-1), respectively. The average bond lengths, the intermetallic distances and bond angles within the $\{\text{Fe}_2(\mu\text{-CN})_4\text{Co}_2\}$ core in this light-induced paramagnetic state show that the obtained crystal structure is virtually identical to the one obtained at 230 K (Tables III–1 and S.III–1) and similar to the thermally quenched phase. Moreover, it confirms that light irradiation (even at 83 K) is more efficient to obtain the metastable paramagnetic phase at low temperatures than the thermal quenching, as also observed from magnetic measurements (Figure III-1 left).

III.2.3.2. $\{[(\text{Tp}^*)\text{Fe}(\text{CN})_3]_2[\text{Co}(\text{diMebpy})_2]_2\}(\text{OTf})_2\cdot\text{H}_2\text{O}\cdot 2\text{DMF}$ (**2**)

Complex **2** is a methyl functionalized version of complex **1** that preserved thermally and photo-induced ET associated with a change of magnetic and optical properties. It exhibits thermally reversible electron-transfer crossover at $T_{1/2} = 174 \text{ K}$ between paramagnetic $\{\text{Fe}^{\text{III}}_2\text{Co}^{\text{II}}_2\}$ and diamagnetic $\{\text{Fe}^{\text{II}}_2\text{Co}^{\text{III}}_2\}$ states (Figure III-1 right).^{6g,9} Under white-light irradiation at 10 K, it is possible to convert the diamagnetic $\{\text{Fe}^{\text{II}}_2\text{Co}^{\text{III}}_2\}$ phase into the paramagnetic $\{\text{Fe}^{\text{III}}_2\text{Co}^{\text{II}}_2\}$ one (Figure III-1 right).^{6g,9} The crystal structures have previously been reported for the high temperature phase at 250 K and for the low temperature phase at 120 K.^{6g,9}

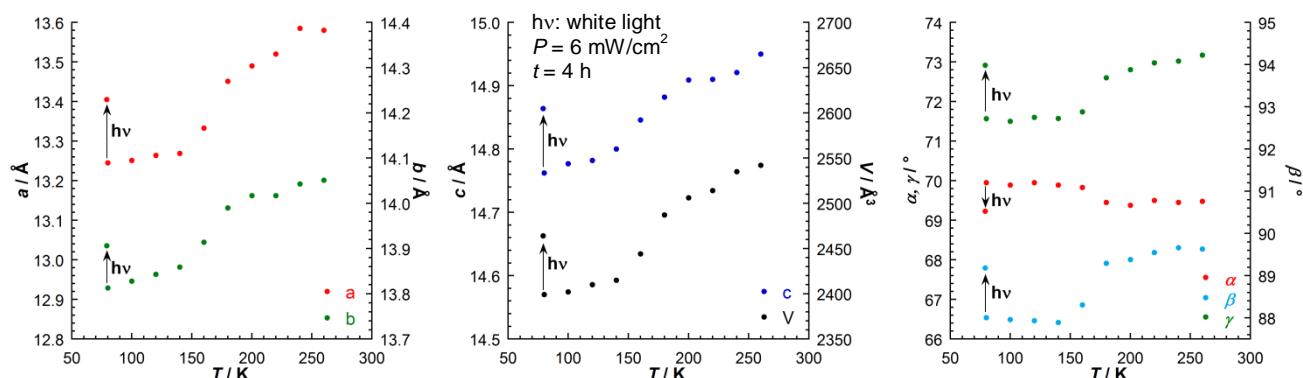
To study the photo-induced ET on a single crystal of **2** and to determine the structure of the photo-induced state, detailed XRD studies were performed at various temperatures and under white light irradiation in collaboration with Prof. Eric Collet at Institut de Physique de Rennes (Université Rennes 1). Thus, crystal structures of **2** were refined in three different states and at two different temperatures (Figure III-4, Tables III–2 and S.III–2).

In the case of compound **2** it was possible to record the variation of the lattice parameters versus temperature (Figure III-3), since there the ET is not associated with a structural first order phase transition (that could fracture the crystal).

Table III-2. Unit-cell parameters, average metal-to-ligand bond lengths, metal-to-metal distances and deformation of the Co coordination sphere for **2** under different experimental conditions, for **3** at 100 K and for **4** at 120 K.

	(2)		(3)	(4)
	240 K	80 K	80 K	120 K
	$\{Fe^{III}_2Co^{II}_2\}$	light off $\{Fe^{II}_2Co^{III}_2\}$	light on $\{Fe^{III}_2Co^{II}_2\}$	$\{Fe^{III}_2Co^{II}_2\}$
Crystal system	Triclinic	Triclinic	Triclinic	Triclinic
Space group	$P\bar{1}$	$P\bar{1}$	$P\bar{1}$	$P\bar{1}$
a, Å	13.585(10)	13.248(10)	13.405(10)	13.084(2)
b, Å	14.041(10)	13.813(10)	13.906(10)	13.958(2)
c, Å	14.921(10)	14.761(10)	14.864(10)	14.647(3)
α , °	69.503(6)	69.949(7)	69.232(7)	113.044(7)
β , °	89.664(6)	88.004(7)	89.180(7)	91.226(8)
γ , °	73.024(6)	71.569(7)	72.920(7)	105.495(8)
V, Å ³	2535.0(3)	2399.1(3)	2464.0(3)	2348.0(7)
$\langle Fe-C \rangle$, Å	1.926	1.882	1.920	1.920
$\langle Fe-N \rangle$, Å	1.990	2.035	1.989	2.003
$\langle Co-N \rangle$, Å	2.127	1.926	2.115	2.130
Fe(1)··Co(1), Å	5.100	4.889	5.112	5.139
Fe(1)··Co(1)', Å	5.114	4.895	5.104	5.060
Fe··Fe, Å	7.148	6.782	7.088	7.073
Co··Co, Å	7.296	7.052	7.356	7.350
$\Sigma(N-Co-N)^a$, °	58.5	35.9	59.4	59.61

$$^a \Sigma = \sum_{i=1}^{12} |90 - \varphi_i|, \text{ where } \varphi_i \text{ are } N-Co-N \text{ bond angles}$$

**Figure III-3.** Thermal evolution on cooling of lattice parameters for complex **2**.

Similarly to the χT product (from magnetic measurements Figure III-1 right) during the ET associated $\{Fe^{III}_2Co^{II}_2\} \rightarrow \{Fe^{II}_2Co^{III}_2\}$ thermal crossover, a decrease in the values of lattice parameters was observed upon cooling, except for the α angle that increased (Figure III-3). After white light irradiation at 80 K ($P = 6 \text{ mW/cm}^2$, $t = 4 \text{ h}$) due to the photo-induced ET, an increase of lattice parameters was observed, except the α angle that decreased. The values of lattice parameters observed in the photo-induced metastable paramagnetic phase are similar to those measured for thermodynamic paramagnetic phase above 200 K and extrapolate in an almost linear trend the thermal contraction of the unit cell.

X-ray structural analysis performed at 240 and 80 K (before and after white light irradiation) (Figure III-4, Tables III-2 and S.III-2) show that compound **2** crystallizes in the triclinic $P\bar{1}$ space group with one molecule in the unit cell. The structure of the central fragment is essentially similar to that in compound **1** (Figure III-2), with a square shaped core, in which Fe and Co ions are alternately bridged by cyanide ions. In the crystal packing, trifluoromethanesulfonate counter anions, lattice DMF and H_2O molecules are also

present. In structures of **2**, the cationic $\{\text{Fe}_2(\mu\text{-CN})_4\text{Co}_2\}$ core is nearly planar (Figure III-4). The tridentate Tp^* ligand facially coordinates to the Fe ion, and the remaining coordination sites are occupied by three cyanide carbon atoms. Two of the three cyanide ions from the Fe sites coordinate in bridging mode to the Co ions, while the free non-bridging cyanide groups adopt an *anti* orientation relative to the $\{\text{Fe}_2(\mu\text{-CN})_4\text{Co}_2\}$ plane. The coordination sphere around each Co ion is completed by two bidentate diMeby ligands.

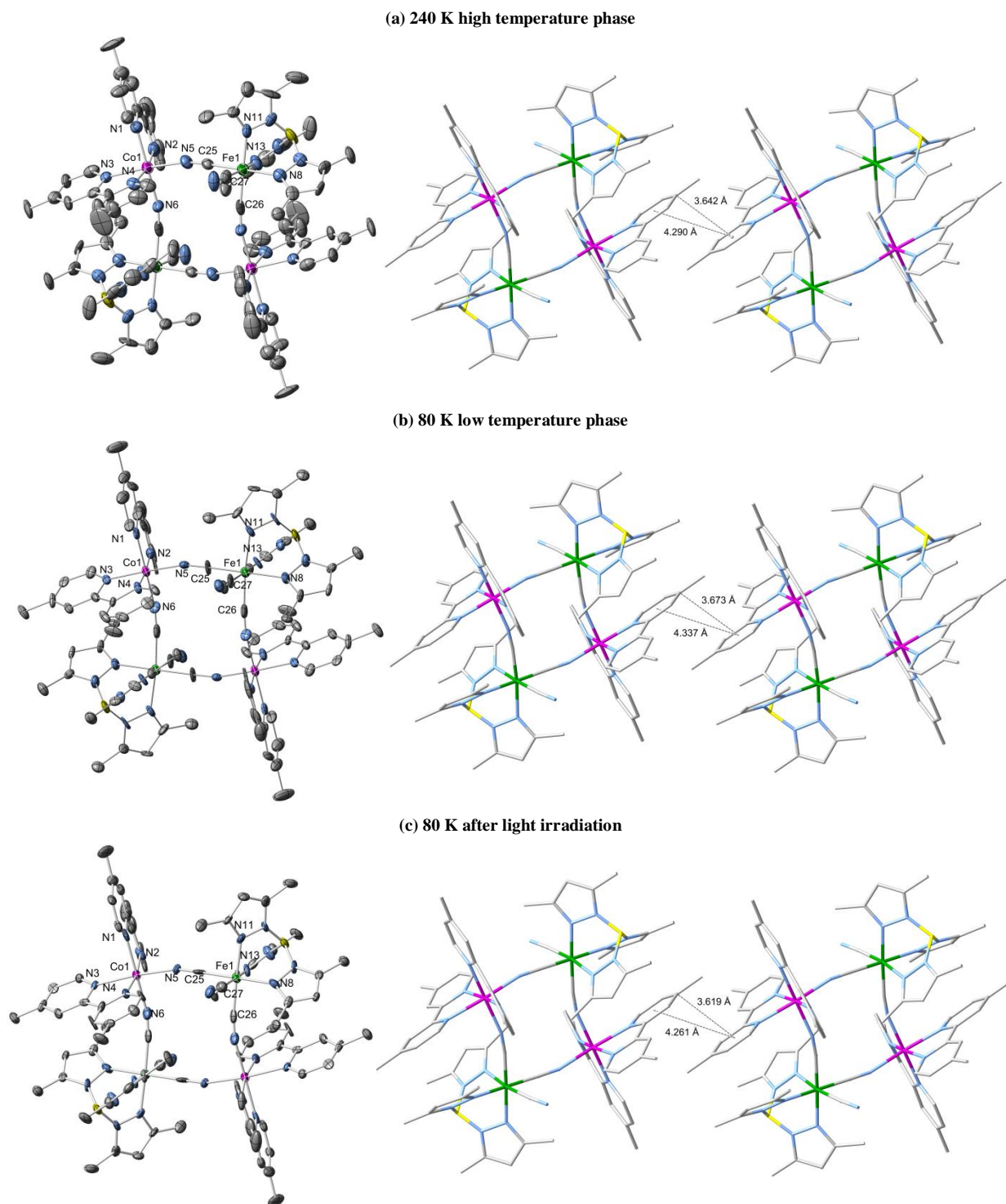


Figure III-4. (left) Cationic portion of **2** in its: (a) high temperature phase at 240 K; (b) low temperature phase collected at 80 K; and (c) photo-induced metastable paramagnetic phase at 80 K. Thermal ellipsoids are at 50% probability. (right) Packing arrangement illustrating π - π interactions present between adjacent complexes of **2** along the crystallographic *b*-direction under different experimental conditions. All anions, lattice solvent and hydrogen atoms are eliminated for clarity.

At 240 K (Figure III-4a), the average Fe-C (1.926 Å), Fe-N (1.990 Å) and Co-N (2.127 Å) bond distances (Tables III-2 and S.III-2) are in close agreement with those expected for Co^{II} HS and Fe^{III} LS metal ions, considering the valence sum bond analysis and charge compensation. The separations between adjacent metal ions within the cyanide-bridged units (Fe(1)··Co(1) and Fe(1)··Co(2) of 5.10 and 5.11 Å, respectively), and the C(25)-Fe(1)-C(26) (90.8°), N(5)-Co(1)-N(6) (89.7°), N(5)-C(25)-Fe(1) (177.3°) bond angles suggest that the tetranuclear core in **2** has a nearly planar square shape. Nevertheless, interatomic Fe··Fe (7.15 Å) and Co··Co (7.3 Å) distances and Co-N-C angles ranging between 164.0 and 166.6° show that the $\{Fe_2(\mu-CN)_4Co_2\}$ has a significantly distorted geometry (Figure III-4a) in comparison with **1**. The values of the N-Co-N angles (Table S.III-2) show a distorted coordination sphere around the HS Co^{II} ions, as judged by the $\Sigma_{(N-Co-N)}$ parameter of 58.5° (Table III-2).

After cooling to 80 K in the dark, the structure of the green crystal (Figure III-4b) reveals shorter average Fe-C and Co-N bond distances of 1.882 and 1.926 Å, respectively (Tables III-2 and S.III-2). The shorter average Co-N bond distances by ca. 0.2 Å are characteristic of Co^{III} LS ions formed after thermally induced ET associated with the $\{Fe^{III}_2Co^{II}_2\} \rightarrow \{Fe^{II}_2Co^{III}_2\}$ conversion. While the changes in average Fe-C and Fe-N bond distances at 80 K differ only slightly (by ~ 0.03 Å) from those observed at 240 K and correspond well to Fe^{II} LS ions (Table III-2). As the result of metal-to-ligand bond length decrease, the interatomic Fe··Fe (6.78 Å) and Co··Co (7.05 Å) distances inside the $\{Fe_2(\mu-CN)_4Co_2\}$ core shortened as well. The change in values of the N-Co-N angles shows a less distorted coordination sphere for the Co^{III} LS ion ($\Sigma_{(N-Co-N)} = 35.9^\circ$) than that measured for the Co^{II} HS site at 240 K.

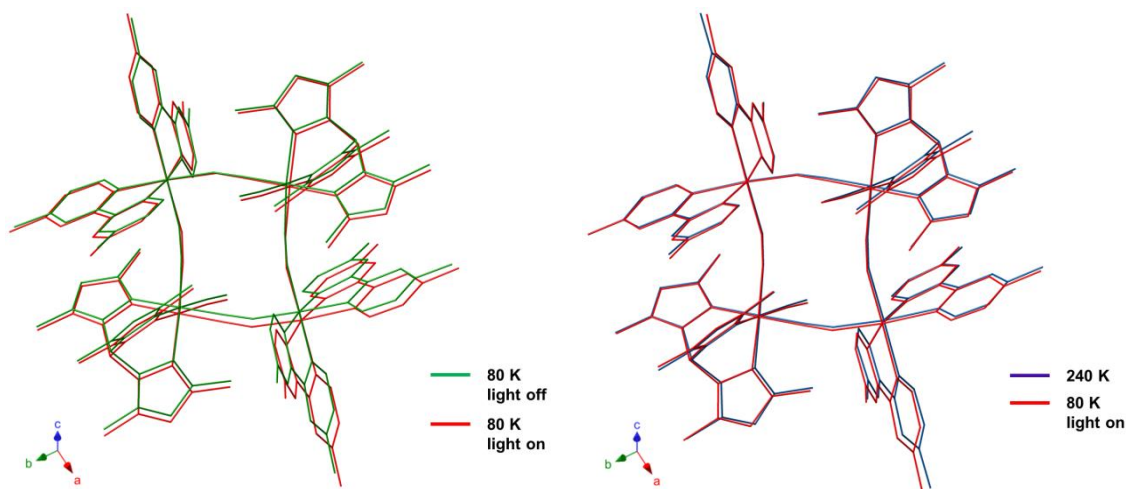


Figure III-5. Superimposed structures of the $\{Fe_2(\mu-CN)_4Co_2\}$ cationic core in **2** emphasizing the differences observed under different experimental conditions. (left) Differences observed before and after white light irradiation at 80 K ($P = 6$ mW/cm², $t = 4$ h). (right) Comparison of the structures corresponding to the thermodynamic high temperature paramagnetic phase and to the metastable light induced paramagnetic state.

Many structural parameters changed after the irradiation with white light at 80 K ($P = 6$ mW/cm², $t = 4$ h). Firstly, changes were observed from the unit cell determination measurements (Figure III-3). Thus, most of the lattice parameters increased in value (except the α angle that decreased) if compared with those measured at 80 K in the dark. Besides the changes in the unit cell size, the increase of the average Co-N distance from 1.926 Å (at 80 K in the dark) to 2.115 Å was observed after white light irradiation, as the result of photo-induced ET associated with the $\{Fe^{II}_2Co^{III}_2\} \rightarrow \{Fe^{III}_2Co^{II}_2\}$ conversion. A comparison of the

structures before and after white light irradiation can be found in the Figure III-5 left. In the photo-induced phase, the average Fe-C and Fe-N bond distances as well as intermetallic Fe(1) \cdots Co(1) and Fe(1) \cdots Co(2) separations along the cyanide bridge showed values very close to those measured at 240 K (Table III-2). Nevertheless, the cationic {Fe₂(μ -CN)₄Co₂} core at 80 K after white light irradiation has a slightly different geometry from the one determined at 240 K (Figure III-5 right). Thus, the interatomic Fe \cdots Fe (7.09 Å) distance is shorter while Co \cdots Co (7.36 Å) one is longer (Table III-2). The N-Co-N bond angles show a slightly more distorted coordination sphere around Co (Table III-2). Moreover, Fe-C-N and C-Fe-C bond angles have values that are higher or smaller than those observed at 240 K by 1-3°.

Similarly to **1**, square molecules form weak intermolecular π - π type interactions between several adjacent diMebpy molecules coordinated to Co^{II} ions along the *b*-axis in crystal packing of **2** (Figures III-4 and III-6 top), but {Fe₂Co₂} complexes are more separated than in **1** (Figure S.III-3). A steric hindrance generating slightly weaker π - π interactions, i.e. longer overlap distances, is induced by the methyl groups present at the 4- and 4'- positions on the bipyridine ligands. Consequently, the bipyridine centroid-to-centroid distances in complex **1** vary from 3.88 to 4.14 Å (Figure S.III-3) while in complex **2** they are ranging between 4.26 and 4.34 Å (Figure III-4 right), suggesting the presence of significantly weaker elastic interactions between complexes in the crystal structure.^{6g,9} Therefore, the square complex **2** shows a Boltzmann conversion between the paramagnetic excited {Fe^{III}₂Co^{II}₂} state and diamagnetic {Fe^{II}₂Co^{III}₂} ground state (Figure III-1 right). Besides intermolecular π - π interactions, the non-bridging cyanides are involved in H-bond with the co-crystallized water molecule, which is also H-bound to a DMF molecule. The existence of H-bonds was deduced from N \cdots O_w and O_w \cdots O_{DMF} distances of 2.964 and 3.044 Å, respectively, at 240 K. In the low temperature diamagnetic phase before white light irradiation, these contacts are slightly shorter (2.930 and 3.014 Å, respectively), while in the light induced paramagnetic phase, they increase above the 240 K values to 2.971 and 3.057 Å, respectively. Complex **1** shows similar H-bonds, except that the measured values, corresponding to this kind of contacts, are about 0.2 Å shorter (Figure S.III-4).

III.2.3.3. {[Tp*]Fe(CN)₃]₂[Co(diMebpy)₂]₂}(ClO₄)₂·2DMF (**3**)

X-ray crystal structure analysis of complex **3** was performed at 250 and 100 K (Tables III-2 and S.III-3). No structural changes specific to a thermally induced intramolecular ET were observed on cooling the red crystal of **3** from 250 to 100 K (Table S.III-3), suggesting that this compound is always in a paramagnetic {Fe^{III}₂Co^{II}₂} state. Complex **3** crystallizes in the triclinic *P*-1 space group with a square-shaped tetranuclear core, in which Fe and Co ions are alternately bridged by cyanide ions in the same way as in **1** and **2**. The unit cell consists of a centro-symmetric cyanido-bridged {Fe₂Co₂} square, two free perchlorate ions and two DMF molecules. The structure of the cationic {Fe₂(μ -CN)₄Co₂} part at 100 K is showed in Figure III-6 left.

The Fe ions are coordinated by tridentate Tp* ligand with a facial configuration, and the remaining coordination sites are occupied by three cyanide carbon atoms. Two of these three cyanide ions bridge to Co ions, while the remaining one coordinates only to Fe. The two bidentate diMebpy ligands chelate each Co ion, and the bridging cyanide groups occupy the *cis* positions of the Co sites (Figure III-6 left). The average Co-N bond lengths of about 2.13 Å at 100 K and 250 K are characteristic of Co^{II} HS ions, while the average

Fe-C (1.92 Å) and Fe-N (2.00 Å) (Table III-2) are similar to those measured for Fe^{III} LS ions in the paramagnetic states of **1** and **2**.

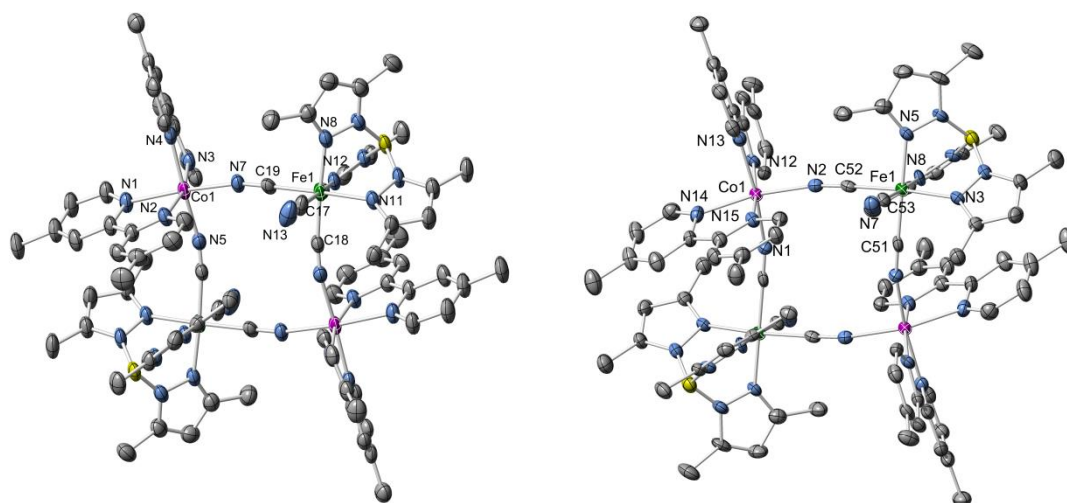


Figure III-6. (left) The structure of the complex cation in **3** at 100 K. (right) The structure of the complex cation in **4** at 120 K. Thermal ellipsoids are at 50% probability. All anions, lattice solvent molecules, and hydrogen atoms are omitted for clarity. Color scheme: C grey, Co pink, Fe green, N blue, B yellow.

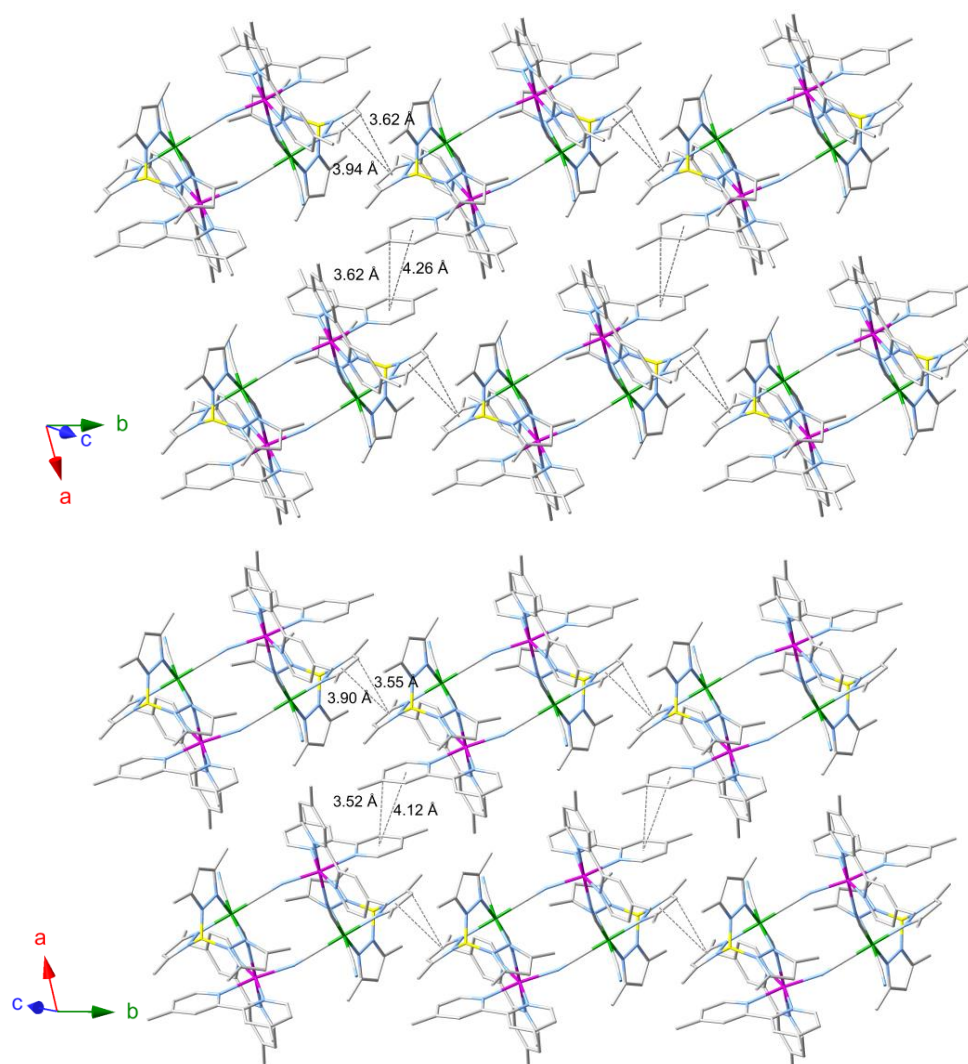


Figure III-7. Perspective view of the crystal packing of **2** at 80 K in light-induced paramagnetic state (top) and **3** at 100 K (bottom) illustrating π - π interactions between molecular squares. Counter anions, hydrogen atoms and solvent molecules are omitted for clarity.

The $\{\text{Fe}_2(\mu\text{-CN})_4\text{Co}_2\}$ core in **3** adopts a distorted square geometry similar to the one observed for **2** in its paramagnetic state. Nevertheless, the bond-angles, N(5)-Co(1)-N(7) ($89.27(14)^\circ$) and C(18)-Fe(1)-C(19) ($91.08(16)^\circ$), are close to orthogonality. The cyanide bridges are notably bent especially at the cobalt sites, both Co-N-C angles are $165.2(3)$ and $165.5(4)^\circ$, while the Fe-C-N angles range between $172.7(3)$ and $178.7(4)^\circ$ (Table S.III-3). The two Fe–CN–Co edges are quasi identical since the Fe(1) \cdots Co(1) and Fe(1) \cdots Co(2) distances are 5.139 and 5.104 Å, respectively, while the Fe \cdots Fe and Co \cdots Co distances are 7.073 and 7.350 Å. Both iron and cobalt ions are six-coordinate. The FeN₃C₃ environment is less distorted than the CoN₆ surrounding. The distortion parameter (Σ) for the Co^{II} HS ion has a value of 59.6° and is very close to the one measured in **2** for the light-induced paramagnetic structure.

Weak intermolecular π - π type interactions are present between adjacent diMeby ligands coordinated to Co^{II} ions and between adjacent pyrazole rings from the capping Tp* ligand on Fe^{III} site along the crystallographic *b* axis. These weak interactions lead to a supramolecular 2D-like structure with centroid-to-centroid distances between diMeby planes of 4.12 Å and between pyrazole planes of 3.94 Å (Figure III-7 bottom). The distances corresponding to intermolecular interactions in **3** are slightly shorter than those measured for complex **2** in its light-induced paramagnetic $\{\text{Fe}^{\text{III}}_2\text{Co}^{\text{II}}_2\}$ state at 80 K (Figure III-7 top). Since complex **3** at 100 K is in the $\{\text{Fe}^{\text{III}}_2\text{Co}^{\text{II}}_2\}$ paramagnetic state, according to structural analysis, the light-induced paramagnetic $\{\text{Fe}^{\text{III}}_2\text{Co}^{\text{II}}_2\}$ state of **2** was chosen for comparison. The shorter intermolecular contacts between the adjacent capping ligands in the crystal packing of **3** may be explained by the presence of a smaller ClO₄⁻ counter-anion. As can be observed from the unit cell volumes measured for **2** (2464.0 Å³) and **3** (2348.0 Å³), a denser crystal packing is formed in **3** (Table III-2). Therefore, a too dense crystal packing caused by a smaller counter-anion can be considered as one of the factors that blocks the thermally induced ET.

III.2.3.4. $\{[(\text{Tp}^*)\text{Fe}(\text{CN})_3]_2[\text{Co}(\text{diMeby})_2]_2\}(\text{OTs})_2 \cdot 6\text{DMF}$ (**4**)

The structural analysis of a dark red crystal of **4** was performed at 120 K after cooling it from 250 K at 1 K·min⁻¹. Complex **4** crystallizes in the same triclinic *P*-1 space group, as previously reported for complexes **1**, **2** and **3**. The crystal structure consists of a discrete cyanide-bridged tetranuclear cationic core (Figure III-6 right), two *para*-toluenesulfonate anions (OTs⁻) and six co-crystallized DMF molecules.

The analysis of the average Co-N (2.12 Å), Fe-C (1.925 Å) and Fe-N (1.997 Å) bond distances (Tables III-2 and S.III-4) shows that the $\{\text{Fe}_2(\mu\text{-CN})_4\text{Co}_2\}$ core is composed of Co^{II} HS and Fe^{III} LS ions. The geometry of the $\{\text{Fe}_2(\mu\text{-CN})_4\text{Co}_2\}$ square is significantly more distorted than in **2** or **3**. Even though the two Fe–CN–Co edges are quasi identical (the Fe(1) \cdots Co(1) and Fe(1) \cdots Co(2) distances are 5.118 and 5.127 Å, respectively), the Fe \cdots Fe and Co \cdots Co distances within the core are significantly different at 7.489 and 6.992 Å, respectively (Table III-2). The cyanide bridges are bent especially at the cobalt sites, both Co-N-C angles are $163.7(5)$ and $168.5(5)^\circ$ (Table S.III-4). The N-Co-N angles (Table S.III-4) reveal a more distorted coordination sphere around the HS Co^{II} ion in **4** than in **2** or **3**, as it can be observed from the $\Sigma_{(N\text{-Co-N})}$ parameter of 69.36° (Table III-2).

The presence of large OTs⁻ counter-anions and six DMF per molecular square in the crystal packing of **4** contributes to a better separation of tetranuclear $\{\text{Fe}_2(\mu\text{-CN})_4\text{Co}_2\}$ units. Thus, no π - π type interactions are

observed between adjacent diMebpy ligands coordinated to the Co^{II} ions, while the centroid-to-centroid distances between pyrazole planes (from capping Tp^* ligand on Fe^{III} sites) increased to 4.58 Å (Figure III-8).

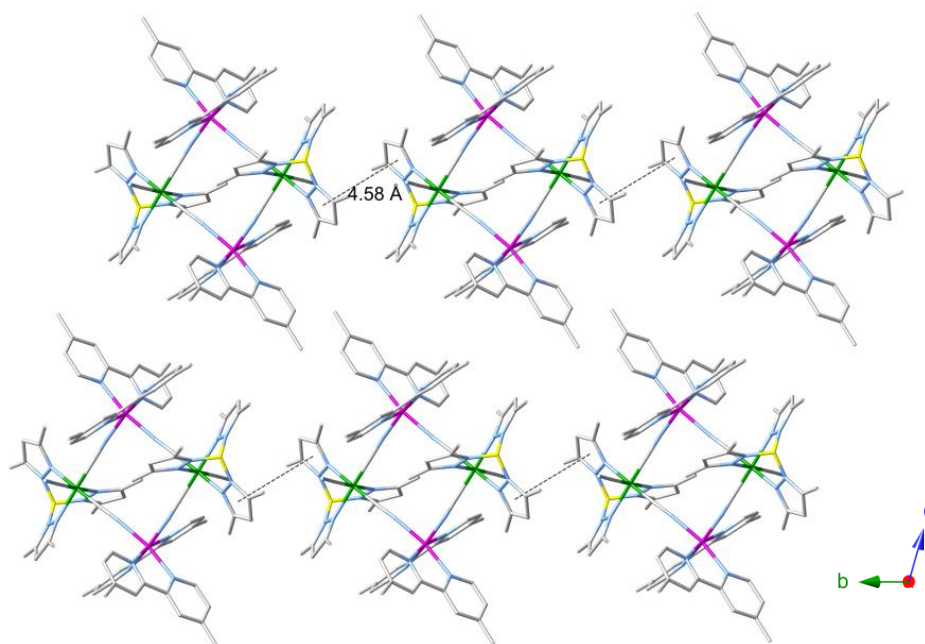


Figure III-8. Perspective view of the crystal packing of **4** at 120 K, illustrating π - π interactions between molecular squares. Counter anions, hydrogen atoms and solvent molecules are omitted for clarity.

III.2.3.5. Structural comparison of compounds (**2**), (**3**) and (**4**): influence of the counter-anion

The aim for the preparation of compounds **3** and **4** with counter-anions different than the one in **2** was to study the counter-anion effect on the ET process in functionalized $\{[(Tp^*)Fe(CN)_3]_2[Co(diMebpy)_2]\}^{2+}$ system in solid state. Studies of the counter-anion effect over the ET properties of $\{Fe_2Co_2\}$ squares have not been reported so far. To synthesize a family of closely related complexes, $\{[(Tp^*)Fe(CN)_3]_2[Co(diMebpy)_2]\}X_2$ (preferably varying only in the choice of X), common solvent and synthetic procedures were applied, since synthetic variations can affect the crystal structure and the properties of the final compounds. The solubility and the reactivity of the chosen starting materials allowed successful preparation of a series of $\{[(Tp^*)Fe(CN)_3]_2[Co(diMebpy)_2]\}X_2$ complexes (where X = OTf for **2**; ClO_4^- for **3**; and OTs for **4**).

At the first sight the overall shape of the $\{[(Tp^*)Fe(CN)_3]_2[Co(diMebpy)_2]\}^{2+}$ system in **2**, **3** and **4** appears to be very similar since the Fe and Co ions are alternately bridged by cyanide ions to form a square shaped core, in which, the tridentate Tp^* ligand facially chelates the Fe ion, while the coordination sphere around each Co ion is completed by two bidentate diMebpy ligands. But even with the ligands remaining the same across the three crystallographically characterized compounds, the ET process was observed only in the original compound **2**. Thus, structural perturbations inside the crystal packing such as the change of the molecular shape and weaker/stronger intermolecular interactions induced by anion exchange can either facilitate or inhibit the intramolecular ET in cyanido-bridged $\{Fe_2Co_2\}$ molecular squares.

As can be observed from the compared crystallographic data for **2**, **3** and **4** showed in Table III-2 and Figure III-9, the cationic core in **3** has a structural geometry very similar to the one observed for **2** in both light-induced or thermodynamic paramagnetic states. Therefore the absence of the intramolecular ET in **3**

may be explained by the presence of shorter intermolecular contacts (and as result stronger intermolecular interactions) between adjacent square molecules. Adjacent diMe bpy ligands coordinated to the Co^{II} ions and adjacent pyrazole rings from capping Tp^* ligand on Fe^{III} site form π - π type interactions (Figure III-7 bottom). The measured values for these short contacts are slightly shorter in **3** than **2** (Figure III-7 top). But the presence of weaker intermolecular interactions in **4** (Figure III-8) with longer separations between the square molecules than in **2** and **3** might bring to a conclusion that the denser crystal packing caused by a smaller anion is not the only parameter that influences the ET process. Indeed, no thermally induced ET was observed in **4**, according to the structural analysis. Both metal ions at low temperature show bond-lengths corresponding to the Co^{II} HS and Fe^{III} LS ions, suggesting that **4** is always in paramagnetic state. In contrary to **3**, the square core in **4** has a significantly more distorted geometry than in **2** (Table III-2 and Figure III-9). The $\{[(\text{Tp}^*)\text{Fe}(\text{CN})_3]_2[\text{Co}(\text{diMe bpy})_2]_2\}^{2+}$ system in **4** shows a significantly more distorted Co^{II} coordination sphere ($\Sigma_{(\text{N-Co-N})} = 69.36^\circ$, Table III-2) and significantly bent Co-N-C angles ($163.7(5)$ and $168.5(5)^\circ$, Table S.III-4). The presence of larger anions contributes to a bigger unit cell volume, a better separation between squares and much weaker intermolecular interactions. No significant short contacts are observed between adjacent diMe bpy ligands coordinated to the Co^{II} ions in **4**, while the centroid-to-centroid separation between pyrazole rings (from capping Tp^* ligand on Fe^{III} sites) is also quite large about 4.58 \AA (Figure III-8). Thus, the crystal structure of compound **4** differs from others by a more distorted tetranuclear core and by weaker intermolecular interactions. In the case of compound **4**, the organization inside the crystal, governed by large OTs^- anions, influences the geometrical structure of the heterometallic core and the final ET properties.

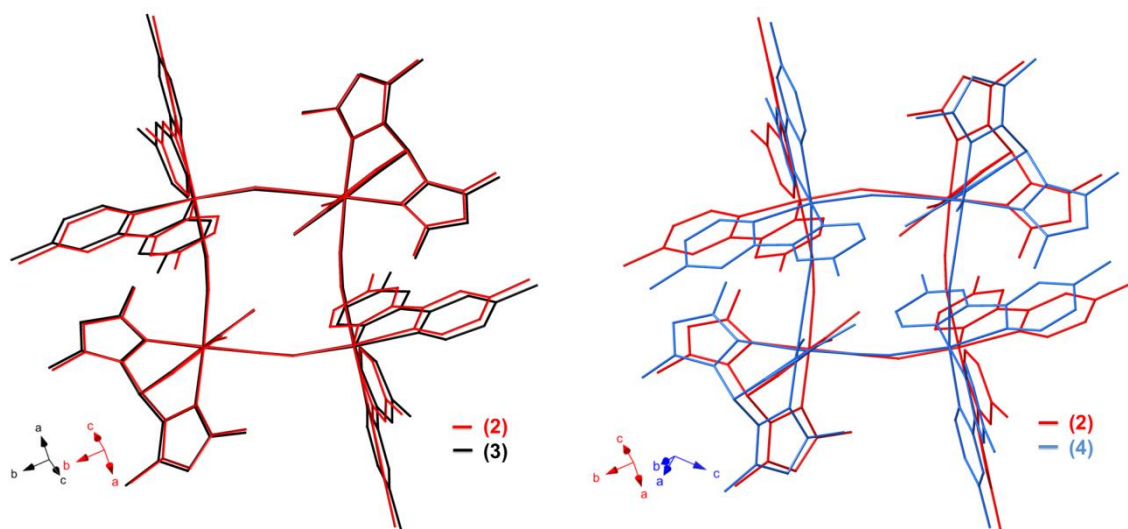


Figure III-9. Superimposed structures of the $\{\text{Fe}_2(\mu\text{-CN})_4\text{Co}_2\}$ cationic cores emphasizing the structural differences. (left) Comparison of the structures corresponding to the paramagnetic light-induced $\{\text{Fe}^{\text{III}}_2\text{Co}^{\text{II}}_2\}$ phase in **2** at 80 K and always paramagnetic **3** at 100 K. (right) Comparison of the structures corresponding to the paramagnetic light-induced $\{\text{Fe}^{\text{III}}_2\text{Co}^{\text{II}}_2\}$ phase in **2** at 80 K and always paramagnetic **4** at 120 K.

Prepared compounds differ not only by the counter-anion, structure of the tetranuclear core and intermolecular short contacts, but by the solvation inside the crystal packing, as well. In the structure of **2**, there are present two DMF molecules and a water molecule, while in the packing of **3** and **4** only DMF molecules are present (two DMF molecules in **3** and six DMF molecules in **4**). Since the applied synthetic and crystallization methods were identical for the three compounds, it appears that the nature of the counter-

anion influences the solvation inside the crystal packing. Indeed the nature of the co-crystallized solvents and the resulting intermolecular interactions between different molecules modify the properties of the final compounds. Thus, another important difference between **2**, **3** and **4** is the presence of water molecule in **2** which forms H-bonds with the nitrogen atom from the non-bridging cyanides (on Fe sites) and with one of the DMF molecules. Similar H-bonding interactions are present in **1**. The intramolecular electron transfer observed in these systems is a redox process dependent on the redox potentials of the Fe and Co sites. Apparently, the presence of short intermolecular contacts, such as an H-bond with a water molecule, modifies the electronic density and the redox potential around the Fe ion, allowing the occurrence of the intramolecular ET.

The performed structural analysis of compounds **2**, **3** and **4** showed that the counter-anion exchange around the $\{[(Tp^*)Fe(CN)_3]_2[Co(diMebpy)_2]_2\}^{2+}$ system affects the occurrence of the ET process. The perturbations induced by counter-anion modification influence several parameters such as the geometry of the $\{Fe_2(\mu-CN)_4Co_2\}$ core, the intermolecular weak interactions and the solvation. Therefore, the obtained data allows concluding that ET process in cyanido-bridged molecular $\{Fe_2Co_2\}$ squares is strongly dependent on the structure of the tetranuclear core that is influenced by the environment it is placed in.

III.2.4. Optical reflectivity studies

In order to check the optical properties of the obtained complexes and an eventual ET transfer induced color change, solid state reflectivity spectra were collected in the spectral range between 500 and 1000 nm, at different temperatures. As the reflectivity data for **1** and **2** are very similar and have already been reported,^{6c,6g,9} only the temperature dependent reflectivity spectra of **3** and **4** in comparison with **2** will be described.

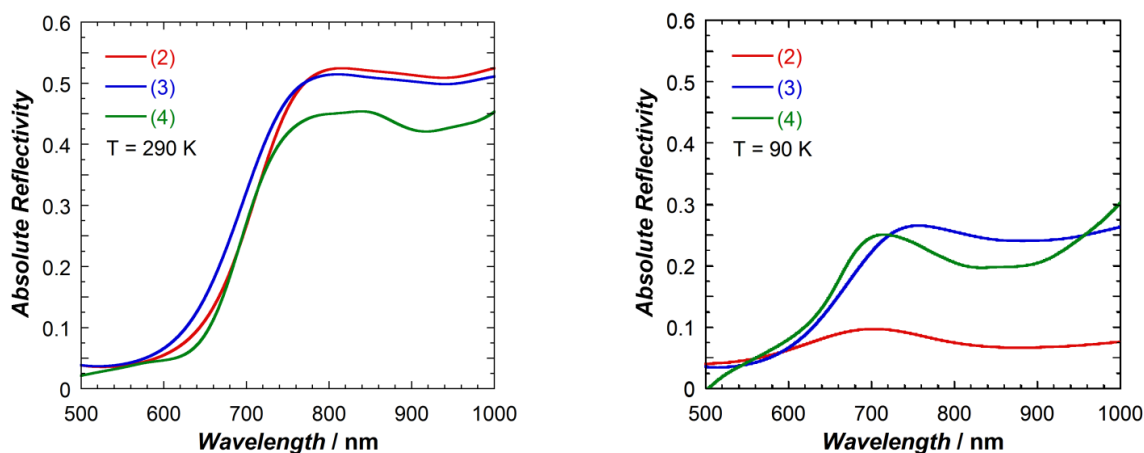


Figure III-10. Comparison of the reflectivity spectra of **2** with **3** and **4** at 290 K (left) and at 90 K (right).

At 290 K, the reflectivity spectra of **2**, **3** and **4** are very similar and present strong absorption between 500 and 700 nm (absolute reflectivity at 550 nm $R_{550}=0.04$ for **2**, **3** and **4**, Figure III-10 left). The absorption at higher wavelengths is stronger in **4** ($R_{850} = 0.45$), while in **2** and **3** is almost of the same magnitude (R_{850} being 0.52 for **2** and 0.50 for **3**).

On cooling red crystals of **2** become green. Therefore, at 90 K the complex becomes strongly absorbent above 700 nm ($R_{850} = 0.07$, Figure III-10 right), the hallmark signature of the thermally-induced

electron-transfer between Co^{II} and Fe^{III} ions.^{6b-c,6g,9} Compounds **3** and **4** showed an increase in absorption intensity at 850 nm. The observed increase is not as intense in **3** and **4** (R_{850} being 0.24 and 0.20, respectively) as the one observed for **2** (Figure III-10 right), but still is suggesting a certain change of optical properties. No thermally ET transfer was observed for **3** and **4**, according to structural data. Thus, it is likely that on surface of the studied samples we can observe a thermally induced ET, but since the absorbance intensity did not increase as much as in **2** (or in **1**^{6c} which has reflectivity spectra very similar to **2**) we can state that it is likely only a surface effect.

III.2.5. Magnetic measurements

Both compounds **1** and **2** undergo thermally and photo-induced intramolecular electron transfer as the result of that the paramagnetic $\{\text{Fe}^{\text{III}}_{\text{LS}}(\mu\text{-CN})\text{Co}^{\text{II}}_{\text{HS}}\}$ species can be converted reversibly into the diamagnetic $\{\text{Fe}^{\text{II}}_{\text{LS}}(\mu\text{-CN})\text{Co}^{\text{III}}_{\text{LS}}\}$ species. The detailed discussions on magnetic properties of **1** and **2** were reported previously (Figure III-1).^{6c,6g,9} Therefore, in this section, the magnetic properties of **3** and **4** in comparison with **2** are discussed (Figure III-11).

Temperature dependent magnetic measurements were carried out between 1.8 and 280 K and are shown in Figure III-11 as the thermal dependence of the χT product. Above 250 K, the χT product remains nearly constant ($\sim 6.5 \text{ cm}^3 \cdot \text{K/mol}$ for **2** and **3**, and $\sim 6.8 \text{ cm}^3 \cdot \text{K/mol}$ for **4**) that is in agreement with values expected for a 2:2 ratio of magnetically isolated $\text{Fe}^{\text{III}}_{\text{LS}}$ ($S = 1/2$, $g \approx 2.6$) and $\text{Co}^{\text{II}}_{\text{HS}}$ ($S = 3/2$, $g \approx 2.4$) centers. For **2**, slowly decreasing the temperature (0.4 K/min) from 240 to 120 K affords a gradual decrease of χT value in **2**, approaching $0.51 \text{ cm}^3 \cdot \text{K/mol}$ at 120 K then $0.08 \text{ cm}^3 \cdot \text{K/mol}$ at 1.8 K, therefore suggesting thermally generated diamagnetic $\{\text{Fe}^{\text{II}}_{\text{LS}}(\mu\text{-CN})\text{Co}^{\text{III}}_{\text{LS}}\}$ units as a result of the intramolecular ET (black curve on Figure III-11).

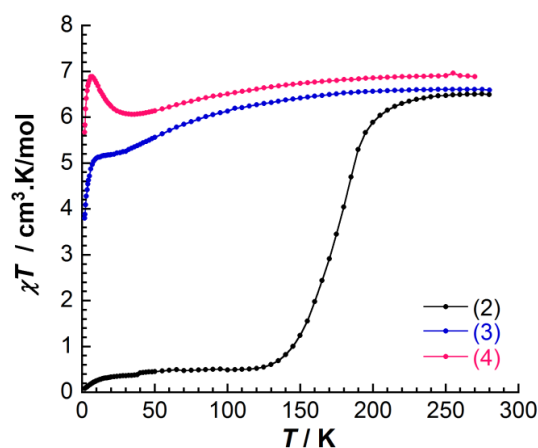


Figure III-11. Temperature dependence of the χT product (where χ defined as the molar magnetic susceptibility and equal to M/H ; M = magnetization and H = external magnetic field) for compounds **2** (black, 0.5 T, 0.4 Kmin⁻¹), **3** (blue, 0.1 T, 0.4 Kmin⁻¹) and **4** (pink, 0.1 T, 0.4 Kmin⁻¹), solid lines are guides for the eyes.

As expected from the temperature dependent structural investigations, compounds **3** and **4** do not exhibit any ET associated conversion between paramagnetic and diamagnetic species on cooling. The χT product for **3** and **4** remains roughly constant down to 120 K then decreases to values of $5.2 \text{ cm}^3 \cdot \text{K/mol}$ for **3** and $6.0 \text{ cm}^3 \cdot \text{K/mol}$ for **4** likely due to the spin-orbit coupling of the high spin Co^{II} ion. On further cooling below 30 K, the χT product for **3** reaches a plateau and remains relatively constant until 10 K then it abruptly

decreases to $3.8 \text{ cm}^3\cdot\text{K/mol}$ at 1.8 K. At low temperatures (below 30 K), compound **4** has a different behaviour than **3**. The χT product for **4** increases to a value of $6.9 \text{ cm}^3\cdot\text{K/mol}$ at 7 K, then as the temperature is lowered it decreases to $5.7 \text{ cm}^3\cdot\text{K/mol}$ at 1.8 K. The observed behavior in **4** suggests the presence of ferromagnetic interactions between Fe^{III} and Co^{II} ions with weak intermolecular antiferromagnetic interactions. Similar magnetic behavior corresponding to intramolecular ferromagnetic couplings between Fe^{III} and Co^{II} spin carriers was reported for complex **1** in its paramagnetic photo-induced phase (Figure III-1 left, green plot). The magnetic behavior observed for **3** and **4** is similar, but it seems that the intermolecular antiferromagnetic interactions are significantly stronger in **3**. This is confirmed by the particularly short contacts between square complexes in **3** (See Section III.2.3.3, Figure III-7 bottom). Intermolecular π - π type interactions occur between adjacent diMeby ligands and between adjacent pyrazole rings from capping Tp^* ligands along the crystallographic b axis. As already mentioned, these interactions lead to a supramolecular 2D-like structure with centroid-to-centroid distances between diMeby planes of 4.12 \AA and between pyrazole planes of 3.94 \AA (Figure III-7 bottom). In contrast, complexes are more isolated in **4** with no π - π type interactions observed between diMeby ligands, while the centroid-to-centroid distances between pyrazole planes (from capping Tp^* ligands) increased to 4.58 \AA (Figure III-8). Additional evidence for ferromagnetic exchange between Fe^{III} and Co^{II} spin carriers in **3** and **4** is found in the field-dependence of magnetization plots (Figure S.III-5). At 1.8 K, the magnetization value is monotonically increasing upon applying the external dc fields, without showing S-shape curves that could be indicative for the presence of the antiferromagnetic interactions. Moreover the magnetization curves show an absence of magnetization saturation which is consistent with magnetic anisotropy of the Co^{II} ions (Figure S.III-5).

III.3. Conclusions and perspectives

In Chapter III, four tetranuclear $\{Fe_2Co_2\}$ molecular square compounds were investigated in terms of synthesis, structural characterizations, and magnetic properties. Previously reported^{6c,6g,9} compounds **1** and **2** were synthesized and characterized with the aim to prove the photo-magnetic effect on single crystals and to study the nature of the photo-induced states. Another two new compounds, **3** and **4**, were synthesized with the goal to study the perturbation of the ET process in functionalized $\{[(Tp^*)Fe(CN)_3]_2[Co(diMeby)_2]_2\}^{2+}$ system through changing the counter-anion, a change that has not yet been studied with respect to $\{Fe_2Co_2\}$ molecular squares.

The photo-crystallographic investigations of compounds **1** and **2** showed that the light induced metastable paramagnetic phase is, as claimed and expected, composed of $\{Fe^{III}_{LS}(\mu-CN)Co^{II}_{HS}\}$ units. Moreover, in the case of complex **1** it was possible to determine that light irradiation is a more efficient way to obtain the metastable paramagnetic phase than the thermal quenching method. In the case of compound **2**, it was possible to observe that the photo-induced paramagnetic phase is slightly different in structure than the thermodynamic one observed at high temperatures.

The structural and magnetic studies of the family of closely related complexes, $\{[(Tp^*)Fe(CN)_3]_2[Co(diMeby)_2]_2\}X_2$ (compounds **2**, **3** and **4**) showed that the occurrence of the ET process in solid state is strongly affected by the exchange of the counter-anion. The counter-anion induced

perturbations influence several parameters such as the geometry of the $\{\text{Fe}_2(\mu\text{-CN})_4\text{Co}_2\}$ core, the intermolecular interactions, the solvation and the ET process. Therefore, we can conclude that electron transfer in cyanido-bridged molecular $\{\text{Fe}_2\text{Co}_2\}$ squares is strongly dependent on the structural environment, which is influenced by the nature of counter-anion.

As a perspective towards a better understanding of counter-anion influence on ET process in cyanido-bridged molecular $\{\text{Fe}_2\text{Co}_2\}$ squares, it can be suggested the synthesis of new complexes with other counter-anions, including diamagnetic ones like BF_4^- , PF_6^- , SbF_6^- , ReO_4^- , BPh_4^- or paramagnetic ones like $[\text{FeCl}_4]^-$ or $[\text{ReF}_6]^{2-}$, which has a different charge. Besides synthesis of novel compounds changing of the crystallization conditions (i.e. solvents) of the previously reported compounds (**1**, **2**, **3** and **4**) can offer a better view of the effect that solvation inside the crystal packing can have on ET process. In particular, polar solvents should be able increase the ET characteristic temperature, as was observed in solutions for **1**.^{6g,9} On the other hand, the chemical tuning (by functionalization, counter-anion exchange or variation of crystallization solvents and conditions) of ET properties in molecular $\{\text{Fe}_2\text{Co}_2\}$ squares is time consuming. It appears much easier to control the intramolecular electron transfer in solutions,^{6g,9} since they offer an environment which lacks lattice packing restraints and highlights the molecular nature of the observed behavior.

Another promising perspective based on further functionalization of the bipyridine ligands on the Co site has been successfully applied in the next chapters.

III.4. Supporting materials

III.4.1. Experimental protocols

Preparation of $Co(OTf)_2$. 50 mL of trifluoromethanesulfonic acid (2.4 g, 16 mmol) solution in methanol were added dropwise to the $CoCO_3$ (0.95 g, 8 mmol) suspension in 20 mL of methanol. The mixture was stirred until CO_2 gas stopped to form. Then the solution was filtered and concentrated under reduced pressure. $Co(OTf)_2$ was precipitated as a pink solid by adding a large excess of diethyl ether. The compound was dried in vacuum at 383 K. The yield was 2.3 g (82 %). Elemental analysis – Calc. (Found) for $C_2CoF_6O_6S_2$ ($Co(CF_3SO_3)_2$): C, 6.73 (6.40). Selected FT-IR data (ATR, cm^{-1}): 1225 (vs), 1191 (vs), 1023 (vs), 626 (m), 593 (m).

Preparation of $Co(OTs)_2 \cdot 6H_2O$. In a 250-mL round-bottomed flask equipped with a reflux condenser were mixed $CoCO_3$ (8.54 g, 71.8 mmol), p-toluenesulfonic acid monohydrate (27.4 g, 144 mmol) and 20 mL of water. The mixture was refluxed for 5 h. The resulting reddish-pink solution was filtered while hot. The filtrate was cooled to room temperature and pale orange blocks formed after 1 h. The crystals were collected by filtration and dried overnight under vacuum at room temperature. A second crop of crystals was obtained by concentration and cooling of the mother liquor. The yield was 28.5 g (78 %). Elemental analysis – Calc. (Found) for $C_{14}H_{26}CoO_{12}S_2$ ($Co(CH_3C_6H_4SO_3)_2 \cdot 6H_2O$): C, 33.01 (32.56); H, 5.14 (5.05); S, 12.59 (12.32). Selected FT-IR data (ATR, cm^{-1}): 3065 (w), 3039 (w), 1180 (vs), 1122 (vs), 1035 (s), 1009 (s), 812 (s), 676 (s), 563 (s).

Preparation of $(NEt_4)[(Tp^*)Fe(CN)_3]$. Dropwise addition of KTp^* (0.5 g, 1.48 mmol) dissolved in 2.5 mL of methanol to $Fe(acac)_3$ (0.5 g, 1.41 mmol) solution in 2.5 mL of methanol afforded a dark brown mixture that was stirred for ~ 2 h. A reddish precipitate was isolated by filtration and dried. Afterwards it was re-dissolved in 5 mL of acetonitrile and treated with 0.6 g of $(NEt_4)CN$ (3.8 mmol) in 5 mL of acetonitrile. The mixture was stirred for 2 h at 50°C. The excess of $(NEt_4)CN$ was removed by column chromatography (silica gel, CH_3CN). The compound was purified by recrystallization from methanol solution layered with diethyl ether. The yield was 0.25 g (60 %). Elemental analysis – Calc. (Found) for $C_{26}H_{46}BFeN_{10}O_2$ ($(NEt_4)[(Tp^*)Fe(CN)_3] \cdot 2H_2O$): C, 52.28 (52.65); H, 7.76 (7.52); N, 23.45 (24.39). Selected FT-IR data (ATR, cm^{-1}): 2982 (m), 2934 (m), 2549 (m), 2115 (s), 1540 (vs), 1447 (vs), 1415 (vs), 1392 (vs), 1370 (vs), 1199 (vs), 1060 (vs), 997 (m), 785 (vs), 777 (vs), 645 (s).

Preparation of $\{[(Tp^*)Fe(CN)_3]_2[Co(bpy)_2]_2\}(OTf)_2$ (1). $[NEt_4][[(Tp^*)Fe(CN)_3] \cdot 2H_2O$ (168 mg, 0.3 mmol) was treated with $Co(OTf)_2$ (107 mg, 0.3 mmol) in 5 mL of wet DMF under argon to afford a red solution that was allowed to stir for 2 h. Then 2,2'-bipyridine (94 mg, 0.6 mmol) was added and the mixture was stirred for 10 min and filtered. Dark red crystals were obtained by slow diffusion of diethyl ether in the DMF solution. The yields was 0.23 g (69.9 %). Elemental analysis – Calc. (Found) for $C_{90}H_{108}B_2Co_2F_6Fe_2N_{30}O_{12}S_2$ ($\{[(Tp^*)Fe(CN)_3]_2[Co(bpy)_2]_2\}(OTf)_2 \cdot 2H_2O \cdot 4DMF$): C, 48.45 (48.25); H, 4.89 (4.85); N, 18.83 (18.91). Selected FT-IR data (ATR, cm^{-1}): 3077 (w), 2928 (w), 2544 (w), 2150 (s), 2128 (m), 1664 (vs), 1596 (s), 1542 (s), 1441 (vs), 1414 (s), 1385 (s), 1367 (s), 1260 (vs), 1155 (s), 1029 (vs), 773 (s), 636 (s), 573 (m).

Preparation of $\{[(\text{Tp}^*)\text{Fe}(\text{CN})_3]_2[\text{Co}(\text{diMeppy})_2]_2\}[\text{X}]_2$ (2-4). $[\text{NEt}_4][(\text{Tp}^*)\text{Fe}(\text{CN})_3] \cdot 2\text{H}_2\text{O}$ (168 mg, 0.3 mmol) was treated with 0.3 mmol of $\text{Co}(\text{X})_2$ (for **2** with 107 mg of $\text{Co}(\text{OTf})_2$; for **3** with 109.7 mg of $\text{Co}(\text{ClO}_4) \cdot 6\text{H}_2\text{O}$; for **4** with 153 mg of $\text{Co}(\text{OTs})_2 \cdot 6\text{H}_2\text{O}$) in 5 mL of wet DMF under argon to afford a red solution that was allowed to stir for 2 h. Then 4,4'-dimethyl-2,2'-bipyridine (diMeppy, 114 mg, 0.6 mmol) was added and the mixture was stirred for 20 min and filtered. Dark red crystals were obtained by slow diffusion of diethyl ether in the DMF solution. The yields were 0.23 g (69.9 %) for **2**, 0.22 g (72.7 %) for **3** and 0.27 g (71.4 %) for **4**. Elemental analysis – Calc. (Found) for (**2**) $\text{C}_{92}\text{H}_{108}\text{B}_2\text{Co}_2\text{F}_6\text{Fe}_2\text{N}_{28}\text{O}_9\text{S}_2$ ($\{[(\text{Tp}^*)\text{Fe}(\text{CN})_3]_2[\text{Co}(\text{diMeppy})_2]_2\}(\text{OTf})_2 \cdot \text{H}_2\text{O} \cdot 2\text{DMF}$): C, 50.70 (50.36); H, 5.00 (4.94); N, 18.00 (18.13). Selected FT-IR data (ATR, cm^{-1}): 2926 (w), 2857 (w), 2546 (w), 2151, 2116 (w), 1664 (s), 1614 (s), 1541 (s), 1444 (s), 1414 (s), 1385 (s), 1369 (s), 1263 (vs), 1202 (s), 1138 (s), 1062 (s), 1031 (s), 824 (s), 793 (s), 635 (vs), 572 (s). Elemental analysis – Calc. (Found) for (**3**) $\text{C}_{90}\text{H}_{106}\text{B}_2\text{Cl}_2\text{Co}_2\text{Fe}_2\text{N}_{28}\text{O}_{10}$ ($\{[(\text{Tp}^*)\text{Fe}(\text{CN})_3]_2[\text{Co}(\text{diMeppy})_2]_2\}(\text{ClO}_4)_2 \cdot 2\text{DMF}$): C, 52.42 (52.27); H, 5.18 (5.09); N, 19.02 (19.11). Selected FT-IR data (ATR, cm^{-1}): 2926 (w), 2855 (w), 2545 (w), 2149 (m), 2119 (w), 1671 (vs), 1614 (vs), 1542 (s), 1445 (s), 1414 (s), 1386 (s), 1369 (s), 1204 (m), 1086 (vs), 1061 (vs), 1016 (s), 920 (m), 824 (s), 786 (s), 691 (m), 645 (m), 622 (vs). Elemental analysis – Calc. (Found) for (**4**) $\text{C}_{116}\text{H}_{148}\text{B}_2\text{Co}_2\text{Fe}_2\text{N}_{32}\text{O}_{12}\text{S}_2$ ($\{[(\text{Tp}^*)\text{Fe}(\text{CN})_3]_2[\text{Co}(\text{bpy})_2]_2\}(\text{OTs})_2 \cdot 6\text{DMF}$): C, 55.78 (55.69); H, 5.97 (5.89); N, 17.94 (18.07). Selected FT-IR data (ATR, cm^{-1}): 3059 (w), 2924 (w), 2855 (w), 2535 (w), 2146 (s), 2118 (w), 1669 (vs), 1655 (vs), 1612 (s), 1543 (m), 1489 (m), 1446 (s), 1410 (s), 1382 (s), 1368 (s), 1195 (s), 1120 (m), 1092 (m), 1062 (s), 1035 (m), 1012 (s), 919 (m), 819 (m), 800 (m), 778 (m), 679 (vs), 658 (m), 645 (m), 568 (m), 561 (m).

III.4.2. FT-IR spectroscopic analyses

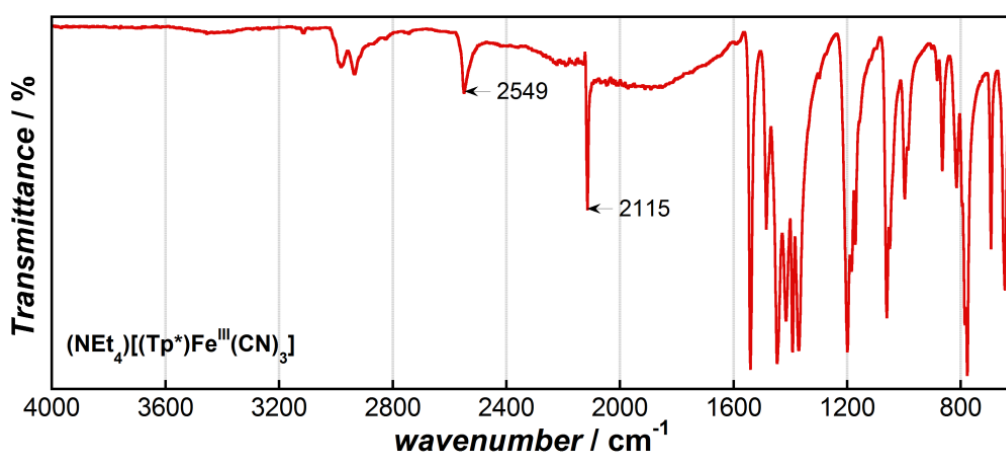


Figure S.III-1. FT-IR spectrum of tricyanido-metallate precursor $(\text{NEt}_4)[(\text{Tp}^*)\text{Fe}(\text{CN})_3]$ at room temperature.

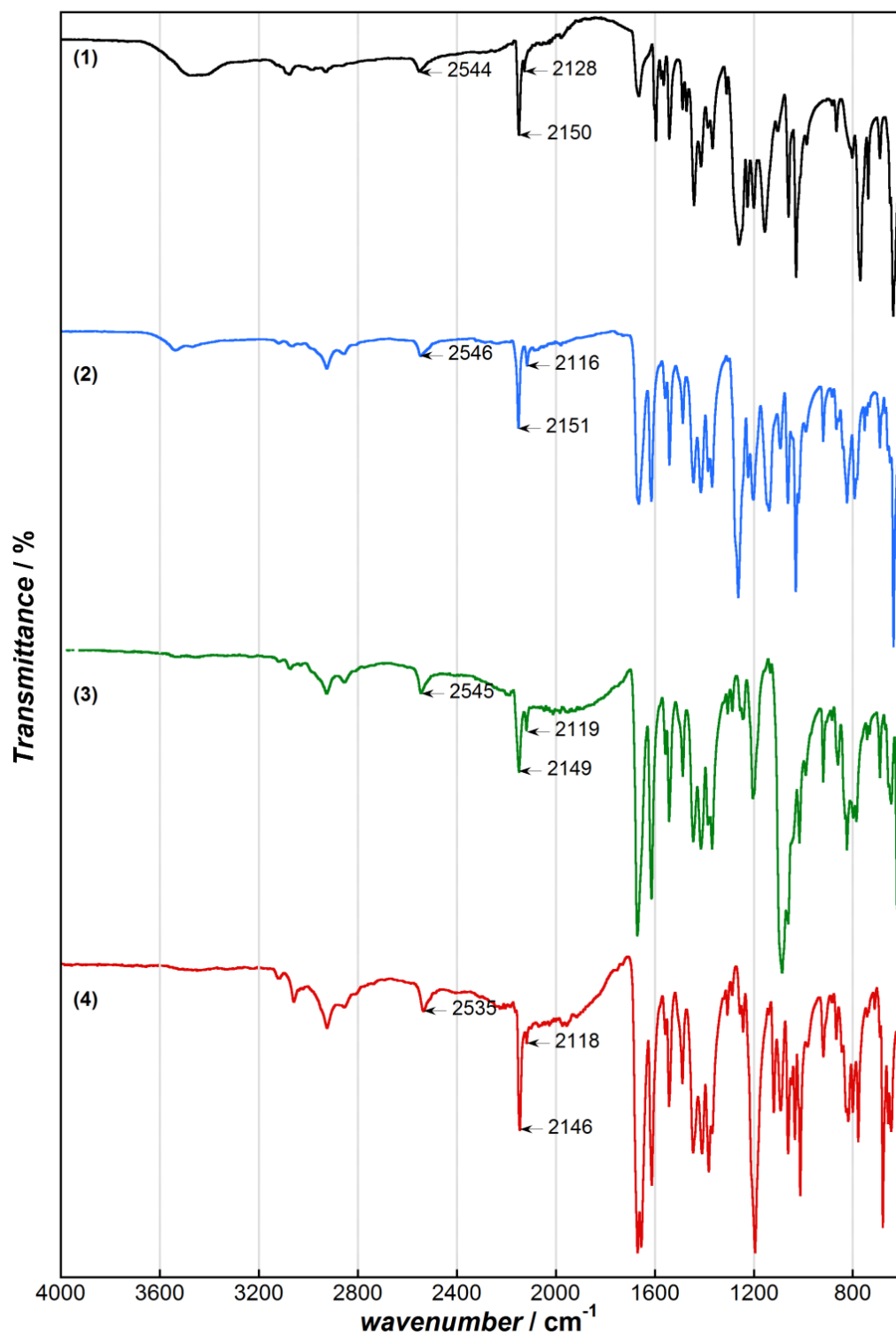


Figure S.III-2. FT-IR spectra of compounds 1 – 4 at room temperature.

III.4.3. Crystallographic data for (1), (2), (3) and (4)

Table S.III-1. Crystallographic data for 1 at various temperatures in its different phases.

Temperature	230 K high temperature phase	90 K quenched from 300 K	120 K low temperature phase	84 K low temperature phase	83 K after white light irradiation
Crystal color	dark red	dark red	dark green	dark green	dark red
Moiety formula	$C_{76}H_{76}B_2Co_2Fe_2N_{26}$, $2(CF_3O_3S)$, $3(C_3H_7NO)$, $3(H_2O)$				
Empirical formula	$C_{87}H_{103}B_2Co_2F_6Fe_2N_{29}O_{12}S_2$				
Formula weight	2176.23				
Crystal system	Triclinic				
Space group	$P\bar{1}$				
Wavelength, Å	0.71073				
a, Å	13.6685(11)	13.560(2)	13.3401(10)	13.3171(9)	13.5151(7)
b, Å	13.8537(9)	13.7708(19)	13.4448(9)	13.4405(8)	13.7665(5)
c, Å	14.8485(12)	14.805(2)	14.8307(12)	14.7961(10)	14.7657(7)
α , °	99.514(3)	99.932(6)	100.515(3)	100.494(3)	99.894(2)
β , °	93.620(3)	94.494(7)	94.288(3)	94.330(3)	94.611(2)
γ , °	107.868(3)	107.213(6)	106.561(3)	106.519(3)	107.283(2)
V, Å ³	2619.8(3)	2576.4(7)	2484.0(3)	2473.7(3)	2558.8(2)
Z	1				
ρ_{calcd} , g/cm ³	1.379	1.403	1.455	1.461	1.412
μ , 1/mm	0.703	0.715	0.741	0.744	0.719
Reflections collected	62198	56131	80919	59992	91328
Independent reflections	9654	9413	9020	9033	9379
R_1^a	0.0462	0.0717	0.0621	0.0620	0.0479
wR_2^a	0.1529	0.2067	0.1850	0.1818	0.1398
GoF ^a	1.068	1.047	1.057	1.053	1.047
Selected bond distances (Å)					
Co(1)-N(1)	2.087(4)	2.038(5)	1.905(5)	1.905(5)	2.073(4)
Co(1)-N(2)	2.090(4)	2.059(5)	1.908(5)	1.905(5)	2.081(4)
Co(1)-N(10)	2.127(4)	2.103(4)	1.947(5)	1.951(5)	2.127(4)
Co(1)-N(12)	2.130(4)	2.093(5)	1.947(5)	1.941(5)	2.119(4)
Co(1)-N(11)	2.146(4)	2.101(5)	1.953(5)	1.954(5)	2.136(4)
Co(1)-N(13)	2.151(4)	2.106(5)	1.957(5)	1.952(5)	2.132(4)
Fe(1)-C(2)	1.914(5)	1.925(6)	1.879(6)	1.877(6)	1.917(5)
Fe(1)-C(1)	1.917(4)	1.912(6)	1.889(6)	1.887(6)	1.912(5)
Fe(1)-C(3)	1.926(5)	1.939(6)	1.921(6)	1.919(6)	1.930(6)
Fe(1)-N(8)	1.994(4)	2.010(5)	2.037(5)	2.037(5)	1.986(4)
Fe(1)-N(6)	2.004(4)	2.027(5)	2.039(5)	2.035(5)	2.005(5)
Fe(1)-N(4)	2.009(4)	2.019(5)	2.051(5)	2.052(5)	2.001(4)
Selected bond angles (°)					
N(1)-Co(1)-N(2)	96.09(15)	95.42(18)	93.60(2)	93.43(19)	95.71(16)
N(1)-Co(1)-N(10)	94.19(15)	93.77(17)	93.4(2)	93.42(19)	93.64(16)
N(2)-Co(1)-N(10)	89.86(15)	90.61(17)	87.89(19)	88.10(2)	90.93(16)
N(1)-Co(1)-N(12)	91.87(15)	89.68(17)	88.2(2)	88.50(2)	89.90(16)
N(2)-Co(1)-N(12)	93.77(15)	93.72(18)	93.2(2)	93.00(2)	94.19(16)
N(2)-Co(1)-N(11)	91.41(15)	89.84(18)	89.6(2)	89.70(2)	89.55(16)
N(10)-Co(1)-N(11)	76.66(16)	77.94(18)	82.5(2)	82.50(2)	76.81(16)
N(12)-Co(1)-N(11)	96.75(15)	98.19(18)	95.8(2)	95.50(2)	99.13(16)
N(1)-Co(1)-N(13)	89.37(15)	90.76(18)	89.9(2)	90.10(2)	90.81(16)
N(10)-Co(1)-N(13)	99.12(15)	96.74(17)	95.6(2)	95.50(2)	97.24(16)
N(12)-Co(1)-N(13)	76.64(15)	78.52(18)	83.2(2)	83.20(2)	77.20(17)
N(11)-Co(1)-N(13)	84.80(15)	85.21(18)	87.1(2)	87.10(2)	85.49(16)
C(2)-N(2)-Co(1)	173.8(4)	176.7(4)	176.60(5)	176.6(5)	177.1(4)
C(1)-N(1)-Co(1)	176.6(4)	175.2(4)	175.60(5)	175.5(5)	175.3(4)
C(2)-Fe(1)-C(1)	85.52(18)	85.9(2)	88.10(2)	88.0(2)	85.0(2)
C(2)-Fe(1)-C(3)	85.68(19)	89.1(3)	89.50(3)	89.9(3)	88.7(2)
N(1)-C(1)-Fe(1)	178.8(4)	175.3(5)	174.20(5)	174.3(5)	175.7(4)
N(2)-C(2)-Fe(1)	175.5(4)	178.6(5)	177.80(5)	177.3(5)	179.1(5)
N(3)-C(3)-Fe(1)	178.8(5)	178.6(6)	177.90(6)	178.0(6)	178.3(5)

^a $I > 2\sigma(I)$, $R_1 = \sum(|F_o| - |F_c|)/\sum|F_o|$, $wR_2 = \{\sum[w(F_o^2 - F_c^2)^2]/\sum w(F_o^2)^2\}^{1/2}$, GoF (goodness of fit on F^2) = $\{\sum[w(F_o^2 - F_c^2)^2]/(n-p)\}^{1/2}$, where n is the number of reflections and p is the total number of refined parameters.

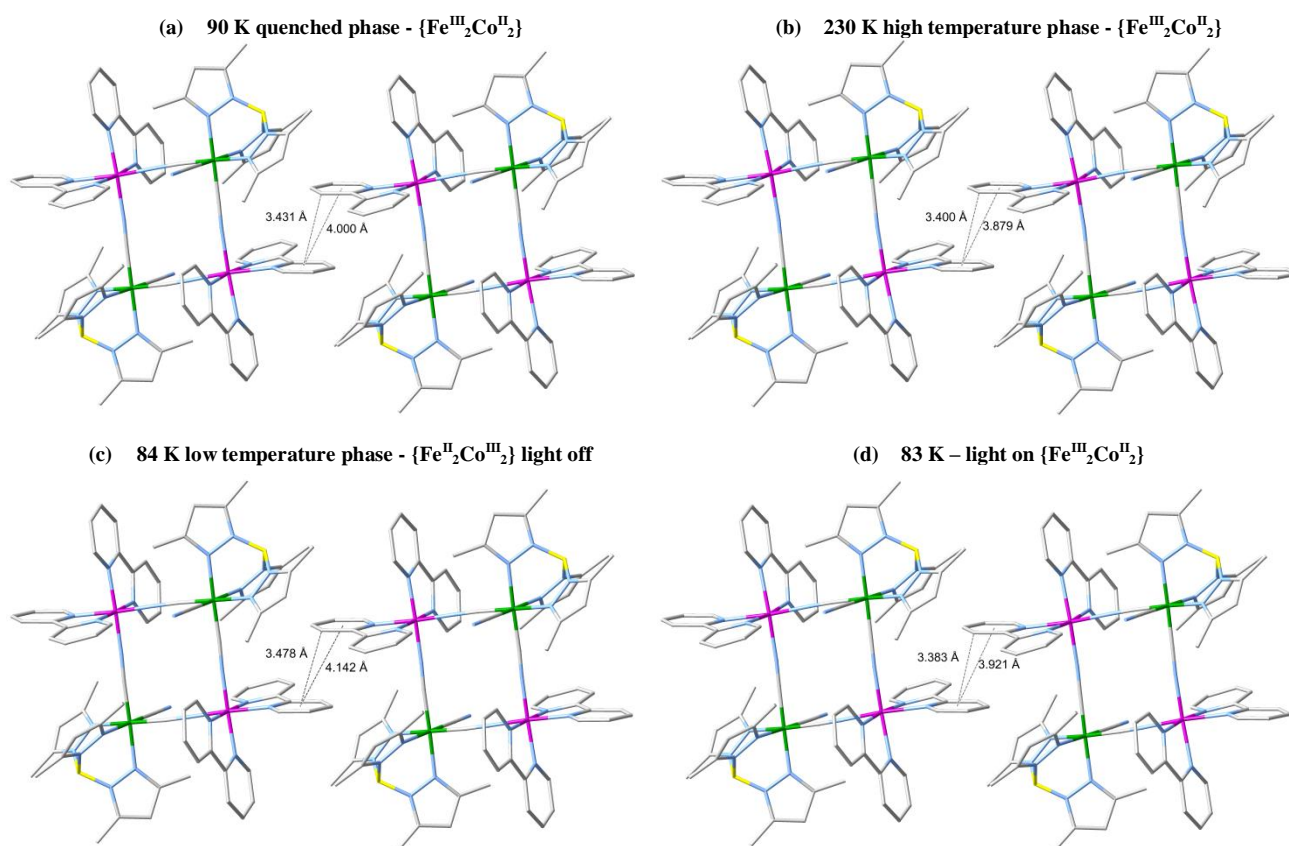


Figure S.III-3. Packing arrangement illustrating π - π interactions present between adjacent complexes of **1** along the crystallographic b -direction under different experimental conditions. All anions, lattice solvent and hydrogen atoms are eliminated for clarity.

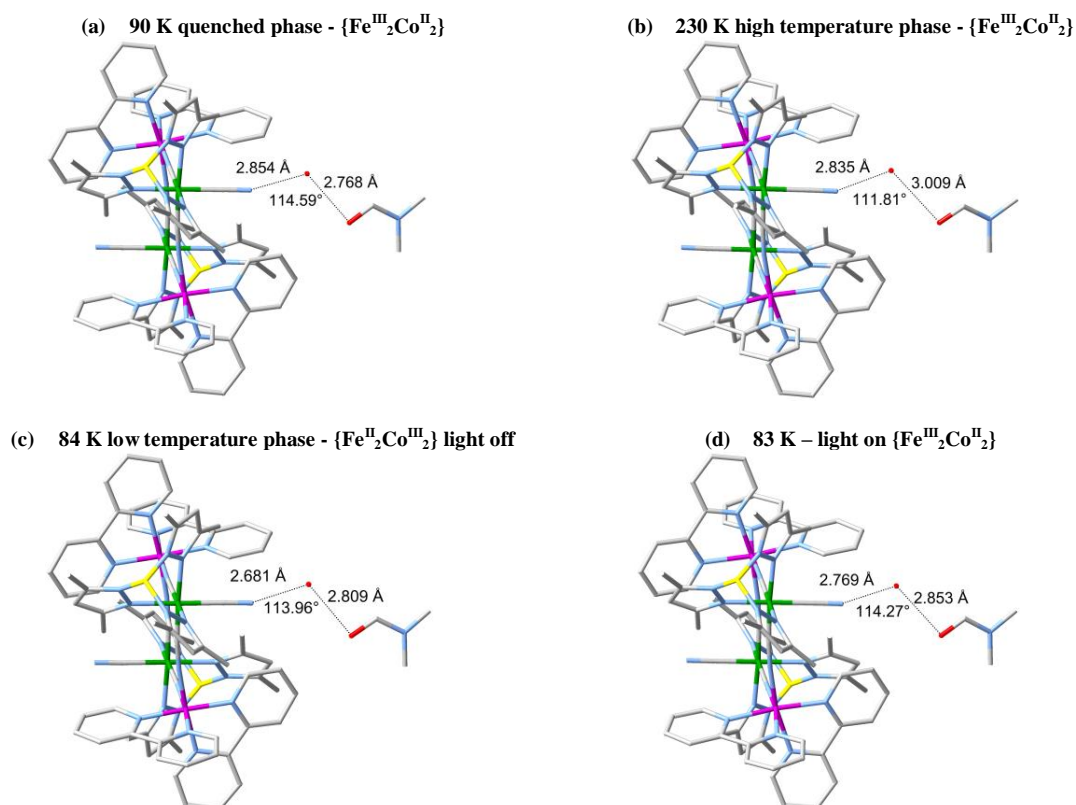


Figure S.III-4. View of the intermolecular short contacts in crystal packing of **1** under different experimental conditions.

Table S.III-2. Crystallographic data for **2** at various temperatures in its different phases.

Temperature	240 K	80 K	80 K
	high temperature phase	low temperature phase	after light irradiation
Crystal color	dark red	dark green	dark red
Moiety formula	C ₈₄ H ₉₂ B ₂ Co ₂ Fe ₂ N ₂₆ , 2(CF ₃ O ₃ S), 2(C ₃ H ₇ NO), (H ₂ O)		
Empirical formula	C ₉₂ H ₁₀₈ B ₂ Co ₂ F ₆ Fe ₂ N ₂₈ O ₉ S ₂		
Formula weight	2179.32		
Crystal system	Triclinic		
Space group	P $\bar{1}$		
Wavelength, Å	0.71073		
a, Å	13.5850(10)	13.2480(10)	13.4050(10)
b, Å	14.0410(10)	13.8130(10)	13.9060(10)
c, Å	14.9210(10)	14.7610(10)	14.8640(10)
α , °	69.503(6)	69.949(7)	69.232(7)
β , °	89.664(6)	88.004(7)	89.180(7)
γ , °	73.024(6)	71.569(7)	72.920(7)
V, Å ³	2535.0(3)	2399.1(3)	2464.0(3)
Z	1		
ρ_{calcd} , g/cm ³	1.428	1.508	1.469
μ , 1/mm	0.724	0.765	0.745
Reflections collected	19030	17635	17994
Independent reflections	10704	10017	10232
R_1^a	0.0741	0.0660	0.0733
wR_2^a	0.1446	0.1257	0.1394
GoF ^a	0.759	0.653	0.702
	Selected bond distances (Å)		
Co(1)-N(1)	2.142(7)	1.954(6)	2.124(7)
Co(1)-N(2)	2.114(8)	1.943(7)	2.113(7)
Co(1)-N(3)	2.172(6)	1.959(6)	2.149(6)
Co(1)-N(4)	2.115(7)	1.911(6)	2.103(7)
Co(1)-N(5)	2.107(7)	1.911(6)	2.104(7)
Co(1)-N(6)	2.111(7)	1.876(6)	2.099(7)
Fe(1)-C(25)	1.909(9)	1.855(8)	1.909(9)
Fe(1)-C(26)	1.930(9)	1.890(9)	1.940(9)
Fe(1)-C(27)	1.939(9)	1.900(8)	1.910(10)
Fe(1)-N(8)	1.982(7)	2.029(6)	1.963(7)
Fe(1)-N(11)	1.993(6)	2.040(6)	2.001(6)
Fe(1)-N(13)	1.995(7)	2.037(6)	2.002(7)
	Selected bond angles (°)		
N(1)-Co(1)-N(2)	77.4(3)	82.6(3)	77.6(3)
N(1)-Co(1)-N(3)	89.6(2)	90.9(2)	90.6(2)
N(1)-Co(1)-N(4)	97.7(3)	94.4(3)	97.0(3)
N(1)-Co(1)-N(5)	93.1(2)	90.4(2)	92.0(2)
N(2)-Co(1)-N(3)	94.5(3)	92.2(3)	94.8(3)
N(2)-Co(1)-N(5)	96.1(3)	92.0(2)	96.1(2)
N(2)-Co(1)-N(6)	95.1(3)	94.9(3)	97.2(3)
N(3)-Co(1)-N(4)	76.2(3)	83.0(3)	76.8(3)
N(3)-Co(1)-N(6)	89.0(2)	88.5(2)	88.7(2)
N(4)-Co(1)-N(5)	93.3(3)	92.8(3)	92.5(3)
N(4)-Co(1)-N(6)	89.4(3)	88.0(3)	88.0(3)
N(5)-Co(1)-N(6)	89.7(3)	90.4(3)	89.7(2)
C(25)-N(5)-Co(1)	166.6(8)	164.7(6)	164.2(7)
C(26)-N(6)-Co(1)	164.0(7)	168.8(6)	164.9(7)
C(25)-Fe(1)-C(26)	90.8(3)	92.5(3)	91.3(3)
C(25)-Fe(1)-C(27)	86.4(3)	85.0(3)	83.2(3)
N(5)-C(25)-Fe(1)	177.3(9)	177.1(7)	179.0(8)
N(6)-C(26)-Fe(1)	174.0(8)	174.4(6)	172.9(8)
N(7)-C(27)-Fe(1)	174.5(8)	174.1(7)	173.4(7)

^a $I > 2\sigma(I)$, $R_1 = \sum(|F_o| - |F_c|)/\sum|F_o|$. $wR_2 = \{\sum[w(F_o^2 - F_c^2)^2]/\sum[w(F_o^2)^2]\}^{1/2}$. GoF (goodness of fit on F^2) = $\{\sum[w(F_o^2 - F_c^2)^2]/(n-p)\}^{1/2}$, where n is the number of reflections and p is the total number of refined parameters.

Table S.III-3. Crystallographic data for **3** at 100 and 250 K.

Temperature	250 K	100 K
Crystal color	dark red	dark red
Moiety formula	$C_{84}H_{92}B_2Co_2Fe_2N_{26}, 2(ClO_4), 2(C_3H_7NO)$	
Empirical formula	$C_{90}H_{106}B_2Cl_2Co_2Fe_2N_{28}O_{10}$	
Formula weight	2062.10	
Crystal system	Triclinic	
Space group	$P\bar{1}$	
Wavelength, Å	0.71073	
a, Å	13.191(3)	13.084(2)
b, Å	14.097(3)	13.958(2)
c, Å	14.739(3)	14.647(3)
α , °	113.177(8)	113.044(7)
β , °	90.673(10)	91.226(8)
γ , °	105.633(8)	105.495(8)
V, Å ³	2404.9(9)	2348.0(7)
Z	1	
ρ_{calcd} , g/cm ³	1.424	1.458
μ , 1/mm	0.763	0.781
Reflections collected	67613	72871
Independent reflections	10179	8747
R_1^a	0.0593	0.0553
wR_2^a	0.1921	0.1629
GoF ^a	1.033	1.059
Selected bond distances (Å)		
Co(1)-N(5)	2.085(4)	2.075(4)
Co(1)-N(7)	2.107(3)	2.098(3)
Co(1)-N(4)	2.132(3)	2.125(3)
Co(1)-N(3)	2.142(3)	2.149(3)
Co(1)-N(2)	2.149(3)	2.155(3)
Co(1)-N(1)	2.181(3)	2.175(3)
Fe(1)-C(17)	1.914(5)	1.917(4)
Fe(1)-C(18)	1.920(5)	1.922(5)
Fe(1)-C(19)	1.927(4)	1.922(4)
Fe(1)-N(8)	1.997(3)	1.997(3)
Fe(1)-N(11)	2.014(3)	2.001(3)
Fe(1)-N(12)	2.009(3)	2.012(3)
Selected bond angles (°)		
N(2)-Co(1)-N(1)	75.65(12)	75.56(12)
N(3)-Co(1)-N(1)	90.88(12)	90.84(12)
N(4)-Co(1)-N(1)	90.05(13)	90.56(13)
N(4)-Co(1)-N(2)	98.00(13)	98.26(13)
N(4)-Co(1)-N(3)	76.66(13)	76.72(13)
N(5)-Co(1)-N(1)	90.54(13)	90.46(14)
N(5)-Co(1)-N(2)	89.58(14)	89.37(14)
N(5)-Co(1)-N(3)	95.66(14)	95.65(14)
N(5)-Co(1)-N(7)	89.21(13)	89.27(14)
N(7)-Co(1)-N(2)	93.50(13)	93.34(12)
N(7)-Co(1)-N(3)	99.94(13)	100.23(13)
N(7)-Co(1)-N(4)	91.65(13)	91.19(13)
C(18)-N(5)-Co(1)	166.1(3)	165.2(3)
C(19)-N(7)-Co(1)	166.2(3)	165.5(4)
C(18)-Fe(1)-C(19)	90.70(16)	91.08(16)
C(19)-Fe(1)-C(17)	83.54(17)	83.32(17)
N(7)-C(19)-Fe(1)	178.7(4)	178.7(4)
N(5)-C(18)-Fe(1)	172.6(3)	172.7(3)
N(13)-C(17)-Fe(1)	175.5(4)	175.5(4)

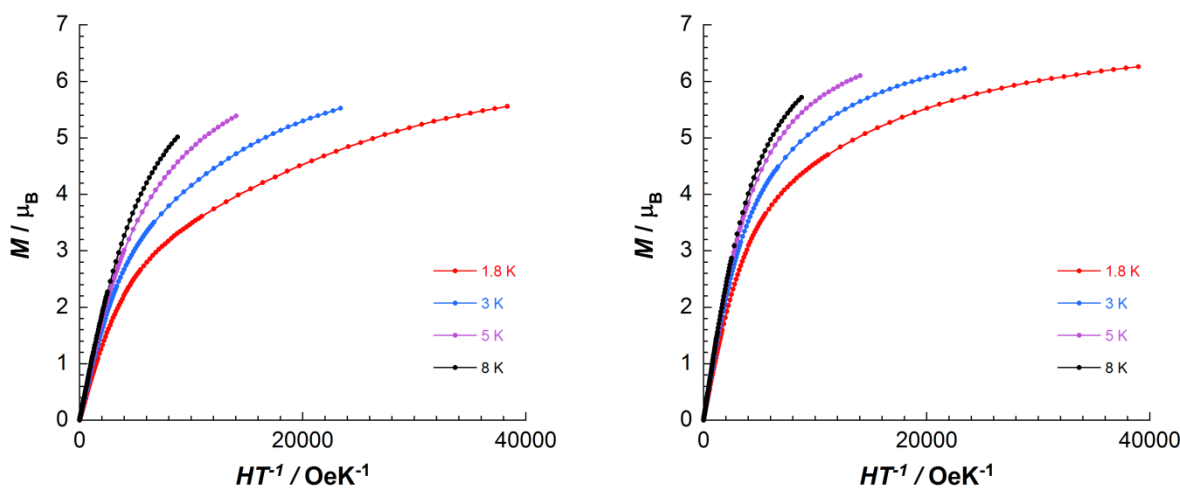
^a $I > 2\sigma(I)$, $R_1 = \sum(|F_o| - |F_c|)/\sum|F_o|$, $wR_2 = \{\sum[w(F_o^2 - F_c^2)^2]/\sum[w(F_o^2)^2]\}^{1/2}$. GoF (goodness of fit on F^2) = $\{\sum[w(F_o^2 - F_c^2)^2]/(n-p)\}^{1/2}$, where n is the number of reflections and p is the total number of refined parameters.

Table S.III-4. Crystallographic data for **4** at 120 K.

Temperature	120 K	Selected bond distances (Å)	
Crystal color	dark red	Co(1)-N(1)	2.090(5)
Moiety formula	$C_{84}H_{92}B_2Co_2Fe_2N_{26}$, $2(C_7H_7O_3S)$, $6(C_3H_7NO)$	Co(1)-N(12)	2.105(5)
Empirical formula	$C_{116}H_{148}B_2Co_2Fe_2N_{32}O_{12}S_2$	Co(1)-N(15)	2.110(5)
Formula weight	2497.96	Co(1)-N(1)	2.116(5)
Crystal system	Triclinic	Co(1)-N(13)	2.145(5)
Space group	$P\bar{1}$	Co(1)-N(14)	2.153(5)
Wavelength, Å	0.71073	Fe(1)-C(52)	1.908(6)
a, Å	13.813(4)	Fe(1)-C(53)	1.930(7)
b, Å	15.847(4)	Fe(1)-C(51)	1.937(6)
c, Å	16.115(4)	Fe(1)-N(5)	1.974(5)
α , °	101.448(12)	Fe(1)-N(8)	1.988(5)
β , °	97.680(11)	Fe(1)-N(3)	2.029(5)
γ , °	114.931(11)	Selected bond angles (°)	
V, Å ³	3040.0(14)	N(1)-Co(1)-N(14)	83.43(19)
Z	1	N(12)-Co(1)-N(1)	95.02(19)
ρ_{calcd} , g/cm ³	1.364	N(12)-Co(1)-N(13)	76.26(19)
μ , 1/mm	0.609	N(12)-Co(1)-N(14)	99.87(19)
Reflections collected	86047	N(13)-Co(1)-N(14)	91.11(19)
Independent reflections	11303	N(15)-Co(1)-N(1)	94.9(2)
R_1^a	0.0788	N(15)-Co(1)-N(13)	93.31(19)
wR_2^a	0.2379	N(15)-Co(1)-N(14)	76.71(19)
GoF ^a	1.104	N(2)-Co(1)-N(1)	91.32(19)
		N(2)-Co(1)-N(12)	91.60(19)
		N(2)-Co(1)-N(13)	95.85(19)
		N(2)-Co(1)-N(15)	92.78(19)
		C(51)-N(1)-Co(1)	163.7(5)
		C(52)-N(2)-Co(1)	168.5(5)
		C(52)-Fe(1)-C(53)	84.6(2)
		C(52)-Fe(1)-C(51)	86.1(2)
		N(1)-C(51)-Fe(1)	175.9(5)
		N(2)-C(52)-Fe(1)	176.1(5)
		N(7)-C(53)-Fe(1)	178.5(6)

^a $I > 2\sigma(I)$, $R_1 = \sum(|F_o| - |F_c|)/\sum|F_o|$. $wR_2 = \{\sum[w(F_o^2 - F_c^2)^2]/\sum[w(F_o^2)^2]\}^{1/2}$. GoF (goodness of fit on F^2) = $\{\sum[w(F_o^2 - F_c^2)^2]/(n-p)\}^{1/2}$, where n is the number of reflections and p is the total number of refined parameters.

III.4.4. Magnetic measurements

**Figure S.III-5.** Magnetization versus H/T plots at different temperatures for **3** (left) and **4** (right).

III.5. References

1. (a) Sato, O.; Iyoda, T.; Fujishima, A.; Hashimoto, K. *Science* **1996**, 272, 704-705; (b) Sato, O.; Einaga, Y.; A. Fujishima, A.; K. Hashimoto, K. *Inorg. Chem.* **1999**, 38, 4405-4412; (c) Sato, O.; Tao, J.; Zhang, Y.-Z. *Angew. Chem.* **2007**, 119, 2200-2236; (d) Sato, O.; Tao, J.; Zhang, Y.-Z. *Angew. Chem., Int. Ed.* **2007**, 46, 2152-2187.
2. Catala, L.; Volatron, F.; Brinzei, D.; Mallah, T. *Inorg. Chem.* **2009**, 48, 3360-3370.
3. (a) Beltran, L. M. C.; Long, J. R. *Acc. Chem. Res.* **2005**, 38, 325-334; (b) Rebilly, J.-N.; Mallah, T. *Struct. Bonding* **2006**, 122, 103-131; (c) Wang, S.; Ding, X.-H.; Zuo, J.-L.; You, X.-Z.; Huang, W. *Coord. Chem. Rev.* **2011**, 255, 1713-1732; (c) Newton, G. N.; Nihei, M.; Oshio, H. *Eur. J. Inorg. Chem.* **2011**, 3031-3042.
4. (a) Wang, S.; Zuo, J.-L.; Zhou, H.-C.; Choi, H. J.; Ke, Y.; Long, J. R.; You, X.-Z. *Angew. Chem., Int. Ed.* **2004**, 43, 5940-5943; (b) Li, D.; Clérac, R.; Parkin, S.; Wang, G.; Yee, G. T.; Holmes, S. M. *Inorg. Chem.* **2006**, 45, 5251-5253; (c) Li, D.; Parkin, S.; Wang, G.; Yee, G. T.; Clérac, R.; Wernsdorfer, W.; Holmes, S. M. *J. Am. Chem. Soc.* **2006**, 128, 4214-4215; (d) Schelter, E. J.; Karadas, F.; Avendano, C.; Prosvirin, A. V.; Wernsdorfer, W.; Dunbar, K. R. *J. Am. Chem. Soc.* **2007**, 129, 8139-8149; (e) Freedman, D. E.; Jenkins, D. M.; Iavarone, A. T.; Long, J. R. *J. Am. Chem. Soc.* **2008**, 130, 2884-2885; (f) Li, D.; Parkin, S.; Wang, G.; Yee, G. T.; Prosvirin, A. V.; Holmes, S. M. *Inorg. Chem.* **2005**, 44, 4903-4905.
5. (a) Nihei, M.; Ui, M.; Yokota, M.; Han, L.; Maeda, A.; Kishida, H.; Okamoto, H.; Oshio, H. *Angew. Chem., Int. Ed.* **2005**, 44, 6484-6487; (b) Herchel, R.; Boca, R.; Gembicky, M.; Kozisek, J.; Renz, F. *Inorg. Chem.* **2004**, 43, 4103-4105; (c) Shatruck, M.; Dragulescu-Andrasi, A.; Chambers, K. E.; Stoian, S. A.; Bominaar, E. L.; Achim, C.; Dunbar, K. R. *J. Am. Chem. Soc.* **2007**, 129, 6104-6116; (d) Boldog, I.; Munoz-Lara, F. J.; Gaspar, A. B.; Munoz, M. C.; Sereidyuk, M.; Real, J. A. *Inorg. Chem.* **2009**, 48, 3710-3719.
6. (a) Berlinguette, C. P.; Dragulescu-Andrasi, A.; Sieber, A.; Galan-Mascaros, J. R.; Güdel, H.-U.; Achim, C.; Dunbar, K. R. *J. Am. Chem. Soc.* **2004**, 126, 6222-6223; (b) Li, D.; Clérac, R.; Roubeau, O.; Harté, E.; Mathonière, C.; Le Bris, R.; Holmes, S. M. *J. Am. Chem. Soc.* **2008**, 130, 252-258; (c) Zhang, Y.; Li, D.; Clérac, R.; Kalisz, M.; Mathonière, C.; Holmes, S. M. *Angew. Chem., Int. Ed.* **2010**, 49, 3752-3756; (d) Mercuriol, J.; Li, Y.; Pardo, E.; Risset, O.; Seuleiman, M.; Rousselière, H.; Lescouëzec, R.; Julve, M. *Chem. Commun.* **2010**, 46, 8995-8997; (e) Nihei, M.; Sekine, Y.; Suganami, N.; Oshio, H. *Chem. Lett.* **2010**, 39, 978-979; (f) Nihei, M.; Sekine, Y.; Suganami, N.; Nakazawa, K.; Nakao, H.; Murakami, Y.; Oshio, H. *J. Am. Chem. Soc.*, **2011**, 133, 3592-3600; (g) Siretanu, D.; Li, D.; Buisson, L.; Bassani, D. M.; Holmes, S. M.; Mathonière, C.; Clérac, R. *Chem.-Eur. J.* **2011**, 17, 11704-11708. (h) Hilfiger, M.; Chen, M.; Brinzari, T.; Nocera, T.; Shatruck, M.; Petasis, D.; Musfeldt, J.; Achim, C.; Dunbar, K. R. *Angew. Chem., Int. Ed.* **2010**, 49, 1410-1413; (i) Funck, K. E.; Prosvirin, A. V.; Mathonière, C.; Clérac, R.; Dunbar, K. R. *Inorg. Chem.* **2011**, 50, 2782-2789; (j) Bernhardt, P. V.; Martinez, M. *Inorg. Chem.* **1999**, 38, 424-425.
7. Bleuzen, A.; Marvaud, V.; Mathonière, C.; Sieklucka, B.; Verdager, M. *Inorg. Chem.* **2009**, 48, 3453-3466.
8. (a) Heinrich, J. L.; Berseth, P. A.; Long, J. R. *Chem. Commun.* **1998**, 1231-1232; (b) Klausmeyer, K. K.; Rauchfuss, T. B.; Wilson, S. R. *Angew. Chem. Int. Ed.* **1998**, 37, 1694-1696; (c) Klausmeyer, K. K.; Wilson, S. R.; Rauchfuss, T. B. *J. Am. Chem. Soc.* **1999**, 121, 2705-2711; (d) Gu, Z.-G.; Liu, W.; Yang, Q.-F.; Zhou, X.-H.; Zuo, J.-L.; You, X.-Z. *Inorg. Chem.* **2007**, 46, 3236-3244; (e) Gu, Z.-G.; Liu, W.; Yang, Q.-F.; Zhou, X.-H.; Zuo, J.-L.; You, X.-Z. *Inorg. Chem.* **2007**, 46, 3236-3244; (f) Nihei, M.; Ui, M.; Hoshino, N.; Oshio, H. *Inorg. Chem.* **2008**, 47, 6106-6108.
9. Siretanu, D. *PhD Thesis*, Univ. of Bordeaux 1, **2011**.
10. (a) Kitchen, J. A.; White, N. G.; Jameson, G. N. L.; Tallon, J. L.; Brooker, S. *Inorg. Chem.* **2011**, 50, 4586-4597; (b) Tafili-Kryeziu, M.; Weil, M.; Muranaka, T.; Bousseksou, A.; Hasegawa, M.; Jun A.; Linert, W. *Dalton Trans.*, **2013**, 42, 15796-15804; (c) Yamada, M.; Hagiwara, H.; Torigoe, H.; Matsumoto, N.; Kojima, M.; Dahan, F.; Tuchagues, J.-P.; Re, N.; Iijima, S. *Chem. Eur. J.* **2006**, 12, 4536-4549.
11. Li, D.; Parkin, S.; Wang, G.; Yee, G.T.; Holmes, S.M. *Inorg. Chem.* **2006**, 45, 1951-1959.
12. Nakamoto, K. *Infrared and Raman Spectra of Inorganic and Coordination Compounds*, 5th Ed. John Wiley and Sons: New York, **1997**.
13. Kaiba, A.; Shepherd, H. J.; Fedouai, D.; Rosa, P.; Goeta, A. E.; Rebbani, N.; Létard, J. F.; Guionneau, P. *Dalton Trans.*, **2010**, 39, 2910-2918.

Chapter IV
Revealing and Tuning the Electron Transfer
Properties by Solubilization of Functionalized
Molecular Squares

Table of Contents for Chapter IV:

IV.1. Introduction	IV.143
IV.2. Synthesis and characterizations of functionalized molecular {Fe ₂ Co ₂ } squares in solid state	IV.144
IV.2.1. Synthetic procedures and FT-IR characterizations	IV.144
IV.2.2. Structural investigations of functionalized molecular {Fe ₂ Co ₂ } squares	IV.145
IV.2.2.1. {[Tp*]Fe(CN) ₃] ₂ [Co(diC6bpy) ₂] ₂ }[OTf] ₂ ·2DMF (5).....	IV.146
IV.2.2.2. {[Tp*]Fe(CN) ₃] ₂ [Co(diC13bpy) ₂] ₂ }[OTf] ₂ ·H ₂ O·3CH ₃ OH (6).....	IV.148
IV.2.3. Reflectivity studies	IV.150
IV.2.4. Magnetic measurements	IV.151
IV.3. Analytical characterizations of functionalized molecular {Fe ₂ Co ₂ } squares in diluted solutions ...	IV.152
IV.3.1. UV-Vis spectroscopic characterizations 5 and 6 in diluted solutions	IV.153
IV.3.2. Magnetic properties of 5 and 6 in solutions	IV.155
IV.4. Conclusions and perspectives	IV.158
IV.5. Supporting materials	IV.160
IV.5.1. Experimental protocols.....	IV.160
IV.5.2. Crystallographic data for 5 and 6	IV.161
IV.5.3. UV-Vis studies in diluted solutions of 5 and 6	IV.163
IV.5.4. Magnetic measurements in solid state.....	IV.165
IV.5.5. Magnetic measurements in solutions	IV.166
IV.6. References	IV.168

IV.1. Introduction

In this fourth chapter, the functionalization of the tetranuclear cyanido-bridged $\{\text{Fe}_2\text{Co}_2\}$ squares with long alkyl chains is described. Adding long alkyl chains to the outer periphery (Figure IV-1) can induce new possibilities for the dispersion or self-organization of the complexes in solution, mesophases or the solid state. Such approach can improve the solubility of a magnetic material in various solvents that could make easier the fabrication of thin films and coatings, or even liquid phase processing.

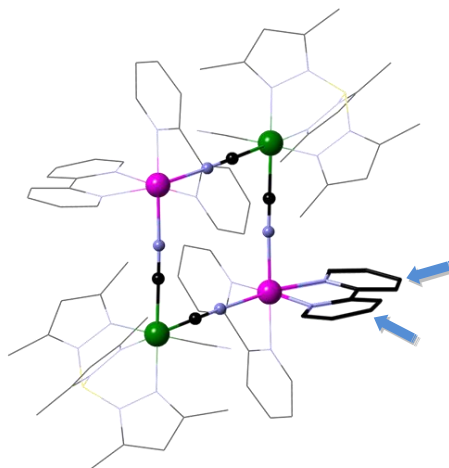


Figure IV-1. Schematic representation of the strategy used to get more soluble systems by functionalizing bipyridine ligand in 4- and 4'- positions (blue arrows). The core and only one bipyridine ligand are emphasized in the shown $\{[(\text{Tp}^*)\text{Fe}(\text{CN})_3]_2[\text{Co}(\text{bpy})_2]_2\}^{2+}$ complex. Color scheme: Fe green, Co pink, B yellow, N blue, C black.

The main motivation of the design of hybrid magnetic materials is to obtain systems exhibiting novel synergetic effects and to preserve the original magnetic behavior (eventually improving it). But, besides the benefits, the functionalization of organic ligands of known molecular magnetic materials may significantly alter their original properties, as well. The functionalization of pyridine-based ligands used for the synthesis of $\{\text{Fe}_2\text{Co}_2\}$ square complexes appears to be an efficient way to control the ET induced switching of magnetic and optical properties. Through the methyl functionalization of the bipyridine (bpy) ligands in **1** ($\{[(\text{Tp}^*)\text{Fe}(\text{CN})_3]_2[\text{Co}(\text{bpy})_2]_2\}(\text{OTf})_2 \cdot 2\text{H}_2\text{O} \cdot 4\text{DMF}$,¹ see also Chapter III), compound **2** ($\{[(\text{Tp}^*)\text{Fe}(\text{CN})_3]_2[\text{Co}(\text{diMebpy})_2]_2\}(\text{OTf})_2 \cdot \text{H}_2\text{O} \cdot 2\text{DMF}$,^{2,3} where diMebpy = 4,4'-dimethyl-2,2'-bipyridine, see also Chapter III) was obtained, preserving the magnetic and optical bistability driven by thermally and photoinduced intramolecular electron transfer process in solid state. This system with improved solubility showed the possibility to transfer the solid state properties of $\{\text{Fe}_2\text{Co}_2\}$ complexes into a wide range of solvents. Moreover, a fine-tuning of the electron transfer and associated magnetic and optical properties of **2** in solution was demonstrated over a broad range of temperatures by simply adjusting the solvent composition and polarity.^{2,3} Another square system with *tert*-butyl groups in 4- and 4'- positions on bpy ligands $\{[(\text{Tp}^*)\text{Fe}(\text{CN})_3]_2[\text{Co}(\text{dtbbpy})_2]_2\}(\text{PF}_6)_2 \cdot 2\text{MeOH}$ (where dtbbpy = 4,4'-di-*tert*-butyl-2,2'-bipyridine) exhibits electron transfer process in solid state and in butyronitrile solutions, that is induced by the temperature and/or by protonation.⁴

In this chapter, two new functionalized complexes $\{[(\text{Tp}^*)\text{Fe}(\text{CN})_3]_2[\text{Co}(\text{diC6bpy})_2]_2\}[\text{OTf}]_2 \cdot 2\text{DMF}$ (**5**) and $\{[(\text{Tp}^*)\text{Fe}(\text{CN})_3]_2[\text{Co}(\text{diC13bpy})_2]_2\}[\text{OTf}]_2 \cdot \text{H}_2\text{O} \cdot 3\text{CH}_3\text{OH}$ (**6**) (where diC6bpy = 4,4'-dihexyl-2,2'-

bipyridine, and diC13bpy = 4,4'-ditridecyl-2,2'-bipyridine) are investigated with the aim to probe the effect of the functionalization on intramolecular ET process in cyanido-bridged $\{\text{Fe}_2\text{Co}_2\}$ molecular squares and to determine if their switching properties can be transferred in a general manner to different solvents. The full characterization of compounds **5** and **6** in solid state, and in solutions is described.

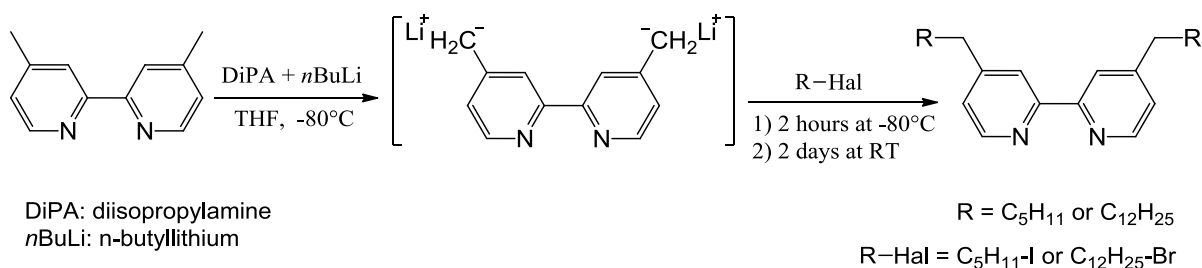
The preliminary work related to the synthesis of the complex **6** presented in this chapter was performed by Diana Siretanu during her PhD thesis (CRPP, 2008 – 2011).³ For a better understanding of functionalization effect in solid state and in solutions, the complete investigations of complexes **5** and **6** are presented together within this chapter.

IV.2. Synthesis and characterizations of functionalized molecular $\{\text{Fe}_2\text{Co}_2\}$ squares in solid state

IV.2.1. Synthetic procedures and FT-IR characterizations

In order to apply the functionalization strategy (Figure IV-1), the diC6bpy and diC13bpy ligands were first synthesized. A large variety of functionalizations can be done on the bipyridine ligand.⁵ The ligands with alkyl chains in 4- and 4'- positions were synthesized from the 4,4'-dimethyl-2,2'-bipyridine following a reported protocol.^{5a} The synthesis generally proceeds in good yields when the alkylation is performed at low temperatures (193 K/-80°C) with the corresponding 1-bromo- or 1-iodoalkane in the presence of lithium diisopropylamide (Scheme IV-1). The 4,4'-dihexyl-2,2'-bipyridine (diC6bpy) was purified by column chromatography, while the 4,4'-ditridecyl-2,2'-bipyridine (diC13bpy) was purified by recrystallization from ethanol (see Section IV.5.1 for detailed protocols).

Scheme IV-1. Reaction scheme for the synthesis of 4,4'-dialkyl-2,2'-bipyridine ligands.



Functionalized complexes **5** and **6** were prepared using the same precursors $(\text{NEt}_4)[(\text{Tp}^*)\text{Fe}(\text{CN})_3]$ and $\text{Co}(\text{OTf})_2$, and the same synthetic procedure (see Sections III.2.1 and IV.5.1 for details) adapted from the previously reported syntheses of complexes **1** and **2**.¹⁻³ Due to the presence of long alkyl chains, we had doubts that it was possible to obtain single-crystals of **5** and **6**. Preliminary crystallization tests showed that addition of diethyl ether to the reaction mixture of **5** allows precipitation of red powder that shows IR stretching bands characteristic to cyanido-bridged $\{\text{Fe}_2\text{Co}_2\}$ square complexes in the FT-IR spectra (Figure IV-2 left).¹⁻⁴ The strong stretching band at 2149 cm^{-1} corresponds to the cyanide groups in bridging mode^{1-3,6,7} and a weaker one at 2118 cm^{-1} is specific to the free terminal cyanide on the Fe sites.^{1-3,8,9} Both signatures are observed in the FT-IR spectrum of the raw powder (Figure IV-2 left). The presence of the B-H stretching band from the Tp* ligand at 2554 cm^{-1} and the intense C-H bands at 2927 and 2856 cm^{-1} (from diC6bpy

ligand) confirms, as well, the formation of functionalized complex **5**. The red color of the raw powder of **5** and the high energies of C≡N and B-H bands suggest that the system is in the paramagnetic $\{\text{Fe}^{\text{III}}_{\text{LS}}(\mu\text{-CN})\text{Co}^{\text{II}}_{\text{HS}}\}$ state.¹⁻⁴ Fortunately, it was possible to obtain single-crystals of **5** by layering the DMF solution of the reaction mixture with diethyl ether. The FT-IR spectrum of the dark red crystals of **5** is identical to the one recorded for the raw powder (Figure IV-2 left).

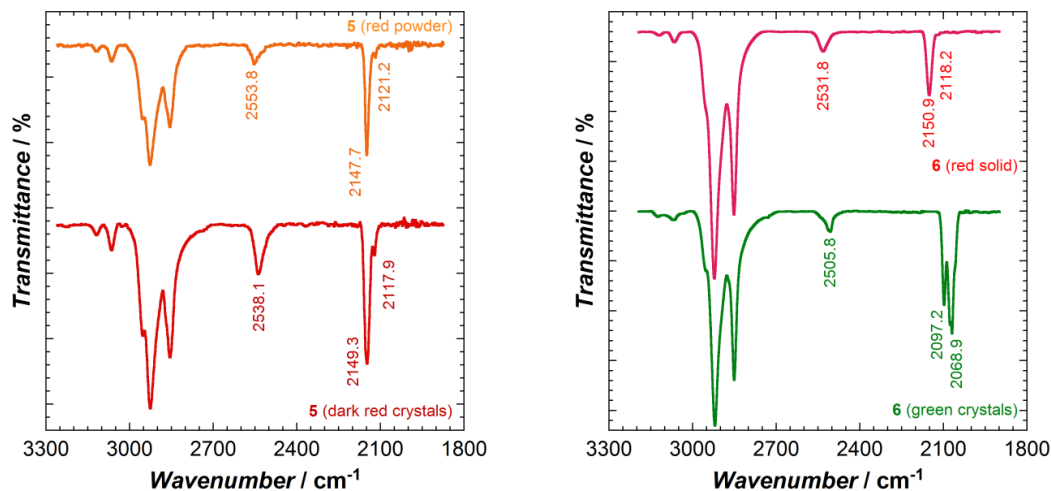


Figure IV-2. FT-IR spectra collected between 3300 and 1800 cm^{-1} at 290 K: (left) for the raw powder and crystals of **5**; (right) for solvated green crystals and dry red crystals of **6**.

Addition of diethyl ether to the reaction mixture of **6** in DMF did not allow precipitation of the raw powder of **6** and showed that the functionalized compound is very well soluble in ether. Therefore it was impossible to crystallize **6** using ether diffusion and layering techniques. Moreover, the red powder of **6** obtained after the evaporation of the reaction mixture is very well soluble at room temperature in most of the solvents. Nevertheless, crystals of **6** could be obtained by cooling down its methanol solution to 253 K (-20 °C). The crystals are well shaped green prisms, which re-dissolve at room temperature, forming a red solution, but re-crystallize again when temperature is decreased. The green crystals of **6** turn irreversibly red if they are kept outside the mother liquor. The FT-IR spectra of these two solid forms are represented in Figure IV-2 right. The spectrum of the red solid is very similar to the room temperature FT-IR spectra of compounds **1**, **2** and **5**. Only the stretching bands around 2900 cm^{-1} are stronger that is in good agreement with tridecyl chains present on the 4- and 4'- positions of the bipyridine. The FT-IR spectrum of green crystals shows bathochromic shifts of the peaks to lower energies. The B-H stretch shifts to 2505 cm^{-1} and C≡N stretches are present at 2097 and 2069 cm^{-1} that is characteristic to diamagnetic $\{\text{Fe}^{\text{II}}_{\text{LS}}(\mu\text{-CN})\text{Co}^{\text{III}}_{\text{LS}}\}$ pairs in the green crystals of **6** (Figure IV-2 right),^{1,3,7-9} whereas the dried red crystals agree with the paramagnetic $\{\text{Fe}^{\text{III}}_{\text{LS}}(\mu\text{-CN})\text{Co}^{\text{II}}_{\text{HS}}\}$ state of the square complex.

IV.2.2. Structural investigations of functionalized molecular $\{\text{Fe}_2\text{Co}_2\}$ squares

In order to determine whether the functionalized complexes undergo ET process and the associated structural changes, single crystals of complexes **5** and **6** were subjected to temperature dependent X-ray diffraction analysis. Crystal structures of compound **5** were determined at 100 and 260 K. The crystals of **6** are green up to 280 K. At higher temperatures (around 310 K for a crystal in Paratone-N oil), the color turns

red, but unfortunately, the compound is not crystalline anymore. The heating causes the evaporation of the intermolecular solvent and the loss of the crystallinity. Therefore, the X-Ray analysis for red $\{\text{Fe}^{\text{III}}_2\text{Co}^{\text{II}}_2\}$ state in **6** could not be performed. Green solvated crystals of **6** in $\{\text{Fe}^{\text{II}}_2\text{Co}^{\text{III}}_2\}$ state can be obtained again only by recrystallization of the red complex in an appropriate solvent at low temperatures.

IV.2.2.1. $\{[(\text{Tp}^*)\text{Fe}(\text{CN})_3]_2[\text{Co}(\text{diC6bpy})_2]_2\}[\text{OTf}]_2 \cdot 2\text{DMF}$ (**5**)

X-ray crystal structure analysis of complex **5** was performed at 260 and 100 K (Tables IV–1 and S.IV–1). No structural changes specific to thermally induced intramolecular ET were observed on cooling the dark red crystal of **5** from 260 to 100 K (Tables IV–1 and S.IV–1), suggesting that compound **5** is always in its paramagnetic $\{\text{Fe}^{\text{III}}_2\text{Co}^{\text{II}}_2\}$ state. Single-crystal X-ray diffraction analysis showed that **5** crystallizes in the monoclinic $P2_1/c$ space group with a square-shaped tetranuclear core, in which Fe and Co ions are alternately bridged by cyanide ions, in the same way as in complexes **1** and **2**.¹⁻³ The unit cell consists of a centrosymmetric cyanido-bridged $\{\text{Fe}_2\text{Co}_2\}$ square, two free trifluoromethanesulfonate ions and two DMF molecules. The structure of the cationic $\{\text{Fe}_2(\mu\text{-CN})_4\text{Co}_2\}$ part at 100 K is showed in Figure IV-3.

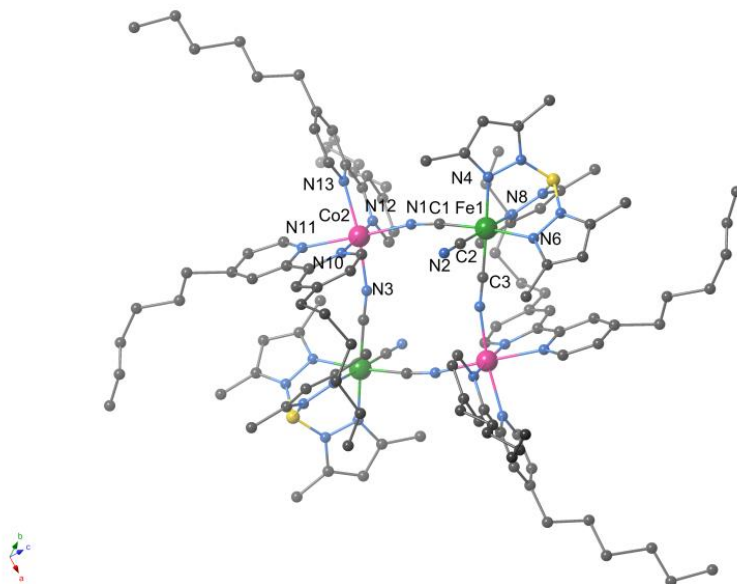


Figure IV-3. Structure of the cationic part of **5** at 100 K. Lattice solvents, anions, and hydrogen atoms are omitted for clarity. Colour scheme: Fe green, Co pink, B yellow, N blue, C grey.

The average Co-N bond length of 2.13 Å at 100 K and 260 K is characteristic of the HS Co^{II} ions, while the average Fe-C (1.92 Å) and Fe-N (2.00 Å) bond distances (Table IV-1) are similar to those measured for the LS Fe^{III} ions in the paramagnetic state of **1** and **2**.

The $\{\text{Fe}_2(\mu\text{-CN})_4\text{Co}_2\}$ core in **5** adopts a significantly distorted square geometry. The bond-angles N(1)-Co(1)-N(3) ($99.3(2)^\circ$) and C(1)-Fe(1)-C(3) ($83.8(2)^\circ$) are far from orthogonality. The cyanide bridges are notably bent especially on the cobalt sites with Co-N-C angles of $165.9(5)$ and $168.3(5)^\circ$, while the Fe-C-N angles range between $176.6(5)$ and $178.2(6)^\circ$ (Table S.IV-1). The Fe-CN-Co edges are quasi identical since the Fe(1) \cdots Co(1) and Fe(1) \cdots Co(2) distances are 5.087 and 5.115 Å, respectively, while the Fe \cdots Fe and Co \cdots Co distances are 7.759 and 6.24 Å, respectively. Both iron and cobalt ions are six-coordinate. The FeN_3C_3 environment is less distorted than the CoN_6 coordination sphere. The distortion parameter (Σ) for HS

Co^{II} ion has a value of 80.4° at 100 K and is bigger than the ones measured for complexes **1** – **4** (see Section III.2.3) in their paramagnetic state.

Table IV-1. Unit-cell parameters, average metal-to-ligand bond lengths, metal-to-metal distances and deformation of the Co coordination sphere for **5** under different experimental conditions, for **6** at 100 K.

	(5)		(6)
	100 K {Fe ^{III} ₂ Co ^{II} ₂ }	260 K {Fe ^{III} ₂ Co ^{II} ₂ }	100 K {Fe ^{II} ₂ Co ^{III} ₂ }
Crystal system	monoclinic	monoclinic	triclinic
Space group	P2 ₁ /c	P2 ₁ /c	P1
a, Å	12.8665(14)	12.939(4)	11.9217(13)
b, Å	29.832(4)	30.070(8)	16.8399(18)
c, Å	19.772(2)	20.136(6)	25.069(3)
α, °	90.00	90.00	78.207(5)
β, °	112.886(7)	112.923(18)	80.997(6)
γ, °	90.00	90.00	78.043(6)
V, Å ³	6991.7(14)	7216(4)	4785.4(9)
<Fe-C>, Å	1.923	1.921	1.880
<Fe-N>, Å	1.996	1.996	2.047
<Co-N>, Å	2.122	2.130	1.928
Fe(1)⋯Co(1), Å	5.087	5.108	4.884
Fe(1)⋯Co(2), Å	5.115	5.107	4.892
Fe⋯Fe, Å	7.759	7.749	7.129
Co⋯Co, Å	6.624	6.656	6.688
Σ(N-Co-N) ^a , °	80.37	81.6	38.5

^a Σ = Σ_{i=1}¹² |90 - φ_i|, where φ_i are N-Co-N bond angles

The functionalization with hexyl chains contributes to a better isolation of {Fe₂(μ-CN)₄Co₂} units in the crystal packing of **5**. No intermolecular short contact, besides weak van-der-Waals interactions between the hydrocarbon chains, are observed between adjacent square complexes inside the crystal packing (as illustrated by Figure IV-4).

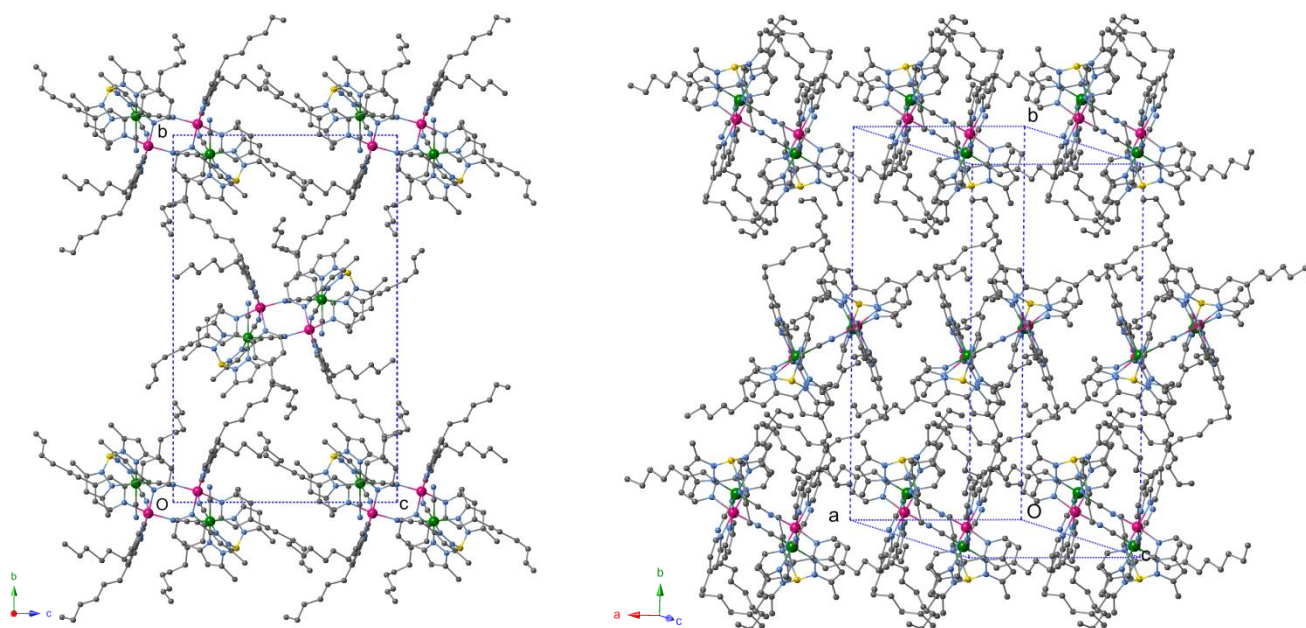


Figure IV-4. Perspective views of the crystal packing of **5** at 100 K. Lattice solvents, anions, and hydrogen atoms are omitted for clarity. Colour scheme: Fe green, Co pink, B yellow, N blue, C grey.

IV.2.2.2. $\{[(\text{Tp}^*)\text{Fe}(\text{CN})_3]_2[\text{Co}(\text{diC13bpy})_2]_2\}[\text{OTf}]_2 \cdot \text{H}_2\text{O} \cdot 3\text{CH}_3\text{OH}$ (**6**)

In contrast to complex **5**, compound **6** is very well soluble in diethyl ether, so it cannot be crystallized in the same manner. Surprisingly, crystals of **6** were obtained by cooling down its methanol solution to 253 K. The crystals of **6** are well shaped green prisms, which re-dissolve at room temperature to form a red solution. But they re-crystallize again when the temperature is decreased. Due to the high solubility at room temperature, the single crystal must be mounted very quickly on the X-ray diffractometer directly at 100 K, otherwise some parts of the crystal alter.

The crystal structure of $\{[(\text{Tp}^*)\text{Fe}(\text{CN})_3]_2[\text{Co}(\text{diC13bpy})_2]_2\}[\text{OTf}]_2 \cdot \text{H}_2\text{O} \cdot 3\text{CH}_3\text{OH}$ (**6**) was solved in triclinic *P1* space group. In contrast to the main parts of the tetranuclear core, some parts of the alkyl chains are not symmetrically equivalent through an inversion center, as it is in complexes **1** – **5**. Moreover, the resolution in *P-1* space group gives unequivocal evidences that there is no center of inversion: in particular, some part of some disordered alkyl chains are too close to coexist with their image generated through the inversion center. Therefore, the crystal structure was solved in *P1* space group using TWIN and BASF commands giving rise to a Flack parameter of 0.5 (racemic or twinned crystal).

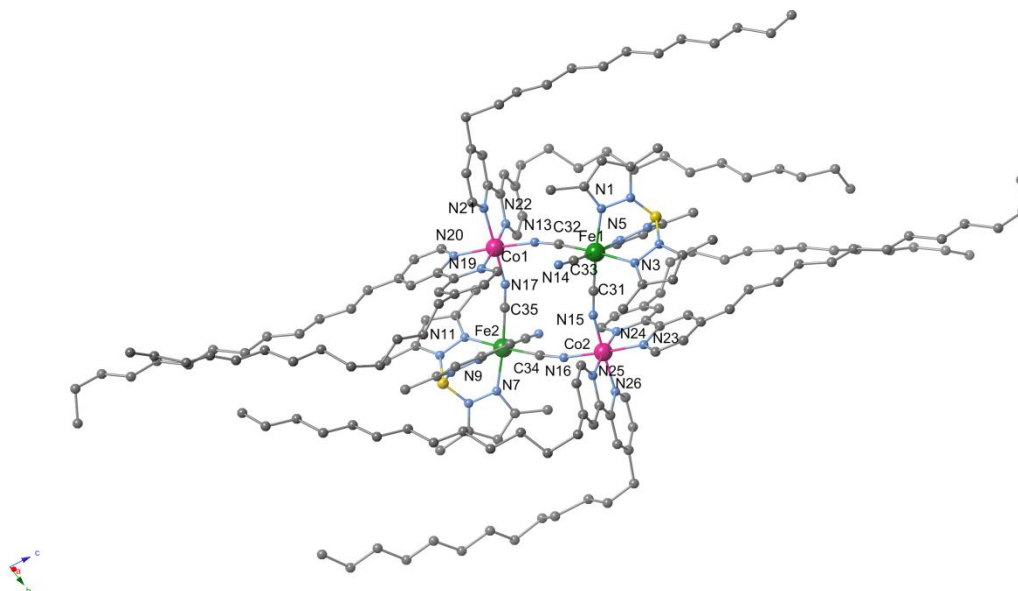


Figure IV-5. Structure of the cationic part of **6** at 100 K. Lattice solvents, anions, and hydrogen atoms are omitted for clarity. Color scheme: Fe green, Co pink, B yellow, N blue, C grey.

The global structure of compound **6** (Figure IV-5), is consistent with that of compound **2** at 100 K in its diamagnetic $\{\text{Fe}^{\text{II}}_{\text{LS}}(\mu\text{-CN})\text{Co}^{\text{III}}_{\text{LS}}\}$ state,^{2,3} as confirmed by the green color of crystals and the FT-IR spectroscopy. The average Co-N bond distances of 1.928 Å suggest that Co ions are trivalent and in LS configuration, while the average Fe-N and Fe-C bond distances of 2.047 Å and 1.880 Å (Table IV-1), respectively, are in the agreement with the values measured for LS Fe^{II} ions.^{1-4,7-9}

The heterometallic cyanido-bridged core has a distorted square shape, based on N(17)-Co(1)-N(13) and C(32)-Fe(1)-C(31) bond angles of 92.2(4)° and 87.8(5)°, respectively. The $\{\text{Fe}(\mu\text{-CN})\text{-Co}\}$ edges are bent. On the cobalt sites, Co-N-C angles are 165.6(8) and 168.7(8)°, while the Fe-C-N angles range between 171.8(9) and 176.5(9)° (Table S.IV-2). The Fe-CN-Co edges are quasi identical and shorter than in **5**: the Fe(1)⋯Co(1) and Fe(1)⋯Co(2) distances are 4.884 and 4.892 Å, respectively. The Fe⋯Fe and Co⋯Co

distances are 7.129 and 6.688 Å, respectively (Table IV-1). The angular distortion parameter on the Co sites has a value of 38.5° that is a few degrees higher than the one measured in **2** in its diamagnetic {Fe^{II}Co^{III}} state at low temperatures. One bipyridine ligand has stretched alkyl chains pointing the *c* unit cell direction, while in the other one, the chains are bent following the direction of stretched chains. Therefore, all chains are arranged along the *c* axis of the unit cell (Figure S.IV-1).

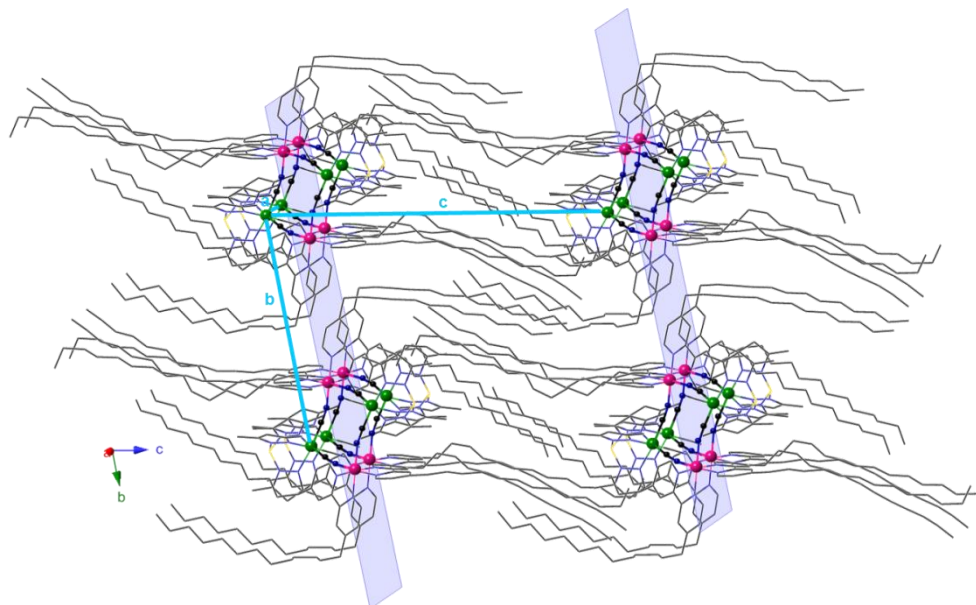


Figure IV-6. Packing diagram of **6** in the *bc* plane emphasizing one unit cell. Lattice solvent molecules, anions, and hydrogen atoms are omitted for clarity. Color scheme: Fe green, Co pink, B yellow, N blue, C grey.

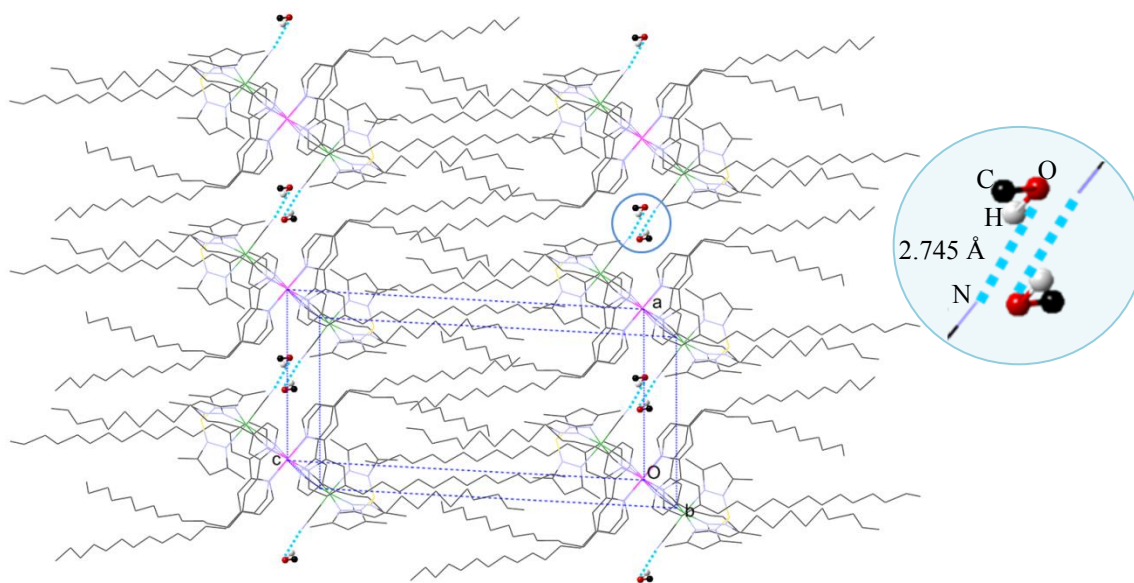


Figure IV-7. Packing diagram of **6** in the *ac* plane illustrating the H bonding between solvent molecules and terminal cyanide groups. Anions and hydrogen atoms are omitted for clarity. Color scheme: Fe green, Co pink, B yellow, N blue, C grey, O red.

As a consequence, the packing of **6** shows a layered structure (Figures IV-6 and S.IV-1). The molecular squares are arranged face to face along the *a* axis in the (*bc*) plane, separated by 11.9217(13) Å equal to the *a* parameter of the unit cell. The aliphatic chains of adjacent layers are strongly interdigitated, separating the layers by 25.069(3) Å, value of the *c* parameter of the unit cell. The alkyl chains are packed

and are separated by about 5 Å. Because of the weak van-der-Waals interactions between the hydrocarbon chains, the thermal motion increases from the beginning to the end of the chains. Methanol molecules form hydrogen bonds¹⁰ with terminal cyanide groups (Figure IV-7). Apparently, the H-bonds with methanol molecules are stabilizing the diamagnetic $\{\text{Fe}^{\text{II}}_2\text{Co}^{\text{III}}_2\}$ state that may be confirmed by the irreversible color change from green to red and by the loss of crystallinity, when the solvated green crystals of **6** are dried under vacuum or heated above 290 K.

IV.2.3. Reflectivity studies

In order to check the optical properties of the obtained complexes, solid state reflectivity spectra were collected between 500 and 900 nm at different temperatures. For the complex **5** and the dry form of compound **6**, the reflectivity spectrum at 280 K presents a strong absorption between 500 and 700 nm, and is similar to the spectra recorded for **1** and **2** in their paramagnetic state.¹⁻³ Absolute reflectivity at 550 nm is $R_{550} = 0.06$ for **5**, and $R_{800} = 0.03$ for red solid form of **6** (Figure IV-8). Between 295 and 10 K, no significant changes are observed, denoting that the compounds do not undergo thermally- or photo-induced electron transfer.

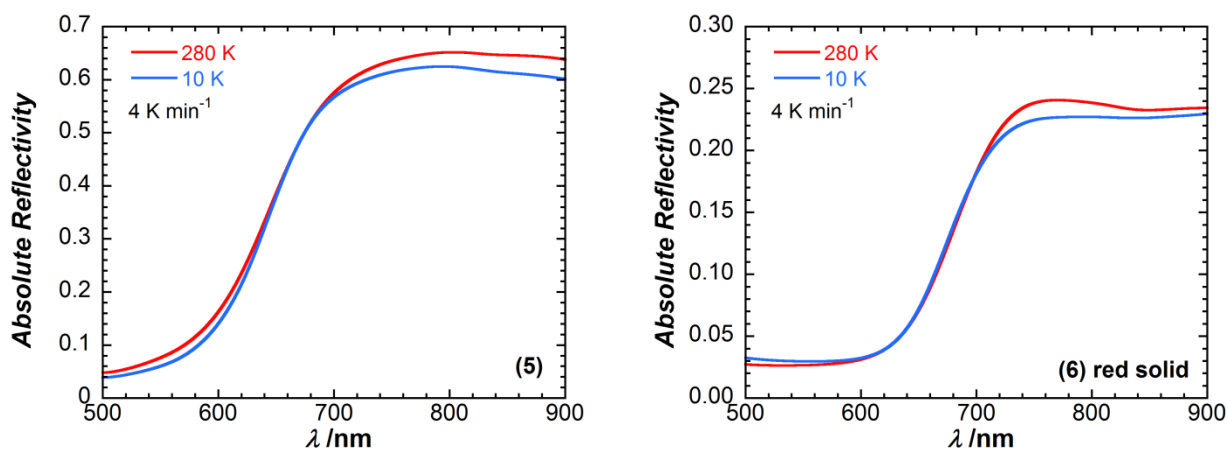


Figure IV-8. Reflectivity spectra of **5** (left) and red crystals of **6** (right) at 10 and 280 K (spectroscopic white light halogen source, $P = 0.5 \text{ mW/cm}^2$).

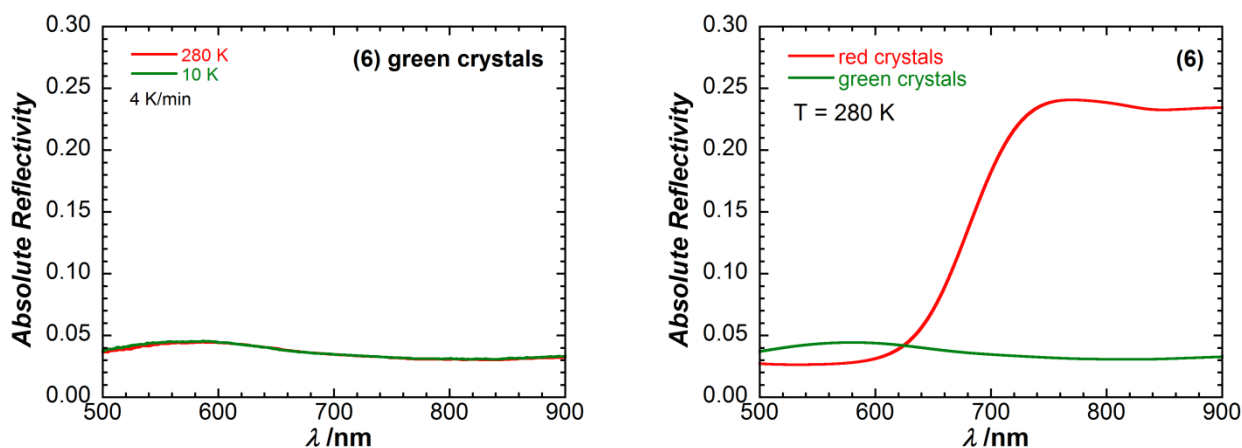


Figure IV-9. Reflectivity spectra of (left) the green crystals of **6** at 10 and 280 K, and (right) the comparison between the reflectivity spectra of green and red crystals of **6** (spectroscopic white light halogen source, $P = 0.5 \text{ mW/cm}^2$).

Solid state reflectivity measurements were also carried out for the solvated green crystals of **6**. The spectra recorded between 280 and 10 K showed no significant changes. The sample remains strongly absorbent in the studied spectral range (Figure IV-9 left), similarly to complexes **1** and **2** in their diamagnetic states.¹⁻³ Moreover, no spectral changes were observed after the irradiation with white light for several hours, meaning that solvated crystals of **6** do not undergo photo-induced electron transfer.

IV.2.4. Magnetic measurements

Magnetic susceptibility measurements (Figure IV-10) confirmed that functionalized molecular squares **5** and **6** do not undergo reversible thermally induced ET and, thus, do not exhibit switching between red paramagnetic state and the green diamagnetic one. The functionalized complex **5** is paramagnetic in the 1.9 – 270 K range, whereas complex **6** undergoes around 300 K an irreversible ET associated with a conversion between diamagnetic and paramagnetic states due to the loss of lattice MeOH molecules.

The temperature dependence of the χT product (where χ is the molar magnetic susceptibility per $\text{Fe}^{\text{III}}_2\text{Co}^{\text{II}}$ unit) for complex **5** shows a value of $7.3 \text{ cm}^3\cdot\text{K/mol}$ high temperatures (Figure IV-10 left). This value is slightly larger than the one expected for the sum of two magnetically isolated low-spin Fe^{III} ions ($S = 1/2$ with $g \approx 2.6$) and two high-spin Co^{II} ions ($S = 3/2$, $g \approx 2.4$). Upon cooling, χT slightly decreases to $7.0 \text{ cm}^3\cdot\text{K/mol}$ at 130 K. After this minimum the χT increases smoothly until ca. 40 K, in line with a ferromagnetic coupling between the Co^{II} and Fe^{III} atoms through the cyanide bridges. At $T < 40 \text{ K}$, χT sharply increases to reach maxima of ca. $11.3 \text{ cm}^3\cdot\text{K/mol}$ at 7.0 K. Then, it further decreases with T because of zero-field splitting or/and antiferromagnetic intermolecular interactions to reach a value of $9.82 \text{ cm}^3\cdot\text{K/mol}$ at 1.8 K. These features are consistent with ferromagnetic interactions inside the tetranuclear core of **5**. Additional evidence for ferromagnetic exchange between Fe^{III} and Co^{II} ions in **5** is found in the field-dependence of magnetization plots. At 1.8 K, the magnetization value is monotonically increasing upon applying the external dc fields, without showing S-shape curves that could be indicative for the presence of antiferromagnetic interactions. Moreover the magnetization curves show an absence of magnetization saturation which is consistent with magnetic anisotropy of the Co^{II} ions (Figure S.IV-5).

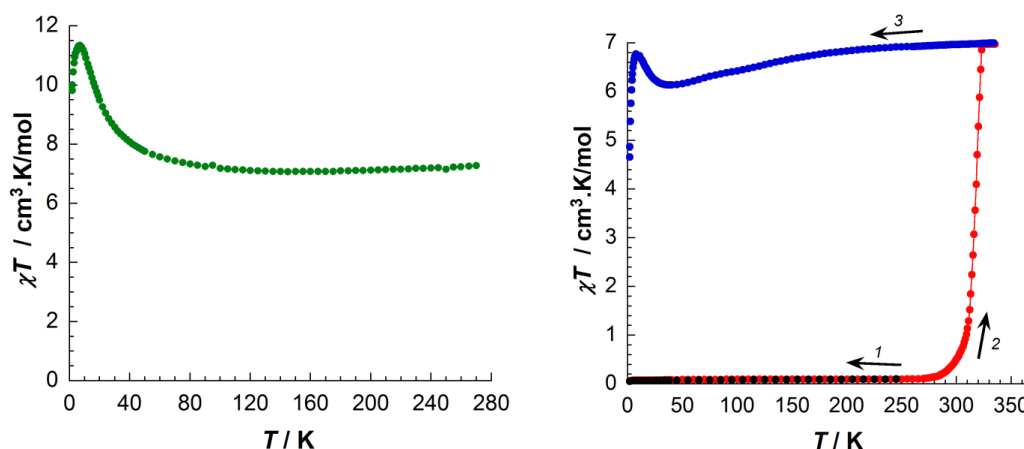


Figure IV-10. Temperature dependence of the χT product (with χ defined as the molar magnetic susceptibility and equal to M/H) for compound **5** at 0.1 T (left) and for compound **6** (right, 1-black on first cooling; 2-red on heating and 3-blue on second cooling at 0.4 K/min, 0.5 T).

The solvation in the functionalized complex **6**, particularly the H-bonded methanol molecules, generates stable diamagnetic $\{\text{Fe}^{\text{II}}_2\text{Co}^{\text{III}}_2\}$ species. The χT values very close to zero ($0.06 \text{ cm}^3\cdot\text{K}/\text{mol}$) (Figure IV-10 right, black curve), when **6** is measured on cooling from 250 K. Similarly to crystallographic analysis, the magnetic measurements confirm that solvated green crystals of **6** are diamagnetic. On heating mode above 295 K, χT values increase up to $7.0 \text{ cm}^3\cdot\text{K}/\text{mol}$ suggesting that the diamagnetic $\{\text{Fe}^{\text{II}}_2\text{Co}^{\text{III}}_2\}$ complexes transform into paramagnetic $\{\text{Fe}^{\text{III}}_2\text{Co}^{\text{II}}_2\}$ species (Figure IV-10 right, red curve). Due to the loss of lattice solvents, an irreversible ET occurred at 316 K. On second cooling, between 330 and 40 K, the χT product is only slightly decreasing from 7.0 to $6.2 \text{ cm}^3\cdot\text{K}/\text{mol}$ due to the intrinsic spin orbit coupling of the cobalt centers. This result confirms that the solvent (methanol) is lost from the crystal lattice when the sample is heated above 280 K and the paramagnetic $\{\text{Fe}^{\text{III}}_2\text{Co}^{\text{II}}_2\}$ units are irreversibly formed. At lower temperatures, the χT values rapidly increases to $\sim 7.0 \text{ cm}^3\cdot\text{K}/\text{mol}$ at 7 K, suggesting that (Figure IV-10 right, blue curve) $\text{Co}^{\text{II}}_{\text{HS}}$ and $\text{Fe}^{\text{III}}_{\text{LS}}$ centers are ferromagnetically coupled like in **5**. Below 7 K, the χT product decreases due to intermolecular antiferromagnetic interactions between adjacent molecular squares or zero-field splitting.

IV.3. Analytical characterizations of functionalized molecular $\{\text{Fe}_2\text{Co}_2\}$ squares in diluted solutions

The structural, spectroscopic and magnetic studies showed that functionalized complexes **5** and **6** do not undergo reversible thermally or photo-induced ET and, thus, do not exhibit switching of magnetic and optical properties associated with an ET process in solid state. The methyl functionalized molecular square, **2**, proved the possibility to transfer the ET driven switching properties of $\{\text{Fe}_2\text{Co}_2\}$ complexes from solid state into solutions with a wide range of solvents.^{2,3}

Table IV-2. Solubility of **2**, **5** and **6** in various solvents and qualitative tests for electron-transfer in their solutions.

Solvents	(2)	(5)	(6)
Water	×	×	×
Nitromethane	red - green	red - green	red - green
Methanol	red - green	red - green	red - green
Acetonitrile	red - green	red - green	red - green
Ethanol	red - green	red - green	red - green
Acetone	red - green	red - green	red - green
Ethyl acetate	×	red - green	red - green
Isopropanol	×	red - green	red - green
Tetrahydrofuran	×	red - green	red - green
Chloroform	red	red - green	red - green
<i>n</i> -Buthanol	×	red - green	red - green
Dichloromethane	red - green	red - green	red - green
Diethyl ether	×	×	red - green
Toluene	×	red	×
Hexane	×	×	×

× insoluble at 298 K; “red” color at all temperatures suggesting the absence of electron-transfer; “red - green” colors at 290 and 77 K suggesting an electron-transfer process in solution.

In order to determine if complexes **5** and **6** can exhibit ET properties and associated switching of their magnetic and optical properties in diluted solutions, the solubility of the functionalized complexes and the

properties of the resulting solutions have been studied. As it was expected, complexes **5** and **6** containing bipyridine ligands functionalized with long alkyl chains are soluble in a broader range of organic solvents in comparison to methyl functionalized complex **2** (Table IV-1).

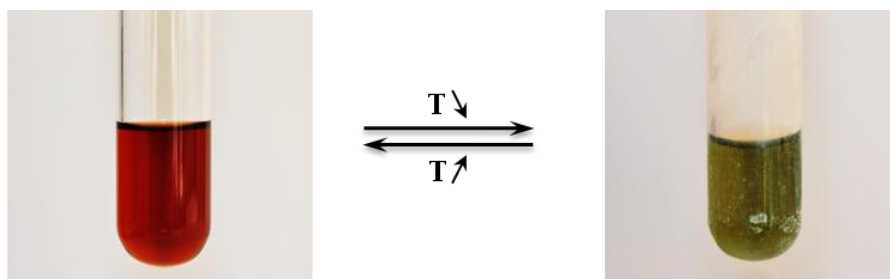


Figure IV-11. Change of color observed when a methanol solution of **5** is cooled from room temperature (left) and cooled down with liquid nitrogen (right).

In contrast to their electronic stability in the solid state, both compounds undergo ET in solution, as demonstrated by the color change of solutions from red at room temperature to green when cooled down to 77 K (Figure IV-11). The observed color change occurs in almost all of the tested solvents (Table IV-2). For the solutions where a change of color was observed, it was assumed that the square configuration of $\{\text{Fe}_2\text{Co}_2\}$ molecules remains intact in solution like for **1** and **2**.

It is important to mention that complexes **2**, **5** and **6** are well soluble in both DMSO and DMF, but no electron transfer associated color change was observed on cooling the red DMSO and DMF solutions. The color of these solutions changes very rapidly in time (from dark red to orange), the UV/Vis spectra are significantly altered. After a certain period of time (about several hours), crystalline materials of the starting materials are obtained, suggesting that these compounds decompose and/or disassemble in these solvents. Moreover, there is no proof about the existence of the $\{\text{Fe}_2\text{Co}_2\}$ molecules in solutions that stay red in the studied range of temperatures. For the solutions where a change of color was observed, it was assumed that the square configuration of $\{\text{Fe}_2\text{Co}_2\}$ molecules remained intact.

IV.3.1. UV-Vis spectroscopic characterizations **5** and **6** in diluted solutions

The ET associated thermochromism observed in solutions of **5** and **6** has been quantitatively studied by temperature dependent UV-Vis spectroscopy in four different solvents (dichloromethane, ethylacetate, acetone and methanol). These measurements have been performed at Institute des Sciences Moléculaires (ISM, Université Bordeaux-1) in collaboration with Dr. D. M. Bassani.

The UV-Vis absorption spectra reported for **2**^{2,3} and those collected for **5** and **6** at room temperature (295 – 300 K) in methanol are very similar (Figure IV-12). A broad absorption band is centered at 450 nm in addition to a small shoulder at ca. 540 nm (Figure IV-12 left). The intense absorption at 450 nm corresponds to a spin- and Laporte-allowed ligand-to-metal charge transfer (LMCT) transition,^{2-4,7,11} while the shoulder at 560 nm may be attributed to a $\text{Co}^{\text{II}} \rightarrow \text{Fe}^{\text{III}}$ metal-to-metal charge transfer (MMCT) transition.^{2-4,7} On cooling, the absorption band at 540 nm decreases progressively in intensity whereas a new absorption band, characteristic to the $\text{Fe}^{\text{II}} \rightarrow \text{Co}^{\text{III}}$ MMCT, appears around 760 nm (Figure IV-12 left). Thus, the spectroscopic data clearly demonstrate that a thermal conversion of $\{\text{Fe}^{\text{III}}_{\text{LS}}(\mu\text{-CN})\text{Co}^{\text{II}}_{\text{HS}}\}$ into $\{\text{Fe}^{\text{II}}_{\text{LS}}(\mu\text{-CN})\text{Co}^{\text{III}}_{\text{LS}}\}$ units

occurs in solution. Furthermore, the presence of an isobestic point at 608 nm suggests that only two species are involved in the thermal inter-conversion process. The temperature dependence of the $\{\text{Fe}^{\text{III}}_{\text{LS}}(\mu\text{-CN})\text{Co}^{\text{II}}_{\text{HS}}\}$ and $\{\text{Fe}^{\text{II}}_{\text{LS}}(\mu\text{-CN})\text{Co}^{\text{III}}_{\text{LS}}\}$ fractions can be deduced from the thermal variation of the 540 and 760 nm absorptions, respectively (Figure IV-12 right). As expected, the two fractions cross each other at 0.5 defining $T_{1/2}$ temperature as the temperature for which equal quantities of $\{\text{Fe}^{\text{III}}_{\text{LS}}(\mu\text{-CN})\text{Co}^{\text{II}}_{\text{HS}}\}$ and $\{\text{Fe}^{\text{II}}_{\text{LS}}(\mu\text{-CN})\text{Co}^{\text{III}}_{\text{LS}}\}$ species are present.

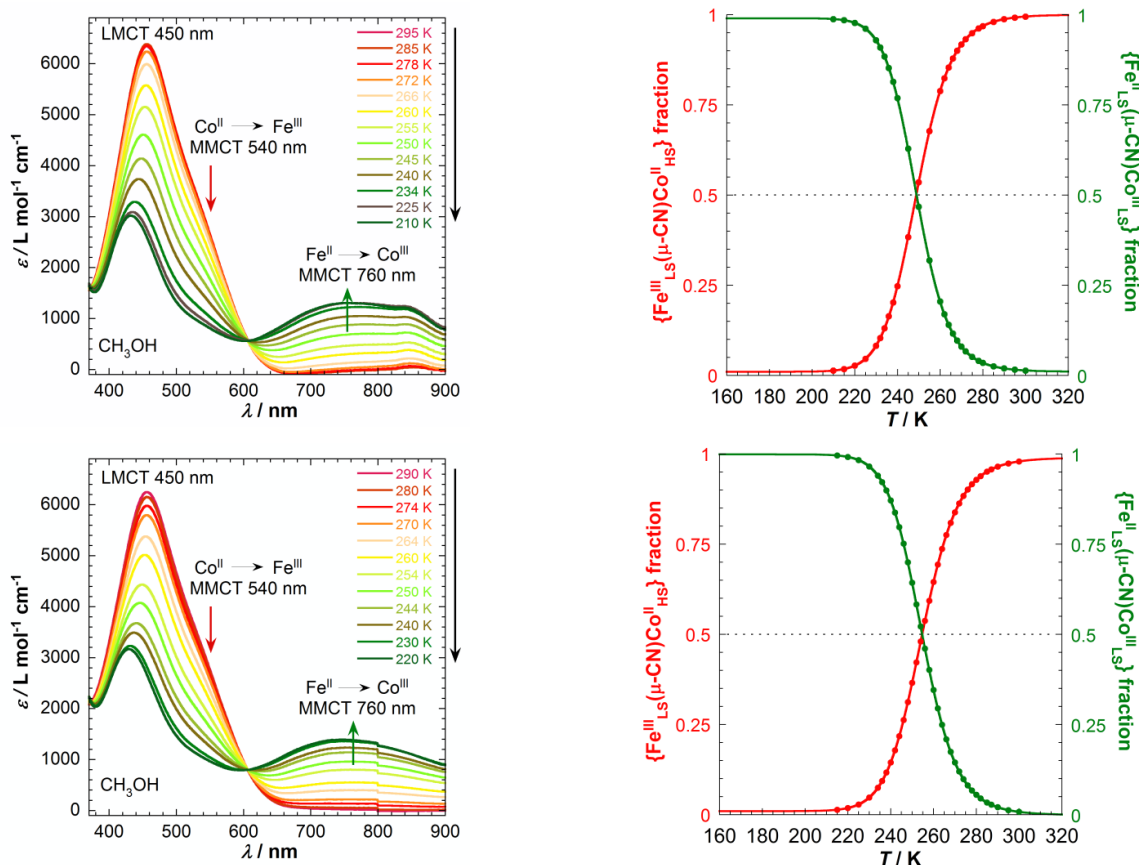


Figure IV-12. (left) UV-Vis spectra for **5** (top) and **6** (bottom) in CH_3OH on cooling mode from 295 K to 210 K (at 0.2 to 0.3 K/min). (right) Temperature dependence of the $\{\text{Fe}^{\text{III}}_{\text{LS}}(\mu\text{-CN})\text{Co}^{\text{II}}_{\text{HS}}\}$ and $\{\text{Fe}^{\text{II}}_{\text{LS}}(\mu\text{-CN})\text{Co}^{\text{III}}_{\text{LS}}\}$ fractions estimated from the absorption intensities at the MMCT bands (≈ 540 nm and ≈ 760 nm) for **5** (top) and **6** (bottom) in CH_3OH , solid lines are the fits to the ideal solution model.¹²

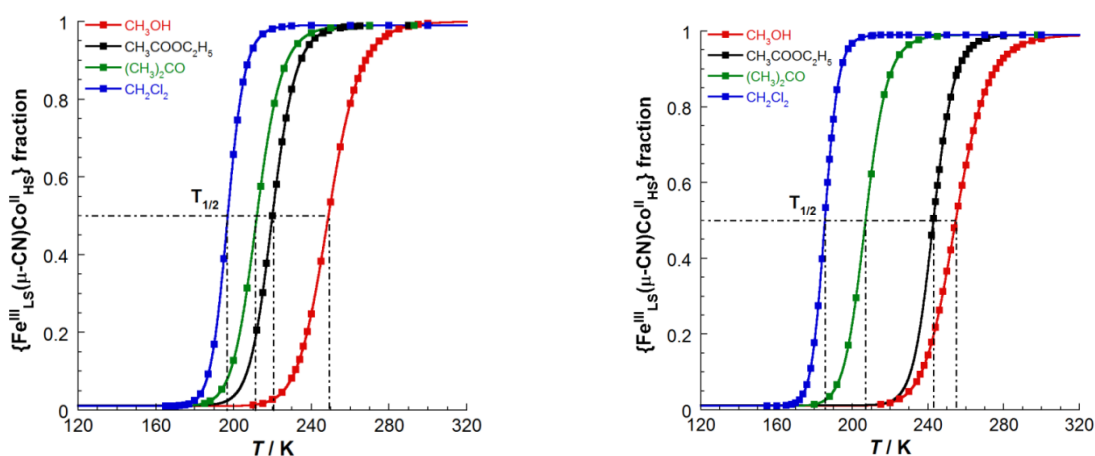


Figure IV-13. Temperature dependence of the $\{\text{Fe}^{\text{III}}_{\text{LS}}(\mu\text{-CN})\text{Co}^{\text{II}}_{\text{HS}}\}$ fraction estimated from the absorption intensities at the MMCT band (≈ 540 nm) for **5** (left) and **6** (right) in different solvents. Solid lines are the fits to the ideal solution model.¹²

For compounds **5** and **6**, the $T_{1/2}$ equals to 249 and 254.7 K, respectively, in methanol (Figure IV-12 and Table IV-3). The UV-Vis spectra recorded in other solvents are similar to those in methanol, and are shown in Figures S-IV.2 and S-IV.3. The only observed difference between various solvents is the shift of the electron transfer characteristic temperature, $T_{1/2}$, as can be observed from Figure IV-13.

The analysis of obtained optical data suggests that only two species ($\{\text{Fe}^{\text{III}}_{\text{LS}}(\mu\text{-CN})\text{Co}^{\text{II}}_{\text{HS}}\}$ and $\{\text{Fe}^{\text{II}}_{\text{LS}}(\mu\text{-CN})\text{Co}^{\text{III}}_{\text{LS}}\}$) are present in solution, due to the thermally induced ET, and thus the temperature dependence of paramagnetic or diamagnetic fractions fits well with the ideal solution model¹² for an equilibrium between two different states:

$$X = X_{LT} + \frac{X_{HT} - X_{LT}}{1 + \exp\left(\frac{\Delta H}{R}\left(\frac{1}{T} - \frac{1}{T_{1/2}}\right)\right)} \quad \text{Eq. IV.1}$$

where X is the $\{\text{Fe}(\mu\text{-CN})\text{Co}\}$ fraction; X_{LT} and X_{HT} are low temperature $\{\text{Fe}^{\text{II}}_{\text{LS}}(\mu\text{-CN})\text{Co}^{\text{III}}_{\text{LS}}\}$ and high temperature $\{\text{Fe}^{\text{III}}_{\text{LS}}(\mu\text{-CN})\text{Co}^{\text{II}}_{\text{HS}}\}$ fractions, respectively; R is the ideal gas constant ($8.314 \text{ J}\cdot\text{K}^{-1}\cdot\text{mol}^{-1}$); ΔH is the enthalpy change; and ΔS is the entropy variation ($\Delta S = \Delta H/T_{1/2}$). The calculated ΔH , $T_{1/2}$, and ΔS are summarized in Table IV-3.

Table IV-3. Thermodynamic parameters obtained from the ideal solution modelling¹² of UV-Vis data for **5** and **6** in different solvents.

	(5)			(6)		
	ΔH , $\text{kJ}\cdot\text{mol}^{-1}$	$T_{1/2}$, K	ΔS , $\text{J}\cdot\text{K}^{-1}\cdot\text{mol}^{-1}$	ΔH , $\text{kJ}\cdot\text{mol}^{-1}$	$T_{1/2}$, K	ΔS , $\text{J}\cdot\text{K}^{-1}\cdot\text{mol}^{-1}$
Methanol	63.7	249.0	255.9	63.4	254.7	248.9
Ethyl acetate	67.4	220.0	306.5	89.4	242.9	368.0
Acetone	58.5	212.0	276.1	61.9	207.0	299.2
Dichloromethane	73.3	197.0	372.4	79.7	185.5	428.4

For both complexes **5** and **6** thermodynamic parameters change from one solvent to another, but the observed characteristic temperatures, $T_{1/2}$, follow the same trend. The lowest $T_{1/2}$ is in dichloromethane, then in acetone, then ethyl acetate and the highest is in methanol. The characteristic temperatures for **6** are higher than those observed for **5**. In the case of ethyl acetate, the values of ΔH or ΔS must be taken with caution as both complexes precipitated during the UV-Vis absorption measurements (Figure S-IV-4).

IV.3.2. Magnetic properties of **5** and **6** in solutions

Additional evidences in support of intramolecular electron transfer in solutions of **5** and **6** were obtained from the magnetic susceptibility measurements (Figure IV-14).

Multiple preliminary tests allowed determination of optimal conditions for the magnetic studies in solutions.³ In order to avoid a thermal hysteresis between cooling and heating modes due to the freezing/melting of the solvent (first order phase transition), temperature dependent measurements on cooling were performed until the freezing point. Such methodology allowed recording superposed cooling and heating curves (Figure S-IV-6). Above the melting or freezing temperature of the solvent, another thermal hysteresis related to precipitation (on cooling) or dissolution (on heating) of the solute (complex **5** or **6**) was observed. Moreover, similar behavior was observed from the temperature dependent UV-visible

spectroscopy, when solubility of compounds **5** and **6** ($C \sim 5 \cdot 10^{-5}$ mol/L) in ethyl acetate decreased abruptly as the temperature was lowered (Figure S.IV-4). It was possible to avoid this extrinsic effect for solutions of **5** in methanol, acetone and dichloromethane by preparation of diluted solutions with the concentration range between 1 and $3 \cdot 10^{-4}$ mol/L. The dilution of solutions (**5** in ethyl acetate and **6** in all four solvents) to the limit of measurability of the magnetometer did not allow suppressing the partial precipitation of the compounds (Figure S.IV-6). This precipitate can be easily seen by eyes when removing the sample from the SQUID magnetometer. Therefore only the magnetic measurements obtained on cooling modes for **5** and **6** are discussed in this part (Figure IV-14).

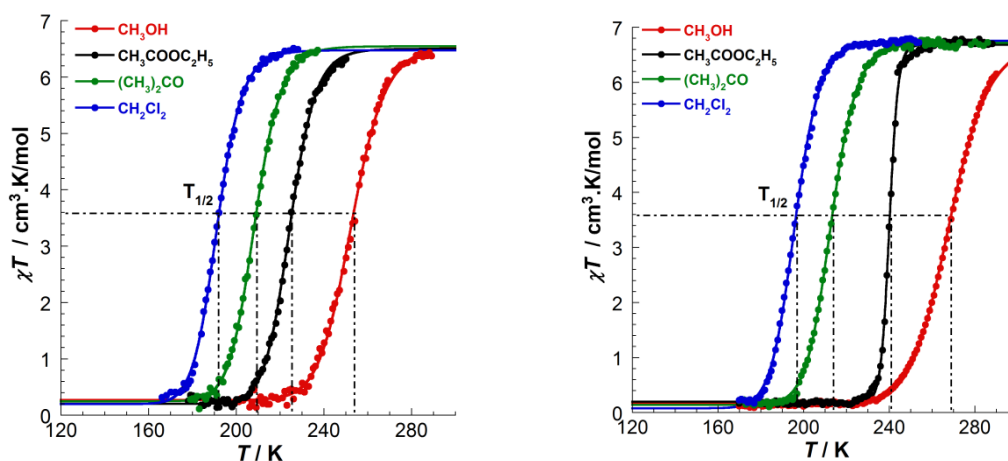


Figure IV-14. χT vs T data for **5** (left) and **6** (right) in methanol, ethylacetate, acetone and dichloromethane solutions (0.4 K/min, 1 T, solid lines are fits to the ideal solution model¹²).

Regardless the complex functionalization and the solvent, the χT product at higher temperatures is essentially the same (around $6.6 \text{ cm}^3 \cdot \text{K/mol}$) for solutions of **5** and **6** that is in agreement with the presence of paramagnetic $\{\text{Fe}^{\text{III}}_2\text{Co}^{\text{II}}_2\}$ complexes. With decreasing temperature, the χT product rapidly decreases to small values (0.26 to $0.35 \text{ cm}^3 \cdot \text{K/mol}$, Figure IV-14), consistent with the presence of diamagnetic $\{\text{Fe}^{\text{II}}_2\text{Co}^{\text{III}}_2\}$ units as the majority species in solution. Practically the same value of the χT product at higher temperatures for both complexes may suggest that in solutions the tetranuclear cores adopt a similar structural geometry and there are no restraints induced by intermolecular interactions as in the solid state.

Table IV-4. Thermodynamic parameters obtained from the ideal solution modelling¹² of magnetic data for **5** and **6** in different solvents.

	(5)			(6)		
	ΔH , $\text{kJ} \cdot \text{mol}^{-1}$	$T_{1/2}$, K	ΔS , $\text{J} \cdot \text{K}^{-1} \cdot \text{mol}^{-1}$	ΔH , $\text{kJ} \cdot \text{mol}^{-1}$	$T_{1/2}$, K	ΔS , $\text{J} \cdot \text{K}^{-1} \cdot \text{mol}^{-1}$
Methanol	68.8	252.8	271.9	65.8	268.2	245.3
Ethyl acetate	71.7	224.5	319.5		240.1	
Acetone	59.5	208.4	286.1	63.4	212.8	297.7
Dichloromethane	53.5	191.3	278.6	55.3	196.0	282.1

The χT vs T data (Figure IV-14) for **5** and **6** are also in good agreement with the ideal solution model¹² (see Eq. IV.1, where X is the χT product, X_{LT} and X_{HT} are χT values at low and at high temperatures, respectively).¹² Calculated thermodynamic parameters ΔH , $T_{1/2}$, and ΔS are summarized in Table IV-4. The thermodynamic parameters have values slightly different from those obtained from optical measurements

(Table IV-3). These differences, especially between $T_{1/2}$ values determined spectrophotometrically and from magnetic measurements, are attributed to differences in the experimental set-ups and to the difficulty of precisely determining molar fractions by UV/Vis studies in cases where the experimentally available temperature range does not cover the entire temperature range of the ET. But as already observed by UV/Vis spectroscopy, the electron-transfer process is strongly influenced by the solvent nature. The characteristic temperatures ($T_{1/2}$) observed from magnetic studies follow the same trend as the ones determined from the absorption spectra. The lowest $T_{1/2}$ is in dichloromethane, then in acetone, and then ethyl acetate, whereas the highest were measured in methanol solutions (Table IV-4).

The $T_{1/2}$ values evaluated and reported previously for complex **2** in various solvents² showed a strong dependence on solvent polarity (Table S.IV-3).¹³ The ET characteristic temperature in solutions of **2** was increasing with the increase of the solvent polarity index. The trend observed for **5** and **6** in the studied solutions shows the same dependence except ethyl acetate solutions. The polarity index of ethyl acetate (4.3) is slightly lower than the polarity index of acetone (5.1).¹³ Therefore it was expected that the $T_{1/2}$ value in acetone would have been higher than the one observed in ethyl acetate. But from both UV-Vis absorption and magnetic susceptibility measurements the $T_{1/2}$ determined for acetone solutions was lower than the ones observed in ethyl acetate solutions. On cooling solutions of **5** and **6** in ethyl acetate, besides thermally induced ET, a partial precipitation of both compounds occurs as well, so the process is more complex. Therefore the characteristic temperature measured in ethyl acetate does not fit the polarity trend and must be taken into consideration with caution.

The increase in solvent polarity shifts $T_{1/2}$ to higher values for complexes **2**, **5** and **6** in solutions. Since the observed change of optical and magnetic properties is associated with an intramolecular redox process it is possible that increasing solvent polarity shifts the reduction potentials (of Fe^{III} ions) to more positive values and makes the reduction step more favorable due to a better solvation of tetranuclear cyanido-bridged core and stronger solute/solvent interactions (i.e. hydrogen-bonding and/or electron-pair donor/acceptor interactions), as have been reported for several organic systems exhibiting ET equilibria.¹⁴

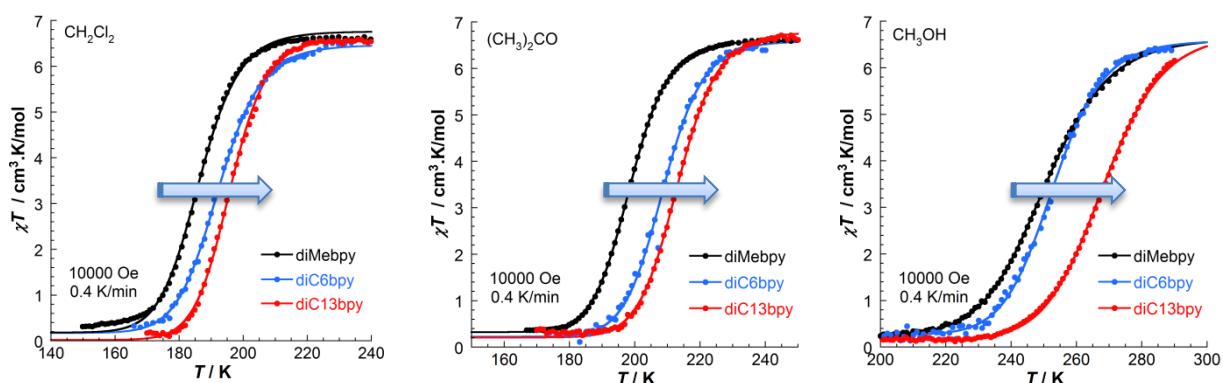


Figure IV-15. Comparison between χT vs T data for complexes **2**, **5** and **6** in dichloromethane (left), in acetone (center) and methanol (right), the solid line are fits to the ideal solution model.¹²

The comparison of magnetic susceptibility measurements of complexes **2**,^{2,3} **5** and **6** solubilized in the same solvent (Figure IV-15) shows that the longer is the alkyl chain on the bipyridine ligand the higher is the characteristic temperature of the ET process. The alkyl chains are known as weak electron donating groups

and the chain length effect over the $T_{1/2}$ respects the following trend: methyl < hexyl < tridecyl. The magneto-optical bistability of the solubilized cyanido-bridged molecular $\{\text{Fe}_2\text{Co}_2\}$ squares can be tuned by the solvent nature or/and by the nature of the functional groups attached to the capping ligands.

IV.4. Conclusions and perspectives

Two new tetranuclear cyanido-bridged complexes $\{[(\text{Tp}^*)\text{Fe}(\text{CN})_3]_2[\text{Co}(\text{diC6bpy})_2]_2\}[\text{OTf}]_2 \cdot 2\text{DMF}$ (**5**) and $\{[(\text{Tp}^*)\text{Fe}(\text{CN})_3]_2[\text{Co}(\text{diC13bpy})_2]_2\}[\text{OTf}]_2 \cdot \text{H}_2\text{O} \cdot 3\text{CH}_3\text{OH}$ (**6**) have been synthesized and their properties in solid state and in solutions have been described by structural, spectroscopic and magnetic methods.

In the solid state no reversible thermally or photo-induced ET was observed in the functionalized complexes **5** and **6**. The functionalization of bipyridine ligands with long alkyl chains and the employed crystallization methods have a significant influence on packing and solvation inside in the crystal. Thus, the functionalized complex **5** is always paramagnetic in the solid state whereas the complex **6** is stabilized in diamagnetic state likely due to methanol molecules H-bonded to terminal cyanides on Fe sites. The presence of such H-bonds most likely induced a shift of the reduction potential on the iron centers in solid state. Moreover, the electron density withdrawing effect is so strong that even under irradiation with white light, as confirmed by reflectivity studies, it has been impossible to convert the diamagnetic $\{\text{Fe}^{\text{II}}_{\text{LS}}(\mu\text{-CN})\text{Co}^{\text{III}}_{\text{LS}}\}$ species into paramagnetic $\{\text{Fe}^{\text{III}}_{\text{LS}}(\mu\text{-CN})\text{Co}^{\text{II}}_{\text{HS}}\}$ ones. On the other hand, the dried compound **6** is stable in the paramagnetic state, as could be observed from the structural, magnetic and optical reflectivity studies.

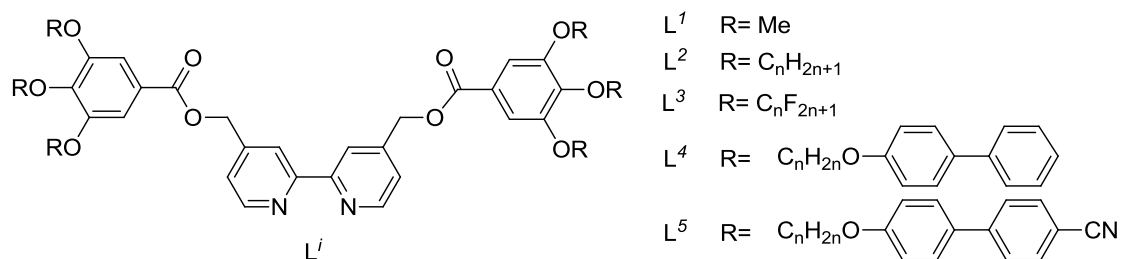
The studies performed in solutions confirmed that the functionalization with long alkyl chains improves the solubility of the molecular $\{\text{Fe}_2\text{Co}_2\}$ squares in organic solvents. Moreover, these investigations revealed that functionalized squares undergo thermally-induced intramolecular ET in diluted solutions and, thus, exhibit switching of their magnetic and optical properties in solutions. Remarkably, a fine-tuning of the electron transfer associated magnetic and optical properties of **5** and **6** in solutions is observed over a broad range of temperature by simply adjusting the solvent polarity or the functionalized ligand of the Co site.

This work demonstrates and generalizes the possibility to observe switchable magnetic and optical properties of the functionalized $\{\text{Fe}_2\text{Co}_2\}$ complexes in solution, and opens up new possibilities to control molecular optical and magnetic properties by tuning the energy of the electron transfer process through variation of solvents and ligand functionalization.

The intramolecular ET between the cyanido-bridged $\text{Fe}^{\text{II/III}}$ and $\text{Co}^{\text{III/II}}$ centers is a redox process that occurs due to a small difference between the Fe and Co redox potentials. The spectroscopic and magnetic studies performed in solutions showed that solvent's polarity has a specific influence on the observed characteristic temperatures ($T_{1/2}$). Apparently, the medium formed by the solvents affects the redox potential of the metal ions, making either smaller or bigger the difference between the Fe and Co redox potentials. Therefore studying the electrochemistry of the molecular squares and their precursors in various solvents may allow a better understanding the solvent and the bpy functionalization effect.

The functionalization with hexyl and tridecyl aliphatic chains helped improving the solubility of the molecular squares. However, this work should not stop at this point and many strategies towards the preparation of hybrid systems exhibiting both ET and self-organization of liquid crystals can be developed. For example, the series of functionalized bpy-based ligands showed in Scheme IV-2 may induce, indeed, liquid crystalline phases, while the functionalization with electron density donating groups stronger than alkyl chains may induce occurrence of ET around room temperature that can make this systems more attractive for future applications.

Scheme IV-2. Representation of the possible functionalizations of the 2,2'-bipyridine ligand



IV.5. Supporting materials

IV.5.1. Experimental protocols

Preparation of 4,4'-diR-2,2'-bipyridines (R: *hexyl* or *tridecyl*). To a three-neck flask containing 4,4'-dimethyl-2,2'-bipyridine (1.22 g, 6.64 mmol), 80 mL of diisopropylamine (1.86 mL, 13.29 mmol) solution in anhydrous THF were added. The resulting mixture was cooled to 193 K, and then 1.58 M solution of *n*-butyllithium in hexane (5.12 mL, 13.29 mmol) was added. After 30 min the obtained dark reddish brown solution was slowly combined with 10 mL of 1-bromoalkane (1-iodopentane 2.63 g or 1-bromododecane 3.30 g, 13.29 mmol) solution in anhydrous THF. The reaction mixture was kept at 193 K for 2 hours, and then it was allowed to warm slowly to room temperature and stirred for 2 more days. The reaction was quenched by adding methanol (100 mL) and then poured into 100 mL of water. The organic material was extracted with diethyl ether (3 x 100 mL), washed with water, dried over anhydrous sodium sulphate and concentrated under reduced pressure. The 4,4'-dihexyl-2,2'-bipyridine (**diC6bpy**) was purified by column chromatography on alumina with dichloromethane/hexane (1:10) mixture used as eluent, the yield was 1.33 g (62 %). ¹H NMR (400 MHz) in CDCl₃ (δ, ppm): 8.56 (d, *J* = 4.9 Hz, 1H), 8.24 (s, 1H), 7.12 (dd, *J* = 7.5, 4.0 Hz, 1H), 2.69 (t, *J* = 6.9 Hz, 2H), 1.76 – 1.59 (m, 2H), 1.45 – 1.15 (m, 7H), 0.88 (t, *J* = 6.9 Hz, 3H). Elemental analysis – Calc. (Found) for C₂₂H₃₂N₂: C, 82.40 (82.29); H, 10.97 (11.01), N 6.63 (6.70). The 4,4'-ditridecyl-2,2'-bipyridine (**diC13bpy**) was recrystallized from ethanol at 253 K as a white microcrystalline product with the yield of 2.83 g (82.0 %). ¹H NMR (CD₃Cl, 400 MHz, ppm): *d* = 8.54 (d, 2H, *J* = 5.0 Hz), 8.21 (s, 2H), 7.11 (dd, 2H, *J* = 6.0, 2.0 Hz), 2.67 (t, 4H, *J* = 7 Hz), 1.67 (m, 4H), 1.3-1.2 (m, 40H), 0.86 (t, 6H, *J* = 7.0 Hz). Anal. Calcd (Found) for C₃₆H₆₀N₂: C, 83.01 (82.94); H, 11.61 (11.67); N, 5.38 (5.41).

Preparation of {[(Tp*)Fe(CN)₃]₂[Co(**diRbpy**)₂]}[OTf]₂ (**5-6**).** [NEt₄][(**Tp***)Fe(CN)₃]·H₂O (165 mg, 0.3 mmol) was treated with Co(OTf)₂ (107 mg, 0.3 mmol) in 5 mL of wet DMF under argon to afford a red solution that was allowed to stir for 2 h. Subsequently, 4,4'-*R,R*-2,2'-bipyridine (for **5**, 195 mg with *R* = C₆H₁₃; for **6**, 302 mg with *R* = C₁₃H₂₇, 0.6 mmol) was added and the mixture was stirred for 2 days and then filtered. Crystals of **5** suitable for X-ray diffraction were obtained by layering diethyl ether over the reaction mixture in DMF, the yield was 55 % (0.22 g). Elemental analysis – Calc. (Found) for (**5**) C₁₃₂H₁₈₆B₂Co₂F₆Fe₂N₂₈O₈S₂ ([(**Tp***)Fe(CN)₃]₂[Co(**diC6bpy**)₂]}(OTf)₂·2DMF): C, 50.70 (50.36); H, 5.00 (4.94); N, 18.00 (18.13). Selected FT-IR data (ATR, cm⁻¹): 2953 (s), 2926 (s), 2856 (s), 2538 (m), 2148 (s), 2121 (w), 1679 (vs), 1613 (vs), 1263 (vs). Diethyl ether was added to the complex **6** (with *R* = C₁₃H₂₇) and the solution was filtered to separate the insoluble impurities. The filtrate was dried under vacuum. The complex **6** crystallizes well from methanol solutions when cooled down to 253 K. The yield was 0.39 g (77.4 %). Elemental analysis – Calc. (Found) for (**6**) C₁₈₄H₂₉₂B₂Co₂F₆Fe₂N₂₆O₈S₂ ([(**Tp***)Fe(CN)₃]₂[Co(**diC13bpy**)₂]}(OTf)₂·2CH₃OH): C, 64.51 (64.45); H, 8.59 (8.46); N, 10.63 (10.69); Selected FT-IR data (ATR, cm⁻¹): (dry) 2922 (vs), 2852 (vs), 2532 (m), 2151 (s), 2119 (vw), 1613 (s), 1261 (vs); (wet) 2920 (vs), 2851 (vs), 2506 (m), 2098 (s), 2069 (s), 1617 (s), 1259 (vs).**

IV.5.2. Crystallographic data for 5 and 6

Table S.IV-1. Crystallographic data for 5 at 100 and 260 K.

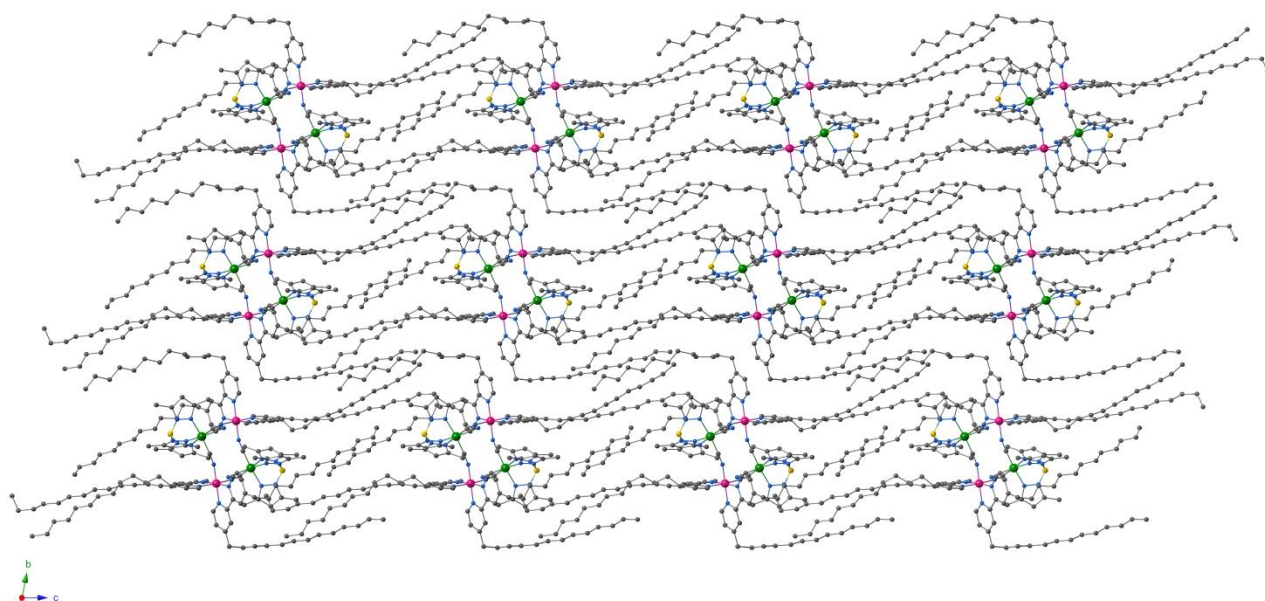
Temperature	100 K	260 K
Crystal color	dark red	dark red
Moiety formula	$C_{124}H_{172}B_2Co_2Fe_2N_{26}, 2(CF_3O_3S), 2(C_3H_7NO)$	
Empirical formula	$C_{132}H_{186}B_2Co_2F_6Fe_2N_{28}O_8S_2$	
Formula weight	2722.39	
Crystal system	Monoclinic	
Space group	$P2_1/c$	
Wavelength, Å	0.71073	
a, Å	12.8665(14)	12.939(4)
b, Å	29.832(4)	30.070(8)
c, Å	19.772(2)	20.136(6)
β , °	112.886(7)	112.923(18)
V, Å ³	6991.7(14)	7216(4)
Z	1	
ρ_{calcd} , g/cm ³	1.293	1.253
μ , 1/mm	0.539	0.522
Reflections collected	76075	161415
Independent reflections	12852	13122
R_1^a	0.0833	0.1200
wR_2^a	0.2740	0.3200
GoF ^a	1.038	1.070
Selected bond distances (Å)		
Co(1)-N(1)	2.085(6)	2.113(7)
Co(1)-N(3)	2.091(5)	2.075(6)
Co(1)-N(13)	2.116(5)	2.119(6)
Co(1)-N(12)	2.128(5)	2.148(5)
Co(1)-N(10)	2.142(5)	2.151(5)
Co(1)-N(11)	2.168(5)	2.176(6)
Fe(1)-C(3)	1.909(6)	1.920(8)
Fe(1)-C(1)	1.912(7)	1.906(9)
Fe(1)-C(2)	1.948(8)	1.936(9)
Fe(1)-N(8)	1.970(5)	1.980(6)
Fe(1)-N(4)	1.996(5)	1.978(6)
Fe(1)-N(6)	2.023(6)	2.029(7)
Fe(1)-Co(1)	5.087	5.108
Fe(1)-Co(2)	5.115	5.107
Fe(1)-Fe(2)	7.759	7.749
Co(1)-Co(2)	6.624	6.656
Selected bond angles (°)		
N(1)-Co(1)-N(3)	99.3(2)	98.2(2)
N(1)-Co(1)-N(13)	93.47(19)	95.2(2)
N(1)-Co(1)-N(12)	92.2(2)	92.1(2)
N(3)-Co(1)-N(12)	90.31(19)	90.4(2)
N(13)-Co(1)-N(12)	76.22(18)	75.5(2)
N(1)-Co(1)-N(10)	92.7(2)	92.2(2)
N(3)-Co(1)-N(10)	88.66(19)	89.7(2)
N(13)-Co(1)-N(10)	103.73(18)	103.5(2)
N(3)-Co(1)-N(11)	84.9(2)	84.2(2)
N(13)-Co(1)-N(11)	85.37(19)	85.8(2)
N(12)-Co(1)-N(11)	99.50(19)	100.4(2)
N(10)-Co(1)-N(11)	75.69(19)	75.2(2)
C(3)-Fe(1)-C(1)	83.8(2)	83.3(3)
C(3)-Fe(1)-C(2)	87.2(3)	88.4(3)
C(1)-Fe(1)-C(2)	85.6(3)	86.6(3)
C(1)-N(1)-Co(1)	168.3(5)	169.5(6)
C(3)-N(3)-Co(1)	165.9(5)	166.8(6)
N(1)-C(1)-Fe(1)	173.6(5)	172.5(6)
N(2)-C(2)-Fe(1)	178.2(6)	176.7(7)
N(3)-C(3)-Fe(1)#1	178.0(6)	178.8(7)

^a $I > 2\sigma(I)$, $R_1 = \Sigma(|F_o| - |F_c|)/\Sigma|F_o|$, $wR_2 = \{\Sigma[w(F_o^2 - F_c^2)]/\Sigma[w(F_o^2)]\}^{1/2}$, GoF (goodness of fit on F^2) = $\{\Sigma[w(F_o^2 - F_c^2)^2]/(n-p)\}^{1/2}$, where n is the number of reflections and p is the total number of refined parameters.

Table S.IV-2. Crystallographic data for **6** at 100 K.

Temperature	100 K	Selected bond distances (Å)	
Crystal color	dark green	Co(1)-N(21)	1.949(8)
Moiety formula	(C ₁₈₀ H ₂₈₂ B ₂ Co ₂ Fe ₂ N ₂₆), 2(CF ₃ O ₃ S), 3(CH ₄ O), H ₂ O	Co(1)-N(22)	1.929(9)
Empirical formula	C ₁₈₅ H ₂₉₆ B ₂ Co ₂ F ₆ Fe ₂ N ₂₆ O ₁₀ S ₂	Co(1)-N(17)	1.885(8)
Formula weight	3473.78	Co(1)-N(13)	1.90(1)
Crystal system	Triclinic	Co(1)-N(19)	1.943(9)
Space group	P1	Co(1)-N(20)	1.96(1)
Wavelength, Å	0.71073	Fe(1)-N(5)	2.040(9)
a, Å	11.9217(13)	Fe(1)-N(3)	2.07(1)
b, Å	16.8399(18)	Fe(1)-N(1)	2.031(8)
c, Å	25.069(3)	Fe(1)-C(31)	1.85(1)
α, °	78.207(5)	Fe(1)-C(33)	1.91(1)
β, °	80.997(6)	Fe(1)-C(32)	1.88(1)
γ, °	78.043(6)	Selected bond angles (°)	
V, Å ³	4785.4(9)	N(21)-Co(1)-N(22)	82.9(4)
Z	1	N(21)-Co(1)-N(13)	89.9(4)
ρ _{calcd.} , g/cm ³	1.201	N(21)-Co(1)-N(19)	93.0(4)
μ, 1/mm	0.406	N(21)-Co(1)-N(20)	92.2(4)
Reflections collected	38313	N(22)-Co(1)-N(17)	93.6(4)
Independent reflections	16215	N(22)-Co(1)-N(13)	89.7(4)
R ₁ ^a	0.1832	N(22)-Co(1)-N(20)	94.8(4)
wR ₂ ^a	0.3435	N(17)-Co(1)-N(13)	92.2(4)
GoF ^a	1.112	N(17)-Co(1)-N(19)	90.4(4)
		N(17)-Co(1)-N(20)	85.9(4)
		N(13)-Co(1)-N(19)	93.2(4)
		N(19)-Co(1)-N(20)	82.5(4)
		Co(1)-N(13)-C(32)	168.7(8)
		Co(1)-N(17)-C(35)	165.6(8)
		Fe(1)-C(33)-N(14)	176.5(9)
		Fe(1)-C(31)-N(15)	175.9(9)
		Fe(1)-C(32)-N(13)	171.8(9)
		C(32)-Fe(1)-C(31)	87.8(5)
		C(32)-Fe(1)-C(33)	88.4(5)
		C(31)-Fe(1)-C(33)	95.5(5)

^a $I > 2\sigma(I)$, $R_1 = \sum(|F_o| - |F_c|) / \sum|F_o|$, $wR_2 = \{\sum[w(F_o^2 - F_c^2)^2] / \sum[w(F_o^2)^2]\}^{1/2}$. GoF (goodness of fit on F^2) = $\{\sum[w(F_o^2 - F_c^2)^2] / (n-p)\}^{1/2}$, where n is the number of reflections and p is the total number of refined parameters.

**Figure S.IV-1.** Packing diagram of **6** in the *bc* plane illustrating interdigitation of the long alkyl chains from diC13bpy ligands.

IV.5.3. UV-Vis studies in diluted solutions of 5 and 6

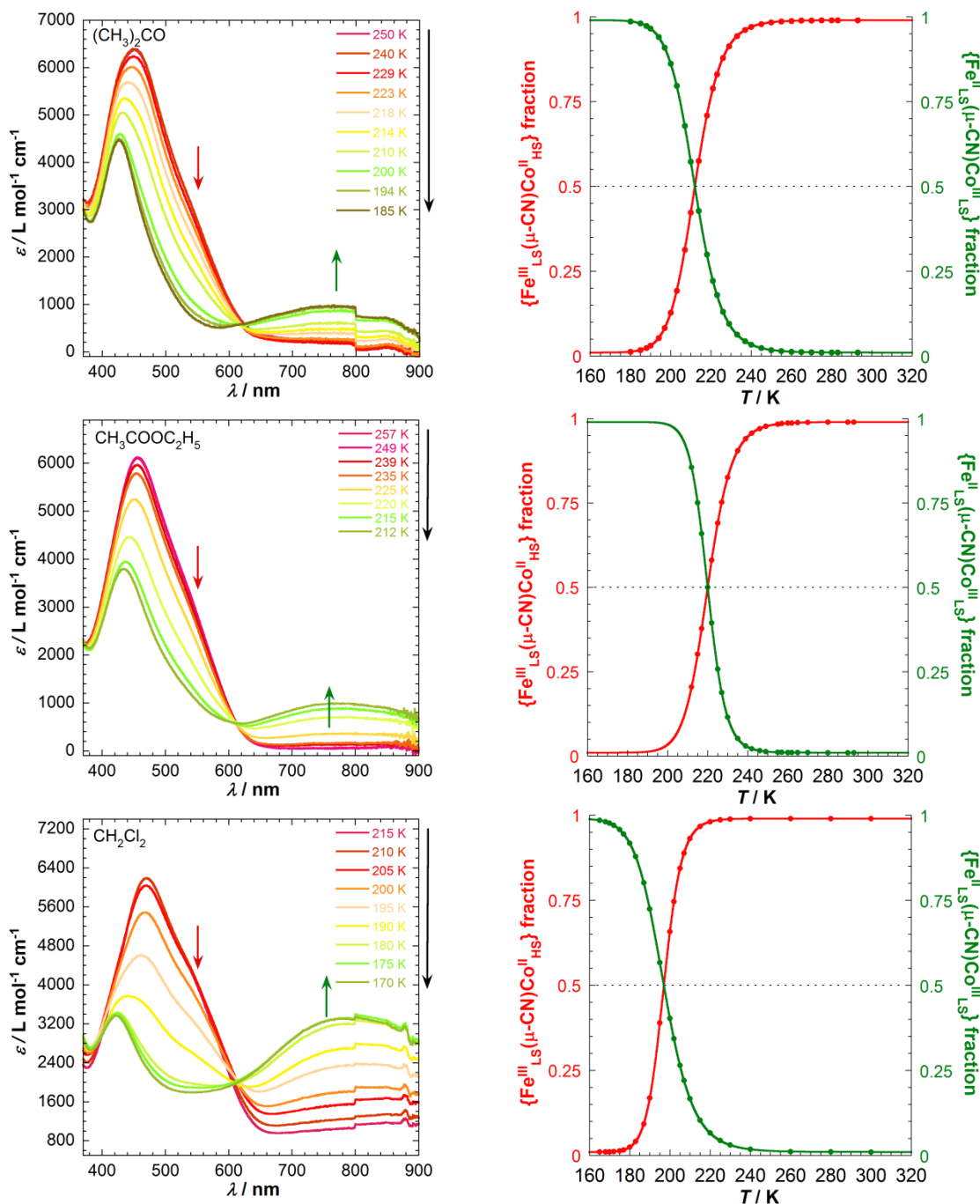


Figure S.IV-2. Left: UV-vis spectra for **5** in acetone (top), ethyl acetate (middle) and dichloromethane (bottom) in cooling mode from 300 K to solvent freezing point (at 0.2 to 0.3 K/min). Right: Temperature dependence of $\{\text{Fe}^{\text{III}}_{\text{LS}}(\mu\text{-CN})\text{Co}^{\text{II}}_{\text{HS}}\}$ (red) and $\{\text{Fe}^{\text{II}}_{\text{LS}}(\mu\text{-CN})\text{Co}^{\text{III}}_{\text{LS}}\}$ (green) fractions estimated from the analyses of absorption intensities at MMCT bands (540 nm and 760 nm, respectively); solid lines are fits of the experimental to an ideal solution model.

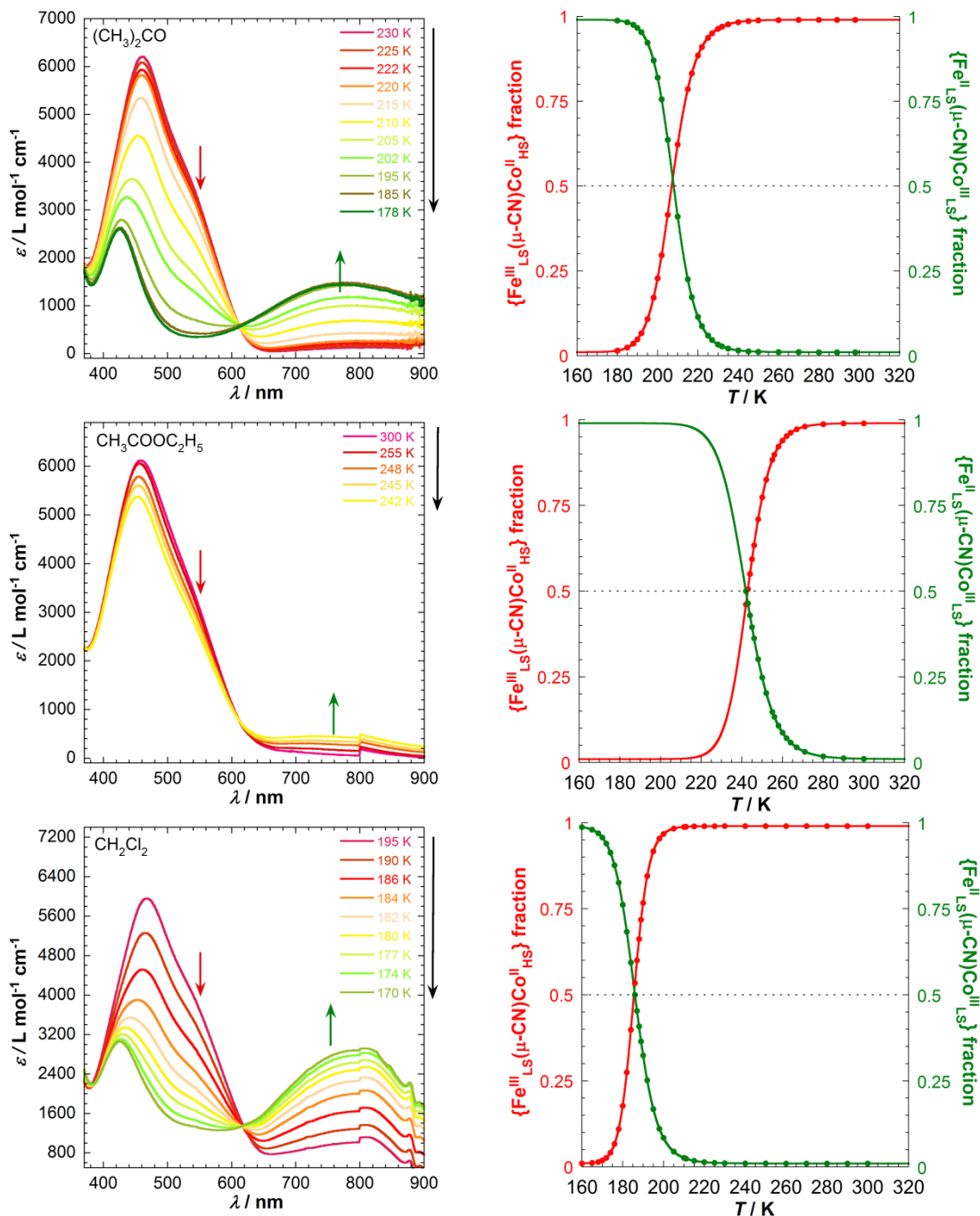


Figure S.IV-3. Left: UV-vis spectra for **6** in acetone (top), ethyl acetate (middle) and dichloromethane (bottom) in cooling mode from 300 K to solvent freezing point (at 0.2 to 0.3 K/min). Right: Temperature dependence of $\{\text{Fe}^{\text{III}}_{\text{LS}}(\mu\text{-CN})\text{Co}^{\text{II}}_{\text{HS}}\}$ (red) and $\{\text{Fe}^{\text{II}}_{\text{LS}}(\mu\text{-CN})\text{Co}^{\text{III}}_{\text{LS}}\}$ fractions estimated from the analyses of absorption intensities at MMCT bands (540 nm and 760 nm, respectively); solid lines are fits of the experimental to an ideal solution model.

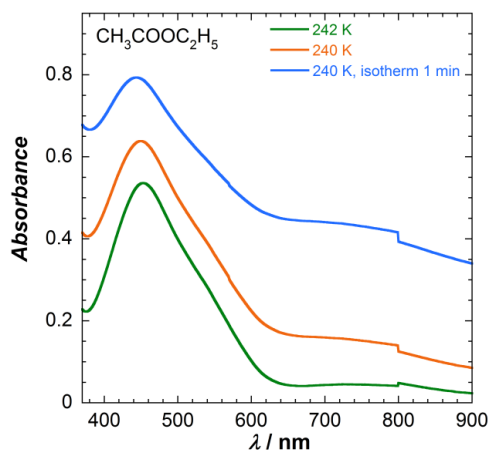


Figure S.IV-4. UV/Vis spectra for **6** in $\text{CH}_3\text{COOC}_2\text{H}_5$ in cooling mode from 242 K to 240 K ($9 \cdot 10^{-5}$ mol/L).

IV.5.4. Magnetic measurements in solid state

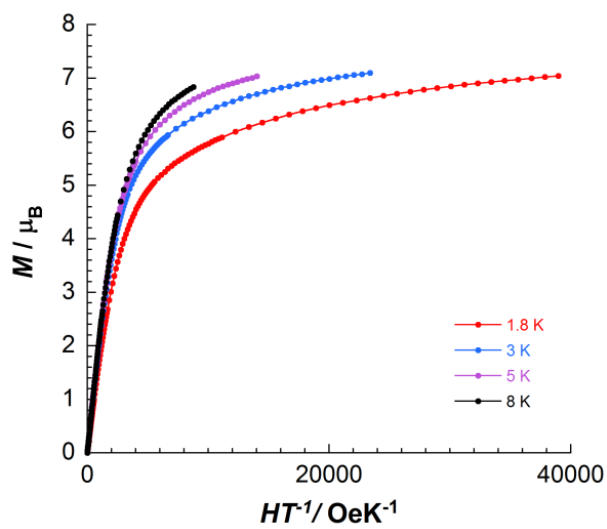


Figure S.IV-5. Magnetization versus HT plots at different temperatures for **5**.

IV.5.5. Magnetic measurements in solutions

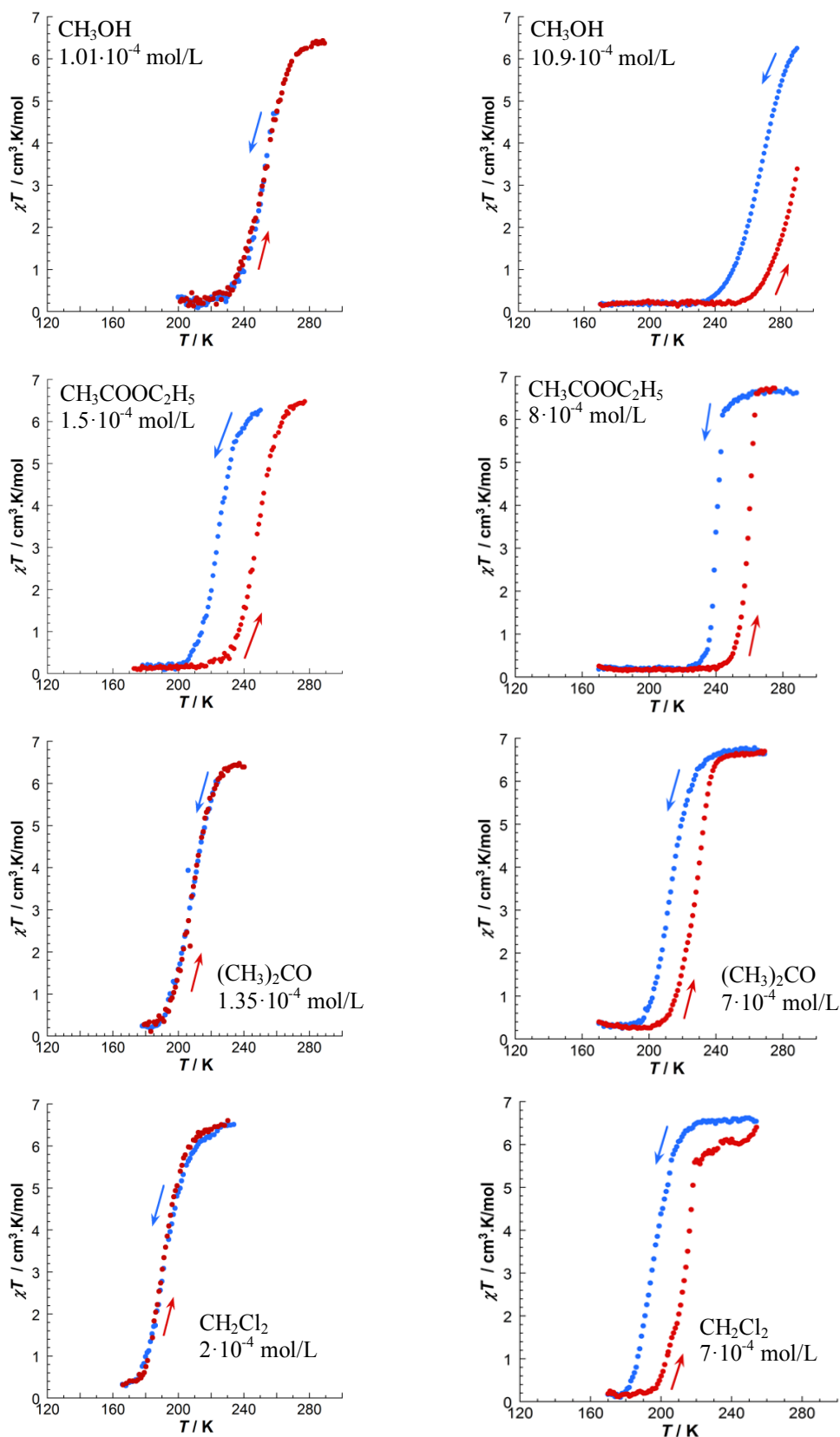


Figure S.IV-6. χT vs T data on cooling (blue dots) and heating (red dots) for **5** (left) and **6** (right) in different solvents (0.4 K/min, 1 T). In several cases, on cooling the sample two processes occur: ET associated with conversion from paramagnetic to diamagnetic state and precipitation of the solute. On heating the sample firstly dissolves and then undergoes ET. Therefore on cooling and heating $T_{1/2}$ have different values and a thermal hysteresis extrinsic to $\{\text{Fe}_2\text{Co}_2\}$ molecular squares in solutions appears

Table S.IV-3. Polarity index of several commonly used solvents.

Solvents	Polarity index (P')¹³
Water	9.0
Nitromethane	6.8
Methanol	6.6
Acetonitrile	6.2
Ethanol	5.2
Acetone	5.1
Butyronitrile	4.6
Ethyl acetate	4.3
Isopropanol	4.3
Tetrahydrofuran	4.2
Chloroform	4.1
<i>n</i> -Buthanol	3.9
Dichloromethane	3.4
Diethyl ether	2.9
Toluene	2.3
Hexane	0.0

IV.6. References

1. Zhang, Y.; Li, D.; Clérac, R.; Kalisz, M.; Mathonière, C.; Holmes, S. M. *Angew. Chem.* **2010**, *122*, 3840-3844; *Angew. Chem., Int. Ed.* **2010**, *49*, 3752-3756.
2. Siretanu, D.; Li, D.; Buisson, L.; Bassani, D. M.; Holmes, S. M.; Mathonière, C.; Clérac, R. *Chem.-Eur. J.* **2011**, *17*, 11704-11708.
3. Siretanu, D. *PhD Thesis*, Univ. of Bordeaux 1, **2011**.
4. (a) Nihei, M.; Sekine, Y.; Suganami, N.; Oshio, H. *Chem. Lett.* **2010**, *39*, 978-979. (b) Nihei, M.; Sekine, Y.; Suganami, N.; Nakazawa, K.; Nakao, H.; Murakami, Y.; Oshio, H. *J. Am. Chem. Soc.*, **2011**, *133*, 3592-3600.
5. (a) Domínguez-Gutiérrez, D.; Paoli, G. D.; Guerrero-Martínez, A.; Ginocchetti, G.; Ebeling, D.; Eiser, E.; Cola, L. D.; Elsevier, C. J. *J. Mater. Chem.* **2008**, *18*, 2762-2750. (b) Pucci, D.; Barberio, G.; Crispini, A.; Francescangeli, O.; Ghedini, M. *Mol. Cryst. Liq. Cryst.* **2003**, *395*, 325-335. (c) Janiak, C.; Deblon, S.; Wu, H. P.; Kolm, M. J.; Klufers, P.; Piotrowski, H.; Mayer, P. *Eur. J. Inorg. Chem.* **1999**, 1507-1521. (d) Garelli, N.; Vierling, P. *J. Org. Chem.* **1992**, *57*, 3046-3051.
6. (a) Berlinguette, C. P.; Dragulescu-Andrasi, A.; Sieber, A.; Galan-Mascaros, J. R.; Güdel, H.-U.; Achim, C.; K. R. Dunbar, *J. Am. Chem. Soc.* **2004**, *126*, 6222-6223. (b) Berlinguette, C. P.; Dragulescu-Andrasi, A.; Sieber, A.; Güdel, H. -U.; Achim, C.; Dunbar, K. R. *J. Am. Chem. Soc.* **2005**, *127*, 6766-6779. (c) Shatruk, M.; Dragulescu-Andrasi, A.; Chambers, K. E.; Stoian, S. A.; Bominaar, E. L.; Achim, C.; Dunbar, K. R. *J. Am. Chem. Soc.* **2007**, *129*, 6104-6116.
7. Li, D.; Clérac, R.; Roubeau, O.; Harté, E.; Mathonière, C.; Le Bris, R.; Holmes, S. M. *J. Am. Chem. Soc.* **2008**, *130*, 252-258.
8. Mercuriol, J.; Li, Y.; Pardo, E.; Risset, O.; Seuleiman, M.; Rousselière, H.; Lescouëzec, R.; Julve, M. *Chem. Commun.* **2010**, *46*, 8995-8997.
9. Li, D.; Parkin, S.; Wang, G.; Yee, G. T.; Prosvirin, A. V.; Holmes, S. M. *Inorg. Chem.* **2006**, *45*, 1951-1959.
10. (a) Desiraju, G. R. *Acc. Chem. Res.* **1996**, *29*, 441. (b) Steiner, T. *Crystallogr. Rev.* **1996**, *6*, 1. (c) Steiner, T. *Chem. Commun.* **1997**, 727.
11. Nihei, M.; Ui, M.; Hoshino, N.; Oshio, H. *Inorg. Chem.* **2008**, *47*, 6106-6108.
12. Atkins, P.; De Paula, J. *Physical Chemistry*, 8th Ed., Oxford University Press, **2006**.
13. (a) Snyder, L. R. *J. Chromatogr. Sci.* **1978**, *16*, 223-234. (b) Rutan, S. C.; Carr, P. W.; Cheong, W. J.; Park, J. H.; Snyder, L. R. *J. Chromatogr. A* **1989**, *463*, 21-37. (c) Barwick, V. J. *Trends Anal. Chem.* **1997**, *16*, 293-309.
14. Reichardt, C. *Solvents and Solvent Effects in Organic Chemistry*, 3rd ed., Wiley-VCH Verlag GmbH & Co. KGaA: Weinheim, **2003**, 137-139, and references therein.

Chapter V
**Functionalization of Molecular {Fe₂Co₂}
Squares with Strongly Donating Methoxy
Group: Electron Transfer Properties in Solid
State and Solutions**

Table of Contents for Chapter V:

V.1. Introduction.....	V.171
V.2. Synthesis and characterizations of functionalized molecular $\{Fe_2Co_2\}$ squares in solid state	V.171
V.2.1. Synthetic procedures and FT-IR characterizations	V.171
V.2.2. Structural investigations	V.173
V.2.2.1. $\{[(Tp^*)Fe(CN)_3]_2[Co(diMeObpy)_2]_2\}(OTf)_2 \cdot 4DMF$ (7)	V.173
V.2.2.2. $\{[(Tp^*)Fe(CN)_3]_2[Co(diMeObpy)_2]_2\}(PF_6)_2 \cdot 2H_2O \cdot 5MeCN$ (8a).....	V.175
V.2.2.3. $\{[(Tp^*)Fe(CN)_3]_2[Co(diMeObpy)_2]_2\}(PF_6)_2 \cdot 6MeCN$ (8b)	V.177
V.2.3. Optical reflectivity studies	V.179
V.2.3.1. Reflectivity measurements for compound 7	V.179
V.2.3.2. Reflectivity measurements for compound 8a	V.179
V.2.3.3. Reflectivity measurements for compound 8b	V.182
V.2.4. Photo-crystallographic investigations of compound 8a	V.185
V.2.5. Magnetic measurements	V.188
V.2.5.1. Magnetic properties of 7	V.188
V.2.5.2. Magnetic and photo-magnetic properties of 8a	V.189
V.2.5.3. Magnetic and photo-magnetic properties of 8b	V.190
V.3. Analytical characterizations of the methoxy functionalized molecular $\{Fe_2Co_2\}$ squares in diluted solutions	V.192
V.3.1. UV-Vis spectroscopic characterizations of 7 and 8 in diluted solutions	V.193
V.3.2. Magnetic properties of 7 and 8 in solutions.....	V.195
V.4. Conclusions and perspectives	V.197
V.5. Preliminary XAS and XMCD investigations.....	V.200
V.6. Supporting materials.....	V.205
V.6.1. Experimental protocols	V.205
V.6.2. Crystallographic data for 7 , 8a and 8b	V.206
V.6.3. Optical reflectivity studies.....	V.210
V.6.4. Magnetic properties in solid state	V.212
V.6.5. UV-Vis spectroscopic characterizations in diluted solutions	V.212
V.6.6. Magnetic measurements in solutions	V.213
V.6.7. XAS and XMCD measurements	V.213
V.7. References	V.215

V.1. Introduction

The capping ligands on the Fe and Co centers in cyanido-bridged $\{Fe_2Co_2\}$ squares have an important role in the occurrence of the intramolecular electron transfer associated with the switching of magnetic and optical properties. This phenomenon can be fulfilled only when the ancillary ligands on both metal centers match well a proper difference value between the redox potentials of the metal ions. Therefore by changing the capping ligands the redox potentials of the concerned sites are modified and, thus, it is possible to obtain systems showing thermally and/or photo-induced intramolecular ET^{1,2,3,4} or to stabilize either the paramagnetic $\{Fe^{III}_2Co^{II}_2\}$ ^{3b,5} or the diamagnetic $\{Fe^{II}_2Co^{III}_2\}$ ^{3b,4b,6} state. In the case of the $\{[(Tp^*)Fe(CN)_3]_2[Co(4,4'-diRbpy)_2]_2\}^{2+}$ systems (where Tp^* = tris(3,5-dimethylpyrazol-1-yl)hydroborate, bpy = 2,2'-bipyridine and $R = H, Me, t-Bu, C_6H_{13}$ or $C_{13}H_{27}$) it was observed^{1,3,4} (see also Chapter IV) that the functionalization of the bpy ligands on Co sites with weak electron donating alkyl groups contributes to an increase of ET characteristic temperature in solid state and/or in solutions. Based on these results and with the aim to determine if the functionalization of bpy ligands with stronger electron density donating groups (i.e. methoxy) can further increase the ET characteristic temperature, the work on functionalization of molecular $\{Fe_2Co_2\}$ squares is continued in this chapter.

By rational choice of the capping ligands, counter-anions and crystallization solvents, it was possible to synthesize three new cyanido-bridged $\{Fe_2Co_2\}$ complexes functionalized with methoxy (MeO) groups in 4- and 4'- positions of the bpy ligand:

(7) – $\{[(Tp^*)Fe(CN)_3]_2[Co(diMeObpy)_2]_2\}(OTf)_2 \cdot 4DMF$ (where $diMeObpy$ = 4,4'-dimethoxy-2,2'-bipyridine, OTf = trifluoromethanesulfonate, DMF = N,N-dimethylformamide);

(8a) – $\{[(Tp^*)Fe(CN)_3]_2[Co(diMeObpy)_2]_2\}(PF_6)_2 \cdot 2H_2O \cdot 5MeCN$ (where $MeCN$ = acetonitrile);

(8b) – $\{[(Tp^*)Fe(CN)_3]_2[Co(diMeObpy)_2]_2\}(PF_6)_2 \cdot 6MeCN$.

The full set of structural, optical and magnetic characterizations of the prepared compounds **7**, **8a** and **8b** are described herein in solid state and in solutions.

V.2. Synthesis and characterizations of functionalized molecular $\{Fe_2Co_2\}$ squares in solid state

V.2.1. Synthetic procedures and FT-IR characterizations

Functionalized complex **7** was synthesized and crystallized according to the procedure employed for preparation of complexes **1** – **6** (see Sections III.2.1, III.4.1, IV.2.1, IV.5.1 and V.6.1), using $(NEt_4)[(Tp^*)Fe(CN)_3]$ and $Co(OTf)_2$ as metal precursors (detailed preparation procedures can be found in Section III.4.1). The dark red color and the high energy values of cyanide (bridging at 2154.1 cm^{-1} and terminal at 2121.7 cm^{-1}) and B-H (at 2532.7 cm^{-1}) stretching bands in the FT-IR spectrum of the obtained crystals (Figure V-1 left) suggest that at room temperature compound **7** is a cyanido-bridged square in its paramagnetic $\{Fe^{III}_2Co^{II}_2\}$ state.^{1,3-5c,6,7}

In the case of compounds **8a** and **8b**, the synthetic strategy was modified with the aim to exchange the OTf anion with PF_6^- . The choice of the hexafluorophosphate as counter-anion was not accidental. The same

counter-anion was used in the preparation of the $\{[(Tp^*)Fe(CN)_3]_2[Co(di-t-Bubpy)_2]_2\}(PF_6)_2 \cdot 2MeOH$ (where di-*t*-Bubpy = 4,4'-di-*tert*-butyl-2,2'-bipyridine) complex which exhibits both thermally and photo-induced ET in solid state, while in butyronitrile solutions it shows thermally and protonation induced ET. Moreover the results reported in Chapter III motivated us to perform also a study on the counter-anion effect of the systems functionalized with methoxy groups.

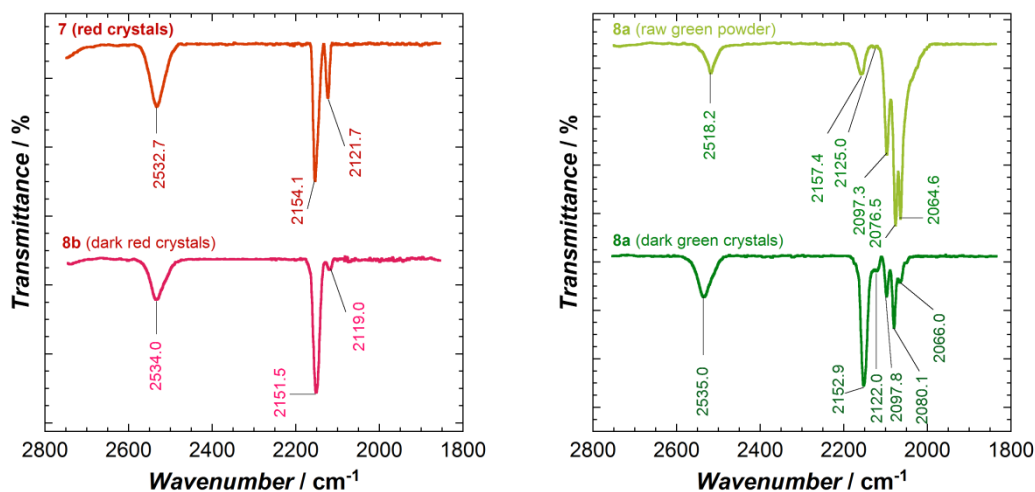


Figure V-1. FT-IR spectra collected between 2800 and 1800 cm⁻¹ at room temperature: (left) for the red crystals of **7** and red crystals of **8b**; (right) for the green powder and green crystals of **8a**.

Compounds **8a** and **8b** are indeed different solvates of the same system, $\{[(Tp^*)Fe(CN)_3]_2[Co(diMeObpy)_2]_2\}(PF_6)_2$ as shown by later structural investigations. The different solvation is achieved when the synthesis is carried out in “wet” or anhydrous solvents. The modified synthetic procedure for preparation of **8a** and **8b** consists in treatment of a diluted solution containing 1 eq. of $Co(OTf)_2$ with 2 eq. of diMeObpy in methanol, followed by the addition of 1 eq. of $(NEt_4)[(Tp^*)Fe(CN)_3]$ and 2 eq. of NBu_4PF_6 . If the synthesis is performed in “wet” methanol, after the addition of NBu_4PF_6 a green powder (**8a**) precipitates from red solution, whereas in the case of anhydrous methanol a red powder (**8b**) is formed. Both powders are poorly soluble in alcohols, especially methanol and ethanol.

The FT-IR analysis of the green powder (Figure V-1 right), showed that the prepared compound is likely a cyanido-bridged square in its diamagnetic $\{Fe^{II}_2Co^{III}_2\}$ state, since the stretching bands corresponding to the bridging (2097 and 2076 cm⁻¹) and terminal (2065 cm⁻¹) cyanides are shifted to lower energies comparing to the ones observed in $\{Fe^{III}_2Co^{II}_2\}$ cyanido-bridged squares.¹⁻⁷ The energy of the $\bar{\nu}_{BH}$ stretching band shifted to a lower energy (2518 cm⁻¹) is confirming the presence of the Fe^{II} ions.⁷ During the FT-IR analysis a small amount of the sample turned irreversibly red after it was pressed inside the ATR accessory of the FT-IR spectrometer, therefore two stretching bands corresponding to the bridging and terminal cyanide ligands (at 2157 and 2125 cm⁻¹, respectively) in $\{Fe^{III}_2Co^{II}_2\}$ cyanido-bridged squares were observed. The observed change of color may correspond to an irreversible ET and indirectly confirm that this green powder is a cyanido-bridged $\{Fe_2Co_2\}$ complex. The dissolution of the green powder in acetonitrile affords a red solution. Green prismatic crystals of **8a** were obtained by slow diffusion of diethyl ether into the red acetonitrile solution. The FT-IR analysis of the green crystals showed a spectrum similar to the one recorded in the case of the green powder (Figure V-1 right), but it is important to mention that the crystals of

8a are less stable to the mechanical stress and turn red after being crashed (for example with the ATR accessory of the FT-IR spectrometer). Therefore, the FT-IR spectrum of the green crystals of **8a** corresponds to a mixture of cyanido-bridged $\{Fe^{III}_2Co^{II}_2\}$ and $\{Fe^{II}_2Co^{III}_2\}$ squares. Due to the poor stability of the **8a** crystals under pressure, the $\bar{\nu}_{CN}$ and $\bar{\nu}_{BH}$ stretching absorptions bands of higher energies corresponding to $\{Fe^{III}_2Co^{II}_2\}$ species are more intense than those at lower energies corresponding to the $\{Fe^{II}_2Co^{III}_2\}$ units (Figure V-1 right). Moreover, it is important to mention that if a crystal of **8a** is kept out of its mother liquor for about 5 – 10 minutes, it turns irreversibly red.

The red prismatic crystals of **8b** were obtained by ether diffusion in acetonitrile solution of the red powder obtained in anhydrous methanol. The FT-IR spectrum (Figure V-1 left) is in a good agreement with the red color suggesting the presence of the $\{Fe^{III}_2Co^{II}_2\}$ units with stretching absorptions specific to bridging (2151.5 cm^{-1}) and terminal (2119 cm^{-1}) cyanides.

V.2.2. Structural investigations

V.2.2.1. $\{[(Tp^*)Fe(CN)_3]_2[Co(diMeObpy)_2]_2\}(OTf)_2 \cdot 4DMF$ (**7**)

Single crystal X-ray diffraction (XRD) studies of a dark red crystal of **7** were performed at 90 K after cooling it from 250 K with a $1\text{ K}\cdot\text{min}^{-1}$ temperature sweep rate. Similar to complexes **1** – **4** (see Chapter III), compound **7** crystallizes in the triclinic $P\bar{1}$ space group, but with a unit cell about twice bigger (Tables V-1 and S.V-I).

Table V-1. Unit-cell parameters, average metal-to-ligand bond lengths, metal-to-metal distances and deformation of the Co coordination sphere for **7** at 90 K, for **8a** at 120 K, and for **8b** under different experimental conditions.

	(7)	(8a)	(b)	
	90 K $\{Fe^{III}_2Co^{II}_2\}$	120 K $\{Fe^{II}_2Co^{III}_2\}$	90 K $\{Fe^{II}_2Co^{III}_2\}$	298 K $\{Fe^{III}_2Co^{II}_2\}$
Crystal system	Triclinic	Monoclinic	Monoclinic	Monoclinic
Space group	$P\bar{1}$	C 2/c	P 21/c	P 21/c
a, Å	13.687(3)	31.980(4)	15.434(4)	15.1202(7)
b, Å	16.247(4)	20.8190(10)	22.124(5)	23.1984(10)
c, Å	27.611(6)	21.593(2)	21.318(4)	21.5742(7)
α , °	87.698(11)	90	90	90
β , °	84.376(11)	129.237(2)	132.717(11)	131.615(2)
γ , °	65.203(10)	90	90	90
V, Å ³	5547(2)	11135.1(18)	5348(2)	5657.6(4)
$\langle Fe-C \rangle$, Å	1.919	1.894	1.899	1.923
$\langle Fe-N \rangle$, Å	1.995	2.056	2.042	2.010
$\langle Co-N \rangle$, Å	2.123	1.925	1.924	2.126
$Fe(1)\cdots Co(1)$, Å	5.091	4.946	4.934	5.166
$Fe(1)\cdots Co(1)'$, Å	5.132	4.942	4.935	5.156
$Fe\cdots Fe$, Å	7.562	7.187	7.186	7.655
$Co\cdots Co$, Å	6.879	6.775	6.765	6.925
$\Sigma(N-Co-N)^a$, °	67.6	45.3	42.4	70.6

^a $\Sigma = \sum_{i=1}^{12} |90 - \varphi_i|$, where φ_i are N-Co-N bond angles

The asymmetric unit inside the crystal lattice is composed of two halves of two discrete complex cations, $[(Tp^*)Fe(CN)_3Co(bpy)_2]$, two strongly disordered trifluoromethanesulfonate ions and four co-crystallized DMF molecules. In both tetranuclear square-shaped cores, Fe and Co ions reside in alternate

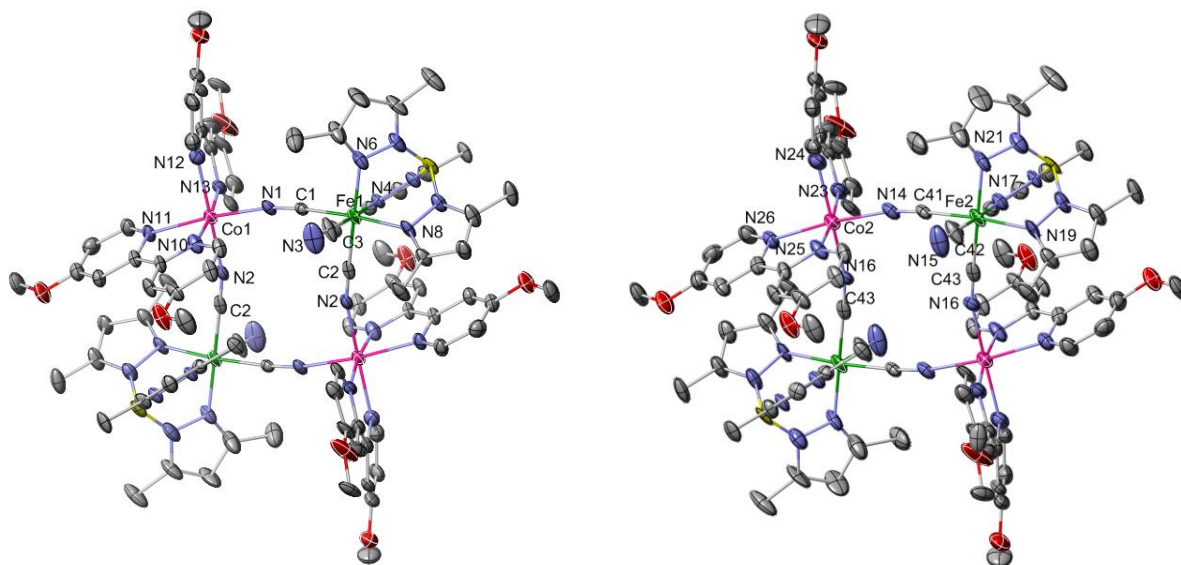


Figure V-2. The structures of the both complex cations in **7** at 90 K. Thermal ellipsoids are at 50% probability. All anions, lattice solvent molecules, and hydrogen atoms are omitted for clarity. Color scheme: C grey, Co pink, Fe green, N blue, O red, B yellow.

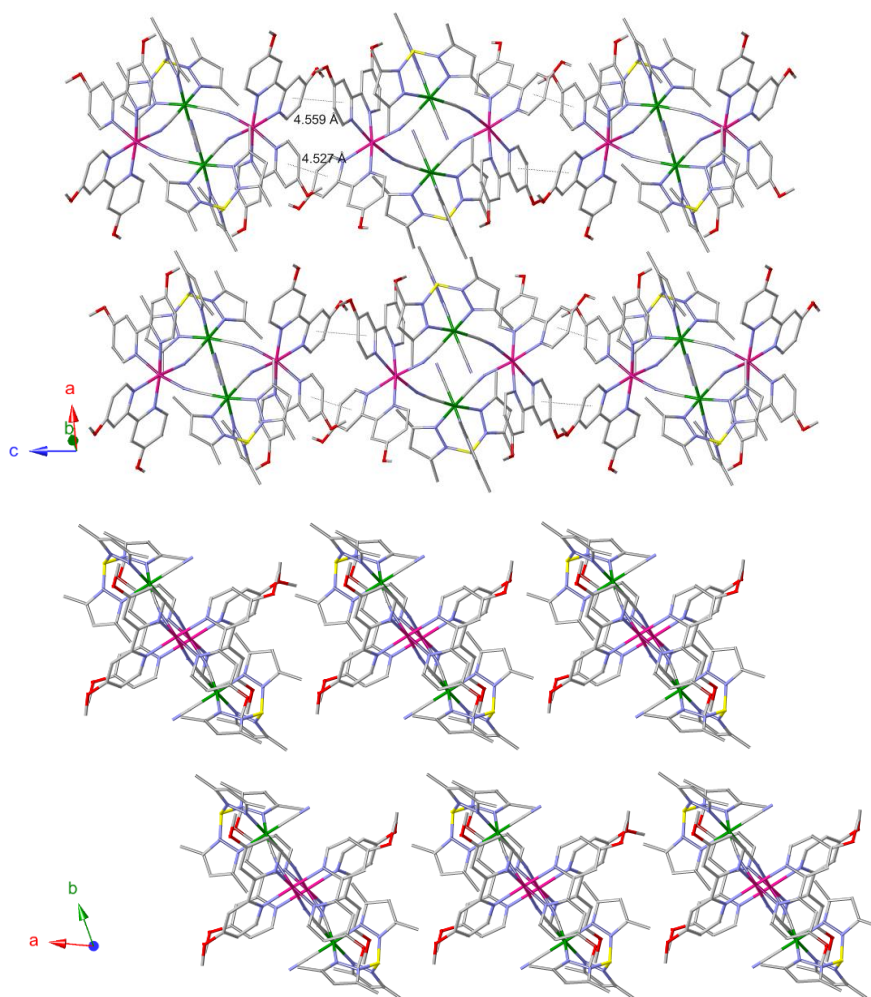


Figure V-3. Perspective views of the crystal packing of **7** at 90 K: (top) along the crystallographic *c* axis illustrating intermolecular short contacts between $\{Fe_2Co_2\}$ squares; (bottom) down the crystallographic *c* axis. Counter anions, hydrogen atoms and solvent molecules are omitted for clarity.

corners and are linked by cyanide ligands to form $\{\text{Fe}(\mu\text{-CN})\text{Co}\}$ pairs; each Fe center bears one terminal cyanide ligand that adopts an *anti* orientation relative to the $\{\text{Fe}_2(\mu\text{-CN})_4\text{Co}_2\}$ plane. The Fe ions are coordinated by tridentate Tp* in a facial configuration, while two bidentate diMeObpy ligands complete the coordination sphere around each Co ion (Figure V-2).

The analysis of the average Co-N (2.123 Å), Fe-C (1.919 Å) and Fe-N (1.995 Å) bond distances (Tables V-1 and S.V-2) shows that both $\{\text{Fe}_2(\mu\text{-CN})_4\text{Co}_2\}$ cores, inside the unit cell, are composed of Co^{II} HS and Fe^{III} LS ions. The geometry of the $\{\text{Fe}_2(\mu\text{-CN})_4\text{Co}_2\}$ squares is significantly more distorted than in complexes **1** – **3**, and is similar to the one observed in **4** (see Chapter III). Even though the two Fe–CN–Co edges are quasi identical (the $\text{Fe}(1)\cdots\text{Co}(1)$ and $\text{Fe}(1)\cdots\text{Co}(1)'$ distances are 5.091 and 5.132 Å, respectively), the Fe \cdots Fe and Co \cdots Co distances within the core are significantly different 7.562 and 6.879 Å, respectively (Table V-1). The cyanide bridges are bent especially at the cobalt sites, Co-N-C angles vary between 165.0(8) and 169.2(8)° (Table S.V-2). The N-Co-N angles (Table S.V-2) reveal a strongly distorted coordination sphere around the HS Co^{II} ion, as it can be observed from the $\Sigma_{(N\text{-Co-N})}$ parameter of 67.6° (Table V-1). No structural changes observed upon cooling the crystal of **7** from 250 to 90 K and the presence of Co^{II} HS and Fe^{III} LS ions in tetranuclear cores strongly suggest no intramolecular ET.

The presence of two OTf^- counter-anions and four co-crystallized DMF molecules per $\{\text{Fe}_2\text{Co}_2\}$ square in the crystal packing of **7** contributes to a good separation of the $\{\text{Fe}_2(\mu\text{-CN})_4\text{Co}_2\}$ units (Figure V-3 bottom). Thus, no π - π type interactions are observed between pyrazole planes of the capping Tp* ligands, as it was observed in **2** – **4**, while adjacent diMeObpy ligands coordinated to the Co^{II} ions form weak intermolecular π - π like interactions (about 4.5 Å) along crystallographic *c* axis (Figure V-3 top).

Several crystal structures of **7** were collected within this work (including high temperatures), unfortunately the refinement factors could not be lowered to reasonable values mainly due to the strongly disordered OTf^- counter-anions.

V.2.2.2. $\{[(\text{Tp}^*)\text{Fe}(\text{CN})_3]_2[\text{Co}(\text{diMeObpy})_2]_2\}(\text{PF}_6)_2\cdot 2\text{H}_2\text{O}\cdot 5\text{MeCN}$ (**8a**)

The crystals of **8a** are green at room temperature. If a crystal is kept outside its mother liquor or heated it turns rapidly red, and is not crystalline anymore. Apparently the evaporation of co-crystallized solvents causes a loss of crystallinity and an irreversible ET (as may be concluded from the color change). Therefore, the X-Ray analysis could not be performed for **8a** at high temperatures. The re-crystallization of the dried red crystals of **8a** by ether diffusion into acetonitrile solution affords red prismatic crystals which have the same structure as the crystals of **8b**. Most likely the repetitive recrystallizations remove the lattice water molecules that stabilize diamagnetic state at room temperature.

X-ray structural analysis performed at 120 K in a sealed glass capillary (Tables V-1 and S.V-3) showed that compound **8a** crystallizes in the monoclinic *C* 2/*c* space group with four molecules in the unit cell. The structure of the central fragment is essentially similar to that of compound **1**¹ in its diamagnetic $\{\text{Fe}^{\text{II}}_2\text{Co}^{\text{III}}_2\}$ state (see also Chapter III), with a square shaped core where Fe and Co ions are alternately bridged by cyanide ions. In the crystal packing, hexafluorophosphate counter anions, lattice MeCN and H₂O molecules are also present. The cationic $\{\text{Fe}_2(\mu\text{-CN})_4\text{Co}_2\}$ core in **8a** is nearly planar (Figure V-4). The tridentate Tp* ligand facially coordinates to the Fe ion, and the remaining coordination sites are occupied by

three cyanide carbon atoms. Two of the three cyanide ions from the Fe sites coordinate in bridging mode to the Co ions, while the free non-bridging cyanide groups adopt as in the other analogs an *anti* orientation relative to the $\{Fe_2(\mu-CN)_4Co_2\}$ plane. The coordination sphere around each Co ion is completed by two bidentate diMeObpy ligands.

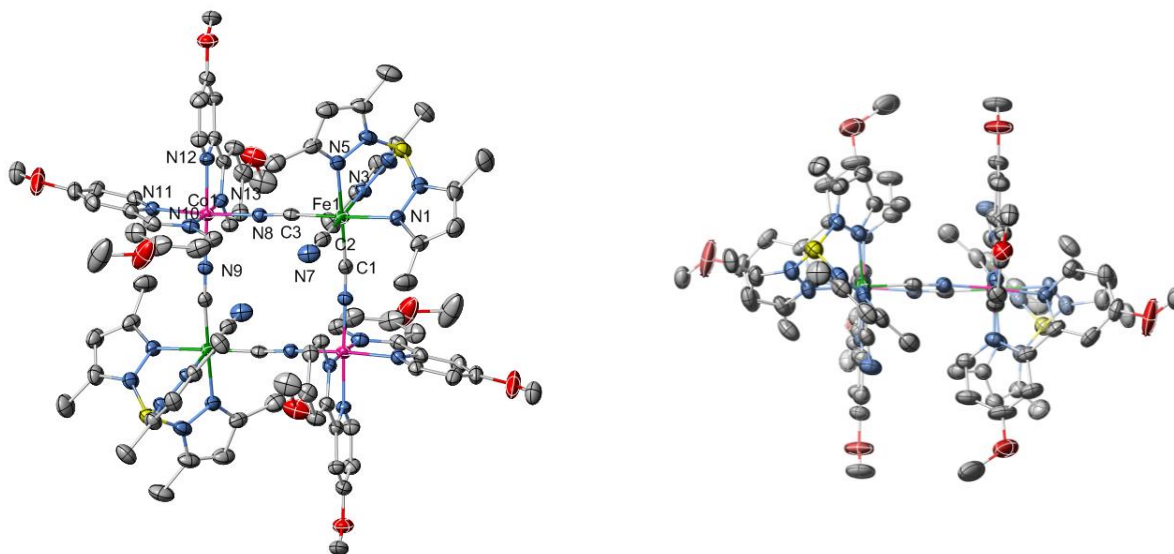


Figure V-4. (left) The structure of the complex cation in **8a** at 120 K. Thermal ellipsoids are at 50% probability. (right) The side view of the complex cation in **8a**, emphasizing the almost planar geometry of the tetranuclear core. All anions, lattice solvent molecules, and hydrogen atoms are omitted for clarity. Color scheme: C grey, Co pink, Fe green, N blue, O red, B yellow.

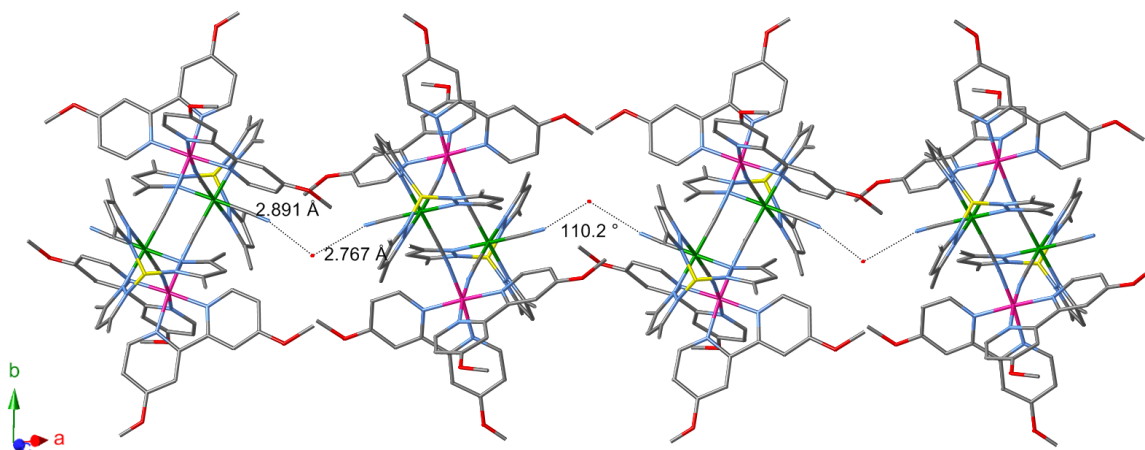


Figure V-5. Packing arrangement illustrating H-bonds present between one co-crystallized H_2O molecule and two adjacent complexes of **8a**. All anions, lattice solvent and hydrogen atoms are eliminated for clarity.

At 120 K, single-crystal XRD studies showed that the $\{Fe_2(\mu-CN)_4Co_2\}$ core is in a diamagnetic state since it contains trivalent Co ions in low spin (LS) configuration (confirmed by average Co-N bond distance of approximately 1.93 Å, Table V-1) and Fe^{II} ions, as results of the charge balance. The $\{Fe_2(\mu-CN)_4Co_2\}$ core is nearly planar since the Fe-C-N angles range between 174.1(4) and 177.1(5)° while Co-N-C angles range between 173.6(4) and 175.6(4)° (Table S.V-3, Figure V-4). The separations between adjacent metal ions within the tetranuclear core through the cyanide bridges ($Fe(1)\cdots Co(1)$ and $Fe(1)\cdots Co(1)'$) are virtually equal, 4.946 and 4.942 Å, respectively. Nevertheless, the C(1)-Fe(1)-C(3) angle (87.91°), $Fe\cdots Fe$ (7.187 Å)

and $Co \cdots Co$ (6.775 Å) distances indicate that **8a** adopts a slightly distorted square structure (Figure V-4, Table V-1). The N-Co-N angles in the Co^{III} LS coordination sphere depart less from orthogonality ($\Sigma_{(N-Co-N)} = 45.2^\circ$) than those measured for the Co^{II} HS ions in **7** (Table V-1).

Similarly to compound **7**, the presence of interstitial MeCN molecules and PF_6^- counter-anions allows a good separation between cationic cores, thus no significant short intermolecular interactions between the $\{Fe_2Co_2\}$ squares are observed inside the crystal packing of **8a**. Each of co-crystallized water molecules forms two hydrogen bonds ($N(7) \cdots O(1)w$, 2.891 Å, and $O(1)w \cdots N(7)'$, 2.767 Å) with two nitrogen atoms from terminal cyanide ligands of two neighboring squares. The observed H-bonds lead to a supramolecular 1D-like structure and likely contribute to the stabilization of the green diamagnetic $\{Fe^{II}_2Co^{III}_2\}$ species in solid state (Figure V-5). Hydrogen-bonds between lattice water molecules and terminal cyanide groups were also observed in **1**¹ and **2**⁴ (see also Chapter III), which exhibit both thermally and photo-induced ET. If in complexes **1** and **2**, bearing bpy or diMeobpy ligands on Co sites, these H-bonds are considered as one of the factors that contribute to the occurrence of intramolecular ET. Then in the case of cyanido-bridged $\{Fe_2Co_2\}$ complexes with diMeObpy ligands, the electron-withdrawing effect of these H-bonds over the redox potential of the Fe centers is enough to stabilize the diamagnetic $\{Fe^{II}_2Co^{III}_2\}$ species in solid state. The same stabilization effect was observed with MeOH molecules H-bonded to terminal cyanide groups in complex **6**^{4b} (see also Chapter IV) and in the recently reported $\{[(Tp)Fe(CN)_3]_2[Co(diCOOEtbpy)_2]_2\}(ClO_4)_2 \cdot 2MeOH$ complex⁶ (where Tp = tri(pyrazol-1-yl)hydroborate and diCOOEtbpy = 4,4'-bis(ethoxycarbonyl)-2,2'-bipyridine).

V.2.2.3. $\{[(Tp^*)Fe(CN)_3]_2[Co(diMeObpy)_2]_2\}(PF_6)_2 \cdot 6MeCN$ (**8b**)

The structural analysis of a dark red prismatic crystal of **8b** (obtained by ether diffusion in acetonitrile solution of the red powder obtained in anhydrous methanol, see Section V.2.1), was performed at 90 and at 298 K (Tables V-1 and S.V-4). Complex **8b** crystallizes in the monoclinic $P2_1/c$ space group. The unit cell consists of two centro-symmetric cyanido-bridged $\{Fe_2Co_2\}$ squares, four hexafluorophosphate ions and twelve MeCN molecules.

When the red crystal of **8b** was placed under cryostream at 90 K, its color changed immediately to dark green. The measured structure of the cationic $\{Fe_2(\mu-CN)_4Co_2\}$ part in **8b** at 90 K (Figure V-6 right) is consistent with the complex **8a** at 120 K and its $\{Fe^{II}_{LS}(\mu-CN)Co^{III}_{LS}\}$ state (Figure V-4). The average Fe-C (1.899 Å), Fe-N (2.042 Å) and Co-N (1.924 Å) bond distances (Tables V-1 and S.V-4) are in close agreement with those expected for Co^{III} LS and Fe^{II} HS metal ions, considering the valence sum bond analysis and charge compensation. The separations between adjacent metal ions within the cyanide-bridged units ($Fe(1) \cdots Co(1)$ and $Fe(1) \cdots Co(1)'$ of 4.934 and 4.935 Å, respectively), and the C(2)-Fe(1)-C(1) (85.1°), N(1)-Co(1)-N(2) (93.2°), N(2)-C(2)-Fe(1) (177.6°) bond angles suggest that the tetranuclear core in **8b** has a nearly planar square shape. Nevertheless, interatomic $Fe \cdots Fe$ (7.187 Å) and $Co \cdots Co$ (6.765 Å) distances and Co-N-C angles of 171.9 and 178.3° show that the $\{Fe_2(\mu-CN)_4Co_2\}$ has a slightly distorted geometry (Figure V-6 right, Tables V-1 and S.V-4) in comparison with **7**. The values of the N-Co-N angles (Table S.V-4) show a distorted coordination sphere around the LS Co^{III} ions, as judged by the $\Sigma_{(N-Co-N)}$ parameter of 42.4° (Table V-1).

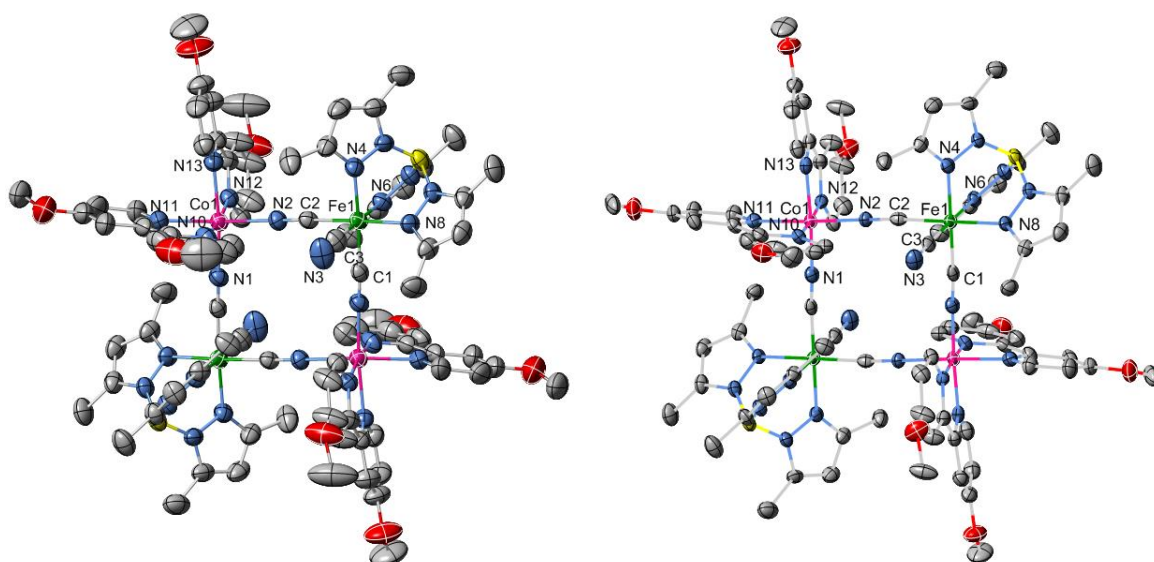


Figure V-6. The structure of the complex cation in **8b** at 298 K (left) and at 90 K (right). Thermal ellipsoids are at 50% probability. All anions, lattice solvent molecules, and hydrogen atoms are omitted for clarity. Color scheme: C grey, Co pink, Fe green, N blue, O red, B yellow.

After heating to 298 K, the structure of the red crystal (Figure V-6) reveals a slightly more distorted tetranuclear core and longer average Fe-C and Co-N bond distances of 1.923 and 2.126 Å, respectively. While the average Fe-N bond distance decreased to 2.010 Å (Tables V-1 and S.V-4). The longer average Co-N bond distances by ca. 0.2 Å are characteristic of Co^{II} HS ions formed after thermally induced ET associated with a $\{Fe^{II}_2Co^{III}_2\}$ to $\{Fe^{III}_2Co^{II}_2\}$ conversion. On the other hand, the changes in average Fe-C and Fe-N bond distances at 298 K differ only slightly (by ~ 0.03 Å) from those observed at 90 K and correspond also well to Fe^{III} LS ions (Table V-1). As the result of metal-to-ligand bond length increase, the interatomic $Fe \cdots Fe$ (7.655 Å) and $Co \cdots Co$ (6.92 Å) distances inside the $\{Fe_2(\mu-CN)_4Co_2\}$ core increased as well. The change in the N-Co-N angles shows a more distorted coordination sphere for the Co^{II} LS ion ($\Sigma_{(N, Co-N)} = 70.6^\circ$) than for the Co^{III} LS site at 90 K.

In the crystal packing of **8b**, $\{Fe_2Co_2\}$ complexes are well separated by hexafluorophosphate anions and interstitial solvents at both 90 and 298 K. The bulkiness of the methoxy groups present on the 4- and 4'-positions of the bipyridine ligands generates a sterical hindrance effect that does not allow any π - π type interactions between diMeObpy ligands. Nevertheless, weak intermolecular edge-to-edge π - π stacking interactions are present between adjacent dimethylpyrazole rings from the Tp* ligand (Figure S.V-1). Similarly to the metal-to-ligand bond lengths, the short-contact distance changes as the result of the intramolecular ET from ~ 3.9 Å at 298 K to ~ 3.8 Å at 90 K (Figure S.V-1).

For the three crystallographically characterized compounds **7**, **8a** and **8b**, structural changes associated with a thermally induced ET process were observed only in the compound **8b**. According to the obtained temperature dependent structural data for the $\{[(Tp^*)Fe(CN)_3]_2[Co(diMeObpy)_2]_2\}^{2+}$ core, it is possible to obtain systems showing thermally induced intramolecular ET associated with switching between $\{Fe^{III}_2Co^{II}_2\}$ and $\{Fe^{II}_2Co^{III}_2\}$ states (**8b**) or to stabilize either the $\{Fe^{III}_2Co^{II}_2\}$ (**7**) or the $\{Fe^{II}_2Co^{III}_2\}$ (**8a**) states that show no thermally induced intramolecular ET process.

As can be deduced from the crystallographic data of **7**, **8a** and **8b** presented in Table V-1, the cationic $\{Fe^{III}_2Co^{II}_2\}$ core in **7** is significantly more distorted than the one observed in **8b** at 298 K with the same electronic configuration on metal centers. The presence of trifluoromethanesulfonate anions and co-crystallized DMF molecules in the crystal packing of **7** strongly influence the molecular structure of the tetranuclear core and contribute to the stabilization of the paramagnetic $\{Fe^{III}_2Co^{II}_2\}$ state. Both **8a** and **8b** complexes show very similar structures at low temperatures (at 120 and 90 K, respectively. See Table V-1), but only the compound **8b** exhibits thermally induced ET, while **8a** is stabilized in the diamagnetic $\{Fe^{II}_2Co^{III}_2\}$ state, likely due to the H-bonded water molecules.

V.2.3. Optical reflectivity studies

Surface reflectivity spectra of complexes **7**, **8a** and **8b** were collected between 500 and 1000 nm, at different temperatures, with the aim to determine the presence of any changes of the optical properties associated with an eventual thermally- and/or photo-induced ET process.

V.2.3.1. Reflectivity measurements for compound **7**

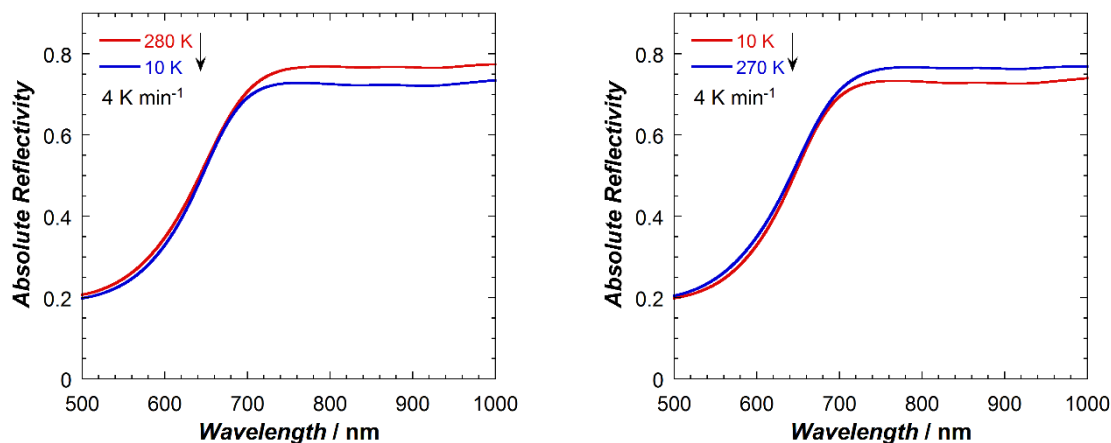


Figure V-7. Reflectivity spectra of **7** at 280 K and 10 K on cooling from 280 K to 10 K (left) and on heating from 10 K to 270 K (right).

The reflectivity spectrum of **7** at 280 K presents a strong absorption between 500 and 700 nm ($R_{550} = 0.22$, while $R_{800} = 0.75$), and is similar to the spectra recorded for other cyanido-bridged $\{Fe_2Co_2\}$ molecular squares in their paramagnetic state.^{1,4} Between 280 and 10 K, no significant changes are observed, denoting that complex **7** does not undergo thermally-induced electron transfer (Figure V-7).

V.2.3.2. Reflectivity measurements for compound **8a**

It is important to mention that the green crystals of **8a** turn red if they are kept outside the mother liquor for more than 5 – 10 min or if they are subjected to a mechanical stress like smoothing the surface during the preparation of a sample for the optical reflectivity measurements. Therefore, the optical reflectivity measurements were carried out between 270 and 10 K on freshly filtered green crystals of **8a**.

At 270 K, the green crystals are strongly absorbent in the studied spectral range ($R_{550} = 0.05$, while $R_{800} = 0.14$, Figure V-8), similarly to **1**¹, **2**⁴, and **6** (see also Chapters III and IV) in their diamagnetic $\{Fe^{II}_2Co^{III}_2\}$ state. Between 270 and 120 K, the complex becomes even more strongly absorbent above 700

nm ($R_{800} = 0.09$, Figure V-8 left) and less absorbent below 600 nm ($R_{550} = 0.06$, Figure V-8 left). The observed weak changes in reflectivity spectra on cooling mode, may be attributed to a thermally induced ET between Co^{II} and Fe^{III} ions in paramagnetic $\{Fe^{III}_2Co^{II}_2\}$ molecular squares formed as defects on the surface of the green crystals of **8a** during the preparation of the reflectivity sample. The presence of a small amount of paramagnetic red $\{Fe^{III}_2Co^{II}_2\}$ defects can be also confirmed by the R_{800} value that is slightly bigger than the one measured for R_{550} , whereas for compounds **1**¹, **2**⁴, and **6** (see also Chapters III and IV) in their

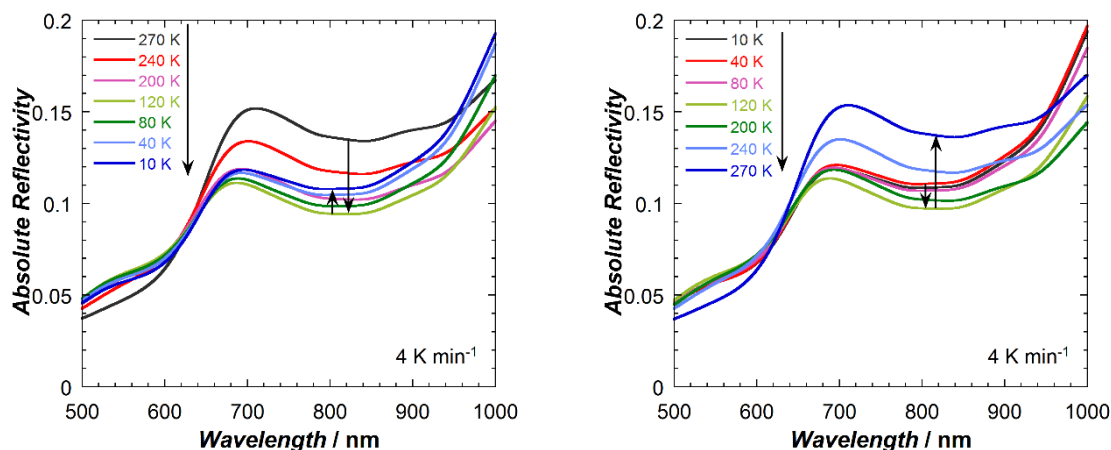


Figure V-8. Optical reflectivity spectra of **8a** at selected temperatures between 280 K and 10 K on cooling (left) and on heating (right).

diamagnetic green $\{Fe^{II}_2Co^{III}_2\}$ state, the observed R_{800} and R_{550} are practically equal. On further cooling from 120 K, the surface of **8a** becomes slightly more reflective in the near-infrared region. Upon heating from 10 K, the reflectivity above 700 nm continues to increase slowly until 70 K. This thermal behavior suggests that the compound might be indeed photo-active and that the diamagnetic green $\{Fe^{II}_2Co^{III}_2\}$ species are partially photo-converted into paramagnetic $\{Fe^{III}_2Co^{II}_2\}$ species below 70 K (even if the irradiation with white-light occurs only during the spectra acquisition). But the further increase of the temperature leads to a decrease of the reflectivity in the near-IR region and at 120 K the spectrum is similar to the one obtained at 120 K in cooling mode indicating the presence of only $\{Fe^{II}_{LS}(\mu-CN)Co^{III}_{LS}\}$ motifs in the square complex. The spectrum at 270 K is similar to the one obtained before the thermal cycle suggesting that the sample is stable under the experimental conditions and the defects induced during the sample preparation recover their high temperature $\{Fe^{III}_{LS}(\mu-CN)Co^{II}_{HS}\}$ state.

An alternative way to visualize the thermal changes of the optical reflectivity spectra is presented in Figure V-9 (left) in the form of the thermal dependence of the reflectivity at 800 ± 5 nm (R_{800}). Upon cooling from 270 K (Figure V-9 left, blue curve), R_{800} decreases from ≈ 0.14 down to ≈ 0.09 at 120 K as a signature of electron transfer occurrence in the $\{Fe^{III}_2Co^{II}_2\}$ defects on sample's surface. At lower temperatures, the reflectivity slightly increases up to 0.11 at 10 K due a weak photo-conversion (induced by the reflectivity source light) of the $\{Fe^{II}_{LS}(\mu-CN)Co^{III}_{LS}\}$ into $\{Fe^{III}_{LS}(\mu-CN)Co^{II}_{HS}\}$ units. Upon warming from 10 K (Figure V-9 left, red curve), R_{800} is increasing up to 0.12 at 60 K, as expected if the photo-conversion is still active in this temperature domain. Above 60 K, the photo-conversion is less efficient than the thermal relaxation process and therefore the reflectivity at 800 nm decreases to recover at 120 K its 0.09 value. The heating

above 120 K leads to a complete reversal of the changes observed on cooling such that at 270 K R_{800} recovers its 0.14 value, which is identical in heating and cooling modes.

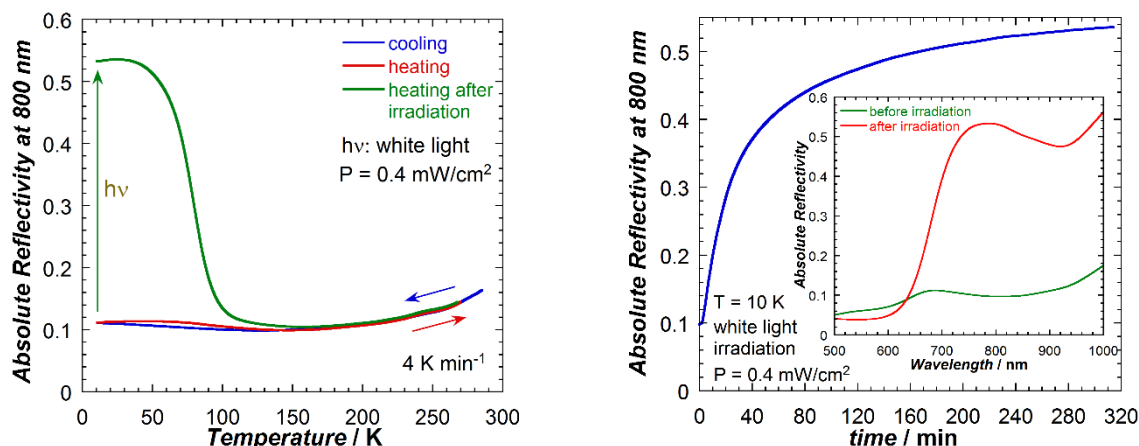


Figure V-9. (left) Thermal evolution of reflectivity signal recorded at $\lambda = 800 \pm 5$ nm (R_{800}) of **8a** in heating (red line) and cooling modes (blue line), and after 5 h of white light irradiation (0.4 mW/cm^2) at 10 K in heating mode (green line). (right) Time evolution of the absolute reflectivity R_{800} under white light irradiation (0.4 mW/cm^2) during 5 h at 10 K; inset: reflectivity spectra at 10 K before and after 5 h of white light irradiation (0.4 mW/cm^2).

In order to verify if compound **8a** is indeed photo-active, the time evolution of the reflectivity, R_{800} , during a white light irradiation was monitored after cooling the complex in the dark from 270 K to 10 K (Figure V-9 right). Irradiating the sample with white light (0.4 mW/cm^2) at 10 K for 5 h results in a significant change of the reflectivity spectra (Figure V-9 right inset). The value of R_{800} increased from 0.1 before irradiation to 0.53 after 5 h of irradiation, whereas the value of R_{550} decreased from 0.06 to 0.03 (Figure V-9 right inset). The reflectivity spectrum recorded after 5 h of white light irradiation (red line Figure V-9 right inset) is quite similar to ones recorded for other cyanido-bridged $\{Fe_2Co_2\}$ molecular squares in their paramagnetic state.^{1,4} Thus, using optical reflectivity measurements, it was possible to reveal the high photosensitivity of **8a** (at least at the samples' surface) under white light irradiation leading to conversion of the diamagnetic green $\{Fe^{II}_{LS}(\mu-CN)Co^{III}_{LS}\}$ pairs into paramagnetic red $\{Fe^{III}_{LS}(\mu-CN)Co^{II}_{HS}\}$ units. The red paramagnetic $\{Fe^{III}_2Co^{II}_2\}$ state is metastable, and increasing the temperature to 150 K (at $4 \text{ K}\cdot\text{min}^{-1}$) results in the recovery of the R_{800} value, 0.1, specific to the thermodynamically favored $\{Fe^{II}_2Co^{III}_2\}$ state.

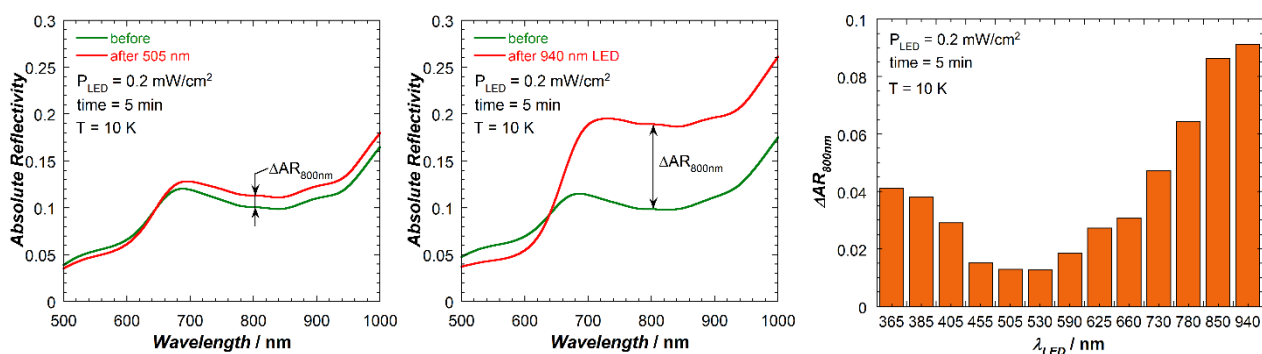


Figure V-10. Optical reflectivity spectra of **8a** at 10 K measured before (green) and after 5 min of irradiation (0.2 mW/cm^2) using wavelengths delivered by 505 nm (left) and 940 nm (center) LED sources. (right) Difference in absolute reflectivity (ΔAR) at 800 nm from the reflectivity spectra of **8a** before and after 5 min of irradiation (0.2 mW/cm^2) at 13 different wavelengths delivered by LED sources at 10 K.

In order to fully characterize the metastable photo-induced $\{Fe^{III}_2Co^{II}_2\}$ state, additional photo-excitation experiments were performed at selected wavelengths ranging from 940 to 365 nm (± 10 nm) using LED sources. The optimal wavelength to photo-convert the diamagnetic $\{Fe^{II}_2Co^{III}_2\}$ state into the paramagnetic $\{Fe^{III}_2Co^{II}_2\}$ one was determined by checking the efficiency of the 13 different LEDs in similar conditions at 10 K: 5 min of irradiation at a power of 0.2 mW/cm^2 (Figures V-10 and S.V-2). Before each excitation, the sample was heated to 250 K and cooled down to 10 K in the dark to fully relax the photo-generated $\{Fe^{III}_2Co^{II}_2\}$ sites. The plot of the difference between the absolute reflectivity at 800 nm before and after LED irradiation, $\Delta AR_{800} = R_{800\text{afterLED}} - R_{800\text{before}}$, as a function of the LED wavelength (Figure V-10 right) revealed that the most efficient wavelength is 940 nm (Figure V-10 center), whereas the least efficient ones are at 505 and 530 nm (Figure V-10 left). It is important to mention that all the LED sources were indeed efficient, explaining why the $\{Fe^{III}_2Co^{II}_2\}$ state can be easily populated with a white light irradiation (Figure V-9 right).

The optical reflectivity studies revealed the photo-sensitivity of **8a** and thus the possibility to convert the diamagnetic green $\{Fe^{II}_2Co^{III}_2\}$ species into a paramagnetic $\{Fe^{III}_2Co^{II}_2\}$ metastable state. Moreover, the additional photo-excitation experiments using LED sources allowed the identification of the wavelength with the highest efficiency to induce the photo-excited state that was useful for further investigations of light-induced ET in complex **8a**.

V.2.3.3. Reflectivity measurements for compound **8b**

Several preliminary tests showed that the ET transfer process (confirmed by the temperature dependent structural investigations) in crystals of **8b**, which are red at room temperature, is strongly dependent on the presence of the interstitial solvent molecules inside the crystal lattice. Therefore the temperature dependent reflectivity studies were performed below room temperature between 280 and 10 K in order to avoid the loss of co-crystallized solvent molecules.

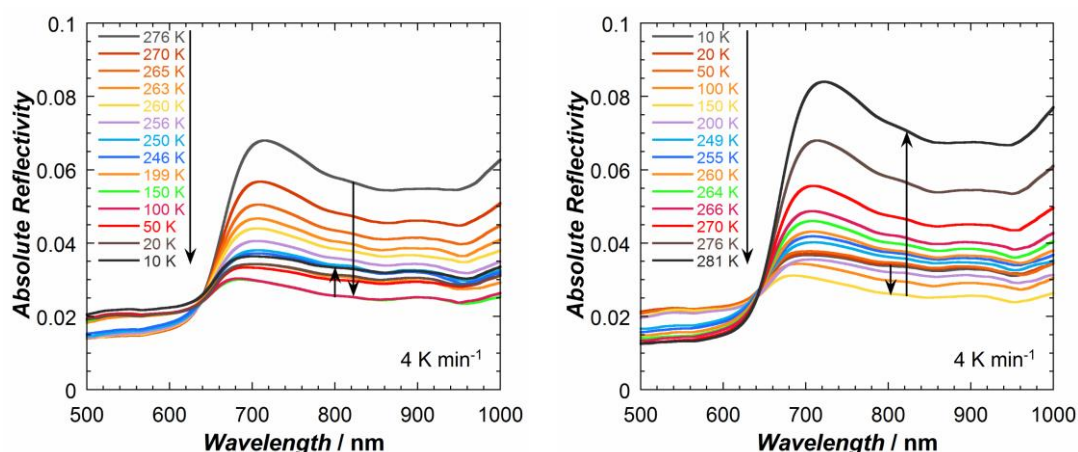


Figure V-11. Optical reflectivity spectra of **8b** at selected temperatures on cooling from 276 to 10 K (left), and on heating from 10 to 281 K (right).

At 276 K, the surface of compound **8b** is strongly absorbent and shows a reflectivity spectrum weak in intensity that contains a strong and broad absorption between 500 and 700 nm (absolute reflectivity at 550 nm $R_{550} = 0.015$) and a slightly higher reflectivity above 700 nm ($R_{800} = 0.06$). The observed strong

absorption of **8b** can be explained by the very dark red color of the crystals at room temperature and/or partial conversion at 276 K of the $\{Fe^{III}_2Co^{II}_2\}$ species into the diamagnetic $\{Fe^{II}_2Co^{III}_2\}$ species that show strong absorption between 500 and 1000 nm.

On cooling from 276 to 246 K, the complex **8b** becomes strongly absorbent above 700 nm (Figure V-11 left) as the result of thermally-induced electron-transfer between Co^{II} and Fe^{III} ions. Upon further cooling until 100 K the reflectivity in the near-IR region continues to decrease, but not as significantly as between 276 and 246 K. Below 100 K, an increase of reflectivity is observed above 700 nm as a possible signature of the photo-induced formation of the paramagnetic $\{Fe^{III}_2Co^{II}_2\}$ species under the spectroscopic white light ($P = 0.4 \text{ mW/cm}^2$) as already observed for **8a**. Heating the sample leads to a complete reversal of the spectral changes observed upon cooling. The spectrum at 276 K is similar to the one obtained before the thermal cycle suggesting that the sample is stable under the experimental conditions, while the further heating until 286 K shows a significant decrease of absorption in the near-IR region, suggesting the occurrence of thermally-induced ET.

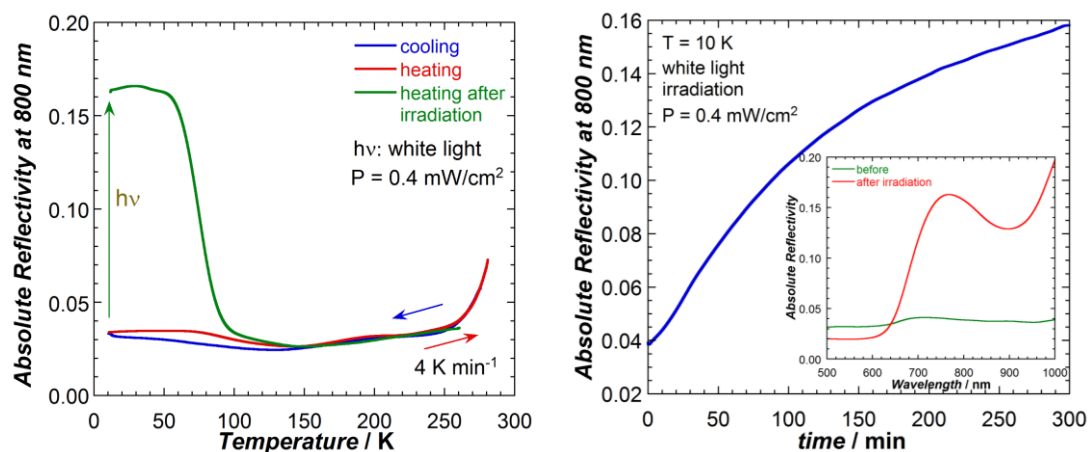


Figure V-12. (left) Thermal evolution of reflectivity signal recorded at $\lambda = 800 \pm 5 \text{ nm}$ (R_{800}) for **8b** in heating (red line) and cooling modes (blue line), and after 5 h of white light irradiation (0.4 mW/cm^2) at 10 K in heating mode (green line). (right) Time evolution of the absolute reflectivity R_{800} under white light irradiation (0.4 mW/cm^2) during 5 h at 10 K; inset: reflectivity spectra at 10 K before and after 5 h of white light irradiation (0.4 mW/cm^2).

The observed thermal evolution of the absolute reflectivity at 800 nm, R_{800} , allows an easier probing of the ET process over the whole temperature range (Figure V-12 left). Upon cooling from 276 K, R_{800} decreases from ≈ 0.06 at 276 K down to ≈ 0.03 at 250 K as a signature of the electron transfer process. Between 250 and 120 K, R_{800} decreases smoothly from 0.03 to 0.025 and below 120 K an increase of R_{800} is observed as a possible signature of a photo-conversion of the diamagnetic $\{Fe^{II}_{LS}(\mu-CN)Co^{III}_{LS}\}$ into paramagnetic $\{Fe^{III}_{LS}(\mu-CN)Co^{II}_{HS}\}$ units by the white light source used for spectra acquisition. The presence of thermal hysteresis effect between 10 and 140 K (Figure V-12 left, red and blue curves) reinforces this hypothesis. Upon heating the sample, a complete reversal of the spectral changes is observed (R_{800} recovers its value of 0.06 at 276 K) showing no thermal hysteresis above 250 K and suggesting that thermally induced ET is associated with a conversion of the diamagnetic $\{Fe^{II}_{LS}(\mu-CN)Co^{III}_{LS}\}$ units into the paramagnetic $\{Fe^{III}_{LS}(\mu-CN)Co^{II}_{HS}\}$ pairs. Whereas the increase of R_{800} to 0.073 at 281 K suggests that the thermal

$\{Fe^{III}_2Co^{II}_2\} \rightarrow \{Fe^{III}_2Co^{II}_2\}$ conversion is not finished at 281K and has a characteristic temperature, $T_{1/2}$, between 250 and 298 K (on the basis of single-crystal XRD data collected at 298 K).

To follow the photo-excitation of **8b**, the sample was cooled down in the dark at 10 K and then exposed to a constant white light ($P = 0.4 \text{ mW/cm}^2$). At 10 K, the optical reflectivity at 800 nm (R_{800}) was monitored in time (Figure V-12 right). After 5 hours of irradiation the reflectivity spectrum changed considerably (Figure V-12 right inset), R_{800} increased from ~ 0.03 to ~ 0.16 but did not reach saturation likely due to a very dark surface of the **8b** sample. The observed effect of the white light irradiation on the reflectivity spectrum is clearly suggesting the presence of a photo-induced ET. Upon heating from 10 to 270 K (at $4 \text{ K}\cdot\text{min}^{-1}$; Figure V-12 right, green curve), R_{800} is staying first stable until 50 K before rapidly decreasing at 95 K as the system is relaxing into its thermodynamic diamagnetic $\{Fe^{II}_2Co^{III}_2\}$ state. Interestingly, this relaxation of the photo-induced $\{Fe^{III}_2Co^{II}_2\}$ species occurs at the same temperature for **8a** and **8b** ($\sim 80 \text{ K}$) whereas at room temperature they show different electronic states.

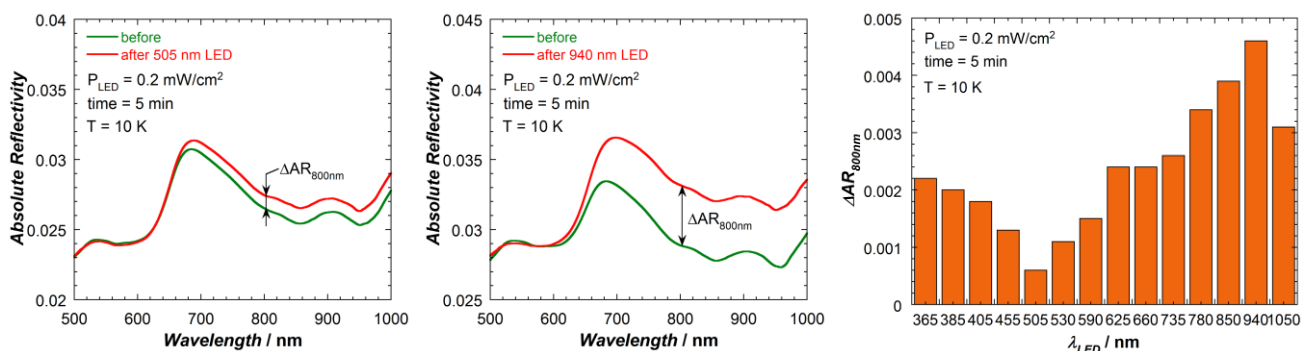


Figure V-13. Optical reflectivity spectra of **8b** at 10 K measured before (green) and after 5 min of irradiation (0.2 mW/cm^2) using wavelengths delivered by 505 nm (left) and 940 nm (center) LED sources. (right) Difference in absolute reflectivity (ΔAR) at 800 nm from the reflectivity spectra of **8b** before and after 5 min of irradiation (0.2 mW/cm^2) at 14 different wavelengths delivered by LED sources at 10 K.

Additional photo-excitation experiments using 14 LED sources of specific wavelengths ranging from 1050 to 365 nm ($\pm 10 \text{ nm}$) were performed on **8b** (Figures V-13 and S.V-3), employing the same experimental protocol as for **8a** (5 minutes of irradiation at 10 K with a LED source at a power of 0.2 mW/cm^2 , see Section V.2.3.2 for details). To summarize and visualize the changes induced by the LED irradiations, the difference of absolute reflectivity at 800 nm (ΔAR_{800}) was plotted as a function of LED wavelength (Figure V-13 right). ΔAR_{800} shows the same LED wavelength dependence for both **8a** and **8b** compounds, with the most efficient wavelength at 940 nm (Figure V-13 center) and the least efficient at 505 nm (Figure V-13 left).

Even though all the employed LED sources are capable to convert $\{Fe^{II}_2Co^{III}_2\}$ to $\{Fe^{III}_2Co^{II}_2\}$ species with different efficiencies on the surface of **8b**, it was decided to verify whether it is possible to observe $\{Fe^{II}_2Co^{III}_2\} \leftrightarrow \{Fe^{III}_2Co^{II}_2\}$ photo-reversibility with different wavelengths at 10 K, as it was reported recently on the basis of magnetic and crystallographic measurements for the molecular square complex of formula $\{[(\text{pzTp})\text{Fe}(\text{CN})_3]_2[\text{Co}(\text{bik})_2]_2\}(\text{ClO}_4)_2 \cdot 2\text{H}_2\text{O}$ (where pzTp = tetrapyrazolylborate, bik = bis(1-methylimidazol-2-yl)ketone).^{2b} To test the ET photo-reversibility in **8b**, the 940 nm LED was chosen for

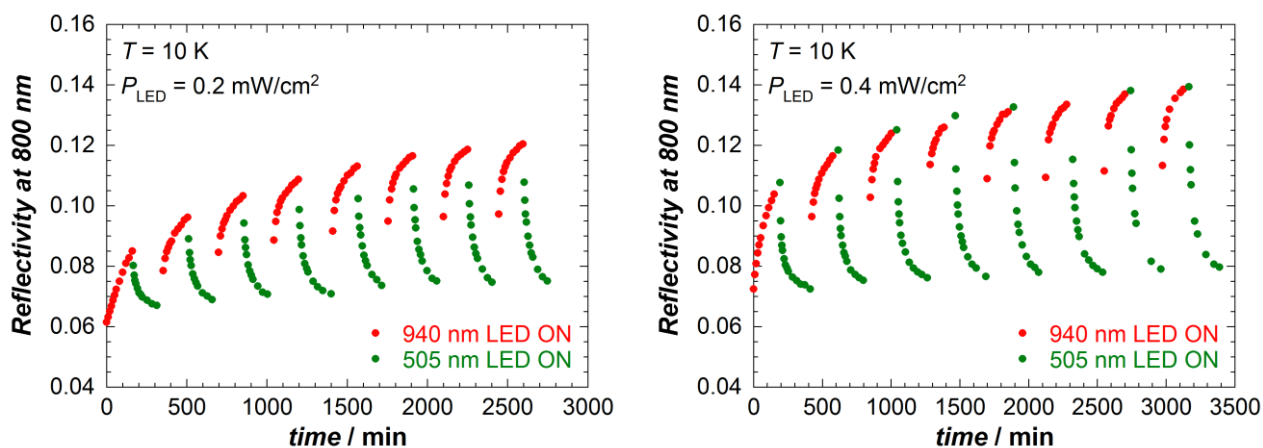


Figure V-14. Time evolution of R_{800} for **8b** during eight successive irradiation cycles with 940 ± 10 nm and 505 ± 10 nm LED sources at 10 K: (left) $P_{LED} = 0.2$ mW/cm², $t_{940LED} = 160$ min, $t_{505LED} = 180$ min; (right) $P_{LED} = 0.4$ mW/cm², $t_{940nmLED} = 200$ min, $t_{505nmLED} = 220$ min.

excitation while the 505 nm LED was chosen to probe de-excitation. During the first set of successive irradiation cycles at 10 K, the power of both LED sources was set to 0.2 mW/cm², with one cycle consisting of 160 min of irradiation with the 940 nm LED followed by 180 min of irradiation with the 505 nm LED. To summarize and visualize the ET photo-reversibility in **8b** induced by the successive LED irradiations at 10 K, the absolute reflectivity at 800 nm (R_{800}) was monitored as a function of time. As judged by the time evolution of R_{800} during the first set of successive irradiation cycles, a photo-reversible effect was observed the surface of **8b** (Figure V-14), but surprisingly the recorded curves do not superimpose. The first 940 nm LED irradiation curve appears to be considerably below the following ones. Moreover each curve corresponding to the excitation with the 940 nm LED source to paramagnetic $\{Fe^{III}_2Co^{II}_2\}$ state (Figure V-14 left: red dots, except the first one) looks quasi-saturated but at different R_{800} values. In contrary to excitation data, the curves corresponding to the irradiation with the 505 nm LED source exhibit quite efficient recovery of the thermodynamic $\{Fe^{II}_2Co^{III}_2\}$ state (Figure V-14 left: green dots), the obtained R_{800} value is higher than the initial one, but is relatively constant after each irradiation cycle. Increasing the power of the LED sources and the time of exposure to LED irradiation showed similar quasi-reversible switching between $\{Fe^{II}_2Co^{III}_2\}$ and $\{Fe^{III}_2Co^{II}_2\}$ states at the surface of **8b** (Figure V-14 left). In order to verify if the observed de-excitation caused by 505 nm LED irradiation is real and not confused with the relaxation in the dark, the latter was monitored. The R_{800} time dependence was measured during three cycles consisting of 180 min exposure to the white light ($P = 0.4$ mW/cm²) followed by 160 min of no irradiation (Figure S.V-4). No significant relaxation was observed in the dark, therefore we can conclude that at least at the surface of **8b** it is possible to observe a $\{Fe^{II}_2Co^{III}_2\} \leftrightarrow \{Fe^{III}_2Co^{II}_2\}$ photo-reversibility with different wavelengths at 10 K. To confirm the nature of the observed photo-switching, it is necessary to perform additional investigations including photo-magnetic measurements on a bulk polycrystalline sample of **8b** and X-ray crystallography under irradiation.

V.2.4. Photo-crystallographic investigations of compound **8a**

Optical reflectivity measurements of **8a** revealed the possibility to photo-convert at 10 K the diamagnetic $\{Fe^{II}_2Co^{III}_2\}$ state into a paramagnetic $\{Fe^{III}_2Co^{II}_2\}$ species at the surface of the studied sample.

Therefore additional single-crystal XRD investigations were performed with the aim to study the photo-induced effect on a single crystal of **8a** and to determine the structure of the photo-induced state. The measurements were performed at 10 K before and after the irradiation with an 808 nm laser source (2 h, $P = 30 \text{ mW/cm}^2$) in collaboration with Prof. Eric Collet at Institut de Physique de Rennes (Université Rennes 1). Thus, crystal structures of **8a** were refined in the two different states at 10 K (Figure V-15, Tables V-2 and S.V-3).

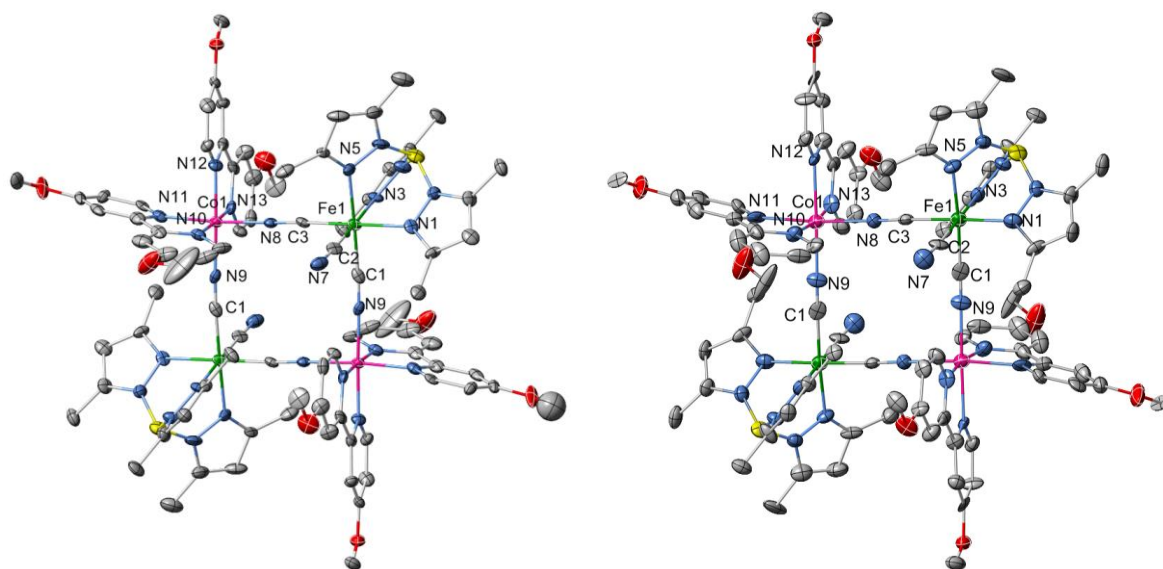


Figure V-15. The structure of the cationic portion of **8a** (left) before and (right) after the irradiation with an 808 nm laser source (2 h, $P = 30 \text{ mW/cm}^2$) at 10 K. Thermal ellipsoids are at 50% probability. All anions, lattice solvent and hydrogen atoms are eliminated for clarity. Color scheme: C grey, Co pink, Fe green, N blue, O red, B yellow.

Table V-2. Unit-cell parameters, average metal-to-ligand bond lengths, metal-to-metal distances and deformation of the Co coordination sphere for **8a** before and after the irradiation with an 808 nm laser source (2 h, $P = 30 \text{ mW/cm}^2$) at 10 K.

	(8a)	
	10 K $\{Fe^{II}_2Co^{III}_2\}$	10 K 808nm $\{Fe^{III}_2Co^{II}_2\}$
Crystal system	Monoclinic	
Space group	C 2/c	
a, Å	31.980(4)	31.933(3)
b, Å	20.8190(10)	21.262(2)
c, Å	21.593(2)	21.772(2)
β , °	129.237(2)	129.010(10)
V, Å ³	11135.1(18)	11486.4(19)
$\langle Fe-C \rangle$, Å	1.887	1.925
$\langle Fe-N \rangle$, Å	2.053	2.010
$\langle Co-N \rangle$, Å	1.925	2.101
Fe(1)···Co(1), Å	4.930	5.143
Fe(1)···Co(1) ^a , Å	4.930	5.135
Fe···Fe, Å	7.144	7.577
Co···Co, Å	6.797	6.945
$\Sigma(N-Co-N)^a$, °	43.9	64.1

$$^a \Sigma = \sum_{i=1}^{12} |90 - \varphi_i|, \text{ where } \varphi_i \text{ are } N-Co-N \text{ bond angles}$$

At 10 K before irradiation, the structure of the square motif in the green crystals of **8a** (Figure V-15, Tables V-2 and S.V-3) shows no significant differences compared with the one determined at 120 K (See Section V.2.2.2, Figure V-4, Tables V-1 and S.V-3). The measured average bond lengths match well with those previously observed for Fe^{II} and Co^{III} ions in LS configurations.

Many structural parameters changed after the irradiation with an 808-nm laser light at 10 K (2 h, $P = 30 \text{ mW/cm}^2$), even if the space group remains $C2/c$. An increase of the unit cell volume by 350 \AA^3 was observed after the irradiation (Table V-2). Important changes in the coordination sphere of the Co ion occurred (Tables V-2 and S.V-3). The average Co–N bond length became $2.086(7) \text{ \AA}$, which is close to that expected for a Co^{II} HS ion, suggesting an almost complete $\{Fe^{II}_2Co^{III}_2\} \rightarrow \{Fe^{III}_2Co^{II}_2\}$ photo-conversion. In addition, the N–Co–N angle values in the HS Co^{II} coordination sphere departed more significantly from orthogonality than those measured for the LS Co^{III} ion (Tables V-2 and S.V-3). Although the Fe coordination sphere showed only smaller differences (Tables V-2 and S.V-3), the change in the Fe charge is visible in the Fe–C bond distances. Whereas the Fe–C bond lengths were about 1.89 \AA before irradiation, the average distance increased to 1.92 \AA after the 808-nm irradiation. Thus, the crystal data match well with the occurrence of a light-induced ET associated with $\{Fe^{II}_2Co^{III}_2\} \rightarrow \{Fe^{III}_2Co^{II}_2\}$ photo-conversion. This process was also accompanied by subtle changes in the geometry of the $\{Fe_2Co_2\}$ square motif. The Fe–Co intramolecular distances became significantly longer (increasing by ca. 0.2 \AA), and the cyanide bridges are slightly more distorted at the Co sites in the metastable paramagnetic state (Table S.V-3).

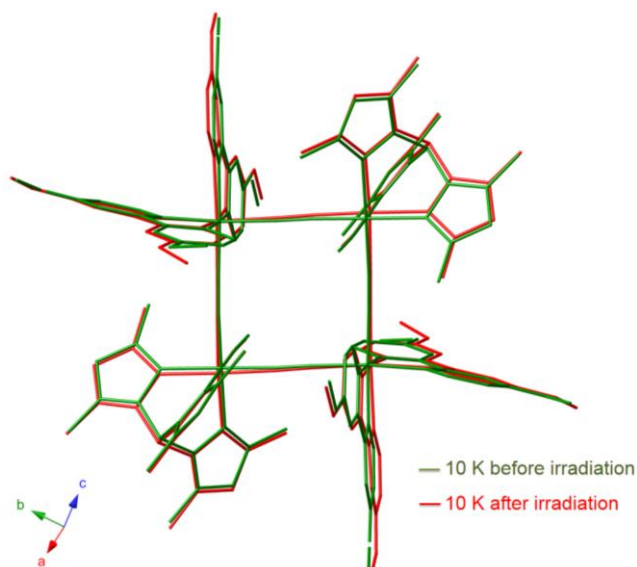


Figure V-16. Superimposed structures of the $\{Fe_2(\mu-CN)_4Co_2\}$ cationic core in **8a** emphasizing the differences observed before and after irradiation with an 808 nm laser source (2 h, $P = 30 \text{ mW/cm}^2$) at 10 K.

The observed light-induced geometrical variations were also accompanied by modifications in the intermolecular interactions. As seen previously in the crystal structure at 120 K, each co-crystallized water molecule forms two hydrogen bonds with two nitrogen atoms from terminal cyanide ligands of two neighboring squares, leading to a supramolecular 1D-like structure (Figure V-5). As the result of the 808-nm irradiation, these H-bonds ($N(7)\cdots O(1)w$ and $O(1)w\cdots N(7)'$) decreased from 2.924 and 2.870 \AA to 2.810 and 2.787 \AA , respectively, at 10 K.

The photo-crystallographic investigations performed at 10 K for the green crystals of **8a** are in agreement with the optical reflectivity study and proved the possibility to convert the diamagnetic $\{Fe^{II}_{LS}(\mu-CN)Co^{III}_{LS}\}$ species into paramagnetic $\{Fe^{III}_{LS}(\mu-CN)Co^{II}_{HS}\}$ units as the result of the intramolecular light induced ET.

V.2.5. Magnetic measurements

According to the structural and optical data, compound **7** does not exhibit an ET process, **8a** is stabilized in the diamagnetic $\{Fe^{II}_2Co^{III}_2\}$ state between 10 and 270 K, but exhibits an $\{Fe^{II}_2Co^{III}_2\} \rightarrow \{Fe^{III}_2Co^{II}_2\}$ conversion as the result of a photo-induced ET, while compound **8b** shows both thermally and light-induced ET. To further investigate the electron transfer mechanism and the resulting changes of the electronic states, the magnetic properties of **7**, **8a** and **8b** as a function of temperature and/or light exposure were studied.

V.2.5.1. Magnetic properties of **7**

As expected, magnetic susceptibility measurements carried out for **7** between 1.8 and 280 K (and shown in Figure V-17 as the thermal dependence of the χT product) did not show any sign of thermally induced ET. Above 170 K, the χT product remains nearly constant around $7.6 - 7.7 \text{ cm}^3 \cdot \text{K/mol}$ that is in good agreement with the expected value for a 2:2 ratio of magnetically isolated Fe^{III}_{LS} ($S = 1/2$, $g \approx 2.6$) and Co^{II}_{HS} ($S = 3/2$, $g \approx 2.6$) centers. The temperature decrease from 170 to 40 K affords a smooth decrease of the χT value to $7.2 \text{ cm}^3 \cdot \text{K/mol}$ likely due to the spin-orbit coupling of the high spin Co^{II} ions. On further cooling below 40 K, the χT product increases to a value of $7.8 \text{ cm}^3 \cdot \text{K/mol}$ at 8 K, then as the temperature is lowered it decreases to $5.3 \text{ cm}^3 \cdot \text{K/mol}$ at 1.8 K. The observed behavior in **7** suggests the presence of ferromagnetic interactions between Fe^{III} and Co^{II} ions with weak intermolecular antiferromagnetic interactions. Similar magnetic behavior was observed for the paramagnetic $\{Fe^{III}_2Co^{II}_2\}$ compound **4** (see section III.2.5) and compound **1** in its paramagnetic photo-induced phase.¹

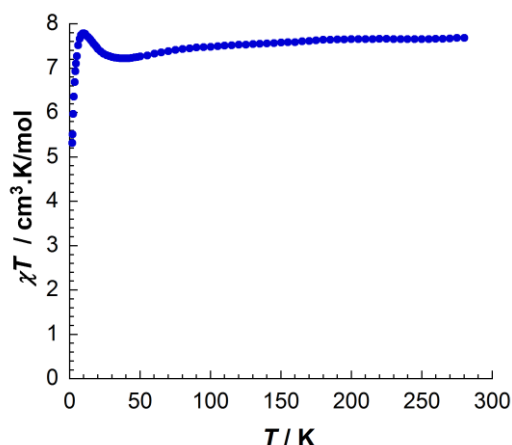


Figure V-17. Temperature dependence of the χT product (with χ defined as the molar magnetic susceptibility and equal to M/H) for compound **7** at 0.1 T.

The plots of the magnetization field-dependence bring an additional evidence of the ferromagnetic exchange between Fe^{III} and Co^{II} ions in **7**. The magnetization is monotonically increasing upon applying the

external dc fields, without showing an inflection point, i.e. “S-shape” curves, that could be indicative for the presence of antiferromagnetic interactions. Moreover, the magnetization curves show an absence of magnetization saturation that is consistent with magnetic anisotropy of the Co^{II} ions (Figure S.V-5 left).

V.2.5.2. Magnetic and photo-magnetic properties of **8a**

The dark green color of the crystals at room temperature suggests that **8a** is in its diamagnetic $\{Fe^{II}_2Co^{III}_2\}$ state. Optical reflectivity measurements and photo-crystallographic investigations at 10 K suggested the possibility to photo-induce the conversion of the diamagnetic $\{Fe^{II}_2Co^{III}_2\}$ state into a metastable paramagnetic $\{Fe^{III}_2Co^{II}_2\}$ state by an intramolecular electron transfer. Therefore, the magnetic and photo-magnetic properties of **8a** were studied.

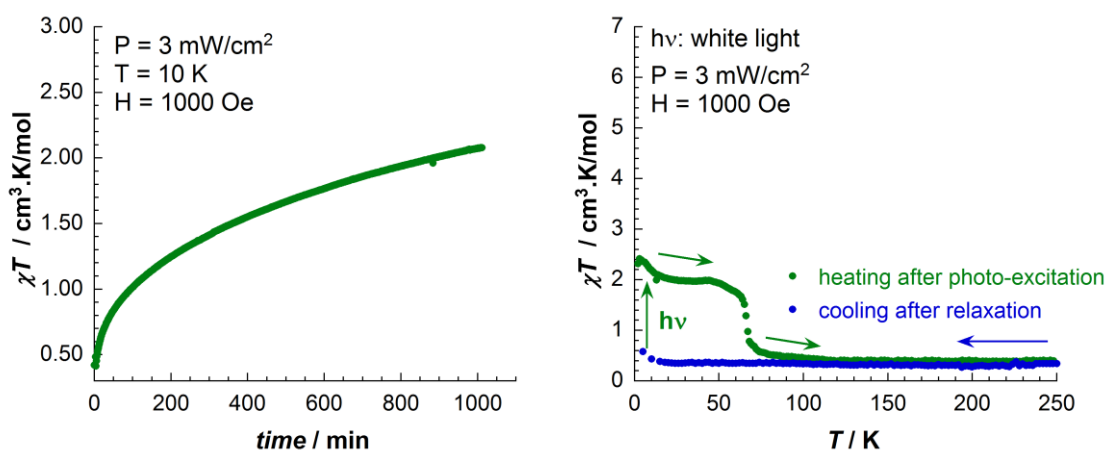


Figure V-18. (left) Time evolution of the χT product for **8a** during the white light irradiation (3 mW/cm^2) at 10 K. (right) Temperature dependence of the χT product for **8a** on heating (green dots, 0.1 T, 0.3 K/min) after the white light irradiation (3 mW/cm^2) at 10 K for ~ 17 h and on cooling from 250 K in the dark (blue dots, 0.1 T, 0.3 K/min).

At 10 K in the dark, the measured χT product was about $0.3 \text{ cm}^3\cdot\text{K/mol}$, confirming that the investigated sample is globally diamagnetic consistently with the presence of two low-spin Co^{III} ($S = 0$) and two low-spin Fe^{II} ($S = 0$) ions. Under irradiation with a white halogen lamp (3 mW/cm^2) at 10 K, the χT product increases with the irradiation time (Figure V-18 left). This increase of the magnetization points out the occurrence of a photo-induced electron transfer associated with the conversion of the diamagnetic $\{Fe^{II}_{LS}(\mu\text{-CN})Co^{III}_{LS}\}$ species into paramagnetic $\{Fe^{III}_{LS}(\mu\text{-CN})Co^{II}_{HS}\}$ ones. Apparently due to an insufficient light-penetration depth and/or relatively low efficiency of the irradiation, an incomplete conversion was observed. The χT product did not reach saturation and the expected values of ca. $6.5 - 7 \text{ cm}^3\cdot\text{K/mol}$ even after ~ 17 h of irradiation; $\chi T = 2.1 \text{ cm}^3\cdot\text{K/mol}$ at 10 K (Figure V-18 left). Upon heating in the dark from 2 to 45 K, the χT product smoothly decreased from $2.5 \text{ cm}^3\cdot\text{K/mol}$ towards $1.9 \text{ cm}^3\cdot\text{K/mol}$, thus suggesting the presence of intramolecular ferromagnetic couplings in the photo-generated $\{Fe^{III}_{LS}(\mu\text{-CN})Co^{II}_{HS}\}$ species (Figure V-18 right), as it was reported for other cyanido-bridged $\{Fe_2Co_2\}$ squares.^{1,2a} Consistently with the reflectivity study, the photo-induced metastable state readily converts into the thermodynamic $\{Fe^{II}_{LS}(\mu\text{-CN})Co^{III}_{LS}\}$ state above 70 K. Upon further heating the χT product recovered the initial value of $0.3 \text{ cm}^3\cdot\text{K/mol}$ and remained constant between 90 and 250 K. The studied polycrystalline sample of **8a** was not heated above 250 K during the magnetic measurements. Indeed preliminary tests

showed that over time (5 – 15 min at room temperature and even after several hours at 120 K under N_2 cryo-flux) the green crystals of **8a** turn irreversibly red, if they are kept out of the mother liquor, likely due to the loss of the lattice solvent molecules. Cooling the sample from 250 to 2 K in the dark showed that **8a** is diamagnetic in this temperature range (Figure V-18 right).

V.2.5.3. Magnetic and photo-magnetic properties of **8b**

Magnetic susceptibility measurements were performed on the crystals of **8b** kept in their mother liquor between 1.8 and 280 K (Figure V-19 left). The χT product below 200 K is nearly constant with a value of $0.36 \text{ cm}^3 \cdot \text{K/mol}$, suggesting that **8b** is in its diamagnetic electronic state, $\{Fe^{II}_2Co^{III}_2\}$. As the temperature was increased from 200 to 280 K, the χT product increased to a value of $8.5 \text{ cm}^3 \cdot \text{K/mol}$, indicating the occurrence of the thermally induced ET (Figure V-19 left). The value of the χT product at 280 K is significantly higher than the expected theoretical value for two non-interacting LS Fe^{III} ($S = 1/2$, $g \approx 2.6$) and two HS Co^{II} ($S = 3/2$) ions. The high value of the χT product may be explained by the presence of a significant orbital contribution to the magnetic moment of the HS Co^{II} ions leading to a g factor around 2.8.^{5a,8} On cooling from 280 K at 0.7 K/min, the measured χT product values traced the profile obtained in heating mode (with the same sweep rate of 0.7 K/min) with no thermal hysteresis suggesting that **8b** displays a thermally reversible crossover between the paramagnetic and diamagnetic states associated with the intramolecular electron-transfer. This kind of thermal behavior is not surprising since no significant intermolecular interactions were observed in the crystal structure of **8b**.

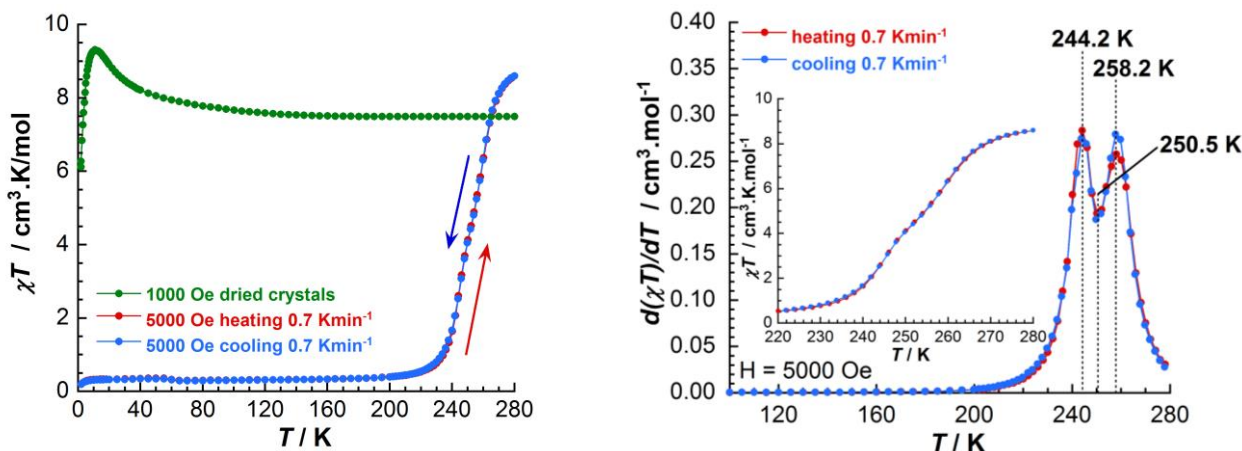


Figure V-19. (left) Temperature dependence of the χT product for the crystals of **8b** in their mother liquor (on heating and cooling, red and blue dots respectively, 0.5 T, 0.7 K/min) and for crystals of **8b** dried in vacuum at room temperature for 12 h (green dots, 0.1 T, 1 K/min). (right) $d(\chi T)/dT$ vs T plot of the temperature dependent susceptibility measurements showed on left of the crystals of **8b** in their mother liquor at 0.5 T on cooling (blue dots) and heating (red dots) with a sweep rate of 0.7 K/min. Inset: the zoom of the χT vs T plot showed on the left between 220 and 280 K.

A closer examination of the recorded χT vs T curves for the crystals of **8b** (Figure V-19 right, inset) revealed that the conversion associated with the ET process between 220 and 280 K occurs in a two-step fashion via a possible intermediate state. This result is confirmed by the $d(\chi T)/dT$ vs T plots (Figure V-19 right) showing the presence of two inflection points around 244 and 258 K. A possible intermediate state is observed in a very narrow temperature range around 250 K for a χT value of $4.2 \text{ cm}^3 \cdot \text{K/mol}$ that is about half of the value measured at 280 K. The occurrence of an intermediate state, composed of $\{Fe^{III}_2Co^{II}_2\}$ and

$\{Fe^{II}Co^{III}\}_2$ complexes in the 1:1 molar ratio inside the crystal packing, was also observed and reported previously for another cyanido-bridged square complex, $\{[(Tp^*)Fe(CN)_3]_2[Co(dtbbpy)_2]_2\}(PF_6)_2 \cdot 2MeOH$ (where $dtbbpy = 4,4'$ -di-*tert*-butyl-2,2'-bipyridine).³

As it was mentioned previously, the crystals of **8b** lose their crystallinity and their ET properties if they are kept outside their mother liquor more than 5 – 10 min. In order to verify the effect of the lattice solvents over ET occurrence, the sample used for magnetic measurements, described above, was kept in vacuum overnight at room temperature and then re-measured in the magnetometer. Thus, as expected, the recorded χT vs T curve (Figure V-19 left, green dots) showed no thermally induced ET and confirmed that lattice solvent loss stabilizes the paramagnetic state. The temperature dependence of the χT product for dried crystals of **8b** shows a value of $7.5 \text{ cm}^3 \cdot \text{K/mol}$ at high temperatures (Figure V-19 left, green dots). This value is slightly larger than the one expected for the sum of two magnetically isolated low-spin Fe^{III} ions ($S = 1/2$) and two high-spin Co^{II} ions ($S = 3/2$) but lower than the one observed for the solvated sample. This difference may be explained by the fact that after the solvent loss the structural geometry of the cyanido-bridged $\{Fe_2Co_2\}$ core has changed inducing a change of the intrinsic magnetic properties of the metal ions. Upon cooling the dried sample, the χT product remained practically constant at $7.5 \text{ cm}^3 \cdot \text{K/mol}$ until 130 K. Below 130 K, the χT increases smoothly down to 40 K, in line with the ferromagnetic coupling between the Co^{II} and Fe^{III} ions through the cyanide bridges. At $T < 40 \text{ K}$, χT sharply increases to reach maxima of ca. $9.3 \text{ cm}^3 \cdot \text{K/mol}$ at 10.0 K. Then, it decreases with temperature, likely because of antiferromagnetic intermolecular interactions and/or the magnetic anisotropy of HS Co^{II} ions, to reach a value of ca. $6.0 \text{ cm}^3 \cdot \text{K/mol}$ at 1.8 K. These features are consistent with significant ferromagnetic interactions inside the tetranuclear core. Additional evidence for ferromagnetic exchange between Fe^{III} and Co^{II} ions in the dried sample of **8b** is found in the field-dependence of magnetization. At 1.8 K, the magnetization value is monotonically increasing upon applying the external dc fields, without showing S-shape curves that could be indicative for the presence of antiferromagnetic interactions. Moreover the magnetization curves show an absence of magnetization saturation as expected in the presence of the Co^{II} magnetic anisotropy (Figure S.V-5 right).

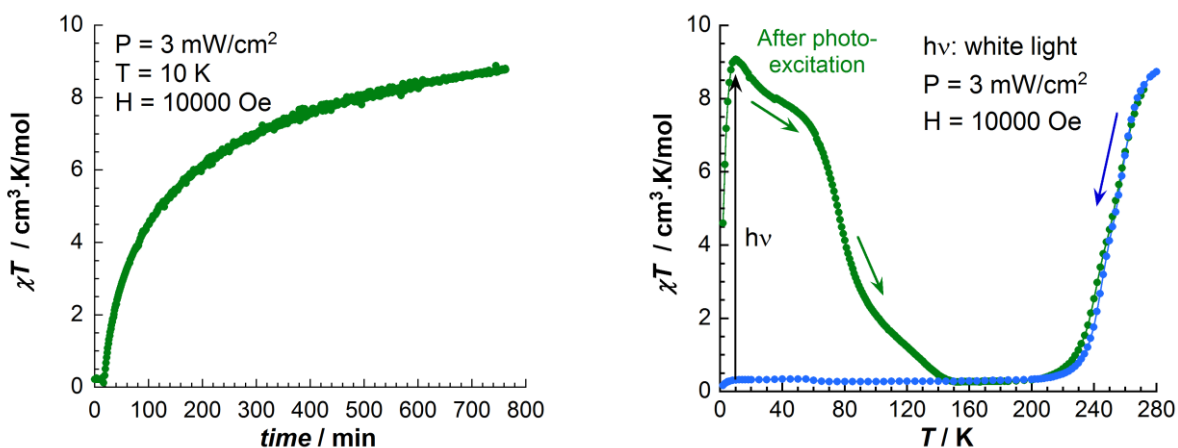


Figure V-20. (left) Time evolution of the χT product for **8b** during the white light irradiation (3 mW/cm^2 , 1 T) at 10 K. (right) Temperature dependence of the χT product for **8b** on heating (green dots, 1 T, 0.3 K/min) after the white light irradiation (3 mW/cm^2) at 10 K for $\sim 13 \text{ h}$ and on cooling from 250 K in the dark (blue dots, 1 T, 0.3 K/min).

Optical reflectivity measurements showed a change of optical properties corresponding to the occurrence of photo-induced intramolecular ET at the surface of the **8b** sample. Therefore photo-magnetic investigations of **8b** were carried out (Figure V-20).

Under white-light irradiation (3 mW/cm^2) at 10 K, the χT product value increased from $0.2 \text{ cm}^3 \cdot \text{K/mol}$ to a value of $8.7 \text{ cm}^3 \cdot \text{K/mol}$ after ~ 13 hours (Figure V-20 left), thus suggesting that $\{Fe^{III}_2Co^{II}_2\}$ complexes are photo-generated. Upon heating in the dark from 2 to 10 K, the χT product increased from 4.5 to $9.1 \text{ cm}^3 \cdot \text{K/mol}$, thus indicating that magnetic anisotropy and/or intermolecular antiferromagnetic interactions are present in the photo-induced phase (Figure V-20 right). In the 10 – 60 K range, χT product decreased towards $7.5 \text{ cm}^3 \cdot \text{K/mol}$, thus suggesting that intramolecular ferromagnetic exchange between LS Fe^{III} and HS Co^{II} ions is operative. Consistent with reflectivity studies (Figure V-12 left), the photo-generated paramagnetic metastable state readily converts into the thermodynamic diamagnetic $\{Fe^{II}_2Co^{III}_2\}$ state in two steps, abrupt one between 60 – 90 K and a smoother one in the 90 – 140 K range. Further increasing of the temperature leads the compound to recover its original paramagnetic $\{Fe^{III}_2Co^{II}_2\}$ state at high temperatures.

At least at the surface of **8b**, optical reflectivity investigations also showed the possibility to observe $\{Fe^{II}_2Co^{III}_2\} \leftrightarrow \{Fe^{III}_2Co^{II}_2\}$ photo-reversibility with different wavelengths at 10 K. Unfortunately the photo-magnetic measurements on a crystalline sample of **8b** have not been performed yet to confirm the occurrence of photo-reversible ET at low temperatures.

V.3. Analytical characterizations of the methoxy functionalized molecular $\{Fe_2Co_2\}$ squares in diluted solutions

The characterizations of compounds **7**, **8a** and **8b**, performed in solid state, have showed that the functionalization of the cyanido-bridged $\{[(Tp^*)Fe(CN)_3]_2[Co(bpy)_2]_2\}^{2+}$ system with electron donating methoxy groups influences significantly the optical and magnetic properties of the final complexes, if combined rationally with other factors like the counter-anion and crystallization solvents. Identification of the right conditions that would contribute to the occurrence of the intramolecular ET is a difficult and time consuming task. It appears much easier to control the ET properties in molecular cyanido-bridged $\{Fe_2Co_2\}$ squares when they are “placed” in solutions^{3b,4} (see also Chapter IV). In solution the constraints induced by the crystal lattice packing are not present anymore and, thus, have no effect over the intrinsic molecular behavior.

The investigations of functionalized complexes **2**,⁴ **5**, and **6**^{4b} (see also Chapters III and IV) in solutions proved the possibility to transfer from solid state or to reveal into a wide range of solvents the ET driven switching properties of the functionalized $\{Fe_2Co_2\}$ complexes. With the aim to determine if the functionalized complexes **7**, **8a** and **8b** can exhibit thermally induced ET in solutions, the properties of the resulting solutions have been investigated.

It is important to mention, that compounds **8a** and **8b** represent different solvates of the same system, $\{[(Tp^*)Fe(CN)_3]_2[Co(diMeObpy)_2]_2\}(PF_6)_2$, stabilized in different electronic states at room temperature. **8a** is a green crystalline solid, whereas **8b** is red at room temperature. The dissolution of the green crystals of **8a** affords a red solution in acetonitrile (and other solvents), while the repeated re-crystallizations of the red

acetonitrile solutions of **8a** yield red crystals of **8b**. Therefore in further investigations of the magnetic and optical properties in solutions, compounds **8a** and **8b** are considered the same compound and referred as compound **8**, $\{[(Tp^*)Fe(CN)_3]_2[Co(diMeObpy)_2]_2\}(PF_6)_2$.

The qualitative tests for ET that consisted in cooling with liquid nitrogen the solutions of **7** and **8** showed a systematic change of color from red to green, pointing out the occurrence of intramolecular ET in solutions of **7** and **8**. The qualitative tests were carried out in several solvents: methanol, ethanol, acetone, acetonitrile, dichloromethane and butyronitrile. Due to the presence of PF_6^- as counter-anion, both solvates of **8** are not soluble in alcohols, especially methanol and ethanol. Similarly to previously reported complexes **1**,^{1,4b} **2**,⁴ **5** and **6**^{4b} (see also Chapters III and IV) it was assumed that the integrity of the $\{Fe_2Co_2\}$ square molecules remained intact in solutions for which the color change was observed.

V.3.1. UV-Vis spectroscopic characterizations of **7** and **8** in diluted solutions

The absorption spectra of **7** (in methanol, Figure V-21 top left, and dichloromethane, Figure S.V-6 left) and **8** (in butyronitrile – PrCN, Figure V-21 bottom left) were measured at different temperatures in cooling mode from room temperature until the freezing point of the solvent.

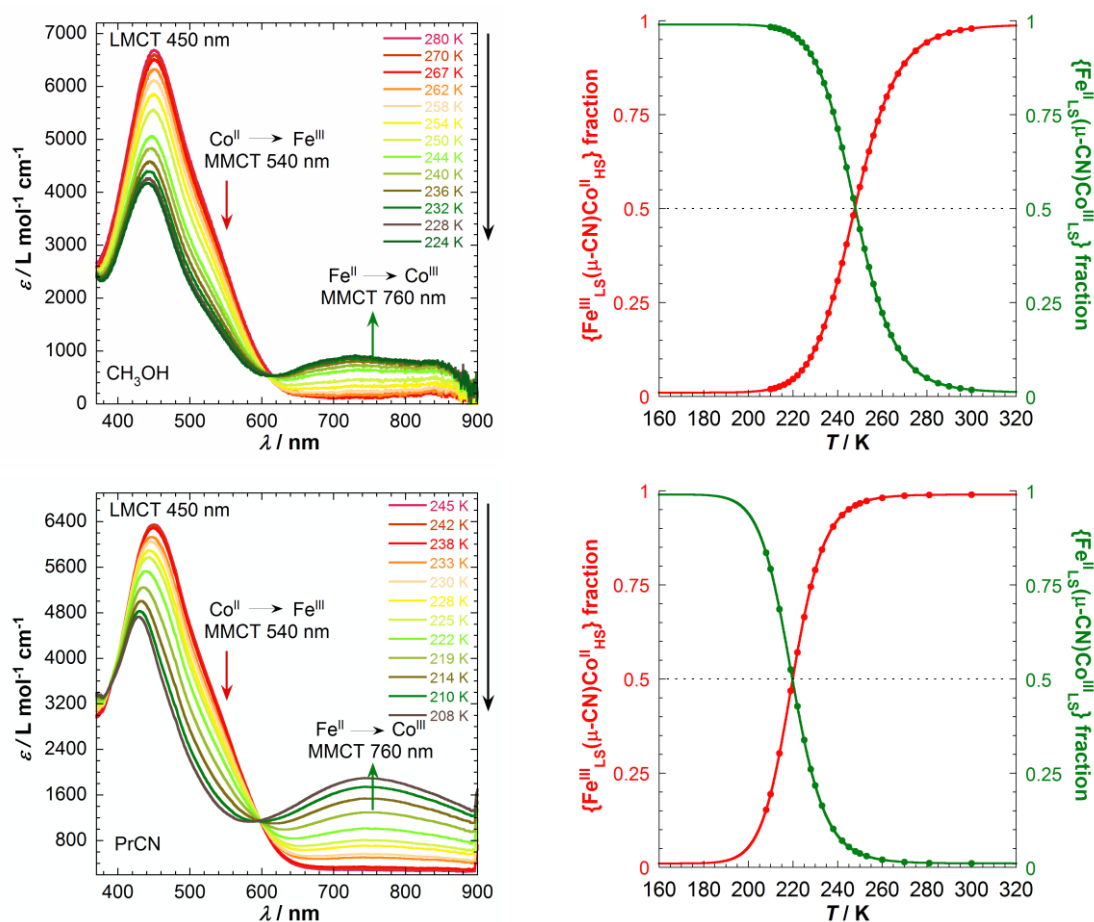


Figure V-21. (left) Selected UV-Vis spectra for **7** in CH_3OH (top) and **8** in PrCN (bottom) on cooling mode from 300 K until the freezing point of the solvent (at 0.2 to 0.3 K/min). (right) Temperature dependence of the $\{Fe^{III}_{LS}(\mu-CN)Co^{II}_{HS}\}$ and $\{Fe^{II}_{LS}(\mu-CN)Co^{III}_{LS}\}$ fractions estimated from the absorption intensities at the MMCT bands (≈ 540 nm and ≈ 760 nm) for **7** in CH_3OH (top) and **8** in PrCN (bottom), solid lines are the fits to the ideal solution model.⁹

The spectra recorded at 300 K showed an intense broad absorption band at 450 nm with a shoulder around 540 nm and matched well with those reported for cyanido-bridged squares in their paramagnetic

$\{Fe^{III}_2Co^{II}_2\}$ state^{2a,3b,4} (see also Sections IV.3.1 and IV.5.3 in Chapter IV). The strong absorption at 450 nm was assigned to the ligand-to-metal charge transfer (LMCT) bands from the Fe and Co chromophores, whereas the shoulder band at 540 nm was assigned to $Co^{II} \rightarrow Fe^{III}$ metal-to-metal charge transfer (MMCT) transition.^{2a,3b,4,10} As the temperature was lowered (Figures V-21 and S.V-5 left), the band at 450 nm is shifted to the higher energy region due to the decrease of the $Co^{II} \rightarrow Fe^{III}$ MMCT band (540 nm) in intensity. Concomitantly, a new broad absorption peak appears, assignable to the $Fe^{II} \rightarrow Co^{III}$ MMCT band at 760 nm.^{2a,3b,4,11} The spectral changes confirmed that solutions of **7** and **8** exhibit a thermally induced ET associated with $\{Fe^{III}_2Co^{II}_2\} \rightarrow \{Fe^{II}_2Co^{III}_2\}$ conversion upon cooling. The temperature dependence of the absorption spectra (Figures V-21 and S.V-5) showed an isosbestic point around 603 – 608 nm (depending on the employed solvent) suggesting that only two species are involved in the thermal inter-conversion process.

Table V-3. Thermodynamic parameters obtained from the ideal solution model⁹ fit of the UV-Vis data for **7** and **8** in different solvents.

	(7)			(8)		
	ΔH , kJ·mol ⁻¹	$T_{1/2}$, K	ΔS , J·K ⁻¹ ·mol ⁻¹	ΔH , kJ·mol ⁻¹	$T_{1/2}$, K	ΔS , J·K ⁻¹ ·mol ⁻¹
Methanol	53.3	247.7	215.2	-	-	-
Butyronitrile	-	-	-	56.6	219.9	257.3
Dichloromethane	72.5	210.0	345.2	-	-	-

The temperature dependence of the $\{Fe^{III}_{LS}(\mu-CN)Co^{II}_{HS}\}$ and $\{Fe^{II}_{LS}(\mu-CN)Co^{III}_{LS}\}$ fractions was deduced from the thermal variation of the 540 and 760 nm absorptions, respectively (Figures V-21 right and S.V-5 right). As expected, the two fractions cross each other at 0.5 defining the $T_{1/2}$ temperature for which equal quantities of $\{Fe^{III}_{LS}(\mu-CN)Co^{II}_{HS}\}$ and $\{Fe^{II}_{LS}(\mu-CN)Co^{III}_{LS}\}$ species are present. This result also confirms the presence in solution of only two species ($\{Fe^{III}_{LS}(\mu-CN)Co^{II}_{HS}\}$ and $\{Fe^{II}_{LS}(\mu-CN)Co^{III}_{LS}\}$), due to the thermally induced ET. Therefore, the temperature dependence of paramagnetic and diamagnetic fractions (Figures V-21 right and S.V-5 right) was fitted with the ideal solution model (see Eq. IV.1 from Section IV.3.1) for an equilibrium between two different states.⁹ An excellent theory/experiment agreement is observed with this simple model (Figures V-21 and S.V-5) and the deduced ΔH , $T_{1/2}$, and ΔS are summarized in Table V-3.

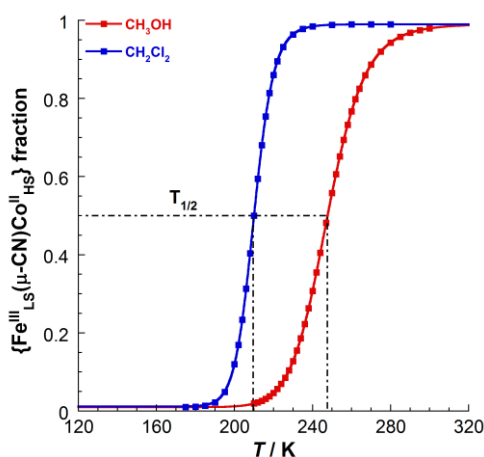


Figure V-22. Temperature dependence of the $\{Fe^{III}_{LS}(\mu-CN)Co^{II}_{HS}\}$ fraction estimated from the absorption intensities at the MMCT band (≈ 540 nm) for **7** in CH_2Cl_2 and CH_3OH . Solid lines are the fits to the ideal solution model.⁹

The estimated thermodynamic parameters have values close to those deduced for complexes **2**,⁴ **5**, and **6**^{4b} (see also Chapter IV, $\Delta H \sim 50 - 75 \text{ kJ}\cdot\text{mol}^{-1}$ and $\Delta S \sim 190 - 350 \text{ J}\cdot\text{K}^{-1}\cdot\text{mol}^{-1}$). Both the enthalpy and the entropy are changing with employed solvents, but no certain solvent polarity dependence could be observed, except for the characteristic temperature, $T_{1/2}$. Both parameters are more than two times greater than the ones reported in solid state,^{1,4,10a} suggesting that the relatively large values might be caused by the reorganization of solvent molecules or any other solvent effect upon electron transfer.

In spite of the fact that the temperature dependence of the absorption spectra was collected only in a few solvents, the obtained results allowed to prove the occurrence of the thermally induced ET in solutions of **7** and **8**. In solid state, the paramagnetic (red) state of complex **7** was stabilized without any evidence of ET. Moreover, the ET characteristic temperature is modified as a function of the employed solvent (Figure V-22), as already discussed for complexes **2**,⁴ **5**, and **6**^{4b} (see also Chapter IV). In fact, the methanol and dichloromethane were chosen for the quantitative investigations of the optical properties in solution because previous studies of **2**,⁴ **5**, and **6**^{4b} (see also Chapter IV) showed that the largest difference between the ET characteristic temperatures were obtained for these solvents due to a large difference between their polarities.

Another important observation was made in the case of compound **8**. Its solvates **8a** and **8b** have a completely different behavior in solid state. The green color of the crystals of **8a** at room temperature, as well as the magnetic susceptibility measurements confirm that the diamagnetic state is stabilized in solid state. On the other hand, during the solubilization, the green crystals afford a red solution that exhibits ET and thermochromism only after cooling with liquid nitrogen. The crystals of **8b** exhibit a thermally induced ET between 200 and 290 K in a two-step fashion via an intermediate state most probably composed of a 1:1 mixture of $\{Fe^{II}_2Co^{III}_2\}$ and $\{Fe^{III}_2Co^{II}_2\}$ complexes at 250 K. No obvious evidences of an intermediate state were observed in solution due to absence of the crystal lattice packing constraints.

V.3.2. Magnetic properties of **7** and **8** in solutions

From the magnetic susceptibility measurements, additional evidences in support of an intramolecular ET in solutions of **7** and **8** were obtained (Figures V-23 and S.V-7). The magnetic susceptibility measurements were carried in dichloromethane for both compounds, in methanol **7**, and in butyronitrile for **8** at concentrations of $6.6 - 10.4 \cdot 10^{-4} \text{ mol/L}$ until the freezing point of the employed solvents. These solvents and concentrations were chosen to avoid any precipitation of the solid during the cooling or freezing of the solvent.

At high temperatures, both complexes showed practically the same χT product around $6.6 \text{ cm}^3\cdot\text{K/mol}$, that is in agreement with the presence of paramagnetic $\{Fe^{III}_2Co^{II}_2\}$ complexes, and is similar to the χT values measured for **2**,⁴ **5**, and **6**^{4b} (see also Chapter IV). With decreasing temperature, the χT product rapidly decreases to small values (0.2 to $0.3 \text{ cm}^3\cdot\text{K/mol}$, Figure V-23), consistent with the observed change of color and with the presence of diamagnetic $\{Fe^{II}_2Co^{III}_2\}$ complexes as the majority species in solution. On heating back, the measured χT product values traced the profile obtained in cooling mode (with the same sweep rate of 0.4 K/min , Figure S.V-7). The same value of the χT product at higher temperatures for both complexes,

may suggest that in solutions the tetranuclear cores adopt a similar structural geometry and there are no intermolecular interactions as in the solid state.

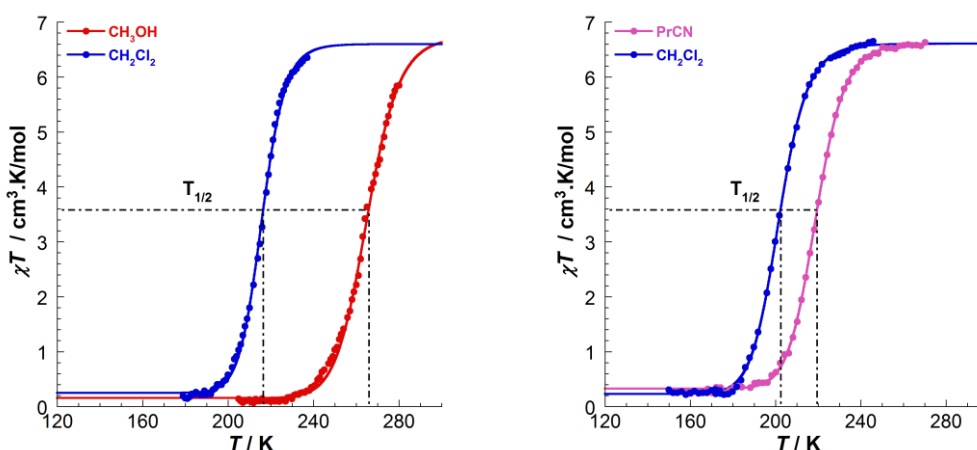


Figure V-23. χT vs T data for the solutions of **7** in methanol and dichloromethane (left) and **8** in dichloromethane and butyronitrile (right), 0.4 K/min on cooling, 1 T, solid lines are fits to the ideal solution model.⁹

Table V-4. Thermodynamic parameters obtained from the ideal solution model⁹ fit of the magnetic data for **7** and **8** in different solvents.

	(7)			(8)		
	ΔH , kJ·mol ⁻¹	$T_{1/2}$, K	ΔS , J·K ⁻¹ ·mol ⁻¹	ΔH , kJ·mol ⁻¹	$T_{1/2}$, K	ΔS , J·K ⁻¹ ·mol ⁻¹
Methanol	60.3	263.7	228.7	-	-	-
Butyronitrile	-	-	-	59.2	218.9	270.3
Dichloromethane	75.0	215.9	347.4	50.9	201.6	252.7

The χT vs T data (Figure V-23) for **7** and **8** are also in good agreement with the ideal solution model (see Eq. IV.1 Chapter IV, where X is the χT product, X_{LT} and X_{HT} are χT values at low and at high temperatures, respectively).⁹ Estimated thermodynamic parameters ΔH , $T_{1/2}$, and ΔS are summarized in Table V-4. The thermodynamic parameters have values slightly different from those obtained from optical measurements (Table V-3). These differences, especially between $T_{1/2}$ values determined spectrophotometrically and from magnetic measurements, are attributed to differences in the experimental set-ups and to the difficulty of accurately determine the temperature during the UV/Vis studies (the temperature measurement is not directly close to the sample). But as already observed by UV-Vis absorption spectroscopy, the electron-transfer process is strongly influenced by the solvent nature. The characteristic temperatures ($T_{1/2}$) observed from magnetic studies follow the same solvent polarity dependence as the ones determined from the absorption spectra. Moreover the observed trend is basically the same as the one observed for compounds **2**,⁴ **5**, and **6**^{4b} (see also Chapter IV) suggesting that thermally induced ET is an intrinsic property of the $\{[(Tp^*)Fe(CN)_3]_2[Co(diRbpy)_2]_2\}^{2+}$ systems that can be easily observed in solutions due to the absence of the crystal lattice packing constraints or strong intermolecular interactions.

Compounds **7** and **8** differ only by the counter-anions (OTf⁻ in **7** and PF₆⁻ in **8**); therefore it was surprising to observe that their solutions in the same solvent (i.e. dichloromethane) show a difference of ca. 14 K between the characteristic temperatures (Table V-4). On the other hand, the nature of the counter-anion has a significant influence on the solubility (**7** is soluble in methanol, while **8** is not), on the dissociation

equilibrium and, thus, on the interactions of the cationic core with solvent molecules. So, it is possible to preliminarily conclude that counter-anions influence the occurrence of ET in cyanido-bridged molecular squares not only in solid state (see Chapter III), but also in solutions.

The functionalization of the bipyridine ligands on Co sites with strongly donating methoxy groups showed an important increase of the ET characteristic temperature. The donating effect of the methoxy groups is observed very well in dichloromethane, when the magnetic susceptibility plots are compared for **2** ($T_{1/2} = 186$ K), **5** ($T_{1/2} = 191$ K), **6** ($T_{1/2} = 196$ K) and **7** ($T_{1/2} = 216$ K) (Figure V-24, compound **7** was chosen for comparison because it has the same counter-anion (OTf^-) as **2**, **5**, and **6**).

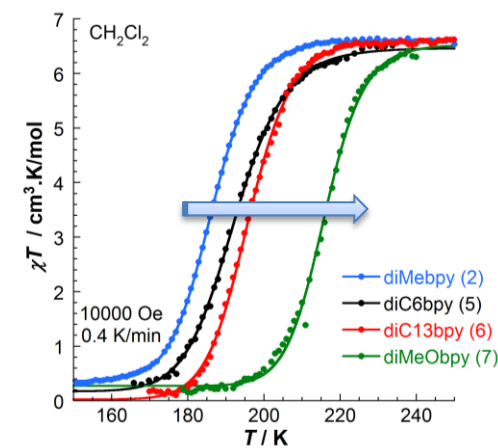


Figure V-24. Comparison between χT vs T data for complexes **2**, **5**, **6** and **7** in dichloromethane, the solid line are fits to the ideal solution model.⁹

The comparison of the χT vs T plots in methanol solutions shows a slightly different behavior, the $T_{1/2}$ value for **7** (264 K) is higher than the ones measured for **2** and **5** (213 and 253 K respectively), but it is about 5 K lower than the one measured for **6** (269 K). The observed behavior can be explained by the fact that on cooling methanol solutions of **6**, the ET occurs in the same time with the precipitation/crystallization of the sample (Figure S.IV–6 right top) that can have influence on the thermodynamic parameters. On the other hand, the observed difference may be explained by the fact that the nature of the ligand functionalization and the solvent's nature (or polarity) are likely not the only parameters that influence the ET properties of cyanido-bridged $\{Fe_2Co_2\}$ squares in solution.

V.4. Conclusions and perspectives

Three new tetranuclear cyanido-bridged $\{Fe_2Co_2\}$ complexes functionalized with methoxy (MeO) groups in 4- and 4'- positions of the bpy ligand on the Co sites were synthesized and their properties were investigated both in solid state and in solution, by structural, spectroscopic and magnetic methods.

The correlation between the structure and the properties of compounds **7**, **8a** and **8b**, observed in solid state, have showed that the functionalization of the cyanido-bridged $\{[(Tp^*)Fe(CN)_3]_2[Co(bpy)_2]_2\}^{2+}$ system with electron donating methoxy groups influences significantly the optical and magnetic properties of the final compound. With the ligands remaining the same across the three compounds, it was possible to stabilize the cyanido-bridged $\{[(Tp^*)Fe(CN)_3]_2[Co(diMeObpy)_2]_2\}^{2+}$ core in various electronic states.

Compound **7** that has a different counter-anion (OTf) and was crystallized under different conditions from the ones employed for **8a** and **8b**, exhibits no ET and is stabilized in its paramagnetic $\{Fe^{III}_2Co^{II}_2\}$ state. Compound **8a** is stabilized in its diamagnetic $\{Fe^{II}_2Co^{III}_2\}$ state that shows no thermally-induced ET between 2 and 300 K, as confirmed by the green color of the crystals at room temperature and the magnetic susceptibility measurements. Optical reflectivity and magnetic measurements of **8a** supported by the photo-crystallographic investigations demonstrated the occurrence of the photo-induced ET associated with a conversion between the diamagnetic $\{Fe^{II}_2Co^{III}_2\}$ and paramagnetic $\{Fe^{III}_2Co^{II}_2\}$ states at low temperatures. Compound **8b** that differs from **8a** only by the solvation inside the crystal lattice exhibits both thermally- and light-induced ET. Magnetic measurements of **8b** showed the occurrence of thermally-induced ET in a two-step fashion via a possible intermediate state that is, most, likely composed of a 1:1 molar mixture of diamagnetic and paramagnetic complexes, as already reported for another cyanido-bridged $\{Fe_2Co_2\}$ molecular square.³

The compared crystallographic data for **7**, **8a** and **8b** presented in Table V-1, showed that the cationic $\{Fe^{III}_2Co^{II}_2\}$ core in **7** is significantly more distorted than the one observed in **8b** at 298 K, with the same electronic configuration on metal centers. The presence of trifluoromethanesulfonate anions and co-crystallized DMF molecules in the crystal packing of **7** strongly influence the geometrical shape of the tetranuclear core and contribute to the stabilization of the paramagnetic $\{Fe^{III}_2Co^{II}_2\}$ state. Both **8a** and **8b** complexes show very similar structures at low temperatures (at 120 and 90 K, respectively. See Table V-1), but only the compound **8b** exhibits thermally induced ET, while **8a** is stabilized in its diamagnetic $\{Fe^{II}_2Co^{III}_2\}$ state, likely due to the H-bonded water molecules. Thus, structural perturbations inside the crystal packing such as the change of the molecular shape and weaker/stronger intermolecular interactions induced by anion exchange can either facilitate or inhibit the intramolecular ET in cyanido-bridged $\{Fe_2Co_2\}$ molecular squares.

Additional optical reflectivity measurements employing different light wavelengths revealed that the diamagnetic $\{Fe^{II}_2Co^{III}_2\}$ state in **8a** and **8b** can be converted into the paramagnetic $\{Fe^{III}_2Co^{II}_2\}$ one by a photo-induced ET using 1050 to 365 nm irradiation wavelengths (with an optimal wavelength of 940 nm, and the least efficient one of 505 nm). Successive light irradiations with 940 nm and 505 nm LED sources proved the possibility of a photo-reversible $\{Fe^{II}_2Co^{III}_2\} \leftrightarrow \{Fe^{III}_2Co^{II}_2\}$ conversion at the surface of **8b**. To confirm the occurrence of the photo-reversible ET in this compound, it will be necessary to perform additional photo-magnetic investigations.

The studies performed in solutions revealed that functionalized squares **7** and **8** (**8a** and **8b** are different solvates of the same system, $\{[(Tp^*)Fe(CN)_3]_2[Co(diMeObpy)_2]_2\}(PF_6)_2$, and were referred as **8** in solution studies) undergo thermally-induced intramolecular ET and, thus, exhibit switching of magnetic and optical properties in diluted solutions. In spite of the fact that the magnetic and optical characterizations were performed only in a few solvents, the obtained results revealed additional information about the occurrence of thermally induced ET in solutions of $\{Fe_2Co_2\}$ molecular squares. It was observed that the ET characteristic temperatures in the same solvent (i.e. dichloromethane) show a difference of ca. 14 K for compounds **7** and **8** that differ only by the counter-anions (OTf in **7** and PF_6^- in **8**). This result highlights the

important role played by the counter-anions in the modulation of ET properties in cyanido-bridged molecular squares not only in solid state (see Chapter III), but also more surprisingly in solutions. The characteristic temperatures ($T_{1/2}$) observed from the magnetic and optical studies of **7** and **8** in solutions follow the same trend as the one observed for compounds **2**,⁴ **5**, and **6**^{4b} (see also Chapter IV) suggesting that thermally induced ET is an intrinsic property of the $\{[(Tp^*)Fe(CN)_3]_2[Co(diRbpy)_2]_2\}^{2+}$ systems that can be easily observed in solutions due to the absence of the crystal lattice packing constraints or the strong intermolecular interactions.

Functionalization with donating methoxy groups shows the possibility to increase the ET characteristic temperature in solid state, if compared with compounds **1** and **2**, and in solutions if compared with compounds **2**, **5**, and **6**. But it is important to point out that in solid state, the desired effect was achieved in combination with several other parameters (counter-anion, co-crystallized solvents, weaker or stronger intermolecular interactions) that influence also the ET properties of the cyanido-bridged $\{Fe_2Co_2\}$ molecular squares.

The functionalization of these remarkable systems should be continued in many ways. The promising direction is to choose a functionalization of the bpy ligand with even stronger electron density donating groups like the dimethylamino group, $-N(CH_3)_2$. On the other hand, it would be worth modulating also the functional groups on the capping ligand of the Fe site. It is for example possible to introduce additional donating methyl groups by exchanging the tris(3,5-dimethylpyrazol-1-yl)hydroborate (Tp^*) ligand with tris(3,4,5-trimethylpyrazol-1-yl)hydroborate that can help reducing the difference between the redox potentials of the Fe and Co ions.

Finally, it is worth noting that although the $\{Fe_2Co_2\}$ square complexes at the present time remain the simplest reported molecular analogs of the more sophisticated FeCo PBAs, they still raise many difficult questions regarding: the coupling between Fe and Co spin carriers in the photo-induced state; and the way ET occurs inside the tetranuclear core (does it occur in both pairs simultaneously or preferentially occurs through one Fe–CN–Co edge). Therefore our current efforts are being devoted to the study of the electronic states involved in the thermal and photo-switching using X-ray absorption spectroscopy (XAS), X-ray magnetic circular dichroism (XMCD) and ultra-fast time-resolved optical spectroscopy experiments (see next Section V.5 for preliminary results).

V.5. Preliminary XAS and XMCD investigations

X-ray absorption spectroscopy (XAS) and X-ray magnetic circular dichroism (XMCD) investigations were carried out at ID12 beamline of ESRF synchrotron (Grenoble, France) in collaboration with Marie-Anne Arrio (IMPMC), Philippe Sainctavit (IMPMC), Andrei Rogalev (ESRF) and Fabrice Wilhelm (ESRF).

XAS is an element and orbital selective spectroscopic tool for geometric and electronic structure elucidation.¹² XMCD is a difference spectrum of two x-ray absorption spectra (XAS) taken in a magnetic field, one taken with left circularly polarized x-rays, and one with right circularly polarized ones.¹² By closely analyzing the difference in the XMCD spectra, information can be obtained on the magnetic properties of the atom, such as its spin, orbital magnetic moment and relative orientations of the neighboring magnetic moments.^{12,13}

Recently, XAS and XMCD investigations were reported for a 1D $\{FeCo\}_n$ coordination polymer (XAS and XMCD at L edges)¹⁴ and a cyanido-bridged molecular $\{Fe_2Co_2\}$ square (XAS at K edges)¹⁵ that exhibit thermally and light-induced ET. In both cases only the changes in electronic states associated with thermally induced ET were investigated. No XAS and XMCD investigations of the metastable light-induced paramagnetic state have been reported previously.

The X-ray absorption near-edge spectra (XANES, that is a type of X-ray absorption) and the dichroic signals (XMCD) at the K edges of cobalt and iron ions for the compound **8b** were recorded and investigated with the following aims: (a) to observe the thermally and photo-induced ET in the molecular cyanido-bridged $\{Fe_2Co_2\}$ square PBAs using these techniques; (b) to determine/confirm the spin and oxidation numbers of the Co and Fe ions in the different states; and (c) to determine the exact nature of the magnetic coupling between Fe and Co ions in the metastable light-induced paramagnetic state. The investigation of the photo-induced state is particularly interesting because macroscopic investigations of molecular cyanido-bridged $\{Fe_2Co_2\}$ squares suggest the presence of ferromagnetic interactions between Co^{II} HS and Fe^{III} LS ions.¹⁴ Whereas previous reports on XMCD measurements at the Co and Fe K edges of the 3D Co/Fe PBAs have shown an antiferromagnetic coupling between Co^{II} HS and Fe^{III} LS ions and offered experimental evidence of the ferrimagnetic nature of the photo-induced metastable state in these 3D materials.¹⁸

As has been mentioned in the previous paragraphs of this chapter, the loss of lattice solvent molecules influences significantly the occurrence of the ET in cyanido-bridged $\{Fe_2Co_2\}$ squares. XAS investigations require ultra-high vacuum conditions. In order to avoid the solvent loss during XAS and XMCD studies the analyzed sample was kept in its mother liquor solution and covered with Kapton film.

XAS spectra at Co and Fe K-edges were recorded for crystals of **8b** to confirm the changes in the electronic state of the metal ions upon thermally induced ET (Figure V-25). In the cobalt K edge absorption spectrum of **8b** at 298 K (Figure V-25 left), the energies of the absorption maximum at 7727 eV (allowed $1s (a_{1g}) \rightarrow 4p (t_{1u})$ transition) and a weak pre-edge at 7712 eV (forbidden $1s (a_{1g}) \rightarrow 3d (t_{2g}, e_g)$ transition) at 298 K indicate the presence of Co^{II} ions.¹⁶ At 2 K, the Co K edge maximum is shifted by 3 eV to higher energy (7730 eV) compared to that at 298 K and fits the energy of the absorption maximum of Co^{III} ions.^{16,17} The high-energy shift of the EXAFS (extended X-ray absorption fine structure) oscillations observed above

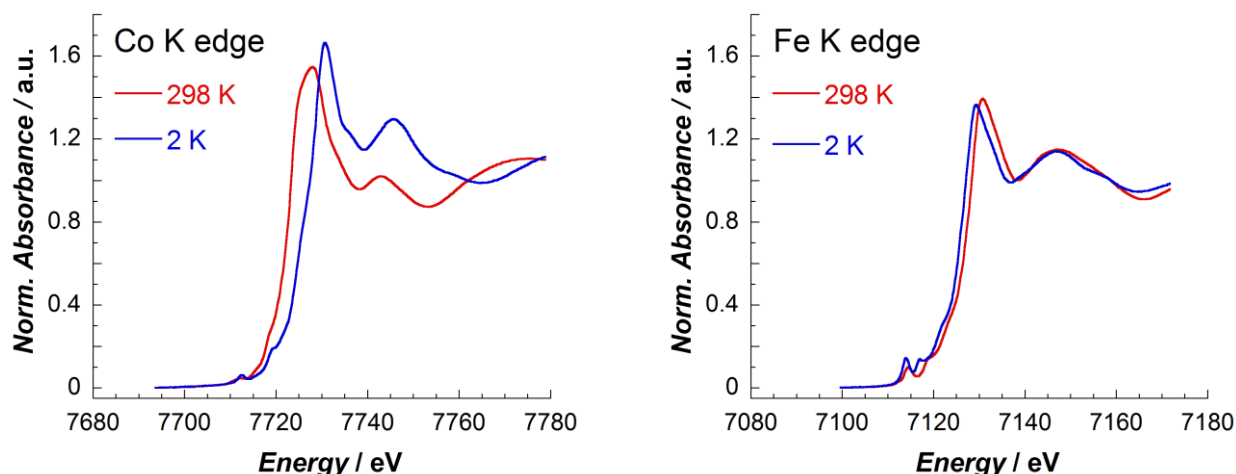


Figure V-25. XANES at Co (left) and Fe (right) K edges at 298 K (red) and 2 K (blue) for **8b**.

7740 eV clearly demonstrates the presence of shorter Co^{III} -to-ligand bonds in **8b** at 2 K (as observed from temperature dependent crystallographic investigations of **8b**, Table V-1, and reported for EXAFS oscillations in 3D Fe/Co PBAs).¹⁸ The iron K edge spectra of **8b** exhibit weaker changes upon thermally induced ET (Figure V-25 right).¹⁶⁻¹⁸ The absorption maximum shifts from 7131 eV at 298 K to 7130 eV at 2 K. These weak changes are not surprising, given the similarity of the spin state (LS) and crystallographic data for the Fe coordination sphere obtained at 298 and 90 K for single crystals of **8b** (Table V-1). The energy of the K edge absorption maximum (7131 eV) at 298 K indicates that the oxidation state of the iron ions is +3.¹⁸ Moreover, the XAS analysis of the Fe^{III} precursor, $(NEt_4)[Fe^{III}(Tp^*)(CN)_3]$, showed the maximum absorption at the same energy value at 2 K (Figure S.V-8) suggesting that the maximum of absorption observed at 2 K for **8b** (7130 eV) is corresponding to the expected Fe^{II} LS ions.

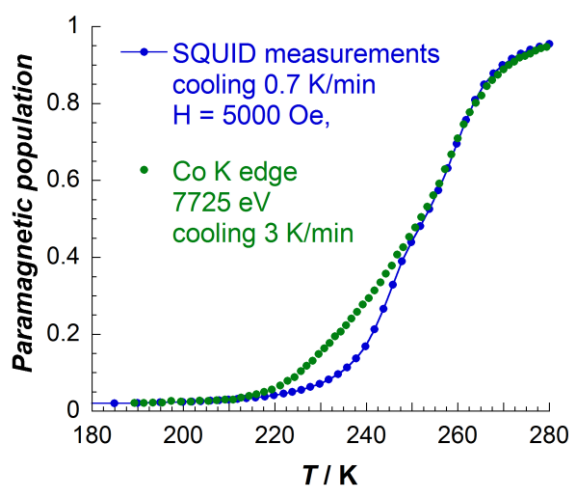


Figure V-26. Temperature dependence of the paramagnetic fractions estimated from the absorption intensities at 7725 eV in the Co K edge (green curve) and from the magnetic susceptibility measurements (blue curve) for **8b**.

The most prominent changes in the Co K edge were observed at the energy of 7725 eV. Therefore the electron transfer phenomenon was also followed as a function of temperature by XANES at this Co K edge energy. The temperature dependence of the paramagnetic $\{Fe^{III}_{LS}(\mu-CN)Co^{II}_{HS}\}$ fractions can be deduced from the thermal variation of the absorption at 7725 eV (Figure V-26). As expected, the obtained XANES

data correlates very well with the data obtained from the magnetic susceptibility measurements (Figure V-26).

After 18 h of excitation with a white light source at 2 K a photo-conversion from diamagnetic to paramagnetic state was observed. XANES spectra on both Fe and Co K edges were gradually changing upon white light irradiation (Figure V-27) giving a clear evidence of a photo-conversion from the diamagnetic to paramagnetic state as the result of intramolecular metal-to-metal photo-induced ET.

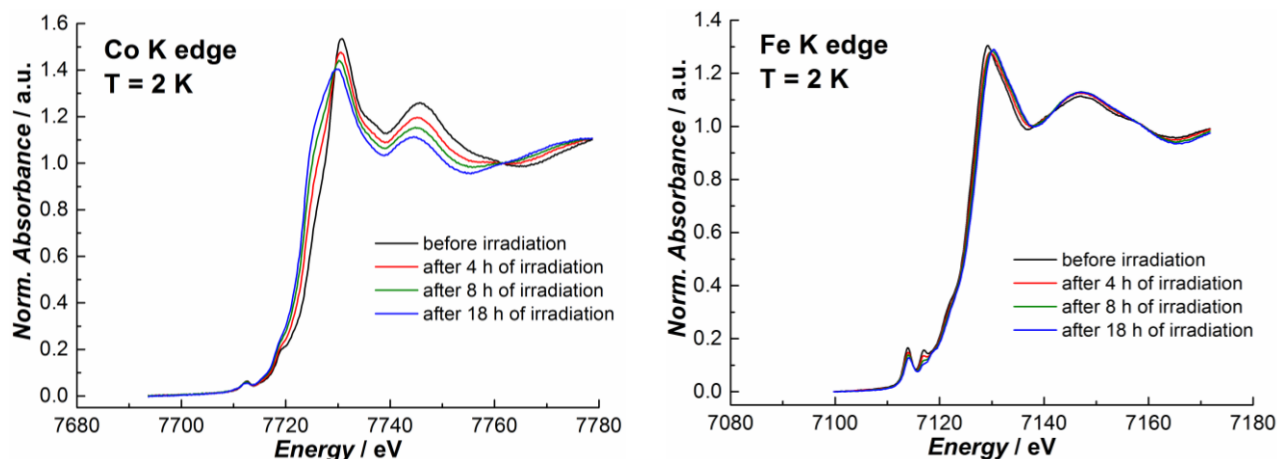


Figure V-27. Changes in XANES at the Co (left) and Fe (right) K edges upon irradiation of **8b** with white light at 2 K.

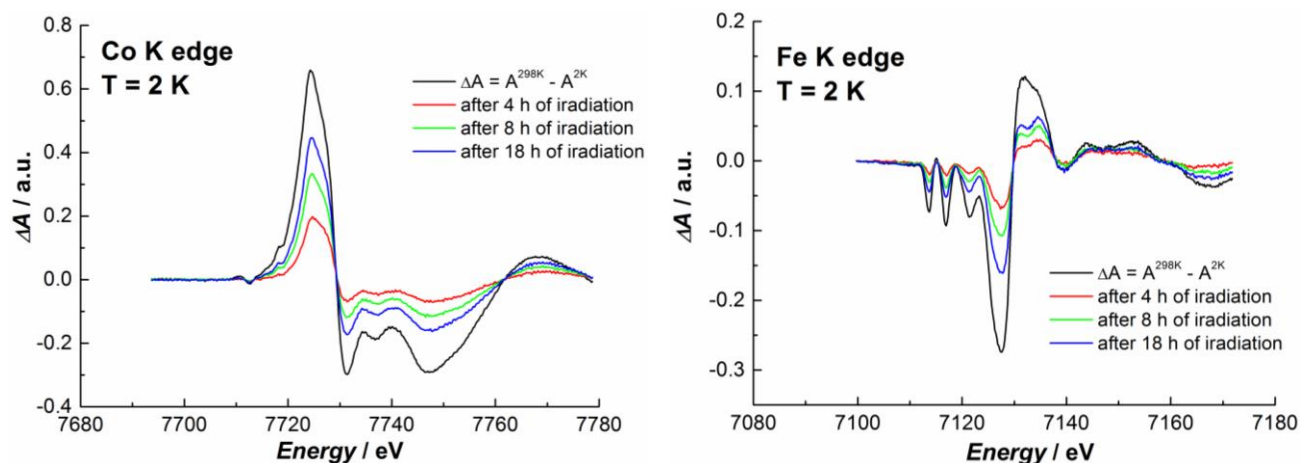


Figure V-28. Evolution of the difference between the room temperature (298 K) XANES and low temperature (2 K) XANES spectra for **8b** before and during white light irradiation at both Co (left) and Fe (right) K edges.

As it was expected significant changes upon photo-irradiation in the XANES spectra were observed at Co K-edge (Figure V-27 left). The absorption maximum on Co K edge shifts from 7730 eV towards lower energies while the absorption at 7725 eV decreases, suggesting conversion of Co^{III} LS ions into Co^{II} HS ions. Photo-induced changes are not that obvious on Fe K edge. For a better observation, the light induced changes were analyzed as the difference between the room temperature (298 K) XANES and low temperature (2 K) XANES spectra of **8b** before and during white light irradiation at both Co and Fe K edges (Figure V-28). This data allowed estimating that approximately 70 %, of the studied sample, were converted from diamagnetic to paramagnetic state during ~ 18 h of irradiation (the conversion ratio was determined by monitoring the intensity at 7725 and 7131 eV in the Co and Fe K edges, respectively). The bulk of the

sample was not fully photo-transformed probably due to the thickness of the sample and/or an insufficient penetration depth of the visible light. This problem is certainly in link with the position of the light source that was far away (60 cm) from the sample despite the use of a focalizing lens.

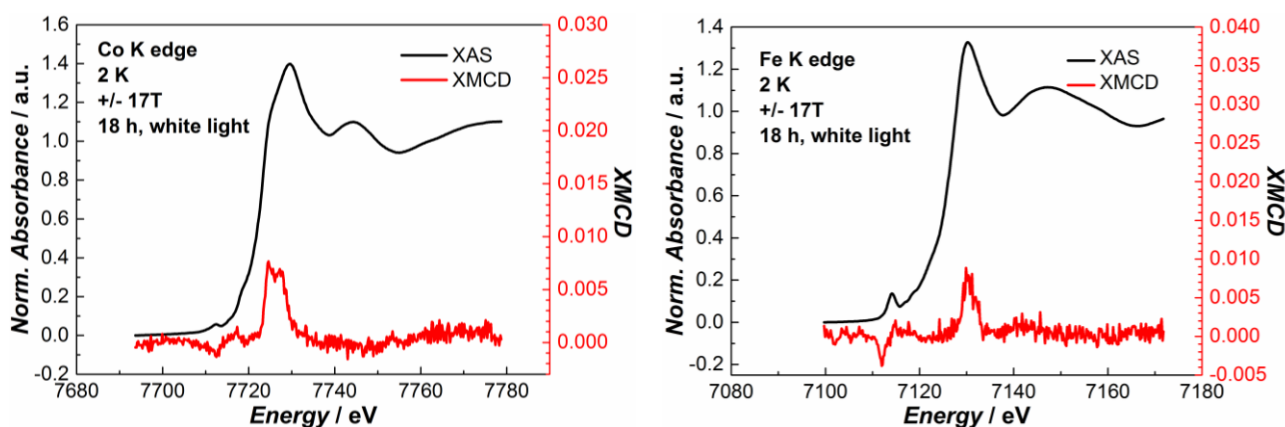


Figure V-29. Isotropic (average, black) and dichroic (XMCD, red) absorption spectra at Co (left) and Fe (right) K edges for **8b**.

Since the light-induced metastable state is paramagnetic, weak XMCD signals (see Annex for experimental details) were observed at Fe and Co K edges at 2 K upon white light irradiation (Figure V-29). As expected, no XMCD signal was observed for the diamagnetic state of **8b**. The intense signal observed in the XMCD spectra corresponds to the allowed transition to the p -symmetry levels of the metal ions (~ 7725 eV at the Co K edge, and ~ 7130 eV at the Fe K edge). The other negative and very weak peak may correspond to forbidden transitions to the d levels of metal ions (~ 7712 eV at the Co K edge, and ~ 7112 eV at the Fe K edge). The presence of a dichroic signal at the K edges is due to the presence of spin-orbit coupling in the metallic p levels in the excited states ($1s^1 3d^n 4p^1$ electronic configuration), and the exchange interaction of the p excited electrons with the $3d$ electrons. The small intensity of the signals ($\sim 0.7\%$ of the isotropic spectra at both edges corresponding to allowed $1s(a_{1g}) \rightarrow 4p(t_{1u})$ transitions) is due to the absence of spin-orbit coupling in the $1s$ level and the weakness of the spin-orbit coupling in the final state.^{18,19} Weak analogous XMCD signals at K edges were also reported previously for 3D networks of Fe/Co PBA.¹⁸ After the photo-excitation experiments, the reversibility of the thermally and photo-induced intramolecular ET was verified. The system recovered its initial state when it was warmed up to 300 K (Figure S.V-9).

For a vacuum dried sample of **8b**, the macroscopic magnetization data (Figure S.V-5 right) show no inflection point that may correspond to the presence of antiferromagnetic interactions between Fe^{III} and Co^{II} ions. Moreover, the temperature dependent magnetic susceptibility measurements for the same sample show a significant increase of the χT product at low temperatures (Figure V-19 left), suggesting a ferromagnetic coupling between the metal ions. Similar behavior in the magnetic susceptibility measurements have been observed for solvated sample of **8b** under white light irradiation at low temperatures (Figure V-20 right). These macroscopic observations find a local counterpart in the dichroic signals. At both Fe and Co K edges, the dichroic signals have the same sign (positive for intense peaks corresponds to the allowed transition to the p levels, and negative for the very weak signals of the forbidden transitions to the d levels). The same signs (or directions) of the XMCD signals from cobalt and iron sites can be *preliminary* considered as a local

characterization of the ferromagnetic coupling between cobalt and iron ions in the photo-induced metastable state of compound **8b**. To confirm these preliminary result and conclusions additional interpretations through theoretical calculations will be necessary.

Within the studies presented in this section, for the first time the photo-induced metastable state in a cyanido-bridged molecular {Fe₂Co₂} square was characterized using XAS and XMCD techniques. Moreover, direct experimental evidences of the ferromagnetic nature of photo-induced metastable state were obtained.

V.6. Supporting materials

V.6.1. Experimental protocols

Preparation of $\{[(Tp^*)Fe(CN)_3]_2[Co(diMeObpy)_2]_2\}[OTf]_2 \cdot 4DMF$ (7**).** $[NEt_4][(Tp^*)Fe(CN)_3] \cdot H_2O$ (165 mg, 0.3 mmol) was treated with $Co(OTf)_2$ (107 mg, 0.3 mmol) in 5 mL of wet DMF under argon to afford a red solution that was allowed to stir for 2 h. Subsequently, 130 mg (0.6 mmol) of 4,4'-dimethoxy-2,2'-bipyridine (diMeObpy) were added and the mixture was stirred for 1 hour and then filtered. Crystals of **7** suitable for X-ray diffraction were obtained by slow diffusion of diethyl ether in the DMF solution, the yield was 64 % (0.23 g). Elemental analysis – Calc. (Found) for $C_{98}H_{120}B_2Co_2F_6Fe_2N_{30}O_{18}S_2$ ($\{[(Tp^*)Fe(CN)_3]_2[Co(diMeObpy)_2]_2\}(OTf)_2 \cdot 4DMF$): C, 48.33 (48.19); H, 4.97 (5.03); N, 17.25 (17.39). Selected FT-IR data (ATR, cm^{-1}): 2928.3 (w), 2857.4 (w), 2532.7 (w), 2154.1 (m), 2121.7 (w), 1668.9 (vs), 1201.8 (s), 1033.9 (s).

Preparation of $\{[(Tp^*)Fe(CN)_3]_2[Co(diMeObpy)_2]_2\}[PF_6]_2 \cdot 2H_2O \cdot 5CH_3CN$ (8a**).** *Note: The solvents used in this synthetic protocol were used as received without further purification (i.e. drying).* The reaction of 107 mg (0.3 mmol) of $Co(OTf)_2$ dissolved in 45 mL of CH_3OH with 130 mg (0.6 mmol) of diMeObpy in 15 mL of CH_3OH gave a pale yellow solution. After stirring for 10 min, $(Et_4N)[(Tp^*)Fe(CN)_3]$ (165 mg, 0.3 mmol) in CH_3OH (5 mL) was added and followed by the addition of solid NBu_4PF_6 (233 mg, 0.3 mmol). The mixture was stirred for 1 h to give a dark red solution and green powder. The green powder was filtrated and dried in air. Dark green crystals of **8a** were obtained by slow diffusion of diethyl ether into the red solution resulting from the dissolution of the green powder in CH_3CN . The yield was 0.12 g (35 %). Selected FT-IR data (ATR, cm^{-1}): 2974.5 (w), 2931.5 (w), 2869.7 (w), 2534.9 (w), 2152.9 (m), 2122.2 (vw), 2097.8 (w), 2080.1 (w), 2066.1 (w), 844.0 (vs).

Preparation of $\{[(Tp^*)Fe(CN)_3]_2[Co(diMeObpy)_2]_2\}[PF_6]_2 \cdot 6CH_3CN$ (8b**).** The dark red crystals of **8b** can be obtained by following the protocol for **8a** and using the anhydrous CH_3OH . Thus, after the addition of NBu_4PF_6 , dark red powder is formed. The slow ether diffusion into the solution resulting from the dissolution of the red powder in CH_3CN , leads to dark red prismatic crystals of **8b** with the yield of 0.16 g (ca. 45 %). Selected FT-IR data (ATR, cm^{-1}): 2973.6 (w), 2929.8 (w), 2858.3 (w), 2534.0 (w), 2151.5 (m), 2119.0 (vw), 844.0 (vs).

V.6.2. Crystallographic data for 7, 8a and 8b

Table S.V-1. Crystallographic data for 7 at 90 K.

Temperature	90 K
Crystal color	dark red
Moiety formula	$C_{84}H_{92}B_2Co_2Fe_2N_{26}O_8, 2(CF_3O_3S), 4(C_3H_7NO)$
Empirical formula	$C_{98}H_{120}B_2Co_2Fe_2N_{32}O_{18}S_2$
Formula weight	2435.49
Crystal system	Triclinic
Space group	$P\bar{1}$
Wavelength, Å	0.71073
a, Å	13.687(3)
b, Å	16.247(4)
c, Å	27.611(6)
$\alpha, ^\circ$	87.698(11)
$\beta, ^\circ$	84.376(11)
$\gamma, ^\circ$	65.203(10)
V, Å ³	5547(2)
Z	2
$\rho_{\text{calcd}}, \text{g/cm}^3$	1.456
$\mu, \text{l/mm}$	0.676
Reflections collected	212115
Independent reflections	21322
R_1^a	0.1445
wR_2^a	0.3454
GoF ^a	1.193
^a $I > 2\sigma(I)$, $R_1 = \sum(F_o - F_c)/\sum F_o $, $wR_2 = \{\sum[w(F_o^2 - F_c^2)^2]/\sum[w(F_o^2)^2]\}^{1/2}$. GoF (goodness of fit on F^2) = $\{\sum[w(F_o^2 - F_c^2)^2]/(n-p)\}^{1/2}$, where n is the number of reflections and p is the total number of refined parameters.	

Table S.V-2. Selected bonds distances and angles in the crystal structure of 7 at 90 K.

Selected bond distances (Å)			
Co(1)-N(1)	2.073(8)	Co(2)-N(14)	2.069(9)
Co(1)-N(10)	2.134(9)	Co(2)-N(16)	2.102(8)
Co(1)-N(11)	2.158(8)	Co(2)-N(23)	2.148(9)
Co(1)-N(12)	2.131(9)	Co(2)-N(24)	2.134(9)
Co(1)-N(13)	2.139(9)	Co(2)-N(25)	2.136(9)
Co(1)-N(2)	2.107(9)	Co(2)-N(26)	2.146(9)
Fe(1)-C(1)	1.900(10)	Fe(2)-C(41)	1.910(10)
Fe(1)-C(2)	1.924(11)	Fe(2)-C(42)	1.926(11)
Fe(1)-C(3)	1.932(10)	Fe(2)-C(43)	1.921(11)
Fe(1)-N(4)	1.998(8)	Fe(2)-N(17)	1.997(8)
Fe(1)-N(6)	1.975(9)	Fe(2)-N(19)	2.014(9)
Fe(1)-N(8)	2.014(9)	Fe(2)-N(21)	1.974(9)
Selected bond angles (°)			
N(1)-Co(1)-N(2)	94.0(3)	N(14)-Co(2)-N(16)	93.9(3)
N(1)-Co(1)-N(12)	89.8(3)	N(14)-Co(2)-N(23)	92.7(3)
N(1)-Co(1)-N(10)	92.4(3)	N(14)-Co(2)-N(24)	90.0(3)
N(2)-Co(1)-N(10)	91.2(3)	N(14)-Co(2)-N(25)	92.2(3)
N(12)-Co(1)-N(10)	99.8(4)	N(16)-Co(2)-N(23)	92.4(3)
N(1)-Co(1)-N(13)	92.6(3)	N(16)-Co(2)-N(25)	91.1(3)
N(2)-Co(1)-N(13)	92.3(3)	N(16)-Co(2)-N(26)	84.6(3)
N(12)-Co(1)-N(13)	76.4(3)	N(24)-Co(2)-N(23)	76.4(3)
N(2)-Co(1)-N(11)	84.7(3)	N(24)-Co(2)-N(25)	99.7(4)
N(12)-Co(1)-N(11)	93.7(3)	N(24)-Co(2)-N(26)	93.7(3)
N(10)-Co(1)-N(11)	76.1(3)	N(25)-Co(2)-N(26)	76.1(3)
N(13)-Co(1)-N(11)	98.9(3)	N(26)-Co(2)-N(23)	99.0(3)
C(1)-Fe(1)-C(2)	85.8(4)	C(41)-Fe(2)-C(43)	85.5(4)
C(1)-Fe(1)-C(3)	85.0(4)	C(41)-Fe(2)-C(42)	84.8(4)
C(2)-Fe(1)-C(3)	90.6(5)	C(43)-Fe(2)-C(42)	90.9(5)
N(1)-C(1)-Fe(1)	174.4(9)	N(14)-C(41)-Fe(2)	175.5(9)
N(2)-C(2)-Fe(1)	176.4(9)	N(16)-C(43)-Fe(2)	176.8(9)
N(3)-C(3)-Fe(1)	178.8(10)	N(15)-C(42)-Fe(2)	179.5(12)
C(1)-N(1)-Co(1)	169.2(8)	C(41)-N(14)-Co(2)	168.5(8)
C(2)-N(2)-Co(1)	165.0(8)	C(43)-N(16)-Co(2)	165.5(8)

Table S.V-3. Crystallographic data for **8a** at various temperatures and for the different phases.

Temperature	120 K	10 K	10 K 808 nm
Crystal color	dark green	dark green	dark red
Moiety formula	$C_{84}H_{92}B_2Co_2Fe_2N_{26}O_8, 2(PF_6), 5(C_2H_3N), 2H_2O$		
Empirical formula	$C_{94}H_{111}B_2Co_2F_{12}Fe_2N_{31}O_{10}P_2$		
Formula weight	2376.20		
Crystal system	Monoclinic		
Space group	C 2/c		
Wavelength, Å	0.71073		
a, Å	32.134(5)	31.980(4)	31.933(3)
b, Å	21.044(5)	20.8190(10)	21.262(2)
c, Å	21.827(5)	21.593(2)	21.772(2)
β , °	129.099(5)	129.237(2)	129.010(10)
V, Å ³	11455(4)	11135.1(18)	11486.4(19)
Z	4		
ρ_{calcd} , g/cm ³	1.366	1.490	1.445
μ , 1/mm	0.646	0.691	0.670
Reflections collected	66310	38753	21001
Independent reflections	13139	11985	11369
R_1^a	0.0790	0.1213	0.1200
wR_2^a	0.2044	0.3580	0.3413
GoF ^d	1.174	1.042	0.960
Selected bond distances (Å)			
Co(1)-N(8)	1.898(4)	1.914(8)	2.068(11)
Co(1)-N(9)	1.902(4)	1.896(8)	2.070(11)
Co(1)-N(11)	1.933(4)	1.938(8)	2.095(11)
Co(1)-N(10)	1.935(4)	1.937(9)	2.110(9)
Co(1)-N(13)	1.939(4)	1.926(9)	2.110(8)
Co(1)-N(12)	1.945(4)	1.940(7)	2.155(9)
Fe(1)-C(1)	1.889(5)	1.880(10)	1.946(15)
Fe(1)-C(3)#1	1.890(5)	1.876(10)	1.921(14)
Fe(1)-C(2)	1.903(5)	1.904(12)	1.907(12)
Fe(1)-N(3)	2.042(4)	2.027(8)	1.993(9)
Fe(1)-N(1)	2.057(4)	2.055(8)	1.999(11)
Fe(1)-N(5)	2.069(4)	2.078(8)	2.038(10)
Co(1)-N(8)	1.898(4)	1.914(8)	2.068(11)
Co(1)-N(9)	1.902(4)	1.896(8)	2.070(11)
Co(1)-N(11)	1.933(4)	1.938(8)	2.095(11)
Co(1)-N(10)	1.935(4)	1.937(9)	2.110(9)
Selected bond angles (°)			
N(8)-Co(1)-N(9)	93.24(16)	92.9(3)	93.9(4)
N(9)-Co(1)-N(11)	92.05(16)	92.6(3)	93.1(4)
N(8)-Co(1)-N(10)	93.47(17)	93.5(4)	95.8(4)
N(9)-Co(1)-N(10)	87.77(16)	88.5(3)	91.1(4)
N(11)-Co(1)-N(10)	82.59(17)	82.6(4)	76.4(4)
N(8)-Co(1)-N(13)	89.03(16)	89.0(3)	90.9(4)
N(9)-Co(1)-N(13)	93.52(16)	92.8(3)	93.8(4)
N(11)-Co(1)-N(13)	94.78(16)	94.8(3)	96.3(4)
N(8)-Co(1)-N(12)	89.28(16)	89.4(3)	89.8(4)
N(11)-Co(1)-N(12)	85.71(16)	85.3(3)	84.5(4)
N(10)-Co(1)-N(12)	95.62(16)	95.4(3)	97.3(4)
N(13)-Co(1)-N(12)	82.97(16)	83.3(3)	77.4(4)
C(1)-Fe(1)-C(3)	87.91(19)	88.2(4)	84.8(5)
C(1)-Fe(1)-C(2)	86.61(19)	86.7(4)	84.3(4)
C(3)-Fe(1)-C(2)	87.7(2)	88.1(4)	85.9(5)
N(9)-C(1)-Fe(1)	174.1(4)	174.8(9)	177.3(10)
N(7)-C(2)-Fe(1)	177.1(5)	174.4(9)	175.1(12)
N(8)-C(3)-Fe(1)	175.9(4)	176.6(8)	177.5(9)
C(1)-N(9)-Co(1)	173.6(4)	174.2(8)	173.8(9)
C(3)-N(8)-Co(1)	175.6(4)	175.8(8)	177.9(9)

^a $I > 2\sigma(I)$, $R_1 = \sum(|F_o| - |F_c|)/\sum|F_o|$. $wR_2 = \{\sum[w(F_o^2 - F_c^2)^2]/\sum[w(F_o^2)^2]\}^{1/2}$. GoF (goodness of fit on F^2) = $\{\sum[w(F_o^2 - F_c^2)^2]/(n-p)\}^{1/2}$, where n is the number of reflections and p is the total number of refined parameters.

Table S.V-4. Crystallographic data for **8b** at various temperatures and for the different phases.

Temperature	298 K	90 K
Crystal color	dark red	dark red
Moiety formula	$C_{84}H_{92}B_2Co_2Fe_2N_{26}O_8, 2(PF_6), 6(C_2H_3N)$	
Empirical formula	$C_{96}H_{110}B_2Co_2F_{12}Fe_2N_{32}O_8P_2$	
Formula weight	2381.22	
Crystal system	Monoclinic	
Space group	P 21/c	
Wavelength, Å	0.71073	
a, Å	15.1202(7)	15.434(4)
b, Å	23.1984(10)	22.124(5)
c, Å	21.5742(7)	21.318(4)
β , °	131.615(2)	132.717(11)
V, Å ³	5657.6(4)	5348(2)
Z	2	
ρ_{calcd} , g/cm ³	1.350	1.451
μ , 1/mm	0.651	0.691
Reflections collected	195501	57861
Independent reflections	11332	10092
R_1^a	0.0755	0.0741
wR_2^a	0.2465	0.2163
GoF ^a	1.139	1.070
Selected bond distances (Å)		
Co(1)-N(1)	1.900(5)	2.113(4)
Co(1)-N(10)	1.916(5)	2.124(4)
Co(1)-N(11)	1.932(4)	2.168(4)
Co(1)-N(12)	1.941(4)	2.119(5)
Co(1)-N(13)	1.948(5)	2.142(4)
Co(1)-N(2)	1.905(4)	2.087(4)
Fe(1)-C(1)	1.881(6)	1.924(5)
Fe(1)-C(2)	1.891(5)	1.921(5)
Fe(1)-C(3)	1.926(6)	1.924(6)
Fe(1)-N(4)	2.050(4)	2.002(4)
Fe(1)-N(6)	2.042(4)	2.005(4)
Fe(1)-N(8)	2.033(4)	2.022(4)
Selected bond angles (°)		
N(1)-Co(1)-N(10)	90.53(18)	89.40(15)
N(1)-Co(1)-N(11)	90.03(18)	92.31(15)
N(1)-Co(1)-N(12)	93.75(18)	92.88(17)
N(1)-Co(1)-N(2)	93.23(18)	95.36(16)
N(10)-Co(1)-N(11)	82.92(19)	76.12(15)
N(10)-Co(1)-N(13)	93.11(18)	100.64(18)
N(11)-Co(1)-N(12)	95.99(18)	96.02(17)
N(11)-Co(1)-N(13)	86.00(18)	83.39(16)
N(12)-Co(1)-N(13)	82.55(18)	76.2(2)
N(2)-Co(1)-N(10)	93.54(18)	93.96(16)
N(2)-Co(1)-N(12)	87.30(18)	93.56(17)
N(2)-Co(1)-N(13)	91.00(18)	91.00(16)
C(1)-N(1)-Co(1)	177.0(4)	171.9(4)
C(2)-N(2)-Co(1)	173.6(4)	178.3(4)
C(1)-Fe(1)-C(2)	88.1(2)	85.08(19)
C(1)-Fe(1)-C(3)	86.7(2)	86.2(2)
C(2)-Fe(1)-C(3)	86.7(2)	85.9(2)
N(1)-C(1)-Fe(1)	175.2(4)	176.0(4)
N(2)-C(2)-Fe(1)	174.3(5)	177.6(4)
N(3)-C(3)-Fe(1)	174.8(5)	177.2(6)

^a $I > 2\sigma(I)$, $R_1 = \Sigma(|F_o| - |F_c|)/\Sigma|F_o|$, $wR_2 = \{\Sigma[w(F_o^2 - F_c^2)^2]/\Sigma[w(F_o^2)^2]\}^{1/2}$. GoF (goodness of fit on F^2) = $\{\Sigma[w(F_o^2 - F_c^2)^2]/(n-p)\}^{1/2}$, where n is the number of reflections and p is the total number of refined parameters.

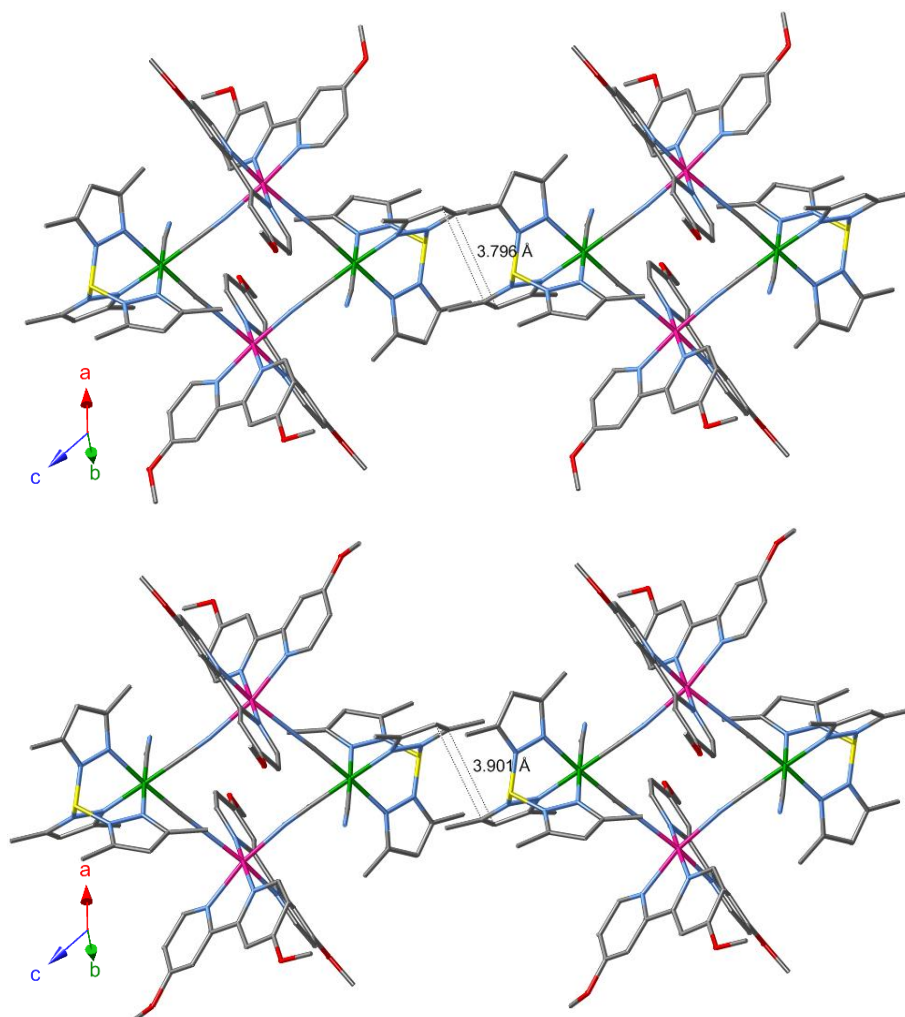


Figure S.V-1. Packing arrangement illustrating π - π interactions present between adjacent complexes in **8b** under different experimental conditions: at 90 K (top), at 298 K (bottom). All anions, lattice solvent and hydrogen atoms are eliminated for clarity.

V.6.3. Optical reflectivity studies

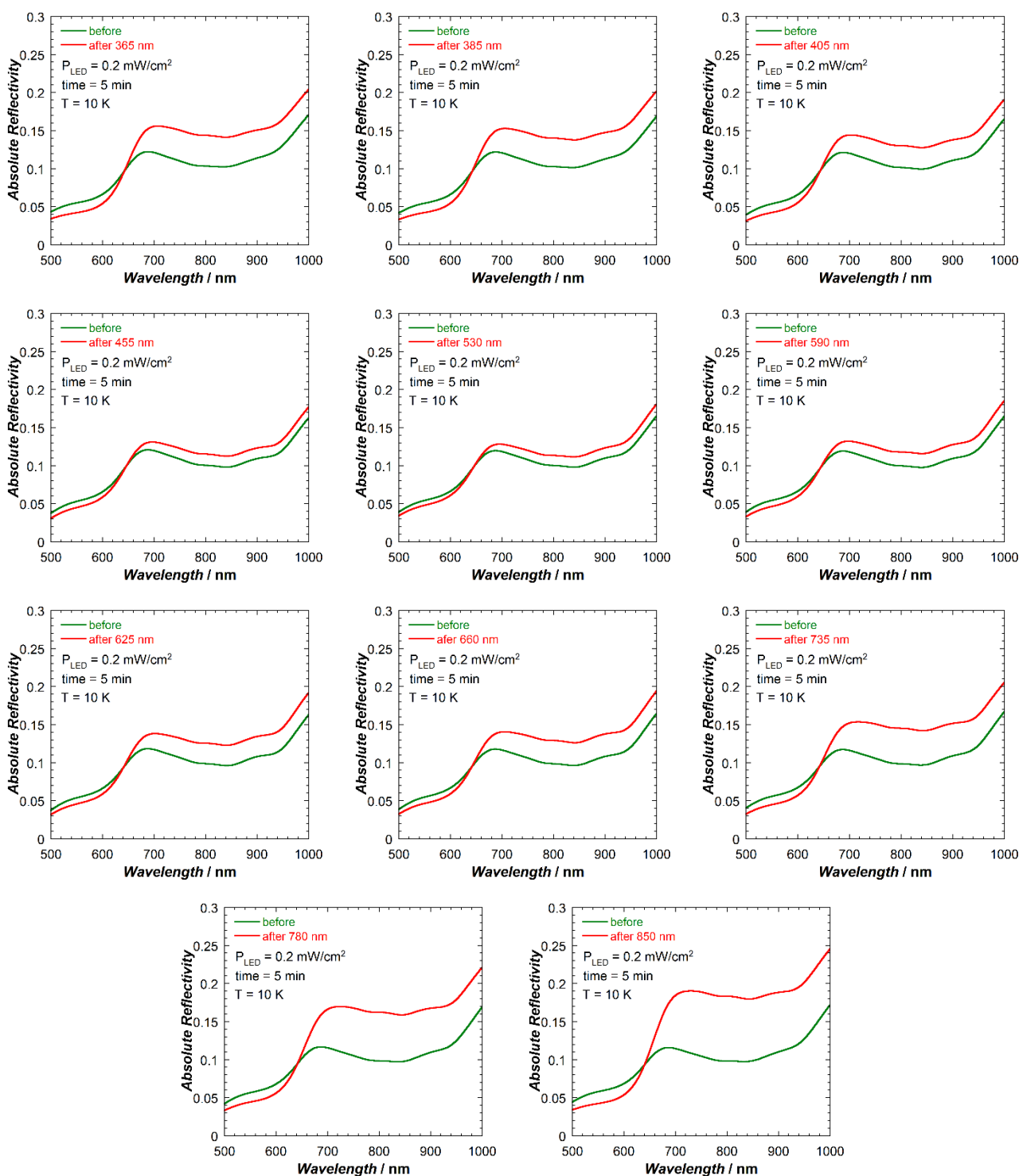


Figure S.V-2. Optical reflectivity spectra of **8a** at 10 K measured before (green) and after 5 min of irradiation (0.2 mW/cm^2) at different wavelengths delivered by 11 different LED sources.

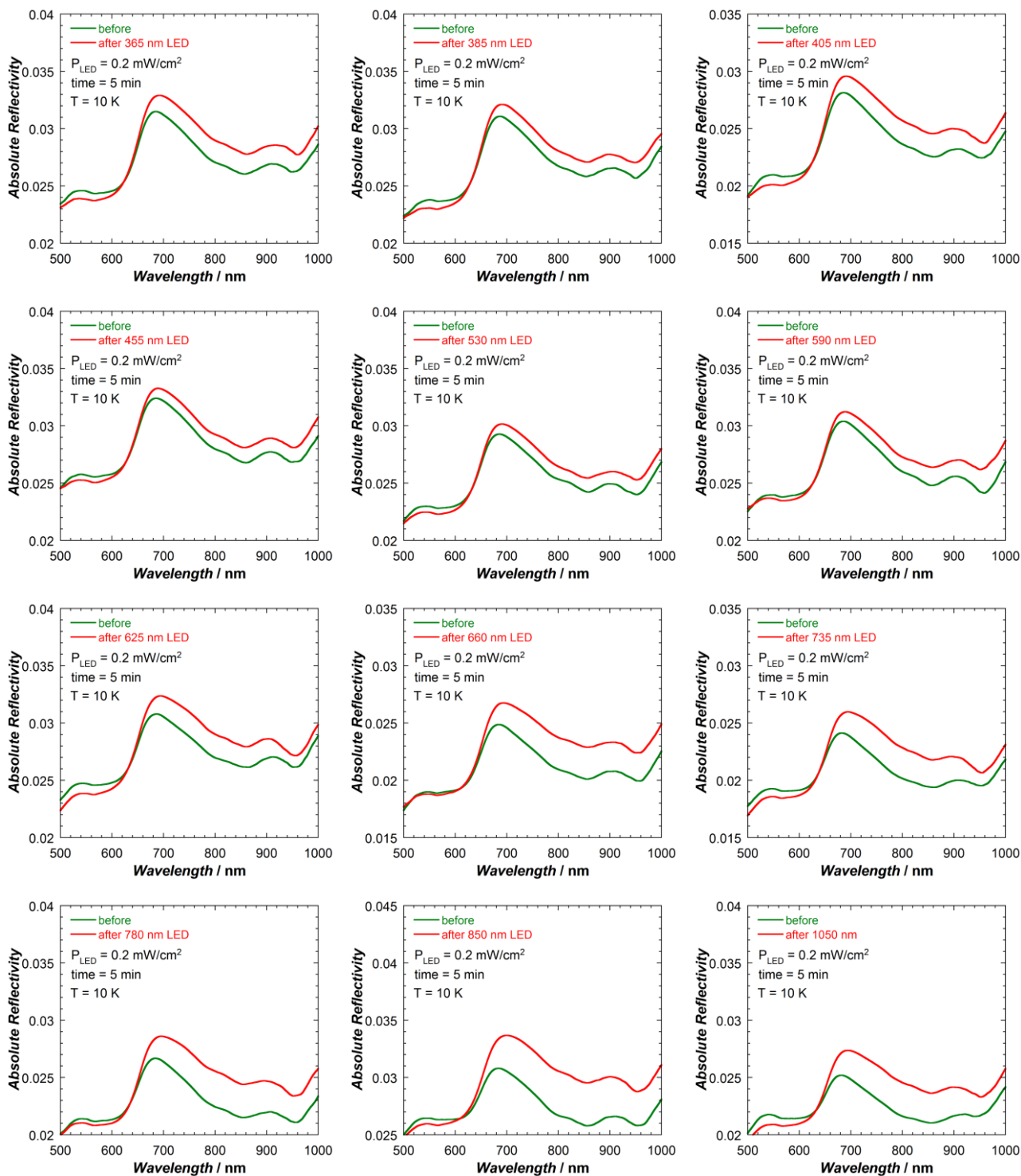


Figure S.V-3. Optical reflectivity spectra of **8b** at 10 K measured before (green) and after 5 min of irradiation (0.2 mW/cm^2) at different wavelengths delivered by 12 different LED sources.

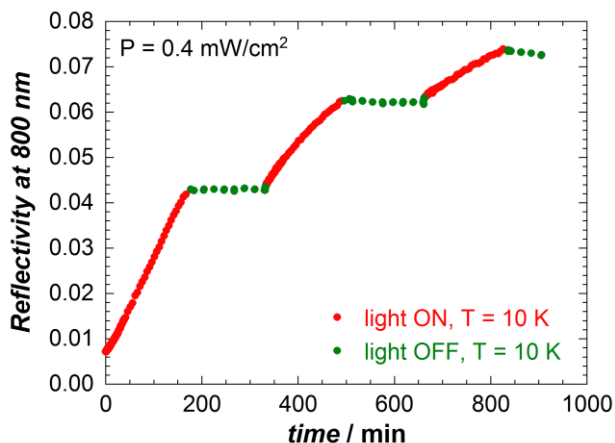


Figure S.V-4. Time evolution of R_{800} for **8b** during three successive cycles of 180 min irradiation with white light (0.4 mW/cm^2) by 160 min of no irradiation.

V.6.4. Magnetic properties in solid state

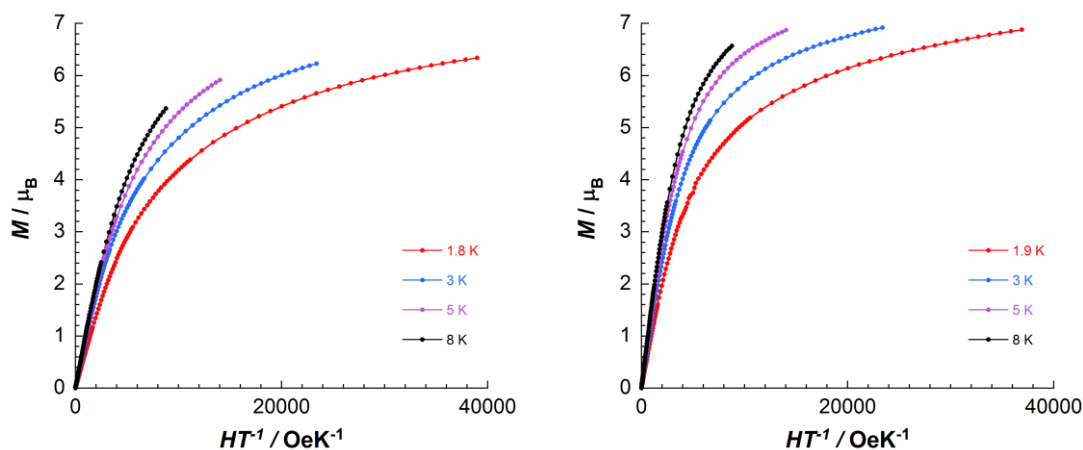


Figure S.V-5. Magnetization (M) versus H/T plots at different temperatures for **7** (left) and dried crystals of **8b** (right).

V.6.5. UV-Vis spectroscopic characterizations in diluted solutions

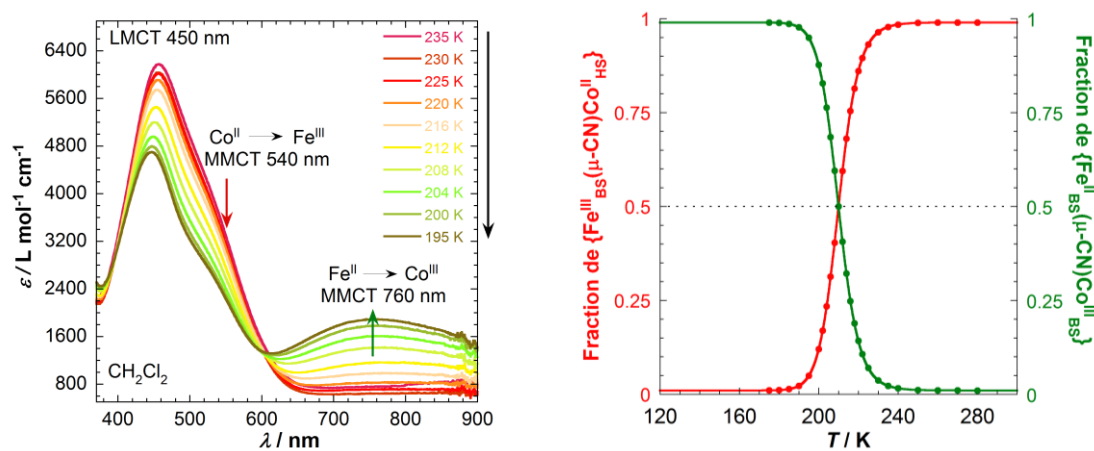


Figure S.V-6. (left) Selected UV-Vis spectra for **7** in CH_2Cl_2 on cooling mode from 235 K to 195 K (at 0.2 to 0.3 K/min). (right) Temperature dependence of the $\{\text{Fe}^{\text{III}}_{\text{LS}}(\mu\text{-CN})\text{Co}^{\text{II}}_{\text{HS}}\}$ and $\{\text{Fe}^{\text{II}}_{\text{LS}}(\mu\text{-CN})\text{Co}^{\text{III}}_{\text{LS}}\}$ fractions estimated from the absorption intensities at the MMCT bands ($\approx 540 \text{ nm}$ and $\approx 760 \text{ nm}$) for **7** in CH_2Cl_2 , solid lines are the fits to the ideal solution model.

V.6.6. Magnetic measurements in solutions

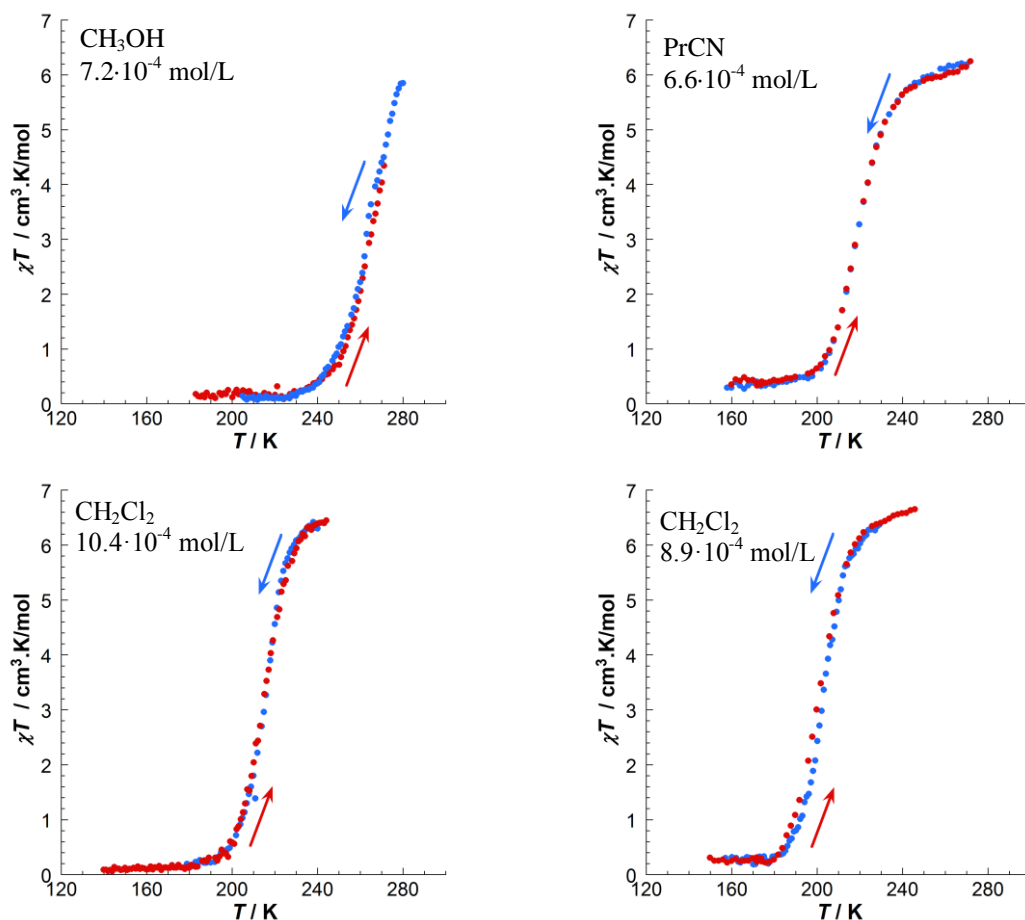


Figure S.V-7. χT vs T data on cooling (blue dots) and heating (red dots) for **7** (left) and **8** (right) in different solvents (0.4 K/min, 1 T).

V.6.7. XAS and XMCD measurements

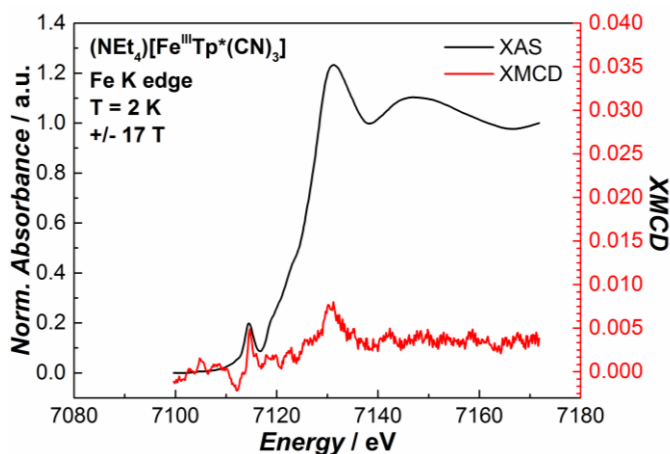


Figure S.V-8. Isotropic (average, black) and dichroic (XMCD, red) absorption spectra at and Fe (right) K edge for $(\text{NEt}_4)[\text{Fe}^{\text{III}}\text{Tp}^*(\text{CN})_3]$.

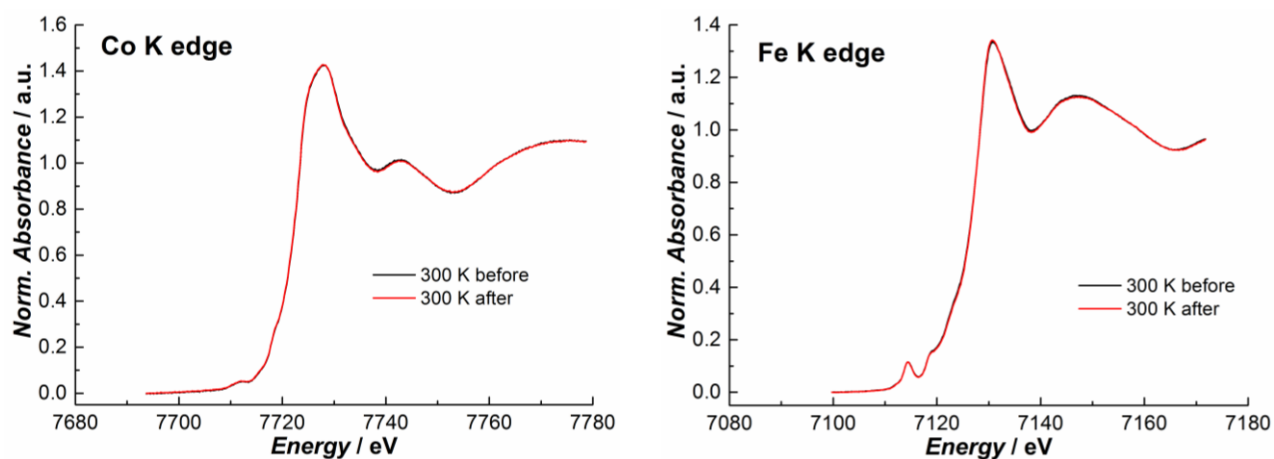


Figure S.V-9. The XANES at room temperature at Fe and Co K edges emphasizing reversibility, after relaxation from photo-induced state for **8b**.

V.7. References

1. Zhang, Y.; Li, D.; Clérac, R.; Kalisz, M.; Mathonière, C.; Holmes, S. M. *Angew. Chem., Int. Ed.* **2010**, *49*, 3752-3756.
2. (a) Mercuriol, J.; Li, Y.; Pardo, E.; Risset, O.; Seuleiman, M.; Rousselière, H.; Lescouëzec, R.; Julve, M. *Chem. Commun.* **2010**, *46*, 8995-8997; (b) Mondal, A.; Li, Y.; Seuleiman, M.; Julve, M.; Toupet, L.; Buron-Le Cointe, M.; Lescouëzec, R. *J. Am. Chem. Soc.*, **2013**, *135*, 1653-1656.
3. (a) Nihei, M.; Sekine, Y.; Suganami, N.; Oshio, H. *Chem. Lett.* **2010**, *39*, 978-979; (b) Nihei, M.; Sekine, Y.; Suganami, N.; Nakazawa, K.; Nakao, H.; Murakami, Y.; Oshio, H. *J. Am. Chem. Soc.*, **2011**, *133*, 3592-3600.
4. (a) Siretanu, D.; Li, D.; Buisson, L.; Bassani, D. M.; Holmes, S. M.; Mathonière, C.; Clérac, R. *Chem.-Eur. J.* **2011**, *17*, 11704-11708; (b) Siretanu, D. *PhD Thesis*, Univ. of Bordeaux 1, **2011**.
5. (a) Pardo, E.; Verdaguer, M.; Herson, P.; Rousselière, H.; Cano, J.; Julve, M.; Lloret, F.; Lescouëzec, R. *Inorg. Chem.* **2011**, *50*, 6250-6262; (b) Dong, D.-P.; Xiao, J.-Q.; Zhuang, P.-F.; Zheng, H.; Zhao, L.; Cheng, H.; Liu, T.; Duan, C.-Y. *Inorg. Chem. Commun.*, **2012**, *21*, 84-87; (c) Li, D.; Parkin, S.; Wang, G.; Yee, G. T.; Prosvirin, A. V.; Holmes, S. M. *Inorg. Chem.* **2005**, *44*, 4903-4905.
6. Cao, L.; Tao, J.; Gao, Q.; Liu, T.; Xia, Z.; Li, D. *Chem. Commun.*, **2014**, *50*, 1665-1667.
7. Li, D.; Parkin, S.; Wang, G.; Yee, G.T.; Holmes, S.M. *Inorg. Chem.* **2006**, *45*, 1951-1959.
8. (a) Lloret, F.; Julve, M.; Cano, J.; Ruiz-García, R.; Pardo, E. *Inorg. Chim. Acta* **2008**, *361*, 3432. (b) Pardo, E.; Ruiz-García, R.; Lloret, F.; Faus, J.; Julve, M.; Journaux, Y.; Delgado, F. S.; Ruiz-Pérez, C. *Adv. Mater.* **2004**, *16*, 1597-1600. (c) Pardo, E.; Ruiz-García, R.; Lloret, F.; Faus, J.; Julve, M.; Journaux, Y.; Novak, M. A.; Delgado, F. S.; Ruiz-Pérez, C. *Chem.-Eur. J.* **2007**, *13*, 2054-2066. (d) Pardo, E.; Train, C.; Lescouëzec, R.; Journaux, Y.; Pasán, J.; Ruiz-Pérez, C.; Delgado, F. S.; Ruiz-García, R.; Lloret, F.; Paulsen, C. *Chem. Commun.* **2010**, *46*, 2322-2324. (e) Berlinguette, C. P.; Dragulescu-Andrasi, A.; Sieber, A.; Güdel, H.-U.; Achim, C.; Dunbar, K. R. *J. Am. Chem. Soc.* **2005**, *127*, 6766-6779.
9. Atkins, P.; De Paula, J. *Physical Chemistry*, 8th Ed., Oxford University Press, **2006**.
10. (a) Li, D.; Clérac, R.; Roubeau, O.; Harté, E.; Mathonière, C.; Le Bris, R.; Holmes, S. M. *J. Am. Chem. Soc.* **2008**, *130*, 252-258. (b) Nihei, M.; Ui, M.; Hoshino, N.; Oshio, H. *Inorg. Chem.* **2008**, *47*, 6106-6108. (c) Nihei, M.; Ui, M.; Hoshino, N.; Oshio, H. *Inorg. Chem.* **2008**, *47*, 6106-6108.
11. (a) Bernhardt, P.V.; Bozoglian, F.; Macpherson, B. P.; Martínez, M. *Coord. Chem. Rev.* **2005**, *249*, 1902-1916. (b) Bernhardt, P. V.; Bozoglian, F.; Macpherson, B. P.; Martínez, M. *Dalton Trans.* **2004**, 2582-2587.
12. Stöhr, J.; Siegmann, H. C. *Magnetism – From Fundamentals to Nanoscale Dynamics, Part III, Polarized Electron and X-Ray Techniques*, Springer Berlin Heidelberg: Berlin; **2006**, 351-476.
13. Brouder, C.; Kappler, J. P. in Beaurepaire, E., Carrière, B., Kappler, J. P. (Eds.) *Magnetism and Synchrotron Radiation*, Editions de Physique, Les Ulis, Springer: New York; **1997**, 19-32.
14. Baker, M. L.; Kitagawa, Y.; Nakamura, T.; Tazoe, K.; Narumi, Y.; Kotani, Y.; Iijima, F.; Newton, G. N.; Okumura, M.; Oshio, H.; Nojiri, H. *Inorg. Chem.*, **2013**, *52*, 13956-13962.
15. Sekine, Y.; Nihei, M.; Kumai, R.; Nakao, H.; Murakami, Y.; Oshio, H. DOI: 10.1039/C3CC48820A
16. Cartier dit Moulin, C.; Villain, F.; Bleuzen, A.; Arrio, M.-A.; Sainctavit, P.; Lomenech, C.; Escax, V.; Baudalet, F.; Dartyge, E.; Gallet, J. J.; Verdaguer, M. *J. Am. Chem. Soc.* **2000**, *122*, 6653-6658
17. Bleuzen, A.; Lomenech, C.; Escax, V.; Villain, F.; Varret, F.; Cartier dit Moulin, C.; Verdaguer, M. *J. Am. Chem. Soc.* **2000**, *122*, 6648-6652.
18. Champion, G.; Escax, V.; Cartier dit Moulin, C.; Bleuzen, A.; Villain, F.; Baudalet, F.; Dartyge, E.; Verdaguer, M. *J. Am. Chem. Soc.*, **2001**, *123*, 12544-12546.
19. Carra, P.; König, H.; Thole, B. T.; Altarelli, M. *Physica B* **1993**, *192*, 182-184.

General Conclusions

In the field of molecule-based magnetism, functionalization of molecule-based molecular materials is one of directions that may, indeed, allow these molecular systems to be used in future applications. Our strategic approach in this thesis is to functionalize single-molecule magnets, and electron transfer systems towards more soluble systems and liquid crystal phases. We herein summarize the principal results obtained during this thesis work.

In the first chapter, general theoretical aspects of the single molecule magnets and electron-transfer systems were defined offering the readers the opportunity to understand easily the following Chapters II to V. Various examples of hybrid soft molecule-based magnetic materials have been described, in order to illustrate the interest of the coordination chemistry towards this class of multifunctional compounds that have promising properties to respond to technological demands. Regarding this, we attempted to get hybrid molecular soft systems in order to organize and shape magnetic complexes in controlled assemblies via a chemical control of their intrinsic magnetic properties via rational functionalization of the organic ligands.

In Chapter II, two different functionalization strategies were applied to obtain hybrid single molecule magnets. The functionalization with strongly lipophilic groups failed in obtaining products with less oriented and symmetric phases than the known cubic arrangements, but still resulted to be successful in the thermal control of the induced 3D self-organization of the Mn_{12} SMMs. Thus, by varying chain density around the rigid core, it was possible to stabilize crystalline cubic organization or thermotropic cubic mesophases of different symmetries. The second chosen strategy oriented towards functionalization by grafting a mesogenic promoter via a flexible spacer, showed that functionalized complexes form a hexagonal self-organization in layered smectic phase over a wide range of temperatures. The rational choice of the mesogenic promoter allowed a control of the thermal properties of hybrid molecular materials. The specific molecular design in this case contributed to the formation of hybrid molecular materials possessing several properties and allowed tuning of parameter characteristics of the original Mn_{12} -based core. As it was expected, all synthesized complexes preserved their magnetic properties after the functionalization process. Significant difference in magnetic relaxation was observed, resulting from the different ratio of JT isomers, which appears to be influenced by the structure of the ligand and the intermolecular interactions it may induce.

Chapters III – V were dedicated to functionalization of cyanido-bridged molecular squares that exhibit thermally or photo-induced ET, therefore these three chapters are summarized together herein. Even though it was not possible, at this point, to induce self-organizational properties within this class of molecule-based materials via functionalization of the bipyridine ligands, several other important achievements in this intriguing field were obtained. First of all, it was shown that the change of the counter-anion induces perturbations that influence several parameters such as the geometry of the $\{Fe_2(\mu-CN)_4Co_2\}$ core, the intermolecular interactions, the solvation and, correspondingly, the occurrence of the ET process in solid state of these systems. The structural geometry of the cyanido-bridged core is strongly influenced by the

employed functionalization as well. The bulkier is the structure of the functionalized ligand the more distorted is the shape of the final complex and, as a result, the occurrence of a thermally or light-induced ET becomes impossible. The nature of the functional groups allows modulation of the thermally and/or photo-induced ET in solid state and/or in solutions, and thus offers a tool to control this process. But, it is important to point out that in solid state the desired effect is achieved in combination with several other parameters (counter-anion, co-crystallized solvents, weaker or stronger intermolecular interactions) that influence the ET properties in cyanido-bridged $\{\text{Fe}_2\text{Co}_2\}$ molecular squares. The studies performed in solutions confirmed that the functionalization with long alkyl chains improves the solubility of the molecular $\{\text{Fe}_2\text{Co}_2\}$ squares in organic solvents. Moreover, these investigations revealed that functionalized squares (that show no evidence of ET in solid state) undergo thermally-induced intramolecular ET in diluted solutions and, thus, exhibit switching of their magnetic and optical properties in solutions. Remarkably, a fine-tuning of the electron transfer associated magnetic and optical properties in solutions is observed over a broad range of temperatures by simply adjusting the solvent polarity or the functionalized ligand of the Co site. Furthermore, these studies suggest that thermally-induced ET is an intrinsic property of the $\{[(\text{Tp}^*)\text{Fe}(\text{CN})_3]_2[\text{Co}(\text{diRbpy})_2]_2\}^{2+}$ systems that can be easily observed in solutions due to the absence of the crystal lattice packing effects or strong intermolecular interactions. Thus, the molecular nature of the observed process is highlighted.

As summarized in the previous paragraphs, the functionalization of SMM and ET complexes has been well achieved and offered an opportunity to observe and control the original properties within the designed materials. The work on functionalization of the remarkable systems, presented within this work, can be continued in many ways as has been detailed in conclusions part of each chapter. Liquid crystalline properties and improved solubility are not the only features that can be induced in a magnetic system. Via rational functionalization it is possible to control (tune) the physical properties via various effects of the functional groups; to induce affinity towards particular surfaces that may allow, as well, the control over the organization of the molecular materials in a device; or to induce biocompatibility that can make molecular magnetic materials promising candidates for targeted drug delivery or magnetic resonance imaging. Therefore the foregoing investigations of hybrid (or rationally functionalized) magnetic systems would give a valuable contribution to various research fields.

Annex

A1: Physico-chemical methods

Elemental analysis (EA)

Elemental analyses (C, H and N) were performed following the classical Pregl–Dumas technique on a ThermoFischer Flash EA 1112 instrument at the Institut de Chimie de la Matière Condensée de Bordeaux (ICMCB). The results of this microanalysis are shown in mass fractions of each element in the compound.

Thermogravimetric analyses (TGA)

Thermogravimetric analyses were carried out using samples of 10 – 20 mg, at 5 K/min in the nitrogen atmosphere using a thermogravimetric analyzer Setaram TAG 16.

Fourier transformed infrared (FT-IR) analysis

The FT-IR spectra were recorded between 4000 and 550 cm^{-1} on a Thermal Scientific Nicolet™ 6700 ATR (attenuated total reflectance) spectrometer equipped with a Smart iTR diamond window.

Nuclear magnetic resonance

^1H NMR spectra were collected with JEOL ECS 400 instrument at room temperature, using CDCl_3 or CD_3CN as solvent. Chemical shifts of ^1H NMR signals were quoted to internal standard TMS ($\delta = 0.00$ ppm) and expressed as chemical shifts in ppm (δ), multiplicity, coupling constant (Hz), and relative intensity.

Single crystal X-ray analysis

The X-ray diffraction data for the single crystals of $[\text{Mn}_{12}\text{O}_{12}(\text{L}^1)_{16}(\text{H}_2\text{O})_3]$, **1**, **3–7**, **8a** and **8b** were collected with a Bruker APEX II diffractometer, using graphite monochromated MoK_α radiation ($\lambda = 0.71073$ Å). The program SAINT was used to integrate the data, which were thereafter corrected for absorption using SADABS.¹ The structure was solved by direct methods and refined by least squares on F^2 with SHELXL-97.² All non-hydrogen atoms were refined anisotropically. Hydrogen atoms were assigned to ideal positions using the appropriate HFIX command in SHELXL-97. Irradiation of the crystals of **1** with white light ($P = 3$ mW/cm^2) at 83 K was performed with a halogen-tungsten light source (Leica CLS 150 XD tungsten halogen source) coupled through an optical fiber that was directed towards the analyzed crystal. Light was kept on during out of equilibrium data collections.

Structural investigations of compounds **2** (at various temperatures and under continuous white light irradiation from the sample illumination lamp of the diffractometer $P = 6$ mW/cm^2) and **8a** (at 10 K before and after irradiation with a 808 nm laser source, $P = 30$ mW/cm^2) were performed on a four-circle Oxford Diffraction Xcalibur 3 diffractometer (MoK_α radiation) with a 2D Sapphire 3 CCD detector (Institut de Physique de Rennes, Université Rennes 1). The single crystals were placed either in an Oxford Diffraction Helijet helium-flow cryostat, allowing reaching 10 K (**8a**) or in an Oxford Cryosystems nitrogen-flow

cryostat, at 80 K (2), for the complete data collection. The unit cell parameters and the data reduction were obtained with CrysAlis software from Oxford Diffraction.³ The structures were solved with SIR-97⁴ and refined with SHELXL-97.

Small and wide angle X-ray scattering (SAXS and WAXS)

X-Ray scattering experiments at small and wide angles were collected on a home-made experimental set-up equipped with a Rigaku Nanoviewer (XRF microsource generator, MicroMax 007HF), with an 1200-W rotating anode ($\lambda = 1.54180 \text{ \AA}$) coupled to a confocal Max-FluxH Osmic mirror (Applied Rigaku Technologies) and a MAR345 image plate detector (Marresearch GmbH). The studied samples were mounted in glass capillaries of 1 mm diameter. Diffraction patterns were integrated with the FIT2D software.⁵

Polarized optical microscopy

The thermal behavior and the optical textures of the compounds were studied with an Olympus BX51TRF polarizing microscope equipped with a Mettler Toledo FP82HT hot-stage.

Differential scanning calorimetry

The transition temperatures and enthalpies changes were measured by differential scanning calorimetry with a Q2000 TA instrument. DCS traces were recorded at different scanning rates, from 1 to 10 K/min in a nitrogen environment. Measurements were carried out using closed Tzero aluminium pans. Calibration of temperature and melting enthalpy was performed with an indium and tin sample. Transition enthalpies changes were deduced by integration of the DSC peaks after polynomial baseline corrections.

UV/Vis analysis

UV/Vis spectra were recorded between 350 and 1000 nm using a Varian Cary 5000 UV/Vis recording spectrophotometer at Institut des Sciences Moleculaires (ISM). Variable temperature UV/Vis data were obtained using an Oxford Liquid Nitrogen Cryostat Optistat^{ON} (static) equipped with an Oxford ITC502 controller operating between 77 and 300 K.

Reflectivity analysis

Surface reflectivity measurements were performed on a home-built system at different temperatures ranging from 10 to 300 K using freshly filtered compounds. Heating and cooling rates were maintained at 4 K·min⁻¹ during the measurements. This setup collects the light reflected by the sample (sum of direct and diffuse reflected light) that is analyzed by a high-sensitivity Hamamatsu 10083CA spectrometer between 500 and 1000 nm. The spectra are compared to a white reference obtained with a NIST traceable standard for reflectance (SphereOptics, ref SG3054). The background, collected with the light source switched off, is subtracted from all measurements. The reflectivity can be plotted as a function of temperature, time, or

wavelength. Different light emitting diodes (LEDs) operating between 365 and 1050 nm and bought from Thorlabs were used for excitation measurements. As the samples are potentially photosensitive, the light exposure time was minimized during all the experiments keeping the samples in the dark except during the spectra measurements when white light is shined on the sample surface ($P = 0.4 \text{ mW/cm}^2$). The temperature dependence of the reflectivity spectra was followed during a cycle of cooling–heating. For all the excitation/de-excitation experiments performed at 10 K, the sample was initially placed at this temperature keeping the sample in the dark to avoid any excitation.

Magnetic measurements

Magnetic susceptibility measurements were carried out on a Quantum Design SQUID magnetometer MPMS-XL (CRPP) operating between 1.8 and 400 K for applied dc fields ranging from -7 to 7 T. Measurements in solid state were performed on a microcrystalline samples that were filtered from its mother liquor and dried in air less than 2 minutes prior the use. Experiments in solution were carried out in sealed plastic straws under argon. Magnetic data was corrected for the sample holder and diamagnetic contributions for all magnetic measurements. Photomagnetic measurements were performed at ICMCB using a halogen-tungsten light source (Leica CLS 150 XD tungsten halogen source adjustable from 0.5 mW/cm^2 to 1 W/cm^2) coupled through an optical fiber directed into the magnetometer cavity. Samples of ca. 3 mg were packed into a thermoformed plastic straw placed about 3.5 cm from the optical fiber (the power of the irradiation light was chosen carefully to find a good compromise between minimizing thermal heating of the sample and maximizing the photoconversion efficiency). Sample temperatures were corrected for the light-induced heating (average $\pm 2 \text{ K}$ at 10 K under white light irradiation), and the calibration of experimental sample temperatures was referenced to the data collected in absence of light.

XAS (XANES) and XMCD measurements

The experiments have been performed on the ID12 beamline of the ESRF synchrotron (Grenoble, France).⁶ The flux of circularly polarized photons delivered by a helical undulator is monochromatized by a Si(111) two-crystal monochromator. The absorption is recorded in total fluorescence yield by a silicon diode. More instrumental information can be found in ref 6.

The XMCD signal has been measured by reversing both the photon helicities and the direction of the magnetic induction and was obtained by the appropriate averaging of the various cross sections. For a given energy, the XMCD signal is the difference between the XAS spectra with right and left circularly polarized X-rays. The specimen magnetization is parallel to the photons wave vector, and in the electric dipole approximation, reversing the photon helicity is equivalent to reversing the magnetic induction. Spectra are recorded in a fixed magnetic field (either +17 or -17 T), and the circular polarization is flipped at each energy point.

A2: List of abbreviations

1D	One-dimensional
2D	Two-dimensional
3D	Three-dimensional
<i>ac</i>	Alternating current
AcOH	Acetic acid
AD	Anno Domino
bik	bis(1-methylimidazol-2-yl)ketone
bpy	2,2'-bipyridine
Col	Columnar
Cr	Crystal/crystalline phase
CRPP	Centre de Recherche Paul Pascal
Cub	Cubic phase
<i>dc</i>	Direct current
diC13bpy	4,4'-ditridecyl-2,2'-bipyridine
diC6bpy	4,4'-dihexyl-2,2'-bipyridine
diCOOEtbpy	4,4'-bis(ethoxycarbonyl)-2,2'-bipyridine
diMebpy	4,4'-methyl-2,2'-bipyridine
diMeObpy	4,4'-dimethoxy-2,2'-bipyridine
DLS	Dynamic light scattering
DMF	N,N-dimethylformamide
DSC	Differential scanning calorimetry
dtbbpy	4,4'-di- <i>tert</i> -butyl-2,2'-bipyridine
EA	Elemental analysis
ESRF	European synchrotron radiation facility
ET	Electron transfer
EXAFS	Extended X-ray absorption fine structure
FR	Fast relaxing
FT-IR	Fourier transform infrared spectroscopy
HS	High spin
HT	High temperature
I	Isotropic phase
ICMCB	Institut de Chimie de la Matière Condensée de Bordeaux
IMPMC	Institut de minéralogie, de physique des matériaux et de cosmochimie
ISM	Institut des Sciences Moleculaires
JT	Jahn-Teller

LC	Liquid crystal
LED	Light emitting diode
LMCT	Ligand-to-metal charge transfer
LS	Low spin
LT	Low temperature
MeCN	Acetonitrile
MMCT	Metal-to-metal charge transfer
Mn ₁₂ -OAc	[Mn ₁₂ O ₁₂ (O ₂ CCH ₃) ₁₆ (H ₂ O) ₄] or Mn ₁₂ -acetate
-N(CH ₃) ₂	Dimethylamino group
NEt ₄ ⁺	Tetraethylammonium
NMR	Nuclear magnetic resonance
OTf	Trifluoromethanesulfonate (CF ₃ SO ₃ ⁻)
OTs ⁻	<i>para</i> -Toluenesulfonate
P	Power
PB	Prussian blue
PBA	Prussian blue analogue
Ph	Phenyl
p <i>K</i> _a	Logarithmic acid dissociation constant
POM	Polarized optical microscopy
PrCN	Butyronitrile
pz ₃ CCH ₂ OH	2,2,2-tris(pyrazolyl)ethanol
pzTp	Tetrapyrazolylborate
R-trz	4-(alkyl)-1,2,4-triazole
sal	Salicylaldehyde
SAXS	Small angle X-ray scattering
SC	Spin crossover
SCM	Single-chain magnet
Sm	Smectic phase
SMM	Single-molecule magnet
SR	Slow relaxing
S _T	Spin ground state
<i>t</i> Bu	<i>tert</i> -Butyl
T _C	Curie temperature
TGA	Thermogravimetric analysis
THF	Tetrahydrofuran
tmphen	3,4,7,8-tetramethyl-1,10-phenanthroline
Tp	tri(pyrazol-1-yl)hydroborate
Tp*	tris(3,5-dimethylpyrazol-1-yl)hydroborate

trien	Triethylenetetramine
WAXS	Wide angle X-ray scattering
XANES	X-ray absorption near-edge spectra
XAS	X-ray absorption spectroscopy
XMCD	X-ray magnetic circular dichroism
XRD	X-ray diffraction

A3: Physical constants

	Symbol	Value	Units SI	CGS
Avogadro constant	N_A	6.02217	10^{23} mol^{-1}	
Boltzmann constant	k_B	1.38062	$10^{-23} \text{ J}\cdot\text{K}^{-1}$	$10^{-21} \text{ erg}\cdot\text{G}^{-1}$
Bohr magneton	μ_B	9.27410	$10^{-24} \text{ J}\cdot\text{T}^{-1}$	$10^{-16} \text{ erg}\cdot\text{K}^{-1}$
Electron volt	eV	1.60219	10^{-19} J	10^{-11} erg
Vacuum permeability	μ_0		$4\pi 10^{-7} \text{ N}\cdot\text{A}^{-2}$	1
Molar gas constant	R	8.31446	$\text{J}\cdot\text{mol}^{-1}\cdot\text{K}^{-1}$	$10^7 \text{ erg}\cdot\text{mol}^{-1}\cdot\text{K}^{-1}$

References:

1. Sheldrick, G. M. *SADABS*, Version 2.03; Bruker Analytical X-Ray Systems: Madison, WI, **2000**.
2. Sheldrick, G. M. *Acta Cryst.* **2008**, *A64*, 112-122.
3. *CrysAlis RED*, Version 1.171.32.5; Oxford Diffraction Ltd, **2007**.
4. Altomare, A.; Burla, M.C.; Camalli, M.; Cascareno, G.; Giacovazzo, C.; Guagliardi, A.; Moliterni, A. G. G.; Polidori, G.; Spagna R. *J. Appl. Cryst.* **1999**, *32*, 115-119.
5. (a) Hammersley, A. P. *ESRF Internal Report, ESRF97HA02T*, **1997**; (b) www.esrf.eu/computing/scientific/FIT2D/
6. <http://www.esrf.eu/UsersAndScience/Experiments/Elect-StructMagn/ID12/>

Résumé

Dans ce domaine en pleine croissance qu'est la science des matériaux, les matériaux moléculaires connaissent un intérêt relativement récent et émergent, qui est motivé par le développement rapide de nouvelles technologies qui requièrent des matériaux toujours plus performants.^{1,2} Les systèmes moléculaires présentent des avantages synthétiques par rapport aux matériaux traditionnels puisqu'ils utilisent des précurseurs bien définis avec une géométrie contrôlée et ne nécessitent pas de méthodes de production coûteuses en énergie. Le choix rationnel des briques moléculaires permet un contrôle efficace de la structure finale des matériaux et ainsi de leurs propriétés physiques.^{3,4} Le développement de matériaux construits à partir de motifs moléculaires, assemblés et conçus pour induire des propriétés magnétiques intéressantes et parfois préméditées, a donné naissance au domaine du magnétisme moléculaire.

Les matériaux magnétiques ont été à l'origine d'avancées technologiques majeures devenues indispensables dans notre société.^{5,6} Ces composants magnétiques sont omniprésents dans nos vies comme par exemple dans les générateurs, les moteurs, les haut-parleurs, les microphones, les commutateurs, les capteurs, les systèmes de stockage de l'information, et bien d'autres. Jusque dans les années 80, les matériaux magnétiques les plus étudiés, étaient composés de métaux purs, d'alliages métalliques ou d'oxydes métalliques.⁶ La préparation et traitement de tels matériaux nécessitent de hautes températures et des procédés métallurgiques très consommateurs en énergie. D'autre part l'optimisation des systèmes de stockage de l'information exige une continuelle miniaturisation de la taille des unités de stockage. Cependant, les matériaux magnétiques traditionnels présentent des limitations à cet égard puisqu'ils ne peuvent conserver leur aimantation au-dessous d'une certaine taille.^{6,7} Par conséquent, le développement de nouveaux matériaux magnétiques basés sur des précurseurs moléculaires a connu un véritable essor ces dernières décennies. En comparaison avec les nanoparticules inorganiques qui sont intrinsèquement polydisperses en taille, les systèmes moléculaires sont parfaitement monodisperses en taille, volume, forme, et charge, puisque les précurseurs moléculaires sont tous identiques. Ils sont également solubles dans des solvants usuels et le caractère modulaire de ces matériaux offre l'opportunité d'affiner leurs propriétés. En outre, certains de ces matériaux moléculaires exhibent des propriétés magnétiques remarquables, qui sont rares ou inexistantes dans les matériaux inorganiques. Par exemple, des systèmes moléculaires présentant des phénomènes de conversion de spin (SC),⁸ du photomagnétisme,⁹ ou des comportements de molécule-aimant (SMM)¹⁰ ou de chaîne-aimant (SCM)¹¹ ont été découverts. D'autre part, les matériaux moléculaires peuvent présenter des propriétés supplémentaires comme la transparence, le thermo- ou photochromisme, la solubilité, la conductivité/superconductivité, la faible densité, la biocompatibilité et/ou la recyclabilité offrant ainsi des solutions pratiques pour de nouveaux besoins technologiques.¹² Un autre avantage important de ces matériaux moléculaires est la possibilité de moduler finement les propriétés chimiques et physiques par le design des précurseurs moléculaires et en particulier par la modification des ligands.

Durant ces dernières années, des efforts de recherche considérables ont été dédiés à la synthèse de systèmes à l'échelle nanométrique, afin par exemple de réduire la taille des unités magnétiques dans les dispositifs de stockage de l'information. Les matériaux moléculaires pourraient répondre à cette attente en donnant l'opportunité de stocker l'information à l'échelle moléculaire en utilisant par exemple les prometteuses SMMs.^{6,8-10,13} Toutefois, si ces propriétés et applications potentielles sont souvent mises en

valeur dans les études fondamentales, à ce jour, aucun de ces composants magnétiques n'a été exploité industriellement pour concevoir des dispositifs commerciaux.¹⁴

Même si les propriétés magnétiques sont les principales motivations dans le domaine du magnétisme moléculaires, le développement de matériaux moléculaires multifonctionnels est une thématique de recherche également cruciale. En effet, la plupart des composés magnétiques sont produits sous forme de poudres ou de solides cristallins, tandis que les dispositifs technologiques nécessitent un certain degré d'auto-organisation. Ainsi, un des grands défis dans le domaine du magnétisme moléculaire est de mettre en forme ces composés au sein de matériaux technologiquement viables. À cet égard, la chimie moléculaire offre des possibilités uniques, car elle permet de concevoir de nouveaux matériaux hybrides qui combinent plusieurs propriétés physiques dans un même système, ce qui est difficile, voire impossible à réaliser en chimie du solide ou en chimie inorganique. Afin d'obtenir des matériaux hybrides magnétiques avec des propriétés avancées, la modification de la partie organique des matériaux moléculaires par des substituants connus pour induire des propriétés physiques supplémentaires (phases liquide-cristallines ou augmentation de la solubilité) est une stratégie de choix car elle peut apporter des comportements multifonctionnels et/ou des effets de synergie entre propriétés.

L'objectif principal de cette thèse est de développer des matériaux hybrides magnétiques avec des propriétés améliorées *via* une fonctionnalisation rationnelle de complexes moléculaires magnétiques bien connus. La conception d'hybrides magnétiques est une des principales thématiques de recherche du groupe Matériaux Moléculaires et Magnétisme au Centre de Recherche Paul Pascal. La stratégie mise en œuvre consiste à modifier des complexes magnétiques connus en fonctionnalisant leurs ligands organiques avec divers substituants permettant d'induire des propriétés liquide-cristalline, ou tout simplement, permettant d'améliorer la solubilité dans des solvants usuels. Bien que cette approche puisse sembler évidente, elle est encore relativement peu développée et seuls quelques groupes de recherche étudient actuellement cette stratégie pour créer de nouveaux matériaux hybrides magnétiques. Cette approche peut être bénéfique pour: (i) isoler et protéger le cœur magnétique par une enveloppe organique limitant ainsi les interactions entre les objets; (ii) orienter, aligner et organiser les unités magnétiques, grâce à l'auto-organisation des mesophases; (iii) avoir la fluidité nécessaire pour la mise en forme de ces matériaux; (iv) améliorer la solubilité et/ou la stabilité thermique; et (v) contrôler ou améliorer les propriétés chimiques ou physiques de l'objet original.

Dans ce travail, nous avons cherché à concevoir et d'étudier de nouveaux matériaux hybrides basés sur deux systèmes moléculaires connus pour posséder des propriétés magnétiques remarquables: (a) le complexe dodecanucléaire $[Mn_{12}]$ de formule générale $[Mn_{12}O_{12}(OAc)_{16}(H_2O)_4]$, qui fait partie de la grande famille des molécule-aimants (SMM) et (b) les carrés moléculaires cyanido-pontés $\{Fe_2Co_2\}$ de formule $\{[(Tp^*)Fe(CN)_3]_2[Co(bpy)_2]_2\}[OTf]_2$, qui sont classés dans la catégorie des complexes à transfert d'électron.

Ce manuscrit de thèse comprend cinq chapitres qui couvrent les deux systèmes moléculaires suivants: les molécule-aimants, et les systèmes à transfert d'électron. Ainsi, les concepts fondamentaux des deux systèmes moléculaires choisis pour ces travaux sont résumés dans la première partie du chapitre I. Dans la deuxième partie de ce chapitre, une étude bibliographique fait un bref état de l'art des études menées sur des hybrides magnétiques possédant des propriétés de cristal-liquides ou de systèmes solubles.

Dans la deuxième partie de ces travaux, nous avons choisi des ligands porteurs de chaînes (cyanobiphenyloxy)decyle et (biphenyloxy)decyle (Schéma R-2) et d'étudier les complexes $[\text{Mn}_{12}]$ correspondants. Avec pour but de réduire les interactions intermoléculaires, et ainsi la température de clarification, le promoteur mésomorphe biphenyle (ligand HL⁶) a été utilisé et comparé à son analogue cyanobiphenyle (ligand HL⁵).

Les six complexes $[\text{Mn}_{12}]$ ont été synthétisés avec succès et entièrement caractérisés. En contraste avec le complexe original $[\text{Mn}_{12}\text{-OAc}]$ qui se décompose au-dessus de 320 K, les nouveaux composés sont thermiquement stables jusqu'à 420 K avec les ligands portant de longues chaînes et jusqu'à 470 K avec le ligand 4-méthoxybenzoate.

A partir des mesures de susceptibilité magnétique *ac* (Figure R-1), la conservation du comportement molécule-aimant a été confirmée pour tous les composés. Les complexes présentent également un isomérisme Jahn-Teller (JT) comme le montrent les mesures de la partie imaginaire de la susceptibilité *ac* et la structure rayons X du complexe modèle. Des différences significatives de la relaxation magnétique résultant de la variation du ratio en isomères JT, ont été observées selon la fonctionnalisation appliquée.

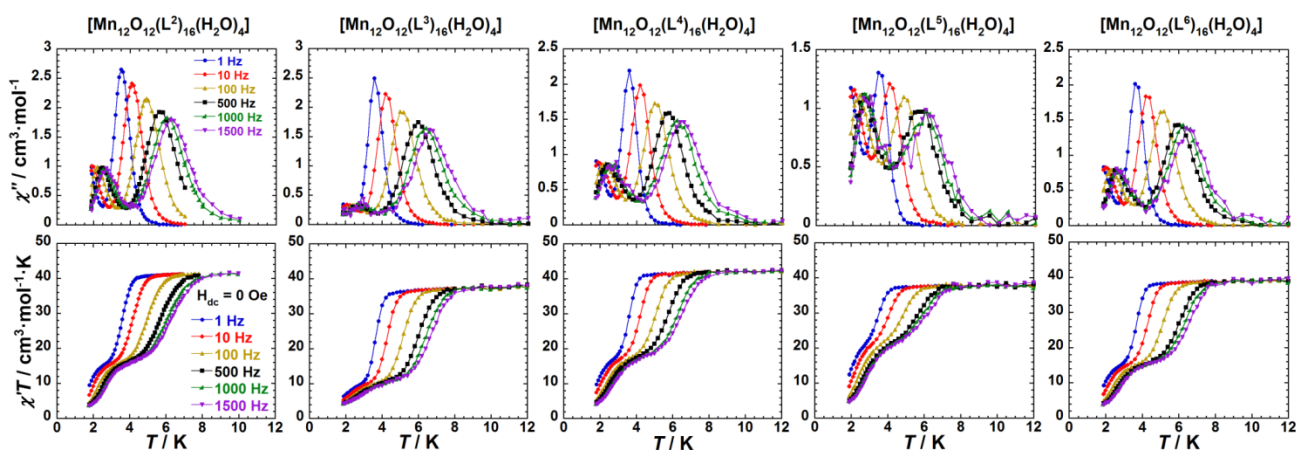


Figure R-1. $\chi'T$ et χ'' en fonction de la température pour les complexes $[\text{Mn}_{12}\text{O}_{12}(\text{L}^i)_{16}(\text{H}_2\text{O})_4]$ ($i = 2 - 6$), mesurés sous différentes fréquences d'oscillation (1-1500 Hz) à champ dc nul. Les lignes solides sont des guides pour les yeux.

Notre première stratégie consistant à greffer un nombre variable de chaînes lipophiles autour du cœur rigide $[\text{Mn}_{12}]$, n'a pas permis l'obtention de mésophases moins orientés et symétriques comme nous l'espérions mais a néanmoins permis un contrôle de l'auto-organisation 3D. Ainsi, en variant le nombre de chaînes autour du cœur magnétique, il est possible de stabiliser une organisation cristalline cubique dans le cas du composé $[\text{Mn}_{12}\text{O}_{12}(\text{L}^2)_{16}(\text{H}_2\text{O})_4]$ ou des mésophases cubiques thermotropes de différentes symétries pour les complexes $[\text{Mn}_{12}\text{O}_{12}(\text{L}^3)_{16}(\text{H}_2\text{O})_4]$ et $[\text{Mn}_{12}\text{O}_{12}(\text{L}^4)_{16}(\text{H}_2\text{O})_4]$. L'organisation à l'intérieur des mésophases cubiques est d'origine moléculaire et est régie par la forme globale du cœur rigide, tandis que les chaînes aliphatiques offrent la fluidité nécessaire à l'auto-organisation. De la même façon que pour les propriétés magnétiques, l'organisation et la symétrie à l'intérieur des mésophases cubiques dépendent non seulement du nombre de groupements fonctionnels, mais aussi de la position des substituants sur les ligands benzoate. Le design moléculaire spécifique a dans ce cas contribué à la formation de matériaux moléculaires hybrides

possédant plusieurs propriétés et a permis de moduler les paramètres caractéristiques du cœur $[\text{Mn}_{12}]$ original.

En appliquant la seconde stratégie de fonctionnalisation consistant à greffer des promoteurs mésogéniques *via* des espaceurs flexibles, il a été possible d'obtenir deux nouveaux complexes hybrides possédant des propriétés de cristal-liquide et de molécule-aimant. Deux promoteurs mésogéniques différents ont été utilisés dans ce travail. Malgré l'encombrement du cœur $[\text{Mn}_{12}]$, il a été possible dans les deux cas d'induire des phases smectiques thermotropes. Même si quelques exemples de complexes de type $[\text{Mn}_{12}]$ fonctionnalisés par des promoteurs mésogéniques (groupe cyanobiphényle) et présentant des mésophases smectiques sont déjà décrits dans la littérature, l'arrangement des cœurs magnétiques était difficile à établir par les précédentes mesures de SAXS (Small Angle X-ray Scattering).^{19b,c} Dans le cas des composés développés dans ce travail, il a été possible d'observer clairement un arrangement hexagonal de courte portée des unités magnétiques par les mesures de SAXS (Figure R-2).

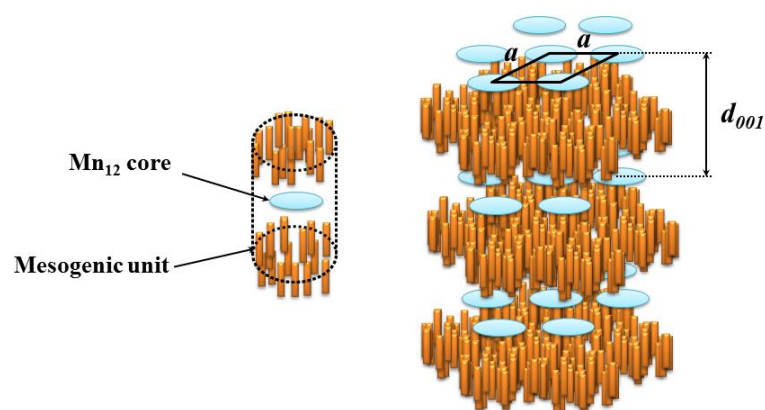


Figure R-2. Représentation schématique de l'organisation lamellaire des complexes au sein des mésophases smectiques. Les groupes équatoriaux sont omis pour plus de clarté.

Probablement, le raccourcissement de la longueur de l'espaceur aliphatique (un carbone de moins) par rapport aux précédents systèmes décrits dans la littérature, a permis une certaine stabilisation de l'arrangement des cœurs $[\text{Mn}_{12}]$ au sein de la structure lamellaire induite par les groupements mésogènes. En outre, le greffage de groupement biphényle a permis une diminution du point de clarification et, à notre connaissance, le complexe $[\text{Mn}_{12}\text{O}_{12}(\text{L}^{\circ})_{16}(\text{H}_2\text{O})_4]$ présente la plus basse température de clarification jamais observée pour des complexes $[\text{Mn}_{12}]$ fonctionnalisés avec des promoteurs mésogéniques. Bien que les deux systèmes ont des structures similaires et ont la même organisation au sein des mésophases, le rapport en isomères JT y est considérablement différent. Ceci pourrait être lié à la différence des promoteurs mésogéniques terminaux qui induiraient une interdigitation supérieure avec les promoteurs biphényle par rapport aux groupes cyanobiphényle. Ainsi, les interactions intermoléculaires induites par des groupes cyanobiphényle ou biphényle déforment différemment le cœur magnétique et, par conséquent, affectent différemment leurs propriétés magnétiques.

Les chapitres III à V sont dédiés à la fonctionnalisation des carrés moléculaires tetranucléaires cyanido-ponté $\{\text{Co}_2\text{Fe}_2\}$ de formule générale $\{[(\text{Tp}^*)\text{Fe}(\text{CN})_3]_2[\text{Co}(\text{L})_2]_2\}(\text{X})_2$ (avec $\text{Tp}^* = \text{tris}(3,5\text{-diméthylpyrazol-1-yl})\text{hydroborate}$, $\text{X} = \text{contre-ion monovalent}$, $\text{L: bpy} = 2,2'\text{-bipyridine}$ or $\text{diMe bpy} = 4,4'$

dimethyl-2,2'-bipyridine). Ces objets moléculaires sont prometteurs pour le développement et l'étude de matériaux moléculaires photo- ou magnéto-commutables. Dans ces systèmes, la commutation réversible des propriétés magnétiques et optiques est due à un transfert d'électron intramoléculaire (ET) à la suite d'une perturbation externe comme la variation de température, de pression ou l'application de lumières (Figure R-3).²⁰

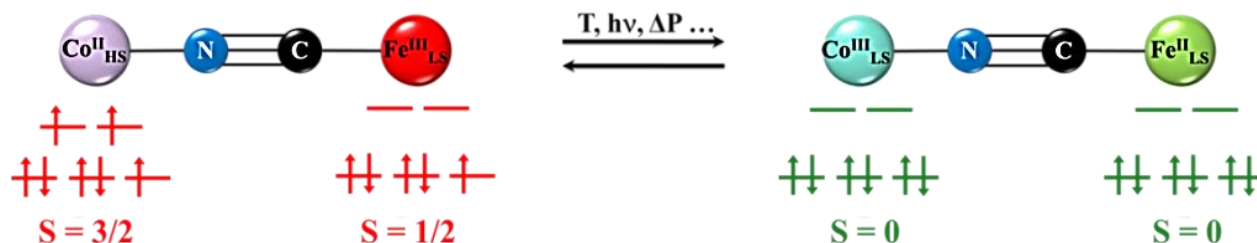


Figure R-3. Représentation schématique du transfert d'électron métal-métal induit par un stimuli externe dans le cas d'une paire cyanido-pontante $\{\text{Fe}^{\text{II}}_{\text{BS}}\text{Co}^{\text{III}}_{\text{BS}}\}/\{\text{Fe}^{\text{III}}_{\text{BS}}\text{Co}^{\text{II}}_{\text{HS}}\}$ (BS : bas spin et HS : haut spin).

Même s'il n'a pas été possible à ce stade, d'induire des propriétés d'auto-organisation pour cette classe de matériaux moléculaires par la fonctionnalisation des ligands bipyridine, plusieurs autres réalisations importantes ont été obtenues.

Le chapitre III est dédié à l'étude structurale de carrés moléculaires $\{\text{Fe}_2\text{Co}_2\}$ (récemment décrits par notre équipe),^{20a} et à l'étude du transfert d'électron à l'état solide dans des complexes $\{[(\text{Tp}^*)\text{Fe}(\text{CN})_3]_2[\text{Co}(\text{diMebpy})_2]_2\}(\text{X})_2$ ayant des contre-anions X différents. En effet, bien que ce type de modification ait été largement étudié pour les complexes à conversion de spin,²¹ l'influence du contre-anion dans les systèmes à transfert d'électron $\{\text{Fe}_2\text{Co}_2\}$ n'a fait l'objet d'aucune étude. Ainsi dans ce chapitre, nous présentons la synthèse, l'étude structurale et les propriétés magnétiques de quatre carrés moléculaires $\{\text{Fe}_2\text{Co}_2\}$:

- (1) – $\{[(\text{Tp}^*)\text{Fe}(\text{CN})_3]_2[\text{Co}(\text{bpy})_2]_2\}(\text{OTf})_2 \cdot 3\text{H}_2\text{O} \cdot 3\text{DMF}$;^{20a}
- (2) – $\{[(\text{Tp}^*)\text{Fe}(\text{CN})_3]_2[\text{Co}(\text{diMebpy})_2]_2\}(\text{OTf})_2 \cdot \text{H}_2\text{O} \cdot 2\text{DMF}$;^{20e}
- (3) – $\{[(\text{Tp}^*)\text{Fe}(\text{CN})_3]_2[\text{Co}(\text{diMebpy})_2]_2\}(\text{ClO}_4)_2 \cdot 2\text{DMF}$;
- (4) – $\{[(\text{Tp}^*)\text{Fe}(\text{CN})_3]_2[\text{Co}(\text{diMebpy})_2]_2\}(\text{OTs})_2 \cdot 6\text{DMF}$,

(avec bpy = 2,2'-bipyridine, diMebpy = 4,4'-diméthyl-2,2'-bipyridine, Tp* = tris(3,5-diméthylpyrazol-1-yl)hydroborate, OTf = trifluorométhanesulfonate, OTs = *para*-toluènesulfonate, and DMF = N,N-diméthylformamide)

L'étude photo-cristallographique des composés **1** et **2** a montré que l'état métastable paramagnétique photo-induit est, comme nous avons prévu et décrit, composé de paires $\{\text{Fe}^{\text{III}}_{\text{BS}}(\mu\text{-CN})\text{Co}^{\text{II}}_{\text{HS}}\}$. En outre, dans le cas du complexe **1**, il a été possible de montrer que l'irradiation lumineuse est un moyen plus efficace pour obtenir la phase métastable paramagnétique que le procédé de piégeage thermique. Dans le cas du composé **2**, nous avons observé que l'état paramagnétique photo-induit est structuellement légèrement différent de celui obtenu à des hautes températures.

Les études structurales et magnétiques des analogues $\{[(\text{Tp}^*)\text{Fe}(\text{CN})_3]_2[\text{Co}(\text{diMebpy})_2]_2\}\text{X}_2$ (composés **2**, **3** and **4**) ont montré que le processus de transfert d'électron à l'état solide est fortement affecté

par l'échange du contre-anion. La nature des contre-anions influe sur de multiples paramètres comme la géométrie du cœur $\{\text{Fe}_2(\mu\text{-CN})_4\text{Co}_2\}$, les interactions intermoléculaires, la solvataion et ainsi que le processus ET. Par conséquent, nous pouvons conclure que le transfert d'électrons dans les carrés moléculaires $\{\text{Co}_2\text{Fe}_2\}$ est fortement dépendant de l'environnement structural, qui est influencé par la nature du contre-anion.

Le quatrième chapitre est consacré à la synthèse et étude de nouveaux carrés moléculaires $\{\text{Co}_2\text{Fe}_2\}$ fonctionnalisés par de longues chaînes alkyle. Ces derniers ont été obtenus en utilisant des ligands bipyridine porteurs en positions 4 et 4' de chaînes hexyle ou tridecyle (Figure R-4). L'ajout de longues chaînes alkyles peut offrir de nouvelles possibilités pour disperser ou auto-organiser ces objets dans l'état solide, dans des mésophases ou en solutions. Une telle approche permet d'améliorer la solubilité de ces complexes magnétiques dans divers solvants et pourrait ainsi rendre plus facile la fabrication de films et couches minces, ou plus simplement de systèmes liquides.

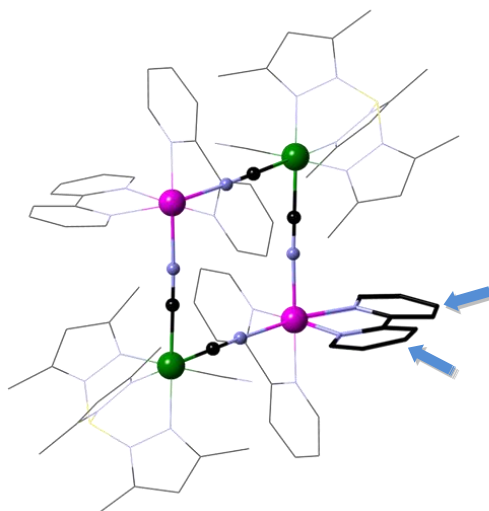


Figure R-4. Représentation schématique de la stratégie utilisée pour obtenir des systèmes plus solubles en modifiant les positions 4 et 4' des ligands bipyridine (flèches bleues). Couleurs du schéma Fe : vert, Co : rose, B : jaune, N : bleu, C : noir.

Deux nouveaux complexes $\{[(\text{Tp}^*)\text{Fe}(\text{CN})_3]_2[\text{Co}(\text{diC6bpy})_2]_2\}[\text{OTf}]_2$ (**5**) et $\{[(\text{Tp}^*)\text{Fe}(\text{CN})_3]_2[\text{Co}(\text{diC13bpy})_2]_2\}[\text{OTf}]_2$ (**6**) (avec diC6bpy = 4,4'-dihexyl-2,2'-bipyridine, et diC13bpy = 4,4'-ditridecyl-2,2'-bipyridine) ont été synthétisés et leurs propriétés à l'état solide et en solutions ont été étudiées.

A l'état solide aucun processus de transfert d'électron réversible (thermique ou photo-induit) n'est observé pour les complexes **5** et **6** (Figure R-5).

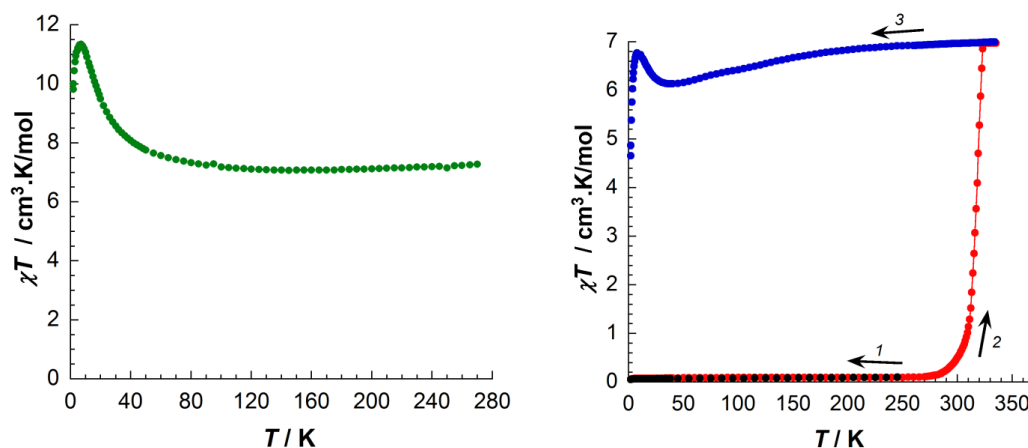


Figure R-5. Produit χT en fonction de la température pour les composés **5** à 0.1 T (gauche) et **6** (droite, 1-noir : 1^{er} refroidissement; 2-rouge 1^{er} chauffage et 3-bleu 2^{ème} refroidissement à 0.4 K/min, 0.5 T).

La fonctionnalisation avec de longues chaînes alkyle et les méthodes de cristallisation utilisées ont une influence significative sur l'organisation et solvataion des complexes au sein du cristal. Ainsi, le complexe **5** est toujours paramagnétique à l'état solide tandis que le complexe **6** est stabilisé à l'état diamagnétique, probablement en raison de liaisons hydrogène entre des molécules de méthanol et des cyanures sur les sites de fer. La présence de telles liaisons hydrogène induit très probablement un changement du potentiel redox des ions fer à l'état solide. L'effet électroattracteur est si fort que même sous irradiation avec une lumière blanche, il a été impossible de convertir l'espèce diamagnétique $\{\text{Fe}^{\text{II}}_{\text{BS}}(\mu\text{-CN})\text{Co}^{\text{III}}_{\text{BS}}\}$ en l'espèce paramagnétique $\{\text{Fe}^{\text{III}}_{\text{BS}}(\mu\text{-CN})\text{Co}^{\text{II}}_{\text{HS}}\}$, comme l'a confirmé l'étude de réflectivité. D'autre part, le composé **6** séché est stable à l'état paramagnétique, comme le révèle les études structurales, magnétiques et de réflectivité optique.

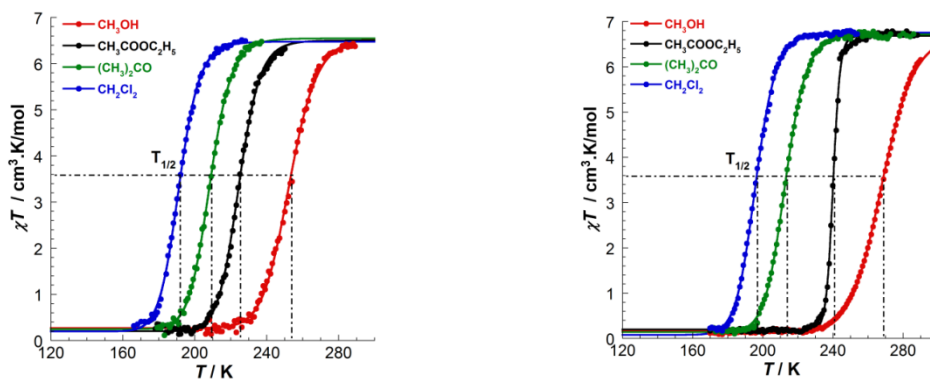


Figure R-6. Mesures χT vs T pour **5** (gauche) et **6** (droite) dans des solutions de méthanol, d'éthylacétate, d'acétone et de dichlorométhane (0.4 K/min, 1 T, les lignes pleines sont des courbes modèles pour des solutions idéales).

Les études effectuées en solutions ont confirmé que la fonctionnalisation avec de longues chaînes alkyle améliore la solubilité des complexes $\{\text{Fe}_2\text{Co}_2\}$ dans de nombreux solvants organiques. D'autre part, ces études ont révélé la présence de processus de transfert d'électron réversibles et intramoléculaires induits thermiquement, montrant ainsi la commutation des propriétés magnétiques et optiques de ces composés en solutions (Figure R-6). Remarquablement, le processus de transfert d'électron, associé au changement des propriétés magnétiques et optiques, peut être ajusté sur une large gamme de température en modifiant simplement la nature du solvant (polarité) ou des ligands coordonnés aux ions cobalt.

Ainsi le travail présenté dans le chapitre IV a démontré qu'il est possible d'obtenir des propriétés magnétiques et optiques commutables en solution pour des complexes $\{\text{Fe}_2\text{Co}_2\}$ fonctionnalisés. Nous avons aussi montré la possibilité de contrôler aisément ces propriétés physiques en ajustant l'énergie nécessaire au processus de transfert d'électron grâce au choix judicieux du solvant de travail ou des substituants sur les ligands bipyridine.

Dans le chapitre V, l'objectif a été de déterminer si la fonctionnalisation des ligands bpy avec des substituants plus électrodonneurs (c'est-à-dire méthoxy) pourrait encore augmenter la température caractéristique du transfert d'électron. Par un choix rationnel du ligand, des contre-anions et des solvants de cristallisation, il a été possible de synthétiser trois nouveaux carrés moléculaires $\{\text{Co}_2\text{Fe}_2\}$:

(7) – $\{[(\text{Tp}^*)\text{Fe}(\text{CN})_3]_2[\text{Co}(\text{diMeObpy})_2]_2\}(\text{OTf})_2 \cdot 4\text{DMF}$ (avec $\text{diMeObpy} = 4,4'$ -diméthoxy-2,2'-bipyridine, $\text{OTf} = \text{trifluorométhanesulfonate}$, $\text{DMF} = \text{N,N}$ -diméthylformamide);

(8a) – $\{[(\text{Tp}^*)\text{Fe}(\text{CN})_3]_2[\text{Co}(\text{diMeObpy})_2]_2\}(\text{PF}_6)_2 \cdot 2\text{H}_2\text{O} \cdot 5\text{MeCN}$ (avec $\text{MeCN} = \text{acétonitrile}$);

(8b) – $\{[(\text{Tp}^*)\text{Fe}(\text{CN})_3]_2[\text{Co}(\text{diMeObpy})_2]_2\}(\text{PF}_6)_2 \cdot 6\text{MeCN}$.

La corrélation entre la structure et les propriétés physiques observées pour les composés **7**, **8a** et **8b** à l'état solide, a montré que la fonctionnalisation du complexe $\{[(\text{Tp}^*)\text{Fe}(\text{CN})_3]_2[\text{Co}(\text{bpy})_2]_2\}^{2+}$ avec des groupes électrodonneurs méthoxy influence de manière significative les propriétés optiques et magnétiques du composé final. Bien que la composition chimique du cœur $\{[(\text{Tp}^*)\text{Fe}(\text{CN})_3]_2[\text{Co}(\text{diMeObpy})_2]_2\}^{2+}$ soit la même pour les trois composés, il a été possible de stabiliser ces carrés moléculaires dans différents états électroniques. Le composé **7** qui a un contre-anion différent (OTf) et a été cristallisé dans des conditions différentes de celles utilisées pour **8a** et **8b**, ne présente aucun transfert d'électron et est stabilisé dans sa forme paramagnétique $\{\text{Fe}^{\text{III}}_2\text{Co}^{\text{II}}_2\}$ (Figure R-7 à gauche). Le composé **8a** est stabilisé dans son état diamagnétique $\{\text{Fe}^{\text{II}}_2\text{Co}^{\text{III}}_2\}$ et ne montre aucun transfert d'électron thermo-induit entre 2 et 300 K, comme le confirme la couleur verte des cristaux à température ambiante et les mesures de susceptibilité magnétique (Figure R-7 au centre, courbe bleue). Les mesures optiques de réflectivité et photomagnétiques (Figure R-7 au centre, courbe verte), soutenues par l'étude photo-cristallographique, ont démontré la présence d'un processus de transfert d'électron photo-induit accompagné d'une conversion de la forme diamagnétique $\{\text{Fe}^{\text{II}}_2\text{Co}^{\text{III}}_2\}$ à l'état paramagnétique $\{\text{Fe}^{\text{III}}_2\text{Co}^{\text{II}}_2\}$ à basses températures. Le composé **8b** qui quant à lui ne diffère de **8a** que par la solvatation à l'intérieur de la maille cristalline présente un processus de transfert d'électron aussi bien thermo- que photo-induit (Figure R-7 à droite). La comparaison des structures cristallographiques des composés **7**, **8a** et **8b** montrent que le cœur $\{\text{Fe}^{\text{III}}_2\text{Co}^{\text{II}}_2\}$ dans **7** est sensiblement plus distordu que celui observé dans **8b** pour la même configuration électronique des ions métalliques. La présence d'anions trifluorométhanesulfonate et de molécules de DMF co-cristallisées dans le cristal de **7** influencent fortement la forme géométrique du cœur tétranucléaire et contribuent à la stabilisation de l'état paramagnétique $\{\text{Fe}^{\text{III}}_2\text{Co}^{\text{II}}_2\}$.

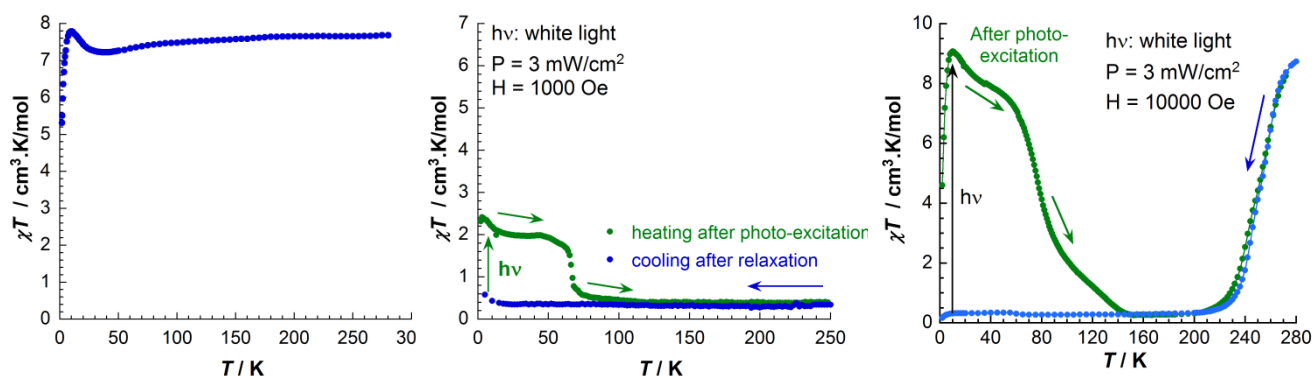


Figure R-7. (Gauche) Produit χT en fonction de la température pour le composé **7** à 0.1 T. (Centre) Produit χT en fonction de la température pour le composé **8a** en mode chauffage (points verts, 0.1 T, 0.3 K/min) après irradiation sous lumière blanche (3 mW/cm^2) à 10 K pendant ~ 17 h en mode refroidissement depuis 250 K et à l'abri de lumière (points bleus, 0.1 T, 0.3 K/min). (Droite) Produit χT en fonction de la température pour le composé **8b** en mode chauffage (points verts, 0.1 T, 0.3 K/min) après irradiation sous lumière blanche (3 mW/cm^2) à 10 K pendant ~ 13 h et en mode refroidissement depuis 250 K et à l'abri de lumière (points bleus, 0.1 T, 0.3 K/min).

Les études effectuées en solutions ont révélé que les carrés moléculaires **7** et **8** (**8a** et **8b** constitue le même système $\{[(\text{Tp}^*)\text{Fe}(\text{CN})_3]_2[\text{Co}(\text{diMeObpy})_2]_2\}(\text{PF}_6)_2$ dans un état de solvation différent à l'état solide, et est donc noté **8** dans les études en solutions) subissent un transfert d'électron thermo-induit, et par conséquent, une commutation des propriétés magnétiques et optiques en solutions diluées. Bien que les mesures magnétiques et optiques ont été réalisées dans seulement quelques solvants, les résultats obtenus ont donné des informations importantes sur le phénomène de transfert d'électron thermo-induit en solution de ces carrés moléculaires et de mettre à jour des différences significatives entre les deux complexes (Figure R-8).

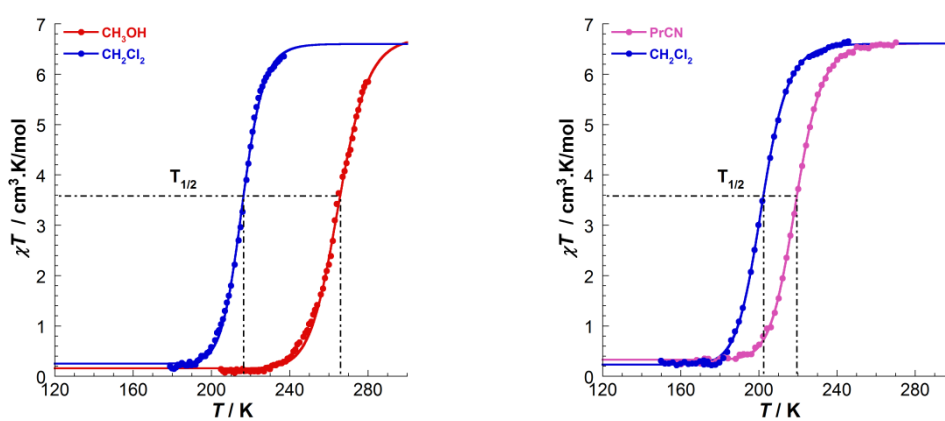


Figure R-8. Mesures χT vs T pour **7** dans des solutions de méthanol et dichlorométhane (gauche) et **8** dans des solutions de dichlorométhane et butyronitrile (droite), 0.4 K/min en mode refroidissement, 1 T. Les lignes pleines sont des courbes modèles pour des solutions idéales.

En effet, les deux composés qui ne diffèrent que par leurs contre-anions (OTf^- pour **7** et PF_6^- pour **8**), présentent des températures caractéristiques $T_{1/2}$ différentes d'environ 14 K pour le même solvant (dichlorométhane). Ce résultat met en lumière le rôle important joué par les contre-anions sur le processus de transfert d'électron non seulement à l'état solide mais aussi, plus étonnamment, en solutions. Les températures caractéristiques ($T_{1/2}$) des composés **7** et **8** en solutions suivent la même tendance que celle observée pour les composés **2**, **5** et **6**, suggérant que le phénomène de transfert d'électron thermo-induit est

une propriété intrinsèque des systèmes $\{[(\text{Tp}^*)\text{Fe}(\text{CN})_3]_2[\text{Co}(\text{diRbpy})_2]_2\}^{2+}$ et qui peut être facilement observée en solution en raison de l'absence d'effet cristallin ou de fortes interactions intermoléculaires.

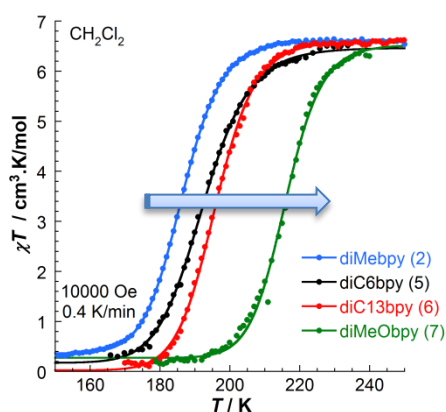


Figure R-9. Comparaison des mesures χT vs T entre les complexes **2**, **5**, **6** et **7** dans le dichlorométhane, les lignes pleines sont des courbes modèles pour des solutions idéales.

La fonctionnalisation avec des groupes électrodonneurs méthoxy permet une augmentation notable de la température caractéristique du transfert d'électron aussi bien à l'état solide (si l'on compare avec les composés **1** et **2**) mais aussi dans le cas de solutions comme l'illustre la comparaison entre **7** et les complexes **2**, **5** et **6** (Figure R-9). Il est cependant important de souligner que, à l'état solide, d'autres paramètres (contre-ions, solvants co-cristallisés, interactions intermoléculaires) entrent en jeu et influencent sensiblement le processus de transfert d'électron.

En résumé, un important travail de fonctionnalisation a été effectué sur deux systèmes magnétiques connus (la molécule-aimant $[\text{Mn}_{12}]$ et les complexes à transfert d'électron $\{\text{Fe}_2\text{Co}_2\}$) afin d'obtenir des matériaux hybrides magnétiques présentant des propriétés de cristal-liquide ou permettant d'améliorer la solubilité de ces systèmes. Les stratégies de fonctionnalisation utilisées, se sont avérées tout à fait prometteuses pour induire ces propriétés mais aussi pour moduler les caractéristiques optiques et/ou magnétiques de ces systèmes. Le travail de fonctionnalisation de ces fascinants systèmes peut être poursuivi de bien des manières et compte tenu du fait que peu d'exemples utilisant ces mêmes approches de fonctionnalisation ont été décrits à ce jour, ces travaux pourraient apporter une contribution précieuse dans le domaine.

Références:

1. Bruce, D.; O'Hare, D.; Walton, R. (Eds) *Molecular Materials*, John Wiley & Sons: Chichester, **2010**, 378.
2. Bradshaw, D.; Claridge, J. B.; Cussen, E. J.; Prior, T. J.; Rosseinsky, M. J. *Acc. Chem. Res.*, **2005**, *38*, 273-282.
3. Dinolfo, P. H.; Hupp, J. T. *Chem. Mater.*, **2001**, *13*, 3113-3125.
4. Öhrström, L.; Larsson, K. *Molecule-based materials*, Elsevier Science: Amsterdam, **2005**.
5. Miller, J. S.; Epstein, A. J. *Molecule-based Magnets: An Introduction*, in: Turnbull, M. M.; Sugimoto, T.; Thompson, L. K. (Eds) *Molecule-Based Magnetic Materials*, ACS Symposium Series, **1996**, *644*, 1-13.
6. Coey, J. M. D. *Magnetism and Magnetic Materials*, Cambridge University Press: New York, **2010**.

7. Skumryev, V.; Stoyanov, S.; Zhang, Y.; Hadjipanayis, G.; Givord, D.; Nogués, J. *Nature*, **2003**, 850-853.
8. Gütllich, P.; Goodwin, H. A. *Spin Crossover in Transition Metal Compounds I–III, Topics in Current Chemistry*; Springer-Verlag: Berlin, **2004**; Vols. 233-235.
9. (a) Decurtins, S.; Gütllich, P.; Köhler, C.P.; Spiering, H.; Hauser, A. *Chem. Phys. Lett.*, **1984**, *105*, 1-4. (b) Sato, O.; Iyoda, T.; Fujishima, A.; Hashimoto, K. *Science*, **1996**, *272*, 704-705; (c) Sato, O.; Einaga, Y.; A. Fujishima, A.; K. Hashimoto, K. *Inorg. Chem.*, **1999**, *38*, 4405-4412.
10. (a) Caneschi, A.; Gatteschi, D.; Sessoli, R.; Barra, A. L.; Brunel, L. C.; Guillot, M. *J. Am. Chem. Soc.*, **1991**, *113*, 5873-5874. (b) Sessoli, R.; Tsai, H. L.; Schake, A. R.; Wang, S. Y.; Vincent, J. B.; Foltling, K.; Gatteschi, D.; Christou, G.; Hendrickson, D. N.; *J. Am. Chem. Soc.*, **1993**, *115*, 1804-1816. (c) Sessoli, R.; Gatteschi, D.; Caneschi, A.; Novak, M. A. *Nature*, **1993**, *365*, 141-143.
11. (a) Caneschi, A.; Gatteschi, D.; Lalioi, N.; Sangregorio, C.; Sessoli, R.; Venturi, G.; Vindigni, A.; Rettori, A.; Pini, M. G.; Novak, M. A. *Angew. Chem., Int. Ed.*, **2001**, *40*, 1760-1763. (b) Clérac, R.; Miyasaka, H.; Yamashita, M.; Coulon, C. *J. Am. Chem. Soc.*, **2002**, *124*, 12837-12844. (c) Coulon, C.; Miyasaka, H.; Clérac, R. *Struct. Bond.*, **2006**, *122*, 163-206.
12. Linert, W.; Verdaguer, M. (Eds) *Molecular Magnets Recent Highlights*, Springer-Verlag Wien: New York, **2003**.
13. Rogez, G.; Donnio, B.; Terazzi, E.; Gallani, J.-L.; Kappler, J.-P.; Bucher, J.-P.; Drillon, M.; *Adv. Mater.*, **2009**, *21*, 4323-4333.
14. Gatteschi, D.; Cornia, A.; Mannini, M.; Sessoli, R. *Inorg. Chem.*, **2009**, *48*, 3408-3419 and references therein.
15. (a) Tirelli, N.; Cardullo, F.; Habicher, T.; Suter, U.W.; Diederich, F. *J. Chem. Soc. Perkin Trans. 2* **2000**, 193-198. (b) Deschenaux, R.; Donnio, B.; Guillon, D. *New J. Chem.* **2007**, *31*, 1064-1073.
16. (a) Date, R.W.; Fernandez Iglesias, E.; Rowe, K. E.; Elliott, J. M.; Bruce, D.W. *Dalton Trans.* **2003**, 1914-1931. (b) Camerel, F.; Ziessel, R.; Donnio, B.; Guillon, D. *New J. Chem.* **2006**, *30*, 135-139.
17. Zhang, T.; Liu, S.; Kurth, D. G.; Faul, C. F. J. *Adv. Funct. Mater.* **2009**, *19*, 642-652.
18. (a) Molard, Y.; Dorson, F.; Cîrcu, V.; Roisnel, T.; Artzner, F.; Cordier, S. *Angew. Chem. Int. Ed.* **2010**, *49*, 3351-3355. (b) Mocanu, A. S.; Amela-Cortes, M.; Molard, Y.; Cîrcu, V.; Cordier, S. *Chem. Commun.* **2011**, *47*, 2056-2058
19. (a) Terazzi, E.; Bourgogne, C.; Welter, R.; Gallani, J.-L.; Guillon, D.; Rogez, G.; Donnio, B. *Angew. Chem., Int. Ed.* **2008**, *47*, 490-495. (b) Terazzi, E.; Jensen, T. B.; Donnio, B.; Buchwalder, K.; Bourgogne, C.; Rogez, G.; Heinrich, B.; Gallani, J.-L.; Pigué, C. *Dalton Trans.*, **2011**, *40*, 12028-12032. (c) Terazzi, E.; Rogez, G.; Gallani, J.-L.; Donnio, B. *J. Am. Chem. Soc.*, **2013**, *135*, 2708-2722.
20. (a) Zhang, Y.; Li, D.; Clérac, R.; Kalisz, M.; Mathonière, C.; Holmes, S. M. *Angew. Chem., Int. Ed.* **2010**, *49*, 3752-3756; (b) Mercurol, J.; Li, Y.; Pardo, E.; Risset, O.; Seuleiman, M.; Rousselière, H.; Lescouëzec, R.; Julve M. *Chem. Commun.* **2010**, *46*, 8995-8997; (c) Nihei, M.; Sekine, Y.; Suganami, N.; Oshio, H. *Chem. Lett.* **2010**, *39*, 978-979; (d) Nihei, M.; Sekine, Y.; Suganami, N.; Nakazawa, K.; Nakao, H.; Murakami, Y.; Oshio, H. *J. Am. Chem. Soc.*, **2011**, *133*, 3592-3600; (e) Siretanu, D.; Li, D.; Buisson, L.; Bassani, D. M.; Holmes, S. M.; Mathonière, C.; Clérac, R. *Chem.-Eur. J.* **2011**, *17*, 11704-11708.
21. (a) Kitchen, J. A.; White, N. G.; Jameson, G. N. L.; Tallon, J. L.; Brooker, S. *Inorg. Chem.* **2011**, *50*, 4586-4597; (b) Tafili-Kryeziu, M.; Weil, M.; Muranaka, T.; Bousseksou, A.; Hasegawa, M.; Jun A.; Linert, W. *Dalton Trans.*, **2013**, 42, 15796-15804; (c) Yamada, M.; Hagiwara, H.; Torigoe, H.; Matsumoto, N.; Kojima, M.; Dahan, F.; Tuchagues, J.-P.; Re, N.; Iijima, S. *Chem. Eur. J.* **2006**, *12*, 4536-4549.

Fonctionnalisation raisonnée de matériaux moléculaires magnétiques: vers des systèmes cristaux liquides, solubles, et aux propriétés physiques modulables

Ce travail de thèse a été dédié à l'élaboration et l'étude de nouveaux matériaux hybrides obtenus par la fonctionnalisation de molécule-aimants (en anglais single-molecule magnets, SMMs) et de complexes à transfert d'électron. Le premier chapitre fait un état de l'art des deux classes de composés magnétiques utilisées dans ce travail : les molécule-aimants et les systèmes à transfert d'électrons. Une brève description des systèmes magnétiques hybrides présents dans la littérature est ensuite présentée dans le but d'illustrer les motivations qui ont conduit à ce travail. Le chapitre II décrit la fonctionnalisation des molécule-aimants de type $[Mn_{12}]$ dans le but d'obtenir des systèmes cristaux liquides hybrides. Deux approches ont été étudiées : (a) la fonctionnalisation des ligands périphériques avec des groupements fortement lipophiles (longues chaînes alkyle) ou (b) le greffage de promoteurs mésogènes par l'intermédiaire d'espacesurs aliphatiques flexibles. Les chapitres III à V présentent les études sur des carrés moléculaires à ponts cyanure $\{Fe_2Co_2\}$ qui montrent un transfert d'électron thermo- et photo-induit. Le chapitre III discute de la possibilité de moduler le processus de transfert d'électron de ces carrés moléculaires *via* le changement du contre anion. La fonctionnalisation du carré moléculaire $\{Fe_2Co_2\}$ avec de chaînes aliphatiques et son impact induit sur les propriétés physiques à l'état solide et en solutions sont décrits dans le chapitre IV. Le chapitre V discute de l'effet de la fonctionnalisation avec des groupements fortement électrodonneurs, tels que les groupements méthoxy, sur le processus de transfert d'électron des carrés moléculaires $\{Fe_2Co_2\}$.

Mot clés: magnétisme moléculaire ; molécule-aimant ; transfert d'électron ; cristal liquide ; systèmes solubles

Rational functionalization of molecular magnetic materials: towards liquid crystalline phases, improved solubility and modulation of physical properties

The work presented in this thesis was focused on the design and investigation of novel hybrid materials *via* ligand functionalization of the single-molecule magnets (SMMs) and electron transfer complexes. Chapter I contains general information about these two classes of the magnetic systems. In order to illustrate the motivation behind our work, a brief review on previously reported soft hybrid magnetic systems, is presented. Chapter II is dedicated to the functionalization of $[Mn_{12}]$ -based SMMs towards hybrid liquid crystalline systems *via* two different approaches: (a) the functionalization of peripheral ligands with strongly lipophilic groups (long alkyl chains), or (b) the grafting of mesogenic promoters through flexible aliphatic spacers. Chapters III – V are focused on cyanido-bridged molecular $\{Fe_2Co_2\}$ squares that exhibit thermally or photo-induced electron transfer. Thus, in Chapter III, the possibility to modulate the electron transfer properties in $\{Fe_2Co_2\}$ molecular squares *via* the use of different counter-anion is discussed. The functionalization with long aliphatic chains and its influence over the properties of $\{Fe_2Co_2\}$ molecular squares in solid state and solutions are discussed in Chapter IV. Finally, the effect of the ligand functionalization with strongly electron density donating groups (methoxy) over the electron transfer properties of $\{Fe_2Co_2\}$ molecular squares is investigated in Chapter V.

Keywords: molecular magnetism; single-molecule magnet; electron transfer; liquid crystal; soluble systems